

# PROCEEDINGS OF SPIE



SPIE—The International Society for Optical Engineering

## ***Light-Emitting Diodes: Research, Manufacturing, and Applications III***

**E. Fred Schubert  
Ian T. Ferguson  
H. Walter Yao**  
*Chairs/Editors*

**27-28 January 1999  
San Jose, California**

**DISTRIBUTION STATEMENT A**  
Approved for Public Release  
Distribution Unlimited

**19991103 037**



**Volume 3621**

# REPORT DOCUMENTATION PAGE

Form Approved  
OMB NO. 0704-0188

Public Reporting burden for this collection of information is estimated to average 1 hour per response, including the time for reviewing instructions, searching existing data sources, gathering and maintaining the data needed, and completing and reviewing the collection of information. Send comment regarding this burden estimates or any other aspect of this collection of information, including suggestions for reducing this burden, to Washington Headquarters Services, Directorate for Information Operations and Reports, 1215 Jefferson Davis Highway, Suite 1204, Arlington, VA 22202-4302, and to the Office of Management and Budget, Paperwork Reduction Project (0704-0188.) Washington, DC 20503.

1. AGENCY USE ONLY (Leave Blank)		2. REPORT DATE July 1999		3. REPORT TYPE AND DATES COVERED Final Report	
4. TITLE AND SUBTITLE Light-Emitting Diodes: Research, Manufacturing, and III				5. FUNDING NUMBERS  DAAD19-99-1-0136	
6. AUTHOR(S) E. Fred Schubert, Ian T. Ferguson, H. Walter Yao, Chairs/Editors					
7. PERFORMING ORGANIZATION NAME(S) AND ADDRESS(ES) International Society for Optical Engineering P.O. Box 10, Bellingham, Washington 98227-0010				8. PERFORMING ORGANIZATION REPORT NUMBER	
9. SPONSORING / MONITORING AGENCY NAME(S) AND ADDRESS(ES)  U. S. Army Research Office P.O. Box 12211 Research Triangle Park, NC 27709-2211				10. SPONSORING / MONITORING AGENCY REPORT NUMBER  ARO 39187.1-EL-CF	
11. SUPPLEMENTARY NOTES The views, opinions and/or findings contained in this report are those of the author(s) and should not be construed as an official Department of the Army position, policy or decision, unless so designated by other documentation.					
12 a. DISTRIBUTION / AVAILABILITY STATEMENT  Approved for public release; distribution unlimited.				12 b. DISTRIBUTION CODE	
13. ABSTRACT (Maximum 200 words)  High-efficient light emitting diodes (LEDs) emitting red, amber, green, blue, and ultraviolet light have been obtained through the use of an InGa <sub>N</sub> active layers instead of GaN active layers. Red LEDs with an emission wavelength of 680 nm which emission energy was smaller than the band-gap energy of InN were fabricated mainly resulting from the piezoelectric field due to the strain. The localized energy states caused by In composition fluctuation in the InGa <sub>N</sub> active layer seem to be related to the high efficiency of the InGa <sub>N</sub> -based emitting devices in spite of having a large number of threading dislocations. InGa <sub>N</sub> single-quantum-well-structure blue LEDs were grown on epitaxially laterally overgrown GaN (ELOG) and sapphire substrates. The emission spectra showed the similar blue shift with increasing forward currents between both LEDs. The output power of both LEDs was almost the same, as high as 6 mW at a current of 20 mA. These results indicate that the In composition fluctuation is not caused by dislocations, the dislocations are not effective to reduce the efficiency of the emission, and that the dislocations form the leakage current pathway in InGa <sub>N</sub> .					
14. SUBJECT TERMS				15. NUMBER OF PAGES	
				16. PRICE CODE	
17. SECURITY CLASSIFICATION OR REPORT UNCLASSIFIED	18. SECURITY CLASSIFICATION ON THIS PAGE UNCLASSIFIED	19. SECURITY CLASSIFICATION OF ABSTRACT UNCLASSIFIED	20. LIMITATION OF ABSTRACT  UL		

NSN 7540-01-280-5500

Standard Form 298 (Rev.2-89)  
Prescribed by ANSI Std. Z39-18  
298-102



PROCEEDINGS OF SPIE  
SPIE—The International Society for Optical Engineering

# ***Light-Emitting Diodes: Research, Manufacturing, and Applications III***

**E. Fred Schubert  
Ian T. Ferguson  
H. Walter Yao**  
*Chairs/Editors*

**27–28 January 1999  
San Jose, California**

*Sponsored by*  
SPIE—The International Society for Optical Engineering

*Cooperating Organization*  
DARPA—Defense Advanced Research Projects Agency

*Published by*  
SPIE—The International Society for Optical Engineering



**Volume 3621**

SPIE is an international technical society dedicated to advancing engineering and scientific applications of optical , photonic, imaging, electronic, and optoelectronic technologies.



The papers appearing in this book comprise the proceedings of the meeting mentioned on the cover and title page. They reflect the authors' opinions and are published as presented and without change, in the interests of timely dissemination. Their inclusion in this publication does not necessarily constitute endorsement by the editors or by SPIE. The views, opinions, and/or findings contained herein should not be construed as official U.S. Department of the Army position, policy, or decision, unless so designated by other documentation.

Please use the following format to cite material from this book:

Author(s), "Title of paper," in *Light-Emitting Diodes: Research, Manufacturing, and Applications III*, E. Fred Schubert, Ian T. Ferguson, H. Walter Yao, Editors, Proceedings of SPIE Vol. 3621, page numbers (1999).

ISSN 0277-786X  
ISBN 0-8194-3091-9

Published by  
**SPIE—The International Society for Optical Engineering**  
P.O. Box 10, Bellingham, Washington 98227-0010 USA  
Telephone 360/676-3290 (Pacific Time) • Fax 360/647-1445

Copyright ©1999, The Society of Photo-Optical Instrumentation Engineers.

Copying of material in this book for internal or personal use, or for the internal or personal use of specific clients, beyond the fair use provisions granted by the U.S. Copyright Law is authorized by SPIE subject to payment of copying fees. The Transactional Reporting Service base fee for this volume is \$10.00 per article (or portion thereof), which should be paid directly to the Copyright Clearance Center (CCC), 222 Rosewood Drive, Danvers, MA 01923. Payment may also be made electronically through CCC Online at <http://www.directory.net/copyright/>. Other copying for republication, resale, advertising or promotion, or any form of systematic or multiple reproduction of any material in this book is prohibited except with permission in writing from the publisher. The CCC fee code is 0277-786X/99/\$10.00.

Printed in the United States of America.



# Contents

vii	<i>Conference Committee</i>
ix	<i>Introduction</i>

## KEYNOTE ADDRESS

---

- 2 **InGaN-based UV/blue/green/amber LEDs [3621-01]**  
T. Mukai, M. Yamada, S. Nakamura, Nichia Chemical Industries, Ltd. (Japan)

## SESSION 1 III-NITRIDE LIGHT-EMITTING DIODES

---

- 16 **Progress and status of visible light-emitting diode technology (Invited Paper) [3621-02]**  
R. S. Kern, Hewlett-Packard Co.
- 28 **InGaN blue light-emitting diodes with optimized n-GaN layer [3621-03]**  
I. Eliashevich, Y. Li, A. Osinsky, C. A. Tran, M. G. Brown, R. F. Karliceck, Jr., Emcore Corp.
- 37 **Gallium-nitride-based LEDs on silicon substrates (Invited Paper) [3621-05]**  
N. A. Bojarczuk, S. Guha, IBM Thomas J. Watson Research Ctr.
- 43 **Growth and characterization of high-efficiency InGaN MQW blue and green LEDs from large-scale-production MOCVD reactors (Invited Paper) [3621-06]**  
C. A. Tran, R. F. Karliceck, Jr., M. G. Brown, I. Eliashevich, A. Gurary, R. A. Stall, Emcore Corp.

## SESSION 2 III-NITRIDES AND RELATED MATERIALS

---

- 52 **Optical properties of InGaAsN: a new 1-eV bandgap material system (Invited Paper) [3621-07]**  
E. D. Jones, N. A. Modine, A. A. Allerman, I. J. Fritz, S. R. Kurtz, A. F. Wright, Sandia National Labs.; S. T. Tozer, X. Wei, Florida State Univ.
- 64 **Time-resolved photoluminescence measurements of InGaN light-emitting diodes, films, and multiple quantum wells [3621-08]**  
M. Pophristic, F. H. Long, Rutgers Univ.; C. A. Tran, I. T. Ferguson, R. F. Karliceck, Jr., Emcore Corp.
- 73 **Optical anisotropy of GaN/sapphire studied by generalized ellipsometry and Raman scattering [3621-09]**  
C. Yan, H. W. Yao, Univ. of Nebraska/Lincoln; J. M. Van Hove, A. M. Wowchak, P. P. Chow, SVT Associates; J. M. Zavada, U.S. Army Research, Development and Standardization Group (UK)

## SESSION 3 ORGANIC AND POLYMER LEDs

---

- 86 **Organic electroluminescent displays (Invited Paper) [3621-12]**  
J. Shen, J. Yang, Arizona State Univ.

- 93 **Application of polyfluorenes and related polymers in light-emitting diodes** [3621-13]  
M. T. Bernius, M. Inbasekaran, E. P. Woo, W. W. Wu, L. Wujkowski, Dow Chemical Co.
- 103 **Improved lifetime and efficiency of organic light-emitting diodes for applications in displays (Invited Paper)** [3621-14]  
W. Kowalsky, T. Benstem, A. Böhrer, S. Dirr, H.-H. Johannes, D. Metzdorf, H. Neuner, J. Schöbel, Technische Univ. Braunschweig (Germany)

---

#### SESSION 4 III-As AND III-P LEDs

---

- 116 **Growth of InGaAlP HB-LEDs in a large-scale-production reactor** [3621-15]  
S. Li, D. A. Collins, S. Vatanapradit, M. Ferreira, P. A. Zawadzki, R. A. Stall, I. Eliashevich, J. E. Nering, Emcore Corp.
- 124 **Optical studies of InAs/In(As,Sb) single quantum well (SQW) and strained-layer superlattice (SLS) LEDs for the mid-infrared (MIR) region** [3621-17]  
H. Hardaway, J. Heber, P. Möck, M. J. Pullin, T. Stradling, P. J. P. Tang, C. Phillips, Imperial College of Science, Technology and Medicine (UK)
- 134 **Temperature dependence of magneto-optical properties of  $\text{Zn}_{1-x}\text{Mn}_x\text{Se}$**  [3621-18]  
Y.-X. Zheng, L.-Y. Chen, B. Xu, D.-L. Qian, Y.-J. Zhang, S.-Y. Wang, R.-J. Zhang, S.-M. Zhou, N. Dai, Y.-F. Wei, D.-M. Huang, Fudan Univ. (China)
- 143 **White LED (Invited Paper)** [3621-20]  
G. Bogner, A. Debray, G. Heidel, OSRAM Opto Semiconductor GmbH (Germany); K. Höhn, Siemens AG (Germany); U. Müller, OSRAM GmbH (Germany); P. Schlotter, Fraunhofer-Institut für Angewandte Festkörperphysik (Germany)
- 151 **High-efficiency top-emitting microcavity light-emitting diodes** [3621-21]  
P. Royo, J. F. Carlin, J. Spicher, R. P. Stanley, R. Houdré, Ecole Polytechnique Fédérale de Lausanne (Switzerland); V. Bardinal, Laboratoire d'Analyse et d'Architecture des Systèmes/CNRS (France); U. Oesterle, M. Ilegems, Ecole Polytechnique Fédérale de Lausanne (Switzerland)
- 160 **16.8% external quantum efficiency from a planar LED** [3621-22]  
C. Dill, R. P. Stanley, U. Oesterle, M. Ilegems, Ecole Polytechnique Fédérale de Lausanne (Switzerland)
- 170 **Uniformity of GaInAsP/GaInAsP multiquantum well structures grown in multiwafer reactors** [3621-23]  
M. Deufel, M. Heuken, R. Beccard, H. Juergensen, AIXTRON AG (Germany); E. Woelk, AIXTRON Inc.
- 179 **Engineering high-quality  $\text{In}_x\text{Ga}_{1-x}\text{P}$  graded composition buffers on GaP for transparent substrate light-emitting diodes** [3621-10]  
A. Y. Kim, E. A. Fitzgerald, Massachusetts Institute of Technology

---

#### SESSION 5 NOVEL STRUCTURES AND MATERIALS

---

- 190 **Control of spontaneous emission in photonic crystals** [3621-24]  
M. Boroditsky, R. B. Vrijen, Univ. of California/Los Angeles; T. F. Krauss, Univ. of Glasgow (UK); R. Coccioli, Univ. of California/Los Angeles; R. J. Bhat, Corning, Inc.; E. Yablonovitch, Univ. of California/Los Angeles

- 198 **Infrared light-emitting diodes with lateral outcoupling taper for high extraction efficiency** [3621-25]  
W. Schmid, F. Eberhard, M. Schauler, M. Grabherr, R. King, M. Miller, E. Deichsel, G. Stareev, U. Martin, R. Jäger, J. Joos, R. Michalzik, K. J. Ebeling, Univ. of Ulm (Germany)
- 206 **Frequency limits of high-efficiency non-resonant cavity light-emitting diodes** [3621-26]  
P. L. Heremans, R. Windisch, IMEC (Belgium); A. Knobloch, Univ. Erlangen-Nürnberg (Germany); J. Potemans, B. Dutta, IMEC (Belgium); G. H. Döhler, Univ. Erlangen-Nürnberg (Germany); G. Borghs, IMEC (Belgium)
- 213 **Size dependence of record-efficiency non-resonant cavity light-emitting diodes** [3621-27]  
R. Windisch, P. L. Heremans, B. Dutta, S. Nemeth, IMEC (Belgium); A. Knobloch, G. H. Döhler, Univ. Erlangen-Nürnberg (Germany); G. Borghs, IMEC (Belgium)
- 221 **Realization of highly efficient and high-speed resonant cavity LED for coupling to plastic optical fibers** [3621-28]  
R. Bockstaele, T. Coosemans, C. Sys, L. Vanwassenhove, A. Van Hove, B. Dhoedt, I. Moerman, P. van Daele, R. G. Baets, Univ. of Ghent (Belgium) and IMEC (Belgium)
- 230 **Solid-source molecular beam epitaxy growth and characteristics of resonant cavity light-emitting diodes** [3621-29]  
M. J. Saarinen, S. Orsila, M. Toivonen, P. Savolainen, T. Kuuslahti, V. Vilokinen, P. Melanen, P. Sipilä, M. Pessa, Tampere Univ. of Technology (Finland)
- 237 **Efficiency improvement in light-emitting diodes based on geometrically deformed chips** [3621-30]  
S. J. Lee, S. W. Song, Chungnam National Univ. (Korea)
- 249 **Diode light sources for retinal scanning displays** [3621-31]  
D. C. Bertolet, N. Bertram, J. R. Lewis, A. A. Gross, Microvision, Inc.
- 258 *Addendum*
- 259 *Author Index*

## Conference Committee

### *Conference Chairs*

**E. Fred Schubert**, Boston University  
**Ian T. Ferguson**, Emcore Corporation  
**H. Walter Yao**, University of Nebraska/Lincoln

### *Program Committee*

**Isamu Akasaki**, Meijo University (Japan)  
**Hiroshi Amano**, Meijo University (Japan)  
**Steven P. DenBaars**, University of California/Santa Barbara  
**Kathy Doverspike**, Cree Research, Inc.  
**Robert M. Fletcher**, Hewlett-Packard Company  
**Paul L. Heremans**, IMEC (Belgium)  
**Jürgen Jahns**, FernUniversität Hagen (Germany)  
**Jack L. Jewell**, Picolight Inc.  
**Rebecca H. Jordan**, Eastman Kodak Company  
**Lionel C. Kimerling**, Massachusetts Institute of Technology  
**Jeffrey N. Miller**, Hewlett-Packard Laboratories  
**Eli Yablonovitch**, University of California/Los Angeles  
**Yang Yang**, University of California/Los Angeles

### *Session Chairs*

- 1    III-Nitride Light-Emitting Diodes  
    **E. Fred Schubert**, Boston University  
    **Steven P. DenBaars**, University of California/Santa Barbara
- 2    III-Nitrides and Related Materials  
    **H. Walter Yao**, University of Nebraska/Lincoln  
    **Eric D. Jones**, Sandia National Laboratories
- 3    Organic and Polymer LEDs  
    **Yang Yang**, University of California/Los Angeles  
    **Ian T. Ferguson**, Emcore Corporation
- 4    III-As and III-P LEDs  
    **Robert M. Fletcher**, Hewlett-Packard Company  
    **John M. Zavada**, U.S. Army Research, Development and Standardization Group (UK)
- 5    Novel Structures and Materials  
    **Ian T. Ferguson**, Emcore Corporation  
    **E. Fred Schubert**, Boston University

## **Introduction**

This volume records the third conference dedicated to light-emitting diodes (LEDs). It was held during SPIE Photonics West in San Jose, California, on January 27–28, 1999.

The proceedings contains 26 invited and contributed papers appearing in five sessions, and one keynote address. The papers cover LEDs emitting in the ultraviolet, visible, and infrared regions of the optical spectrum. LEDs are used for display, communication, and other applications, and this volume provides an overview of the currently rapid progress of this field.

We thank the authors, program committee members, session chairs, and their affiliations for providing this valued and timely update on LED research, manufacturing, and applications.

**E. Fred Schubert  
Ian T. Ferguson  
H. Walter Yao**

## **Keynote Address**

# InGaN-based uv/blue/green/amber/red LEDs

T. Mukai, M. Yamada and S. Nakamura

Department of Research and Development, Nichia Chemical Industries, Ltd.,  
491 Oka, Kaminaka, Anan, Tokushima 774, Japan

## Abstract

High-efficient light emitting diodes (LEDs) emitting red, amber, green, blue, and ultraviolet light have been obtained through the use of an InGaN active layers instead of GaN active layers. Red LEDs with an emission wavelength of 680 nm which emission energy was smaller than the band-gap energy of InN were fabricated mainly resulting from the piezoelectric field due to the strain. The localized energy states caused by In composition fluctuation in the InGaN active layer seem to be related to the high efficiency of the InGaN-based emitting devices in spite of having a large number of threading dislocations. InGaN single-quantum-well-structure blue LEDs were grown on epitaxially laterally overgrown GaN (ELOG) and sapphire substrates. The emission spectra showed the similar blue shift with increasing forward currents between both LEDs. The output power of both LEDs was almost the same, as high as 6 mW at a current of 20 mA. These results indicate that the In composition fluctuation is not caused by dislocations, the dislocations are not effective to reduce the efficiency of the emission, and that the dislocations form the leakage current pathway in InGaN.

**Keywords:** InGaN, GaN, LEDs, blue, green, amber, SQW, ELO, dislocations

## 1. Introduction

Light-emitting diodes (LEDs) are ultimate solid-state light sources. At present, incandescent bulb lamps and fluorescent lamps are used as light sources for many applications. However, these conventional light sources are old, traditional glass-vacuum-type light sources with poor reliability and durability and a low luminous efficiency. In the past, the electronic circuit was made of a glass vacuum tube in spite of poor reliability and durability. Now, however, all electronic circuits are highly reliable solid-state semiconductor circuits. Thus, only light sources are still made of old traditional technology, not solid-state semiconductors. Recently, however, the development of InGaN-based compound semiconductors opened the way to all-solid-state semiconductor light sources. The brightness and durability of solid-state LEDs make them ideal for use in displays and light sources, while semiconductor laser diodes have been used in everything from optical communications systems to compact disk players. These applications have been limited, however, by the lack of materials that can efficiently emit blue and green light. Full-color displays, for example, require at least three primary colors, usually red, green and blue, to produce any visible color. Such a combination is also needed to make a white-light-emitting device that would be more durable with less power consumption than conventional incandescent bulbs or fluorescent lamps. Recently, however, III-V nitride-based materials have opened the way for a realization of high-efficient uv/blue/green/amber LEDs.

## 2. III-V nitride-based semiconductors

III-V nitride-based semiconductors have a direct band gap that is suitable for blue light-emitting devices. The band gap energy of aluminum gallium indium nitride (AlGaInN) varies between 6.2 and 1.89 eV, depending on its composition, at room temperature (RT). Thus, by using these semiconductors, red to ultraviolet-emitting devices can be fabricated. In 1992, authors [1] succeeded in growing a high quality InGaIn films for the first time which emitted a strong band to band emission from green to uv by changing the In content of InGaIn using novel two-flow MOCVD method. Also, Nakamura et al. fabricated first InGaIn/GaN double-heterostructure (DH) LEDs in 1993 [2]. Finally, they [3] could grow InGaIn multi-quantum-well (MQW) structure and confirmed an enhanced strong PL intensity from a quantized energy levels of the InGaIn well layer with a thickness of 25 Å for the first time. A small amount of indium adding into the GaN is very important to

obtain a strong band to band emission because GaN without the indium cannot emit a strong band to band emission at RT. This reason is considered to be related to deep localized energy states caused by In composition fluctuation [4-8].

Using above InGaN, in 1994, Nakamura et al. developed first blue InGaN/AlGaN double heterostructure LEDs [9] and, then developed blue/green InGaN single-quantum-well (SQW) structure LEDs in 1995 [10]. Then, ultraviolet (UV)/amber LEDs [11-13] and first demonstration of RT violet laser light emission in InGaN-MQW/GaN/AlGaN-based heterostructures under pulsed operations were achieved [14]. All of these light-emitting devices use an InGaN active layer instead of a GaN active layer because it is difficult to fabricate a highly efficient light-emitting device using a GaN active layer, the reason for which is still not well known. Also, the InGaN active layer in these LEDs include a large number of threading dislocations (TDs) from  $1 \times 10^8$  to  $1 \times 10^{12} \text{ cm}^{-2}$  originating from the interface between GaN and the sapphire substrate due to a large lattice mismatch of 13.5 % [15]. The TDs are considered to be formed as a result of a complex set of interactions including the interface energy, the nucleation density, island coalescence, and etc. [16,17]. In spite of these large number of dislocations, the efficiency of the InGaN-based LEDs is much higher than that of the conventional III-V compound semiconductor (AlGaAs and AlInGaP)-based LEDs. In many conventional optoelectronic devices, the device performance has been limited by the control of both point defects and structural defects in these materials. However, these recent reports now suggest that III-V nitride-based devices are less sensitive to dislocations than conventional III-V semiconductors.

Chichibu et al. [18] studied the emission mechanisms of GaN and InGaN quantum wells (QWs) by comparing their optical properties as a function of TD density, which was controlled by lateral epitaxial overgrowth (LEO) technique. PL intensity was slightly strengthened by reducing TD density from  $1 \times 10^{10} \text{ cm}^{-2}$  to nearly zero (less than  $1 \times 10^6 \text{ cm}^{-2}$ ). Also, the major PL decay time was independent of the TD density. These results suggested that the emission mechanisms are unaffected by TDs. TDs are considered to simply reduce the net volume of light-emitting area. This effect is less pronounced in InGaN QWs where carriers are effectively localized at certain potential minimum caused by In composition fluctuation in the QWs to form quantized excitons [4-8] before being trapped in nonradiative pathways at TDs, resulting in pronounced slow decay time (1-40 ns). The depth of these localized energy states with a small In composition fluctuation is enhanced by the large band gap bowing of the InGaN [19]. Assuming that the lateral spacing of the effective bandgap (potential) minimum determines the carrier diffusion length in InGaN, the carrier diffusion length was estimated to be less than 60 nm [8]. Absence of change in the Stokes-like shift due to reduction of TD density revealed that the effective bandgap fluctuation in InGaN QWs was not due to a phase separation initiated by TDs [20,21].

The localized states of InGaN layer play a key role of the high efficiency only for LEDs. On the LDs, only InGaN has been used as the active layer because laser oscillation using GaN or AlGaN active layer under current injection has not been achieved. Thus, also for LDs, the InGaN seems to play an important role in forming the localized states that lead to emission. However, the operating current density of the LD is one order higher than that of the LEDs. Thus, in the InGaN active layer of the LDs, some of the injected carriers easily overflow the localized states formed by the In composition fluctuation and they recombine nonradiatively at the nonradiative recombination centers formed by the large number of TDs. Or the localized excitons are easily screened by a large number of injected carriers. Considering about these results, there is a possibility that a small amount of In into the GaN reduces the number of nonradiative recombination centers formed by point or nanopipe defects [22,23] dramatically and also forms the localized energy states due to the In composition fluctuation.

Here, present progress of InGaN-based LEDs are described considering about the role of InGaN layer, referring the previous works as mentioned above.

### 3. InGaN-based UV/blue/green/amber/red LEDs

The reason why InGaN-based LEDs are so efficient in spite of large number of TDs has not been clarified yet [15]. However, there is a clue for the reason. The high-efficient LEDs can be obtained only using InGaN active layer for the LED and LDs. When the active layer of the LEDs is GaN or AlGaN, the efficiency of LEDs is considerably low [11,12]. The PL intensity of band-to band-emission of GaN layer [24] was much weaker than that of InGaN layer [25] when they were grown by MOCVD. Thus, the InGaN active layer is considered to be related to the high-efficiency of the LEDs and LDs in spite of having a large number of TDs.



III-V nitride films were grown using the two-flow MOCVD method, the details of which have been previously described [26,27]. The growth was conducted at atmospheric pressure. Sapphire with (0001) orientation (C-face) and two inch diameter was used as the substrate. The green LED device structures consisted of a 300 Å GaN buffer layer grown at a low temperature (550°C), a 5- $\mu\text{m}$ -thick layer of n-type GaN:Si, a 30-Å-thick active layer of undoped  $\text{In}_{0.45}\text{Ga}_{0.55}\text{N}$ , a 600-Å-thick layer of p-type  $\text{Al}_{0.2}\text{Ga}_{0.8}\text{N:Mg}$ , and a 0.15- $\mu\text{m}$ -thick layer of p-type GaN:Mg. The active region formed a SQW structure consisting of a 30 Å  $\text{In}_{0.45}\text{Ga}_{0.55}\text{N}$  well layer sandwiched by 5  $\mu\text{m}$  n-type GaN and 600 Å p-type  $\text{Al}_{0.2}\text{Ga}_{0.8}\text{N}$  barrier layers. The In composition of the InGa $\text{N}$  well layer was nearly zero for UV LEDs [11,12], and 0.2 for blue LEDs [10]. Here, the In composition was determined assuming that the bowing parameter of InGa $\text{N}$  was 1 eV [28]. However, recent studies revealed that the bowing parameter of InGa $\text{N}$  is much higher than 1 eV [19,29]. In that case, the In content in the InGa $\text{N}$  layer should be much smaller than the above values. For UV LEDs, the thickness of the undoped InGa $\text{N}$  well layer was changed to 55 Å and an  $\text{Al}_{0.2}\text{Ga}_{0.8}\text{N}$  barrier layer was used for both n- and p-type barrier layers. The fabrication of LED chips was as described in other papers [26].

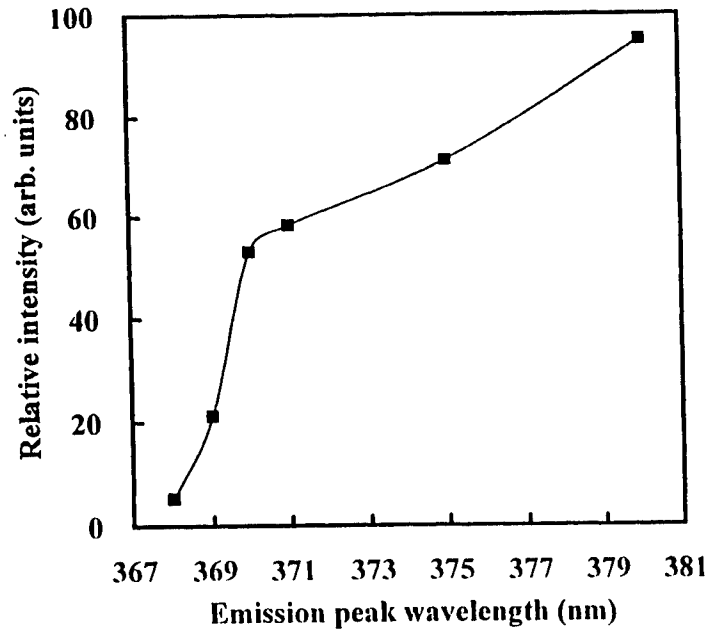


Fig. 1. Relative output power of UV InGa $\text{N}$  SQW LEDs as a function of emission peak wavelength with different In mole fractions in the active layer.

Figure 1 shows the relative output power as a function of the emission peak wavelength of UV LEDs [11,12]. The output power of the UV LEDs containing a small amount of In in the active layer, with the emission wavelength of 380 nm was about 20 times higher than that containing no In with the emission wavelength of 368 nm. With decreasing In composition in the active layer, which means that the emission peak wavelength becomes shorter, the output power decreases dramatically. Thus, high-power UV LEDs can be obtained only when using the InGa $\text{N}$  active layer with relatively high In composition. This is related to the large localized energy states caused by In composition fluctuation in the InGa $\text{N}$  well layer [4-8]. When electrons and holes are injected into the InGa $\text{N}$  active layer of the LEDs, these carriers are captured by the localized energy states before they are captured by the nonradiative recombination centers caused by the large number of TDs. At these large localized energy states, localized excitons with a relatively high binding energy due to a quantum well structure are formed to recombine radiatively. Without In in the active layer, there are no In composition fluctuations that

from the large localized energy state in the InGaN active layer. Thus, the quantum-confined Stark effect (QCSE) resulting from the piezoelectric field due to the strain becomes dominant [30-33]. This field, if strong enough, will induce a spatial separation of the electron and hole wave functions in the well. Then, the wave function overlap decreases and the interband recombination rate is reduced. Also, there is no In composition fluctuation where carriers are captured by the localized energy states before they are captured by the nonradiative recombination centers. Thus, the efficiency of the UV LEDs becomes extremely low when the active layer is GaN or InGaN with a small amount of In, as shown in Fig. 1. When the emission peak wavelength becomes shorter than 371 nm, the output power decreases dramatically probably due to an additional reason of a self absorption of the light by n- and p-type GaN contact layers.

Next, amber LEDs were fabricated by increasing the In composition of the InGaN well layer. Figure 2 shows the emission spectra of amber InGaN and AlInGaP LEDs at a forward current of 20 mA at RT. For comparison, the spectrum of commercially available amber AlInGaP LED fabricated on an absorbing substrate of GaAs (Type: HLMP-DL32, Hewlett Packard) [34] is also shown. The peak wavelength and the full-width at half-maximum (FWHM) of the emission spectra of the amber InGaN LEDs were 594 nm and 50 nm, respectively, and those of amber AlInGaP LEDs were 591 nm and 17 nm, respectively. The spectrum width of the InGaN LEDs is relatively broad mainly due to a phase separation of InGaN during growth, which was reported recently [4-8]. In view of the spectrum width, the amber AlInGaP LEDs seem to have superior color purity. In regard to the application of LEDs, however, in the color range from red to yellow, it is hard for the human eye to detect the difference in color purity caused by a spectrum width difference of 16 nm to 50 nm.

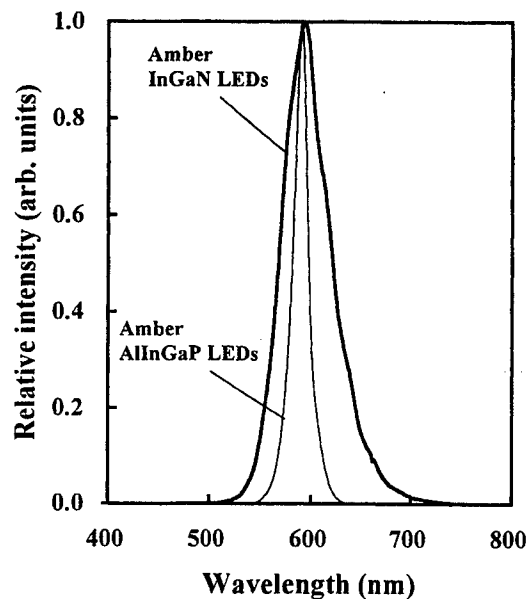


Fig. 2. The emission spectra of amber InGaN and AlInGaP LEDs at a forward current of 20 mA.

Figure 3 shows the output power of amber InGaN and AlInGaP LEDs as a function of the ambient temperature from -30 °C to +80 °C. The output powers of amber InGaN and AlInGaP LEDs at 25 °C were 1.4 mW and 0.66 mW, respectively. The output power of InGaN LEDs was about twice as high as that of AlInGaP LEDs. The output power of each LED was normalized to 1.0 at 25 °C. When the ambient temperature was increased from RT to 80 °C, the output power of amber AlInGaP LEDs decreased dramatically to half that at RT due to a carrier overflow caused by a small band offset between the active layer and cladding layers [34]. In the AlInGaP system, the band offset is small under a lattice-matched condition between the AlInGaP epilayer and GaAs substrate [34]. On the other hand, the temperature dependence of amber InGaN LEDs is relatively weak. When the ambient temperature is increased from RT to 80 °C, the output power of amber InGaN LEDs only decreases to 90 % of that at RT, probably due to a small carrier overflow caused by a large band offset between

the active layer and cladding layers. In terms of the temperature dependence of the LEDs, InGaN LEDs are much superior to the AlInGaP LEDs. The temperature dependence of blue/green InGaN-based LEDs and conventional red AlInGaP LEDs are also shown in Fig. 4. In the figure, InGaN-based LEDs show much superior temperature dependence of the output power in comparison with that of conventional LEDs.

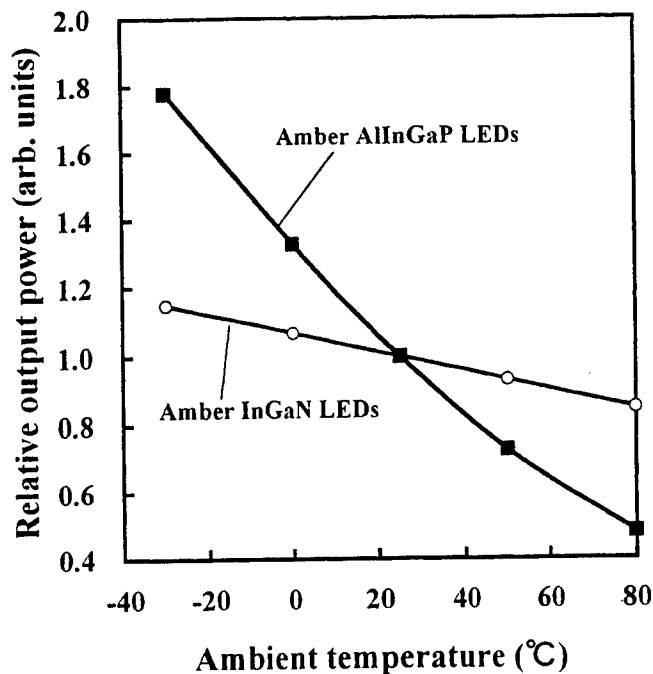


Fig. 3. The output power of amber InGaN and AlInGaP LEDs as a function of the ambient temperature from -30 °C to +80 °C. The output power of each LED was normalized to 1.0 at 25 °C.

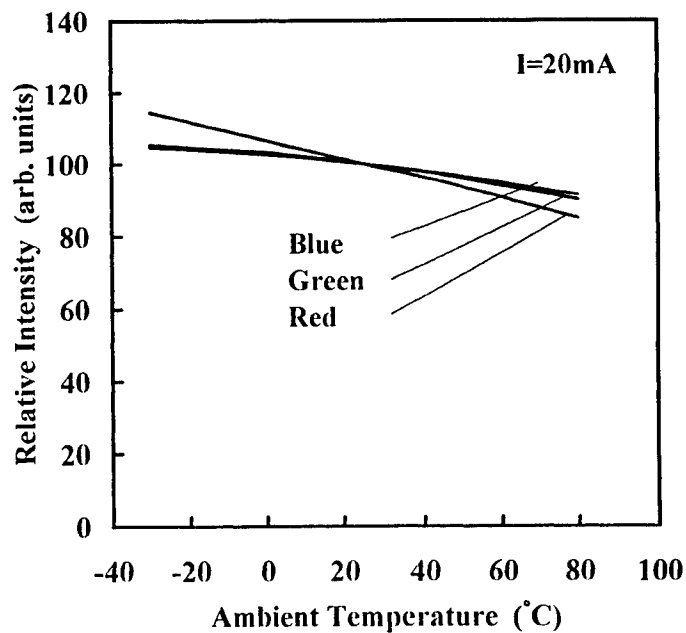


Fig. 4. The output power of blue/green InGaN and red AlInGaP LEDs as a function of the ambient temperature from -30 °C to +80 °C. The output power of each LED was normalized to 1.0 at 25 °C.

Red InGaN SQW LEDs were also fabricated by further increasing the In composition and thickness of InGaN well layers in the above LED structure. The In composition and thickness of the InGaN well layer were changed to approximately 50 % and 60 Å, respectively. Here, the In composition was determined assuming that the bowing parameter of InGaN was 1 eV [28]. Figure 5 shows the emission spectrum of red InGaN SQW LED at forward currents of 10 mA, 20 mA and 40 mA. At a current of 10 mA, the peak wavelength is 680 nm (1.82 eV), which peak emission energy is lower than a band-gap energy of InN (1.89 eV) [35]. When the current was changed from 10 mA to 40 mA, a large blueshift of the peak wavelength was observed from 680 nm to 630 nm. The output power of the red LED was as low as 0.3 mW at a current of 20 mA. This lower emission energy than the bandgap energy of InN can be explained only by the QCSE. The blueshift of the electroluminescence (EL) of the InGaN SQW LEDs with increasing operating current can be explained by the QCSE resulting from piezoelectric fields [30-33], when the In composition and thickness of the InGaN well layer are large. However, a higher efficiency of the LEDs with increasing strain in the SQW upon increasing the In content in the InGaN well layers, was observed from UV to green LEDs [10-13,26] as shown in Figs. 1 and 6.

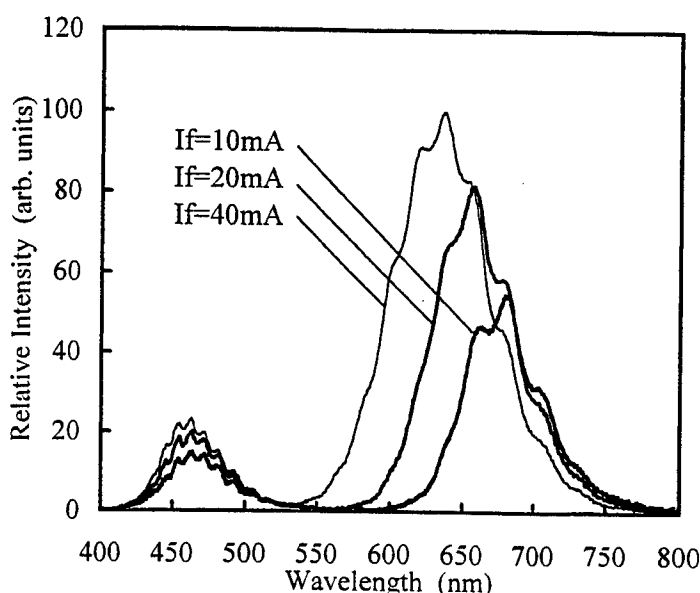


Fig. 5. Emission spectra of red InGaN SQW LEDs at different operating currents.

Figure 6 shows the external quantum efficiency as a function of the emission wavelength of InGaN-based UV, blue, green and amber LEDs. The blue and green LEDs have the highest efficiency of 12 % in spite of a large QCSE with a relatively strong stress due to a large lattice mismatch between InGaN well layer and GaN barrier layers. These phenomena cannot be explained only by the QCSE. It may be that the localization effects induced by In composition fluctuations must overcome these intrinsic limitations due to the piezoelectric field. In Fig. 5, there is an additional emission peak at a wavelength of around 470 nm, which is probably originated from a low In composition InGaN formed by the phase separation of the InGaN well layer due to a high In composition of the well layer [36]. This additional emission peak of 470 nm also demonstrates the phase separation of InGaN layer [36], which means the In composition fluctuation in the well layer. Considering about these results, the emission wavelength of the red LED dependence on the current (blueshift) is dominated by both of the band-filling effect and the screening effect of the QCSE due to a large In composition and large thickness of the InGaN well layer.

Figure 7 shows the cross-sectional TEM images of the LD structure grown directly on the sapphire substrate. The detail structure of the LD is described in other papers [37]. From the cross-sectional TEM, the TD density was estimated to be as high as  $1 \times 10^{10}$  to  $10 \times 10^{10} \text{ cm}^{-2}$  in the InGaN-based LDs, which was originated from the interface of GaN/sapphire. The InGaN-based LEDs has also the same order of TDs in the InGaN active layer [15]. In spite of this large number of

dislocations, these LEDs have the external quantum efficiency as high as 12 %, as shown in Fig. 6. The conventional LEDs, such as infrared/red AlGaAs and red/yellow AlInGaP LEDs, cannot have the high efficiency when the dislocation density is  $> 1 \times 10^3 \text{ cm}^{-2}$ . Thus, only InGaN-based LEDs are insensitive to dislocations from the standpoint of efficiency.

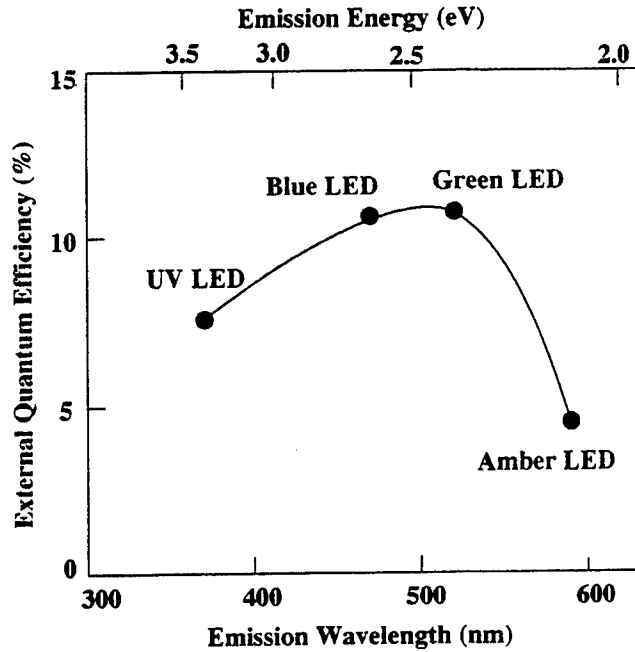


Fig. 6. External quantum efficiency as a function of the emission wavelength of InGaN-based UV, blue, green and amber LEDs.

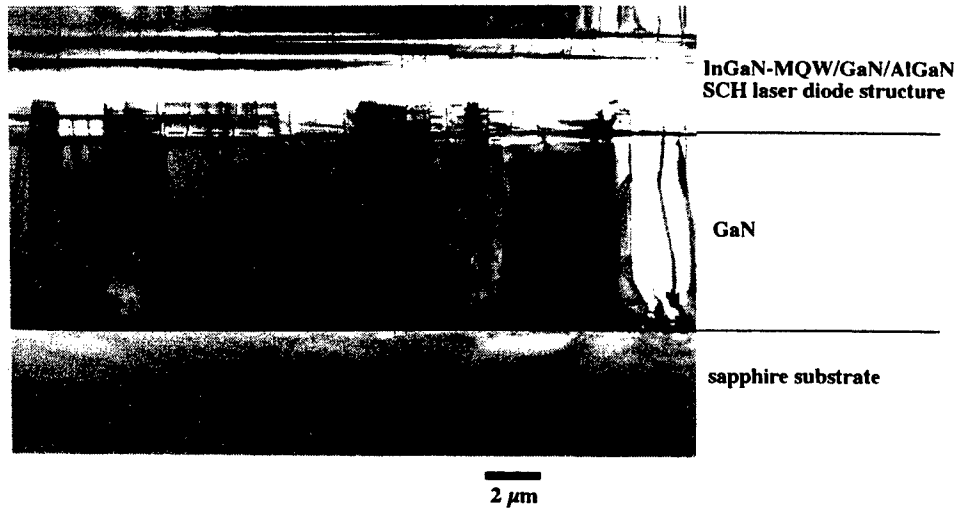


Fig. 7. Cross-sectional TEM images of the LD structure grown directly on the sapphire substrate.

Epitaxially laterally overgrown GaN (ELOG) on sapphire substrate was developed recently to reduce the number of threading dislocations in the GaN epitaxial layers [38,39]. Using the ELOG, the number of threading dislocations was reduced significantly to almost zero in the GaN grown on the  $\text{SiO}_2$  stripe mask. Thus, there is a great interest in fabricating LEDs using the ELOG substrate which has a small number of dislocations in order to study the role of these dislocations in

the InGaN-based LEDs. For the study, blue InGaN SQW structure LEDs as mentioned above were fabricated on the ELOG and sapphire substrates [40]. The selective growth of GaN was performed on a 2- $\mu\text{m}$ -thick GaN layer grown on a (0001) C-face sapphire substrate. The 2- $\mu\text{m}$ -thick silicon dioxide ( $\text{SiO}_2$ ) mask was patterned to form 4- $\mu\text{m}$ -wide stripe windows with a periodicity of 12  $\mu\text{m}$  in the GaN  $\langle 1-100 \rangle$  direction. After 10- $\mu\text{m}$ -thick GaN was grown on the  $\text{SiO}_2$  mask pattern, the coalescence of the selectively grown GaN made it possible to obtain a flat GaN surface over the entire substrate. We call this coalesced GaN the ELOG. Figure 8 shows cross-sectional TEM image of the ELOG substrate. In the underlayer of 2- $\mu\text{m}$ -thick GaN layer, the TD density of order of  $1 \times 10^{10} \text{ cm}^{-2}$  was observed due to a large lattice mismatch between GaN and sapphire substrate. The TDs, originating from the GaN/sapphire interface, propagate to the regrown GaN layer within the window regions of the mask. It is important to note that the TDs extend only to just above the window areas. In contrast, there were no observable TDs in the overgrown layer on the  $\text{SiO}_2$  mask area. However, a few short edge-on dislocation segments parallel to the interface plane were observed in the GaN layer on the  $\text{SiO}_2$  mask area. These dislocations were parallel to the (0001) plane via the extension of the vertical threading dislocations after a  $90^\circ$  bend in the regrown region. These dislocations did not subsequently propagate to the surface of the overgrown GaN layers. We examined the defect density by plan-view TEM observation of the surface of the ELOG substrates. The number of dislocations on the  $\text{SiO}_2$  mask area was almost zero (lower than  $1 \times 10^6 \text{ cm}^{-2}$ ), and that on the window area was approximately  $2 \times 10^7 \text{ cm}^{-2}$ . As the dislocation density of conventional GaN was of the order of  $1 \times 10^{10} \text{ cm}^{-2}$ , the number of the TDs was reduced considerably when the ELOG substrate was used. After obtaining a 15- $\mu\text{m}$ -thick ELOG substrate, a InGaN SQW blue LED structure was grown on the substrate.

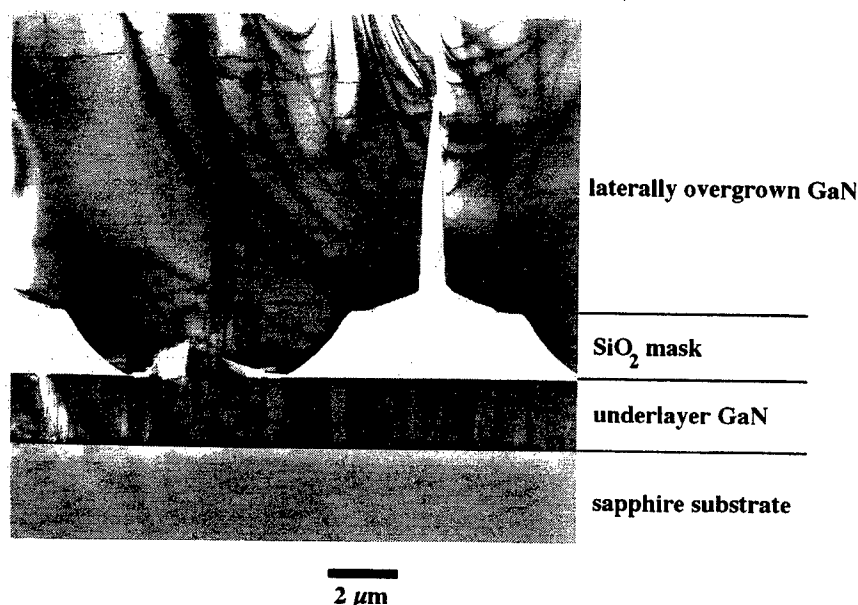


Fig. 8. Cross-sectional TEM micrograph of the laterally overgrown GaN layer on a  $\text{SiO}_2$  mask and window area.

At first, emission spectra of the LEDs were measured [40]. At a forward current of 20 mA at RT, the peak wavelength and the full-width at half maximum (FWHM) of the emission spectra of the LED on ELOG were 470 nm and 27 nm, respectively, and those on sapphire were 464 nm and 26 nm, respectively. The peak wavelength of the LED on ELOG is somewhat longer than that on sapphire probably due to a growth fluctuation. There is no significant difference between in the spectra of both LEDs. The broad spectral width is due to an In composition fluctuation in the InGaN well layer and the QCSE. This means that the size of the fluctuation is the same in both LEDs in spite of a large difference in the dislocation density. Thus, the fluctuations are not related to the dislocations [20,21]. The ELOG and GaN on sapphire had average dislocation densities of  $7 \times 10^6 \text{ cm}^{-2}$  and  $1 \times 10^{10} \text{ cm}^{-2}$ , respectively. Here, average dislocation density of the ELOG on sapphire was obtained by dividing the dislocation density of  $2 \times 10^7 \text{ cm}^{-2}$  on the window region by the ratio of (stripe periodicity of 12  $\mu\text{m}$ ) / (window width of 4  $\mu\text{m}$ ) because the dislocation density on the  $\text{SiO}_2$  stripe region was almost zero.

The size of LED chip is as large as  $350\ \mu\text{m} \times 350\ \mu\text{m}$ . Each LED chip includes many window and  $\text{SiO}_2$  stripe regions. Therefore, we used an average dislocation density for the ELOG on sapphire. When the LED was observed by a microscope under a forward current bias condition, no inhomogeneities of blue emission intensity over the entire surface of the LED chip was observed. There was no emission intensity fluctuation on the surface of the LED depending on the dislocation density fluctuation periodically across the window and  $\text{SiO}_2$  stripe regions. Thus, it is also concluded that a large number of dislocations on the widow region are not effective to reduce the efficiency of the blue emission.

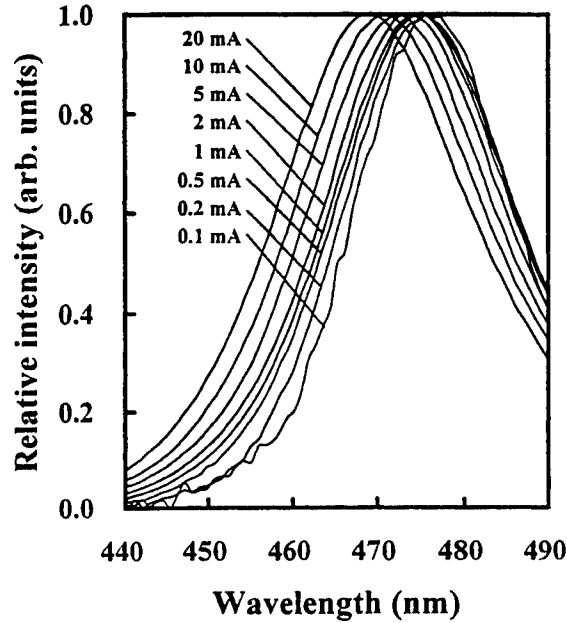


Fig. 9. The emission spectra of blue InGa<sub>N</sub> SQW LED grown on ELOG substrate at various forward currents.

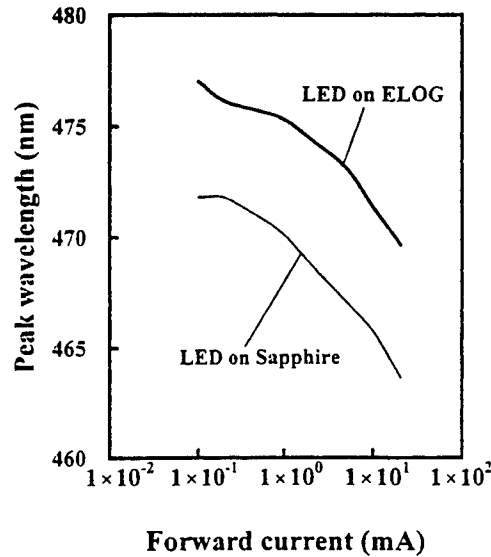


Fig. 10. The peak wavelengths of emission spectra of blue InGa<sub>N</sub> SQW LEDs grown on ELOG and on sapphire substrates as a function of the forward current.

Figure 9 shows the emission spectra of the blue InGa<sub>N</sub> SQW LEDs at forward currents from 0.1 mA to 20 mA. In the spectra, the blue shift is easily observed due to a band-filling effect of the deep localized energy states and a screening

effects of the QCSE. These localized states have been considered to be formed by defects, impurities, or fluctuations of the InGaN quantum well composition and/or thickness. The latter can also be interpreted in terms of quantum dot formation. Among these explanations of the localized state origins, the In composition fluctuation in the InGaN well layer is most plausible at present [4-8]. Figure 10 shows the peak wavelength of both LEDs as a function of the forward current. Both LEDs showed the same peak wavelength dependence on the current, which implies the same blue shifts. Thus, the dislocations are not directly related to the formation of the localized energy states [20,21]. As mentioned above, these localized states are probably formed by the In composition fluctuation in the InGaN well layer due to a natural phase separation of InGaN during growth [36]. Using the ELOG and sapphire substrates, the same blue shifts was observed in the case of both LEDs. Therefore, assuming that the localized states are formed by the In composition fluctuation in the InGaN well layer, the dislocation related composition fluctuation is eliminated because the dislocation density of the epilayer on the ELOG is relatively small [20,21]. The screening effects of the QCSE also contribute to the blueshifts with increasing the currents.

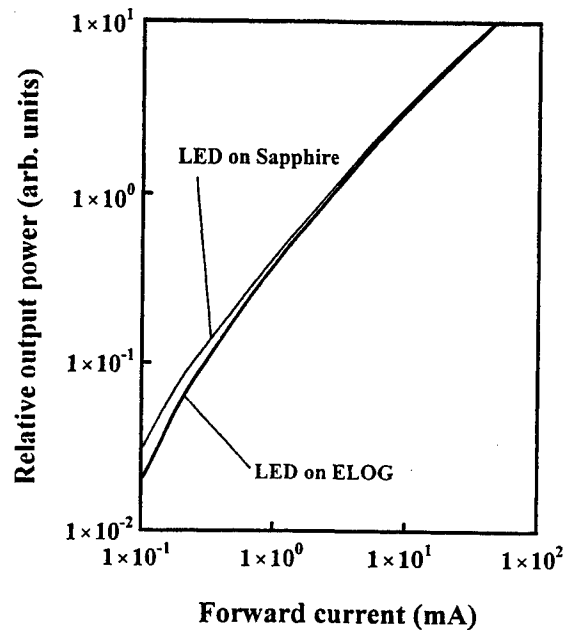


Fig. 11. The relative output power of blue InGaN SQW LEDs grown on ELOG and on sapphire substrates as a function of the forward current.

Figure 11 shows the relative output power of both LEDs as a function of the forward current. The output power of both LEDs at a current of 20 mA was 6 mW, which is equal to the external quantum efficiency of 11 %. In spite of a large number of dislocations, the LED on sapphire had the same output power as that on ELOG. Thus, the dislocation are not effective to reduce the efficiency of the emission. If the dislocations work as nonradiative recombination centers effectively, the output power of the LED on ELOG have to be much higher than that on sapphire due to a small number of average dislocation density.

Figure 12 shows the reverse biased I-V characteristics of both LEDs. At a reverse bias voltage of -20 V, the reverse current of the LED on the ELOG was 0.009  $\mu$ A, and that on sapphire was 1  $\mu$ A. Under the reverse bias condition, the LED on sapphire had a considerable amount of leakage current. This leakage current under forward and reverse biased conditions is probably caused by the dislocations because the LEDs on sapphire have a considerable amount of leakage current and many dislocations. The same results of the increase of the leakage current due to a high dislocation density were already reported previously by Sasaoka et al. [41] on the InGaN/InGaN MQW LEDs. These results indicate that In composition fluctuation is not caused by dislocations, the dislocations are not effective as nonradiative recombination centers in InGaN, and that the dislocations form the leakage current pathway in InGaN.

Thus, the localization induced by the In composition fluctuations seem to be a key role of the high efficiency of the InGaN-based LEDs in spite of the large number of TDs and the large piezoelectric fields [42]. When the electrons and holes



are injected into the InGaN active layer of the LEDs, these carriers are captured by the localized energy states before they are captured by the nonradiative recombination centers caused by the large number of dislocations. It was reported that the TDs served as a nonradiative recombination center in GaN and InGaN [43,44]. These localized energy states can be formed only in InGaN films during the growth due to a phase separation of the InGaN [4-8]. Assuming that the lateral spacing of the effective bandgap (potential) minimum determines the carrier diffusion length in InGaN, the diffusion length was estimated to be less than 60 nm from the spatially resolved CL spectrum mapping measurement [8]. Sugahara et al [44] also concluded that the efficiency of light emission is high as long as the minority carrier diffusion length is shorter than the dislocation spacing. Considering about these previous results, the carrier diffusion length determined by the potential fluctuation due to InGaN phase separation must be less than the dislocation spacing in the InGaN layer in order to obtain high-efficient InGaN-based LEDs [42].

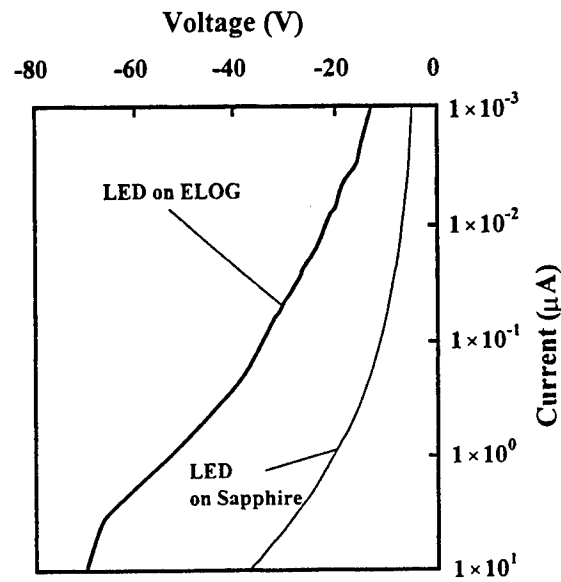


Fig. 12. The I-V characteristics of blue InGaN SQW LEDs grown on ELOG and on sapphire substrates under reverse biased conditions.

#### 4. Conclusion

UV/blue/green/amber/red InGaN-based LEDs were obtained using an InGaN active layer instead of a GaN active layer. The red LEDs with an emission wavelength of 680 nm, which emission energy is smaller than the band-gap energy of InN, were fabricated, probably resulting from the piezoelectric field due to the strain. In the red LEDs, a phase separation of the InGaN layer was clearly observed in the emission spectra, where blue and red emission peaks appeared. In terms of the temperature dependence of the LEDs, InGaN LEDs are much superior to the conventional red and amber LEDs due to a large band offset between the active and cladding layers. The localized energy states caused by In composition fluctuation in the InGaN active layer are related to the high efficiency of the InGaN-based LEDs in spite of having a large number of dislocations and having a large QCSE. Considering about the previous results, the carrier diffusion length determined by the potential fluctuation due to InGaN phase separation must be less than the dislocation spacing in the InGaN layer in order to obtain high-efficient InGaN-based LEDs.

#### References

- [ 1 ] S. Nakamura and T. Mukai, Jpn. J. Appl. Phys. **31**, L1457 (1992).
- [ 2 ] S. Nakamura, M. Senoh and T. Mukai, Jpn. J. Appl. Phys. **32**, L8 (1993).
- [ 3 ] S. Nakamura, T. Mukai, M. Senoh, S. Nagahama and N. Iwasa, J. Appl. Phys. **74**, 3911 (1993).

- [4] S. Chichibu, T. Azuhata, T. Sota, and S. Nakamura, Appl. Phys. Lett. **69**, 4188 (1996).
- [5] S. Chichibu, T. Azuhata, T. Sota, and S. Nakamura, Appl. Phys. Lett. **70**, 2822 (1997).
- [6] Y. Narukawa, Y. Kawakami, Sz. Fujita, Sg. Fujita, and S. Nakamura, Phys. Rev. **B55**, 1938R (1997).
- [7] Y. Narukawa, Y. Kawakami, M. Funato, Sz. Fujita, Sg. Fujita, and S. Nakamura, Appl. Phys. Lett. **70**, 981 (1997).
- [8] S. Chichibu, K. Wada, and S. Nakamura, Appl. Phys. Lett. **71**, 2346 (1997).
- [9] S. Nakamura, T. Mukai and M. Senoh, Appl. Phys. Lett. **64**, 1687 (1994).
- [10] S. Nakamura, M. Senoh, N. Iwasa, S. Nagahama, T. Yamada and T. Mukai, Jpn. J. Appl. Phys. **34**, L1332 (1995).
- [11] T. Mukai, D. Morita and S. Nakamura, J. Crystal Growth **189/190**, 778 (1998).
- [12] T. Mukai, M. Yamada and S. Nakamura, Jpn. J. Appl. Phys. **37**, L1358 (1998).
- [13] T. Mukai, H. Narimatsu and S. Nakamura, Jpn. J. Appl. Phys. **37**, L479 (1998).
- [14] S. Nakamura, M. Senoh, S. Nagahama, N. Iwasa, T. Yamada, T. Matsushita, H. Kiyoku, and Y. Sugimoto, Jpn. J. Appl. Phys. **35**, L74 (1996).
- [15] S. D. Lester, F. A. Ponce, M. G. Craford, and D. A. Steigerwald, Appl. Phys. Lett. **66**, 1249 (1995).
- [16] D. Kapolnek, X. H. Wu, B. Heying, S. Keller, B. Keller, U. K. Mishra, S. P. Denbaars, and J. S. Speck, Appl. Phys. Lett. **67**, 1541 (1995).
- [17] X. H. Wu, P. Fini, S. Keller, E. J. Tarsa, B. Heying, U. K. Mishra, S. P. DenBaars, and J. S. Speck, Jpn. J. Appl. Phys. **35**, L1648 (1996).
- [18] S. Chichibu, H. Marchand, M. Minsky, S. Keller, P. Fini, J. Ibbetson, J. Speck, J. E. Bowers, E. Hu, U. K. Mishra, S. P. Denbaars, T. Deguchi, T. Sota, and S. Nakamura, Appl. Phys. Lett. **74** (1999) [in press for 3/1/1999 issue]
- [19] M. D. McCluskey, C. G. Van de Walle, C. P. Master, L. T. Romano, and N. M. Johnson, Appl. Phys. Lett. **72**, 2725 (1998).
- [20] H. Sato, T. Sugahara, Y. Naoi, and S. Sakai, Jpn. J. Appl. Phys. **37**, 2013 (1998).
- [21] S. Keller, U. K. Mishra, S. P. Denbaars, and W. Seifert, Jpn. J. Appl. Phys. **37**, L431 (1998).
- [22] E. J. Tarsa, B. Heying, X. H. Wu, P. Fini, S. P. Denbaars, and J. S. Speck, J. Appl. Phys. **82**, 5472 (1997).
- [23] F. A. Ponce, D. P. Bour, W. Gotz, and P. J. Wright, Appl. Phys. Lett. **68**, 57 (1996).
- [24] S. Nakamura, T. Mukai and M. Senoh, Jpn. J. Appl. Phys. **31**, 2883 (1992).
- [25] S. Nakamura, T. Mukai and M. Senoh, Jpn. J. Appl. Phys. **32**, L16 (1993).
- [26] S. Nakamura and G. Fasol, The Blue Laser Diode, 1st ed. (Springer-Verlag, Heidelberg, 1997).
- [27] S. Nakamura, Jpn. J. Appl. Phys. **30**, L1705 (1991).
- [28] S. Nakamura, Microelec. J. **25**, 651 (1994).
- [29] T. Takeuchi, H. Takeuchi, S. Sota, H. Sakai, H. Amano and I. Akasaki, Jpn. J. Appl. Phys. **36**, L177 (1997).
- [30] T. Takeuchi, S. Sota, M. Katsuragawa, M. Komori, H. Takeuchi, H. Amano and I. Akasaki: Jpn. J. Appl. Phys. **36**, L382 (1997).
- [31] D. L. Smith and C. Mailhot: Phys. Rev. Lett. **58**, 1264 (1987).
- [32] M. B. Nardelli, K. Rapcewicz and J. Bernholc: Appl. Phys. Lett. **71**, 3135 (1997).
- [33] J. S. Im, H. Kollmer, J. Off, A. Sohmer, F. Scholz and A. Hangleiter: Phys. Rev. **B57**, R9435 (1998).
- [34] F. A. Kish and R. M. Fletcher, AlInGaP Light-Emitting Diodes, ed G. B. Stringfellow and M. G. Craford (Academic Press, San Diego, 1997) Semiconductors and Semimetals, Vol. 48, Chap. 5, p.149.
- [35] S. Strite and H. Morkoç, J. Vac. Sci & Technol. **B10**, 1237 (1992).
- [36] I. Ho and G. B. Stringfellow, Appl. Phys. Lett. **69**, 2701 (1996).
- [37] S. Nakamura, M. Senoh, S. Nagahama, N. Iwasa, T. Yamada, T. Matsushita, H. Kiyoku, Y. Sugimoto, T. Kozaki, H. Umemoto, M. Sano, and K. Chocho, Jpn. J. Appl. Phys. **36**, L1568 (1997).
- [38] A. Usui, H. Sunakawa, A. Sakai, A. Yamaguchi, Jpn. J. Appl. Phys. **36**, L899 (1997).
- [39] O. H. Nam, M. D. Bremser, T. Zheleva, R. F. Davis, Appl. Phys. Lett. **71**, 2638 (1997).
- [40] T. Mukai, K. Takekawa and S. Nakamura, Jpn. J. Appl. Phys. **37**, L839 (1998).
- [41] C. Sasaoka, H. Sunakawa, A. Kimura, M. Nido, A. Usui and A. Sakai, J. Crystal Growth, **189/190**, 61 (1998).
- [42] S. Nakamura, **281**, 956 (1998).
- [43] S. J. Rosner, E. C. Carr, M. J. Ludowise, G. Girolami, and H. I. Erikson, Appl. Phys. Lett. **70**, 420 (1997).
- [44] T. Sugahara, H. Sato, M. Hao, Y. Naoi, S. Kurai, S. Tottori, K. Yamashita, K. Nishino, L. T. Romano, and S. Sakai, Jpn. J. Appl. Phys. **37**, L398 (1998).



---

## **SESSION 1**

### **III-Nitride Light-Emitting Diodes**

# Progress and status of visible light emitting diode technology

R. Scott Kern\*

Hewlett-Packard Company, Optoelectronics Division, San Jose, CA 95131

## ABSTRACT

The light emitting diode (LED) is the dominant type of compound semiconductor device in terms of the epitaxial area of material produced as well as the number of devices fabricated and sold. Recent breakthroughs have resulted in dramatic performance increases for visible LEDs. Very high performance devices are commercially available using the AlGaInP materials system for red, orange and yellow and the InGaN system for green and blue. External quantum efficiencies greater than 10% are available for most colors, with greater than 20% having been achieved in red to orange. Currently, the luminous performance of LEDs exceeds that of traditional incandescent lamps for colors from red to green.

As a result of these advances, LEDs are becoming competitive in applications such as large area signs, traffic signals and automobile lighting. By mixing red, blue and green LEDs or by using phosphor-converted blue or ultraviolet devices, the creation of white light can be achieved, opening up additional applications. A review of the applications for high-brightness LED technology will also be presented.

**Keywords:** AlGaInP, InGaN, LED, OMVPE

## 1. INTRODUCTION

Organometallic vapor phase epitaxy (OMVPE) is the dominant growth technique in the high-volume production of AlGaInP and InGaN LEDs. A review of the properties and deposition of AlGaInP alloys as well as GaN and its alloys will be described. Data will also be presented on AlGaInP and InGaN chip designs and performance. Finally, a summary of state of the art device performance characteristics and an outlook for future possibilities for high-brightness visible LED technology will be detailed.

## 2. PROPERTIES AND GROWTH OF PHOSPHIDE AND NITRIDE LED MATERIALS

### 2.1. AlGaInP alloys

High-quality AlGaInP material is produced by growing an alloy of  $(\text{Al}_x\text{Ga}_{1-x})_{0.5}\text{In}_{0.5}\text{P}$  that is lattice-matched to a GaAs substrate. The energy band gap of AlGaInP materials is complicated by an effect known as atomic ordering<sup>1</sup>, or the formation of a monolayer scale GaP-InP (or AlP-InP) superlattice on {111} crystal planes. This occurs naturally under certain growth conditions and results in a reduction (up to 190 meV) in the band gap energy. Disordered AlGaInP can be obtained by growth on misoriented substrates (e.g., 15° from (100) toward [110]) or by post-growth annealing and is generally favored for high brightness LEDs since a lower Al-composition is needed to achieve a given wavelength. As such, the remainder of this discussion will focus on disordered material.

For disordered  $(\text{Al}_x\text{Ga}_{1-x})_{0.5}\text{In}_{0.5}\text{P}$  alloys, the luminescence efficiency is primarily limited by the direct-indirect band gap crossover. The energy band gaps for the direct and indirect valleys can be calculated as<sup>2,3</sup>:

$$E_T(x) = 1.91 + 0.61 x \quad (\text{eV}) \quad (1)$$

$$E_X(x) = 2.19 + 0.085 x \quad (\text{eV}) \quad (2)$$

These relationships predict the  $\Gamma$ -X crossover at 555 nm (2.23 eV) at an alloy composition of  $x = 0.53$ . The  $\lambda = 555$  nm crossover is consistent with both the shortest wavelength  $(\text{Al}_x\text{Ga}_{1-x})_{0.5}\text{In}_{0.5}\text{P}$  LEDs fabricated to date<sup>4,5</sup> and the shortest wavelength stimulated emission obtained from  $(\text{Al}_x\text{Ga}_{1-x})_{0.5}\text{In}_{0.5}\text{P}$  at an alloy composition of  $x = 0.56$ <sup>6</sup>. The exact position of the direct-indirect transition becomes critical when shorter wavelength devices are produced. In Figure 1, 300 K PL intensity is plotted against the Al composition of the  $(\text{Al}_x\text{Ga}_{1-x})_{0.5}\text{In}_{0.5}\text{P}$  alloy, and shows a marked decrease (Note the logarithmic scale.) as the  $x = 0.53$  composition is approached. Similarly, the efficiency of AlGaInP LED devices is very

\* Correspondence: E-mail: scott\_kern@hp.com, Phone: +1 (408) 435-4595, Fax: +1 (408) 435-6335

sensitive to wavelength in the yellow-green portion of the spectrum and drops rapidly as the wavelength gets shorter and more carriers populate the indirect X valley. Of course, the shorter wavelength devices also suffer from reduced carrier confinement in the active layer and more O incorporation in higher Al-composition active layers<sup>2</sup>.

The AlGaInP system is suitable for producing double heterostructure (DH) LEDs with both high injection efficiency and suitable carrier confinement. Since lattice matching to the GaAs substrate can be maintained for all ratios of Al to Ga, confining layers of both  $(\text{Al}_{0.7}\text{Ga}_{0.3})_{0.5}\text{In}_{0.5}\text{P}$  and InAlP are commonly used in DH devices. A band diagram of a typical  $(\text{Al}_x\text{Ga}_{1-x})_{0.5}\text{In}_{0.5}\text{P}$  DH is shown in Figure 2. The active layer can be tuned for emission from 650 nm ( $x = 0$ ) to 555 nm ( $x \sim 0.53$ ) and is typically between 0.3  $\mu\text{m}$  and 1  $\mu\text{m}$  thick.

N-type doping<sup>7</sup> of AlGaInP confining layers by OMVPE is usually performed using Te (DETe) or Si ( $\text{SiH}_4$  or  $\text{Si}_2\text{H}_6$ ). While both dopants can be used to create n-type layers, there are certain problems associated with each of them. For example, Te is a volatile impurity which exhibits a problematic memory effect and the thermal decomposition of  $\text{SiH}_4$  is incomplete at typical growth temperatures ( $T_p$ ), resulting in higher Si incorporation as growth temperature increases. However,  $\text{Si}_2\text{H}_6$  has a lower thermal stability and is less sensitive to growth temperature<sup>8</sup>. Regardless, high electron concentrations ( $>1 \times 10^{18} \text{ cm}^{-3}$ ) are easily obtained in  $(\text{Al}_x\text{Ga}_{1-x})_{0.5}\text{In}_{0.5}\text{P}$ .

In contrast, p-type doping of AlGaInP presents considerably more difficulty. The most common choices for p-type dopants are Zn (DMZn) and Mg ( $\text{Cp}_2\text{Mg}$ ). Like Te, Zn is very volatile, requiring a high partial pressure and frequent source changes. Higher O incorporation in the higher Al-content material may also contribute to the low hole concentration by compensating the Zn dopants. On the other hand, Mg is less volatile and has a smaller temperature dependence than Zn; however,  $\text{Cp}_2\text{Mg}$  also exhibits a memory effect, which includes a "Mg-delay" as the  $\text{Cp}_2\text{Mg}$  adheres to plumbing and reactor surfaces before incorporating into the growing film<sup>9</sup>. In addition, as the Al concentration increases, obtaining a sufficiently high hole concentration becomes more difficult, resulting from the larger ionization energy of Zn acceptors in the wider band gap material<sup>10</sup>. Also, passivation of acceptors by unintentional hydrogen incorporation during OMVPE growth and post-growth cooldown has been observed in AlGaInP alloys<sup>11</sup>. The degree of passivation depends on the post-growth cooling ambient and the sample cap layer design. Re-activation of the dopants occurs upon sample annealing as the hydrogen leaves the crystal. Considering the above difficulties, achieving high carrier concentrations over many growth runs is more challenging for holes than it is for electrons.

## 2.2. GaN and its alloys

Gallium nitride and all compositions of its alloys (AlGaIn, InGaIn and AlInGaIn) are direct band gap materials that exhibit a range of band gap energies<sup>12</sup> from 1.9 eV (InN) to 3.4 eV (GaN) to 6.2 eV (AlN). This makes them favorable for producing light emitters throughout the visible spectrum and partially into the ultraviolet. However, unlike the AlGaInP case, the materials that make up the AlN-GaN-InN materials system are much less understood and characterized.

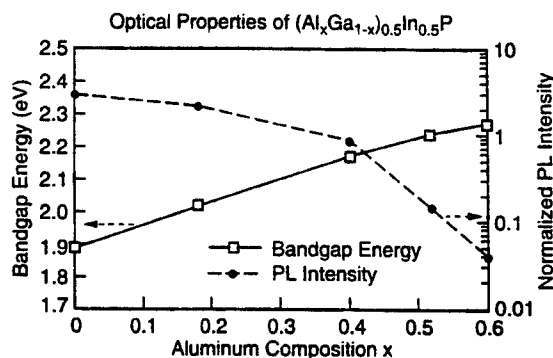


Figure 1. Photoluminescence (PL) intensity and band gap energy of  $(\text{Al}_x\text{Ga}_{1-x})_{0.5}\text{In}_{0.5}\text{P}$  alloys as a function of alloy composition  $x$ . Note the rapid decline in intensity as the  $x = 0.5$  composition is approached. Reprinted from *Semiconductors and Semimetals*, Vol. 48, *High Brightness Light Emitting Diodes*, eds. G. B. Stringfellow and M. G. Craford, 1997 with permission from Academic Press.

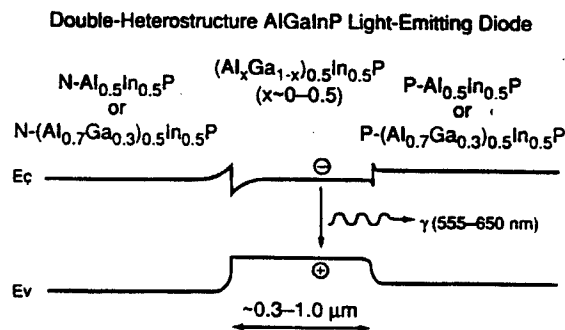


Figure 2. Schematic diagram of the energy band structure of a typical double-heterostructure  $(\text{Al}_x\text{Ga}_{1-x})_{0.5}\text{In}_{0.5}\text{P}$  LED. Reprinted from *Semiconductors and Semimetals*, Vol. 48, *High Brightness Light Emitting Diodes*, eds. G. B. Stringfellow and M. G. Craford, 1997 with permission from Academic Press.

Table I. Comparison of nitride materials properties with various substrates<sup>12</sup>

Material	Lattice Parameter (Å)	Thermal Conductivity (W cm <sup>-1</sup> K <sup>-1</sup> )	Coefficient of Thermal Expansion (K <sup>-1</sup> )
AlN(0001)	a = 3.112 c = 4.982	2.5	4.15 × 10 <sup>-6</sup> 5.27 × 10 <sup>-6</sup>
GaN(0001)	a = 3.189 c = 5.185	1.3	5.59 × 10 <sup>-6</sup> 7.75 × 10 <sup>-6</sup>
InN(0001)	a = 3.548 c = 5.760	-	-
6H-SiC(0001)	a = 3.080 c = 15.12	4.9	4.20 × 10 <sup>-6</sup> 4.68 × 10 <sup>-6</sup>
Al <sub>2</sub> O <sub>3</sub> (0001)	a = 4.758 c = 12.99	0.5	7.50 × 10 <sup>-6</sup> 8.50 × 10 <sup>-6</sup>

One of the critical issues for III-V nitride epitaxy is the choice of a suitable substrate. Unlike other III-V materials that are deposited on either homoepitaxial or lattice-matched substrates, bulk GaN (and AlN) single crystal substrates are not commercially available, although they have been produced in research laboratories<sup>13-16</sup>. As a result, alternate substrates, none of them capable of adequately matching the lattice and thermal properties of the nitrides, have been extensively studied. Table I shows the properties of the nitride materials and various substrates used in nitride epitaxy.

By far, the majority of the epitaxial growth of nitrides is performed on sapphire (Al<sub>2</sub>O<sub>3</sub>) and silicon carbide (SiC) substrates which are well suited for the extreme thermal and corrosive environment experienced during nitride epitaxial growth. In both cases, large differences in lattice parameter and coefficient of thermal expansion between the substrate and the epilayer(s) create problems with respect to producing high quality films. Thus, OMVPE growth of GaN directly on either substrate at typical growth temperatures (1000-1100 °C) has been shown to result in films with very poor electrical, optical and structural properties. However, the insertion of a thin nucleation layer remedies this problem and allows the crystal grower the ability to improve the quality of the layers considerably. Specifically, when using sapphire substrates, a thin AlN<sup>17</sup> or GaN<sup>18</sup> buffer layer is deposited at temperatures between 450 and 700 °C. The use of these intermediate nucleation layers markedly improves the quality and properties of the subsequently grown GaN which is grown at temperatures >1000 °C<sup>17</sup>. On these nucleation layers, GaN growth proceeds via a multistep process<sup>19</sup> including recrystallization and geometric selection until an oriented domain structure emerges as shown in Figure 3. In contrast, growth on SiC substrates is usually initiated at high temperature (>1000 °C) with the deposition of a thin buffer layer of AlN<sup>20</sup>, which has a much better lattice match to SiC than does GaN. Regardless of the substrate used, high quality GaN can be

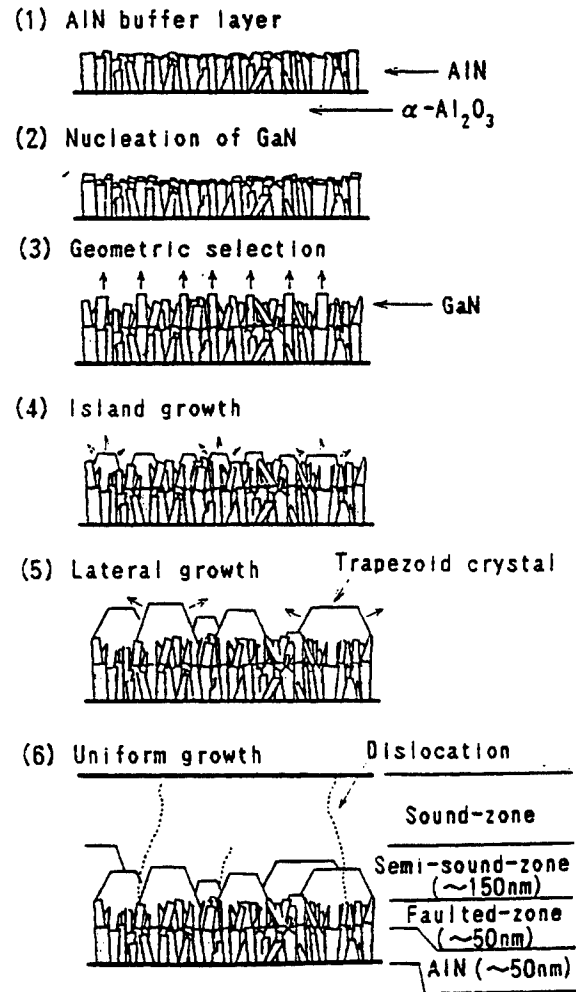


Figure 3. Schematic diagrams showing the growth process of GaN on sapphire. Reprinted from *Journal of Crystal Growth* 115, K. Hiramatsu, S. Itoh, H. Amano, I. Akasaki, N. Kawano, T. Shiraishi, and K. Oki, "Growth mechanism of GaN grown on sapphire with AlN buffer layer by MOVPE", pp. 628-633, 1991, with permission from Elsevier Science.

grown by OMVPE with the introduction of a suitable nucleation layer between the substrate and epitaxial film. However, due to the cost and availability issues associated with SiC substrates, sapphire is the predominant substrate used for nitride epitaxy and LED production. As such, LEDs produced on sapphire will be the primary focus of this text.

Growing InGaN, the active region in nitride optoelectronic devices involves decreasing the deposition temperature substantially from that used in (Al)GaN deposition. Due to the low dissociation of temperature of InN, the growth of high quality InGaN must be performed at temperatures of 850 °C or lower. Complicating matters, the cracking efficiency of NH<sub>3</sub> decreases dramatically with decreasing temperature due to the high kinetic barrier for breaking the N-H bonds in the molecule. Since temperatures used in the growth of InGaN are higher than the decomposition temperature of the TMIn source, the result can be the formation of In droplets if a suitable amount of activated N is not present on the surface of the growing layer<sup>21-24</sup>.

Other matters related to the materials system also make high quality InGaN layers difficult to produce. Lattice mismatch between both InGaN/GaN and InGaN/AlGaN can both be as high as 10% or more, generating misfit dislocations and promoting three-dimensional growth and mosaicity even at very low layer thicknesses<sup>25</sup>. Poor interfacial areas between different compositional layers are also likely due to poor nucleation of the mismatched layer due to low deposition temperature, lattice parameter mismatch and low surface mobility of adatoms. Phase separation<sup>26,27</sup> and spinodal decomposition<sup>28</sup> due to solid phase immiscibility<sup>29,30</sup> have also been reported for InGaN.

To combat these problems, several techniques have been simultaneously applied in order to achieve the highest quality InGaN layers. First, InGaN films are grown at temperatures that are much lower than those used for GaN to reduce the dissociation of In-N bonds and the reevaporation of In. It is found that significant In does not begin to incorporate until growth is performed below 850 °C<sup>31</sup>. Second, InGaN films are often grown using V/III ratios significantly higher than those used in GaN growth in order to offset the reduction in NH<sub>3</sub> cracking efficiency and to partially suppress the decomposition of the In-N bonds<sup>32,33</sup>. Third, due to etching of In by H<sub>2</sub> even at very low concentrations, N<sub>2</sub> is usually used as the carrier gas for InGaN growth<sup>31,34,35</sup>. Fourth, the brightest LEDs employ quantum wells 3 nm or less in thickness<sup>36-38</sup>, thus reducing the effects of the lattice and phase incompatibility that exists. Despite these advances in the deposition of high quality InGaN, differences in the growth conditions between (Al)GaN and InGaN force the crystal grower to successfully implement at least two growth interrupts in order to achieve the gradients in temperature, growth ambient and NH<sub>3</sub> concentration necessary to deposit nitride optoelectronic devices.

Similar to AlGaInP, n-type doping of GaN is usually performed using Si (SiH<sub>4</sub> or Si<sub>2</sub>H<sub>6</sub>) and p-type doping with Mg (Cp<sub>2</sub>Mg). Both Si and Mg atoms preferentially incorporate on the Group III metal (Ga) lattice site and introduce shallow levels in the band gap. In general, nitride films can be doped very heavily n-type (>10<sup>19</sup> cm<sup>-3</sup>); however, cracking of the films becomes a progressively more significant issue as layer thickness and doping increase. As a result, n-GaN films are usually 3-4 μm thick and doped at levels <10<sup>19</sup> cm<sup>-3</sup>. Similar to AlGaInP, high p-type conductivity is difficult to achieve in the nitrides. In fact, as deposited, GaN:Mg films are highly resistive due to the presence of Mg-H complexes that form during growth and on cooling. These complexes effectively remove the acceptor level from the band gap<sup>39</sup>. In order to achieve conductivity, the dopant is generally activated by low-energy electron-beam irradiation (LEEBI)<sup>40</sup> or by thermal annealing<sup>41</sup>. Since Mg is a relatively deep acceptor dopant, it is heavily compensated and only a small portion of it is ionized at room temperature, incorporation levels typically run about one to two orders of magnitude higher than the hole concentration achieved. Thus, films containing hole concentrations in the 10<sup>17</sup>-10<sup>18</sup> cm<sup>-3</sup> range have Mg concentration levels above 10<sup>19</sup> cm<sup>-3</sup>, seriously challenging the solubility limits of the host (GaN) material<sup>42,43</sup>. In fact, the hole concentration has been demonstrated to increase with increasing Mg concentration to a point, before showing a negative correlation, indicative of the crossing of a solubility limit. Even the most conductive p-GaN films exhibit resistivities 20-50 times higher than those achieved in the n-type layers of typical InGaN LEDs.

### 3. LED CHIP DESIGNS

#### 3.1. AlGaInP LED chips

A typical AlGaInP LED device (Figure 4) consists of a cube-shaped chip (p-side up) with a circular top contact in the center of the chip. Due to poor current spreading laterally through the p-type layer in this geometry, recombination occurs only in the region below the top contact, which subsequently absorbs a significant portion of the resulting light emission. A modified top contact geometry (e.g. with current spreading fingers) is sometimes used to combat this problem. However,



this solution is only moderately effective for current spreading in the case of AlGaInP LEDs that rely solely on high resistance ( $x > 0.7$ )  $(\text{Al}_x\text{Ga}_{1-x})_{0.5}\text{In}_{0.5}\text{P}$  upper-confining layers.

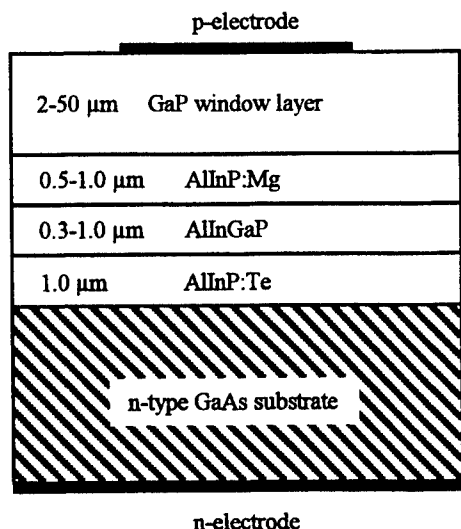


Figure 4. Schematic diagram of an AlGaInP LED. Reprinted from *Semiconductors and Semimetals*, Vol. 48, *High Brightness Light Emitting Diodes*, eds. G. B. Stringfellow and M. G. Craford, 1997 with permission from Academic Press.

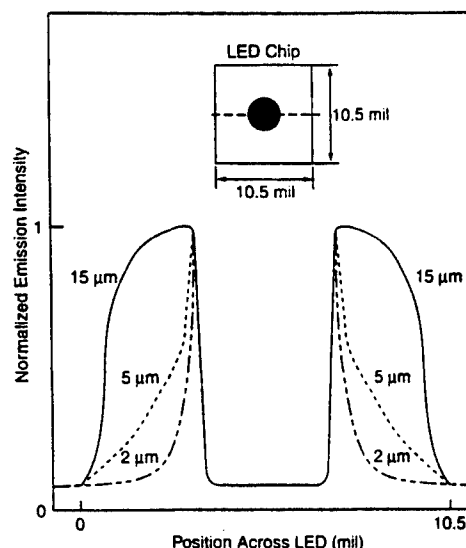


Figure 5. Emission intensity across an AlGaInP LED chip with different GaP window thicknesses. Reprinted from *Semiconductors and Semimetals*, Vol. 48, *High Brightness Light Emitting Diodes*, eds. G. B. Stringfellow and M. G. Craford, 1997 with permission from Academic Press.

The most effective solution to the problem of current spreading in high-brightness AlGaInP LEDs is the growth of a highly conductive transparent window layer on top of the AlGaInP DH. Both AlGaAs and GaP have been successfully employed as window layers on AlGaInP LEDs. The AlGaAs window was developed at Toshiba Corporation<sup>44</sup>, and the GaP window structure was pioneered at Hewlett-Packard Company<sup>4</sup>.  $\text{Al}_x\text{Ga}_{1-x}\text{As}$  is a convenient choice of window material because it is lattice matched to the AlGaInP DH, is transparent from the red to yellow-green when  $x > 0.7$  and can be heavily doped p-type. Additionally, OMVPE can be used to grow the  $\text{Al}_x\text{Ga}_{1-x}\text{As}$  directly on top of the DH as part of a single epitaxial growth run. The largest potential drawback to the use of  $\text{Al}_x\text{Ga}_{1-x}\text{As}$  as a window layer, however, is its instability with respect to water vapor (hydrolyzation)<sup>45</sup>. GaP windows also have the advantages of good transparency and high p-doping, but exhibit a 3.6% lattice mismatch to the underlying AlGaInP DH layers. TEM investigation of the GaP to DH interface reveals a dense network of dislocations in the first 100-200 nm of the GaP, but these dislocations do not propagate downward into the area where they could harm the quality of the DH. The presence of these dislocations does not adversely affect the conductivity or transparency of the window. The GaP may be grown by OMVPE, or made much thicker ( $\sim 50 \mu\text{m}$ ) by hydride vapor phase epitaxy (VPE) regrowth on the DH. The effect of GaP window thickness on current spreading efficiency is demonstrated in Figure 5. The normalized intensity profile across the LED chip is plotted as a function of position. Outside the dip in the curve created by the ohmic contact, the effect of improved current spreading with increasing window thickness is shown by the nearly flat intensity profile for the  $15 \mu\text{m}$  thickness.

Another technique to avoid top contact shadowing in AlGaInP LEDs is the use of a current-blocking structure. In this case current is forced to spread away from the top contact by using a reverse biased p-n junction to block current from flowing into the active layer under the top contact. This structure has been successfully combined with a thin ( $\sim 5\text{-}7 \mu\text{m}$ ) AlGaAs window in the production of commercial high-brightness AlGaInP LEDs<sup>46</sup>.

### 3.2. Further advances resulting in improved light extraction for AlGaInP LED chips

The ultimate measure of LED performance is the external quantum efficiency, or the number of photons emitted per the number of electrons (or holes) injected. In general, the external efficiency of LEDs is much lower than the internal efficiency due to the difficulty in extracting light from the high-index semiconductor chip. The light generation in the

active layer of the device is randomly directed. For a generic AlGaInP LED grown on GaAs, the photons traveling toward the top surface of the chip have a reasonable probability of escape, while the light headed for the GaAs substrate will most likely be absorbed by the lower band gap substrate material. High-brightness AlGaInP LEDs often incorporate features aimed at improving the light extraction efficiency. For example, more of the upward traveling photons can be extracted through the same "window" layers that were described previously for their utility as current spreaders<sup>5</sup>. In order to capture some of the downward propagating light, the growth of distributed Bragg reflectors (DBRs) to reflect light back up to the chip surface has been used successfully. Also, a new technology exists to replace the absorbing GaAs substrate with a transparent substrate, and results in the escape of even more of the downward traveling light.

Consider the simplified schematic of an AlGaInP LED chip shown in Figure 6. The AlGaInP DH of this chip is thin ( $<5 \mu\text{m}$ ) and is grown directly on the GaAs substrate. The amount of upward traveling light that can be emitted from this chip is determined by Snell's law, which states the critical angle for total internal reflection as:

$$\theta_c = \sin^{-1}(n_1/n_2) \quad (3)$$

where  $n_2$  is the index of refraction of the GaP window and  $n_1$  is the index of the medium surrounding the chip. Using 3.4 as the index of the window, we obtain a critical angle of  $17.1^\circ$  for emission into air. When the chip is encapsulated in low-index epoxy ( $n_1 \sim 1.5$ ), the critical angle increases to  $26.2^\circ$ . The apex of the upward directed cone (called an acceptance cone) of Figure 6 is double the critical angle in each case, and represents the rays of light that may escape from an infinitesimal emitting area within the chip. The extraction ratio of the cone is simply

$$(1 - \cos \theta_c)/2 = 0.051 \quad (4)$$

for the encapsulated device. Next, taking into account the Fresnel losses

$$\text{Losses} = (n_1/n_2 - 1)^2 / (n_1/n_2 + 1)^2 \quad (5)$$

at the chip/epoxy interface, there is an additional loss of 15%. Thus, we are left with only a 4.4 % extraction efficiency when only the top cone is available for emission.

The effect of window thickness on the light extraction efficiency of AlGaInP LEDs can be understood by considering the sideways directed cone (Window thickness has little effect on top cone extraction.) drawn in Figure 6. Only one of the four possible side cones is drawn for simplicity. For the case of a thin window, many of the rays nearly parallel to the active layer will be totally internally reflected from the top of the chip and absorbed in the substrate before reaching the sidewall. The fraction of the side light captured from an infinitesimal active area may be calculated from the solid angle of intersection between the sideways escape cone and the sidewall of the window layer. Integrating the solid angle of intersection over the total emitting area for each of the four sidewalls results in the total side light extraction efficiency. Clearly, as the light extraction window gets thicker, the angle of intersection increases until the entire half-cone shown in Figure 6 is accommodated. Calculations on the extraction efficiency of a single cone is  $\sim 4.4\%$ . Thus, an AlGaInP chip with a suitably thick window layer may have a theoretical extraction efficiency (for the top cone plus the four half side cones) approaching  $\sim 13\%$ . Good agreement between the theory and experiment exists, demonstrating the advantage of growing thick GaP window layers on top of AlGaInP DH layers by hydride VPE.

While large improvements in light extraction are possible by using a thick window layer, most of the light is still lost in the absorbing GaAs substrate. Two approaches for reducing the amount of light lost in the substrate have been used successfully in commercial AlGaInP devices and are shown schematically in Figure 7. Figure 7 (a) shows a device containing a highly reflective DBR grown between the active layer and the substrate as well as a current blocking layer and thin ( $5\text{--}7 \mu\text{m}$ ) window layer to facilitate current spreading. Such a device structure has yielded external quantum efficiencies as high as  $\sim 7\%$  for AlGaInP devices operating at  $610 \text{ nm}$ <sup>47</sup>. Figure 7 (b) depicts a transparent substrate (TS)

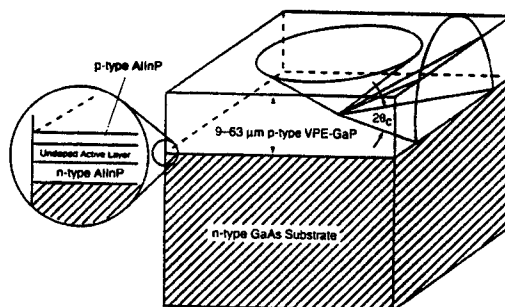


Figure 6. Simplified schematic of an AlGaInP chip with a thick VPE GaP window. The top and one of the four side acceptance cones are indicated. Reprinted from *Semiconductors and Semimetals*, Vol. 48, *High Brightness Light Emitting Diodes*, eds. G. B. Stringfellow and M. G. Craford, 1997 with permission from Academic Press.

device formed by lattice matched OMVPE growth of a DH on a GaAs substrate, followed by a compound semiconductor wafer bonding process to replace the GaAs with a thick GaP substrate<sup>48</sup>.

Comparing the light extraction efficiencies of the two devices of Figure 7, we again invoke the cones of acceptance. A comparison of DBR LEDs and TS AlGaInP LEDs is shown in Figure 8. The DBR device shown in Figure 8 (a) can at best result in 2 full escape cones for single pass light, or an extraction efficiency of  $2 \cdot 4.4\% = 8.8\%$ . This assumes little side emission in the device, which consists of only a thin window grown by OMVPE. For practical DBR devices, the limited angular bandwidth of the mirror reflectivity can result in imperfect capture of the bottom escape cone, especially when considering encapsulated devices. The TS AlGaInP device shown in Figure 8 (b) can result in the extraction of 6 full escape cones for the ideal case, or  $6 \cdot 4.4\% = 26.4\%$ . However, top and bottom contact absorption may play a significant role in the TS device, with the absence of any current blocking structure, reducing the effective escape cones to between 5 and 6 (22-26.4% extraction efficiency). Absorption in the active layer will also detract from the light extraction of both DBR and TS LEDs. The above calculations ignore any additional light extraction from randomization effects or from the extraction of multiple pass light from the chip (most prevalent in the TS structure). However, from the above arguments, the TS AlGaInP LED structure results in a two-fold increase in light extraction efficiency compared to an absorbing substrate (AS) AlGaInP LED with a thick GaP window and a 250% improvement over a thin window DBR LED.

The improved light extraction of TS AlGaInP LEDs is shown experimentally in Figure 9. Here, we compare the light and current (L-I) curves of an (a) AS AlGaInP LED lamp (with a GaP window) to (b) a TS AlGaInP lamp made from the same wafer. As expected, the improved light extraction from the TS device results in a doubling of the light output of the AS device. The wafer-bonded TS AlGaInP devices have been shown to be

compatible with high volume production<sup>49</sup> while matching the reliability performance of AS AlGaInP LEDs<sup>50</sup>.

The high external quantum efficiencies attainable in TS AlGaInP LEDs are plotted in Figure 10 as a function of wavelength. The device structures consist of  $\sim 1 \mu\text{m}$   $(\text{Al}_x\text{Ga}_{1-x})_{0.5}\text{In}_{0.5}\text{P}$  active layers sandwiched inside  $\text{In}_{0.5}\text{Al}_{0.5}\text{P}$  confining layers in the configuration shown in Figure 7 (b). The highest external quantum efficiency ( $\sim 23.7\%$ ) is obtained at 635 nm, while the efficiencies degrade significantly at shorter wavelengths, falling to  $\sim 2.2\%$  at 571.4 nm. At 635 nm, the external quantum efficiency is consistent with the above arguments concerning light extraction efficiency, assuming a high internal efficiency. While absorption in the chip may worsen somewhat at shorter wavelengths, there is clearly an erosion of internal efficiency for AlGaInP LEDs at shorter wavelengths. This is expected for wavelengths near the direct-indirect transition as carriers begin to populate the indirect minima according to Boltzmann statistics. The internal quantum efficiency can be computed as:

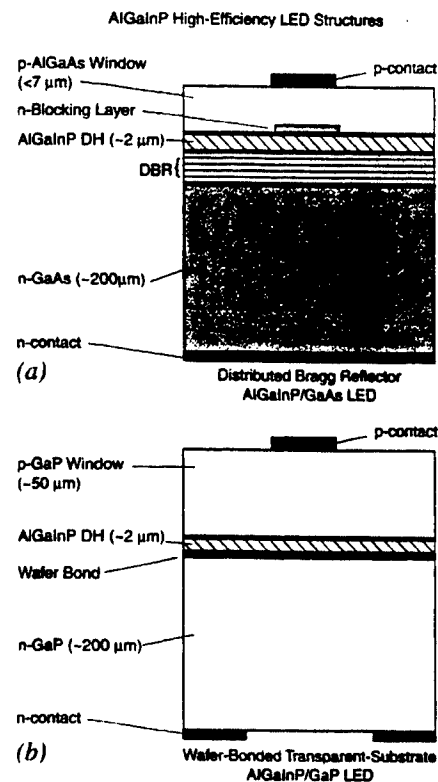


Figure 7. Schematic representation of (a) DBR AlGaInP LED structure with a thin window layer and (b) a wafer-bonded TS AlGaInP LED. Reprinted from *Semiconductors and Semimetals*, Vol. 48, *High Brightness Light Emitting Diodes*, eds. G. B. Stringfellow and M. G. Craford, 1997 with permission from Academic Press.

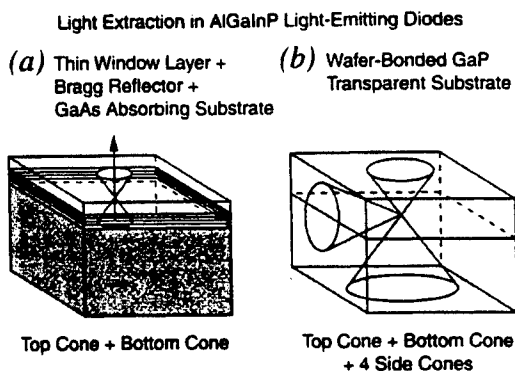


Figure 8. Schematic depiction of light extraction in (a) a DBR LED ( $\sim 2$  cones) and (b) a TS LED ( $\sim 6$  cones). Reprinted from *Semiconductors and Semimetals*, Vol. 48, *High Brightness Light Emitting Diodes*, eds. G. B. Stringfellow and M. G. Craford, 1997 with permission from Academic Press.

$$\eta_{int} = \{1 + (\tau/\tau_{nr})(1 + N \exp[-\Delta E/kT])\}^{-1} \quad (6)$$

where  $\tau_r$  and  $\tau_{nr}$  are the radiative and non-radiative lifetimes respectively,  $N$  is the relative density of states in the indirect minima, and  $\Delta E$  is the energy separation between the direct and indirect minima. Multiplying Equation 6 by the extraction efficiency for TS AlGaInP LEDs yields the theoretical curves for  $\eta_{ext}$  drawn in Figure 10 for three different  $\tau_r/\tau_{nr}$  ratios: (a) 3.5, (b) 1.3 and (c) 0.2, corresponding to  $\eta_{int}$  values of (a) 82%, (b) 43% and (c) 22%. The experimental data shown in Figure 10 show a much larger short-wavelength decrease in  $\eta_{ext}$  than predicted from carrier overflow. Smaller carrier confinement and injection efficiency may contribute to this decrease in the 570-590 nm wavelength regime, but the general trend toward lower internal efficiency at shorter wavelengths has been attributed to increasing concentrations of non-radiative recombination centers in higher Al-composition active layers<sup>51</sup>. The incorporation of oxygen<sup>52</sup> into AlGaInP has been directly correlated to decreases in  $\eta_{ext}$ . Clearly, the growth of high-quality AlGaInP LEDs by OMVPE requires great attention to issues of source purity and reactor integrity to minimize the degradation in internal quantum efficiency due to incorporation of non-radiative defects.

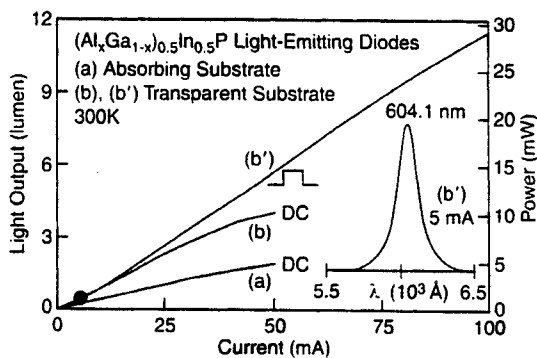


Figure 9. Light output vs. drive current for (a) an AS AlGaInP LED and (b) a TS AlGaInP LED. The curve labeled (b') is the TS LED in (b) operated in pulsed mode. Reprinted from *Semiconductors and Semimetals*, Vol. 48, *High Brightness Light Emitting Diodes*, eds. G. B. Stringfellow and M. G. Craford, 1997 with permission from Academic Press.

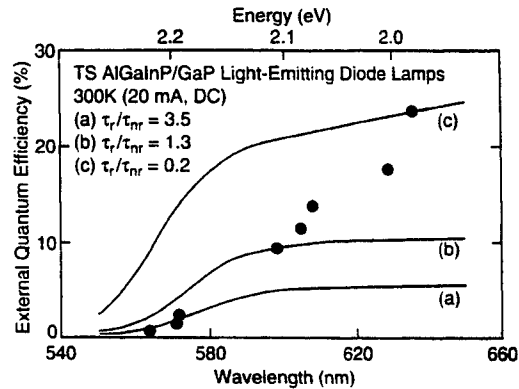


Figure 10. External quantum efficiency vs. wavelength for TS AlGaInP/GaP LEDs and theoretical fits obtained using Boltzmann statistics for radiative/non-radiative lifetime ratios of (a) 3.5, (b) 1.3 and (c) 0.2. Reprinted from *Semiconductors and Semimetals*, Vol. 48, *High Brightness Light Emitting Diodes*, eds. G. B. Stringfellow and M. G. Craford, 1997 with permission from Academic Press.

### 3.3. InGaN LED Chips

Generally, InGaN LEDs are grown with the p-side up on insulating sapphire substrates. Since the substrate itself is not conductive, nitride chips require that etching be performed to expose the n-type layer and that both contacts be placed on the top side of the device. Early versions of InGaN LEDs<sup>53,54</sup> relied on a DH structure involving a thick InGaN active region that was codoped with Si and Zn to achieve a donor-acceptor (D-A) transition for the light emission mechanism. Problems associated with the saturation of this emission center, very broad emission spectra and package degradation due to the considerable quantity of short wavelength (generally UV) light led to the introduction of a thinner active medium consisting of single quantum well (SQW) or multiple quantum well (MQW) InGaN active region LEDs whose emission was based on band gap transitions. By using these quantum well structures, researchers have been able to eliminate the co-doping feature of InGaN LEDs resulting in brighter devices with improved spectral quality and reliability.

A typical Hewlett-Packard InGaN LED chip is shown in Figure 11. The InGaN LED device structures consist of an InGaN/GaN composite nucleation layer, a GaN:Mg intermediate layer, a 3.5  $\mu\text{m}$  thick layer of GaN:Si, an InGaN active region containing either a SQW or MQW stack, a 300  $\text{\AA}$  thick layer of  $\text{Al}_{0.05}\text{Ga}_{0.95}\text{N:Mg}$  and a 0.2  $\mu\text{m}$  thick layer of GaN:Mg. Since the p-type GaN:Mg and AlGaIn:Mg layers are relatively resistive and thin, the p-type contact placed on these layers is generally a thin, semi-transparent metal designed to achieve suitable current spreading (thus overcoming the poor conductivity of the thin p-type AlGaIn and GaN layers) and transparency for light to escape. Figure 11 shows the

typical contact and device patterning used in H-P's blue, cyan and green InGaN LED production. It is important to note that, unlike the LEDs schematics presented for the AlGaInP case, both the n- and p-contacts are placed on the topside of the InGaN LED device after a mesa is etched to reveal the n-type GaN. This is due to the insulating substrate on which the structure is deposited.

Unlike AlGaInP, InGaN LEDs, are grown on substrates that are transparent to the emitted light. Thus, the primary focus to improving the efficiency of InGaN LEDs primarily involves the improvement of the internal efficiency. Due to the large lattice and thermal mismatches<sup>12</sup> in the AlN-GaN-InN-sapphire system, considerable care must be taken to ensure high quality interfaces. The growth of InGaN is performed at conditions far from equilibrium (i.e., at very low temperature relative to the growth of the other layers within the structure) on a surface that may contain a high density of pits and pinholes due to the high dislocation density. When the wafers are raised to higher temperature to grow the remainder of the structure, there exists the possibility of phase separation, clustering and dissociation. Additionally, due to the difficulties in achieving highly doped p-type (Al)GaN and the very short minority carrier diffusion length for holes in this materials system, achieving the accurate placement of the p-n junction in these structures is paramount to attaining high performance LEDs.

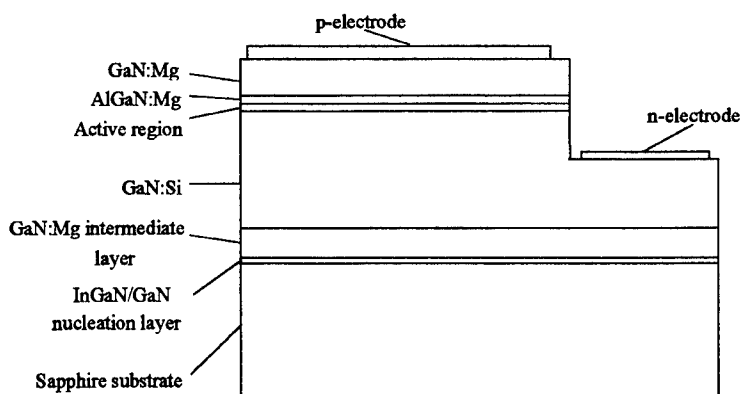


Figure 11. Schematic of a Hewlett-Packard InGaN LED. The active region depicted can consist of either a single or multiple quantum well.

#### 4. SUMMARY AND CONCLUSIONS

A review of the current techniques used to maximize the efficiency of a new class of high-brightness LEDs based on the  $(\text{Al}_x\text{Ga}_{1-x})_{0.5}\text{In}_{0.5}\text{P}$  material system has been presented. The commercialization of AlGaInP technology using OMVPE has resulted in a number of sophisticated device structures to enhance performance, including double heterostructure (DH) active regions, current blocking layers, and current spreading layers that address the problem of efficient carrier injection across useful areas of the chip. Devices with enhanced light-extraction efficiency have been produced by VPE growth of GaP on top of the AlGaInP DH, by OMVPE growth of DBRs for improved bottom-light extraction, and by the development of a TS AlGaInP technology utilizing compound semiconductor wafer bonding. As a result of these advances, AlGaInP LEDs now have luminous efficiencies that far exceed those of conventional LEDs. In fact, the best TS AlGaInP devices now exceed the luminous efficiency of unfiltered incandescent bulbs ( $\sim 15 \text{ lm/W}$ ) over the yellow-green to red wavelength range.

With the commercialization of InGaN quantum well LEDs in the blue through green spectral regions, there now exist solid-state light sources spanning the entire visible spectral region. Figure 12 shows the luminous efficiency versus wavelength for the current state-of-the-art in commercial visible LEDs. High-brightness LEDs in the yellow-green through red-orange spectral region are commercially produced with the AlGaInP material system and in the

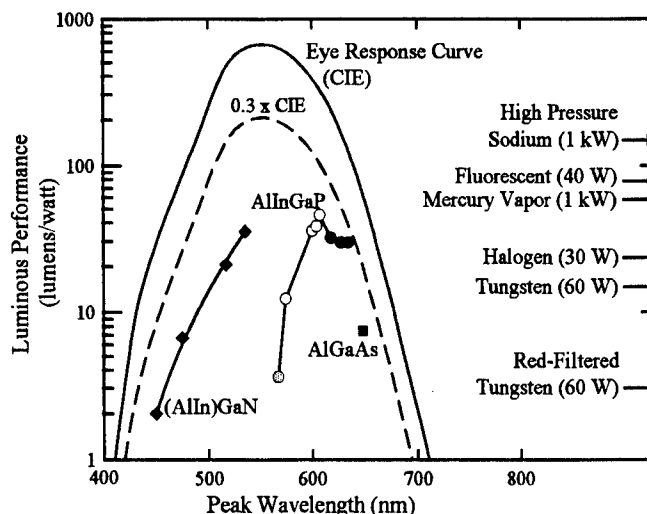


Figure 12. The luminous performance of various LED material systems vs. emission wavelength.

red spectral region with the transparent-substrate AlGaAs material system. In addition, Figure 12 shows luminous performance values for a number of conventional light sources and also the human eye response curve (CIE curve) which describes the theoretical limit for luminous efficiency. The  $0.3 \times$  CIE curve is included for reference. To the right side of the chart are the performance levels for numerous conventional lighting sources. At wavelengths from 500 nm to 650 nm, LED sources can easily compete in efficiency with tungsten filament and halogen lamps.

It is readily apparent that solid-state LEDs are rapidly encroaching upon the performance levels of traditional light sources and in most cases significantly exceed filtered filament-based light of a specific color. Several major markets are being addressed with these newly developed solid state light sources. Automobile exterior lighting has been moving rapidly to incorporate transparent-substrate AlGaInP technology into high-mount stop lights (HMSLs) and into the full amber and red-orange taillight assembly. Full color outdoor changeable message signs and full-motion video displays have been adopting (Al)InGaP and AlGaInP technologies and will continue to proliferate as costs are reduced. Traffic signal applications have begun to incorporate red AlGaInP and AlGaAs LEDs for stop lights and are moving toward incorporating amber and blue-green LEDs to produce a completely LED-based signal head.

All of these new markets are rapidly expanding and will provide enormous growth opportunities for the LED industry in the future. The inherent advantages of LED technology over incandescent lamps include high reliability, low power consumption, and a tolerance for harsh environmental conditions. Currently, LEDs are already serious contenders for many outdoor lighting applications. Continued improvement in materials growth and device technology will allow LEDs to compete with an ever broader range of traditional lighting sources.

## REFERENCES

1. A. Goyma, T. Suzuki, K. Kobayashi, S. Kawata, I. Hino, and T. Yuasa, "Evidence for the existence of an ordered state in  $\text{Ga}_{0.5}\text{In}_{0.5}\text{P}$  grown by metalorganic vapor phase epitaxy and its relation to band-gap energy," *Appl. Phys. Lett.* **50**, pp. 673-675 (1987).
2. D.S. Cao, A. W. Kimball, and G. B. Stringfellow, "Atmospheric pressure organometallic vapor-phase epitaxial growth of  $(\text{Al}_x\text{Ga}_{1-x})_{0.51}\text{In}_{0.49}\text{P}$  (x from 0 to 1) using trimethylalkyls," *J. Appl. Phys.* **67**, pp. 739-744 (1990).
3. A. D. Prins, J. L. Sly, A. T. Meney, D. J. Dunstan, E. P. O'Reiley, A. R. Adams, and A. Valster, "High pressure determination of AlInGaP band structure," *J. Phys. Chem. Solids* **56**, pp. 349-352 (1995).
4. R. M. Fletcher, C. P. Kuo, T. D. Osentowski, K. H. Huang, M. G. Craford, and V. M. Robbins, "The growth and properties of high performance AlInGaP emitters using a lattice mismatched GaP window layer," *J. Electron. Mater.* **20**, pp. 1125-1130 (1991).
5. K. H. Huang, J. G. Yu, C. P. Kuo, R. M. Fletcher, T. D. Osentowski, L. J. Stinson, M. G. Craford, and A. S. H. Liao, "Twofold efficiency improvement in high performance AlInGaP light-emitting diodes in the 555-620 nm spectral region using a thick GaP window layer," *Appl. Phys. Lett.* **61**, pp. 1045-1047 (1992).
6. C. P. Kuo, R. M. Fletcher, T. D. Osentowski, M. G. Craford, D. W. Nam, N. Holonyak, Jr., K. C. Hsieh, and J. E. Fouquet, "Stimulated emission in  $\text{In}_{0.5}(\text{Al}_x\text{Ga}_{1-x})_{0.5}\text{P}$  quantum well heterostructures," *J. Crystal Growth* **93**, pp. 389-395 (1988).
7. G. B. Stringfellow, "The role of impurities in III/V semiconductors grown by organometallic vapor phase epitaxy," *J. Crystal Growth* **75**, pp. 91-100 (1986).
8. T. F. Kuech, E. Veuhoff, and B. S. Meyerson, "Silicon doping of GaAs and  $\text{Al}_x\text{Ga}_{1-x}\text{As}$  using disilane in metalorganic chemical vapor deposition," *J. Cryst. Growth* **68**, pp. 48-53 (1984).
9. Y. Nishikawa, H. Sugawara, and Y. Kokubun, "Anomalous Mg incorporation behavior in InGaAlP grown by metalorganic chemical vapor deposition," *J. Crystal Growth* **119**, pp. 292-296 (1992).
10. Y. Nishikawa, M. Ishikawa, Y. Tsuburai, and Y. Kokubun, "Effects of Zn electrical activity on band gap energy in Zn-doped InGaAlP grown by metalorganic chemical vapor deposition," *Jpn. J. Appl. Phys.* **28**, pp. L2092-L2094 (1989).
11. S. Minagawa, and M. Kondow, "Effect of substrate orientation on Zn-doping of AlGaInP grown by atmospheric pressure organometallic vapor phase epitaxy," *J. Electron. Mater.* **19**, pp. 597-599 (1990).
12. S. Strite and H. Morkoç, "GaN, AlN, and InN: A review," *J. Vac. Sci. Technol.* **B10**, pp. 1237-1266 (1992).
13. S. Porowski, "High pressure growth of GaN-new prospects for blue lasers," *J. Cryst. Growth* **166**, pp. 583-589 (1996).

14. C. M. Balkas, Z. Sitar, T. Zheleva, L. Bergman, R. Nemanich, and R. F. Davis, "Sublimation growth and characterization of bulk aluminum nitride single crystals," *J. Cryst. Growth* **179**, pp. 363-370 (1997).
15. S. Kurai, K. Nishino, and S. Sakai, "Nucleation control in the growth of bulk GaN by sublimation method," *Jpn. J. Appl. Phys.* **36B**, pp. L184-L186 (1997).
16. V. A. Ivantsov, V. A. Sukhoveev, and V. A. Dmitriev, "GaN Crystals Grown from a Liquid Phase at Reduced Pressure," *Mater. Res. Soc. Symp. Proc.* **468**, pp. 143-148 (1997).
17. I. Akasaki, H. Amano, Y. Koide, K. Hiramatsu, and N. Sawaki, "Effects of AlN buffer layer on crystallographic structure and on electrical and optical properties of GaN and  $\text{Ga}_{1-x}\text{Al}_x\text{N}$  ( $0 < x \leq 0.4$ ) films grown on sapphire substrate by MOVPE," *J. Cryst. Growth* **98**, pp. 209-219 (1989).
18. S. Nakamura, "GaN growth using GaN buffer layer," *Jpn. J. Cryst. Growth* **30**, pp. L1705-L1707 (1991).
19. K. Hiramatsu, S. Itoh, H. Amano, I. Akasaki, N. Kawano, T. Shiraishi, and K. Oki, "Growth mechanism of GaN grown on sapphire with AlN buffer layer by MOVPE," *J. Cryst. Growth* **115**, pp. 628-633 (1991).
20. T. W. Weeks, Jr, M. D. Bremser, K. S. Ailey, E. Carlson, W. G. Perry, and R. F. Davis, "GaN thin films deposited via organometallic vapor phase epitaxy on  $\alpha(6H)\text{-SiC}(0001)$  using high-temperature monocrystalline AlN buffer layers," *Appl. Phys. Lett.* **67**, pp. 401-403 (1995).
21. M. Shimizu, K. Hiramatsu, and N. Sawaki, "Metalorganic vapor phase epitaxy growth of  $(\text{In}_x\text{Ga}_{1-x}\text{N}/\text{GaN})$  layered structures and reduction of indium droplets," *J. Cryst. Growth* **145**, pp. 209-213 (1994).
22. C. J. Sun, J. W. Yang, Q. Chen, B. W. Lim, M. Z. Anwar, M. A. Khan, H. Temkin, D. Weismann, and I. Brenner, "Photoluminescence study of high quality InGaN/GaN single heterojunctions," *Appl. Phys. Lett.* **69**, pp. 668-671 (1996).
23. S. M. Bedair, F. G. McIntosh, J. C. Roberts, E. L. Piner, K. S. Boutros, and N. A. El-Masry, "Growth and characterization of In-based nitride compounds," *J. Cryst. Growth* **178**, pp. 32-44 (1997).
24. H. Lu, M. Thonthathiri, Z. Wu, and I. Bhat, "Study of indium droplets formation on the  $\text{In}_x\text{Ga}_{1-x}\text{N}$  films by single crystal x-ray diffraction," *J. Electron. Mater.* **26**, pp. 281-284 (1997).
25. H. Sato, Y. Naoi, and S. Sakai, "X-ray diffraction analysis of GaN and GaN/InGaN/GaN double-hetero structures grown on sapphire substrate by metalorganic chemical vapor deposition," *Jpn. J. Appl. Phys.* **36**, pp. 2018-2021 (1997).
26. L. T. Romano, M. D. McCluskey, B. S. Krusor, D. P. Bour, C. Chua, S. Brennan, and K. M. Yu, "Phase separation in annealed InGaN/GaN multiple quantum wells," *J. Cryst. Growth* **189/190**, pp. 33-36 (1998).
27. R. Singh, D. Doppalapudi, T. D. Moustakas, and L. T. Romano, "Phase separation in InGaN thick films and formation of InGaN/GaN double heterostructures in the entire alloy composition," *Appl. Phys. Lett.* **70**, pp. 1089-1091 (1997).
28. N. A. El-Masry, E. L. Piner, S. X. Liu, and S. M. Bedair, "Phase separation in InGaN grown by metalorganic vapor phase epitaxy," *Appl. Phys. Lett.* **72**, pp. 40-42 (1998).
29. I. Ho and G. B. Stringfellow, "Solid phase immiscibility in GaInN," *Appl. Phys. Lett.* **69**, pp. 2701-2703 (1996).
30. A. Wakahara, T. Tokuda, X. Z. Dang, S. Noda, and A. Sasaki, "Compositional inhomogeneity and immiscibility of a GaInN ternary alloy," *Appl. Phys. Lett.* **71**, pp. 906-908 (1997).
31. S. Nakamura and T. Mukai, "High-quality InGaN films grown on GaN films," *Jpn. J. Appl. Phys.* **31**, pp. L1457-L1459 (1992).
32. P. A. Grudowski, C. J. Eiting, J. Park, B. S. Shelton, D. J. H. Lambert, and R. D. Dupuis, "Properties of InGaN quantum-well heterostructures grown on sapphire by metalorganic chemical vapor deposition," *Appl. Phys. Lett.* **71**, pp. 1537-1539 (1997).
33. A. Koukitu, N. Takahashi, T. Taki, and H. Seki, "Thermodynamic analysis of MOVPE growth of  $\text{In}_x\text{Ga}_{1-x}\text{N}$ ," *J. Cryst. Growth* **170**, pp. 306-311 (1997).
34. A. Koukitu, N. Takahashi, T. Taki, and H. Seki, "Thermodynamic analysis of  $\text{In}_x\text{Ga}_{1-x}\text{N}$  alloy composition grown by metalorganic vapor phase epitaxy," *Jpn. J. Appl. Phys.* **35**, pp. L673-L675 (1996).
35. E. L. Piner, M. K. Behbehani, N. A. El-Masry, F. G. McIntosh, J. C. Roberts, K. S. Boutros, and S. M. Bedair, "Effect of hydrogen on the indium incorporation in InGaN epitaxial films," *Appl. Phys. Lett.* **70**, pp. 461-464 (1997).
36. S. Nakamura, M. Senoh, N. Isawa, and S. Nagahama, "High-brightness InGaN blue, green and yellow light-emitting diodes with quantum well structures," *Jpn. J. Appl. Phys.* **34A**, pp. L797-L799 (1995).

37. S. Nakamura, M. Senoh, N. Isawa, and S. Nagahama, "High-power InGa<sub>N</sub> single-quantum-well-structure blue and violet light-emitting diodes," *Appl. Phys. Lett.* **67**, pp. 1868-1870 (1995).
38. S. Nakamura, M. Senoh, N. Isawa, S. Nagahama, T. Yamada, and T. Mukai, "Superbright green InGa<sub>N</sub> single-quantum-well-structure light-emitting diodes," *Jpn. J. Appl. Phys.* **34**, pp. L1332-L1335 (1995).
39. J. Neugebauer, and C. G. V. d. Walle, "Role of hydrogen in doping of GaN," *Appl. Phys. Lett.* **68**, pp. 1829-1831 (1996).
40. H. Amano, M. Kito, K. Hiramatsu, and I. Akasaki, "P-type conduction in Mg-doped GaN treated with low-energy electron beam irradiation," *Jpn. J. Appl. Phys.* **28**, pp. L2112-L2114 (1989).
41. S. Nakamura, N. Iwasa, M. Senoh, and T. Mukai, "Hole compensation mechanism in p-type GaN films," *Jpn. J. Appl. Phys.* **31A**, pp. 1258-1266 (1992).
42. C. Yuan, T. Salagaj, A. Gurary, A. G. Thompson, W. Kroll, R. A. Stall, C.-Y. Hwang, M. Schurman, Y. Li, W. E. Mayo, Y. Lu, S. Krishnakutty, I. K. Shmagin, R. M. Kolbas, and S. J. Pearton, "Investigation of n- and p-type doping of GaN during epitaxial growth in a mass production scale multiwafer-rotating-disk reactor," *J. Vac. Sci. Technol. B* **13**, pp. 2075-2080 (1995).
43. D. P. Bour, H. F. Chung, W. Götz, L. Romano, B. S. Krusor, D. Hofstetter, S. Rudaz, C. P. Kuo, F. A. Ponce, N. M. Johnson, M. G. Craford, and R. D. Bringans, "Characterization of OMVPE-Grown AlGaInN Heterostructures," *Mater. Res. Soc. Proc.* **449**, pp. 509-518 (1997).
44. H. Sugawara, M. Ishikawa, and G. Hatakoshi, "High-efficiency InGaAlP/GaAs visible light-emitting diodes," *Appl. Phys. Lett.* **58**, pp. 1010-1012 (1991).
45. J. M. Dallesasse, N. El-Zein, N. Holonyak, Jr., K. C. Hsieh, R. D. Burnham, and R. D. Dupuis, "Environmental degradation of Al<sub>x</sub>Ga<sub>1-x</sub>As-GaAs quantum-well heterostructures," *J. Appl. Phys.* **68**, pp. 2235-2238 (1990).
46. H. Sugawara, K. Itaya, H. Nozaki, and G. Hatakoshi, "High-brightness InGaAlP green light-emitting diodes," *Appl. Phys. Lett.* **61**, pp. 1775-1777 (1992).
47. K. Itaya, H. Sugawara, and G. Hatakoshi, "InGaAlP visible light laser diodes and light-emitting diodes," *J. Cryst. Growth* **138**, pp. 768-775.
48. F. A. Kish, F. M. Steranka, D. C. Defever, D. A. Vanderwater, K. G. Park, C. P. Kuo, T. D. Osentowski, M. J. Peanasky, J. G. Yu, R. M. Fletcher, D. A. Steigerwald, M. G. Craford, and V. M. Robbins, "Very high-efficiency semiconductor wafer-bonded transparent-substrate (Al<sub>x</sub>Ga<sub>1-x</sub>)<sub>0.5</sub>In<sub>0.5</sub>P/GaP light-emitting diodes," *Appl. Phys. Lett.* **64**, pp. 2839-2841 (1994).
49. G. E. Hofler, D. A. Vanderwater, D. C. Defever, F. A. Kish, M. D. Camras, F. M. Steranka, and I.-H. Tan, "Wafer bonding of 50-mm diameter GaP to AlInGaP-GaP light emitting diode wafers," *Appl. Phys. Lett.* **69**, pp. 803-805 (1996).
50. F. A. Kish, D. A. Vanderwater, D. C. Defever, D. A. Steigerwald, G. E. Hofler, K. G. Park, and F. M. Steranka, "Highly reliable and efficient semiconductor wafer-bonded AlInGaP/GaP light emitting diodes," *Electron. Lett.* **32**, pp. 132-134 (1996).
51. M. Suzuki, M. Ishikawa, K. Itaya, Y. Nishikawa, G. Hatakoshi, Y. Kokubun, J. Nishizawa, and Y. Oyama, "Electrical characterization of Si-donor-related shallow and deep states in InGaAlP alloys grown by metalorganic chemical vapor deposition," *J. Cryst. Growth* **115**, pp. 498-503 (1991).
52. M. Suzuki, K. Itaya, Y. Nishikawa, H. Sugawara, and M. Okajima, "Reduction of residual oxygen incorporation and deep levels by substrate misorientation in AlInGaP alloys," *J. Cryst. Growth* **133**, pp. 303-308 (1993).
53. S. Nakamura, T. Mukai, and M. Senoh, "Candela-class high-brightness InGa<sub>N</sub>/AlGa<sub>N</sub> double-heterostructure blue-light-emitting diodes," *Appl. Phys. Lett.* **64**, pp. 1687-1689 (1994).
54. S. Nakamura, T. Mukai, and M. Senoh, "High-brightness InGa<sub>N</sub>/AlGa<sub>N</sub> double-heterostructure blue-green-light-emitting diodes," *J. Appl. Phys.* **76**, pp. 8189-8191 (1994).



# InGaN blue light-emitting diodes with optimized n-GaN layer

Ivan Eliashevich\*, Yuxin Li†, Andrei Osinsky‡, Chuong A. Tran, Michael G. Brown,  
Robert F. Karlicek, Jr.

Emcore Corporation, 394 Elizabeth Ave., Somerset NJ 08873

## ABSTRACT

In the extensive research dedicated recently to metal-organic chemical vapor deposition (MOCVD)-grown high-efficiency GaN LED device design, a significant effort has been made to increase the conductivity of p-GaN layers, while n-GaN layers received relatively little attention. We demonstrated, both experimentally and theoretically, that the resistivity of n-GaN layers has a profound effect on blue InGaN LED performance. Optimization of n-GaN epitaxial layers allows the achievement of device series resistances below 15 Ohms and forward voltages as low as 2.9 Volts at 20 mA. We have also shown that contactless measurements of sheet resistivity of the entire LED epitaxial structure closely correlate with the ohmic resistance of the GaN layer measured in the fabricated devices. This provides an excellent non-destructive characterization tool for n-GaN optimization. Insufficient n-GaN conductivity is shown to trigger a distinct degradation mechanism by initiating current crowding in a localized device area. InGaN LED lamps with optimized n-GaN layers had a high external quantum efficiency and a good long-term reliability.

**Keywords:** gallium nitride, n-GaN, light-emitting diode, resistivity, reliability

## 1. INTRODUCTION

High-efficiency blue and green GaN light-emitting diodes were rapidly developed by a number of academic and industrial laboratories after their first introduction by S. Nakamura et al. in the early 1990s<sup>1,2</sup>. In spite of that, basic properties of the new GaN-based materials and devices still continue to present significant challenges for researchers (light generation mechanisms in InGaN low-dimensional structures, details of p-dopant activation in GaN, and transport properties of columnar epitaxial GaN, to name a few). Furthermore, fierce competition between research groups often prevented early publication of interesting results, especially those related to device design and degradation modes (e.g. physics of transparent metal contact formation). This paper intends to fill in one of the gaps in the overall GaN LED publicly available body of knowledge by clarifying some effects of n-GaN layer doping on device performance and reliability.

GaN LED structures grown on insulating sapphire substrate require both n-type and p-type ohmic contacts to be applied to the same side of the epitaxial wafer. Access to the bottom side of the p-n junction (usually, n-type) is provided by etching a mesa structure through the top p-type layers and p-n junction into n-type material. N-type ohmic contact may be subsequently formed to the exposed n-GaN surface while p-type contact is made to the mesa top surface. As a result of such contact geometry, lateral current path optimization becomes necessary in order to achieve uniform light emission and low series resistance in the range of current densities and temperatures corresponding to the LED operating conditions.

When considering the optimum thickness of the n-GaN layer, several limitations should be taken into account imposed by the lattice-mismatch between the sapphire substrate and the epitaxial GaN structure. Usually, a low growth temperature nucleation layer is deposited immediately on the substrate and that layer necessarily has an extremely high dislocation density. A few microns of high growth temperature GaN or nitride heterostructure material is required to remove the active region away from the highly defective surface. Cracking of the epitaxial film may occur above certain critical thickness

\*Correspondence: Email: elia@emcore.com; WWW: <http://www.emcore.com>; Telephone: 732 271 9090x4129; Fax: 732 560-5790

†Current address: Anadigics, Inc., 35 Technology Drive, Warren, New Jersey 07059

‡Current address: NZ Applied Technologies, 8A Gill Street, Woburn, Massachusetts 01801

which depends, among other factors, on the doping level of the layer. That critical thickness decreases with increased impurity level in Si-doped n-GaN. A recently issued US patent<sup>3</sup> suggests a three-layer structure intended to prevent cracking and allow a thicker defect reduction GaN layer to be grown. The proposed structure consists of a thick ( $\sim 3.5 \mu\text{m}$ ) undoped buffer followed by a thin ( $< 0.4 \mu\text{m}$ ) n-doped contact layer and a lightly n-doped cladding layer providing optimum electron injection into the InGaN active region. However, optimization of the lateral current path resistance in the structure is not considered and is likely to present a problem due to insufficient thickness of the contact layer. Experiments and calculations presented in this paper are based on a traditional structure with a single n-layer which serves as a defect reduction, lateral current spreading, n-contact, and cladding layer simultaneously. We believe our approach to the optimization of n-GaN layer is applicable to the current spreading and reliability improvement in a variety of LED structures.

## 2. MATERIAL GROWTH AND CHARACTERIZATION

LED epitaxial structures were grown on [0001]-oriented sapphire by MOCVD as described in a separate publication<sup>4</sup>. The multi-layer structures consisted of an undoped GaN nucleation layer,  $4 \mu\text{m}$ -thick Si-doped n-GaN layer, an undoped InGaN multi-quantum well (MQW) active layer, a Mg-doped p-AlGaIn cladding layer, and a Mg-doped p-GaN contact layer. Silane and  $\text{Cp}_2\text{Mg}$  were used as n-type and p-type dopant sources, respectively. The structures used in this experiment differed by the doping level of n-GaN layer varying from  $\sim 5 \times 10^{16} \text{ cm}^{-3}$  (background carrier concentration) to  $3 \times 10^{18} \text{ cm}^{-3}$ . Acceptors in the p-layers were activated by rapid thermal annealing (RTA), producing a typical carrier concentration of approximately  $7 \times 10^{17} \text{ cm}^{-3}$ . Carrier concentration and mobility in p-type and n-type layers were measured in single-layer samples using the Hall technique with dot contacts in a Van der Pauw configuration. Hole mobility in  $2 \mu\text{m}$ -thick p-GaN films varied between 10 and  $20 \text{ cm}^2\text{V}^{-1}\text{s}^{-1}$ . Electron mobility in  $2 \mu\text{m}$ -thick n-GaN films as a function of carrier concentration is shown in Figure 1.

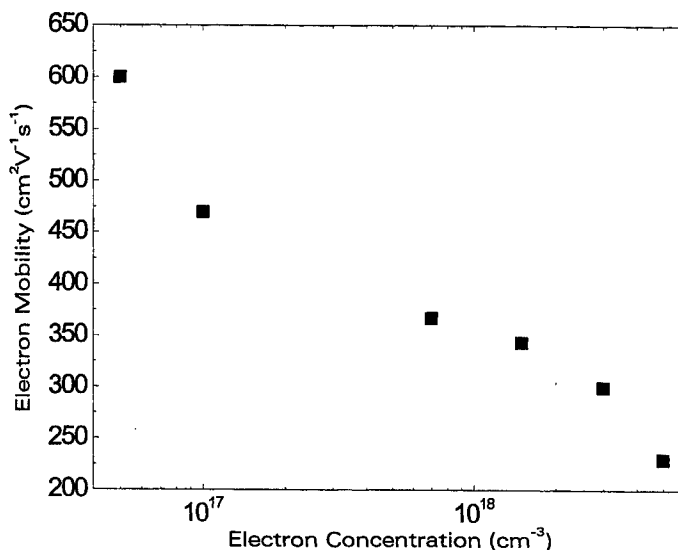


Figure 1. Hall electron mobility vs carrier concentration in  $2 \mu\text{m}$ -thick n-GaN samples.

Sheet resistivity of the full LED structures was measured using Lehigh 1310B Resistivity Mapper. Based on Hall measurement results, we believe the Lehigh data to be representative of the n-GaN resistivity only, since low-mobility p-type layers hardly contribute to the overall conductance. Figure 2 shows a comparison of the n-GaN conductivity calculated from the Hall and Lehigh data. The results are in excellent agreement at high doping levels, while Hall conductivity is consistently lower than Lehigh for the samples with electron concentration below  $1 \times 10^{18} \text{ cm}^{-3}$ . This may be explained by relatively poor geometric and electrical quality of dot contacts to low-doped n-GaN. By comparison, contactless Lehigh measurements may be expected to be more accurate for low-doped samples.

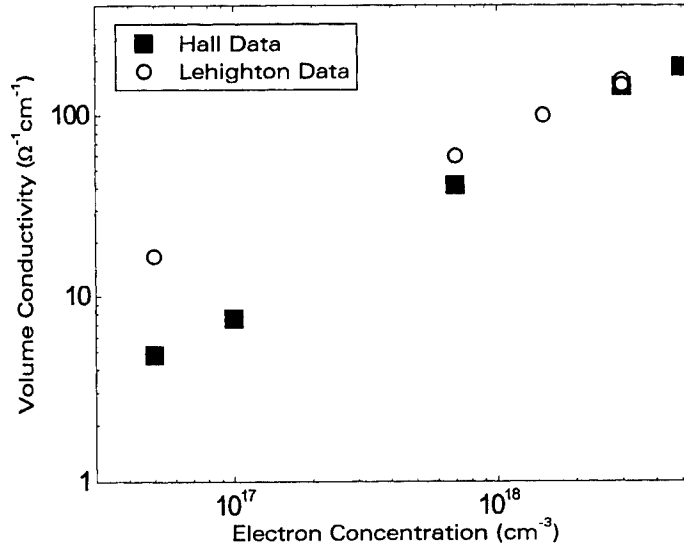


Figure 2. Volume n-GaN conductivity vs carrier concentration. Solid squares - calculated from Hall data for 2  $\mu\text{m}$ -thick n-GaN films. Open circles - calculated from Lehigh resistivity data for LED structures with 4  $\mu\text{m}$ -thick n-GaN layers).

### 3. DEVICE FABRICATION

A typical LED device test structure is shown in Figure 3. The mesa formation allowing an access to n-GaN layers was defined by Reactive Ion Etching using standard photolithographic techniques with  $400 \times 400 \mu\text{m}^2$  total chip area and  $\sim 350 \times 350 \mu\text{m}^2$  mesa area. A Ni/Au transparent metal contact was deposited on p-GaN surface on top of the mesa in order to improve lateral current spreading. Ti/Al n-pad providing ohmic contact to the RIE etched n-GaN surface and Ni/Au p-bonding pad (both pads had  $\sim 100 \mu\text{m}$  diameter) were defined using standard photolithographic techniques, deposited by e-beam evaporation, and annealed by RTA. For power measurements and aging tests, wafers were separated into individual chips using high-speed Kulicke & Soffa 982-6 Wafer Saw. Chips were mounted on TO-18 transistor headers with silver-filled epoxy, and wire-bonded.

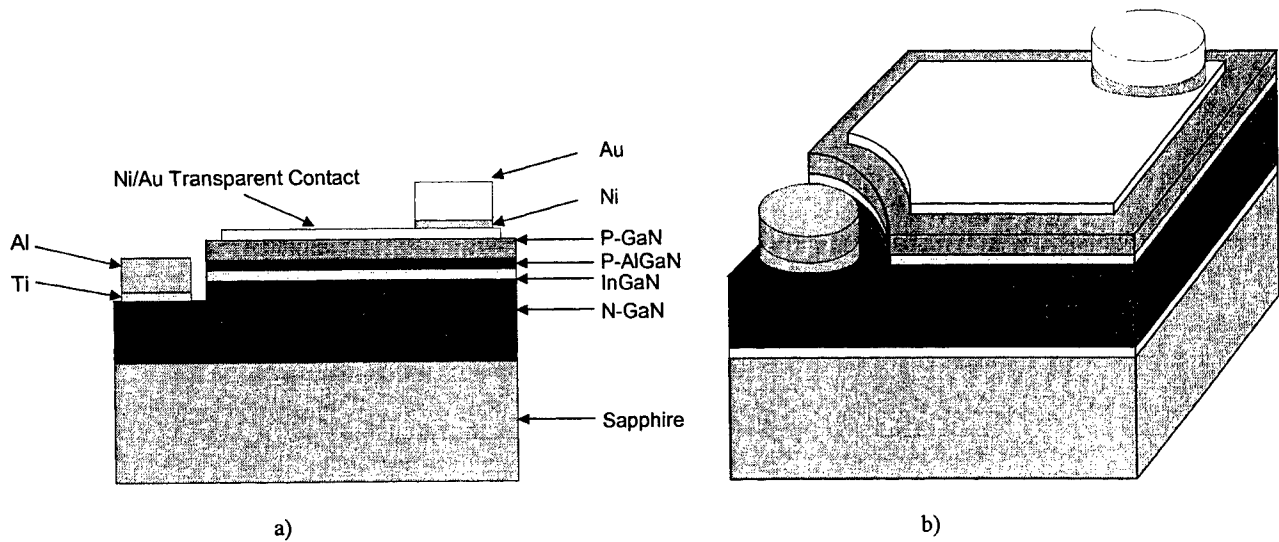


Figure 3. The structure of InGaN blue LED: a) schematic cross section; b) chip overview.

N-type ohmic contact specific resistivity measured using a circular transmission line pattern was well below  $1 \times 10^{-4} \Omega \text{cm}^2$  for all samples, corresponding to n-contact resistance  $< 1 \Omega$ . In order to directly evaluate the n-GaN layer contribution to the total resistivity of the actual devices, n-pad to n-pad resistances were measured for adjacent die on wafers before separation using a 4-wire method. Current path geometry in this test approximately corresponds to the lateral current path through n-GaN layer during the diode operation. Figure 4 demonstrates a reduction of n-GaN layer resistance with increased Si doping and an excellent correlation with Lehighton resistivities measured on the same wafers before processing. Such a correlation provides a non-destructive post-growth characterization tool capable of early detection of the n-GaN-related problems associated with silane source depletion, background Mg compensation, or high defect density in the grown material. This method is far superior to the Hall technique for quick and accurate evaluation of the whole epitaxial wafer immediately after growth without any additional sample preparation.

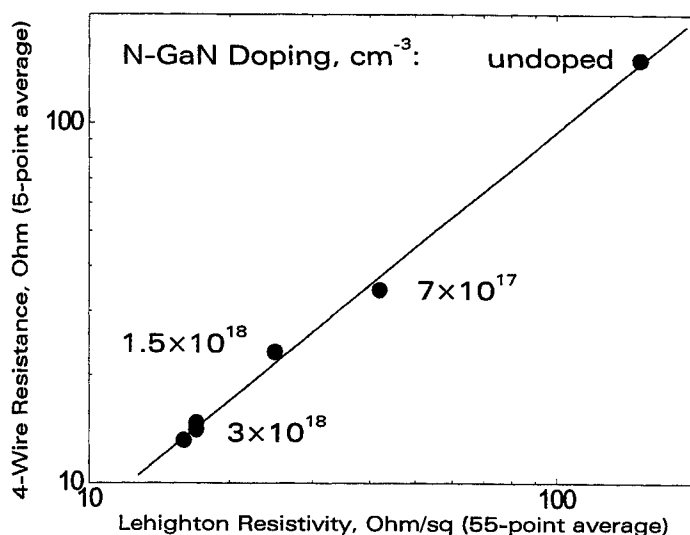


Figure 4. N-pad to n-pad resistance for GaN LEDs with varying n-GaN doping vs Lehighton resistivity of as-grown epitaxial wafers. Solid line shows linear fit.

#### 4. LATERAL CURRENT PATH CALCULATIONS

In order to understand how n-GaN conductivity affects LED current-voltage characteristics, light output, and reliability, possible current paths from p-pad to n-pad need to be analyzed. Cross-section of the LED structure showing two adjacent devices on a wafer is shown in Figure 5.

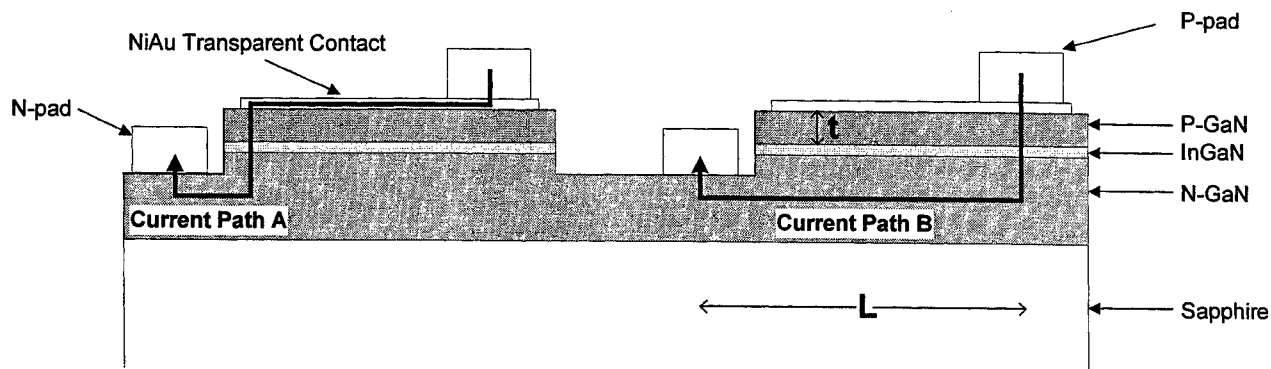


Figure 5. Current flow geometry in GaN LED with lateral current path.

The transparent Ni/Au metal layer may be considered a perfect current spreader with negligible contribution to the total resistance, and only the vertical component of the p-layers' resistance is significant. We shall ignore the resistance of the ohmic contacts here for simplification. Total voltage drop  $V_T$  along an arbitrary current path between the two contacts is then given by the sum of voltage drops across the p-layers  $V_p$ , p-n junction  $V_j$ , and n-layer  $V_n$  as

$$V_T = V_p + V_j + V_n = j\rho_p t + (nkT/e) \times (1 + \ln j/j_0) + j\rho_n l \quad (1)$$

where  $j$  is the current density,  $\rho_p$  and  $t$  are vertical resistivity and thickness of p-type layers,  $n$  is the diode ideality factor,  $k$  is the Boltzmann constant,  $T$  is the junction temperature,  $e$  is the elementary charge,  $j_0$  is the saturation current density,  $\rho_n$  and  $l$  are lateral resistivity of n-GaN and length of the lateral current path through the n-type layer. Two extreme cases of the lateral current paths are shown in Figure 5. Path A corresponds to the case when all lateral current spreading occurs in the transparent contact while the voltage drop across the n-layer is minimal, i.e.  $l \sim 0$ . Path B corresponds to the opposite situation when all lateral current spreading occurs in the n-layer, i.e.  $l = L$ , where  $L$  is the distance between p- and n-pads.

Perfectly uniform current spreading across the active area of the LED is possible when total voltage drop across Path A

$$V_T^A = j\rho_p t + (nkT/e) \times (1 + \ln j/j_0) \quad (2)$$

is equal to the voltage drop across Path B

$$V_T^B = j\rho_p t + (nkT/e) \times (1 + \ln j/j_0) + j\rho_n L \quad (3)$$

which gives a condition

$$\rho_n L \ll \rho_p t + j^{-1} \times (nkT/e) \times (1 + \ln j/j_0) \quad (4)$$

When the resistivity of the n-GaN layer is low enough for condition (4) to be observed, all current paths have equal resistance, causing the current density and light emission intensity to be uniform across the mesa surface. The voltage drop across the p-n junction  $V_j$  is typically larger than  $V_p$ , and  $L \gg t$ . As a result, resistance of the n-GaN along the lateral current path  $\rho_n L$  may still be comparable or higher than the vertical resistance of the p-type layers and ohmic contacts. Condition (4) only assures uniform current spreading but series resistance of the device may still be limited by n-GaN conductivity.

Current path A becomes preferable to any other when n-GaN conductivity is insufficient to meet condition (4). In this case, current is crowding into that path, and light emission region is limited to the edge of the mesa immediately adjacent to the n-contact pad. This process is usually self-enhancing, since series resistance and voltage drop across the junction in semiconductors tend to decrease with higher current density due to local heating, increased local carrier concentration, and minority carrier leakage through the heterostructure space-charge region. In addition to low n-GaN conductivity, other factors making such current crowding more likely include high overall current injection (due to  $j^{-1}$  factor in (4)), and high operating temperature which also reduces voltage drop across the junction and may negatively affect electron mobility. This phenomenon is highly undesirable in most LED structures, since current crowding may make far-field emission pattern of an LED less uniform. It may also jeopardize device reliability by increasing the rate of defect generation and propagation in the localized region with high injection current density.

Condition (4) may be easily estimated numerically. For room temperature conditions and operating current  $\sim 20$  mA, voltage drop across the p-n junction  $V_j$  roughly corresponds to the bandgap of the active region  $E_g/e \sim 2.7$  V. For p-GaN resistivity estimated from Hall measurement data to be  $\rho_p \sim 0.6 \Omega\text{cm}$ , thickness of p-GaN layer  $\sim 0.3 \mu\text{m}$ , and  $L \sim 350 \mu\text{m}$ , condition (4) for the conductivity of n-GaN material becomes  $\sigma_n = 1/\rho_n \gg 4 \Omega^{-1}\text{cm}^{-1}$ . As can be seen from Figure 2, electron concentration in n-GaN only needs to be above  $5 \times 10^{17} \text{ cm}^{-3}$  for this condition to be met.

## 5. LED PERFORMANCE

Current-voltage characteristics and light emission patterns of the LEDs with varying n-GaN doping were recorded using HP4145 Semiconductor Parameter Analyzer and Polaroid MicroCam photographic camera mounted on an optical

microscope. Indeed, at room temperature we observed uniform light intensity for any n-GaN doping level equal or higher than  $7 \times 10^{17} \text{ cm}^{-3}$ . Total device series resistance measured from p-pad to n-pad at 20 mA operation current point varied from 15 to 50  $\Omega$  and exceeded the n-pad to n-pad n-GaN resistance by  $\sim 1$  to 25  $\Omega$  depending on the contributions from p-type ohmic contacts and p-type GaN and AlGaIn layers. As shown in Figure 6, for the LEDs with the highest n-GaN doping of  $3 \times 10^{18} \text{ cm}^{-3}$ , and optimized transparent contact annealing, total series resistance dropped below 15  $\Omega$ . For the same diodes, forward voltage as low as 2.9 V at 20 mA was consistently observed which is, to the best of our knowledge, the lowest value reported in the literature.

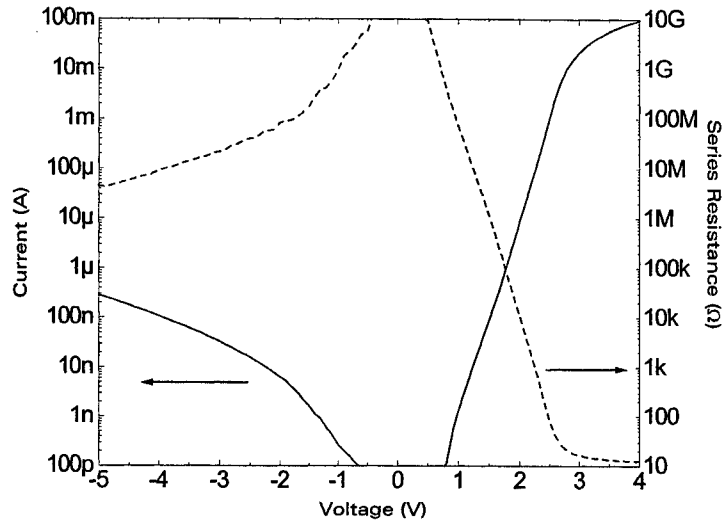


Figure 6. Current-voltage (left axis) and resistance-voltage (right axis) characteristics for GaN LEDs with n-GaN doping  $3 \times 10^{18} \text{ cm}^{-3}$ .

Total output power from the chips mounted on headers was measured in an integrating sphere with Si detector. Power output above 3 mW at 20 mA was achieved, with a linear power-current characteristic in a wide range of operating currents (see Figure 7).

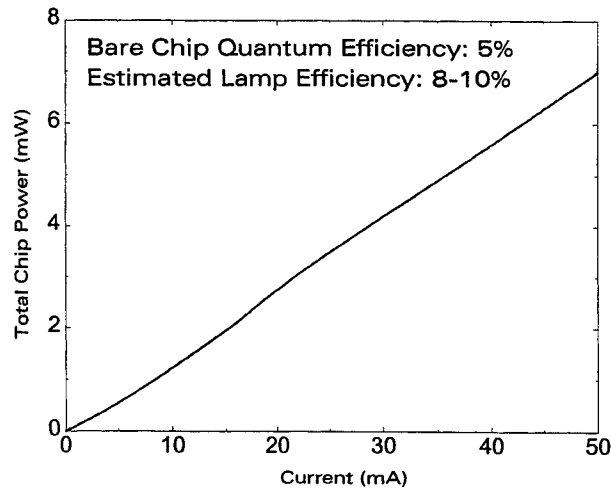


Figure 7. Power-current characteristic for GaN LED with n-GaN doping  $3 \times 10^{18} \text{ cm}^{-3}$ .

The only devices demonstrating current crowding at room temperature were those with n-GaN doped only unintentionally to  $\sim 5 \times 10^{16} \text{ cm}^{-3}$ . Series resistance of those devices was in the range 80-130  $\Omega$ , consistently below the n-pad to n-pad resistance

of  $\sim 150 \Omega$ , unlike in the LEDs with doped n-GaN. This corresponds to the current path A, where the carriers do not spread all the way across the resistive n-GaN layer.

## 6. LED RELIABILITY

Aging tests were performed for LEDs with n-GaN doping  $7 \times 10^{17}$ ,  $1.5 \times 10^{18}$ , and  $3 \times 10^{18} \text{ cm}^{-3}$  at the ambient temperature  $55^\circ\text{C}$  and injection current 30 mA in constant current control mode. Devices were taken out of the environmental chamber for periodic measurements of current-voltage characteristics and output power. Visual inspection was performed after 1000 hours of aging. For most LEDs tested in this experiment the power drop observed after 1000 hours of aging did not exceed 25% of the initial value.

As mentioned in Section 4, the condition (4) imposed on the n-GaN conductivity by the requirement of uniform current density across the active region should become more stringent at higher injection currents and elevated temperatures. The wafers with n-GaN doping  $7 \times 10^{17}$  and  $3 \times 10^{18} \text{ cm}^{-3}$  were pre-screened at the combined stress conditions of injection current up to 40 mA and hot chuck temperature up to  $85^\circ\text{C}$  and hardly demonstrated any immediately noticeable change in the light emission uniformity. However, pronounced current crowding near the mesa edge adjacent to the n-contact pad was observed at room temperature in the LED chips with the lowest n-GaN doping of  $7 \times 10^{17} \text{ cm}^{-3}$  after the completion of aging (Figure 8). This permanent current redistribution is accompanied by a dramatic forward voltage drop by 0.5 - 1 V across the diode and a significant increase in the reverse current leakage. Wafers with n-GaN doping  $1.5 \times 10^{18}$  and  $3 \times 10^{18} \text{ cm}^{-3}$  had a perfectly uniform light emission after the end of aging (Figure 9) and did not exhibit any substantial forward or reverse voltage change. We conclude that the root cause of the current crowding appearance is still the insufficient n-GaN conductivity at the  $7 \times 10^{17} \text{ cm}^{-3}$  doping level and the observed phenomena may be explained within the framework of the voltage drop equations (1)-(4).

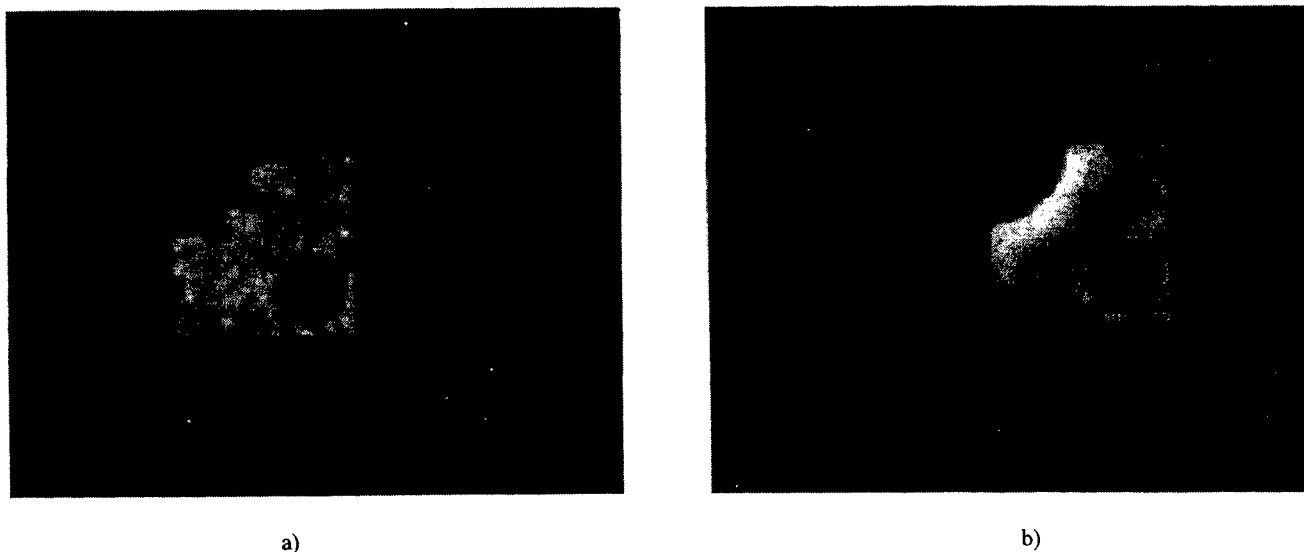


Figure 8. Microphotographs of GaN LED with n-GaN doping  $7 \times 10^{17} \text{ cm}^{-3}$  tested at 20 mA, RT:  
a) before aging; b) after 1000 hours of aging at 30 mA,  $55^\circ\text{C}$ .

In order to explain the current crowding degradation mode, two questions need to be answered:

- Why is current crowding triggered during aging but not in wafer-level tests performed at a higher current and temperature?
- How does it become permanent and start to show up at the standard operating conditions?

The first problem may be explained by a difference in thermal resistances between a device on the wafer and a chip on header. High thermal impedance ( $\sim 500^\circ\text{C/W}$ ) for a separated chip attached to a small header by epoxy bond may lead to the junction temperature of the diode which is significantly ( $\Delta T = 50^\circ\text{C}$  or more) higher than the header temperature, thus

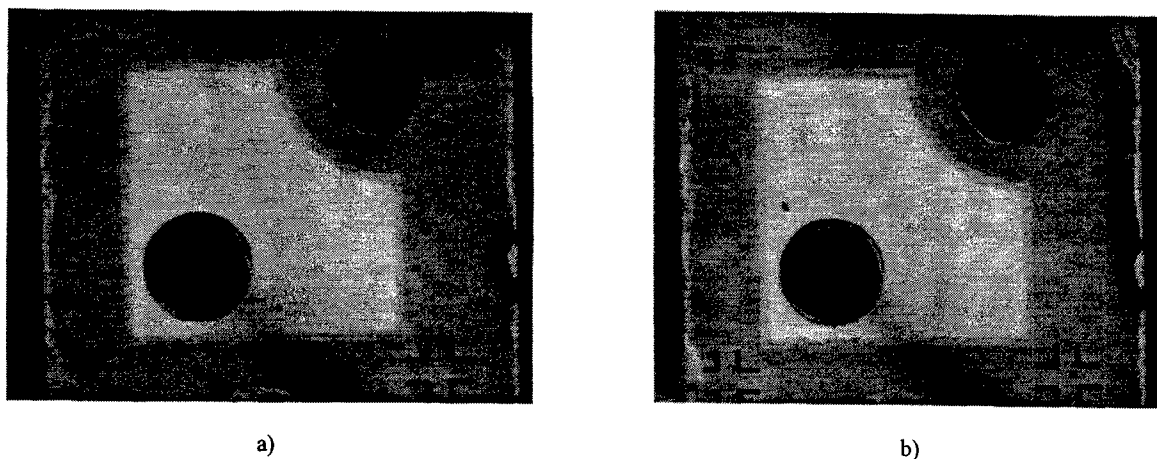


Figure 9. Microphotographs of GaN LED with n-GaN doping  $1.5 \times 10^{18} \text{ cm}^{-3}$  tested at 20 mA, RT:  
a) before aging; b) after 1000 hours of aging at 30 mA, 55°C.

exceeding the temperature used in wafer-level tests. Also, a mechanism of the permanent current redistribution during aging may be proposed which does not need the initial current crowding to be very pronounced. We believe that a positive feedback loop is formed by an initially slightly higher current density near the mesa edge inducing a local resistivity reduction due to one or more of the following processes:

- local annealing of the transparent ohmic contact;
- contact metal migration along defect tubes under electrical current stress<sup>5</sup>;
- activation of Mg acceptors due to dehydrogenation of Mg-H complexes by injected hot electrons<sup>6</sup>.

Any of those processes would cause an irreversible local decrease of the total voltage drop across the lateral current path A (see Figure 5) and make it a preferred channel at the low as well as high temperature and injection current density. The assumption of metal migration is also consistent with the increase in the reverse leakage current in the damaged diodes.

## 7. CONCLUSIONS

In conclusion, an approach to the optimization of n-GaN conductivity in GaN LEDs with lateral current path is proposed and tested which is based on the analysis of the contributions from different parts of the structure to the total voltage drop across the diode. Devices with 4  $\mu\text{m}$ -thick n-GaN layer Si-doped to  $3 \times 10^{18} \text{ cm}^{-3}$  demonstrate extremely low forward voltage of 2.9 V, low series resistance of less than 15  $\Omega$ , and output power of 3 mW at 20 mA injection current. 1000 hour aging test at 30 mA and 55°C reveals a stable operation of the diodes with n-GaN doping at or above  $1.5 \times 10^{18} \text{ cm}^{-3}$  and a distinct failure mode triggered by insufficient n-doping in the diodes with lower doping levels. Finally, Lehigh resistivity measurements are shown to be a reliable non-destructive evaluation tool for post-growth n-GaN conductivity control, a method superior to the Hall resistivity test.

## ACKNOWLEDGEMENTS

The authors are indebted to Mr. Joseph Potopowicz for his help with device assembly and reliability testing. We are also grateful to Mr. James Nering and his group for continuous wafer processing assistance. Discussions of wafer characterization methods with Mr. Paul Cooke were very helpful and insightful. This paper would be impossible without die separation technique developed by Mr. Anthony DiCarlo.



## REFERENCES

1. S. Nakamura, T. Mukai, and M. Senoh, "High-Power GaN P-N Junction Blue-Light-Emitting Diodes," *Jap. J. Appl. Phys.* **30**, pp. L1998-L2001, 1991.
2. S. Nakamura, T. Mukai, and M. Senoh, "Candela-class high-brightness InGaN/AlGaIn double-heterostructure blue light-emitting diodes," *Appl. Phys. Lett.* **64**, pp. 1687-1689, 1994.
3. S. L. Rudaz (Inventor), "Maximizing Electrical Doping while Reducing Material Cracking in III-V Semiconductor Devices," U.S. Patent # 5,729,029, 1998.
4. C. A. Tran, R. F. Karlicek Jr., M. G. Brown, I. Eliashevich, A. Gurary, and R. Stall, "Growth and Characterization of high-efficiency InGaN MQW Blue and Green LEDs from large-scale production MOCVD Reactors," to be published in *Light-Emitting Diodes: Research, Manufacturing, and Applications*, E. Fred Schubert, Editor, Proc. SPIE, 1999.
5. M. Osinsky, J. Zeller, P.-C. Chiu, B. S. Phillips and D. Barton, "AlGaIn/InGaIn/GaN blue light emitting diode degradation under pulsed current stress," *Appl. Phys. Lett.* **69**, pp. 898-900, 1996.
6. F. Manyakhin, A. Kovalev, and A. E. Yunovich, "Aging Mechanisms of InGaIn/AlGaIn/GaN Light-Emitting Diodes Operating at High Currents," *MRS Internet J. Nitride Semicond. Res.* **3**, 53, 1998.

# Gallium nitride based LEDs on silicon substrates

Nestor A. Bojarczuk, Supratik Guha  
IBM T. J. Watson Research Center, Yorktown Heights, NY 10598.

## ABSTRACT

We describe the growth and characteristics of GaN based light emitting diodes grown on Si(111) substrates. We show that the UV electroluminescence of such diodes can be used to generate fluorescence in organic color converters so that multicolored hybrid nitride-organic light emitting diodes that emit in the visible can be prepared.

## 1. INTRODUCTION

Gallium nitride based light emitters offer two attractive features. Firstly, the degradation performance of nitride based light emitting diodes (LEDs) are relatively insensitive to the presence of large densities of threading and planar defects. This is unlike the behavior of light emitters based on other compound semiconductors such as GaAs or ZnSe. Therefore, one can be highly optimistic about a nitride based optoelectronics technology on silicon--the most convenient substrate in microelectronics--inspite of a large lattice mismatch (19%) between GaN and Si and the consequent presence of a large density of defects. Secondly, the short wavelength UV electroluminescence from nitride LEDs can be used to excite color converters in order to obtain "color-downconverted" light emission at selected longer wavelengths--an approach potentially attractive for small displays or lamps. Recently we have demonstrated the first gallium nitride based light emitting diodes grown on silicon substrates. The AlGaIn/GaN double heterostructure diodes were grown by molecular beam epitaxy on Si(111) wafers, turned on between 4.5-6.5 volts, and emitted in the UV at ~360 nm and in the violet at ~420 nm. We have also demonstrated multicolored light emitting diodes (LEDs) on a silicon wafer using such UV/violet GaN LEDs on Si(111) in conjunction with organic dye based color converters. When applied on top of the nitride diodes, these color converters absorb the nitride LED electroluminescence at ~ 360 nm, and fluoresce in the green (~530 nm), and orange (~600 nm). Thus, multicolored light emitters may be made to operate side by side on the same Si wafer in an approach that may be attractive for miniature GaN based displays.

## 2. EXPERIMENTAL

Gallium nitride based light emitting diode structures on silicon were grown by molecular beam epitaxy (MBE) using a radio frequency source for nitrogen delivery. Silicon substrates oriented along <111> were cleaned via a standard "RCA clean" process, followed by a dip in a HF:H<sub>2</sub>O solution. This produces a H terminated Si surface and the hydrogen is then desorbed in vacuum by outgassing the Si wafer at ~600 °C. Growth of the nitrides is initiated by first growing a thin (~8 nm) AlN buffer layer on the Si at ~850°C. We find that the growth of the AlN layer ensures a single crystal epilayer while direct nucleation of GaN can result in a tendency towards polycrystalline GaN growth. Following the GaN growth, double heterostructure n:AlGaIn/GaN active region/p:AlGaIn diodes were grown [1]. The n type doping was achieved using Si while Mg was used for p doping. Aluminum compositions varied from approximately 5% to 15%. Light emitting diodes were made by evaporating thin transparent Ni-Au contacts (about 200-300 microns square) for the top p layer and using the heavily n doped Si substrate as the bottom n electrode. Use of the substrate as an electrode significantly reduces diode fabrication complexity. Color conversion was achieved by use of commercial organic laser dyes dissolved in an appropriate organic matrix. In our case, the commercially available deep UV resist UV2HS was used as the matrix due to its suitability for spinning on and its transparency to visible light. The green color converter was a 0.1% Coumarin 540a/1% Coumarin 450/UV resist mixture, while the orange dye was a 0.1% DCM/1% Coumarin 535/ UV resist mixture. The rationale behind the use of dye mixtures can be found in ref. 2. The dyes were applied to the surface of the nitride LED using a micro-pipette and allowed to solidify.

### 3. RESULTS AND DISCUSSION

Figure 1 shows the dc I-V characteristics of a set of light emitting diodes. In forward bias, the diodes start emitting light between 4.5 to 6 volts and typical currents are 14-65 mA at 12V in forward bias. Reverse leakage currents vary from 10 to 130  $\mu$ A at -10V. As can be seen from the figure there is variation in the I-V parameters from diode to diode, a consequence we believe, of non-uniformities in the growth. Clearly, the electrical characteristics are inferior compared to that for MOCVD grown diodes [3,4]. This will be discussed later. The electroluminescence spectrum from a diode is shown in Figure 2. The peak is at  $\sim$ 360 nm, corresponding to near band edge emission. The light output is weak compared to MOCVD material, though it is clearly visible under normal room illumination conditions. There is a long wavelength tail in the visible at  $>400$  nm. Intensity of the deep level visible emission varies from diode to diode and also sample to sample. This appears to be related to variations in the growth conditions. From preliminary observations, growth of the active layer at lower temperatures ( $<750^\circ\text{C}$ ) appears to promote stronger deep level emission.

An ultraviolet semiconductor LED brings about possibilities for new applications, especially if it is feasible on a convenient substrate such as Si. As described earlier, color conversion to visible wavelengths may be brought about with the use of the organic color converters. Figure 3 shows the results of the color conversion using the orange and green color converters described in the previous section. The orange emission ( $\sim$ 600 nm peak) in Figure 3 is the fluorescence due to the dopant dye, DCM. DCM emits at  $\sim$ 640 nm in a liquid, polar solvent, however in a solid polymeric matrix the fluorescence shifts to shorter wavelengths. The small peak at  $\sim$ 360 nm in Figure 3a is due to unabsorbed electroluminescence. The green emission in Figure 3b peaks at  $\sim$ 530 nm and is due to fluorescence from the Coumarin 540a dye.

The color conversion efficiencies of the organic color converters is a relevant issue. For color converted diodes to be practical, it is expected that conversion efficiencies should be at least 30%. We have carried out measurements of external fluorescence efficiencies of dye combinations spun onto glass substrates and these measurements yield efficiencies in the 10-15% range [5]. Assuming no scattering of light in the film, and the absence of backside reflection, we have estimated that a flat thin film color converter would emit  $\sim$ 13% of the total fluorescence from the front surface due to total internal reflection. It appears therefore that the internal fluorescence efficiencies of the dyes are very high. Enhancement of the light extraction may be possible by modification of the color converting surface in the form of micro-lenses.

The above data clearly demonstrate the feasibility and potential for such hybrid semiconductor-organic light emitters. They are attractive for miniature displays where arrays of nitride LEDs on Si substrates can be coated with organic color converters for multicolor emission. The drawback here is the efficiency of MBE grown light emitting diode structures, which as discussed earlier in this paper, are presently inadequate and not comparable to MOCVD grown material. We find that diodes grown by MBE on the more commonly used sapphire and silicon substrates are similar in their performance. This indicates that the diode performance appears to be limited due to the growth technique itself. This is consistent with the argument that GaN has a tendency to dissociate to Ga and  $\text{N}_2$  at high temperatures, particularly in a high vacuum atmosphere where an adequate nitrogen overpressure cannot be maintained. In a highly defective GaN epilayer this results in thermal etching and a poor microstructure at high temperatures ( $>850^\circ\text{C}$ ). This appears to severely limit the quality of MBE grown GaN. On the other hand, there seem to be no reports of GaN based light emitting diodes grown by MOCVD on Si substrates even though high quality GaN diodes are grown routinely on sapphire or SiC substrates. The reason for this is possibly related to the compatibility between Si and AlN or GaN at high temperatures. From annealing experiments of GaN based diode structures we find that at high ( $\sim 1100^\circ\text{C}$ ) temperatures GaN/AlN/Si structures are unstable. Al and Ga form eutectics with Si. Dissociation of AlN or GaN locally due to the presence of heterogeneities at the interface at high temperatures can result in a Al-Si liquid which would then break down the interface. Growths by MOCVD are carried out at high ( $>1000^\circ\text{C}$ ) and therefore the stability of the nitride-Si can be a serious issue. MBE growth temperatures are typically at  $<850^\circ\text{C}$ , where the interface is stable. MOCVD grown nitride diodes on the other hand can be of high quality, MBE grown diodes are not. The issue then is one of creating a stable nitride-silicon interface, perhaps via the use of an intermediate barrier layer, so that high temperature MOCVD growths can be carried out successfully on silicon.

### REFERENCES

1. S. Guha, N. A. Bojarczuk, Appl. Phys. Lett. **72**, 415 (1998).
2. S. Guha, N. A. Bojarczuk, Appl. Phys. Lett. **73**, 1487 (1998).
3. S. Nakamura, T. Mukai, M. Senoh, Appl. Phys. Lett. **64**, 1687 (1994).

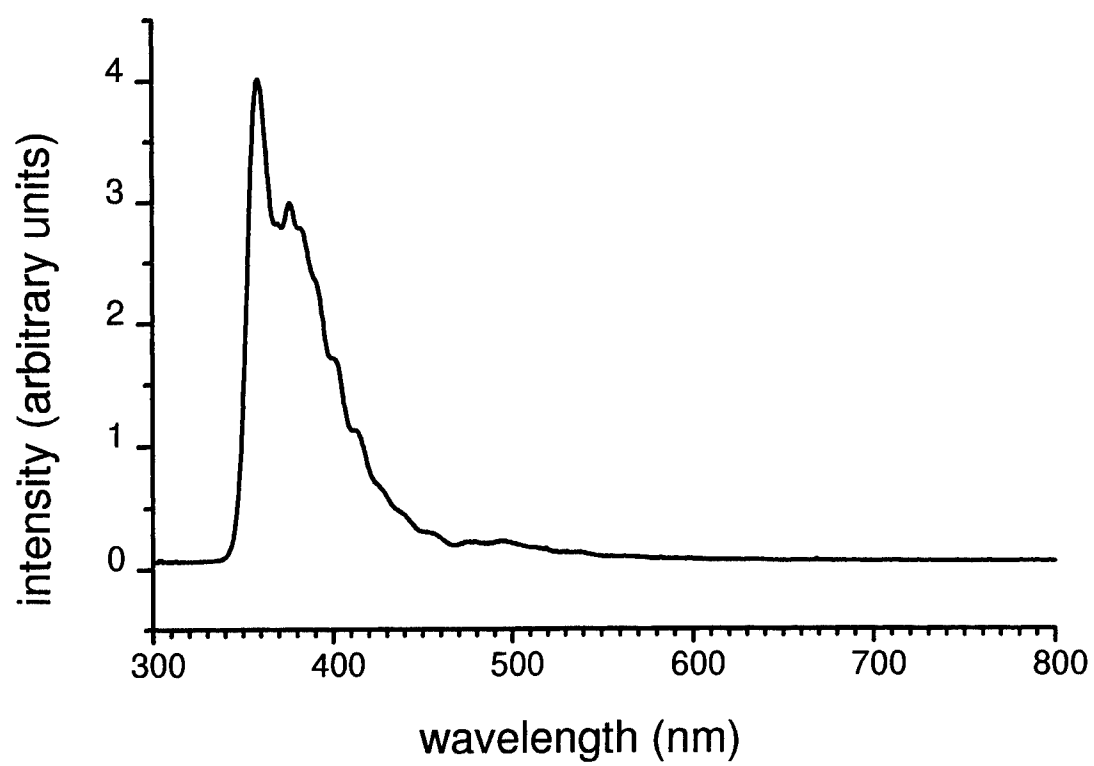
4. S. N. Mohammed and H. Morkoc, Proc. IEEE **83**, 1306 (1995).
5. S. Guha, R. A. Haight, N. A. Bojarczuk, D. W. Kisker, J. Appl. Phys. **82**, 4126 (1997).

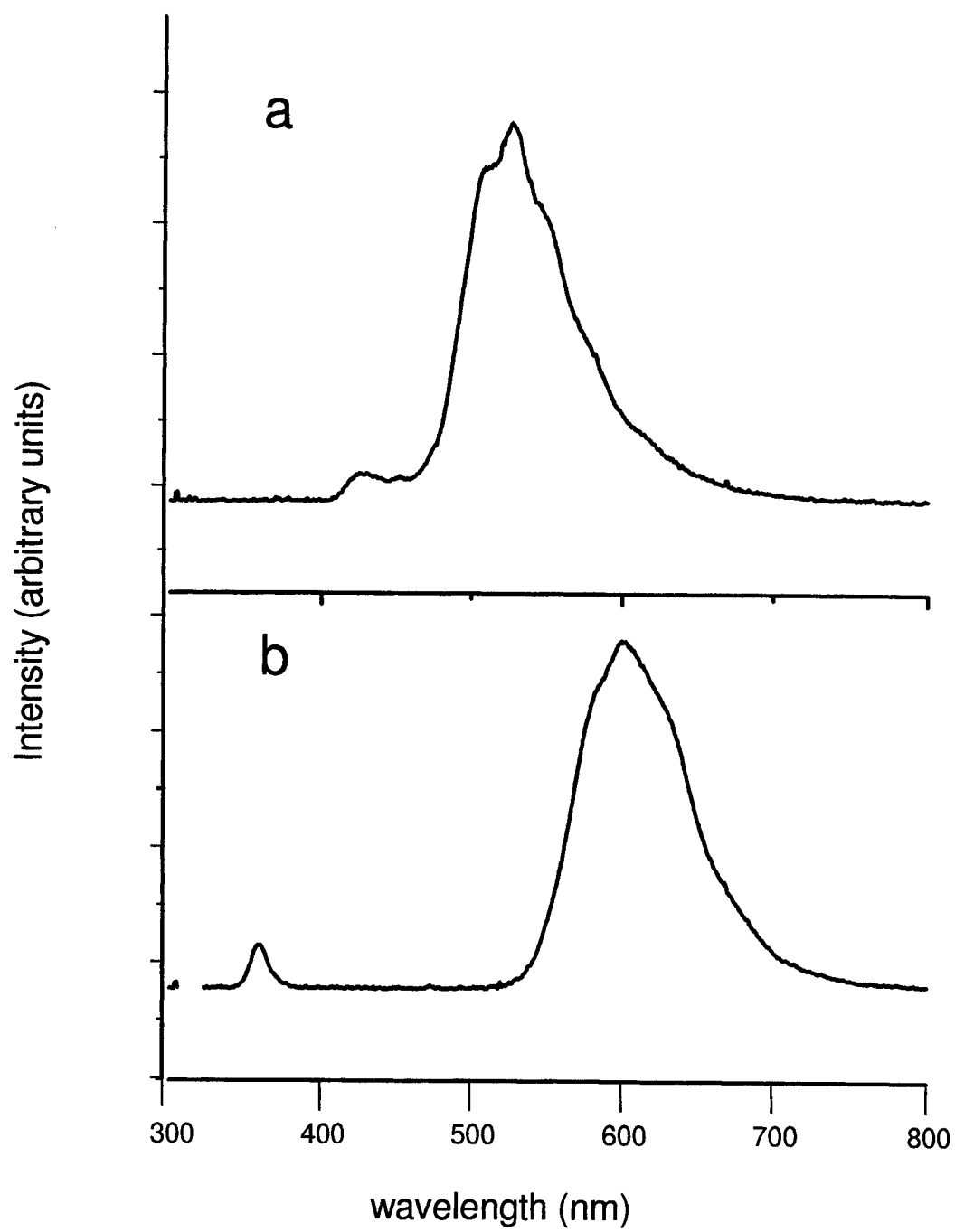
### FIGURE CAPTIONS

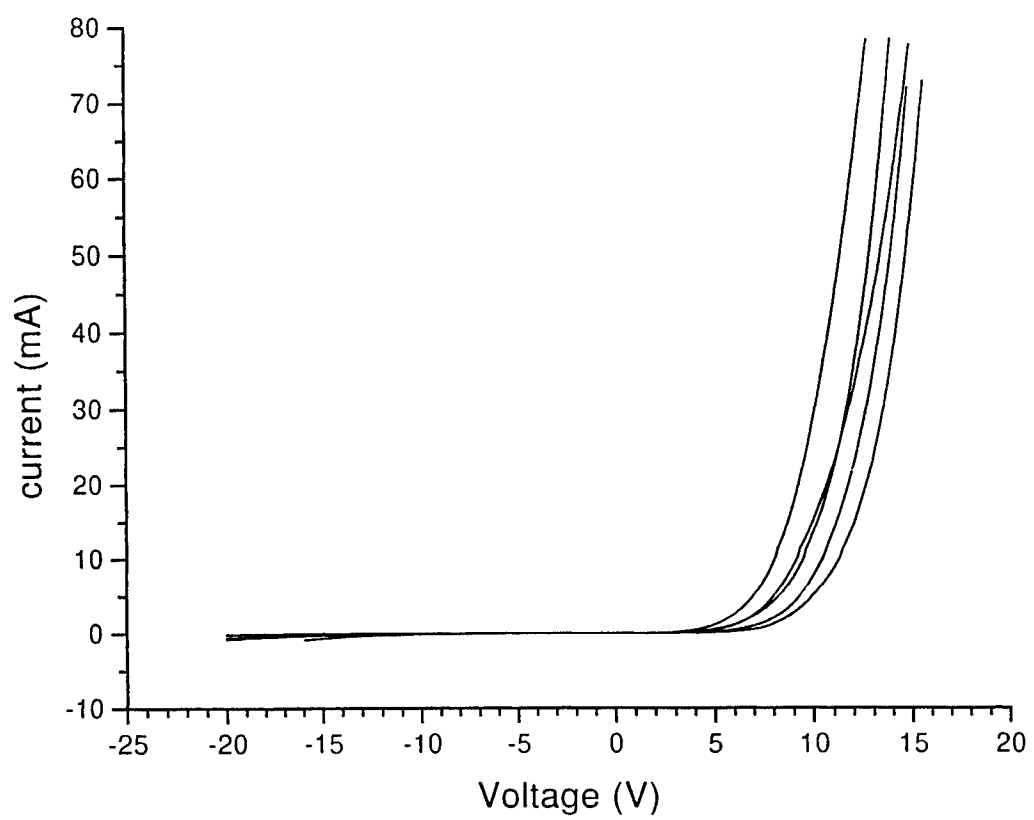
Figure 1: I-V characteristics of a set of 300x300 micron diodes.

Figure 2: Electroluminescence spectrum from a AlGaIn/GaN/GaN double heterostructure LED on Si.

Figure 3: Hybrid diode spectra from: (a) the orange color converter based diode; and (b) the green converter based diode.







# Growth and Characterization of high-efficiency InGaN MQW Blue and Green LEDs from large-scale production MOCVD Reactors

C. A. Tran\*, R. F. Karlicek Jr., M. G. Brown, I. Eliashevich, A. Gurary and R. Stall  
Emcore Corp. 394 Elizabeth Avenue, NJ 08807 USA

\*email : Tran@emcore.com

## ABSTRACT

As more advances are made in the performance of GaN-based devices, a trend toward the use of large scale MOCVD reactors for epitaxial growth of GaN-based device structures is clear. In this paper we describe the use of Emcore's SpectraBlue™ reactor for large-scale manufacturing of Blue and Green LEDs. The high throughput growth of GaN based LEDs is demonstrated without compromising LED uniformity or overall performance. In-situ control of key parameters critical to the production of high quality LEDs, such as buffer layer growth is now feasible using in-situ reflectance spectroscopy. Film properties as well as LED device performance are discussed.

## I. INTRODUCTION

The commercialization of high brightness blue and green LEDs [1] and the recent announcement of reliable III-N laser diodes [2] clearly demonstrates the enormous potential of the III-N material system. MOCVD has become the growth technique of choice for large scale manufacturing of these devices. In LEDs and Laser Diodes (LDs), the active layer consists of either a single InGaN/GaN quantum well or multiple quantum wells (MQW) [2]. Despite rapid advances in growth technology, high indium containing InGaN alloys are still difficult to achieve using MOCVD due to the high volatility of indium and low pyrolysis efficiency of ammonia. The indium incorporation is strongly dependent on temperature and attempts to obtain long wavelength devices can produce indium droplets on the surface of the InGaN films. This problem must be overcome in a production MOCVD reactor where thickness and wavelength uniformity is a critical factor in obtaining high device yields and low operating costs. This paper addresses these issues and demonstrates the high throughput growth of very high brightness blue and green MQW LEDs in an Emcore Turbodisc SpectraBlue™ reactor on six 50 mm wafers in a single run.

## II. THE GROWTH OF III-NITRIDES FOR HIGH-BRIGHTNESS LEDs

InGaN MQWs and MQW LEDs were grown in an EMCORE SpectraBlue™ multi-wafer *Turbodisc* MOCVD system. The details of the *TurboDisc*-reactor technology have been described elsewhere [3]. This system is equipped with a double walled water-cooled stainless steel chamber, a two-zone filament heater, a UHV loadlock and can be used for deposition on up to six 50 mm wafers. The reactor chamber and loadlock are shown in Figure 1. Rotation speeds can be controlled up to 1500 rpm without loss of the substrates and a low thermal mass heater and wafer carrier assembly exhibit rapid heating and cooling rates. The temperature controlled top reactor flange is specially designed to prevent premature mixing of the growth precursors, eliminating the occurrence of parasitic adduct formation known to be a serious problem in the growth of nitrides. Viewports on the top of the growth chamber gives access to the wafer surface and are used for in-situ reflectance spectroscopy as well as pyrometric monitoring of the wafer carrier temperature.

In-situ reflectance spectroscopy is a powerful technique for monitoring the epitaxial growth while in progress. The method is simple and can be used to track the growth process during rotation even if only one wafer (off center) is used. This method is similar to using pyrometric interferometry described by Nakamura [4] but the thickness resolution and signal to noise ratio of in-situ reflectometry is much higher at the shorter wavelength (600nm) used in our studies, so the film morphology can be monitored at almost any thickness.



Interferometric monitoring of the shorter wavelengths (600 nm) used in our growth can be particularly useful in the process development mode. Figure 2 shows an example where three GaN samples were grown using different buffer layer growth conditions. The development of a smooth surface morphology (as shown from the oscillations in the reflectivity) during GaN growth is observed for all 3 samples but it occurs at different times after growth of the buffer layer. It is well known [4] that growth process of GaN films on GaN buffer layers consists of island growth of GaN around buffer layer nucleation sites, followed by lateral growth of GaN islands and coalescence of these islands. According to this model, the coalescence of GaN islands in sample A is much slower than samples B and C. In sample A, surface was very rough at the first 1000 seconds of growth and then gradually became flat. In contrary, sample B and C exhibited very smooth surface at the beginning as shown by an immediate rise of the reflectivity as soon as the growth of GaN at high temperature starts. A smooth initial GaN surface does not guarantee a good surface as the growth develops further as seen in sample C where the decrease in the reflectivity shows that the surface degraded quickly after 1 micron of GaN was deposited. These studies and subsequent LED performance correlation with the in-situ reflectance patterns show that a reasonably slow recovery of surface flatness following the initiation of high temperature GaN growth gives results superior to those obtained from growth conditions producing a rapid reflectivity recovery

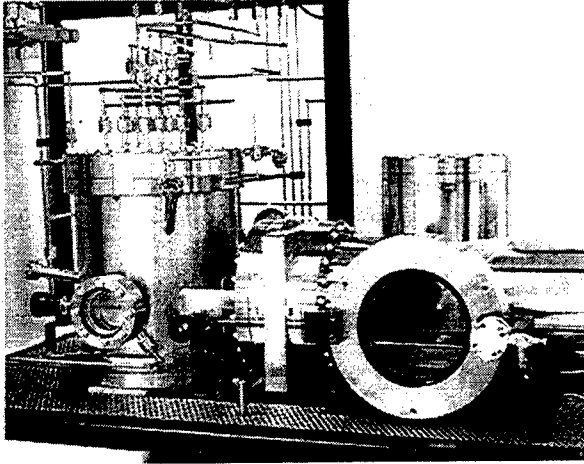


Fig.1 : Growth chamber and loadlock for the SpectraBlue reactor

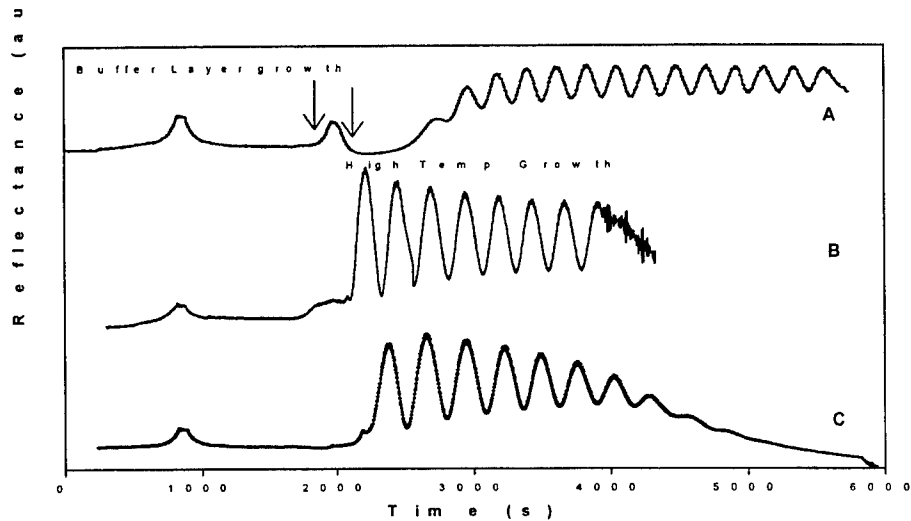


Fig.2 : In-situ reflectance signal in real time of 3 GaN layer growth under different conditions for the low temperature buffer layer. Arrows indicate initiation of the buffer layer growth and high temperature growth. Note that surface of the sample A was not smooth at the beginning but then is smooth for the whole growth time, in contrary with the sample C

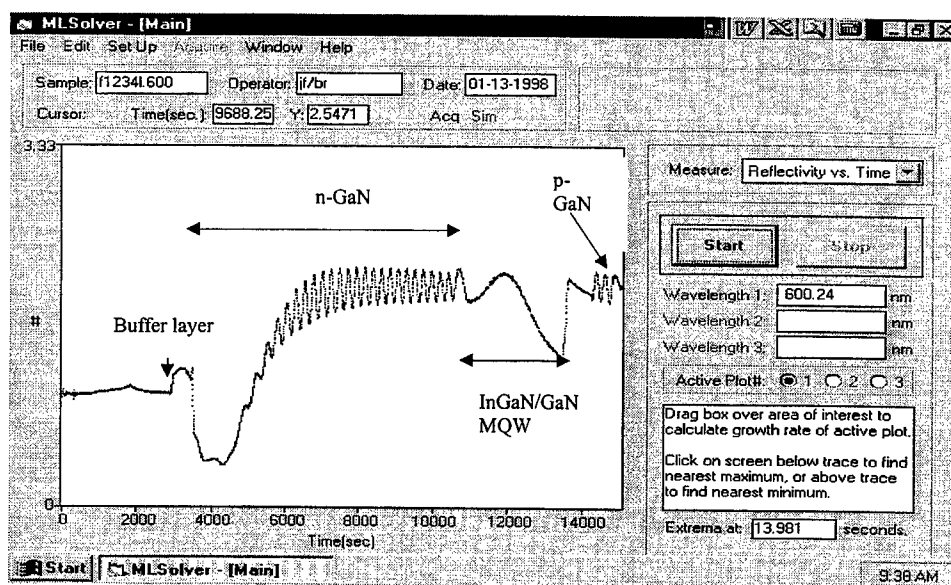


Fig.3 : A snap shot of data from an LED growth run using the simple and powerful in-situ reflectance spectroscopy

Figure 3 shows an in-situ reflectance pattern of a LED growth. It can be used to monitor growth rate and surface roughness in real-time.

### III . PROPERTIES OF GaN AND InGaN/GaN MQWs

Undoped GaN exhibits a background carrier concentration in mid  $10^{16}/\text{cm}^{-3}$  with a mobility in excess of  $600 \text{ cm}^2/\text{vs}$  at room temperature and  $1500 \text{ cm}^2/\text{vs}$  at 80K. Table 1 summarizes properties of undoped GaN as well as n- and p-doped GaN  $2 \mu\text{m}$  thick films. Some details of the film properties can be found in Ref.[5].

	Carrier Conc. ( $\text{cm}^{-3}$ )	Mobility (RT)	(002) FWHM (arcsecs)	(102) FWHM (arcsecs)
Undoped GaN	$5 \times 10^{16}$	550-650	200-300	350-450
Si-doped	$3-5 \times 10^{18}$	230-300	200-300	350-450
Mg-doped	$7-10 \times 10^{17}$	10-20	250-350	400-500

Table 1: Summary of GaN film properties

InGaN/GaN single quantum well (SQW) and MQWs were grown at temperatures between  $700-800^\circ\text{C}$ . The primary focus of this work has been on MQW growth because LEDs with MQW active layer show better brightness at high drive current than SQW LEDs. High indium containing InGaN MQWs are difficult to achieve using MOCVD due to the high volatility of indium and low pyrolysis efficiency of ammonia. The indium incorporation is strongly dependent on temperature and under some growth conditions indium droplets may appear on the surface of the InGaN films. It is normal for high brightness InGaN LEDs to exhibit an emission wavelength longer than expected from the In content measured by normal non-

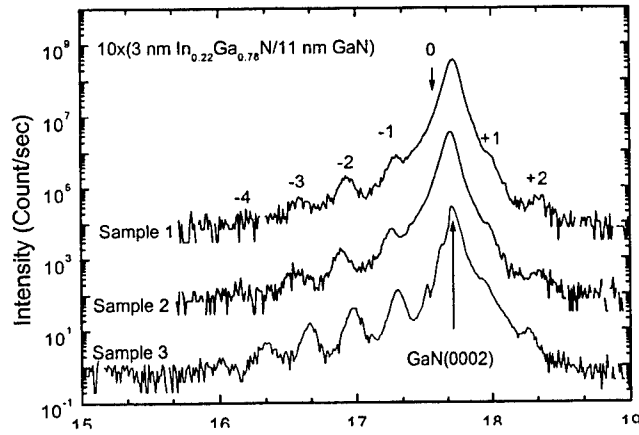


Fig. 4: (002) X-ray diffraction pattern of 3 MQWs consisting of 10 periods of 3nm  $\text{In}_{0.22}\text{Ga}_{0.78}\text{N}$  and 11nm GaN. These MQWs were grown under different growth conditions but indium composition was kept unchanged

by indium-rich clusters within InGaN wells.

Figure 4 shows the (0002) reflection obtained with  $\omega/2\theta$  scans along the growth direction for 3 MQWs consisting of 10 periods of 3nm  $\text{In}_{0.22}\text{Ga}_{0.78}\text{N}$  and 11nm of GaN. The zero-order diffraction peak corresponds to an average indium composition of  $\sim 5\%$  for the entire MQW or 22% indium in the InGaN layers. The actual indium composition may be even less than 22% due to biaxial strain in InGaN layers related to lattice mismatch between the InGaN

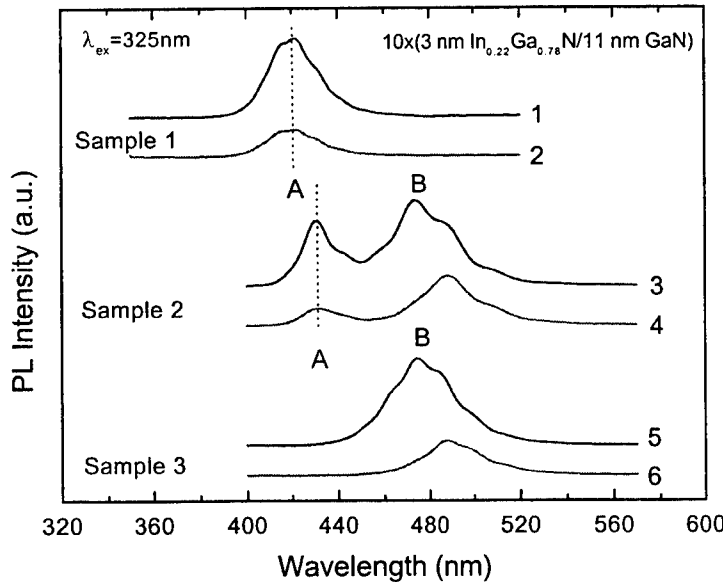


Fig. 5: Room-temperature PL spectra of 3 MQWs (shown in Fig.4) consisting of 10 periods of 3nm  $\text{In}_{0.22}\text{Ga}_{0.78}\text{N}$  and 11nm GaN at two different excitation powers. Spectra 1, 3 and 5 were taken with an excitation power of  $1\text{W}/\text{cm}^2$ . Spectra 2, 4 and 6 were taken with an excitation power of  $0.2\text{W}/\text{cm}^2$

destructive epitaxy characterizations methods such as x-ray diffraction (XRD) and photoluminescence (PL). Controversy about the mechanism of radiative recombination in InGaN/GaN MQWs with high indium content still exists, with causes for this effect being ascribed to either In segregation or piezoelectric effects associated with strain of the InGaN wells. The low solubility of indium in GaN was calculated to be  $< 6\%$  at  $800^\circ\text{C}$  [6]. Chichibu et al. [7] has recently shown a very large red shift of 500 meV in EL with respect to modulated electro-absorption and photo-voltage in InGaN MQW super-bright green LEDs. The EL was assigned to a recombination of excitons localized

and GaN. Figure 5 shows the PL at room temperature of the same 3 MQW structures shown in Fig.4. Spectra were taken at two different excitation powers ( $1\text{W}/\text{cm}^2$  and  $0.2\text{W}/\text{cm}^2$ , respectively). For sample #1 (denoted as peak A in Fig. 5), only a peak at 430 nm is observed. For sample #2 the peak at 430 nm is seen together with a peak at 488nm. The spectrum of sample #3 is dominated by an intense peak at 488 nm (denoted as peak B in Fig.5). The peak at 430 nm corresponds to an indium composition of 23%, close to the 22% determined by XRD. The peak at 488

nm is interpreted in terms of localization of excitons at potential fluctuations due to phase separation of InGaN into high and low indium content regions. This InGaN phase separation can be enhanced by choosing appropriate growth conditions. In sample #3, the peak at 430 nm is unobservable at any excitation power. We believe that the immiscibility of InN and GaN is the driving force for this phase separation. The formation of InGaN with different compositions may also be a means of reducing strain energy due to lattice mismatch.

At higher excitation power as shown in Fig. 5, the peak position at 430 nm does not shift while the peak at 488nm exhibits a noticeable blue shift of 12nm. This observation supports the assignment of the peak at 430 nm to the band-edge recombination and the peak at 488nm to the recombination at potential fluctuations caused by indium clustering. Note that while in PL the recombination at potential fluctuation (indium-rich InGaN clusters) dominates, in XRD the indium average composition is still determined by the indium contents of the surrounding InGaN layer and not by the indium-rich clusters.

#### IV. MATERIAL UNIFORMITY AND RUN-TO-RUN REPRODUCIBILITY

One important requirement for large scale manufacturing is that the reactor be capable of growing LED structures with good yield and reproducibility without sacrificing device performance. On the basis of the previous discussion, indium incorporation is the most important factor for wavelength uniformity as well as LED brightness. The total intra wafer, inter wafer and run to run epitaxy variations must be small enough to result in an acceptable LED yield. We show as an example typical data for a blue LED structure at 465 nm in Fig. 6, which shows a PL wavelength uniformity for a full LED structure. The total wavelength variation over 22 mm radius (3 mm edge exclusion) is better than 1.5 nm ( $1\sigma$ ).

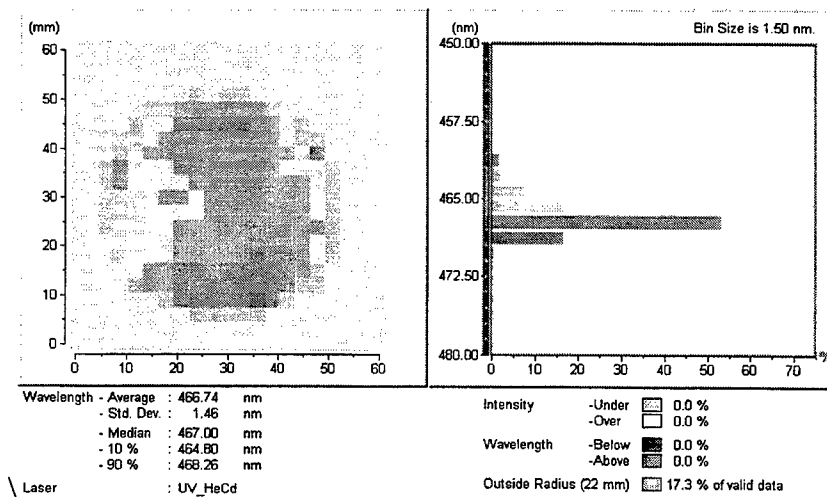


Fig. 6 : Photoluminescence wavelength uniformity of a blue LED structure. The standard deviation is better than 1.5 nm.

Figure 7 shows PL wavelength uniformity for all six 50mm LED wafers from an LED run. Standard deviation from wafer to wafer is better than 2 nm.

Reproducibility is also required in a manufacturing environment. The use of in-situ reflectance spectroscopy to monitor buffer layer growth, growth rate and wafer surface morphology has significantly contributed to developing the hardware and process parameters needed to obtain reproducible LED properties. Run-to-run deviation of the PL averaged wavelength is usually less than 2 nm.

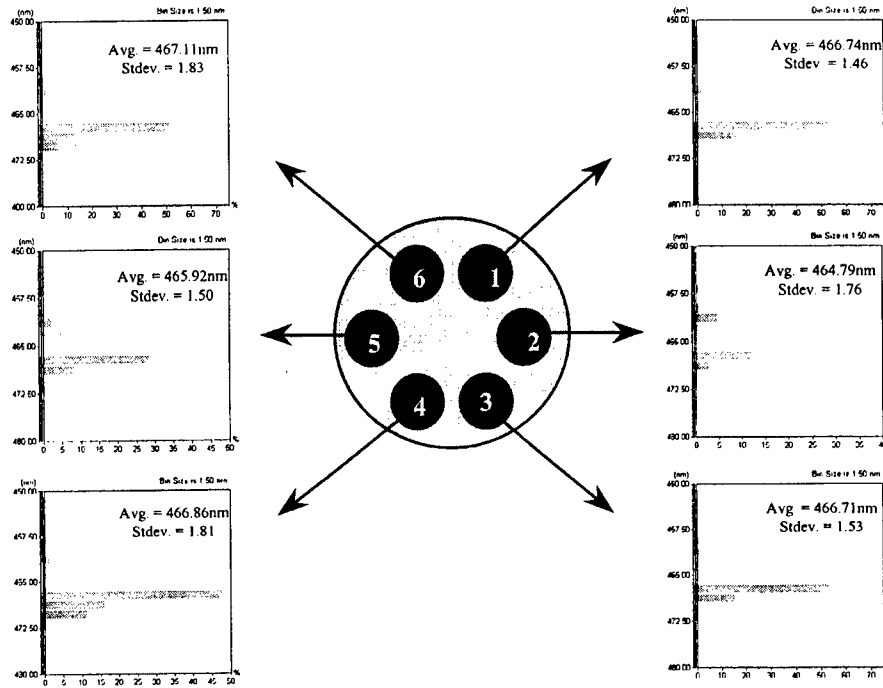


Fig.7 : PL wavelength uniformity from a blue LED run. All six wafers have tight distribution of wavelength with standard deviation better than 2 nm

## V. DEVICE PERFORMANCE

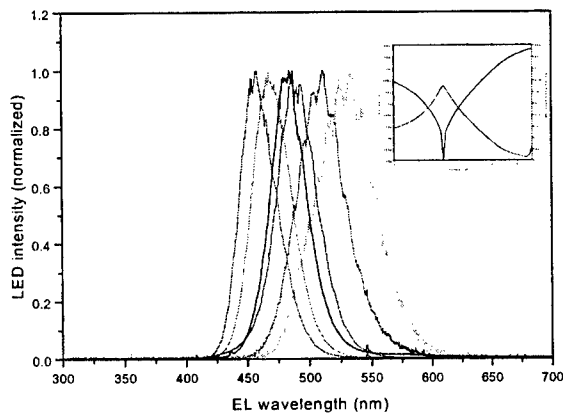


Fig.8 : EL spectra of LEDs at various wavelengths from blue to green color. The inset shows an I-V characteristic of LED

Blue and Green LEDs were fabricated using standard mesa etching and contact fabrication techniques. Figure 8 shows electroluminescence spectra of LEDs with wavelength in the range of 450 – 530 nm which covers blue, cyan and green part of visible light spectrum. An external quantum efficiency of 9% was achieved for devices operating at 465 nm wavelength.

Current-voltage characteristics are presented in the inset of Fig.8. The typical forward voltage at 20 mA is 3.5V. Above 20 mA, the dynamic resistance has a value of ~ 20 Ohm.

## VI. CONCLUSION

We have demonstrated a large scale MOCVD manufacturing system which is able to grow high brightness blue and green LEDs. In situ control of the buffer layer growth is a key factor for this success. InGaN/GaN MQW active layer with emission wavelength in blue-green part of visible spectrum was achieved with very good uniformity and reproducibility. We have showed the relation between indium segregation in InGaN/GaN MQWs and high-brightness LEDs. An external quantum efficiency of 9% has been achieved for 465nm LEDs.

## ACKNOWLEDGEMENT

The authors would like to thank M. Schurman, A. Whitcomb, J. Nering, I. Ferguson, A. Welsh, V. Merai, B. Ronan, M. Gottfriend and T. DiCarlo for very helpful discussion and technical assistance.

## REFERENCES

1. S. Nakamura, T. Mukai, M. Senoh, S. Nagahama, N. Iwasa, *J. Appl. Phys.* **74**, 3911 (1993)
2. S. Nakamura, M. Senoh, N. Iwasa and S. Nagahama, *Appl. Phys. Lett.* **67**, 1868 (1995)
3. G. S. Tompa, P.A. Zawadski, M. McKee, E. Wolak, K. Moy, R. A. Stall, A. Gurary and N. Schumaker, *Mater. Res. Soc. Symp. Proc.* **335**, 241 (1994)
4. S. Nakamura, *Jpn. J. Appl. Phys.* **30**, 1348 (1991)
5. C. A. Tran, R. F. Karlicek Jr., M. Schurman, M. G. Brown, I. Eliashevich, I. Ferguson, R. Stall. To be published in *J. Crys. Growth*. Special issue as Proc. of the IX Int. MOVPE Conference, La Jola, 1998.
6. I-hsiu Ho, G. B. Stringfellow, *Appl. Phys. Lett.* **69**, 2701 (1996)
7. S. Chichibu, T. Azuhata, T. Sota and S. Nakamura, *Appl. Phys. Lett.* **69**, 4188 (1996)



## **SESSION 2**

### **III-Nitrides and Related Materials**



## Optical properties of InGaAsN: A new 1eV bandgap material system

E. D. Jones<sup>†a</sup>, N. A. Modine<sup>a</sup>, A. A. Allerman<sup>a</sup>, I. J. Fritz<sup>a</sup>,  
S. R. Kurtz<sup>a</sup>, A. F. Wright<sup>a</sup>, S. T. Tozer<sup>b</sup>, X. Wei<sup>b</sup>

<sup>a</sup>Sandia National Laboratories, P. O. Box 5800, Albuquerque, NM 87185-0601

<sup>b</sup>National High Magnetic Field Laboratory, Florida State University, Tallahassee, FL 32306-4005

### ABSTRACT

InGaAsN is a new semiconductor alloy system with the remarkable property that the inclusion of only 2% nitrogen reduces the bandgap by more than 30%. In order to help understand the physical origin of this extreme deviation from the typically observed nearly linear dependence of alloy properties on concentration, we have investigated the pressure dependence of the excited state energies using both experimental and theoretical methods. We report measurements of the low temperature photoluminescence energy of the material for pressures between ambient and 110 kbar. We describe a simple, density-functional-theory-based approach to calculating the pressure dependence of low lying excitation energies for low concentration alloys. The theoretically predicted pressure dependence of the bandgap is in excellent agreement with the experimental data. Based on the results of our calculations, we suggest an explanation for the strongly non-linear pressure dependence of the bandgap that, surprisingly, does not involve a nitrogen impurity band. Additionally, conduction-band mass measurements, measured by three different techniques, will be described and finally, the magnetoluminescence determined pressure coefficient for the conduction-band mass is measured.

**Keywords:** InGaAsN, band structure, LDA, photoluminescence, pressure dependent energy gaps, conduction-band mass.

### 1. INTRODUCTION

The quaternary alloy system, InGaAsN, is a new material system that appears to have many exciting and important device applications. Because of a large negative bowing parameter,<sup>1,2</sup> the addition of small amount of nitrogen to the 1.4 eV bandgap energy GaAs system *lowers the energy!* With the bandgap energy of GaN ~ 3.5 eV, normally, one would expect that the GaAsN alloy bandgap energy would increase with nitrogen content. Besides also lowering the bandgap energy, adding indium to GaAsN strain compensates the effect of nitrogen, resulting in a material system with bandgap energies ~ 1eV and lattice matched to GaAs! The InGaAsN alloy system has been identified as a key candidate material for long wavelength laser systems<sup>3-5</sup> and high-efficiency multi-junction solar cells.<sup>6,7</sup> While light emitting diodes (LED) based on InGaAsN have not yet been reported, this could be an ideal system to provide infrared wavelength LED's. Lattice matching allows the design of optoelectronic devices without the inherent problems found in strained systems. Of prime importance is the role of the nitrogen isoelectronic atom: (1) What is the origin of the large bandgap reduction? (2) Are the states extended (band-like) or localized (impurity-like)? (3) How is the nominally light GaAs conduction-band effective mass  $m_c = 0.067$  affected by the addition of nitrogen? For optimum device performance, a better understanding of the electronic properties of this type of alloy system is required.

<sup>†</sup>Correspondence: MS-0601; Email: edjones@sandia.gov; Telephone 505 844 8752; Fax: 505 844 3211

Both first-principles<sup>8-10</sup> and empirical<sup>11-14</sup> theoretical treatments for this material system have concentrated on understanding the dependence of the bandgap energy on nitrogen composition. In the first part of this paper we review previously reported<sup>15</sup> pressure dependent photoluminescence (PL) data together with a first principles local density approximation (LDA) calculation for the band structure and its pressure dependence. It will be shown that, while it is well known that bandgap energies calculated by the LDA method are not accurate, the predicted pressure dependence of the bandgap energy is in excellent agreement with experiment. Similar observations have been reported for silicon.<sup>16</sup> Because of this good agreement, the character of the states is accurately described and we also have confidence that this technique could be useful for understanding the properties of other low concentration alloy systems.

In the second part of the paper, we present conduction-band effective mass determinations using different three different experimental techniques: (1) Studying the bandgap energy dependence as a function of InGaAsN/GaAs quantum-well width. (2) Photorefectance measurements of the ground state and excited state energies of an InGaAsN/GaAs quantum well for various quantum-well widths. (3) Magnetoluminescence measurements of the magnetic field dependence of the InGaAsN exciton diamagnetic shift in bulk epilayers. Additionally, the pressure dependence of the conduction band-mass has also been measured using the magnetoluminescence method.

## 2. EXPERIMENTAL

The structures were grown in a vertical flow, high speed rotating disk, EMCORE GS/3200 metalorganic chemical vapor deposition (MOCVD) reactor. The  $\text{In}_x\text{Ga}_{1-x}\text{As}_{1-y}\text{N}_y$  films were grown using trimethylindium (TMIn), trimethylgallium (TMG), 100% arsine and dimethylhydrazine (DMHy). Dimethylhydrazine was used as the nitrogen source since it has a lower disassociation temperature than ammonia and has a vapor pressure of approximately 110 torr at 18°C. Unintentionally doped InGaAsN was p-type. InGaAsN films for Hall and optical measurements were grown on semi-insulating GaAs orientated 2° off (100) towards <110>. Lattice matched ( $\delta a/a < 8 \times 10^{-4}$ ) films were grown at 600°C and 60 torr using a V/III ratio of 97, a DMHy/V ratio of 0.97 and a TMIn/III ratio of 0.12. The growth rate was 10 Å/s. These conditions resulted in films with an indium mole fraction of  $0.07 \pm 0.005$  and a nitrogen mole fraction of  $0.022 \pm 0.003$ . The composition was determined by calibration growths of GaAsN and InGaAs along with double crystal x-ray diffraction measurements. The nitrogen composition of bulk films was also confirmed from elastic recoil detection measurements. A significant increase in photoluminescence intensity was observed from these films following a post-growth anneal. Ex-situ, post-growth anneals were carried out in a rapid thermal anneal system under nitrogen using a sacrificial GaAs wafer in close proximity to the InGaAsN sample.

The photoluminescence intensity was a maximum for samples annealed either at 700°C for 2 minutes or at 650°C for 30 minutes. Similar results have been reported by Rao *et al.*<sup>17</sup> Transmission electron microscopy measurements indicate that the samples are random and no evidence for clustering or phase separation was observed.<sup>18</sup> The pressure was generated using a small BeCu piston-cylinder diamond anvil cell, 8.75-mm-diameter and 12.5-mm-height.<sup>19</sup> Methanol, ethanol, and water in a ratio of 16:3:1 was used for the pressure medium.<sup>20</sup> The shift in the fluorescence of a small chip of ruby placed in the pressurized volume was used to calibrate the pressure at 4K with an accuracy of  $\pm 0.5$  kbar.<sup>21</sup> A single 600- $\mu\text{m}$ -diameter optical fiber, butted up against one of the diamonds, brought the 1 mW power 5145-nm-wavelength laser to the sample and also collected the PL signal from the sample. A beam splitter system was used to direct the PL signal to an optical monochromator. Depending on the bandgap energy, two liquid-nitrogen-cooled detectors were used to detect the PL signal. For low pressure regimes, where the bandgap energies were near or below 1 eV, a NORTH-COAST EO-817L Ge-detector was employed, while at higher pressures, a standard CCD array was used.

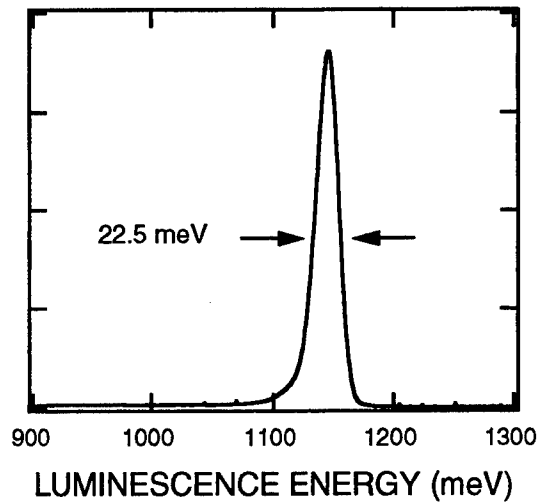


**Figure 1** . Low temperature (4K) PL spectrum for an annealed InGaAsN sample with 2% N. The FWHM = 22.5 meV.

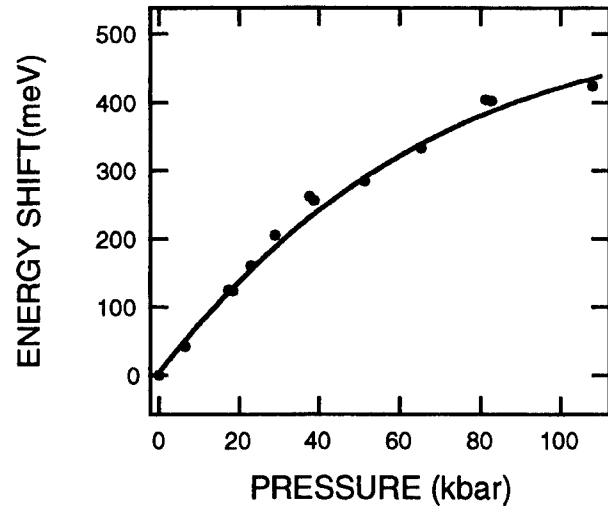


**Figure 2** . Experimental (dots) and theoretical (solid line) shift of the bandgap energy on pressure at 4K for 2% N in InGaAsN.

Photoreflectance spectra were obtained for a variety of MOCVD InGaAsN/GaAs MQW structures. For these experiments, the optical pump source was a blue LED having a 15 degree divergence angle and a peak emission wavelength of 470 nm (Nichia Chemical Industries part number NSPB 300A.). The LED was driven by a square-wave current source operating at 15 mA and 325 Hz. The sample reflectance was measured using a 10 W tungsten-halogen lamp followed by a 0.25-m grating monochromator in conjunction with an InGaAs photodiode detector and a lock-in amplifier.

### 3. DISCUSSION

A typical low temperature (4K) PL spectrum for 2% nitrogen in InGaAsN lattice matched to GaAs is shown in Fig. 1. As can be seen, the 4-K bandgap energy is near 1150 meV, which is significantly less than the 4-K GaAs bandgap energy  $E_g \approx 1515$  meV. The full-width-half-maximum (FWHM) PL linewidth is about 22.5 meV. As mentioned above, the PL intensity increased significantly with annealing. Other optical parameters, such as the FWHM and PL-peak energy appear to remain unaffected by our annealing process. The pressure dependence of the bandgap energy shift data, as determined from by the PL-peak energy, is shown in Fig. 2 as solid circles. The pressure data ranged between ambient and 110 kbar. The solid curve drawn through the data is discussed in the following section, however, it should be noted here that similar studies for GaAs/AlGaAs or InGaAs/GaAs quantum wells exhibit a  $\Gamma$ -X crossing near 40 kbar. For pressures greater than 40 kbar, the X-point becomes the conduction-band ground state and because of large non-radiative recombination paths at the X-point, the PL signal normally disappears.<sup>22</sup> For the InGaAsN pressure data shown in Fig. 2, this is obviously not the case. Thus, to be able to understand the behavior of the InGaAsN system, we need information about its band structure, which will be discussed in Sec 3.1. Section 3.2 presents experimental measurements and estimates for 2% nitrogen InGaAsN alloy conduction-band effective mass while Sec. 3.3 discusses the pressure dependence of the same conduction-band effective mass.

#### 3.1 Band Structure of InGaAsN alloys

In order to model the band structure for the InGaAsN system, we used the Vienna *Ab initio* Simulation Package<sup>23-26</sup> (VASP) to perform first-principles electronic structure calculations based on the Kohn-Sham density functional theory with plane wave basis sets, ultrasoft pseudopotentials,<sup>27</sup> and the local density approximation for the exchange-correlation functional. In construction of the pseudopotentials, the Ga 3d electrons were treated as valence electrons in order to accurately represent any effects of a near resonance with the nitrogen 2s level that has been observed in GaN.<sup>28</sup> We modeled the InGaAsN

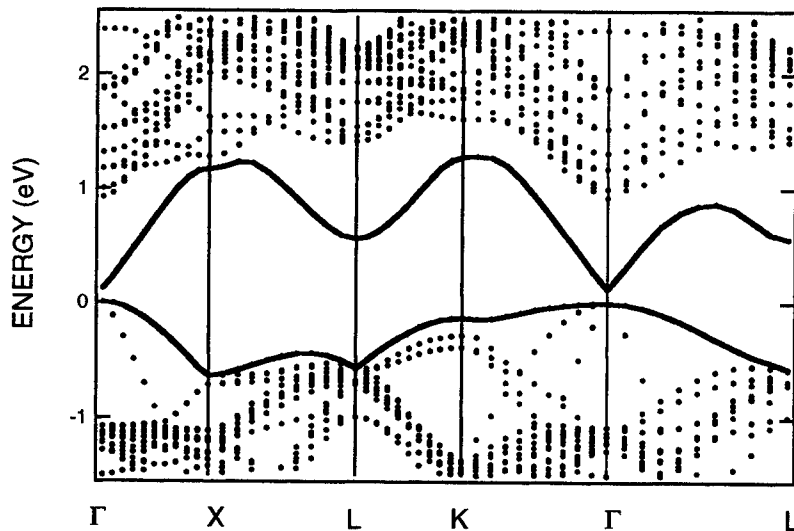


**Figure 3** . First principles local density approximation calculation for 3.3% nitrogen InGaAsN alloy. The solid lines, top and bottom, are respectively the conduction and valence bands.

system in the experimentally relevant concentration range using a series of supercells of the zincblende GaAs structure each with a single arsenic replaced by a nitrogen. The lattice constants of the supercells were varied to simulate the effects of pressure, and for each cell, the ionic positions were relaxed using first-principles forces until the residual forces were less than 20 meV/Å. In all cases, we found that the nitrogen atom remained in the symmetric position during relaxation. In order to compare to experimental data, which is taken as a function of pressure, an *ab initio* calculation of the system pressure was performed. We have investigated supercells with the following stoichiometries: Ga<sub>32</sub>As<sub>31</sub>N, Ga<sub>64</sub>As<sub>63</sub>N, Ga<sub>108</sub>As<sub>107</sub>N, and Ga<sub>128</sub>As<sub>127</sub>N. These cells correspond to nitrogen concentrations of 3.13, 1.56, 0.93 and 0.78%, with the nitrogen atoms ordered in simple cubic, fcc, bcc, and simple cubic lattices respectively. In contrast, the nitrogen atoms in the experimental system are believed to be nearly randomly distributed.<sup>18</sup> However, we found that calculated band structures of our supercells were qualitatively similar despite their differing symmetries, indicating that the nitrogen atoms interact weakly with each other at these low concentrations. Therefore, we believe that our artificially ordered supercells provide an adequate model of the near-band-gap electronic structure of the disordered experimental system. Likewise, we have ignored the presence of In in the experimental system (except for indirect effects due to the change in lattice constant, as will be discussed below). This is justified since experimental studies of InGaAs alloys indicate that the low concentration of indium found in the experimental InGaAsN system has a small effect on the electronic properties.<sup>3,4</sup>

Figure 3 shows a representative band structure for the 3.13% system. It should be noted that the band structure is plotted with respect to the Brillouin zone of a 64-atom cell. Since the nitrogen substitution breaks the symmetry of the underlying zincblende structure, there is no uniquely defined way to “unfold” the band structure into the Brillouin zone of the primitive 2-atom zincblende unit cell. The high symmetry points of the primitive GaAs cell fold into the  $\Gamma$ -point of the 64-atom cell, and therefore in the presence of a real symmetry breaking term (such as produced by nitrogen substitution), we expect interaction between the resulting levels. The valence band and the conduction band are indicated by the heavy solid line. The conduction band is well separated from the other bands throughout most of the Brillouin zone, and it is quite dispersive with a bandwidth more than 1 eV. Likewise, the bands above the conduction band show a substantial amount of dispersion, and there is no evidence of a flat impurity-like band anywhere above the conduction band. The absence of a nitrogen derived impurity-like state is supported by a decomposition of the wave-functions in terms of atomic-like orbitals, which shows that the conduction band has about 5% of its weight on the nitrogen atom, which is by far the highest fraction of any of the bands above the gap. The

calculated bandgap is only 0.12 eV, while the experimental bandgap is of order 1 eV for this concentration of nitrogen. This large error in the bandgap is a well known problem of the LDA. A central result of this paper is that despite this large error in the absolute magnitude of the bandgap, the *change* in bandgap with lattice constant is in excellent agreement with experiment (see Fig. 2).

Figure 2 compares experimental data to results of our theoretical model. The agreement between theory and experiment is excellent. In order to make a meaningful comparison, some nontrivial analysis of the theoretical calculations is required. The basic principle of this analysis is to treat the lattice constant and nitrogen concentration as independent variables, while the bandgap and pressure are treated as dependent variables. The dependent variables are then shifted to remove known LDA errors. In order to obtain results applicable to the 2.0% experimental nitrogen concentration, the bandgap and the pressure are linearly interpolated between the results of 128-atom (1.56% N) and 64-atom (3.13% N) supercells for each lattice constant. Then, results obtained at the experimental lattice constant of GaAs are taken as the reference (assumed to correspond to the experimental zero of pressure), and we plot the change in bandgap against the change in pressure. This procedure compensates for two well known errors of the LDA: (1) The bandgap is severely underestimated, as discussed above. (2) The lattice constant is underestimated by about 1%. The second error may seem to be insignificant compared to the errors in LDA results for some other quantities, but it corresponds to about a 20 kbar error in pressure, which is significant on an experimental scale. Since the experimental GaAs lattice constant is used, this procedure also helps to implicitly compensate for neglecting the In, which is added to the experimental system to match the lattice constant to that of GaAs.

The approach described here could prove useful for similar systems. However, we believe that a reason for the success of our approach is that, with the exception of the largest nitrogen concentration at the largest lattice constant, all of our model systems have a positive bandgap. Previous first-principles calculations for the GaAsN system<sup>8-10</sup> have used high nitrogen concentrations in order to obtain smaller model systems, which are computationally less demanding. At these higher concentrations, the LDA bandgap error is so severe that computed band structures do not have a bandgap. This artificial bandgap collapse leads to unphysical occupations of the electronic states (i.e. conduction-band-like states are occupied, while valence-band-like states are unoccupied), producing a significant error in the electronic charge density. In this regime of strongly negative LDA bandgaps, we are not confident that our simple LDA-based approach to computing the pressure dependence of excited state energies could be applied fruitfully.

A remarkable feature of Fig. 2 is the strongly non-linear dependence of the gap on the pressure. This is in marked contrast to the parent GaAs material and provides additional evidence, beyond the large reduction in the bandgap, that a few percent of nitrogen is producing remarkable changes in the material. In order to understand this nonlinearity, it is necessary to study additional bands above the conduction band. Figure 4 shows the theoretical pressure dependence of the  $\Gamma$ -point energies of several additional bands treated with the same analysis that was used for the conduction band in Fig. 2. Eight energy bands of the sys-

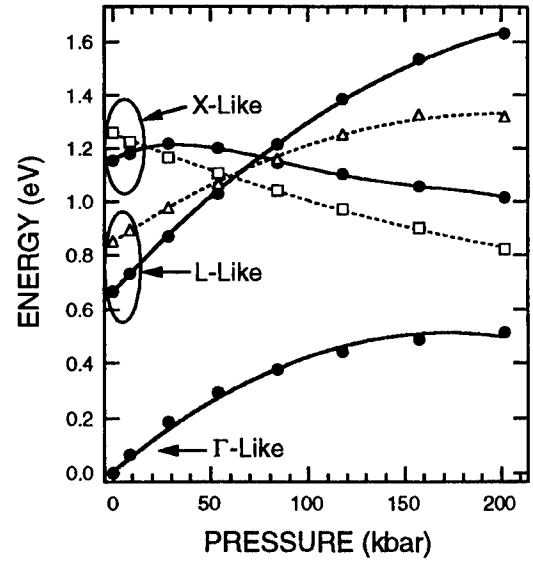


**Figure 4.** Theoretical pressure dependence of the conduction-band states near the bandgap energy minimum for 2% nitrogen GaAsN alloy. The points are calculated and there are three singlets (filled circles), a doublet (open squares), and a triplet state (open triangles).

tem are shown, but these fall into five degenerate groups. The figure shows three singlet states (filled circles), a doublet (open squares), and a triplet state (open triangles).

A common origin of nonlinear behavior of energy levels as a function of a parameter (such as pressure) is band repulsion. Band repulsion results from the mixing (hybridization) of bands in the same representation of the crystal symmetry group in such a way that level crossings are replaced with non-intersecting horizontal curves separated by a gap-like region. In Fig. 4, the highest singlet on the left and the triplet on the upper right bend downward due to repulsion from higher energy bands that have been omitted from the figure in order to improve its clarity. Whether the upper two singlets cross or repel at about 80 kbar can not be determined from the limited number of points that we have calculated, but if they repel, the effect is not very strong. We have chosen to show the bands as crossing in order to aid the eye in following their relationship with the doublet and the triplet. These assignments were chosen by comparing our results for various nitrogen concentrations with results for pure GaAs with the appropriately folded Brillouin zone. This comparison also allows useful, but non-rigorous, assignments of the low energy GaAsN bands at the  $\Gamma$ -point to special points of the primitive 2-atom GaAs Brillouin zone that are folded into the  $\Gamma$ -point. For the bands shown in Fig. 4, we propose the following assignments: (1) The bottom singlet corresponds to the  $\Gamma$ -point of the fundamental cell. (2) The second singlet on the left hand side (the third singlet on the right) plus the triplet correspond to a split quartet formed from the 4 L-points  $(1\ 1\ 1)$ ,  $(1\ \bar{1}\ \bar{1})$ ,  $(\bar{1}\ 1\ \bar{1})$ , and  $(\bar{1}\ \bar{1}\ 1)$ . (3) The remaining singlet plus the doublet correspond to a split triplet consisting of the three X-points (100), (010), and (001). In regions of band repulsion, for example, the character of different bands becomes mixed, and thus these assignments should not be taken too literally. However, we feel that they provide useful labels and help in interpreting the data.

With one exception, all of the bands within a few eV of the gap are observed to regain the degeneracies of pure GaAs to within of a few hundredths of an eV by the time our largest cell (0.78% N concentration) is reached. The exception is the L-derived singlet, which remains split off from the triplet by about 0.1 eV. This suggests that this singlet may evolve into the impurity state observed at very low nitrogen concentrations.<sup>29,30</sup> However, as mentioned above, this state does not act like an impurity state at the technologically interesting concentrations around 2%. Furthermore, the L-derived singlet rises faster than the conduction band throughout the studied pressure range, and we do not see the upward curvature that would be expected if it was repelled by the conduction band. Therefore, we believe that repulsion between the L-derived singlet and the conduction band contributes at most a small amount to the nonlinearity of the conduction band. In contrast, Fig. 4 demonstrates almost textbook repulsion between the X-derived singlet and the conduction band at pressures over 100 kbar, and it is likely that this repulsion continues to lower pressures, even though the effect is obscured by the additional repulsion between the X-derived singlet and a higher state. Based on these observations, we propose that repulsion from the X-derived singlet is the chief cause of the experimentally observed nonlinear dependence of the bandgap on pressure. Based on the above, we conclude that the nonlinear dependence of the bandgap on pressure does not result from localized nitrogen states. Finally, we note that our results are consistent with recent reflectance measurements which show some of the predicted higher energy states.<sup>31,32</sup>

### 3.2 Conduction-band mass for InGaAsN alloys

There are three convenient methods of using optical measurements for masses, and they are: (1) Study the change in luminescence energy in quantum well structures as a function of the quantum-well width. (2) Measure the quantum well energies by photoreflectance measurements as a function of quantum-well width. (3) Measure exciton diamagnetic shifts as a function of magnetic field. A fourth experimental method, low-temperature measurement of far-infrared cyclotron resonance from n-

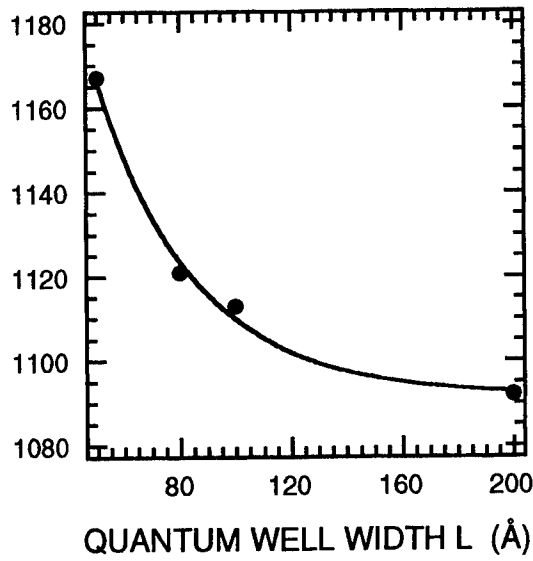


Figure 5. Luminescence energy versus quantum well width  $L$  for InGaAsN/GaAs single quantum wells at 4K. The smooth curve drawn through the data is provided an aid to the eye.

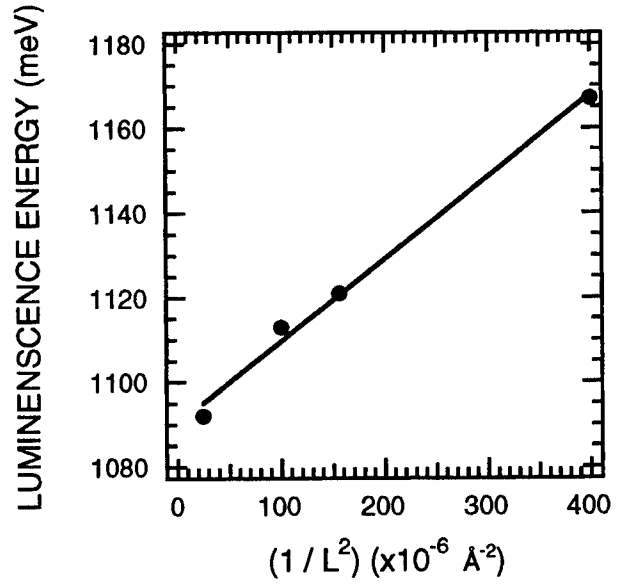


Figure 6. Luminescence energy versus the square of the inverse quantum well width, i.e.,  $L^{-2}$  for InGaAsN/GaAs single quantum wells at 4K. The straight line fitted to the data, yields an estimate for the conduction-band effective mass  $m_c \sim 0.2$ .

type samples was attempted, but because of the low transport mobility ( $\sim 400 \text{ cm}^2/\text{V}\cdot\text{sec}$ ), we not able to observe any cyclotron resonance. However, the question regarding the effect of on the conduction-band mass, if any, from adding a small amount of nitrogen to GaAs will now be addressed.

A series of nominally 2% nitrogen InGaAsN/GaAs quantum wells were grown as previously described in Sec. 2. The widths were estimated from growth rate calibrations. The PL measurements were made at 4K and the resulting dependence of the bandgap energy on the quantum-well width is shown in Fig. 5. The quantum well widths varied between 50 and 200 Å, and as can be seen in Fig. 5, the luminescence energy increases with decreasing quantum well width, the anticipated result. We are interested in comparing the InGaAsN and GaAs masses and thus for purposes of this paper, we will analyze the quantum well data in a simple manner assuming infinite barrier heights. Because all of the mass measurements presented here are only to serve as an illustration of the effect of nitrogen in GaAs, we feel that these simple assumptions are warranted. With the infinite barrier approximation, the luminescence energy is given by

$$E(n) = \frac{\pi^2 \hbar^2 n^2}{2ma^2} = \frac{37600}{m^* L^2}, \quad (L \text{ in } \text{Å}), \quad (1)$$

where  $n = 1, 2, \dots$  is the quantum number of the state,  $m^*$  is the conduction-band effective mass, and  $L$  is the quantum well width. Also assumed here is that the InGaAsN/GaAs quantum-well valence-band effective mass is much heavier than the conduction-band mass, and hence the conduction-band mass and not the reduced mass as expressed in Eq. 1. Because the valence-band offset between 2% nitrogen in InGaAsN and GaAs is believed to be small and only due to the offset from the 7% indium content,<sup>3,4</sup> it is reasonable to assume that quantum confinement has not caused a large splitting between the “pinned” heavy-hole and light-hole valence bands, thereby leading to a “heavy” valence-band mass. Figure 6 shows the dependence of the

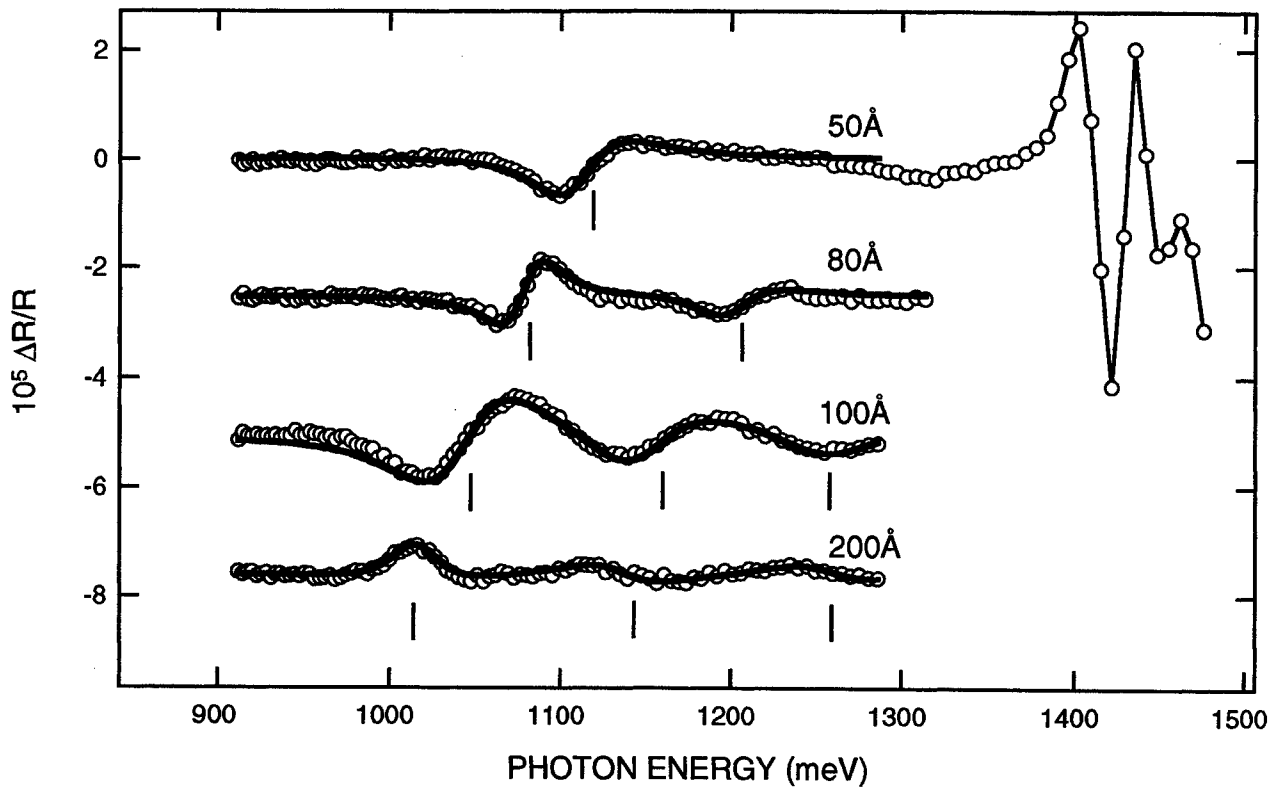


**Figure 7.** Photoreflectance spectra for four InGaAsN/GaAs quantum well structures. The quantum-well widths are indicated in the figure. The solid lines are “fitted” theoretical photoreflectance line shapes to the data. The vertical lines are the critical point energies (i.e., quantum well energies) for each spectrum as calculated by the theoretical line shape fit. As an aid to the eye, the spectra have been offset from each other.

luminescence energy as a function of  $L^{-2}$  for the data shown in Fig. 5, and as can be seen, a straight line can be drawn through the data. From the slope of the line shown in Fig. 6 and with  $n = 1$  in Eq. 1, we derive  $m_c \sim 0.2$ . Possible sources of error in this analysis are the experimental quantum-well widths which are difficult to monitor or control during growth. However, the conduction-band effective mass for GaAs is 0.067 and thus, as in the case of the bandgap energy, we see that the addition of a small amount of nitrogen to GaAs has caused large changes to the 2% nitrogen InGaAsN conduction-band mass.

As mentioned earlier, we have also performed room temperature photoreflectance measurements on the similar structures to those used for the luminescence energy versus quantum-well-width studies. Figure 7 shows photoreflectance spectra for 50, 80, 100 and 200-Å-wide quantum wells. The solid lines are “fitted” theoretical photoreflectance line shapes to the data. The vertical lines are the critical point energies (i.e., quantum well energies) for each spectrum as calculated by the theoretical line shape fit. The difference energy  $\delta E$  from the quantum well states shown in Fig. 7, as vertical lines, gives  $\delta E \sim 120$  meV. We again make the assumption that this energy difference is due entirely to the conduction-band states. With infinite barrier heights, we can arrive at a qualitative estimate for the conduction-band mass from Eq. 1, with the result  $m_c \sim 0.14$ , a mass twice as large as that found for GaAs! However, the two measurements of mass are in reasonable agreement with each other and both lead to the conclusion that the conduction-band mass in InGaAsN is two to three times heavier than found for GaAs.



The last experimental method for an optical determination of the conduction-band mass involves measurements of the exciton diamagnetic shift as a function of magnetic field for 2% nitrogen InGaAsN alloys lattice matched to GaAs. The magnetoexciton diamagnetic shift dependence on magnetic field for ambient pressure is shown as closed circles in Fig. 8. The diamagnetic shifts for varying InGaAsN conduction-band mass  $m_c$  between 0.067 and 0.5 are also indicated in the figure. The theoretical diamagnetic shifts were calculated by the variational approach as described by Greene and Bajaj.<sup>33,34</sup> For the diamagnetic shift calculation presented here, we adapted our quantum-well computer codes<sup>35</sup> which were used to quantify the diamagnetic shift studies in (411)A-oriented GaAs/AlGaAs quantum wells. We account for the 3D (bulk) excitons in InGaAsN by setting the InGaAsN quantum-well width to greater than 200 nm. The trial wavefunctions for the exciton center-of-mass coordinate system are expressed in terms of a Gaussian basis set with the magnetic field perpendicular to the growth direction, i.e., the exciton orbits are in the plane of a 200-nm-wide InGaAsN/GaAs quantum well. The exciton binding energies are calculated for finite values of the height of the 7% indium InGaAsN-GaAs potential barrier. The envelope function method is also employed to account for the finite quantum-well width and height. Besides the low temperature bulk GaAs bandgap energy, the magnetic field strength, and the quantum-well width, some of the relevant physical parameters include: (1) Conduction and valence-band offsets between InGaAsN quantum well and the GaAs barriers. (2) The Luttinger parameters  $\gamma_1$  and  $\gamma_2$  for both the InGaAsN quantum well and GaAs barriers. (3) Conduction and valence-band mass values for the InGaAsN quantum well and GaAs barrier. (4) Low frequency dielectric constants  $\epsilon_0$  for the quantum well and barrier materials. For these calculations, GaAs values for all parameters except the conduction-band mass were used not only for the GaAs barrier, but also for the InGaAsN quantum well. For the present stage of understanding the electronic properties of InGaAsN alloys, these assumptions are reasonable. As can be seen in Fig. 8, a best fit diamagnetic shift dependence on magnetic field occurs for an InGaAsN conduction-band effective mass  $m_c \approx 0.13$ , which is in excellent agreement with the two previous optical determinations presented in this paper of the energy versus quantum-well width studies which gave  $m_c = 0.2$  and the analysis of the quantum-well states of the photoreflectance data which yielded  $m_c = 0.14$ .

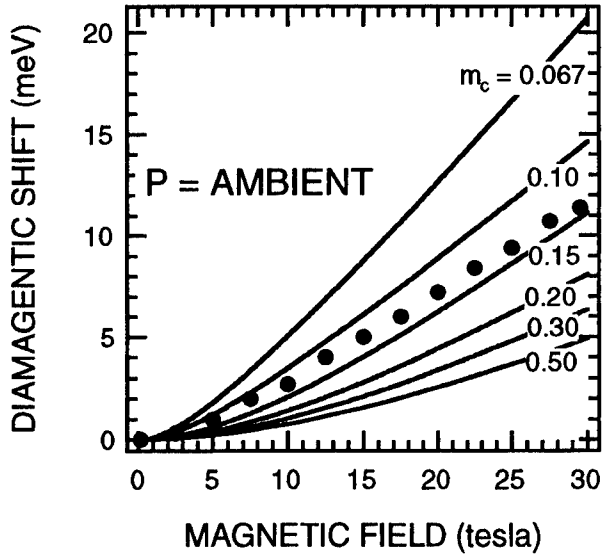


**Figure 8.** Ambient-pressure exciton diamagnetic shift as a function of magnetic field at 2K for 2% nitrogen InGaAsN alloy. The closed circles are the experimental points. The curves, labeled  $m_c = 0.067$  to 0.50, are calculated diamagnetic shifts as a function of mass. The estimated ambient pressure InGaAsN conduction-band effective mass  $m_c$  is about 0.13.

### 3.3 Pressure dependence of the InGaAsN conduction-band effective mass

As mentioned in the experimental section, pressure dependent magnetoluminescence measurements were performed in the pressure range of ambient to 110 kbar and magnetic fields up to 30 tesla. The diamagnetic shift data can be readily analyzed for pressures less than 40 kbar. For higher pressures, the accuracy of the technique fails because of linewidth broadening by the non-hydrostatic component of the pressure medium and also because of an large increase of the conduction-band mass as discussed below. Also, other broadening mechanisms include possible differences to the GaAs elastic constants with the addition of 2% nitrogen. If the elastic constant differences between GaAs and InGaAsN are significant, the application of pressure (including hydrostatic pressure) will lead to anisotropic strain in the InGaAsN epilayer and hence large PL linewidths.

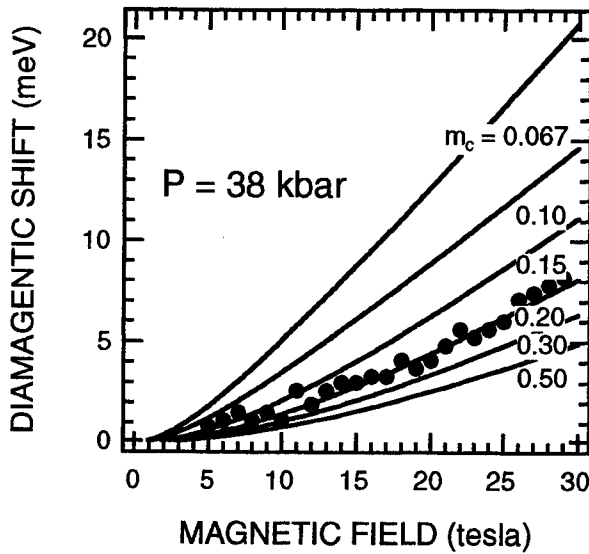


**Figure 9.** Exciton diamagnetic shift as a function of magnetic field and 38 kbar at 2K for the 2% nitrogen InGaAsN alloy. The closed circles are the experimental points. The curves,  $m_c = 0.067$  to 0.50, are theoretical diamagnetic shifts as a function of mass. The estimated InGaAsN conduction-band effective mass at 38 kbar is  $m_c \approx 0.2$ .

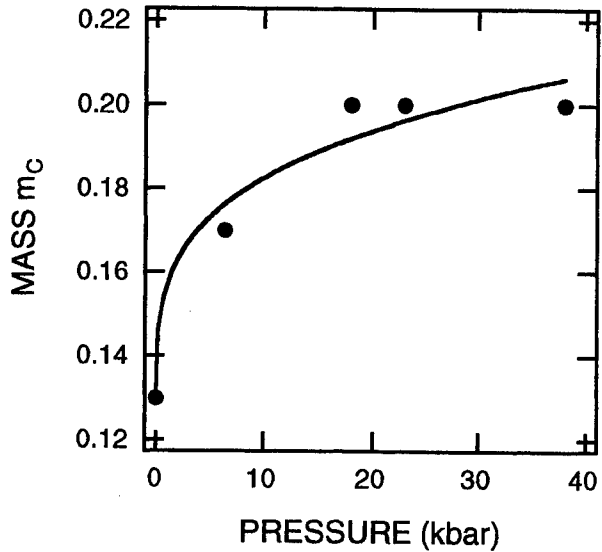


**Figure 10.** The 2-K pressure dependence of the conduction-band mass between ambient pressure and 40 kbar for the 2% nitrogen InGaAsN sample. The smooth curve drawn through the data provides an aid to the eye.

Figure 9 shows the magnetic field dependence of the exciton diamagnetic shift at 38 kbar and  $T = 2\text{K}$ . As is the case with Fig 8, the filled circles are the data points and the curves are calculated shifts as a function of mass. It is apparent from the figure that the conduction-band effective mass is nearly 0.2 in contrast to the  $m_c = 0.13$  found from the ambient pressure data. This large increase to the mass for 2% nitrogen in GaAs is surprising. Recently, we have reported<sup>36</sup> mass measurements as a function of pressure in  $\text{In}_{0.2}\text{Ga}_{0.8}\text{As}/\text{GaAs}$  strained-single-quantum wells and, found that the conduction-band mass ranged from  $\sim 0.07$  to  $\sim 0.085$  for pressures between ambient and 36 kbar in a linear manner. This result for InGaAs/GaAs agrees with expectations<sup>36</sup> based on simple  $k\cdot p$  theory. The large variation and nonlinear behavior of the conduction-band mass for InGaAsN may not be that surprising in light of all of the other mysteries associated with substituting nitrogen for arsenic in GaAs. Figure 10 shows the variation of the effective mass for pressures between ambient and 38 kbar. The smooth curve provides an aid to the eye.

Because of our success in using the LDA calculation to quantify the change in the bandgap energy with pressure (Fig. 2), we performed preliminary LDA calculations for the pressure dependence of the conduction-band mass. But to date, our results are inconclusive and hence will not be discussed here. We can, however, make some qualitative statements by examining the LDA results shown in Fig. 4. As discussed earlier, the band repulsion between the  $\Gamma$ -like and X-like bands at high pressure indicate that strong  $\Gamma$ -X mixing is occurring. Because the mass of the six-fold degenerate X-point in GaAs is heavy ( $m_{Xt} = 1.2$  &  $m_{Xl} = 0.27$ ), we expect that the  $\Gamma$ -X mixing will cause a corresponding increase to the  $\Gamma$ -like conduction-band mass by the heavy X-like mass. Part of the LDA mass calculation will require information about the X-like as well as the L-like masses. In the future, an obvious goal of our LDA calculations will be to replicate the curve shown in Fig. 10.

#### 4. CONCLUSIONS

We have shown that while the first principles LDA calculation for the band structure of InGaAsN yields incorrect values for the bandgap energy, the predicted change in bandgap energy with pressure is in excellent agreement with experiment. Both experiment and calculations show that the lack of crossing of the  $\Gamma$ -like and X-like conduction bands is due to  $\Gamma$ -X mixing. The conduction-band effective mass was measured by three techniques with the result for 2% InGaAsN, lattice matched to GaAs, being that the ambient pressure conduction-band effective mass  $m_c \approx 0.15$ . The pressure dependence of the conduction-band mass is nonlinear and large. The current challenge of the LDA calculation is to account for this behavior.

#### ACKNOWLEDGEMENTS

The authors wish to thank Dr. Yong-Jie Wang of the National High Magnetic Field Laboratory for the far-infrared cyclotron measurements, Dr. D. M. Follstaedt and Dr. Charles Barbour of Sandia National Laboratories for providing the results of their transmission electron microscopy measurements and elastic recoil detection measurements. Sandia is a multiprogram laboratory operated by Sandia Corporation, a Lockheed Martin Company, for the United States Department of Energy under contract DE-AC04-94AL85000. Part of this work was performed at the National High Magnetic Field Laboratory, which is supported by NSF Cooperative Agreement No. DMR-9016241 and by the State of Florida, and by a grant of HPC time from the DoD HPC ARL and CEWES Major Shared Resource Centers. The *ab initio* total-energy and molecular-dynamics package VASP (Vienna *Ab initio* Simulation Package) and the corresponding ultrasoft pseudopotential database were developed at the Institute für Theoretische Physik of the Technische Universität Wien.

#### REFERENCES

1. W. G. Bi and C. W. Tu, "Bowing parameter of the band-gap energy of  $\text{Ga}_x\text{As}_{1-x}$ ," *Appl. Phys. Lett.* **70**, pp. 1608-1610, 1997.
2. L. Malikova, F. H. Pollak, and R. Bhat, "Composition and temperature dependence of the direct band gap of  $\text{GaAs}_{1-x}\text{N}_x$  ( $0 \leq x \leq 0.0232$ ) using contactless electroreflectance," *J. Electronic Materials* **27**, pp. 484-487, 1998.
3. M. Kondow, K. Uomi, A. Niwa, T. Kitatani, S. Watahiki, and Y. Yazawa, "GaInNAs: A novel material for long-wavelength-range laser diodes with excellent high-temperature performance," *Jpn. J. Appl. Phys.* **35**, pp. 1273-1275, 1996.
4. M. Kondow, T. Kitatani, S. Nakatsuka, M. C. Larson, K. Nakahara, Y. Yazawa, M. Okai, and K. Uomi, "GaInNAs: A novel material for long wavelength semiconductor lasers," *IEEE J. Selected Topics in Quantum Electronics* **3**, pp. 719-729, 1997.
5. T. Miyamoto, K. Takeuchi, F. Koyama, and K. Iga, "A novel GaInNAs-GaAs quantum-well structure for long-wavelength semiconductor lasers," *IEEE Photonics Tech. Lett.* **9**, pp. 1448-1450, 1997.
6. Sarah R. Kurtz, D. Myers, and J. M. Olsen, "Projected Performance of Three- and Four Junction Devices Using GaAs and GaInP" in *Proc. 26th IEEE Photovoltaics Spec. Conf.* (IEEE, New York, 1997) pp. 875-878.
7. Steven R. Kurtz, A. A. Allerman, E. D. Jones, J. M. Gee, J. J. Banas, and B. E. Hammons, "InGaAsN solar cells with 1 eV bandgap, lattice matched to GaAs," to be published, *Appl. Phys. Lett.*
8. A. Rubio and M. L. Cohen, "Quasi-particle excitations in  $\text{GaAs}_{1-x}\text{N}_x$  and  $\text{AlAs}_{1-x}\text{N}_x$  ordered alloys," *Phys. Rev. B* **51**, pp. 4343-4346, 1995.
9. J. Neugebauer and C. G. Van de Walle, "Electronic-structure and phase-stability OF  $\text{GaAs}_{1-x}\text{N}_x$  alloys," *Phys. Rev. B* **51**, pp. 10568-10571, 1995.
10. S.-H. Wei and A. Zunger, "Giant and composition-dependent optical bowing coefficient in GaAsN alloys," *Phys. Rev. Lett.* **76**, pp. 664-667, 1996.
11. L. Bellaiche, S.-H. Wei, and A. Zunger, "Localization and percolation in semiconductor alloys," *Phys. Rev. B* **54**, pp. 17568-17576, 1996.
12. L. Bellaiche, S.-H. Wei, and A. Zunger, "Band gaps of GaPN and GaAsN alloys," *Appl. Phys. Lett.* **70**, pp. 3558-3560, 1997.
13. L. Bellaiche, S.-H. Wei, and A. Zunger, "Composition dependence of interband transition intensities in GaPN, GaAsN, and GaPAs alloys," *Phys. Rev. B* **56**, pp. 10233-10240, 1997.

14. L. Bellaiche and A. Zunger, "Effects of atomic short-range order on the electronic and optical properties of GaAsN, GaInN, and GaInAs alloys," *Phys. Rev. B* **57**, pp. 4425-4431, 1998.
15. E. D. Jones, N. A. Modine, A. A. Allerman, S. R. Kurtz, A.F. Wright, S. T. Tozer, and X. Wei, "Band structure of InGaAsN alloys and effects of pressure," submitted to *Phys. Rev. Lett.* (1999).
16. X. Zhu, S. Fahey, and S. G. Louie, "*Ab initio* calculation of pressure coefficients of band gaps of silicon: Comparison of local-density approximation and quasiparticle results," *Phys. Rev. B* **39**, pp. 7840-7847, 1989.
17. E. V. K. Rao, A. Ougazzaden, Y. Le Bellego, and M. Juhel, "Optical properties of low band gap GaAs<sub>(1-x)</sub>N<sub>x</sub> layers: Influence of post-growth treatments," *Appl. Phys. Lett.* **72**, pp. 1409-1411, 1998.
18. D. M. Follstaedt (Unpublished results).
19. S.W. Tozer (Unpublished results).
20. G. J. Piermarini, S. Block, J. D. Barnett, "Hydrostatic limits in liquids and solids to 100 kbar," *J. Appl. Phys.* **44**, pp. 5377-5382, 1973.
21. R. A. Forman, G. J. Piermarini, J. D. Barnett, S. Block, "Pressure measurement made by the utilization of ruby sharp-line luminescence," *Science* **176**, pp. 284-285, 1972.
22. See for example E. D. Jones, S. T. Tozer, and T. Schmiedel, "Pressure dependence of the bandgap energy and the conduction-band mass for an n-type InGaAs/GaAs single-strained quantum well," *Physica E* **2**, pp. 146-150, 1997.
23. G. Kresse and J. Hafner, "*Ab initio* molecular-dynamics for liquid-metals," *Phys. Rev. B* **47**, pp. 558-561, 1993.
24. G. Kresse and J. Hafner, "*Ab-initio* molecular-dynamics simulation of the liquid-metal amorphous-semiconductor transition in germanium," *Phys. Rev. B* **49**, pp. 14251-14269, 1994.
25. G. Kresse and J. Furthmüller, "Efficiency of *ab-initio* total-energy calculations for metals and semiconductors using a plane-wave basis-set," *Comput. Mat. Sci.* **6**, pp. 15-50, 1996.
26. G. Kresse and J. Furthmüller, "Efficient iterative schemes for *ab-initio* total-energy calculations using a plane-wave basis-set," *Phys. Rev. B* **54**, pp. 11169-11186, 1996.
27. D. Vanderbilt, "Soft self-consistent pseudopotentials in a generalized eigenvalue formalism," *Phys. Rev. B* **41**, pp. 7892-7895, 1990.
28. V. Fiorentini, M. Methfessel, and M. Scheffler, "Electronic and structural-properties of GaN by the full-potential linear muffin-tin orbitals method: The role of the d-electrons," *Phys. Rev. B* **47**, pp. 13353-13362, 1993.
29. D. J. Welford, J. A. Bradley, K. Fry, and J. Thompson, "The nitrogen isoelectronic traps in GaAs" in *Physics of Semiconductors*, ed. J. D. Chadi and W. A. Harrison (Springer, New York, 1984) pp. 627-630.
30. X. Liu, M. E. Pistol, L. Samuelson, S. Schwetlick, and W. Seifert, "Nitrogen pair luminescence in GaAs," *Appl. Phys. Lett.* **56**, pp. 1451-1453, 1990.
31. J. D. Perkins, A. Mascarenhas, Y. Zhang, J. F. Geisz, D. J. Friedman, J. M. Olson, and S. R. Kurtz, "Direct observation of resonant-level-induced giant bowing in GaAs<sub>1-x</sub>N<sub>x</sub>," to be published *Phys. Rev. Lett.*, 1999.
32. W. Shan, W. Walukiewicz, and J. W. Ager III, "Band anticrossing in GaInNAs alloys," to be published *Phys. Rev. Lett.*, 1999.
33. R. L. Greene and K. K. Bajaj, "Effect of a magnetic field on the energy levels of a hydrogenic impurity center in GaAs/Ga<sub>1-x</sub>Al<sub>x</sub>As quantum-well structures," *Phys. Rev. B* **31**, pp. 913-918, 1985.
34. R. L. Greene and K. K. Bajaj, "Binding energies of Wannier excitons in GaAs-Ga<sub>1-x</sub>Al<sub>x</sub>As quantum-well structures in a magnetic field," *Phys. Rev. B* **31**, pp. 6498-6502, 1985.
35. E. D. Jones, K. Shinohara, S. Shimomura, S. Hiyamizu, I. Krivorotov, and K. K. Bajaj, "Magneto-excitons in (411)A and (100)-oriented GaAs/AlGaAs multiple quantum well structures," to be published in *Physics and Simulation of Optoelectronic Devices VII*, edited by M. Osinski, P. Blood, and A. Ishibashi, SPIE Conference Proceedings Vol. **3625** (International Society for Optical Engineering, Bellingham, WA, 1999).

# Time-Resolved Photoluminescence Measurements of InGaN

## Light-Emitting Diodes, Films and Multiple Quantum Wells

M. Pophristic <sup>a</sup>, F. H. Long <sup>\*a</sup>, C. Tran <sup>b</sup>, I. T. Ferguson <sup>b</sup>, R. F. Karlicek Jr. <sup>b</sup>

<sup>a</sup> Department of Chemistry, Rutgers University, 610 Taylor Road, Piscataway, NJ 08854-8087

<sup>b</sup> EMCORE Corporation, Somerset, NJ 08873

### ABSTRACT

We have used time-resolved photoluminescence (PL) to examine light-emitting diodes (LEDs) made of InGaN/GaN multiple quantum wells (MQWs) before the final stages of processing. The time-resolved photoluminescence from a dim MQW was quenched by nonradiative recombination centers. The PL kinetics from a bright MQW were not single exponential but stretched exponential, with the stretch parameter  $\beta = 0.59 \pm 0.05$ . The emission lifetime varied with energy, within error  $\beta$  was independent of the emission energy. The stretched exponential kinetics are consistent with significant disorder in the material. Related results for an InGaN film and InGaN/GaN MQWs are also reported. We attribute the disorder to fluctuations of the local indium concentration.

**Keywords:** light-emitting diode, time-resolved photoluminescence, disorder,

### 1. INTRODUCTION

Recently there has been world-wide interest in the use of nitride semiconductors (eg. GaN, InN, and AlN) for opto-electronic devices such as lasers and light-emitting diodes (LEDs). The large changes in physical properties such as band gap, crystal structure, phonon energy, and electronegativity difference between GaN and GaAs, demonstrate that nitride semiconductors are fundamentally distinct from traditional III-V semiconductors. In spite of the impressive progress made in recent years<sup>1</sup> in the development of LEDs and lasers, significant work needs to be done in terms of the optimization of device performance. In order to achieve this goal, the physics underlying the operation of these devices must be better understood. Furthermore, new diagnostic techniques for the characterization of materials and devices will greatly aid in the long-term commercialization of this technology.

It has been recognized that under typical growth conditions there is a positive enthalpy for indium mixing in GaN.<sup>2</sup> Electron microscopy and cathodoluminescence of InGaN has demonstrated the existence of nanometer and micron scale regions of high indium concentration.<sup>3-6</sup> The regions of high indium concentration have a lower band gap than the bulk  $\text{In}_x\text{Ga}_{1-x}\text{N}$ ; therefore, either excitons or carriers are expected to spatially localize in these low energy regions on very fast time scales. It has been hypothesized that the nanoscale regions of high indium concentration are critical to LED operation.<sup>7, 8</sup>

---

\* Correspondence: Email: [fhlong@rutchem.rutgers.edu](mailto:fhlong@rutchem.rutgers.edu); <http://chmwww.rutgers.edu:80/~fhlong/> Telephone 732-445-6359; Fax 732-445-6359

Recently time-resolved photoluminescence (TRPL) has been used to examine nitride semiconductor multiple quantum wells (MQWs) InGaN films at room temperature.<sup>9-12</sup> We present results of time-resolved PL measurements on LED wafers based on InGaN/GaN MQWs.<sup>13</sup> We have found dramatic differences in the time-resolved kinetics between bright and dim devices. Furthermore, the experimental results strongly support the hypothesis that indium phase segregation is present in the bright LEDs. These results suggest that TRPL could be used as an on-line diagnostic for the pre-screening of InGaN LEDs.

## 2. EXPERIMENTAL

The laser used was an amplified and doubled Ti-sapphire laser from Coherent Corporation operating at 250 kHz. The time-resolved photoluminescence (PL) measurements were performed with a Hamamatsu streak camera model C5680. The excitation pulse was at 400 nm (3.10 eV). The excitation power was adjusted by using calibrated neutral density filters. The scattered laser light was filtered with a 420 nm band pass filter. The typical response time was 60 picoseconds and was determined by electrical jitter in the triggering electronics. The laser power used was 1.6 mW, 2.56  $\mu\text{J}/\text{cm}^2$ .

The  $\text{In}_x\text{Ga}_{1-x}\text{N}/\text{GaN}$  light emitting diode structure were grown by metal organic chemical vapor deposition.<sup>8</sup> The average indium mole fraction was about 11 %, as determined by photoluminescence using the strain corrected x-ray measurements of Amano.<sup>14</sup> The whole structure was on c-plane sapphire with 3 microns of unintentionally doped (n-type  $5 \times 10^{16}/\text{cm}^3$ ) GaN as a substrate. The LEDs consists of five layers of  $\text{In}_{0.11}\text{Ga}_{0.89}\text{N}$  35 Å thick and four layers of GaN each 45 Å thick. The two LEDs studied, Sample 1 and Sample 2, were grown under slightly different conditions, leading to large changes in brightness.<sup>8</sup> After final processing, the electroluminescence from Sample 2 was four times brighter than Sample 1, 400  $\mu\text{Watts}$  versus 100  $\mu\text{Watts}$ . The output power was measured at 20 mA and a forward voltage of about 4 volts.<sup>8</sup> The PL maximum of Sample 1 was 425 nm (2.92 eV) and Sample 2 was 440 nm (2.82 eV).

## 3. RESULTS AND DISCUSSION

### 3.1 Light-Emitting Diodes

Previous studies have demonstrated that bulk  $\text{In}_{0.11}\text{Ga}_{0.89}\text{N}$  has a band gap of about 2.95 eV (420 nm).<sup>14</sup> This is well below the excitation energy used in our experiments. However, the band gap of the GaN or GaN layers is well above the 3.10 eV excitation photons; therefore we are selectively exciting the  $\text{In}_{0.11}\text{Ga}_{0.89}\text{N}$  layers. The use of a selective excitation allows for the neglect of carrier diffusion between the GaN barrier layers and the InGaN, this greatly simplifies the analysis of the problem.

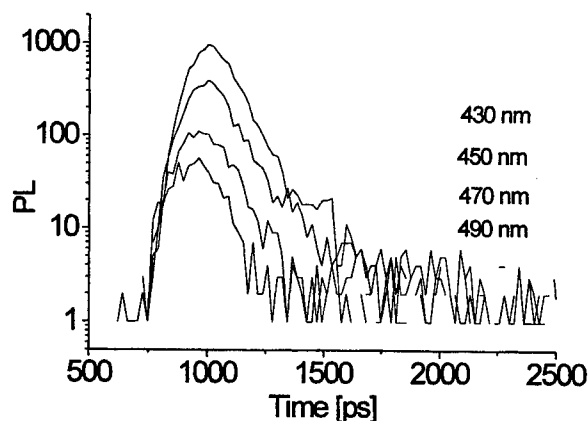


FIG. 1. TRPL from a dim light-emitting diode, Sample 1, at four different wavelengths 430, 450, 470, and 490 nm.

Time-resolved PL data for Sample 1 are shown in Fig. 1. The lifetime of the emission is quite short,  $110 \pm 20$  picoseconds at 440 nm, and the kinetics are not obviously dependent upon wavelength. This lifetime is short compared to other MQWs we have examined under similar conditions. The lifetime of Sample 1 is most likely quenched by non-radiative recombination centers. Time-resolved PL data for Sample 2 is shown in Fig. 2. The kinetics are clearly very wavelength dependent, highly non-exponential, and are clearly on the nanosecond time scale.

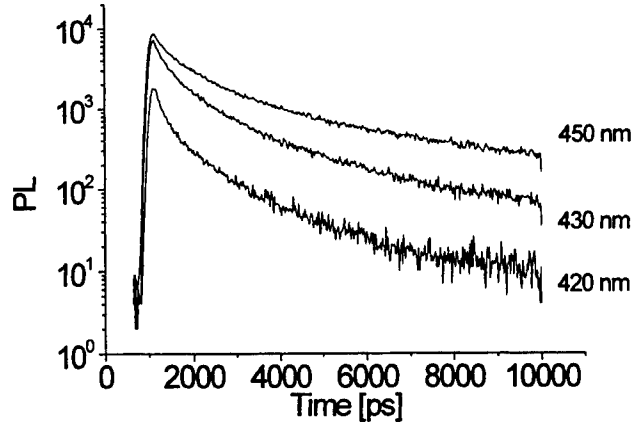


FIG. 2. TRPL from a bright light-emitting diode, Sample 2. The kinetics are highly non-exponential and dependent upon the emission wavelength. Note the time scale change from Fig. 1.

The PL kinetics of Sample 2, the bright LED, can be well-described by a stretched exponential, equation one,

$$I(t) = I_0 \exp(-(t/\tau)^\beta) \quad (1)$$

where  $\beta$  is between 0 and 1 and  $I(t)$  is the PL intensity as a function of time. Stretched exponentials have been used to describe the dynamics of heavily disordered systems for over 100 years.<sup>15</sup> The first observation of stretched exponential photoluminescence decay in a disordered semiconductor was made by Chen *et al.*<sup>16</sup> The TRPL from porous silicon is also well described by a stretched exponential. The underlying physical mechanisms of the porous silicon TRPL are a combination of topological disorder and a distribution of traps with different energies.<sup>17,18</sup> Nanoscale fluctuations in the indium concentration can produce both forms of disorder in InGaN. It is interesting to note that simulations of porous silicon demonstrate that PL from excitons and not uncorrelated electrons and holes yields the characteristic stretched exponential decays.<sup>19</sup>

$\beta$  can be independently determined from  $\tau$  by plotting the double logarithm of the signal versus the  $\ln$  of the time, Fig. 3. The deviation of the data from equation one at early times is due to the undefined slope of equation one at  $t=0$ . A small but clear curvature from stretched exponential behavior is seen at all wavelengths, Fig. 3. Similar deviations from stretched exponential behavior have been recently predicted using a theory for donor-acceptor recombination that includes energetic disorder.<sup>20</sup>

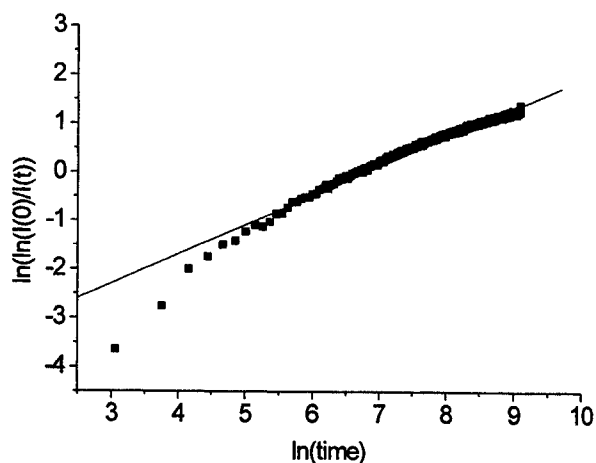


FIG. 3. The experimental value for  $\beta$  and  $\tau$  can be determined by plotting the  $\ln(\ln(I(0)/I(t)))$  versus log time. The emission wavelength was 450 nm (2.76 eV).

In Fig. 4 we plot  $\beta$  and  $\tau$  versus the emission wavelength.  $\beta = 0.59 \pm 0.05$  and within error is independent of emission wavelength. The stretched exponential lifetime varies from 500 picoseconds at 420 nm (2.95 eV) to 3000 ps at 500 nm (2.48 eV). The stretched exponential lifetime for the LED was found to vary exponentially with energy.

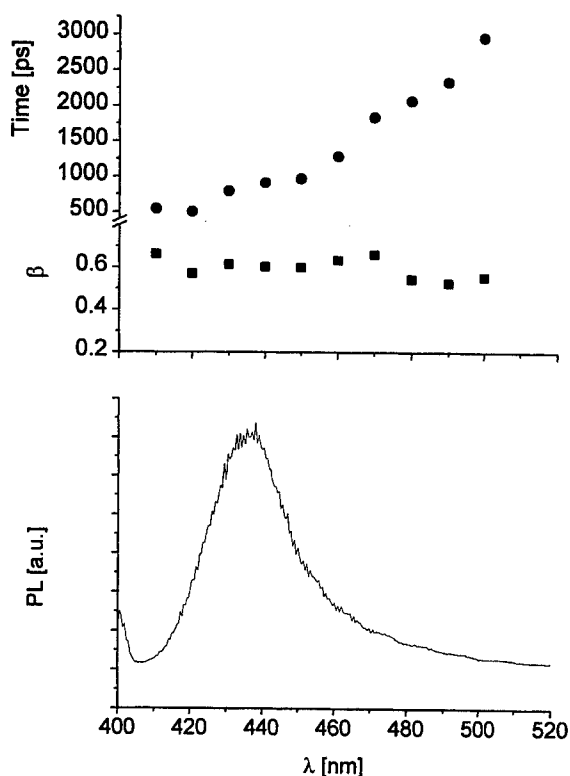


FIG. 4. Analysis of the TRPL from Sample 2. The stretched exponential lifetime is observed to dramatically increase as the emission wavelength is varied from 420 and 500 nm. The average experimental value for the stretch parameter  $\beta = 0.59 \pm 0.05$ , which is within error independent of energy. The time averaged PL spectra is shown on the bottom.



Typically the PL lifetime lengthens with increasing emission wavelength. Fermi's golden rule states that the rate of the transition is proportional to the density of states. Therefore the observed wavelength dependent kinetics can be attributed to increases in the density of states, as the transition energy approaches the band gap energy. We note that the PL maxima from other MQWs<sup>10,11</sup> is at higher energy with respect to our results, this may be due to increased indium concentration fluctuations in our samples. The possible role of tunneling, suggested by the energy dependence of  $\tau$ , is the subject of further investigation.

The importance of piezoelectric fields on the optical properties of  $\text{In}_{0.11}\text{Ga}_{0.89}\text{N}$  has recently been pointed out.<sup>21</sup> The piezoelectric field strength in  $\text{In}_x\text{Ga}_{1-x}\text{N}$  is almost ten times larger than what is observed in less polar semiconductors, such as InGaAs. Intense piezoelectric fields can also explain some of the effects attributed to indium phase segregation, such as the blue shifting of the PL at high carrier concentrations. However studies have shown that at high pulsed laser powers, as in our experiments, the carrier concentration is sufficiently high that the piezoelectric fields are screened.<sup>21</sup> At long times the carrier concentration will have sufficiently reduced that the screening will be incomplete. This is the subject of further investigation.

### 3.2 InGaN Film

We have also investigated InGaN films<sup>22</sup> and multiple quantum wells using time-resolved photoluminescence. We have found that the kinetics of the photoluminescence decays are well described by stretched exponential decays under a wide variety of conditions. Typical results for a high quality 300 Å thick InGaN film are shown in Fig. 5 and Fig. 6.

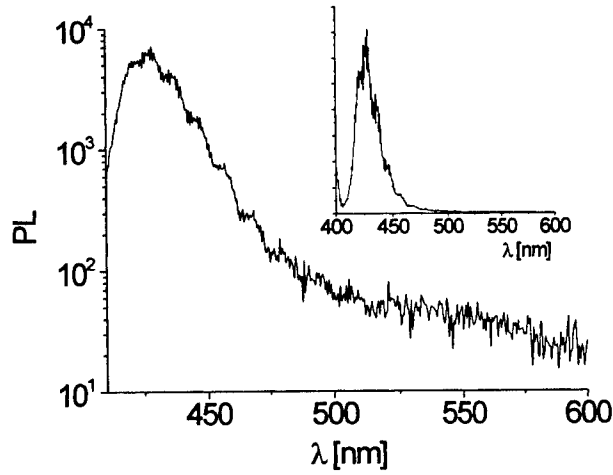


Fig. 5 The time-averaged PL spectra of the  $\text{In}_{0.22}\text{Ga}_{0.78}\text{N}$  film at room temperature measured with 3.10 eV (400 nm) femtosecond pulses. Note the y-axis is a log scale and the clear appearance of tail in PL spectra for wavelengths longer than 475 nm. The low energy tail is due to the emission of localized states most likely associated with the In phase segregation. The high energy side of the PL is cutoff by a long pass filter at 420 nm (2.95 eV). Insert: same spectra on a linear scale.

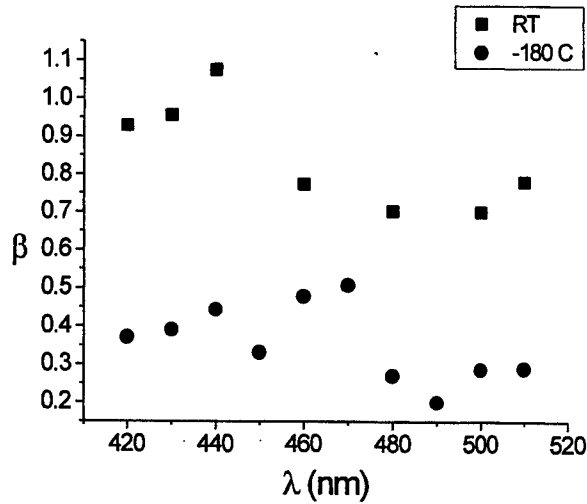


Fig. 6. The stretching parameter  $\beta$  plotted as a function of emission wavelength for both room temperature and 90 K. Same sample as Fig. 5.

The stretching parameter,  $\beta$ , is plotted for different emission energies for both room temperature (squares) and 90 K (circles). At the peak of the photoluminescence,  $\beta$  is near one at room temperature; however, as the sample temperature is lowered  $\beta$  is significantly reduced. Experimental data taken in between the two temperatures is in between the two curves. The lowering of  $\beta$  with temperature is consistent with energetic disorder in the film. At room temperature, there is sufficient thermal energy for the excited state to migrate between different indium sites with different decay rates, thus averaging out the distribution and increasing  $\beta$ . However at lower temperatures this is not the case and the excited state can be trapped in a broad distribution of regions of relatively high indium concentration and different decay rates. Our temperature dependent measurements suggests that the band edge fluctuations in InGaN are of the order of 25 meV. If the band edge fluctuations due to indium phase segregation were much larger, then  $\beta$  would not be almost one at room temperature.

The time-averaged and time-resolved photoluminescence data on the InGaN film support the existence of low energy tail states. In Fig. 5, these appear as a change in the slope of the PL spectra at wavelengths longer than 470 nm. Analogously, the stretching parameter  $\beta$  is observed to be lower in the same spectral region for both room and low temperatures, Fig 6. We attribute the low energy tail states to regions of high local indium concentration inside the film. The size of these regions is most likely characterized by a very broad distribution. Such as distribution is the likely origin of the very broad distribution in rates typical of low values of the  $\beta$ , the stretching parameter. Furthermore, the regions of high indium concentration, which are the microscopic origin of the low energy tail states, are expected to be separated by large distances. Over large distances any migration of the excited state is likely to be minimized, this will also contribute to a small value for the stretching parameter.

### 3.3 InGaN/GaN Multiple Quantum Wells

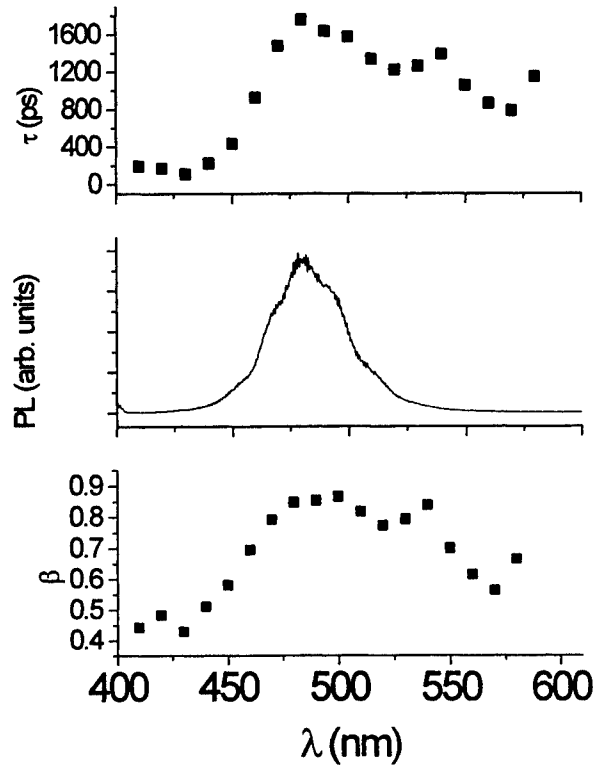


Fig. 7 Analysis of time-resolved photoluminescence data from a heavily segregated multiple quantum well. The indium mole fraction was 0.11; however, the PL maxima occurs at 480 nm (2.58 eV).

Results for a heavily phase segregated multiple quantum well are shown in Fig 7. Again over the entire measured spectral region, the time-resolved photoluminescence decays are clearly stretched exponential. Note that the time constant shown on the top of Fig. 7 is not the single exponential lifetime, but the parameter in equation one. We have observed the general trend that  $\beta$  is maximum at the PL emission maxima and decreases at both higher and lower energies. Similar trends have been calculated in models of porous silicon.<sup>23</sup> This energy dependence of the stretching parameter can be directly attributed to the migration of the excited state to local energy minima.

Theoretical models for stretched exponential behavior include either energetic or topological (e.g. structural) disorder.<sup>15</sup> Because  $\text{In}_x\text{Ga}_{1-x}\text{N}$  has a lower band gap than GaN, fluctuations in the local indium concentration can produce both energetic and topological disorder. In analogy to studies of porous silicon<sup>17,18</sup>, we hypothesize that the energy independence of  $\beta$  at room temperature, Fig. 4, is consistent with topological disorder. In this case, the stretched exponential kinetics may be due to the hopping of localized excitons. High pressure PL measurements on LEDs from Nichia clearly confirm that the emission originates from localized states.<sup>24</sup> Furthermore, there is some experimental evidence from structural measurements that indium concentration fluctuations occur on a variety of distance scales and are possibly fractal.<sup>3,25</sup> Therefore we conclude that the microscopic origin of the disorder causing the stretched exponential kinetics is indium phase segregation and the associated spatial fluctuations of the local indium concentration. The microscopic nature of the quantum dots and their connectivity should have a large effect on the excited state dynamics and thus LED operation.

#### 4. SUMMARY

In summary we have used TRPL to examine wafers of InGaN LEDs before the final stages of processing. We have found that in the bright LED, PL lifetimes at room temperature were on the nanosecond timescale. The PL kinetics were strongly dependent upon the emission wavelength and were well described by a stretched exponential. Both observations are strong experimental evidence for the importance of disorder in actual light-emitting-diodes. We hypothesize that topological disorder associated with the indium concentration fluctuations is critical for the room temperature operation of InGaN LEDs. We also report evidence for the importance of indium alloy fluctuations on the photoluminescence decay kinetics in both InGaN films and multiple quantum wells. It is clear that small changes in the growth conditions can greatly effect the indium alloy fluctuations, our experiment results indicate that such changes greatly alter the excited state dynamics in InGaN systems. Further investigation in this direction is underway.

#### ACKNOWLEDGEMENTS

The authors thank K.P. O'Donnell and L. Pavesi for helpful discussions. FHL would like to thank the Rutgers Research Council for financial support. The authors would also like to thank Bill Cieslik and Hamamatsu Corporation for the loan of the streak camera. Acknowledgement is also made to the donors of the Petroleum Research Fund, administered by the ACS, for the partial support of this research.

#### REFERENCES

- 1 S. Nakamura, M. Senoh, S. Nagahama, N. Iwasa, T. Yamada, T. Matsushita, Y. Sugimoto, and H. Kiyoku, *Applied Physics Letters* **70**, 868-870 (1997).
- 2 I.-h. Ho and G. B. Stringfellow, *Appl. Phys. Lett.* **69**, 2701-2703 (1996).
- 3 S. Chichibu, K. Wada, and S. Nakamura, *Appl. Phys. Lett.* **71**, 2346-2348 (1997).
- 4 S. Chichibu, T. Azuhata, T. Sota, and S. Nakamura, *Appl. Phys. Lett.* **69**, 4188-4190 (1996).
- 5 N. A. El-Masry, E. L. Piner, S. X. Liu, and S. M. Bedair, *Appl. Phys. Lett.* **72**, 40-42 (1998).
- 6 M. D. McCluskey, L. T. Romano, B. S. Krusor, D. P. Bour, N. M. Johnson, and S. Brennan, *Appl. Phys. Lett.* **72**, 1730-1732 (1998).
- 7 S. Nakamura, *Solid State Communications* **102**, 237-248 (1997).
- 8 C. Tran, R. F. Karlicek Jr., R. Stall, M. Schurman, I. Ferguson, A. Onsinski, and J. Rajer, in *Growth of High Efficiency InGaN MQW Blue LEDs*, E-MRS meeting, Strasburg, France, 1998; C. Tran, R. F. Karlicek Jr., M. Schurman, A. Onsinski, V. Meraj, Y. Li, I. Eliashevich, M. G. Brown, J. Nering, I. Ferguson, and R. Stall (to be published) *J. Cryst. Growth*.
- 9 E. S. Jeon, V. Kozlov, Y. K. Song, A. Vertikov, M. Kuball, A. V. Nurmikko, H. Liu, C. Chen, R. S. Kern, C. P. Kuo, and M. G. Craford, *Appl. Phys. Lett.* **69**, 4194-4196 (1996).
- 10 C. K. Sun, T.-L. Chiu, S. Keller, G. Wang, M. S. Minsky, S. P. DenBaars, and J. E. Bowers, *Appl. Phys. Lett.* **71**, 425-427 (1997).
- 11 M. S. Minsky, S. B. Fleischer, A. C. Abare, J. E. Bowers, E. L. Hu, S. Keller, and S. P. DenBaars, *Appl. Phys. Lett.* **72**, 1066-1068 (1998).
- 12 M. Pophristic, F. H. Long, C. Tran, R. F. Kalicek, Z. C. Feng, and I. T. Ferguson, *Appl. Phys. Lett.* **73**, 815-817 (1998).
- 13 M. Pophristic, F. H. Long, C. Tran, R. F. Kalicek, and I. T. Ferguson, *Appl. Phys. Lett.* **73**, 3550-3552 (1998).

- 14 T. Takeuchi, H. Takeuchi, S. Sota, H. Sakai, H. Amano, and I. Akasaki, Jpn. J. Appl. Phys. **36**, L177-L179 (1997).
- 15 H. Scher, M. F. Shlesinger, and J. T. Bender, Physics Today, 26-24 (1991). M. F. Shlesinger, Ann. Rev. Phys. Chem. **39**, 269-290 (1988).
- 16 X. Chen, B. Henderson, and K. P. O'Donnell, Appl. Phys. Lett. **60**, 2672-2674 (1992).
- 17 L. Pavesi and M. Ceschini, Phys. Rev. B **48**, 17625-17628 (1993).
- 18 L. Pavesi, J. Appl. Phys. **80**, 216-225 (1996).
- 19 H. E. Roman and L. Pavesi, J. Phys: Condens. Matter. **8**, 5161-5187 (1996).
- 20 I. Kuskovsky, G. F. Neumark, V. N. Bondarev, and P. V. Pikhitsa, Phys. Rev. Lett. **80**, 2413-2417 (1998).
- 21 T. Takeuchi, S. Sota, M. Katsuragawa, M. Komori, H. Takeuchi, H. Amano, and I. Akasaki, Jpn. J. Appl. Phys. **36**, L382-L385 (1997).
- 22 M. Pophristic, F. H. Long, C. Tran, R. F. Kalicek, Z. C. Feng, and I. T. Ferguson to be published.
- 23 S. Sawada, N. Hamada, and N. Ookubo, Phys. Rev. B **49**, 5236-5242 (1994).
- 24 P. Perlin, V. Iota, B. A. Weinstein, P. Wisniewski, T. Suski, P. G. Eliseev, and M. Osinski, Appl. Phys. Lett. **70**, 2993-2995 (1997).
- 25 P. G. Middleton, K. P. O'Donnell, C. Trager-Cowan, S. C. Bayliss, S. Sapelkin, W. V. D. Stricht, I. Moerman, and P. Demeester, in *The Optical and Structural Properties of InGaN Epilayers with very high Indium content*, E-MRS meeting, Strasburg, France, 1998.

# Optical anisotropy of GaN/sapphire studied by generalized ellipsometry and Raman scattering

Chunhui Yan<sup>a</sup>, H. Walter Yao<sup>\*a</sup>, James M. Van Hove<sup>b</sup>, Andrew M. Wowchak<sup>b</sup>, Peter P. Chow<sup>b</sup>,  
John M. Zavada<sup>c</sup>

<sup>a</sup>University of Nebraska, Center for Microelectronic and Optical Material Research,  
and Department of Electrical Engineering, Lincoln, NE 68588

<sup>b</sup>SVT Associates, Eden Prairie, MN

<sup>c</sup>European Research Office, London, UK

## ABSTRACT

Generalized variable angle spectroscopic ellipsometry (VASE) and Raman scattering have been employed to study the optical anisotropy of GaN/Sapphire structures. The GaN films were grown by hydride vapor phase epitaxy (HVPE) and molecular beam epitaxy (MBE) on both m-plane and c-plane sapphire ( $\alpha$ -Al<sub>2</sub>O<sub>3</sub>) substrates, respectively. Anisotropic optical phonon structure of sapphire have been measured, based on which the optical axis of sapphire substrate has been determined. A 541 cm<sup>-1</sup> TO phonon of GaN grown on m-plane sapphire substrate has been discovered experimentally which is due the coupling of A<sub>1</sub> and E<sub>1</sub> TOs. Optical axis orientation of GaN film on m-sapphire has been fully determined by the anisotropic angular dependence of the coupled TO phonon. Off-diagonal elements A<sub>pst</sub> and A<sub>spt</sub> of transmission VASE (TVASE) are very sensitive parameters related to the optical anisotropy. The optical axis orientation of GaN on m-sapphire has also been accurately determined by TVASE at two special sample positions. The optical anisotropy due to GaN film and sapphire substrate has been successfully separated at 90° sample position allowing to study the optical anisotropy of GaN film only.

**Keywords:** GaN, sapphire, Raman scattering, generalized ellipsometry, optical anisotropy

## 2. INTRODUCTION

The wide band gap semiconductor GaN and related materials, with their excellent thermal conductivity, large breakdown field, and resistance to chemical attack, have a very promising application potential for both high temperature electronic devices and short wave-length optical emitters.<sup>1,2</sup> The recent development of high-brightness, blue and green light emitting diodes (LEDs),<sup>3</sup> room temperature pulsed<sup>4</sup> and continuous-wave (CW)<sup>5</sup> quantum well lasers has greatly encourage researchers to continue the work on these materials. Most of the GaN films were grown on c-plane sapphire substrates, and they usually have wurtzite crystal structure ( $\alpha$ -GaN), which is anisotropic (uniaxial). Several valuable optical property studies have been carried out on the GaN/c-sapphire structure by both Raman<sup>6</sup> and ellipsometry<sup>7</sup>. However, there are not much data available about the optical anisotropy of GaN possibly due to the shortage of GaN samples grown on sapphire substrates other than c-plane orientations. For GaN/c-sapphire case, it is difficult to study the optical anisotropy of GaN film since the polarization of most of the probe light-wave is perpendicular to the optical axis  $\langle c \rangle$ . For GaN grown on m-plane sapphire, on the other hand, its optical axis  $\langle c \rangle$  is certain degree away from the surface normal as pointing out by Matsuoka *et al*<sup>8</sup>, which provides the possibilities for the optical anisotropy study. It was found that the crystal orientation relation between GaN and m-plane sapphire is (01 $\bar{1}$ 3) / (01 $\bar{1}$ 0) as the interface plane, and [03 $\bar{3}$ 2] / [2 $\bar{1}$ 10] as the in-plane orientation preference. Most importantly, it was concluded that GaN grown on m-plane sapphire has a smoother surface, lower background carrier concentration and stronger PL intensity which indicate that GaN grown on m-plane is superior than on c-plane sapphire substrates.. In this work, based on our previous optical anisotropy study of sapphire<sup>9</sup>, a GaN/m-sapphire

\* Correspondence: H. Walter Yao, Email: wyao@Sandia.gov, or hyao1@unl.edu; telephone: 925-294-2169; Fax: 925-294-1489

sample grown by HVPE has been studied by Raman scattering and generalized ellipsometry. The optical axis orientation of GaN film grown on m-plane sapphire has been fully determined by both anisotropic coupled TO phonon and the off-diagonal elements of transmission Jones matrix.

### 3. Theory

#### 2.1 Raman Scattering

It is well known that sapphire and GaN are all optically anisotropic (uniaxial) materials due to their rhombohedral and wurtzite crystal structures. Group theoretical analysis shows that the irreducible representation for the optical modes of sapphire is<sup>10</sup>.

$$\Gamma = A_{1g} + 2A_{1u} + 3A_{2g} + 5E_g + 4E_u, \quad (1)$$

and the irreducible representation for the acoustical modes is  $A_{2u} + E_u$ . Since the unit cell has center-of-inversion symmetry, all vibrations that are Raman allowed are infrared forbidden and vice versa. More specifically, two  $A_{1g}$  modes and five  $E_g$  modes are Raman active only, while two  $A_{2u}$  modes and four  $E_u$  modes are infrared active only. The  $A_{1u}$  and  $A_{2g}$  vibrations are neither infrared nor Raman active.

The irreducible representation of Wurtzite GaN optical phonons is:<sup>11</sup>

$$\Gamma = A_1(z) + 2B_1 + E_1(x, y) + 2E_2, \quad (2)$$

for phonon propagating along or perpendicular to the optical axis  $\langle c \rangle$ . Where x, y, z in parentheses repent the directions of phonon polarization. The  $A_1$  and  $E_1$  modes are both Raman and infrared active, two  $E_2$  modes are only Raman active, and  $B_1$  modes are both Raman and IR silent. Using selection rules of the anisotropic phonon structures of sapphire and GaN, the optical orientation can be quickly determined.

#### 2.2 Generalized Ellipsometry

The variable angle spectroscopic ellipsometry is designed to accurately determine the values of two standard ellipsometry parameters  $\psi$  and  $\Delta$ , which are related to the complex ratio of reflection (or transmission) coefficients for light polarized parallel (p) and perpendicular (s) to the plane of incidence.<sup>12</sup> For isotropic material systems,

$$\rho = \frac{R_p}{R_s} = \tan(\psi)e^{i\Delta}. \quad (3)$$

The electric-field reflection coefficient at an incident angle of  $\phi$  is defined as  $r_p$  ( $r_s$ ) for p (s)- polarized light. They are the diagonal elements of Jones matrix,

$$[J]_{\text{sample}} = \begin{bmatrix} r_p & 0 \\ 0 & r_s \end{bmatrix}. \quad (4)$$

The  $\psi$  and  $\Delta$  are not only dependent on material dielectric responses, also on the surface condition, sample structure, and other properties such as the optical anisotropy.

For the anisotropic material system, the non-diagonal elements of Jones matrix are not necessary to be zero. In the transmission VASE configuration,

$$[J]_{\text{sample}} = \begin{bmatrix} t_{pp} & t_{sp} \\ t_{ps} & t_{ss} \end{bmatrix}. \quad (5)$$

By using the same approach with considerably more algebra involved, we can still predict the  $\psi$  and  $\Delta$  values, but the Fourier coefficients related to  $\psi$  and  $\Delta$  become more complicated.<sup>13</sup> The generalized ellipsometric parameters are defined as below:

$$A_{nEt} = \frac{t_{pp}}{t_{ss}} = \tan \psi_{nE} e^{i\Delta_{nE}}, \quad (6)$$

$$A_{pst} = \frac{t_{ps}}{t_{pp}} = \tan \psi_{ps} e^{i\Delta_{ps}}, \quad (7)$$

$$A_{spt} = \frac{t_{sp}}{t_{ss}} = \tan \psi_{sp} e^{i\Delta_{sp}}, \quad (8)$$

where the  $A_{pst}$  and  $A_{spt}$  describe how much amount p- or s-polarized light becomes s- or p-polarized light after the transmission, respectively. If the optical axis is strictly either perpendicular (perfect c-plane situation) or parallel to the electric field of the incident beam, the Jones matrix is diagonal. While it may not true for GaN films grown on non c-plane sapphire substrates, such as m-plane sapphire substrates since the optical axis of both GaN and sapphire may form an angle respect to the incident polarization so that the off-diagonal elements of Jones matrix may not vanish. The off-diagonal elements  $A_{pst}$  and  $A_{spt}$  are dependent on sample position, angle of incidence, which can be used to determine the optical axis orientation of crystals. Generalized ellipsometry was first introduced by Azzam and Bashara.<sup>14</sup> The recent developments makes this technique more complete and powerful.<sup>15, 16</sup> In a word, the Generalized ellipsometry is a technique which can be used to determined all the elements of Jones matrix of arbitrarily anisotropic and homogeneous layered systems with nonscalar dielectric susceptibilities.

### 3. Experiments

The Raman spectra were taken at room temperature with a SPEX 1877E triple spectrometer equipped with a liquid-nitrogen cooled CCD camera. The excitation light source was an Ar<sup>+</sup> laser operating at 488 nm with the output power kept at 150 mW. A back scattering geometry was employed for all the Raman measurements.

The GaN films used in this work were grown by both HVPE and MBE on m-plane and c-plane sapphire substrates. The backside of the substrate was polished so that the transmission type VASE measurements could be made. The TVASE optical measurements of anisotropic mode were performed in the energy range of 0.75eV to 4eV with a 0.03eV increment at room temperature since the sample is opaque above the GaN band gap 3.4eV. A rotational sample stage allowed us to take the data from different sample positions marked by the angle between the optical axis  $\langle c \rangle$  and the x-axis of the lab coordinates. Multiple angles of incidence from  $-30^\circ$  to  $+30^\circ$  were used in order to see the angular dependence of the optical anisotropy of the GaN/m-sapphire sample.

### 4. Results and discussion

#### 4.1. Optical phonons of sapphire and GaN

Raman scattering is a nondestructive technique used to detect the lattice vibration modes related with crystal orientation and symmetry. A series of Raman scattering measurements have been carried out on c-plane and a-plane sapphire samples. The spectrum of Raman scattering on a c-plane sapphire at back-scattering geometry  $Z(Y, Y+X)\bar{Z}$  are shown in Fig. 1(a). A similar Raman phonon spectrum shown in Fig. 1(b) was obtained from an a-plane sapphire with its optical axis perpendicular to the polarization of the incident laser beam. While a different spectrum shown in Fig. 1(c) was obtained from the same a-plane sapphire with the optical axis parallel to the polarization. Only two TOs appeared for this configuration, and the  $645 \text{ cm}^{-1}$  (LO,  $A_{1g}$ ) is a new phonon which is forbidden in both Fig 1(a) and Fig 1(b) configurations. This indicates that the  $645 \text{ cm}^{-1}$  (LO) mode is allowed or forbidden when the optical axis of the a-plane sample is parallel or perpendicular to the polarization of the Raman probe, respectively.

Optical phonons of GaN films grown on c- and m-plane sapphire substrates are shown in Fig. 2. The dash line refers to the GaN on c-plane sapphire, a  $E_2$  and a  $A_1$  LO phonon are observed at  $569 \text{ cm}^{-1}$  and  $734 \text{ cm}^{-1}$ , respectively. They are consistent with reported values.<sup>17</sup> The solid line represents GaN grown on m-plane sapphire substrate. Except the  $E_2$  and  $E_1$  TOs, a new  $541 \text{ cm}^{-1}$  appeared in the spectrum, which was never reported as the experimental result. Notice that this phonon is not any of the standard zone center phonons propagating along or perpendicular to the optical axis  $\langle c \rangle$ .<sup>11</sup> According to Loudon's theory,<sup>18</sup> this one belongs to a coupled mode of two TO phonons ( $A_1$  TO and  $E_1$  TO) when the angle  $\theta$  between phonon propagation direction  $\langle q \rangle$  and the optical axis  $\langle c \rangle$  is in between of  $0^\circ$  and  $90^\circ$ . For non-zero  $\theta$  values, the coupled modes satisfy the followings:

$$\omega^2(\text{TO}_1) = \omega^2(A_1(\text{TO})) \sin^2 \theta + \omega^2(E_1(\text{TO})) \cos^2 \theta \quad (9)$$

$$\omega^2(\text{TO}_2) = \omega^2(E_1(\text{TO})) \quad (10)$$



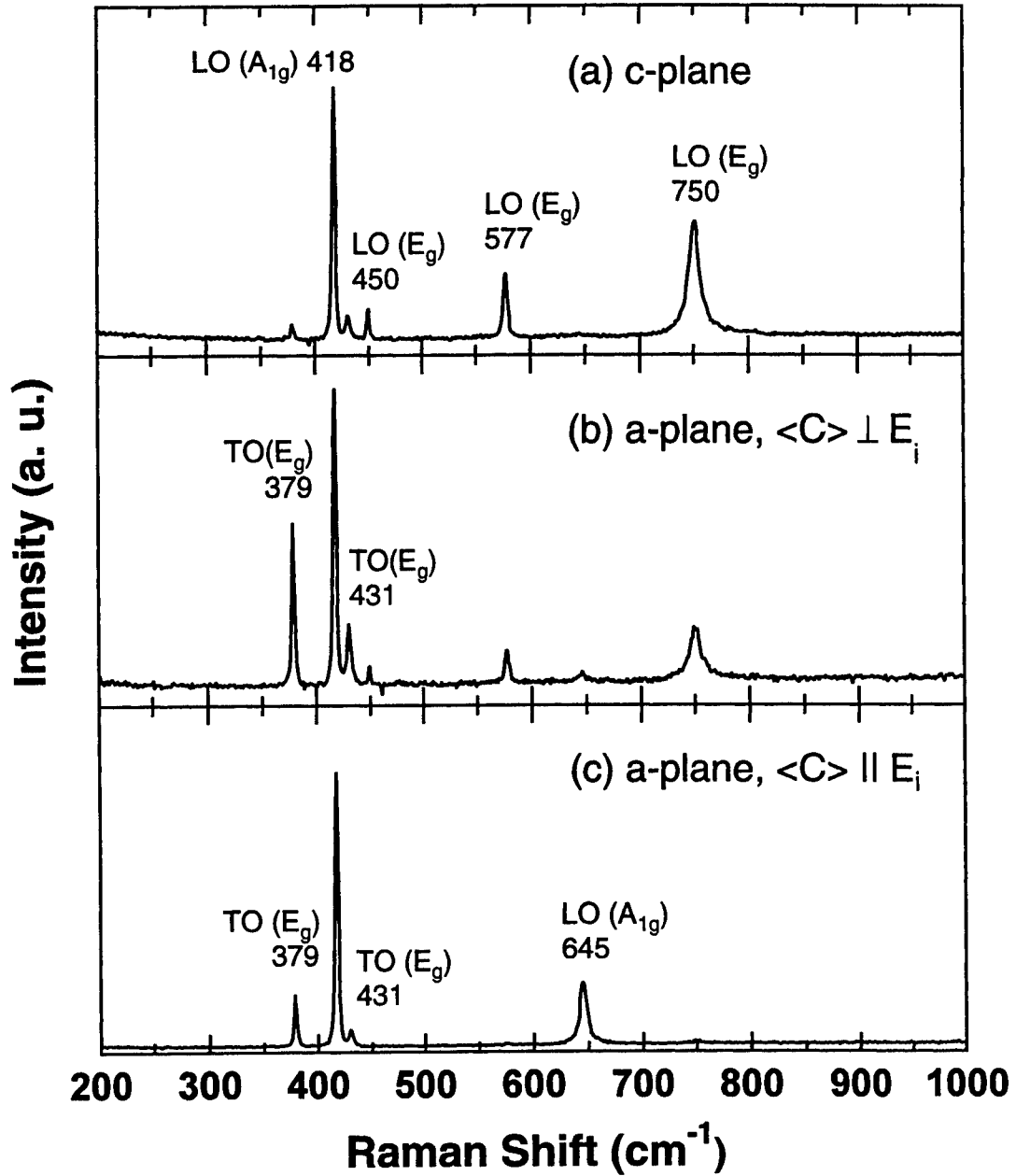


Fig. 1. Optical phonons of sapphire. (a) c-plane; (b) a-plane,  $\langle c \rangle \perp E_i$ ; (c) a-plane,  $\langle c \rangle \parallel E_i$ .

where the  $TO_1$  is the new coupled TO phonon with a strong  $\theta$  angular dependence, and the  $\omega(TO_2)$  is same as  $\omega(E_1 TO)$ . Applying equation (9) to the measured  $541 \text{ cm}^{-1}$  coupled TO phonon mode, the related angle  $\theta$  is about  $58^\circ$ .

In the back scattering geometry, the phonon wave vector  $\langle q \rangle$  is perpendicular to the sample surface. In order to located the orientation of  $\langle c \rangle$  of GaN ( $\langle c \rangle_g$ ), the reference direction  $\langle c \rangle$  of sapphire ( $\langle c \rangle_s$ ) has to be determined first. Based on the analysis of Fig. 1, we can use the  $645 \text{ cm}^{-1}$  LO phonon of sapphire to find the  $\langle c \rangle_s$  position. As shown in Fig. 3, The  $645$

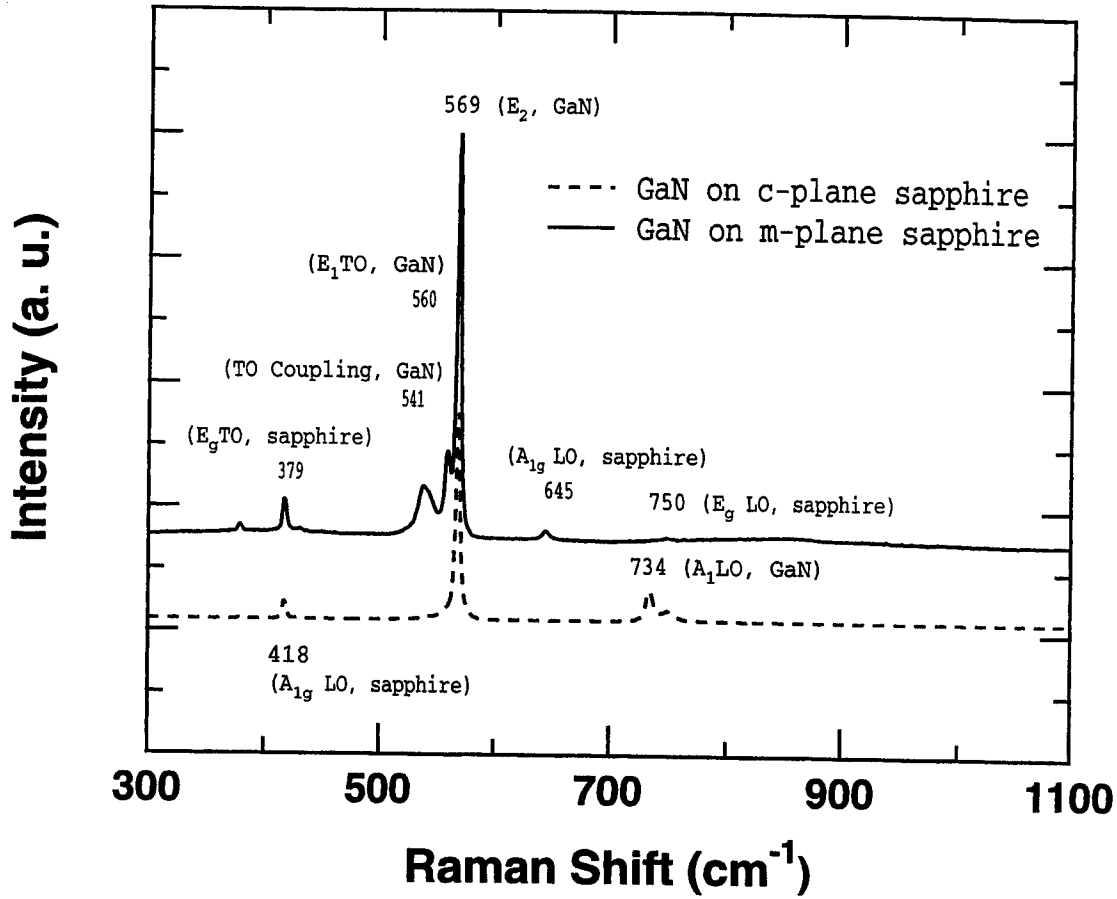


Fig. 2. Optical phonons of GaN films. Dash line is for GaN on c-plane sapphire; solid line is for GaN on m-plane sapphire. 541  $\text{cm}^{-1}$  is the coupled TO phonon of  $A_1$  and  $E_1$  TOs.

$\text{cm}^{-1}$  LO of sapphire is forbidden when  $\langle c \rangle_s$  perpendicular to the polarization (dash line), and it is allowed as  $\langle c \rangle_s$  parallel to the polarization (solid line). Therefore a reference plane can be formed by  $\langle q \rangle$  and  $\langle c \rangle_s$ , which is perpendicular to the sample surface. The task now is to determine where the  $\langle c \rangle_g$  locates at, either in the reference plane or in the plane which is perpendicular to both sample surface and the reference plane. This problem can be solved by tilting the sample to change the angle  $\theta$ . If  $\langle c \rangle_g$  is in the reference plane, by rotating the sample about the x-axis which is perpendicular to the reference plane will result in a maximum angle  $\theta$  change, which should create a different coupled TO phonon according to the equation (9). But the coupled TO frequency will keep unchanged when rotate the sample about the  $\langle c \rangle_s$ . In fact, this is the case for the GaN/m-sapphire sample we have, as shown in Fig. 4 (a). The solid line refers to the Raman data of the untilted sample case, which has the coupled TO at 541  $\text{cm}^{-1}$ . The other dash lines refer to the  $-20^\circ$ ,  $-30^\circ$ ,  $20^\circ$ , and  $30^\circ$  tilted sample cases, which show that the coupled TO phonon moves either to higher or lower wave number indicating the angle  $\theta$  is changed correspondingly with the sample rotations. The coupled TO wave number keeps unchanged while rotates the sample about the  $\langle c \rangle_s$  in our experiment. The calculated and experimental values of the coupled TO phonon frequency as a function of angle  $\theta$  is plotted in Fig. 4 (b). Notice that the relation between  $\theta$  and  $\alpha$  is untrue for

$$\theta = 58^\circ \pm \alpha, \quad (11)$$

where  $\alpha$  is the tilting angle. In stead,

$$\theta = 58^\circ \pm \arcsin[\sin(\alpha) / n_g] \quad (12)$$

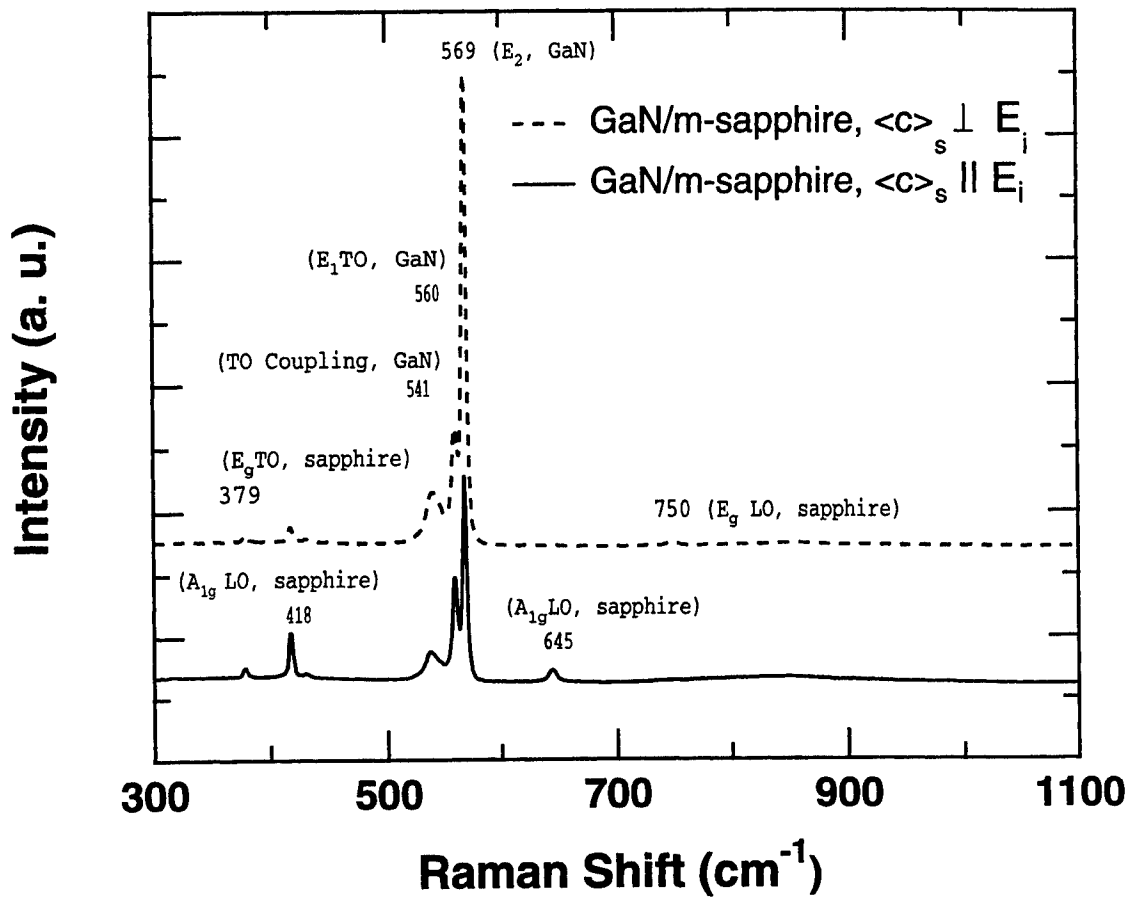


Fig. 3. Optical phonons of GaN film grown on m-plane sapphire substrate at two sample positions respect to the polarization. Dash line represents  $\langle c \rangle_s \perp E_i$  case where  $645 \text{ cm}^{-1}$  LO of sapphire is forbidden, and solid line represents  $\langle c \rangle_s \parallel E_i$  case, where the  $645 \text{ cm}^{-1}$  LO of sapphire is allowed.

is true when the sample is tilted away  $\alpha$  degree. Where  $n_g = 2.4$  is the refractive index of GaN at the probe laser wavelength (488nm). By taking account the interface refraction effect on the  $\langle c \rangle$  direction, the experimental data is in good agreement with the theory.

#### 4.2. Generalized ellipsometry of GaN/m-sapphire

Optical anisotropy can also be measured by generalized ellipsometry, especially the transmission type measurements for transparent materials. The TVASE data of an a-plane sapphire are shown in Fig. 5 as a good example. The data were obtained at  $0^\circ$ ,  $1^\circ$  and  $60^\circ$  sample positions in the range of 0.75 eV to 5.8 eV. The angle of incidence are  $20^\circ$  and  $30^\circ$ , respectively. It can be seen clearly in Fig. 5 (c) that the off-diagonal elements  $A_{pst}$  and  $A_{spt}$  of the Jones matrix have large  $\psi$  values indicating the existence of the optical anisotropy in sapphire crystal. The magnitude of the off-diagonal signal in Fig. 5 (b) is still in reasonable size even for only about  $1^\circ$  difference between  $\langle c \rangle_s$  and x-axis. The zero  $A_{pst}$  and  $A_{spt}$  in Fig. 5 (a) are obtained at the sample position of  $\langle c \rangle_s \parallel x$  (the same result for  $\langle c \rangle \perp x$ ). By finding the zero  $A_{pst}$  and  $A_{spt}$  position, the optical axis of sapphire can thus be fully determined. The results from Fig. 5 agree each other very well with Raman analysis in Fig. 1, but with more accuracy ( $<1^\circ$ ). The one drawback of TVASE method for determining the optical axis is that TVASE can not distinguish the  $0^\circ$  and  $90^\circ$  position since all the off-diagonal elements are zero at these two positions.

In order to reveal the optical anisotropy of GaN, a series of anisotropic mode TVASE measurements have been made on the GaN/m-sapphire sample, as shown in Fig. 6. The selected typical data here are taken from four sample positions:  $0^\circ$ ,  $1^\circ$ ,  $90^\circ$

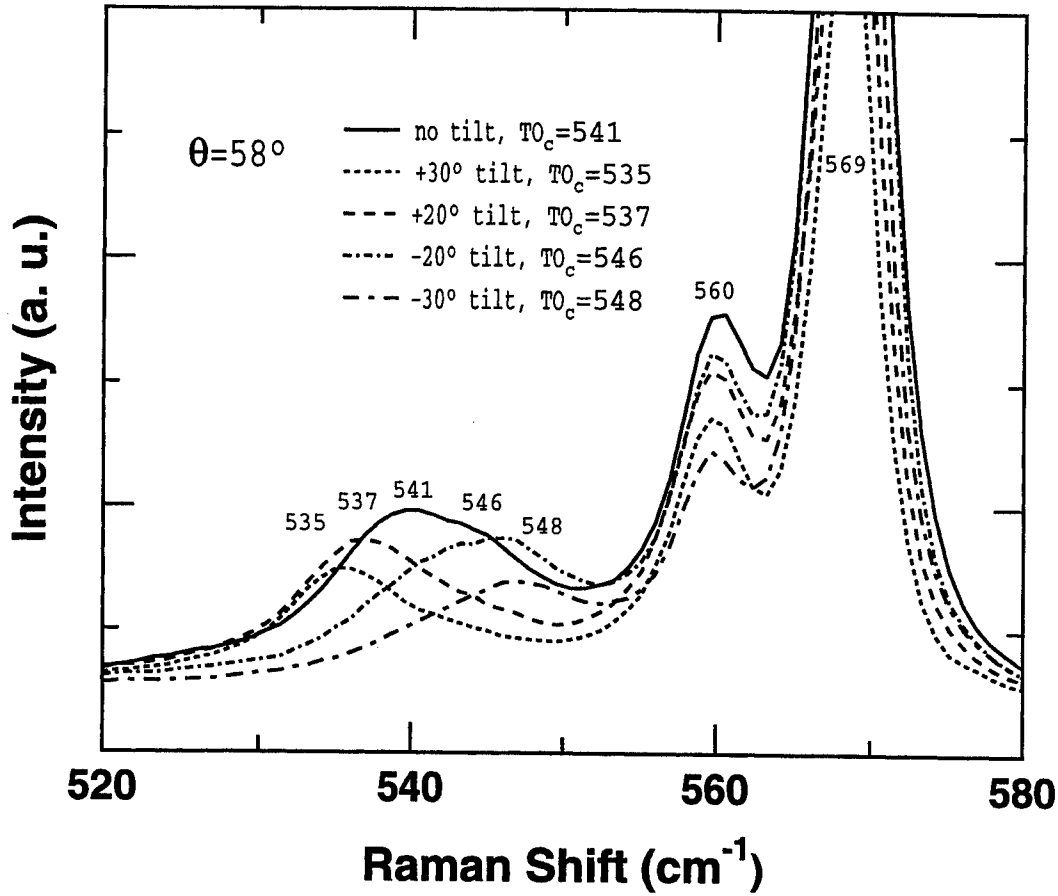


Fig 4. (a) Anisotropic angular dependence of the coupled TO phonon of GaN grown on m-plane sapphire. The sample was rotated about the x-axis which is in the sample surface plane and perpendicular to the sapphire optical axis  $\langle c \rangle_s$ .

and  $92^\circ$ , as shown in Fig. 6. The angle  $\alpha$  is between  $\langle c \rangle_s$  and x-axis. The spectra are cut off at about 3.4 eV since no transmission above the GaN band gap. Multiple angles of incidence ( $0^\circ$ ,  $10^\circ$ ,  $20^\circ$  and  $30^\circ$ ) have been used for collecting strong off-diagonal signal. At  $0^\circ$  position shown in Fig. 6 (a), the off-diagonal elements  $A_{pst}$  and  $A_{spt}$  are all zero. A clear conclusion can be drawn from Fig. 6 (a) is that the optical axis of GaN  $\langle c \rangle_g$  must lay in the plane of incidence somewhere between x-axis and z-axis, since  $\langle c \rangle_g$  could be along neither x-axis nor y-axis direction for the zero  $A_{pst}$  and  $A_{spt}$ , and we already know from Raman scattering that the angle between  $\langle c \rangle_g$  and  $\langle c \rangle_s$  is larger than zero and less than  $90^\circ$ . Recall the calculation result based on the coupled TO phonon mode at  $541 \text{ cm}^{-1}$  and equation (9), the angle  $\theta$  between  $\langle q \rangle$  and  $\langle c \rangle_s$  is about  $58^\circ$ . We now also know that the so-called reference plane formed by  $\langle q \rangle$  and  $\langle c \rangle_s$  defined previously is the plane of incidence. Therefore, The orientation of  $\langle c \rangle_g$  can be fully determined, which is in the reference plane (or the plane of incidence) and  $32^\circ$  away from  $\langle c \rangle_s$  (or x-axis). To test the accuracy of this measurement, another TVASE data was taken at  $1^\circ$  position as shown in Fig. 6 (b). The sizable  $A_{pst}$  and  $A_{spt}$  were detected at all the angles of incidence indicating the sensitivity of TVASE is high enough. At a larger angle position, much bigger pairs of  $A_{pst}$  and  $A_{spt}$  can be obtained, which is a good evidence of the optical anisotropy of the whole structure. However, it is difficult to know how much anisotropy comes from GaN at these positions. Because of the special orientation relationship between  $\langle c \rangle_g$  and  $\langle c \rangle_s$  for GaN on m-plane sapphire, the  $90^\circ$  position can serve very well for this purpose as shown in Fig. 6 (c). The nonzero  $A_{pst}$  and  $A_{spt}$

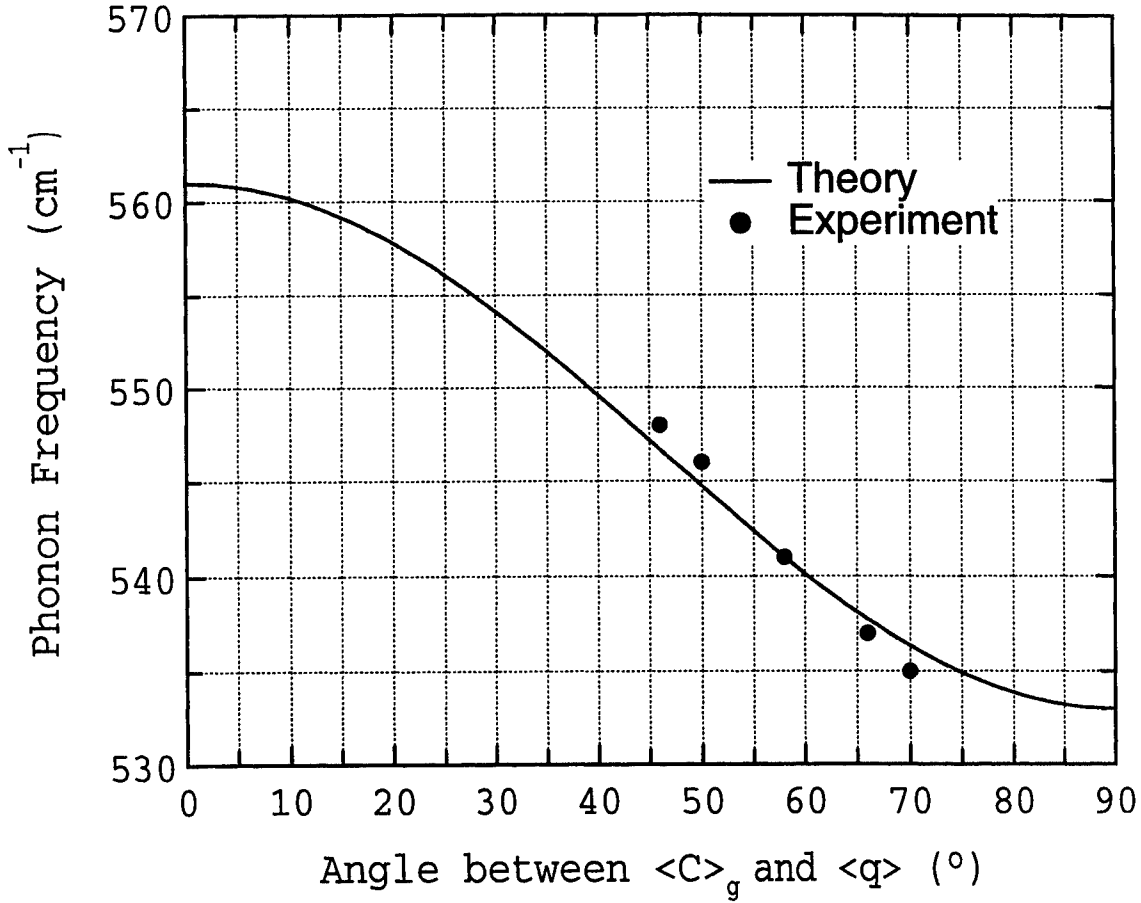


Fig. 4 (b) A comparison of the coupled TO positions from the theoretical calculation and the experimental data.

appeared in Fig. 6 (c) are purely due to the anisotropy of GaN film, since the contribution from sapphire substrate to the  $A_{pst}$  and  $A_{spt}$  is zero. Data in the Fig. 6 (c) is very valuable especially for GaN dielectric functions study. Only two degree away from the  $90^\circ$  position, the  $A_{pst}$  and  $A_{spt}$  are modified by the sapphire substrate dramatically as shown in Fig. 6 (d). This indicates that the optical axis orientation of GaN can be determined accurately.

The angle of incidence dependence of the optical anisotropy is showed in Fig. 7 (a) and (b) refer to two sample positions,  $0^\circ$  and  $90^\circ$ , respectively. The TVASE data was taken at three photon energies of 1.0 eV, 1.6 eV, and 2.2 eV (arbitrary chosen below GaN band gap). The angular increment is  $1^\circ$ . In Fig. 7 (a), the off-diagonal elements are zero in the whole angular range. This is due to that the  $\langle c \rangle_g$  and  $\langle c \rangle_s$  are all in the plane of incidence. In Fig. 7 (b). A different behavior is observed for the same three wavelengths below the band gap. This is because that the optical axis of GaN is in the plane perpendicular to both the sample surface and the plane of incidence. As discuss previously the magnitude of  $A_{pst}$  and  $A_{spt}$  are all contributed by GaN. The  $A_{pst}$  and  $A_{spt}$  are zero at normal incidence at  $90^\circ$  position which is again the proof of  $\langle c \rangle_g$  in the reference plane. The bigger  $A_{pst}$  and  $A_{spt}$  values at larger angle of incidence suggest that a large angle of incidence is usually a better choice for measuring the optical anisotropy by TVASE.

According to the data analysis of both Raman scattering and TVASE, the growth configuration of this GaN/m-sapphire sample is  $(01\bar{1}3)/(0001)$  as the interface plane, and  $[0332]/[0\bar{1}10]$  as the in-plane orientation preference, which is different from the reported structure configuration  $(01\bar{1}3)/(01\bar{1}0)$  as the interface plane, and  $[0332]/[2\bar{1}10]$  as the in-plane orientation preference. we consider this is the other option for GaN grow on m-plane sapphire substrates.

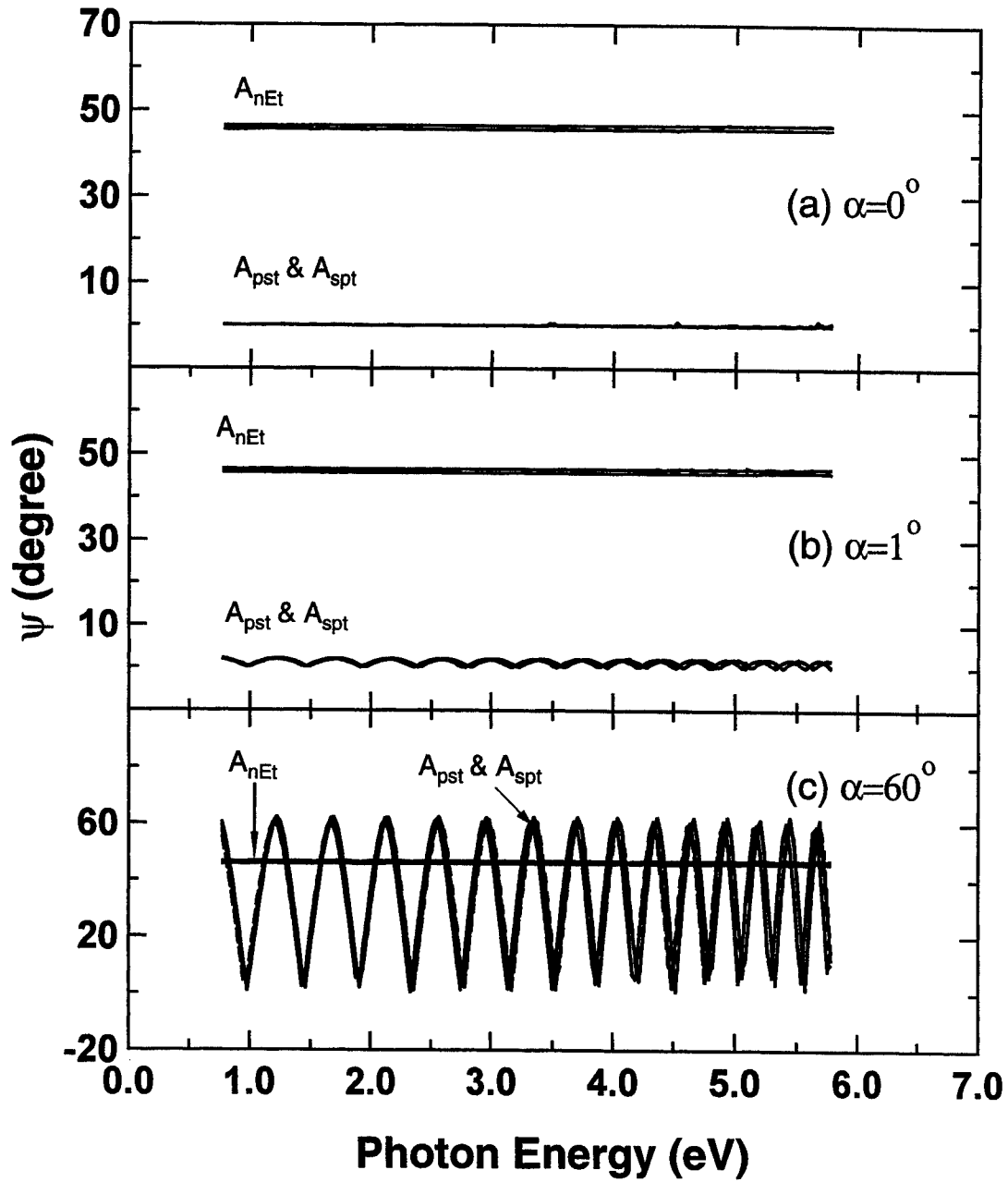


Fig.5. Transmission VASE data of an a-plane sapphire at the angle of incidence of 20° and 30°, respectively. (a)  $\alpha=0^\circ$ ; (b)  $\alpha=1^\circ$ ; (c)  $\alpha=60^\circ$ .  $\alpha$  is the angle between the optical axis and x-axis of the lab coordinates.

### 5. Summary

Optical anisotropy nature of GaN films grown on m-plane sapphire substrates was characterized by Raman scattering and generalized variable angle spectroscopic ellipsometry. A  $541\text{ cm}^{-1}$  phonon of GaN due to the TO coupling was observed experimentally and it agrees very well with the theoretical prediction. The coupled TO phonon of GaN film grown on m-plane sapphire substrate is a good signature of its optical anisotropy, and the angular dependence relation can be used to

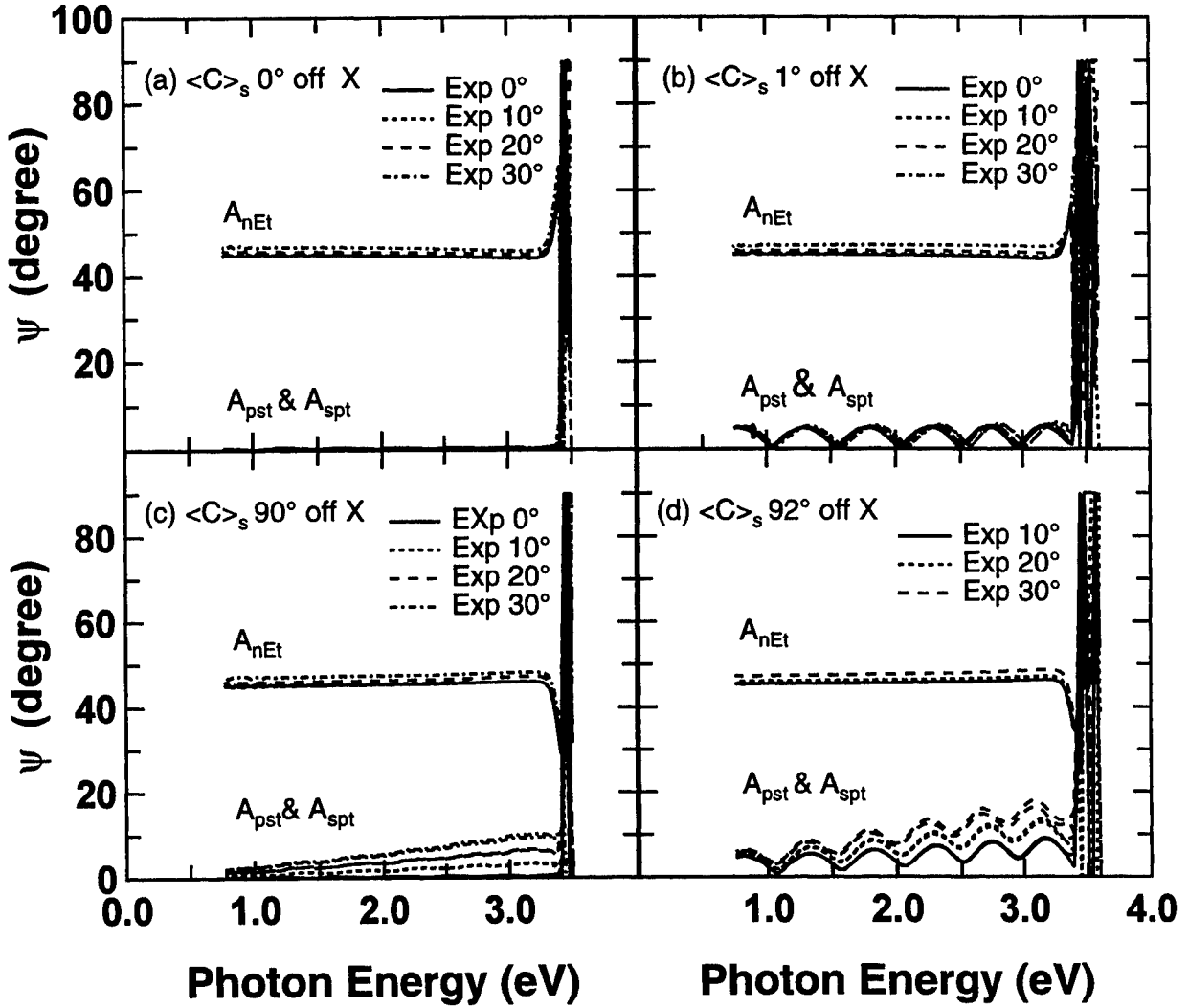


Fig. 6. Transmission VASE data of GaN/m-sapphire at the angle of incidence of 0°, 10°, 20° and 30°, respectively. (a)  $\langle C \rangle_s$ , 0° off x-axis; (b)  $\langle C \rangle_s$ , 1° off x-axis; (c)  $\langle C \rangle_s$ , 90° off x-axis; (d)  $\langle C \rangle_s$ , 92° off x-axis.  $A_{pst}$  and  $A_{spt}$  are the off-diagonal elements of transmission Jones matrix.

determine the location of  $\langle c \rangle_g$ . It is also found that the off-diagonal elements of transmission type Jones matrix are very sensitive to both the sample position and the angle of incident. The optical axis of GaN is fully determined by using the null  $A_{pst}$  and  $A_{spt}$  position at 0°, which is in good agreement with the result from the angular dependence Raman scattering. According to the analysis of both Raman and TVASE, the  $\langle c \rangle_g$  of GaN on m-plane sapphire lies in the reference plane defined by  $\langle q \rangle$  and  $\langle c \rangle_s$ , and it is 32° away from the  $\langle c \rangle_s$ . TVASE measurement at 90° position has given non-zero  $A_{pst}$  and  $A_{spt}$  which are purely due to the anisotropy of GaN film, this kind of data will be very important for the future studies of anisotropic dielectric functions of GaN. A new growth configuration of GaN on m-plane sapphire has been observed as  $(01\bar{1}3)/(0001)$ , and  $[03\bar{3}2]/[0\bar{1}10]$  for the interface plane and in-plane orientation preferences.

#### Acknowledgments

This work was supported by US Army Research Office.

We thank Dr. Richard J. Molnar at MIT Lincoln Laboratories for providing GaN/m-sapphire samples for this study.

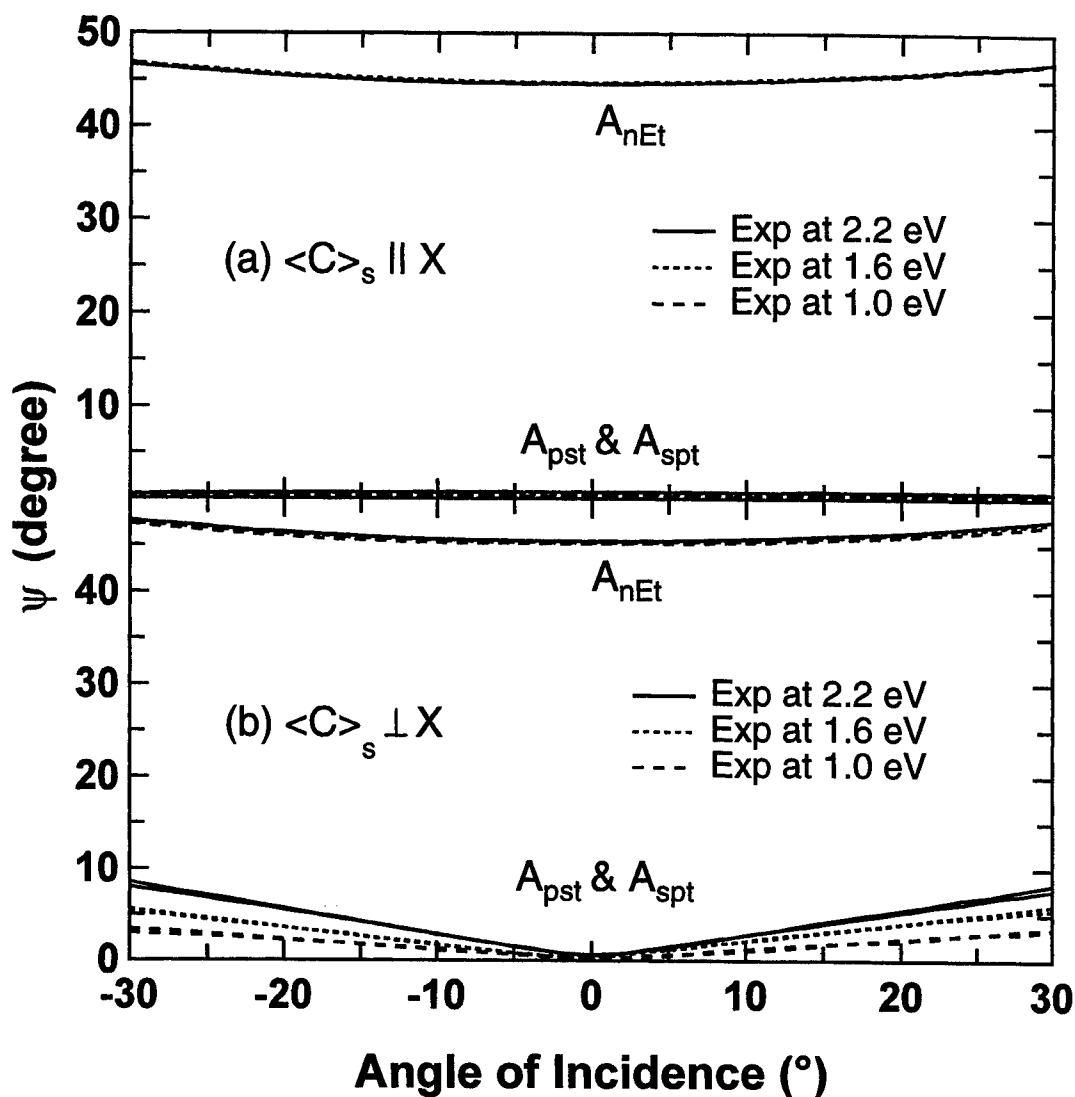


Fig. 7. Incident angular dependence of  $A_{pst}$  and  $A_{spt}$  of GaN/m-sapphire at 1.0, 1.6, and 2.2 eV, respectively. (a)  $\langle c \rangle_s \parallel x$ , (b)  $\langle c \rangle_s \perp x$ .

#### References

1. H. Morkoc, S. Strite, G. B. Gao, M. E. Lin, B. Sverdlov, and M. Burns, "Large-band-gap SiC, III-V nitride, and II-VI ZnSe-based semiconductor device technologies," *J. Appl. Phys.* **76**, pp. 1363-1398, 1994.
2. S. Nakamura, T. Mukai, and M. Senoh, "Candela-class high-brightness InGaN/AlGaIn double-heterostructure blue-light-emitting diodes," *Appl. Phys. Lett.* **64**, pp. 1687-1679, 1994.
3. S. Nakamura, M. Senoh, N. Iwasa, and S. Nagahama, "High-Brightness InGaIn Blue, Green and Yellow Light-Emitting Diodes with Quantum Well Structures," *Jpn. J. Appl. Phys.* **34**, pp. L797-L799, 1995.
4. S. Nakamura, M. Senoh, S. Nagahama, N. Iwasa, T. Yamada, T. Matsushita, H. Kiyoku and Y. Sugimoto, "InGaIn-Based Multi-Quantum-Well-Structure Laser Diodes," *Jpn. J. Appl. Phys.* **35**, pp. L74-L76, 1996.
5. S. Nakamura, M. Senoh, S. Nagahama, N. Iwasa, T. Yamada, T. Matsushita, H. Kiyoku, Y. Sugimoto, T. Kozaki, H. Umemoto, M. Sano, and K. Chocho, "Continuous-wave operation of InGaIn/GaN/AlGaIn-based laser diodes grown on GaN substrates," *Appl. Phys. Lett.* **72**, pp. 2014-2016, 1998.



6. Z. C. Feng, M. Schurman, R. A. Stall, M. Pavlosky and A. Whitley, "Raman scattering as a characterization tool for epitaxial GaN thin films grown on sapphire by turbo disk metal-organic chemical vapor deposition," *Applied Optics* **36**, pp. 2917-2922, 1997.
7. T. Kawashima, H. Yoshikawa, S. Adachi, S. Fuke, and K. Ohtsuka, "Optical properties of hexagonal GaN," *J. Appl. Phys.* **82**, pp. 2528-3535, 1997.
8. T. Matsuoka, "Lattice-matching growth of InGaAlN systems," *Mat. Res. Soc. Symp. Proc.* **395**, pp. 39-50, 1996.
9. H. Yao, C. H. Yan, S. P. Denbaars, J. M. Zavada, "Optical anisotropy studies of sapphire by Raman scattering and spectroscopy transmission ellipsometry," *Mat. Res. Soc. Symp. Proc.* **512**, pp. 411-416, 1998.
10. S. P. S. Porto and R. S. Krishnan, "Raman effect of corundum," *J. Of Chem. Phys.* **47**, pp. 1009-1012, 1967.
11. T. Azuhata, T. Sota, K. Suzuki and S. Nakamura, "Polarized Raman spectra in GaN," *J. Phys.: Condens. Matter* **7**, pp. L129-L133, 1995.
12. R. M. A. Azzam and N. M. Bashara, *Ellipsometry and Polarized Light*, North-Holland, Amsterdam, 1977.
13. M. Schubert, B. Rheinlander, J. A. Wollam, B. Johs, and C. M. Herzinger, "Extension of rotating analyzer ellipsometry to generalized ellipsometry: determination of the dielectric function tensor from uniaxial TiO<sub>2</sub>," *J. Opt. Soc. Am.* **A13**, pp. 875-883, 1996.
14. R. M. A. Azzam, and N. M. Bashara, "Generalized ellipsometry for surface with directional preference: application to diffraction gratings," *J. Opt. Soc. Am.* **62**, pp. 1521-1523, 1972.
15. D. W. Berreman, "Optics in stratified and anisotropic media: 4x4 matrix formulation," *J. Opt. Soc. Am.* **62**, pp. 502-510, 1972.
16. M. Schubert, "Polarization dependent parameters of arbitrarily anisotropic homogeneous layered systems," *Phys. Rev. B*, **53**, pp. 4265-4274, 1996.
17. G. H. Wei, J. Zi, K. M. Zhang, X. D. Xie, "Zone-center optical phonons in wurtzite GaN and AlN," *J. Appl. Phys.* **82**, pp. 4693-4695, 1997.
18. R. Loudon, "The Raman effect in crystals," *Advan. Phys.* **13**, pp. 423-482, 1964.

---

## **SESSION 3**

### **Organic and Polymer LEDs**

# Organic electroluminescent displays

J. Shen<sup>1</sup> and J. Yang

Department of Electrical Engineering and Center for Solid-State Electronics Research  
Arizona State University, Tempe, AZ 85287

## ABSTRACT

Several issues related to the organic electroluminescent devices are reviewed. Numerical simulation results are presented for the trap-charge limited conduction processes. Several experimental observations are explained based on our simulations. Current-voltage characteristics, band and charge profiles are obtained to elucidate the conduction mechanisms with large trap densities. Recombination strength dependence, doping effects, and the interplay among the free, discrete, and exponential trap charges in single- and double-carrier devices are discussed.

Keywords: organic, electroluminescent, light-emitting, trap charge limited (TCL), space charge limited (SCL).

## 1. INTRODUCTION

Electroluminescent (EL) devices based on organic thin films, such as Alq, have shown promising properties for low power, flexible, cost-competitive display applications<sup>[1-4]</sup>. Red, green, and blue light emitting devices are readily available. Devices with luminous efficiency greater than 15 lm/W and lifetime greater than 10,000 hours have been demonstrated. Like its inorganic counterparts, a typical organic light emitting device (OLED) consists of a hole transport layer, an electron transport layer, and a recombination region. Typically, ITO is used as the hole injection electrode and a low work function metal layer (e.g., Mg) is used as the electron injection electrode. In order for the OLED to luminesce, carriers must be injected from the electrodes and transported through the organic layers before they finally recombine. Apparently, both contacts<sup>[5-7]</sup> and the organic layers<sup>[8-14]</sup> affect the device performance. In this article, we discuss several issues related to the bulk carrier transportation in the OLEDs for display applications.

## 2. CHARGE TRANSPORT IN OLED

Experimentally, a power-law current-voltage dependence ( $J \sim V^{l+1}$ ) has often been observed for some OLEDs. Various models have been proposed to interpret the data. To the first order, the single-carrier current density can be written as

$$J = nq\mu E \quad (1)$$

if the diffusion term can be ignored. If  $E \sim V/L$ , then the rest of the voltage dependence to make up the high voltage power factor ( $l+1$ ) has to come from either  $n(V)$  or  $E(V)$ , or the combination of the two. The argument for the voltage dependence of the charge concentration  $n$  is based on the space-charge limited (SCL) conduction theories.<sup>[8-14]</sup> In general, the SCL concentration has the form  $n \sim V^l$ . When the free carrier dominates the space-charge region (trap-free SCL),  $l \sim 1$ ; when the trap with an exponential distribution dominates the space-charge region [trap-charge limited (TCL)],  $l = T_c/T$ , where  $T_c$  is the characteristic temperature and  $l$  can be as high as  $\sim 10$ . On the other hand, the field-dependent mobility can also give rise to a highly nonlinear  $J$ - $V$  relationship which also seem to be able to fit the experimental data well.<sup>[15]</sup> The mobility field dependence is attributed to carrier hopping in disordered systems.<sup>[16]</sup> Most likely both the space charge and the mobility field dependence affect the  $J$ - $V$  relationship. The question is which is more dominant and in what voltage/current range.

### 2.1. Trap-charge limited conduction

<sup>1</sup> Correspondence: Email: [jshen@asu.edu](mailto:jshen@asu.edu); Phone: (602)-965-9517; Fax: (602)-965-8118.

In order to understand the behavior of the space-charge limited conduction processes, we carried out a numerical study. We solved the coupled two-carrier Poisson and current continuity equations. Both the drift and diffusion terms are included. Figure 1 shows the simulated current-voltage ( $J$ - $V$ ) characteristics of a single layer OLED with typical Alq material parameters. Exponential trap distributions are assumed. The three curves correspond to three different trap distributions ( $l = T_c/300 = 5, 7, \text{ and } 9$ ) with the same total trap densities ( $H_p=H_n=10^{19} \text{ cm}^{-3}$ ). Power-law  $J$ - $V$  relationships are obtained, in agreement with previous analytical results and consistent with experimental observations (for example, Ref. [11]). The voltage power factor [the slope in the  $\log(J)\sim\log(V)$  plot] extracted from experimental Alq data falls between our  $l=7$  and  $l=9$  ranges. The analytical derivation determines the power factor to be  $l+1$ , slightly larger than the corresponding extracted slopes from the simulation. At high voltages, the slopes tend to decrease slightly because the device approaches the "trap-filled" limit when the injection level is high. At low voltage ( $V < 2 \text{ V}$ ), our simulated TCL currents continue to decrease more or less following the same trend. Experimentally, a much gradual current-voltage dependence ( $J\sim V$ ) has been observed to intercept the TCL ( $J\sim V^{l+1}$ ) curves at about 2 V (illustrated by the dashed line at  $J=10^{-8} \text{ A/cm}^2$  in Fig. 1); and this voltage is often called the turn-on voltage. The turn-on voltage is generally believed to be coinciding with the flat-band condition in the diode. Below that voltage, the current is attributed to the ohmic conduction by intrinsic or background carriers. We have not been able to reproduce the observed current-voltage characteristics in this low voltage region even when we significantly increase the intrinsic carrier concentration to  $n_i=10^5 \text{ cm}^{-3}$ , which is already uncharacteristically large for the band gap of 2.4 eV. This led us to believe that some other mechanisms may be the cause of the conduction in this region. One possibility, for example, is the discharging effect. During a typical test run, the applied voltage is usually swept from zero to about 20 V or higher. To get an estimate of the magnitudes, we can use the "leaky capacitor" model. The total sheet charge density is  $\sim eV/L=3.4\times 8.85\times 10^{-14}\times 20/(10^{-5}\times 1.6\times 10^{-19})=4\times 10^{12} \text{ cm}^{-2}$ . The discharging process can become very inefficient below the flat-band condition. Thus, the initial current can depend on the history of the device. The evidence manifesting the existence of the discharging effect is the hysteresis associated with the low voltage  $J$ - $V$  tests. The diode can be pre-charged to the opposite polarity by applying a relatively large negative bias. Then the first forward voltage sweep can give rise to a negative current at low voltages ( $V < 2 \text{ V}$ ). Of course, we cannot exclude contact effects either in this low voltage region. Significant deviations from the  $J\sim V^{l+1}$  dependence are also observed for  $l=5$  and  $l=9$  in Fig. 1. After analyzing the corresponding band profiles, our preliminary conclusion is that the  $pn$  junction in the diode is limiting the current for  $l=5$  and the mutual spreading of the positive and negative charges (enlarging of the recombination zone) is enhancing the current for  $l=9$  at low voltages.

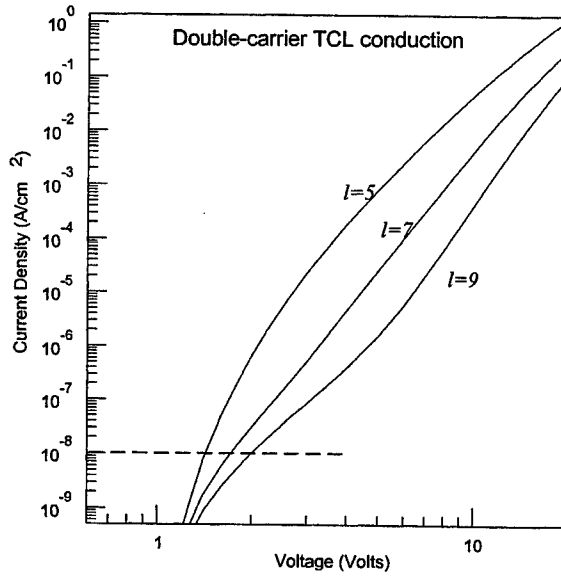


Fig. 1. Calculated TCL current-voltage ( $J$ - $V$ ) characteristics for three  $l$  values ( $l=5, 7, \text{ and } 9$ ). Power law dependence ( $J\sim V^{l+1}$ ) is obtained. The horizontal dashed line at  $J=10^{-8} \text{ A/cm}^2$  illustrates the experimentally observed background current. The parameters we used for this simulation are:  $H_p=H_n=10^{19} \text{ cm}^{-3}$ ,  $T=300\text{K}$ ,  $\epsilon_r=3.4$ ,  $n_i=1 \text{ cm}^{-3}$ ,  $E_g=2.4 \text{ eV}$ ,  $K_b=10^{-4} \text{ cm}^3/\text{s}$ ,  $\mu_n=5\times 10^{-5} \text{ cm}^2/\text{V}\cdot\text{s}$ ,  $\mu_p=0.01\mu_n$ ,  $n_o=p_o=\rho_o=5\times 10^{20} \text{ cm}^{-2}$ ,  $L=60\text{nm}$ . See the parameter definitions in Ref. [14].

## 2.2. Deviations from the classical TCL $J\sim V^{l+1}$ relationship (small $K_b$ )

In Fig. 1 we have used an arbitrary recombination coefficient ( $K_b=10^{-4} \text{ cm}^3/\text{s}$ ) to describe the total contribution summing all the recombination processes (radiative and nonradiative) (see the definition given in Ref. [14]). While accurate determination of the recombination coefficient including all processes is still not readily available, it has been proposed that the Langevin recombination mechanism generally applies to the organic systems.<sup>[17-21]</sup> Based on the Langevin formalism, the recombination coefficient is proportional to the carrier mobility in the following way

$$K_b = \frac{q}{\epsilon} (\mu_n + \mu_p) \quad (2)$$

When we use  $\mu_n=5\times 10^5$  cm<sup>2</sup>/V.s= $100\mu_p$  and  $\varepsilon=3.4\varepsilon_0$  for Alq, the recombination coefficient  $K_b=2.7\times 10^{-11}$  cm<sup>3</sup>/s according to Eq. (2). In order to see how the recombination coefficient may affect the TCL characteristics, we calculated the current-voltage dependence for a series of  $K_b$ 's and the results are shown in Fig. 2. First of all, at a fixed voltage, the current magnitude increases when  $K_b$  decreases. Such an increase in current magnitude is due to the partial cancellation of the positive and negative charges in the device which in turn weakens the electric field. Such a phenomenon has been called the injected plasma limit.<sup>[9,10]</sup> Apparently, a smaller  $K_b$  leads to a larger electron-hole overlap and more effective cancellation of the charges. The calculated charge and energy profiles of a device with  $K_b=10^{-12}$  cm<sup>3</sup>/s is shown in Fig. 3. The recombination zone is broadened and the current is larger as the device is approaching the injected plasma limit. Too broad a recombination zone can be bad for the OLEDs because part of the carriers may flow through the device without the chance to recombine, and part of them may recombine near the electrodes known to have luminescence quenching centers, hurting the luminescence efficiency of the device. The second noticeable feature in the current-voltage characteristics for a smaller  $K_b$  is the decrease in the slope  $[\log(I)/\log(V)]$ . To understand the slope change is not so straightforward. However, it becomes a little clearer if we interpret the slope change in a different way, that is, the amount of the current magnitude increase with smaller  $K_b$  drops when the applied voltage increases. As we know, at a fixed voltage, a smaller  $K_b$  leads to a larger electron-hole overlap (larger recombination zone). On the other hand, for a fixed small  $K_b$  (e.g.,  $K_b=10^{-12}$  cm<sup>3</sup>/s), the electron-hole overlap shrinks as the voltage increases (the recombination term is proportional to  $K_b np$  while the current density is proportional to  $n$  or  $p$ ). Thus for a larger  $V$ , the effective charge cancellation region decreases and the current enhancement due to the charge cancellation becomes less pronounced, which gives rise to the apparent slope change in the  $\log(I)/\log(V)$  curves. As an extreme case, there is no current enhancement from  $K_b=10^{-4}$  cm<sup>3</sup>/s to  $K_b=10^{-8}$  cm<sup>3</sup>/s at 20 V because the electron-hole overlap in either case is insignificant. The point where the current with a smaller  $K_b$  meets with the one with a larger  $K_b$  is also pushed upward (at  $\sim 8$  V for  $K_b=10^{-6}$  cm<sup>3</sup>/s and at  $\sim 20$  V for  $K_b=10^{-8}$  cm<sup>3</sup>/s, etc.). This result is due to the fact that it takes a larger voltage to diminish the electron-hole overlap when  $K_b$  becomes smaller.

It may appear that there would be a discrepancy between the TCL theory and the experimental observations if  $K_b$  is indeed small (the slope is smaller than what is observed). However, many other factors, such as a larger  $T_c$  ( $T_c/T=1$ ) or the field-dependent mobility, can still make corrections to the TCL results to fit a particular experiment. Our study shows that a comprehensive understanding of the physics of the SCL and TCL processes can be very important in interpreting experimental data.

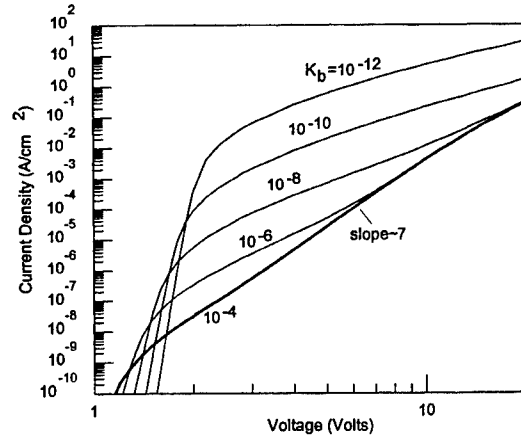


Fig.2. Calculated TCL current-voltage ( $J$ - $V$ ) characteristics for  $l=7$  and several different  $K_b$ 's. The slope  $[\log(I)/\log(V)]$  approaches the analytical value  $(l+1)$  when  $K_b$  is large. For smaller  $K_b$ , the current enhancement due to the charge overlap and the effective charge cancellation reduces the slope. Other device parameters used for this simulation are identical to those given in Fig.1.

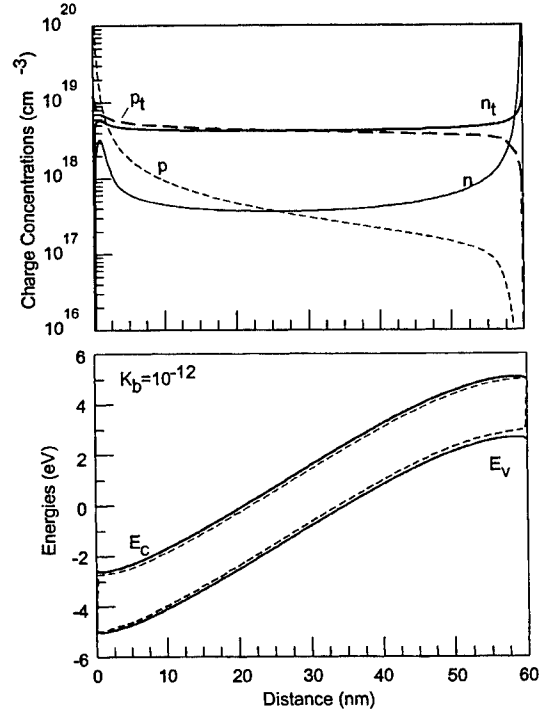


Fig.3. The profiles of a device with a small recombination constant ( $K_b=10^{-12}$  cm<sup>3</sup>/s) at 10 V. Other parameters are kept identical as those in Fig.1 with  $l=7$ . The recombination zone is spreading over a large portion of the device. This is sometimes called the injected plasma limit.

### 3. DOPING EFFECTS

Most fluorescence dye compounds only fluoresce in dilute solutions and the fluorescence is quenched when the compound is made in a condensed phase. The fluorescence solution can either be in solid state and liquid state. When a solid state guest-host solution is made by doping a fluorescence dye in a host matrix, the fluorescence characteristics are determined by the guest molecules provided that the energy transfer from the host molecules to the guest molecules is efficient. This phenomenon in solid state chemistry is known as sensitized luminescence. This method was first used in organic EL systems, such as anthracene doped with tetracene.<sup>[22]</sup> Tang and coworkers then extended this technique to thin film OLEDs.<sup>[2]</sup> They found that the color of the emitted light can be tuned by changing the dopants without changing the overall device structure. With Alq as the host, they were able to shift the emission peak wavelength from 520 nm to 620 nm by changing the dopant. The optimum doping concentration varies from a fraction of a percent to a few percent. This is a very simple way to tune the color of OLED devices. Doping can not only change the emission wavelength, but also improve the device efficiencies by 2-3 folds. Up to date, most of the high efficiency OLED devices are made this way. It should be noted, however, that doping does not always increase the device efficiency. The efficiency of the energy transfer from the host to the guest molecules depends on the relative energy alignment of the two materials. For example, doping perylene in DPVBi does not result in any improvement in device efficiencies.<sup>[23]</sup> On the other hand, doping a distyrylarylene amine in the same host material shows a 2-fold improvement in device efficiency.

We have simulated some aspects of the doping effects numerically, based on the similar numerical models.<sup>[14,24]</sup> We describe the doped layer in one of the following four different ways: (i) the doped layer has a higher concentration of traps than the host, (ii) the doped layer changes the trap distribution characteristic, (iii) the doped layer introduces a discrete trap level in the energy gap of the host, and (iv) the doped layer has a higher recombination rate than the host. Our numerical result reveals the doping-induced changes in the profiles (the energy bands, the charge concentrations, and the electric field, etc.) and the location of the recombination zone. We find that a simple physical picture can be used to explain most of the doping related effects we studied here: The additional trap charge of the doped layer creates a charge imbalance between the positive and negative layers in the OLED; the neutrality requirement finally readjusts the overall charge distribution which in turn determines the location of the recombination zone.

Figure 4 shows the calculated energy and charge profiles of an OLED under TCL conditions, with and without doping.<sup>[24]</sup> We have used parameters that are typical of an Alq layer. Electrons and holes are injected from the right-hand ( $x=60\text{nm}$ ) and left-hand ( $x=0$ ) electrodes, respectively. The n-doped layer is placed at  $x_d=42.5\text{nm}$  and its thickness is  $5\text{nm}$ . Here we have assumed  $H_{nd}=5\times 10^{19}\text{ cm}^{-3}=5H_{n0}$ . The energy profiles of a similar structure without the doped layer are also shown in dot-dashed lines. The most significant change in the device is the shift of the recombination zone toward the doped layer. It is also interesting to see that the recombination zone is not at the doped layer in this particular case. The trap charges directly determine the location of the recombination zone under TCL conditions.

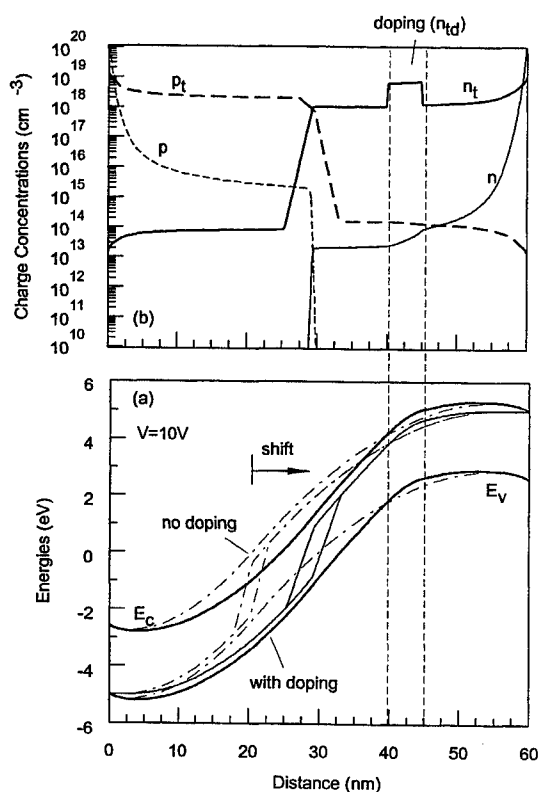


Fig. 4. Calculated energy (a) and charge (b) profiles at 10V of a single layer device with and without a doped layer at  $x_d=42.5\text{nm}$  (with the thickness  $d=5\text{nm}$ ) and the doping density is  $H_{nd}=5\times 10^{19}\text{ cm}^{-3}=5H_{n0}$ . The recombination zone is at  $x \sim 20\text{nm}$  without doping (the thin dot-dashed curves in (a)), and is shifted to  $x \sim 30\text{nm}$  when the doped layer is present (see the arrow). The quasi-Fermi levels ( $F_p$  and  $F_n$ ) are represented by the thin curves inside the energy gap. In the corresponding charge concentration plot [(b), only the profiles with doping are shown], a significant increase in the trapped charge can be seen in the doped layer, which is the cause of the recombination zone shift.

According to the charge neutrality condition which requires the equality between the total positive and negative charges:

$$L_p p(\text{average}) = L_n n(\text{average}) \quad (3)$$

where  $L_p$  and  $L_n$  are the lengths of the  $p$ - and  $n$ -type regions, respectively. Without doping, the averaged trap charges are  $P(\text{ave}) \approx 2 \times 10^{18} \text{ cm}^{-3} \approx 2N_t(\text{ave})$  (one can eyeball it from the  $p_i$  and  $n_i$  curves). Then, we have  $L_p = L_n/2$ , in good agreement with the numerical result (the location of the recombination zone is at  $x \sim 20 \text{ nm}$ ). The free carrier concentrations, on the other hand, differ by a factor of 100 ( $p = 100n$ ) near the recombination zone (Fig. 4, the same result with or without doping). This carrier concentration difference arises from the mobility difference ( $\mu_n = 100\mu_p$ ) and the current continuity requirement ( $j_n \sim n\mu_n = j_p \sim p\mu_p$ ) when the electric field is approximately equal on either side (it is true near the recombination zone). The fact that the free carrier concentrations differ by a factor of 100 while the respective trapped charge concentrations differ by only a factor of 2 is due to the  $I$  factor ( $I = T/T = 7$  in this case):  $p/n_i = (p/n)^{1/I} = (100)^{1/7} \approx 2$ . This result also implies the thermal equilibrium between the free and trapped charges.

When the doped layer is introduced, the trap charges are redistributed. As shown in Fig. 4, the doped layer at  $x_d = 42.5 \text{ nm}$  changes the charge balance. The average trapped electron density in the doped layer is increased to  $\sim 7 \times 10^{18} \text{ cm}^{-3}$ , which effectively increases  $N_t(\text{average})$ , causing the shift of the recombination zone ( $L_n$  decreases). Based on these results, we conclude that if a doped layer changes the trap charge concentration, the trap charge balance is modified and the location of the recombination zone is shifted in the way to satisfy the new charge neutrality condition.

#### 4. EFFECTS OF DISCRETE TRAP LEVELS

The trap energy level can be distributed in some other ways other than the exponential distribution. When traps exist in the energy gap with a single discrete energy  $E_s$ , then the trapped charge concentration is

$$n_t = n_s = \frac{N_s}{1 + \exp[(E_s - F_n)/kT]} \quad (4)$$

where  $F_n$  is the Fermi level, and  $N_s$  is the trap density, assuming the degeneracy factor is equal to one. Because the free carrier concentration is  $n = N_C \exp(F_n/kT)$  with  $N_C$  being the effective density of states of the lowest unoccupied molecular orbitals (assumed to be at zero as an energy level reference), the following relationship between  $n$  and  $n_s$  can be obtained

$$n_s = \frac{N_s}{1 + \theta N_s / n} \quad (5)$$

with  $\theta = (N_C/N_s) \exp(E_s/kT)$ .

The interplay among the free, discrete-trap, and exponential-trap charges is illustrated in Fig. 5, where the charges are plotted as functions of the Fermi level. We first discuss the case where only discrete traps are present. When the Fermi level is below the trap level ( $E_s = -0.5 \text{ eV}$ ), the trap filling rate [the slope in the  $\log(n_s) - F_n$  plot] is the same as the free-carrier concentration increase rate (the slope  $= 1/kT$ ), even though  $n_s$  can be much larger in magnitude than  $n$  (by a factor of  $\theta^{-1}$ ). That is why the D-TCL current has the same voltage dependence as the trap-filled SCL current ( $J \sim V^2$ ). When  $F_n$  approaches  $E_s$ , the discrete traps are quickly filled up and saturated while  $n$  continues to increase with  $F_n$ . Beyond  $F_n = -0.07 \text{ eV}$ , the free carrier concentration becomes larger than  $n_s$ , and the conduction turns into the trap-filled or "trap-free" SCL regime. The region between  $F_n = -0.5 \text{ eV}$  and  $-0.07 \text{ eV}$  is a transition region when  $n$  is still smaller than  $n_s$  but  $n_s$  is no longer increasing. Within this transition region, the free carrier concentration increases by a factor of  $\theta^{-1} \sim 1.7 \times 10^6$  (from point A to point B), which is basically the amount of increase in the current from the D-TCL to the trap-free SCL regions (the voltage change in the transition region is relatively small). Figure 5 can be very helpful because it graphically illustrates the amount of current changes, the boundary between various regions, and how the discrete trap parameters ( $E_s$  and  $N_s$ ) affect the results. For example, if the discrete trap level is shallower than  $E_s = -0.07 \text{ eV}$  (with the same  $N_s$  and  $N_C$ ), then the discrete trap will have little effect on the current-voltage characteristics because the conduction is always in the trap-free SCL region. Similar interesting conclusions can be drawn by moving  $N_s$  and  $N_C$  around.

Adding traps with an exponential energy distribution to the system makes things more interesting and a little bit complicated. For the sets of parameters assumed in Fig. 5, there are possibly four regions: (i) the exponential trap dominated TCL region ( $F_n < -0.6$  eV); (ii) the weak D-TCL region ( $-0.6$  eV  $< F_n < -0.5$  eV); (iii) the transition region ( $-0.5$  eV  $< F_n < -0.07$  eV); and (iv) the trap-filled SCL region ( $-0.07$  eV  $< F_n$ ). In Region (i) the current-voltage characteristic has the form  $J \sim V^{1/2}$ , because the exponential trap is dominant. In Region (ii), the discrete trap takes over and the current-voltage characteristic gradually turns into the  $J \sim V^2$  form, and then changes back toward the  $J \sim V^{1/2}$  dependence in Region (iii). Region (iv) is the trap-filled limit ( $J \sim V^2$ ). Because the magnitude difference between  $n_s$  and  $n_x$  in Regions (ii) and (iii) is not big, we expect more gradual transitions (in the  $J$ - $V$  dependence) between the regions. Similar to what we have discussed above, one can change the values of  $E_s$ ,  $N_s$ ,  $H_n$ , and  $T_c$  in Fig. 5 and study various limiting cases.

Figure 6 shows several calculated current-voltage characteristics of a single-layer device with or without discrete traps. The three thin curves represent the case of single-carrier (electron) injection with various discrete electron trap energies ( $E_s = -0.3, -0.4$  and  $-0.5$  eV). For  $E_s = -0.5$  eV, a sharp transition occurs at  $V \sim 8$  V, corresponding to the trap filling regime. As discussed above, the current magnitude increase in this region is  $\theta^{-1} = (N_s/N_c) \exp(-E_s/kT) = 1.7 \times 10^6$  by using the assumed parameter values ( $N_c = 1.6 \times 10^{20}$  cm $^{-3}$ ,  $N_s = 10^{18}$  cm $^{-3}$ ,  $E_s = -0.5$  eV,  $T = 300$  K), which is in close agreement with the simulation result. This result can also be obtained graphically from Fig. 5 as discussed above. For  $E_s = -0.3$  eV,  $\theta^{-1} = 7 \times 10^{-2}$  so the transition region is very small. What is interesting is the double-carrier injection case with an electron discrete trap at  $E_s = -0.5$  eV (thick solid curves in Fig. 6). The sharp transition region disappears almost completely even though the trap is rather deep. By analyzing the energy and charge profiles of the device, we found that  $p$ - and  $n$ -type regions are formed adjacent to the recombination zone. Unlike the single-carrier case, the electron discrete levels are already full in the  $n$ -region even at a small bias while they are always empty in the  $p$ -region. When the bias is increased, the recombination zone gradually shifts toward the anode, enlarging the  $n$ -region and shrinking the  $p$ -region. So there is no instantaneous transition of all trap levels from empty to full states, which is reflected in the absence of a sharp transition region in the current-voltage characteristics.

## 5. SUMMARY

Several issues related to the carrier transport mechanisms in OLED's with large concentrations of traps have been studied. The current-voltage relationships are simulated for

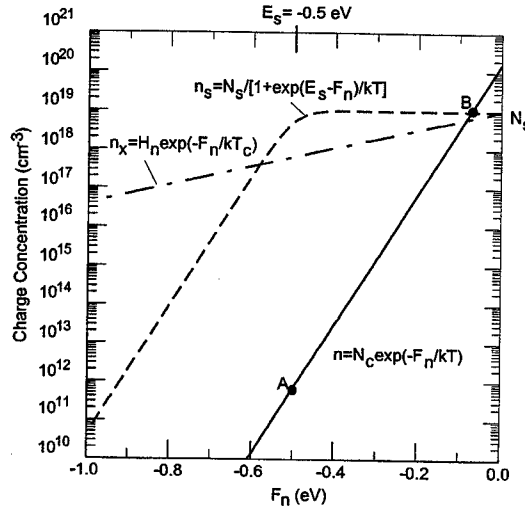


Fig.5. Trends of different electron charges (free electron concentration  $n$ , discrete-trap charge concentration  $n_x$ , and exponential-trap charge concentration  $n_s$ ) in an OLED as functions of the electron Fermi energy  $F_n$ . The discrete trap level is assumed to be at  $E_s = -0.5$  eV in reference to the LUMO ( $=0$ ). The LUMO density is  $N_c = 1.6 \times 10^{20}$  cm $^{-3}$ . Both the exponential-trap density ( $H_n$ ) and discrete-trap density ( $N_s$ ) are assumed to be  $10^{19}$  cm $^{-3}$ .

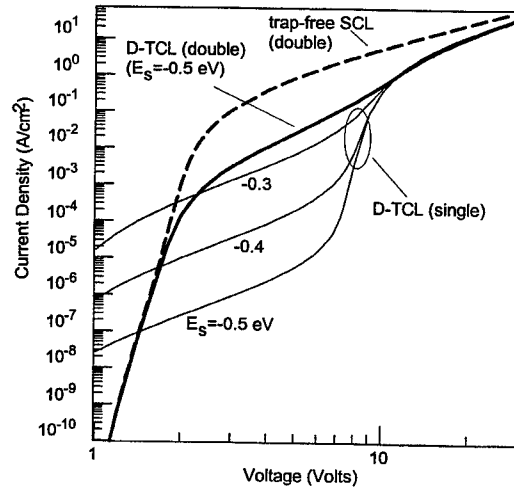


Fig.6. Calculated current-voltage characteristics of several SCL conduction devices without exponential traps. The three thin solid curves correspond to the single-carrier (electron) injection case with three different discrete trap energies. The thick solid curve corresponds to the double-carrier injection case with a discrete electron trap level  $E_s = -0.5$  eV. The thick dashed curve corresponds to the double-carrier trap-free SCL case. The parameters we used according to the notations defined in Ref.[14] are (wherever they apply):  $H_p = H_n = 0$  cm $^{-3}$ ,  $N_s = 10^{18}$  cm $^{-3}$ ,  $T = 300$  K,  $\epsilon_r = 3.4$ ,  $n_i = 1$  cm $^{-3}$ ,  $E_g = 2.4$  eV,  $K_b = 10^{-4}$  cm $^3$ /s,  $\mu_n = 5 \times 10^{-5}$  cm $^2$ /V.s,  $\mu_p = 0.01 \mu_n$ ,  $n_o = p_o = 5 \times 10^{20}$  cm $^{-3}$ ,  $L = 60$  nm.



TCL double-carrier injection OLED's. The characteristic slope of current-voltage curved can be reduced when the recombination constant is small and when the charge overlap and cancellation become effective. Doping effects are also studied. An increase in the amount of trap charges in a doped layer can cause the overall charge redistribution and recombination zone shift. The interplay among the free, discrete-trap, and exponential-trap charges can also lead to some interesting results which had not been predicted before.

## 6. REFERENCES

- [1] C. W. Tang and S. A. VanSlyke, *Appl. Phys. Lett.*, **51**, 913 (1987).
- [2] C. W. Tang, S. A. VanSlyke, and C. H. Chen, *J. Appl. Phys.*, **65**, 3610 (1989).
- [3] J. H. Burroughes, D. D. C. Bradley, A. R. Brown, R. N. Marks, K. Mackay, R. H. Friend, P. L. Burns and A. B. Holmes, *Nature*, **347**, 539 (1990).
- [4] For recent reviews, see N. C. Greenham and R. H. Friend, *Solid State Phys.* **49**, 1 (1995); J. R. Sheats, H. Antoniadis, M. Hueschen, W. Leonard, J. Miller, R. Moon, D. Roitman, and A. Stocking, *Science*, **273**, 884 (1996); and L. J. Rothberg and A. J. Lovinger, *J. Mater. Res.*, **11**, 3174 (1996).
- [5] I. D. Parker, *J. Appl. Phys.* **75**, 1659 (1994).
- [6] V. I. Arkhipov, E. V. Emelianova, Y. H. Tak, H. Bässler, *J. Appl. Phys.* **84**, 848 (1998).
- [7] J. Rommens, M. Van der Auweraer, and F. C. De Schryver, *J. Phys. Chem.* **101**, 3081 (1997).
- [8] P. Mark and W. Helfrich, *J. Appl. Phys.*, **33**, 205 (1962).
- [9] M. A. Lampert and P. Mark, *Current injection in Solids* (Academic, New York, 1970).
- [10] K. C. Kao and W. Hwang, *Electrical Transport in Solids, with Particular Reference to Organic Semiconductors*, Pergamon Press, 1981.
- [11] P. E. Burrows, Z. Shen, V. Bulovic, D. M. McCarty, S. R. Forrest, J. A. Cronin, and M. E. Thompson, *J. Appl. Phys.*, **79**, 7991 (1996).
- [12] P. W. Blom, M. J. M. de Jong, and J. J. M. Vleggaar, *Appl. Phys. Lett.* **68**, 3308 (1996).
- [13] A. J. Campbell, D. D. C. Bradley, and D. G. Lidzey, *J. Appl. Phys.* **82**, 6326 (1997).
- [14] J. Shen and J. Yang, *J. Appl. Phys.* **83**, 7706 (1998).
- [15] A. Ioannidis, E. Forsythe, Y. Gao, M. W. Wu, and E. M. Conwell, *Appl. Phys. Lett.* **72**, 3038 (1998).
- [16] H. Bässler, *Phys. Status Solidi (b)*, **175**, 15 (1993).
- [17] P. Langevin, *Ann. Chem. Phys.* **28**, 289 (1903).
- [18] M. Pope and C. E. Swenberg, *Electronic Processes in Organic Crystals* (Oxford University Press, New York, 1982), p. 502.
- [19] U. Albrecht and H. Bässler, *Phys. Stat. Sol. (b)* **191**, 455 (1995).
- [20] P. W. M. Blom, M. J. M. de Jong, and J. J. M. Vleggaar, *Appl. Phys. Lett.* **68**, 3308 (1996).
- [21] J. C. Scott, S. Karg, and S. A. Carter, *J. Appl. Phys.* **82**, 1454 (1997).
- [22] M. Kawabe, K. Masuda, and S. Namba, *Jpn. J. Appl. Phys.* **10**, 525 (1971).
- [23] C. Hosokawa, H. Higashi, H. Nakamura, and T. Kusumoto, *Appl. Phys. Lett.* **67**, 3853 (1995).
- [24] J. Yang and J. Shen, *J. Appl. Phys.*, **84**, 2105 (1998).

# The Application of Polyfluorenes and Related Polymers in Light Emitting Diodes

Mark Bernius, Michael Inbasekaran, Edmund Woo,  
Weishi Wu\*, and Lisa Wujkowski

Corporate Research and Development  
The Dow Chemical Company, Midland Michigan 48674

## ABSTRACT

We report our progress to date in the materials and processing aspects of developing organic light emitting diode technology based on high molecular weight polymers. A portfolio of fluorene-related polymers are prepared through the coupling of 9,9-disubstituted 2,7-bis-1,3,2-dioxaborolanyl-fluorene with a variety of aromatic dibromides. In the case of fluorene homopolymers, the polyphenylene main chain provides the mechanical, electrical and electronic properties and the C-9 maintains coplanarity of the biphenylene unit and a site for property modification without altering effective conjugation. In the case of alternating polymers, the optical and electronic properties of the polymers are tailored through selective incorporation of different aromatic unit into the system. These polymers are soluble in common organic solvents and are readily processed into uniformed films of high quality by spin casting. Unlike PPV and related materials, LED devices with fluorene polymers in a conventional configuration appear to have electrons as the majority carrier and their performance is markedly improved when modified with an appropriate polymeric hole transporting layer. Bright green light with a luminance of 10000 Cd/m<sup>2</sup> is achieved at a very low drive voltage of <6 V attributable in part to the high hole mobility of fluorene-based polymers.

**Key Words:** Polyfluorenes, Electroluminescent, Photoluminescent, Light emitting diodes.

## 1. INTRODUCTION

Since the first report [1] of polymer light emitting diodes (LED), this topic has experienced an explosive growth in popularity in the research community worldwide. Among the myriad chemical structures studied [2], derivatives and modifications of poly(phenylenevinylene) (PPV) are still receiving the most attention and have shown promise as materials for commercial displays [3]. The basic PPV structure, however, has not lent itself to the generation of blue emitters and is prone to oxidative degradation in the presence of light.

Polyphenylenes (PP), another class of conjugated polymers, have been studied broadly because of their chemical stability and band-gap energies close to the 3 eV required for blue light emission. Much of the interest concentrates on solution-processable versions made soluble by substitutions on the phenylene rings with long-chain alkyl groups. In this way, a number of high molar mass, soluble poly(*p*-phenylene)s have become available for LED work [4]. The steric demand of the solubilizing groups has the drawback of forcing the phenylene groups to be out of conjugation diminishing the interaction of the aromatic  $\pi$ -system, which may adversely affect the performance of these polymers as active components. Ladder structures with long-chain alkyl substituents have been explored as an avenue to maintain coplanarity and solubility. Scherf and Müllen demonstrated that soluble ladder polymers consisting of phenylene units fused together by 5-membered rings could be obtained in relatively high degree of polymerization [5]. However, emission from films of these polymers is yellow instead of the blue observed in solution. It appears these rigid, ribbon-like structures tend to aggregate in the solid state leading to emission from excimers. Inserting 2,5-dialkyl-1,4-phenylene units into the polymer backbones eliminates aggregate formation but reintroduces torsional twist between adjacent phenylene units [6].

Poly(flourene-2,7-diyl) (structure exemplified by **F8** in **Figure 1**) may be regarded as another version of poly(*p*-phenylene) with pairs of phenylene rings locked into a coplanar arrangement by the C-9 atom onto which solubilizing substituents may be placed without introducing additional torsional strain. As implied by the name, fluorene-based compounds are generally highly fluorescent, a requisite feature for electroluminescence applications. This paper describes our work on the synthesis and characterization of a plethora of fluorene homo- and copolymers and their applications to light emitting diodes.

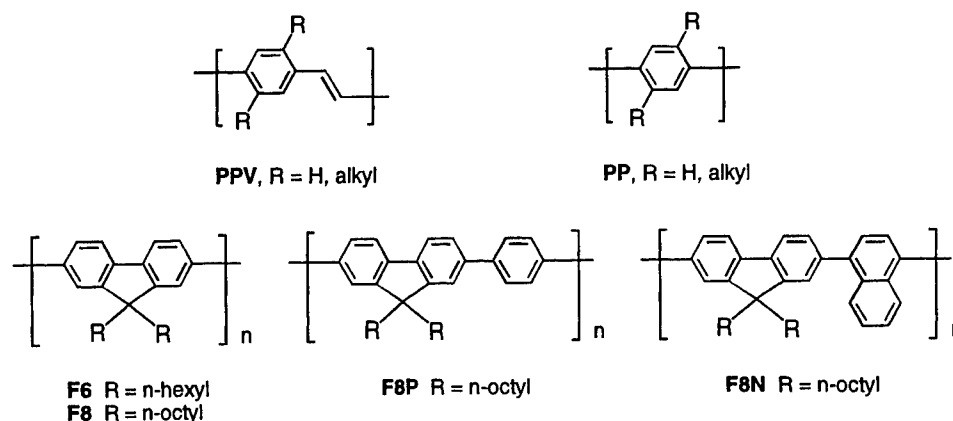


**Figure 1.** Structures of PPV, PP and polyfluorene homopolymers and copolymers.

## 2. FLUORENE HOMOPOLYMERS

The first fluorene-based polymers, via ferric chloride oxidative polymerization of 9-alkyl- and 9,9-dialkylfluorenes, reported by Fukuda and coworkers [7], appear to be relatively low in molar mass, with some degree of branching and non-conjugative linkages through positions other than 2 and 7 [8]. The rather poor regiospecificity is not surprising as Brown and coworkers had found substantial presence of branched polynuclear structures in the oxidative polymerization of benzene [9]. To improve specificity and to minimize branching we chose to access the homopolymers through transition metal-catalyzed reactions of monomeric 2,7-dihalogenated fluorenes.

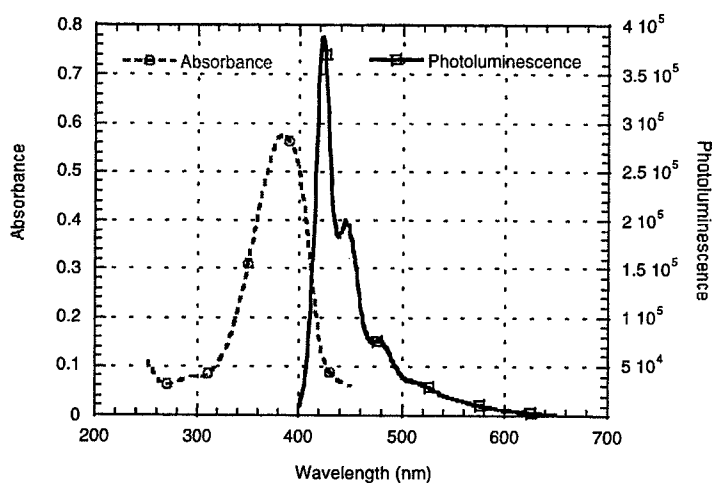
Nickel-catalyzed polymerization of arylene dihalides has been reviewed by Yamamoto [10]. Of particular interest to us was the version first reported by Colon which utilizes zinc as the reducing agent and a truly catalytic amount of *in-situ* generated zero-valent nickel complex [11]. Attempts to apply this reaction to the polymerization of 2,7-dichloro-9,9-di-n-hexylfluorene (and the dibromo analog) succeeded in providing polymers of moderately high degree of polymerization of approximately 50 relative to polystyrene standards. The major impediment to molecular weight built appears to be the limited solubility of the polymer in the highly polar, aprotic solvents required for this reaction. As a result, the growing polymer chains precipitate from the reaction solution effectively suppressing further chain growth.

It is instructive to compare the properties of poly(9,9-di-n-hexylfluorene)s prepared by Ni-catalyzed coupling and oxidative coupling (**Table 1**). The regiospecific polymer obtained by us has a polydispersity typical of a condensation polymer, exhibits a persistent nematic state when a film is heated to about 190°C and is a bright blue emitter [12]. Whereas the polymer reported by Fukuda, although nominally identical, has a significantly lower glass transition temperature, a much higher polydispersity and no indication of order. Whether these differences in polymer properties would be reflected in electronic device performance is unclear but they highlight the impact of chemical defects on properties.

**Table 1.** Properties of Poly(9,9-di-n-hexylfluorenes) (F6).

	Ni-Catalyzed	Oxidative
DP	48	14
Polydispersity	2.4	6.8
DSC		
Glass transition	95°C	55°C
k → n	193°C	none
n → i	249°C	none
Photoluminescence of films	424(s), 445(m), 475(w)	425(m), 495(s)

Because of the non-polar nature of most polyfluorenes, it is unlikely that polymer chain growth can be consistently effected in a highly polar solvent without resorting to high temperature and/or very long reaction time. The nickel-catalyzed coupling reactions are, therefore, not the method of choice for high molecular weight polymers. Furthermore, they would not be suitable for the synthesis of ordered copolymers for the resulting copolymeric structures would be dependent on the relative reactivity and concentrations of the monomers. The palladium-catalyzed synthesis of mixed biphenyls from phenylboronic acid and aryl bromide discovered by Suzuki and coworkers [13] offers the possibility of preparing alternating copolymers and the advantages of being tolerant of a large variety of functional groups, insensitive to the presence of water, and truly catalytic in metallic reagents. Scherf and Müllen [5] reacted alkylated 1,4-phenylene diboronic acids with various dibromobenzophenones in refluxing toluene/aqueous potassium carbonate for 1 day and obtained relatively low molecular weight polymers,  $M_w$  ranging from 600 to 15,000 gram/mole. More recently Tanigaki and coworkers [14] obtained alternating copolymers of modest molecular weight after refluxing in toluene-aqueous sodium carbonate for 72 hours. Optimization of this synthetic method in our laboratories has led to a highly efficient procedure which routinely yields high molecular weight polymers in much shorter reaction times. For example, poly(9,9-di-n-octylfluorene-2,7-diyl) (F8 in Figure 1), of  $M_w > 100,000$  gram/mole was obtained after less than 24 hours of reaction time.

**Figure 2.** Absorption and photoluminescence spectra of poly(9,9-di-n-hexylfluorene-2,7-diyl) (F6).

Polyfluorenes with  $C_6$  or higher substituents at C-9 are all soluble in conventional organic solvents such as aromatic hydrocarbons, tetrahydrofuran, and chlorinated hydrocarbons. Most high molecular weight polymers do not show a very

distinct glass transition, and those with straight alkyl substituents tend to be semicrystalline and exhibit liquid crystallinity (LC). **F8**, for instance, has a very stable LC state that persists up to 270°C [15]. Polymers with branched alkyl substituents, *e.g.*, 2-ethylhexyl, are amorphous. All are strong blue emitters when excited with UV in solution as well as in the solid state. The absorption and photoluminescence spectra of a film of poly(9,9-di-n-hexylfluorene-2,7-diyl) (**F6** in **Figure 2**) are representative of all homopolymers. Absorption spectra are broad and featureless while the photoluminescence spectra show well-defined vibronic structures. The Stokes shift is typically less than 50 meV, a small value in relation to other conjugated polymers and similar to the well-ordered ladder polyphenylenes, indicative of an extended conformation.

### 3. ALTERNATING COPOLYMERS

#### 3.1 Alternating Copolymers with Aromatic Hydrocarbons

Using the Pd-catalyzed polymerization, several high molecular weight alternating copolymers have been prepared from the 2,7-diboronic derivatives of 9,9-dialkylfluorene and dibromoarenes. The impact of steric effect on electronic properties are vividly illustrated by a comparison of the absorption and emission spectra of a **F8** to those of a copolymer with 1,4-dibromobenzene (**F8P**) and 1,4-dibromonaphthalene (**F8N**). Films of these polymers all show broad featureless absorption peaks (**Figure 3**) but different band-gaps (as determined by absorption band edge) and maxima: **F8** with the lowest energy absorption maximum at 386 nm and **F8N** with the highest at 351 nm. These variations can be readily explained by the difference in steric effect. The steric repulsion is expected to be the most severe in **F8N** because of the proximity of the naphthalene *peri*-hydrogen to the C-1 hydrogen of fluorene. Consequently the torsional angle between fluorene and naphthalene would be significantly larger than those between two fluorenes. The electronic properties of **F8P** is intermediate between **F8** and **F8N** and the overall trend re-emphasizes the advantage of fluorene as a building block for polymers with extended conjugation. **F8N** also differs from the other two polymers in several important aspects: it is amorphous, shows no sign of liquid crystallinity, and its photoluminescence spectrum lacks vibronic structure (**Figure 4**).

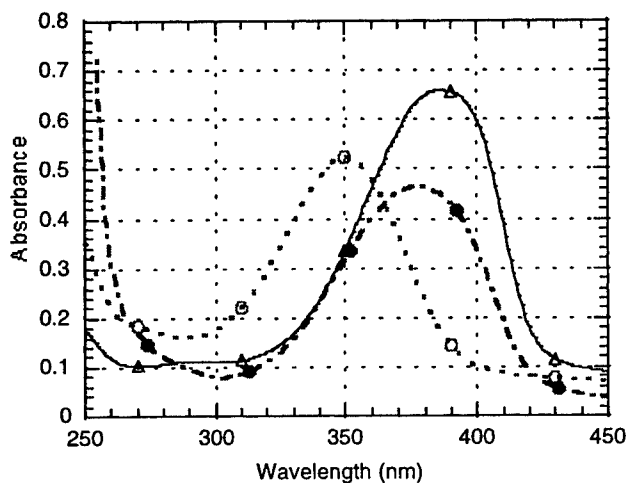


**Figure 3.** Absorption spectra of **F8** (triangles); **F8P** (filled circles) and **F8N** (open circles) films.

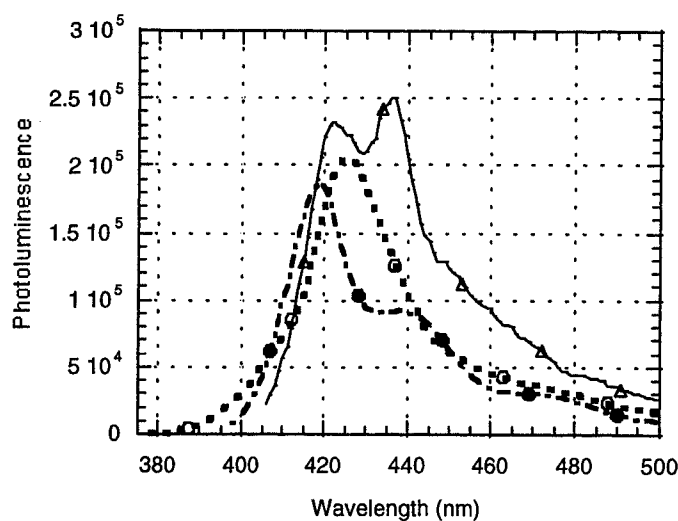


Figure 4. Photoluminescence spectra of F8 (triangles); F8P (filled circles) and F8N (open circles) films.

### 3.2 Alternating Copolymers with Tertiary Aromatic Amines and Thiophene

Tertiary aromatic amines have been known as excellent hole transport materials and have found utility in photoconductors and in light emitting diodes [16]. Polymers with these moieties incorporated into their backbones, however, have been limited to those with non-conjugative comonomers which are expected to have adverse effects on hole transport properties [17]. We reported recently the synthesis of several polymers comprising solely of triarylamine units but they are of relatively low molecular weight owing to the limited solubility of the growing chains in the polymerization solvents [18]. With the Pd-catalyzed polymerization process, it is possible to prepare high molecular weight alternating copolymers consisting of 9,9-dialkylfluorene and various aromatic amines. Representative amines successfully incorporated are shown in Figure 5. These alternating copolymers are all blue emitters, excellent film formers, and soluble in conventional organic solvents. Films of these polymers show distinct and reversible oxidation potentials by cyclic voltammetry and can be cycled repeatedly without any appreciable change. The cyclic voltammetric scan shown in Figure 6, obtained with a film of the alternating copolymer PFB (2c), is typical of all diamine-containing copolymers. The double peaks indicate that both of the amine groups can be oxidized reversibly. Copolymers with triphenylamines, as expected, show only one reversible oxidation. On the basis of their chemical compositions and stability to repeated oxidation these copolymers are expected to be excellent candidates as hole transport materials in light emitting diodes and photoconductors.

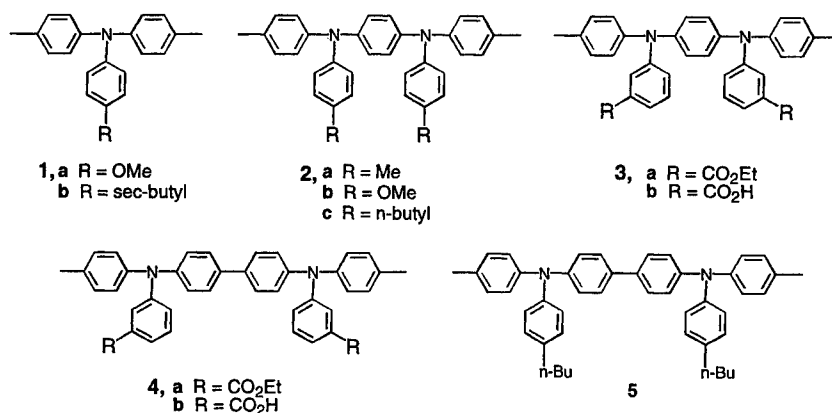


Figure 5. Aromatic Amine comonomers in fluorene alternating copolymers.

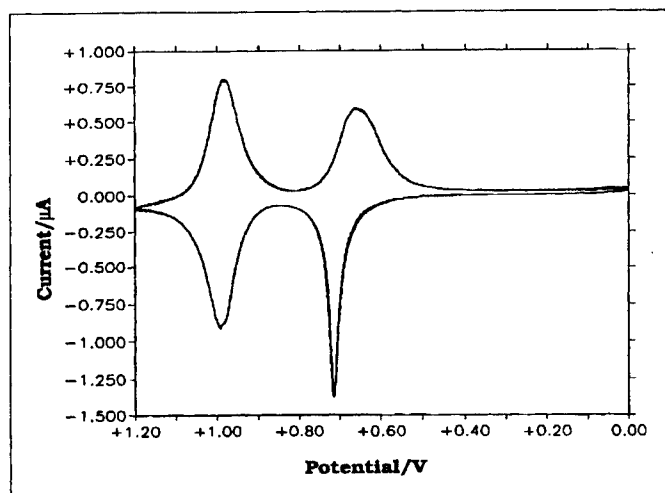


Figure 6. Cyclic voltammogram of PFB film.

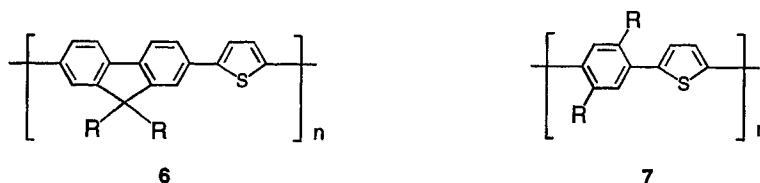
Ionization potentials (based on the first oxidation) and glass transition temperatures of these copolymers are given in Table 2. As can be seen, the copolymer approach provides access to materials with a wide range of properties. The photoluminescence of these copolymers are red-shifted relative to the monomeric amine analogs, lending support to the expectation of substantially more extended conjugation and creation of unique electronic entities in these alternating structures.

Table 2. Properties of Fluorene-Amine Alternating Copolymers

Copolymer	Amine Comonomer	$T_g$ (°C)	Emission Max. (nm)	Ionization Potential (eV)
BFE	4a	137	427	5.29
BFA	4b	220	430, 491	5.28
BFB	5	142	481	5.26
PFE	3a	119	480	5.15
PFA	3b	213	484	5.13
PFMO	2b	120	478	4.98
PFM	2a	76	469	5.04
PFB	2c	132	450	5.09
TFMO	1a	95	437	5.20
TFB	1b	80	431	5.33

The two copolymers (3b and 4b) with carboxylic acid substituents are of particular interest because their solubility characteristics enable the construction of double-layer LED devices without the risk of erosion of the first layer by the solution of the second. All the fluorene homopolymers and copolymers (except those that are highly crystalline) are soluble in aromatic hydrocarbons such as toluene and xylene but the two acidic copolymers, while soluble in polar solvents like DMF, are practically insoluble in these solvents. In a conventional device fabrication process, a DMF solution of one of these acidic polymer is spin-coated onto ITO substrate to serve as the hole transport layer and the resulting film dried by heating. A xylene solution of an emitting fluorene polymer is then applied onto it to yield a two-layer structure with a sharp polymer-polymer interface.

The advantage of dialkylfluorene over 2,5-dialkylphenylene as a monomer in regard to solubilization without interruption of conjugation can be further illustrated by a comparison of the spectral properties of poly(9,9-dialky-2,7-fluorene-alt-2,5-thienylene) (**6**) and poly(2,5-dialkyl-1,4-phenylene-alt-2,5-thienylene) (**7**). A film of the former shows an absorption maximum at about 440 nm, band gap of 2.5 eV, and emits blue-green light. The latter shows an absorption maximum at 335 nm, band gap of about 3.1 eV, and emits blue light [19]. The fluorene copolymer clearly has a more extended conjugation.



#### 4. LIGHT EMITTING DIODES

Fluorene homopolymers so far have yielded rather inefficient single-layer LED devices [20] inspite of their high photoluminescence efficiency in the solid state [21]. Cyclic voltammetry analysis of a film of **F8** indicates an oxidation potential of about 1.4 volts relative to silver, which translates to an ionization potential of about 5.8 eV [22]. Since the band gap of the polymer, estimated from its absorption edge, is about 2.9 eV, accordingly its electron affinity is about 3.1 eV. Thus, devices with ITO anode and calcium cathode should experience facile electron injection but a high barrier to hole injection, and the majority carrier should be electrons rather than holes. The current on-set may occur at low voltage but light on-set should be at substantially higher voltage. This is indeed the case. A device comprising a 150 nm film of **F8** sandwiched between ITO and calcium cathode has light turn-on at about 10 volts and reaches about 100 Cd/m<sup>2</sup> at 20 volts. As reported earlier [23] inserting a hole transport layer between ITO and **F8** results in a device that has light on-set at about 5 volts and reaches 600 Cd/m<sup>2</sup> at 20 volts despite a thicker (200 nm) **F8** film.

The presence of a hole transporting layer has the same beneficial effect in devices with other fluorene polymers. **Figure 7** compares the performance of a single-layer device based on a green-emitting fluorene copolymer to that of a device with a hole transporting layer. The light emitting layer was 150 nm in both cases and the hole transporting layer was a 80 nm film of **BFA** (see Table 2 for **BFA** composition). As stated above, the solubility characteristics of **BFA** is an advantage in constructing double-layer devices with fluorene-based emitters. Its estimated ionization potential of about 5.3 eV, being intermediate between the work function of ITO (4.8 eV) and the estimated ionization potential (5.8 eV) of the emitting polymer, should facilitate hole injection and transport. Despite the increase in total film thickness, the double-layer device was more conductive (current density not shown for purpose of clarity) and more than 10 times brighter at the same bias. At 1000 Cd/m<sup>2</sup> the drive voltage of 9.6 volts and efficiencies are 4.8 Cd/A and 1.6 lumens/watt for the double-layer device versus 16.8 volts, 2.5 Cd/A and 0.5 lumen/watt for the single-layer one. While these findings do not constitute unequivocal proof of electrons as the majority carrier, they do highlight the difference between fluorene polymers and the better known PPV and derivatives which are characterized by holes being the majority carrier.



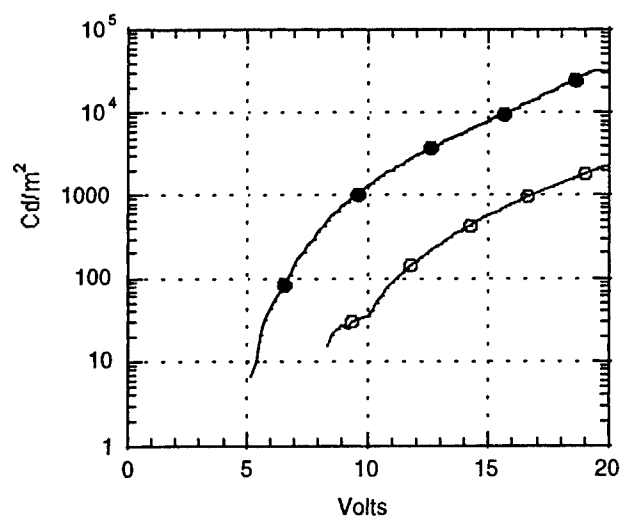


**Figure 7.** Comparison of single-layer to double-layer green devices. single-layer: Emitter (150 nm)/Ca (open circles), double-layer: BFA (80nm)/Emitter(150 nm)/Ca (filled circles).

With the recognition that hole injection/transport is critical to improving device performance, we have continued to optimize the hole transport layer. The result is a significant improvement in efficiency in the green-emitting device. As can be seen in **Figure 8** and **9**, an optimized double layer device has demonstrated a maximum light output of 18,000  $Cd/m^2$  at 6 volts and maximum efficiencies of 7.9  $Cd/A$  and 7.7 lumens/watt respectively. In the cases of some further optimized devices maximum efficiencies of 10 lumens/watt and even higher have also been observed.

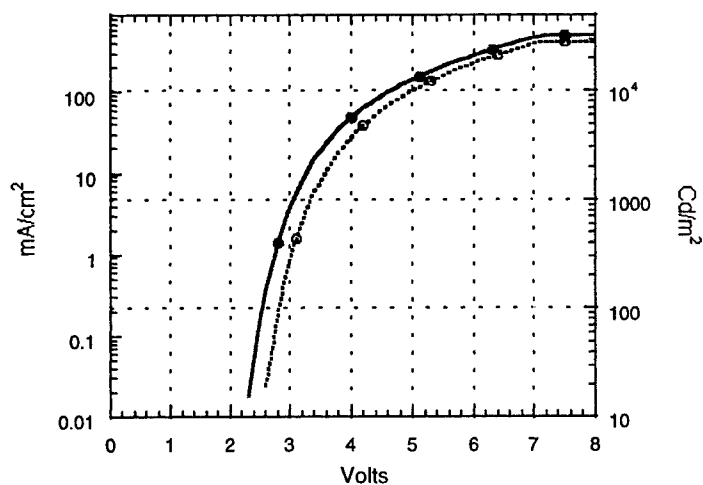


**Figure 8.** JVL characteristics of double-layer green device, HTL (100 nm)/Emitter (75 nm)/Ca; open circle: luminance, filled circle: current density.

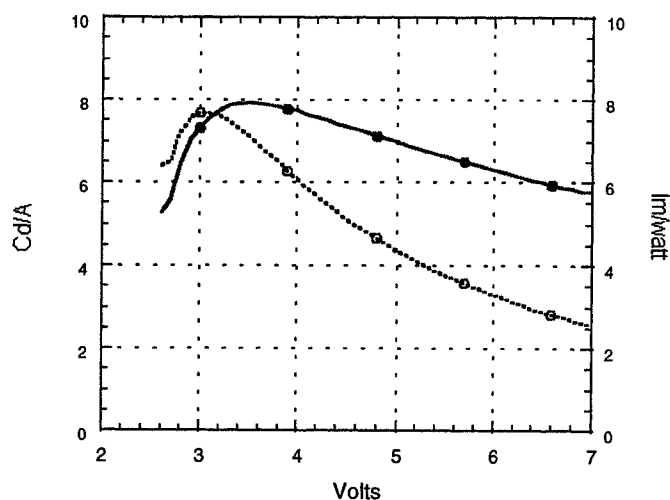


**Figure 9.** Efficiencies of double-layer green device, HTL (100 nm)/Emitter (75 nm)/Ca; open circle: lumens/watt, filled circle: Cd/A.

## 5. CONCLUSION

Our work has shown that fluorene as a monomer offers a number of advantages, the most significant being its ability to impart solubility while maintaining a high degree of delocalization. An improved Pd-catalyzed polymerization procedure has enabled the preparation of a large variety of fluorene homopolymers and copolymers. Unlike PPV and related materials, LED devices with fluorene polymers in a conventional configuration appear to have electrons as the majority carrier and their performance are markedly improved when modified with an appropriate polymeric hole transporting layer. An optimized green-emitting device exhibits very high luminance at very low drive voltage, attributable in part to the high hole mobility of fluorene-based polymers.

## REFERENCES

1. J. H. Burroughes, D. D. C. Bradley, A. R. Brown, R. N. Marks, K. Mackay, R. H. Friend, P. L. Burns, and A. B. Holmes, *Nature*, **347** pp 539-541, 1990.
2. A. Kraft, A. C. Grimsdale, and A.B. HOLMES, *Angew. Chem. Int. Ed.*, **37** pp 402-428, 1998.
3. A. Berntsen, Y. Croonen, C. Liedenbaum, H. Schoo, R.-J. Visser, J. Vleggaar, and P. van de Weijer, *Optical Materials*, **9**, pp 125-133, 1998; I. D. Parker, E. Bagga, P. Bailey, Y. Cao, S. Draeger, A. J. Heeger, J. Kaminski, C. Knudson, J. Long, T. Marx, B. Nollson, J. Peltola, R. Pflanzner, M. Raffetto, T. Ronnfeldt, B. Webber, G. Yu, and C. Zhang, *SID 98 Digest*, pp 15-18, 1998.
4. See for example: M. Rehaln, A.-D. Schlüter, G. Wegner, and W. J. Feast, *Polymer*, **30**, pp1054-1059, 1998; Y. Yang, Q. Pei, and A. J. Heeger, *J. Appl. Phys.*, **79**, pp 934-939, 1996; P. B. Balanda and J. R. Reynold, *Proc. Poly. Mat. Sci. Eng., A.C.S.*, **76**, pp 252, 1997; N. Tanigaki, H. Masuda, and K. Kaerlyama, *Polymer*, **38**, 1221-1226, 1997.
5. U. Scherf. and K. Müllen, *Makromol. Chem., Rapid Commun.*, **12**, pp 489-497, 1991.
6. G. Grem, C. Paar, J. Stample, G. Leising, J. Huber, and U. Scherf, *Chem. Mater.*, **7**, pp 2-4, 1995.
7. M. Fukuda, K. Sawaka, and K. Yoshino, *Jpn. J. Appl. Phys.*, **28**, L pp 1433-1435 1989.

8. M. Fukuda, K. Sawada, and K. Yoshino, *J. Polym. Sci. Polym. Chem. Ed.*, **31**, pp 2465-2471, 1993.
9. C. E. Brown, P. Kovacic, C. A. Wilkie, J. A. Kinsinger, R. E. Hein, S. I. Yaniger, and R.B. Cody, Jr., *J. Polym. Sci., Polym. Chem. Ed.*, **24**, pp 255-267, 1989.
10. T. Yamamoto, *Prog. Polym. Sci.*, **17**, pp1153-1205, 1992.
11. I. Colon, and D. R. Keisey, *J. Org. Chem.*, **51**, pp2627-2637, 1986; I. Colon, and G. T. Kwiatkowski, *J. Polym. Sci. Polym. Chem. Ed.*, **28**, pp 367-383, 1990.
12. E. P. Woo, W.R. Shiang, M. Inbasekaran, G. R. Roof, *U.S. Patent 5708139*, 1998.
13. N. Miyaura, T. Yanagi, and A. Suzuki, *Synthetic Commun.*, **11**, pp513-519, 1981.
14. N. Tanigaki, H. Masuda, and K. Kaeriyama, *Polymer*, **38**, pp 1221-1226, 1997.
15. M. Grell, D. D. C. Bradley, M. Inbasekaran, and E. P. Woo, *Adv. Mater.*, **9**, pp798-802, 1997.
16. C. W. Tang, *Information Display*, pp 16-19, October 1996.
17. See for example: C. Hosokawa, N. Kawasaki, S. Sakamoto, and T. Kusumoto, *Appl. Phys. Lett.*, **61**, pp2503-2505, 1992; J. Kido, G. Harada, and K. Nagai, *Polymers for Advanced Technologies*, **7**, pp31-34, 1991.
18. W. W. Wu, E. P. Woo, and W. R. Shiang, *U.S. Patent 5728801*, 1998.
19. H. Saadeh, T. Goodson, III, and L. Yu, *Macromolecules*, **30**, pp 4602-4612, 1997; M. Fahlman, J. Birgersson, K. Kaeriyama, and W.R. Salaneck, *Syn. Metals*, **75**, pp223-228, 1995.
20. M. Kreyenschmidt, G. Klaerner, T. Fuhrer, J. Ashenurst, S. Karg, W. D. Chen, V. Y. Lee, J. C. Scott, and R. D. Miller, *Macromolecules*, **31**, pp1099-1103, 1998.
21. Q. Pei, and Y. Yang, *J. Am. Chem. Soc.*, **118**, pp 7416-7417, 1996.
22. J. Rault-Berthelot, and M. M. Granger, *Syn. Metals*, **82**, pp 103-109, 1996.
23. A. W. Grice, D. D. C. Bradley, M. T. Bernius, M. Inbasekaran, W. W. WU, and E. P. Woo, *Appl. Phys. Lett.*, **73**, pp 629-631, 1998.

# Improved Lifetime and Efficiency of Organic Light Emitting Diodes for Applications in Displays

Wolfgang Kowalsky\*, Torsten Benstem, Achim Böhler, Siegfried Dirr, Hans-Hermann Johannes,

Dirk Metzdorf, Helge Neuner, Jörg Schöbel

Institut für Hochfrequenztechnik, Technische Universität Braunschweig,

D-38092 Braunschweig, Germany

## Abstract

Organic semiconductors have been intensively studied over the past decades. The potential of this new class of materials for photonic and electronic device applications is demonstrated by successful fabrication of organic and organic-on-inorganic heterostructures for electroluminescent devices, photodetectors, and microwave diodes. The fabrication technology of organic semiconductor devices for photonic applications is discussed. In contrast to spin-on or dipping techniques for fabrication of polymeric films, organic compounds with low molecular weight are sublimated under ultra high vacuum (UHV) conditions. The organic molecular beam deposition (OMBD) technology employed allows the reproducible growth of complex layer sequences with a defined thickness of various organic semiconductors in combination with dielectric films, different metallizations, and indium-tin-oxide layers. Growth rates from 1 – 5 nm/min and substrate temperatures from 77 K to 350 K are used. Efficient organic light emitting diodes with bright emission in the blue (1-AZM-Hex), green (Alq<sub>3</sub>) [tris(8-hydroxyquinoline)-aluminum], and red (Eu-complexes, DCM) spectral region and with low operation voltages are presented. In general, an onset voltage of 2.7 V, efficiencies up to 7 lm/W and a luminance up to  $2 \cdot 10^5 \text{ cd/m}^2$  (cw, RT) are attained for *N,N'*-diphenyl-quinacridone-doped Alq<sub>3</sub> devices. An undoped device can be operated up to 5000h without any loss in brightness and just a small increase of the driving voltage of about 2V.

Embedding emissive organic thin films with a narrow spectral characteristic into planar Fabry-Perot microcavities, a light intensity enhancement and a spatial redistribution of the emission is achieved.

Research and development today expands its scope from the investigation of materials, device physics, and device optimization to peripheral technologies for flat-panel display applications, for instance micro patterning methods for the cathode of an OLED display.

**Keywords:** organic light emitting diode (OLED), organic electroluminescent device, organic molecular beam deposition (OMBD), organic display, microcavity

## 1. Introduction

During the last decade, organic semiconductors have attracted increasing research interest from both academia and industry. Investigations of material properties, device structures and characteristics show that electronic and photonic devices can be successfully prepared from organic compounds. In contrast to spin-on or dipping techniques for the deposition of polymeric films, the organic molecular beam deposition (OMBD) technology allows the subsequent growth of thin solid films under ultrahigh vacuum conditions and leads to the fabrication of complex heterostructures with a layer thickness ranging from single molecular monolayers to a few hundreds of nanometers. Several examples will be discussed: Multilayer structures composed of highly fluorescent molecules and organic semiconductors with preferentially hole or electron transporting properties allow to prepare organic light emitting diodes (OLEDs) for electroluminescence in the blue, green, and red spectral regions at low operation voltages. Further, we will explain a new fabrication technique, which increases the efficiency and lifetime of an OLED, and the influence of a microcavity on a narrow emission spectrum.

\* Correspondence: Fax: +49 531 391 5841

An improved fabrication technique for organic flat-panel displays, which employs substrate microstructure patterning with SiO cathode separators, will be discussed by means of a monochrome OLED display prototype in a 5x7 pixel configuration.

## 2. Organic Materials and Deposition Technology

### 2.1. OMBD (Organic Molecular Beam Deposition)

Fig. 1 shows a schematic diagram of the organic molecular beam deposition (OMBD) system used for the growth of organic thin films. Following the concept of conventional molecular beam epitaxy (MBE) systems, this arrangement consists of two organic growth chambers, a metallization chamber, a sputter chamber, and a preparation chamber for the substrates. Complex layer sequences of various organic semiconductors, dielectric or indium-tin-oxide (ITO) layers, and various metallizations can be deposited without breaking the vacuum. Deposition of organic solids of different crystal structures and lattice constants on arbitrary inorganic semiconductor and amorphous substrates is possible because the molecules of organic crystals are only bound by weak Van der Waals forces.

For reproducible growth conditions, the organic source materials are sublimated from effusion cells provided with mechanical shutters. The cell temperatures vary from 100 to 450°C depending on the organic material. Low deposition rates of 0.1-10 nm/min and the possibility of substrate cooling with liquid nitrogen yield smooth and homogeneous thin films. This growth technique allows organic layers only a few nanometers in thickness to be achieved or even molecular monolayers with the high reproducibility necessary for organic-on-inorganic heterostructures and electroluminescent devices [1].

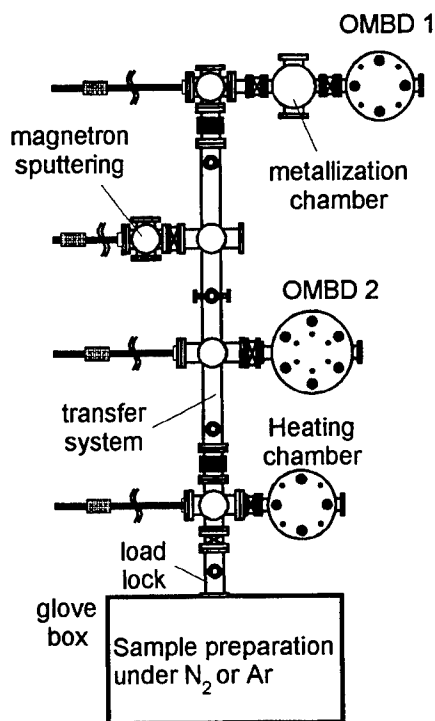


Fig. 1. Thin film processing technique: organic molecular beam deposition (OMBD).

### 2.2. Organic Materials

The molecular structures of the organic materials used in the present investigations are shown in Fig. 2. Molecular structures of the materials shown in Fig. 2(a)-(h) are used as compounds for the fabrication of organic light emitting diodes. The metal chelate complex Alq<sub>3</sub> (tris-(8-hydroxyquinoline) serves as emitter material for the green spectral region. It is also suitable as electron transport layer in double heterostructure devices. Preferentially hole transporting behaviour is observed for CuPc (copper phthalocyanine) and TAD (*N,N'*-diphenyl-*N,N'*-bis(3-methylphenyl)-1,1'-biphenyl-4,4'-diamine) [2]. It is possible to realize a shift from a blue to a red OLED by doping 1-AZM-Hex with Eu(TTFA)<sub>3</sub>Phen (0 wt%: blue, 5 wt%: magenta and

>10 wt%: red emission). As a new layer combination for highly efficient diodes, a layer sequence is used consisting of a hole transport layer of the triphenylamine derivative starburst molecule  $\alpha$ -TNATA [4,4',4''-tris(*N*-(1-naphthyl)-*N*-phenyl-amino)-triphenylamine], a thin electron blocking layer of  $\alpha$ -NPD [*N,N'*-bis(1-naphthyl)-*N,N'*-diphenyl-(1,1'-biphenyl)-4,4'-diamine] and a coevaporated guest-host system of Alq<sub>3</sub> and of a substituted Quinacridone (*N,N'*-diphenyl-quinacridone) for electron transport and emission. The Starburst compound yields very homogeneous and stable thin films with a high glass transition temperature above 100°C which are well suited as hole injection layers due to the very low ionization potential of only about 5.1 eV [3].

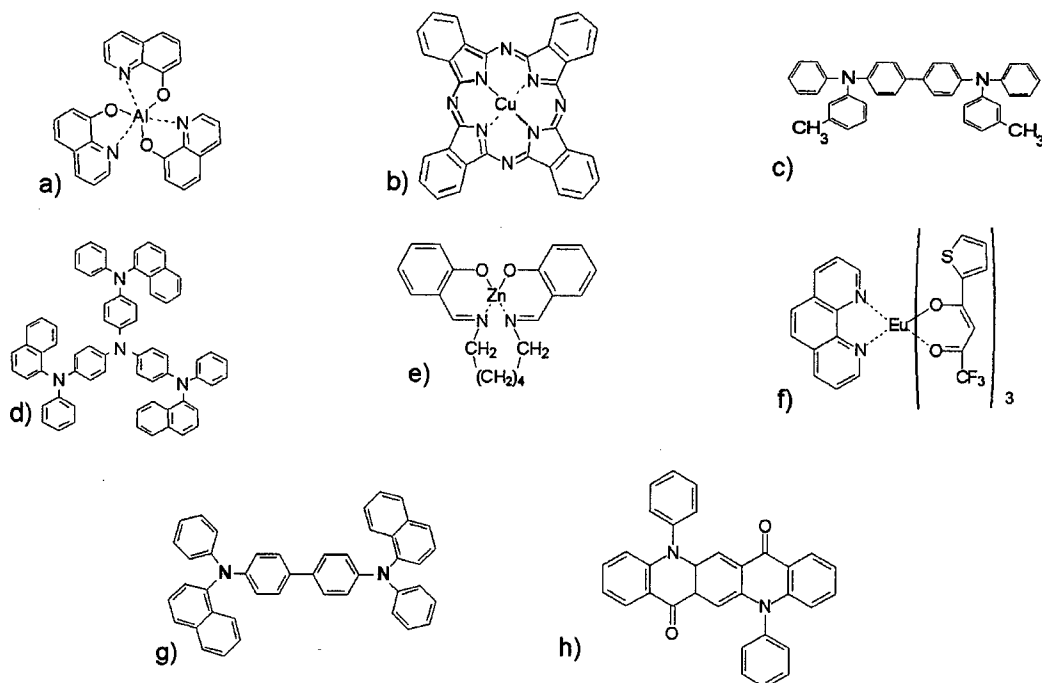


Fig. 2. Molecular structures of (a) Alq<sub>3</sub>, (b) CuPc, (c) TAD, (d)  $\alpha$ -TNATA, (e) 1-AZM-Hex, (f) Eu(TTFA)<sub>3</sub>Phen, (g) NPD, (h) Quinacridon.

### 3. Highly stable and efficient Organic Light Emitting Diodes

#### 3.1. Principle of Operation

The principle of operation of organic light emitting diodes (OLEDs) is similar to that of inorganic light emitting diodes (LEDs). Holes and electrons are injected from opposite contacts into the organic layer sequence and transported to the emitter layer. Recombination leads to the formation of singlet excitons that decay radiatively. In more detail, electrons are injected from a low work function metal contact, e.g. Ca or Mg. The latter is chosen for reasons of stability. A wide-gap transparent indium-tin-oxide (ITO) or polyaniline (PANI) [4] thin film is used for hole injection. In addition, the efficiency of carrier injection can be improved by choosing organic hole and electron injection layers with a low ionization potential (high HOMO (highest occupied molecular orbital) energy) or high electron affinity (low LUMO (lowest unoccupied molecular orbital) energy), respectively. Charge carrier transport properties of organic thin films can rarely be improved significantly by doping. Therefore, preferentially hole or electron transporting organic compounds with sufficient mobility have to be used to transport the charge carriers to the recombination site. The efficiency of electron-hole recombination leading to the creation of singlet excitons is mainly influenced by the overlap of electron and hole densities that originate from carrier injection into the emitter layer. Energy barriers for electrons and holes to both sides of the emitter layer allow to spatially confine and improve the recombination process. The generated singlet excitons will migrate with an average diffusion length of about 20 nm [5] followed by a radiative or non-radiative decay.

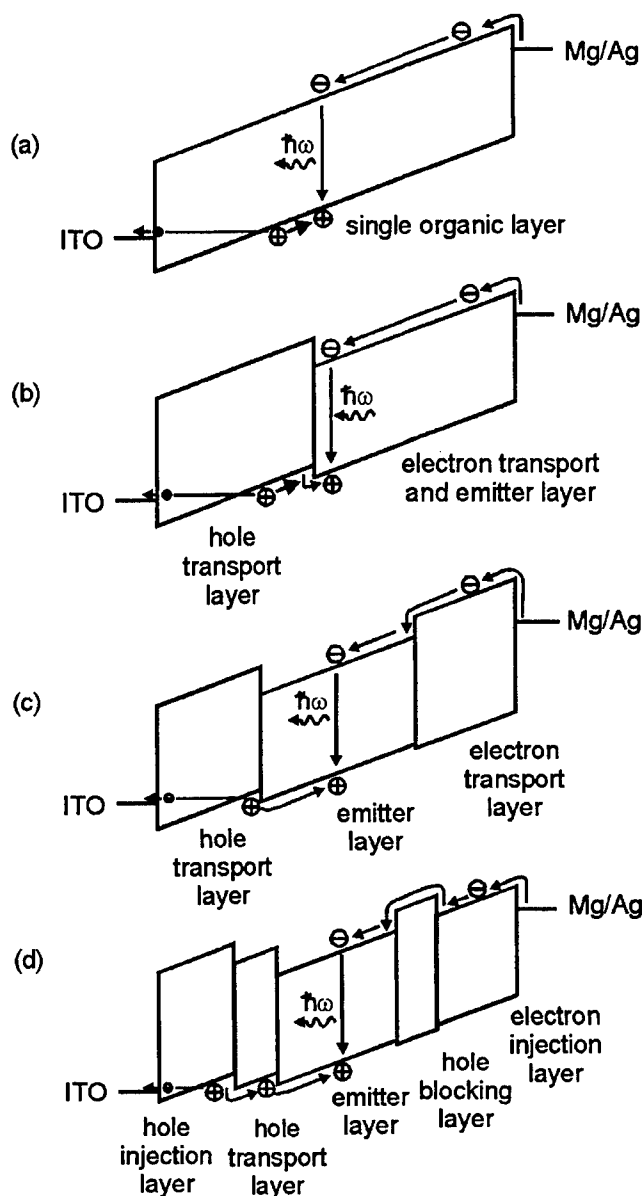


Fig. 3. Layer sequences and energy diagrams for OLEDs with (a) single layer, (b) single heterostructure, (c) double heterostructure, and (d) multilayer structure with separate hole and electron injection and transport layers.

Embedding the emitter layer into transport layers with higher singlet excitation energies leads to a confinement of the singlet excitons and avoids nonradiative decay paths, especially contact quenching. Doping of the emitter layer with organic dye molecules allows to transfer energy from the host to the guest molecule in order to tune the emission wavelength or to increase the luminous efficiency [6]. Efficient device operation do not only depends on the choice of molecules with appropriate electronic and optical properties, but also on the design of the device structure. Fig. 3. shows the layer sequences and energy level diagrams of different structures used for our investigations. Electroluminescence is already achieved with a simple single layer device (Fig. 3(a).), however, the performance is poor since electrons and holes reach the opposite contact and excitons are quenched at the electrodes. The two-layer or single heterostructure device (Fig. 3(b).) introduces a separate hole transport layer. Holes are injected into the combined emitter and electron transport layer and recombine with electrons near the interface. An optimum thickness is found for the combined layer [7] as a result of sufficient distance of the interface to the metal contact and maximum thickness for a given operating voltage. The double heterostructure (Fig. 3(c).) well

known from laser diodes allows to confine both charge carriers and excitons. Unfortunately, energy barriers at the interfaces still impede the transport of electrons and holes from the contacts to the emitter layer. The complex multilayer structure shown in Fig. 3(d), has separate hole injection and transport layers to form a staircase-like path for holes. A similar layer sequence is used for electron injection. The hole blocking layer prevents holes from penetrating into the electron transport layers whereas the electron injection layer has an intermediate LUMO energy to enhance the electron injection from the Mg contact.

### 3.2. Energy Level Measurement by UV Photoelectron Spectroscopy (UPS)

For the design and optimization of multiple-layer OLED structures information on the electron energy levels in organic materials are essential. Generally, different methods can be used to determine these energy levels experimentally: Cyclovoltammetry of the investigated material, which has to be dissolved in an organic solvent, provides the oxidation and reduction potentials, which approximate the HOMO and LUMO, respectively. A thin film surface may be examined in ultrahigh vacuum by means of a Kelvin probe or by UV photoelectron spectroscopy (UPS). While Kelvin probe measurements determine the Fermi level of the organic surface, photoelectron spectroscopy yields the density of valence states, from which the HOMO energy and the ionization potential can be deduced. The photoionization process is depicted on the right side of Fig. 4. The HOMO and deeper electron levels are excited by incident photons, which are commonly generated by a Helium discharge lamp. The difference of the photon energy ( $\text{He(I)}$ , 21.2 eV) and the electron binding energy accounts for a certain kinetic energy of the free electron. Usually, an electrostatic hemispherical or cylindrical analyzer is employed to determine the kinetic electron energy spectrum. The electron binding energies can easily be calculated from this. The secondary electron peak at the low-kinetic-energy side of the photoelectron spectrum is a measure of the vacuum level at the sample surface. All energies are relative to the system Fermi level. Energy calibration is not trivial and is commonly done by measurements of clean metal surfaces.

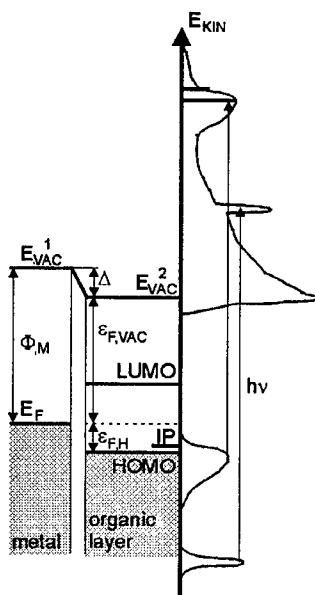


Fig. 4. Metal-organic interface: energy levels and photoionization.

Metal-organic and organic-organic interfaces can be studied with UPS. The subsequent deposition of an organic film allows for the measurement of band bending at the interface. While in small molecule layers band bending is generally not found, several authors have reported dipole layers at metal-organic interfaces. After determination of the metal work function  $\Phi_M$  and the vacuum level  $E_{VAC}^1$  at the metal surface, an organic layer is deposited in situ. Vacuum-level alignment cannot generally be assumed at metal-organic interfaces. The vacuum-level shift  $\Delta$  is directly seen as an energy shift of the secondary electron peak. This is attributed to an interface dipole layer, which may be caused by chemical and/or electrostatical interactions of the materials involved. From the photoelectron spectrum, the energy shift of the HOMO with respect to the metal Fermi level ( $\epsilon_{F,H}$ ), the work function ( $\epsilon_{F,VAC}$ ), and the ionization potential of the organic material are determined.



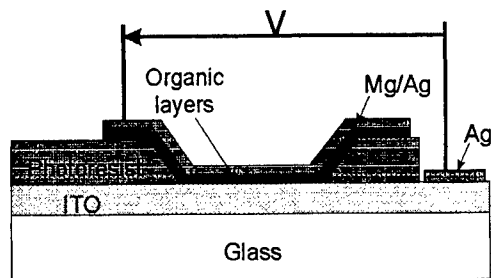


Fig. 5. OLED with an improved device structure.

### 3.3. Characterization and Device Performance

For device characterization, current-voltage and luminance (optical output power)-current characteristics are investigated for cw-operation at room temperature and at normal ambient conditions. The luminance was determined with a Minolta LS-110 luminance meter. A large-area Si photodetector (Advantest) was used to measure the optical output power. The electroluminescence spectra were recorded with a 200 mm monochromator or an Anritsu optical spectrum analyzer.

The internal quantum efficiency of the devices is estimated from the ratio of light generated within the structure to the light detected by a photodetector with limited aperture. Only about 11 - 15% of the total emission is measured due to Fresnel transmission losses, absorption, and total reflection at the interfaces. The results presented correspond to the measured values and no corrections for losses are made.

Parallel to the investigations to find the optimal layer combination and thickness for a highly stable and efficient device, the substrate preparation and the manufacturing process must be optimized in a similar way.

In the following will be described an optimized fabrication technique that leads to an improved device performance. Fig. 5. shows a schematic view of the improved device structure. As the first step of the fabrication technique, the ITO coated glass substrate is cleaned by boiling in organic solvents, ultrasonic agitation and heating. In the second step, windows of  $3.14\text{mm}^2$ , which form the active areas of the OLEDs, are defined by conventional photolithography. The advantage of this structure is evident. The active area of the OLED is completely encapsulated by the remaining photoresist and the overlapping top electrode. Humidity and other ambient influences can also be excluded from causing a deterioration of the OLED performance. An important advantage of the new device is the possibility to evaporate the organic layers and the top electrode without any interruption of the UHV. The influence of the improved device on the performance will be shown by the results of a green emitting single heterostructure device, which consist of a Starburst hole injection layer (60 nm) and an

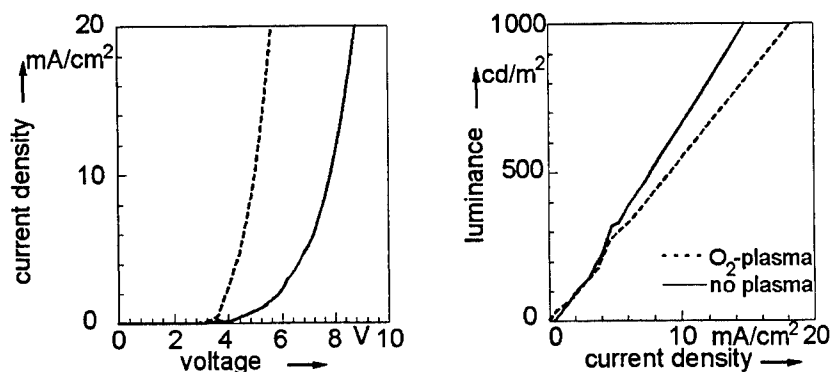


Fig. 6. Influence of a  $\text{O}_2$ -plasma treatment on the current-voltage and luminance-current characteristics.

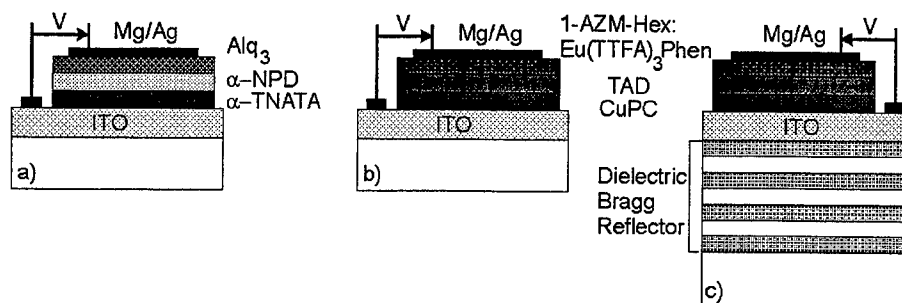


Fig. 7. Different realized heterostructures for the (a) green, (b) blue and red standard device, and (c) red emitting microcavity device.

Alq<sub>3</sub> combined emitter and electron transport layer (60nm). As top electrode a 120 nm Mg and a 120 nm Ag layer is used. Generally, an oxygen plasma treatment is implemented just before placing the substrate into the depositing system. In addition to the performance improvements due to the new device technology, the reactive ion etching treatment in an O<sub>2</sub>-plasma (100W, 2min) reduces the driving voltage by up to 4 V (Fig. 6.).

A typical layer sequence of a highly efficient green emitting device is depicted in Fig. 7(a). The single heterostructure device consists of a  $\alpha$ -TNATA hole injection layer, a  $\alpha$ -NPD hole transport layer and an Alq<sub>3</sub> combined emitter and electron transport layer which is doped with typically <2 % substituted Quinachridone (Fig. 2(h)). Finally, a 120 nm Mg and a 120nm Ag are deposited to form the top electrode.

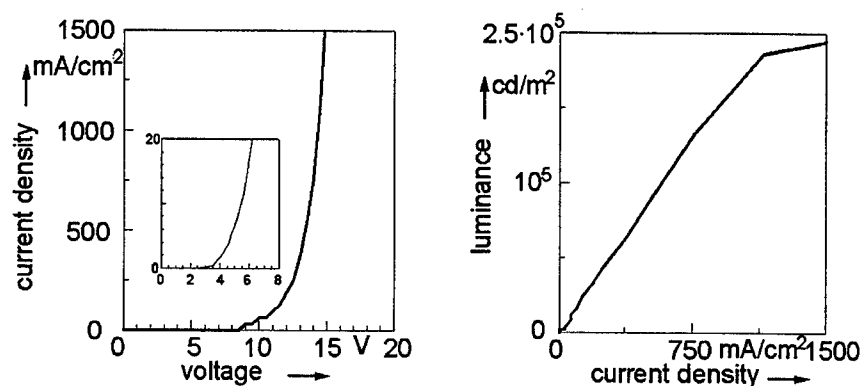


Fig. 8. The current-voltage and luminance-current characteristics of a green emitting high efficient Alq<sub>3</sub>:Qd device.

The current-voltage and luminance-current characteristics of the green doped single heterostructure ( $\alpha$ -TNATA,  $\alpha$ -NPD, Alq<sub>3</sub>:Qd) are shown in Fig. 8. The inset shows a magnification of the lower voltage/current regime. Note the low turn-on voltage of about 2.7 V and the high luminance up to  $2 \cdot 10^5$  cd/m<sup>2</sup> (cw, RT). The luminance efficiency versus current density characteristic of such a device is depicted in Fig. 9. attaining a value as high as 7 lm/W at about 3.4 V and a luminance of 50 cd/m<sup>2</sup>. Fig. 10(a). shows the electroluminescence spectrum of the green Qd-doped OLED with a peak wavelength of 520 nm and a half width of 45 nm and an undoped Diode (60nm Starburst, 60 nm Alq<sub>3</sub>) with a peak wavelength of 535 nm and a half width of 105 nm.

The improved device structure of Fig. 5 combined with an optimized layer sequence leads to highly stable diodes regarding to the lifetime of the device under N<sub>2</sub> atmosphere. Fig. 11. shows a typical lifetime characteristic of an undoped device. The diode is operated with a current-stabilized ac-driving scheme at a time-averaged luminance of 100 cd/m<sup>2</sup>. Two major aspects have to be pointed out: neither an exponential slope at the beginning of the measurement has been observed nor a degradation during the first 4500 h. The device suddenly failed at 5000 h. A slight voltage shift of about 2 V during the total operation time is observed.

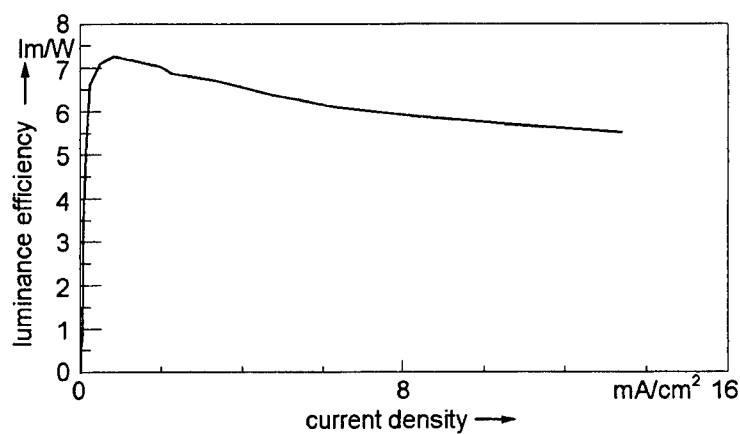


Fig. 9. The luminance efficiency vs. the current density of a Quinacridone-doped  $\text{Alq}_3$  diode.

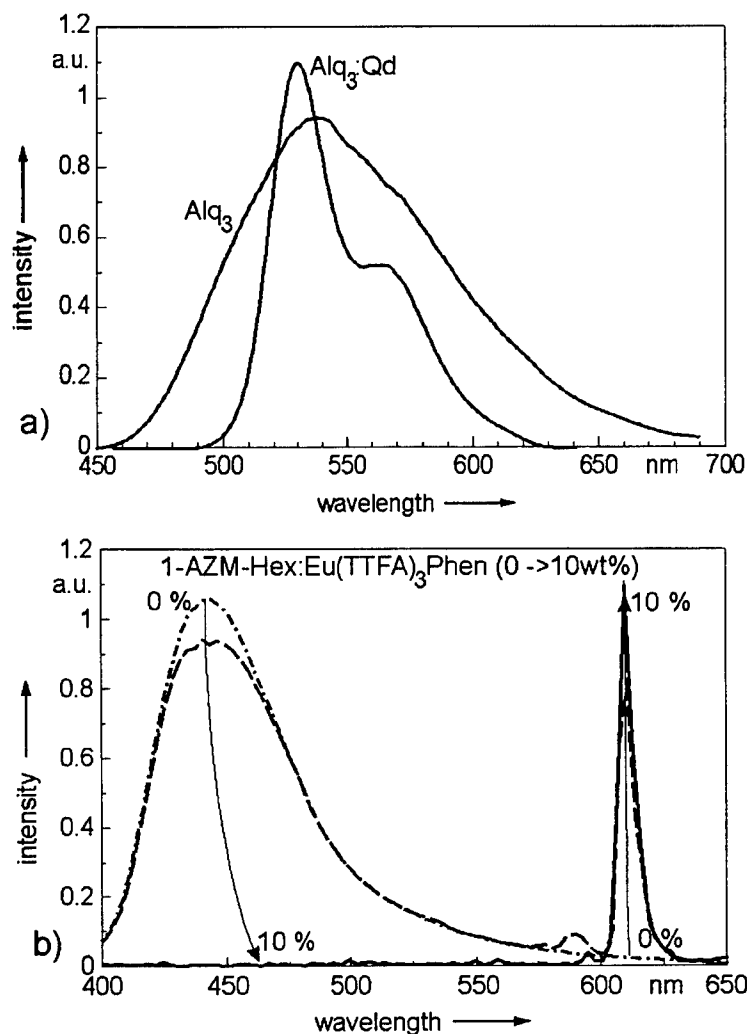


Fig. 10. Electroluminescence spectra of different diodes: (a)  $\text{Alq}_3$  and  $\text{Alq}_3$ :Quinacridone (green), (b) 1-AZM-Hex:  $\text{Eu}(\text{TTFA})_3\text{Phen}$  (blue: 0 wt%, magenta: 5 wt%, and red: >10 wt%).

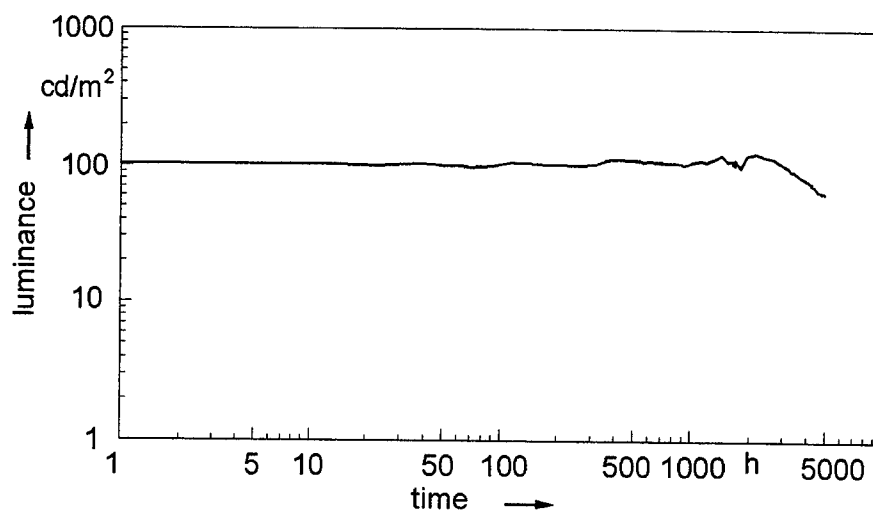


Fig. 11. Typical lifetime result of an undoped green Alq<sub>3</sub> OLED.

In addition to the optimization of the preparation and manufacturing technique of the green Alq<sub>3</sub>-OLED, first steps are made to generate different colors to build a RGB-display (Red, Green, Blue)

One host material (1AZM-Hex) is used for two colors, in which a color shift from the blue to the red is realized by doping the host material with Eu(TTFA)<sub>3</sub>Phen in amounts of 0 wt% to 20 wt%. Fig. 10(b). shows the different emission spectra of an OLED dependent on the guest material concentration. The OLED layer structure is depicted in Fig. 7(b). It is to recognize that the electroluminescence spectra of the 1-AZM-Hex decreases and the Eu(TTFA)<sub>3</sub>Phen spectra appears with the increase of the concentration of the Eu complex and the emission color shifts from blue (0 wt%) over magenta (5 wt%) to red (>10 wt%). Saturation and quenching caused by the Eu complex explains the decrease of the luminance and the higher driving voltage by raising the dopant concentration (Fig. 12).

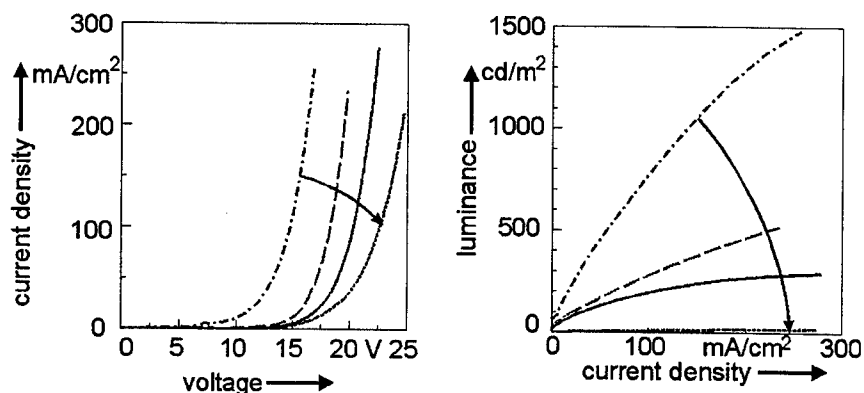


Fig. 12. Current-voltage and luminance-current characteristics of the Eu(TTFA)<sub>3</sub>Phen (0 wt% -> 20 wt%)-doped 1-AZM-Hex guest-host system.

By sandwiching emissive organic layers into a planar Fabry-Perot microcavity, quantum electrodynamical effects offer intensity enhancement and spectral narrowing and spatial redistribution of the emission occur. The microcavity is formed by a semitransparent dielectric Bragg reflector (stack of 3.5  $\lambda/4$  pairs of TiO<sub>2</sub>/SiO<sub>2</sub> layers) and a highly reflective, non transparent mirror: the Mg/Ag cathode. Especially the investigation of a microcavity OLED with an active layer which already has a narrow emission spectrum is interesting for applications requiring saturated colors and/or directive emission, e.g. fiber communications or optical computing [8-10]. The advantage of a material with a narrow emission spectrum compared to a broad one is that there is no spatial color shift but a distinct directed emission.

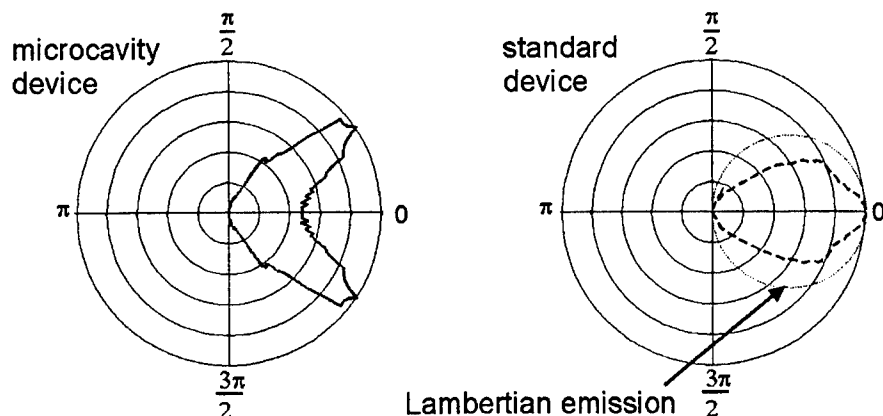


Fig. 13. Angular-dependent electroluminescence spectra of cavity and non-cavity red emitting OLEDs.

Fig. 13. shows the angular dependent emission characteristic of a simultaneously processed conventional OLED and a microcavity OLED (CuPc, TAD, 1- AZM-Hex: EU 10%wt), for which the film thickness of the multilayers is chosen to obtain a resonance at 610 nm (Fig. 7(b,c).). The electrical and luminance characteristics are compared in Fig. 14. The spatial integrated emission intensity of the cavity device (anisotropic radiation) is slightly enhanced compared to the conventional device (isotropic radiation) while the current density vs. voltage curves are not influenced. The narrow electroluminescence spectra of the Eu complex does not change by placing the emission layer into a microcavity device.

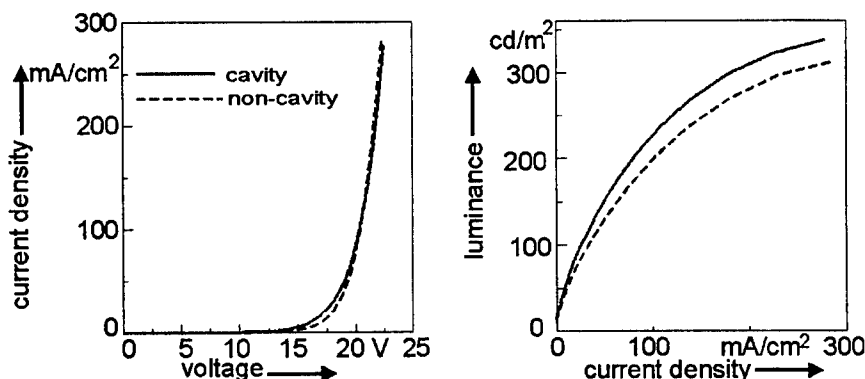


Fig. 14. Current-voltage and luminance-current characteristics of red emitting OLEDs with a  $\text{Eu}(\text{TTFA})_3\text{Phen}$  (10 wt%) doped 1-AZM-Hex guest-host system as emission layer in a cavity structure in comparison to a non-cavity structure.

### 3.4. Micro-Patterning Method for Display Applications

Multilayer organic light emitting diodes have the ability to compete with other emissive technologies, e.g. plasma, vacuum fluorescence, or inorganic thin film electroluminescence displays. A luminance exceeding 100-1000  $\text{cd/m}^2$  and a luminous efficiency of 1-2  $\text{lm/W}$  to 5  $\text{lm/W}$  required for indoor and outdoor flat panel applications [11], respectively, are possible. Low information content displays, e.g. alphanumeric displays, or sign boards, can be fabricated by photolithographic definition of contact patterns of OLED structures. Lightweight and flexible polyaniline (PANI) substrates are suitable for organic electroluminescent displays and offer a large potential for applications.

A possibility to design a display with organic light emitting diodes is a matrix pattern with rows as anode and columns as cathode. To attain the resolution required for example for alphanumeric displays in cellular phones, the pixels must be defined in micrometer dimensions. Therefore, a reproducible patterning by a conventional shadow mask is too complicated because of the high mechanical accuracy required. If the columns of the cathode are defined by an etching or lift-off process after the deposition of the organic multilayers and top electrode, the organic layers would be damaged or totally destroyed by the highly reactive metal etchant or dissolved by organic solvents used in a lift-off process. It follows, that the substrate must define the rows and columns by itself. The ITO anode is structured by an etching process using HCl whereas the rows of the matrix are defined by the remaining photoresist of a conventional photolithography process.

The columns are created by the evaporated organic and top electrode layers extending over the total substrate area. They are separated by  $2\mu\text{m}$  high edges built of  $\text{SiO}_2$ , which is also structured by a lithography process and evaporated under UHV(Fig.15.).  $\text{SiO}_2$  as cathode separator is very stable and the substrate is free of organic materials, so that the matrix structure can be cleaned by organic solvents just before the deposition of the organic layers and the top electrode. With this method, first studies of prototypes are made with a 5x7-matrix display (Fig. 16), which has a pixel size of  $300\mu\text{m} \times 300\mu\text{m}$  and a pixel spacing of  $100\mu\text{m}$ .

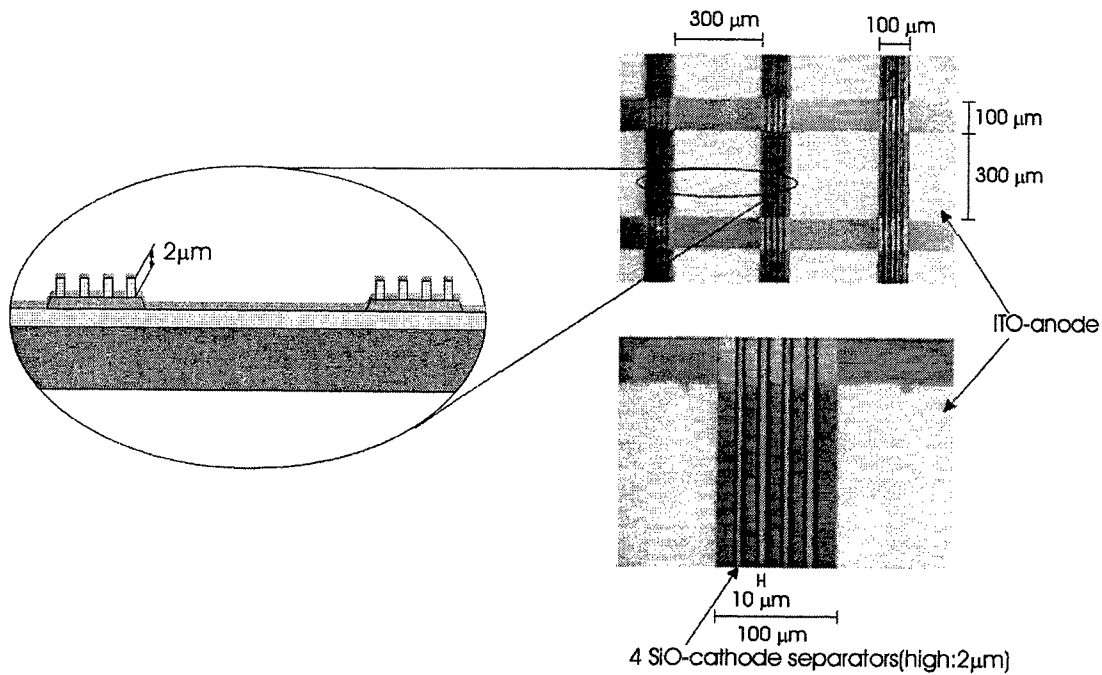


Fig. 15. The substrate structure of an organic matrix display.

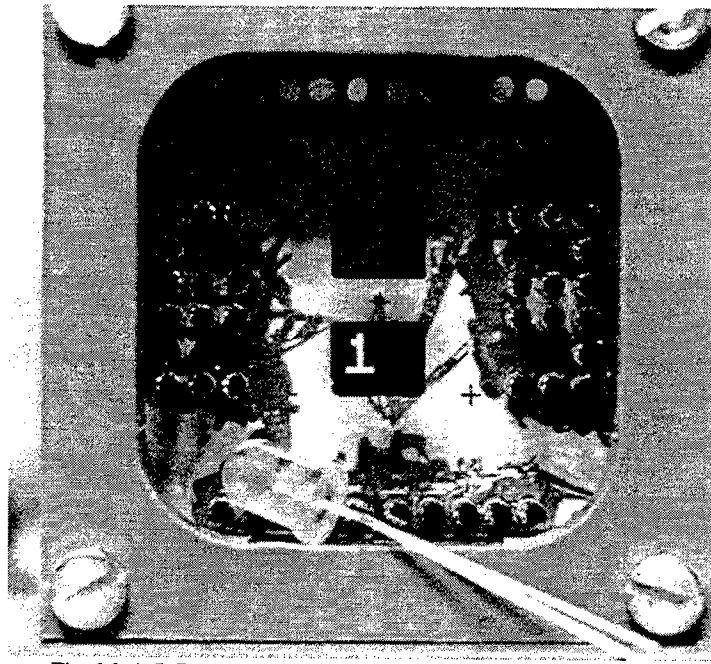


Fig. 16. A 5x7 organic matrix display compared to a conventional LED.

#### 4. Summary

Organic light emitting diodes for the visible spectral region with various multilayer structures were presented. All devices were fabricated by using organic molecular beam deposition technology, which offers ultra-high vacuum growth conditions, precise layer thickness control, the possibility of substrate cooling, and therefore, allows the deposition of homogeneous and smooth organic thin films.

Regarding the operation and performance of OLEDs, improved heterostructure devices lead to drastically increased luminous and quantum efficiencies compared to single layer devices. Blue, green, and red emitting OLEDs based on 1-AZM-Hex (blue), Quinacridone doped and undoped Alq<sub>3</sub> (green), and Eu(TTFA)<sub>3</sub>Phen doped 1-AZM-Hex (red), respectively, showed maximum efficiencies of 7 lm/W. Luminances exceeding 1000 cd/m<sup>2</sup> and lifetimes sufficient for consumer electronics make organic light emitting diodes promising candidates for light-weight flat-panel displays.

As a consequence of the results attained with single OLED devices, first successful investigations for a micro-patterning method for display applications were described and a first prototype of a monochrome display was presented.

#### Acknowledgement

The research on organic materials is funded by the Bundesministerium für Bildung und Forschung (BMBF), by Siemens AG, and by the Volkswagen Stiftung. We gratefully acknowledge their generous financial support.

#### References

- [1] C. Rompf, D. Ammermann, W. Kowalsky, J. Mater. Sci., 11 (1995) 845-848.
- [2] M. Stolka, J. F. Yanus, D. M. Pai, J. Phys. Chem. 88 (1984), 4707-4714.
- [3] Y. Shirota, Y. Kuwabara, H. Inada, T. Wakimoto, H. Nakada, Y. Yonemoto, S. Kawami, K. Imai, Appl. Phys. Lett. 56 (1994), 807-809.
- [4] Y. Yang, E. Westerweele, C. Zhang, P. Smith, A. J. Heeger, J. Appl. Phys. 77 (1995), 694-698.
- [5] C. W. Tang, S. A. VanSlyke, J. Appl. Phys. 65 (1989), 3610-3616.
- [6] Y. Hamada, T. Samo, K. Shibata, K. Kuroki, Jpn. J. Appl. Phys. 34 (1995), L824-826.
- [7] D. Ammermann, A. Böhler, C. Rompf, W. Kowalsky, Proc. IEEE/LEOS Summer Topical Meeting on Flat Panel Display Technology, Keystone, CO, USA, 1995, 31-32.
- [8] T. Tsutsui, C. Adachi, S. Saito, M. Watanabe, M. Koishi, Cem. Phys. Lett. 182 (1991) 143.
- [9] T. Nakayama, Y. Itoh, A. Kakuta, Appl. Phys. Lett. 63 (5) (1993) 594.
- [10] T. Takada, T. Tsutsui, S. Saito, Appl. Phys. Lett. 63 (5) (1993) 2032.
- [11] R. L. Moon, Proc. IS&T's 48<sup>th</sup> Annual Conf., 1995, 386-391

---

## **SESSION 4**

### **III-As and III-P LEDs**



# Growth of InGaAlP HB-LEDs in a Large Scale Production Reactor

S. Li\*, D. A. Collins, S. Vatanapradit, M. Ferreira, P. Zawadzki, R. A. Stall,  
I. Eliashevich, and J. E. Nering  
EMCORE Corporation, Somerset, NJ 08873

## ABSTRACT

The theory, structure, and current manufacturing technologies for InGaAlP high brightness light emitting diodes (HB-LED) emitting in the range of 650 to 585 nm are described in this paper. A state-of-the-art HB-LED MOCVD reactor designed for high volume manufacturing (42 - 2" or 16 - 3" wafers) is demonstrated. Data for thickness and compositional uniformity and reproducibility are presented showing the material quality and reactor stability that can currently be achieved. In addition, device data for InGaAlP HB-LEDs is reported, including brightness, forward voltage, and emission wavelength with excellent intra and inter wafer uniformity and run - to - run reproducibility.

**Keywords:** MOCVD, HB-LED, InGaAlP, MQW, DBR, rotating-disc- reactor

## 1. HB-LED STRUCTURE AND TECHNOLOGY

The structure of a typical high brightness (HB) InGaAlP LED has been described by Chang *et.al.*<sup>1, 2</sup>. The full structure is composed of 6 parts: a GaAs substrate, a distributed Bragg reflector (DBR), an n-type cladding layer, an active region, a p-type cladding layer and a transparent GaP current spreading layer.

### 1.1. Substrate and DBR Reflector

GaAs is commonly chosen as the substrate for InGaAlP based HB LEDs because the quaternary InGaAlP can be perfectly lattice matched to GaAs. This permits the growth of high quality quaternary materials with low defect densities on an inexpensive, high quality substrate. Since GaAs absorbs the photons emitted from the active region, a highly reflective DBR is grown between the substrate and the active region. Both AlGaAs and InGaAlP material systems have been used to grow DBR reflectors; but AlGaAs is normally preferred because it has a higher reflectivity due to its larger refractive index difference between low and high Al content layers, better thermal conductivity, lower cost, and wider growth parameter window than the InGaAlP quaternary. High reflectivity DBRs can always be grown by increasing the number of layers in the DBR design; but there is a trade-off in series resistance, thermal dissipation, and cost. It should be noted that the series resistance is proportional to the number of DBR periods while the reflectivity of the DBR is highly asymptotic. In practice, the number of DBR pairs is optimized to maximize the reflectance within an allowable series resistance range. Typically, this optimization produces DBRs with reflectivity around 97% with minimal impact on the series resistance of the device and the cost of the epitaxial growth process.

### 1.2. Cladding Layers

Typically, both the n- and p-clad layers are composed of InGaAlP with same Al content. In practice, the Al content of the cladding layers is chosen to optimize the efficiency of carrier injection to the active region. In addition, clad doping optimization is important for obtaining low LED forward voltage and high LED brightness. Higher doping reduces the LED operating voltage, but it may reduce LED brightness through free carrier absorption and diffusion into the LED active region. Conventionally, Se, Te, and Si are used as the n-type dopant, but it should be noted that Se-donor binding energy is a function of Al content<sup>3</sup> with the binding energy increasing sharply between  $x \sim 0.3$  to  $x \sim 0.4$ . For the p-clad layer, Zn, Mg, and Be are the common acceptor dopants. The difficulty of p-type doping increases as the Al content of the quaternary increases ( $x > 0.8$ ), especially for Zn and Mg. For Zn, the acceptor binding energy linearly increases with Al content and results in very low conductivity for films with high Al content. Both Mg and Be have been used successfully to dope high Al content quaternaries, but controlling the Mg doping can be difficult due to its complicated doping mechanism<sup>4</sup>. Additional factors to be considered include diffusion and hydrogen passivation of Zn and Mg.

\* Correspondence: Email: sherman@emcore.com; WWW: <http://www.emcore.com>; Telephone: 732 271 9090x4157; Fax: 732 271 9686

### 1.3. Active Regions – DH and MQW

Nominally undoped structures are grown between the n- and p-clads to form the LED active region. Two types of structures are widely used: double heterojunction<sup>5</sup> (DH) and multi-quantum wells<sup>6</sup> (MQW). A DH active region is a single bulk InGaAlP quaternary layer, where the Al content is determined by the desired emission wavelength with shorter wavelengths produced by higher Al content<sup>7</sup>. On the other hand, an MQW active region is composed of lower Al content quaternary quantum wells and higher Al content barriers, where the well width and composition are optimized for the target emission wavelength and the barrier width and composition are optimized to obtain desired carrier confinement and well coupling for high brightness. In practice, barrier compositions of about 60 to 70% Al are normally used to achieve the best carrier confinement because the direct and indirect bandgap crossover occurs in this range. Quantum wells with compressive strain (CS) obtained by increasing the indium content of the well are also widely used, especially for high-speed applications<sup>1</sup> because compressive strain lifts the valance band degeneracy of the well and reduces the heavy hole effective mass. Issues associated with dislocation generation and wavelength shift in the CS MQW structure can be addressed by adjusting the amount of strain in the wells and the Al content and the well thickness. It should be noted that as the Al content increases in the active region the radiation efficiency decreases rapidly, which is mainly caused by the decrease in the separation between direct and indirect bandgap and the increase of the sensitivity to oxygen contamination.

### 1.4. Window Layer

The top layer of an HB LED is a transparent window layer, which not only serves as a current spreading layer to provide uniform carrier injection into the active region but also permits more light to leave the active region. Moreover, the metallic contact, which is opaque and small, is formed directly on the window. Therefore, window optimization plays a critical role in LED performance. Normally, GaP is used for the window layer due to its wide band gap. Doping and thickness of the window layer are optimized to prevent current crowding underneath the contact and enhance light extraction while avoiding free carrier absorption. Detailed studies of GaP window thickness, doping, and its effects on device performance have been published elsewhere.<sup>8,9</sup>

## 2. HB-LED MANUFACTURING IN LARGE SCALE REACTOR

The data presented here were obtained from wafers grown in a large-scale production grade MOCVD reactor, the EMCORE E-400 reactor, which can hold up to 42, 2 inch or 16, 3 inch wafers, as indicated in Fig. 1. The E-400 system is a large diameter vertical flow rotating disc reactor (RDR) consisting of a gas injection inlet and a horizontal susceptor spinning at a relatively high velocity. RDR reactor characteristics have been described in detail by Breiland et.al<sup>10</sup>. Under proper operation, the fluid dynamics of the reactor are characterized by highly reproducible and uniform boundary layer flow providing excellent compositional and growth rate uniformity across the entire growth area. Specially designed source gas manifolds permit abrupt switching of the source gases and the laminar flow patterns in the reactor preserve these abrupt gas fronts allowing the reactor to grow high quality superlattices and thin quantum wells with excellent interface abruptness and reproducibility.

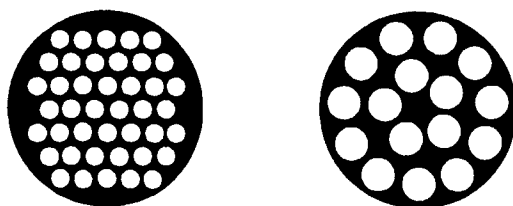


Figure 1. Wafer carriers showing the reactor capacity of each run. (a) 2" - 42 pocket wafer carrier, (b) 3" - 16 pocket wafer carrier

### 2.1. Thickness Uniformity

Thickness uniformity is controlled by the growth rate uniformity of the reactor and the growth rate uniformity can be evaluated by examining the uniformity of the DBR reflector passband center wavelength. For a 625 nm DBR, a 0.8%

thickness uniformity corresponds to 5 nm variation of the passband center wavelength. In this work, the typical wafer to wafer thickness uniformity is about 0.5%, as shown in Fig. 2. This level of uniformity can be easily obtained even following routine reactor maintenance as shown in Fig. 3, where the thickness uniformity is optimized within three calibration runs.

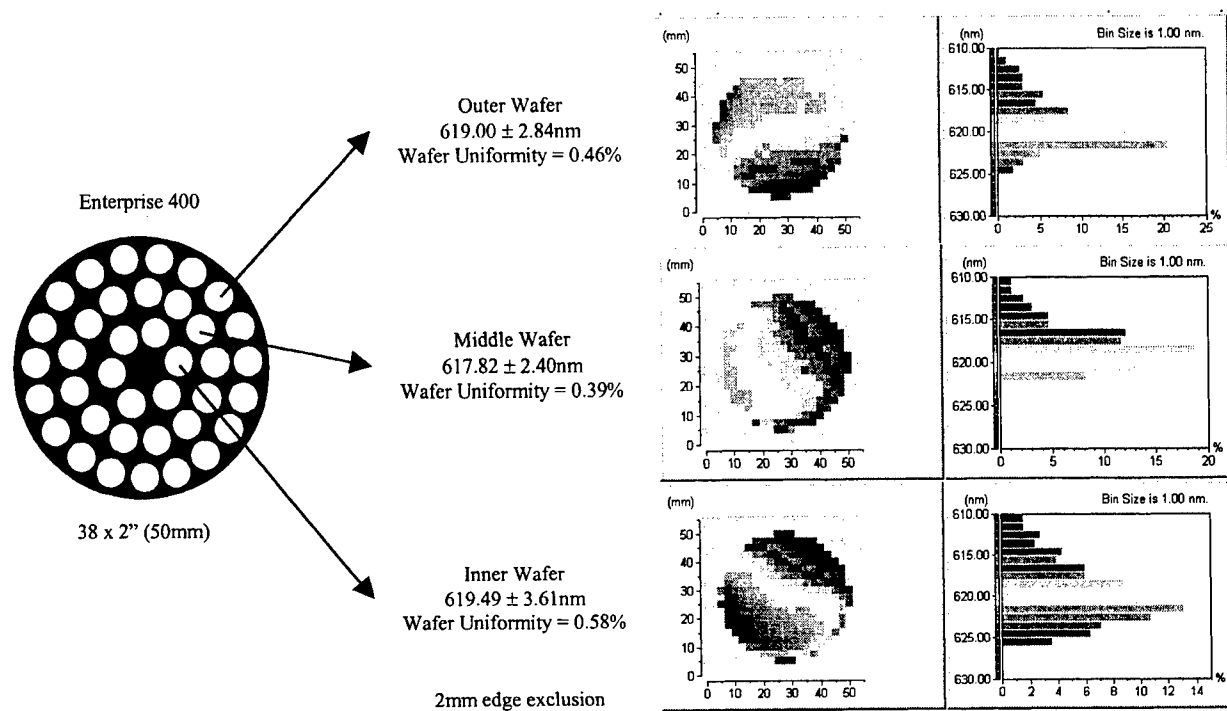


Figure 2. Typical DBR mirror passband center map from inner, middle and outer wafers of a 2'' 38 pocket platter run, where the wafer thickness uniformity is defined as the ratio of standard deviation of the DBR passband center to its average.

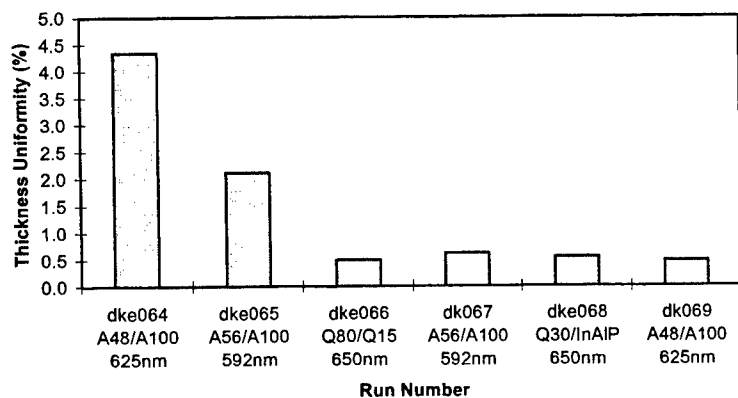


Figure 3. Thickness uniformity profile vs. run number after routine maintenance, where A48 and A56 refer AlGaAs with Al content of 48% and 56%; A100 refers AlAs; Q15, Q30, and Q80 refer InGaAlP with Al content of 15, 30, and 80%.

## 2.2. LED Wavelength Uniformity

LED wavelength uniformity is controlled by both composition and thickness uniformity. For example, an 1% increase in Al content results in about 2 nm PL wavelength decrease, while an 1% indium increase results in about 2 nm PL wavelength increase. It should be noted that indium content is a function of growth temperature as well. Moreover, wafer to

wafer thickness uniformity also affects the MQW LED emission wavelength uniformity<sup>11</sup>. For typical LED structures emitting at 625 nm, the wavelength uniformity is controlled to within 1 nm (standard deviation). Fig. 4 shows a typical wavelength calibration map in which one wafer from each ring of a 50mm x 38 piece wafer carrier is measured. In the data of Fig. 4, a 2 mm edge exclusion was used and the wavelength variation ( $\sigma$ ) was < 1 nm.

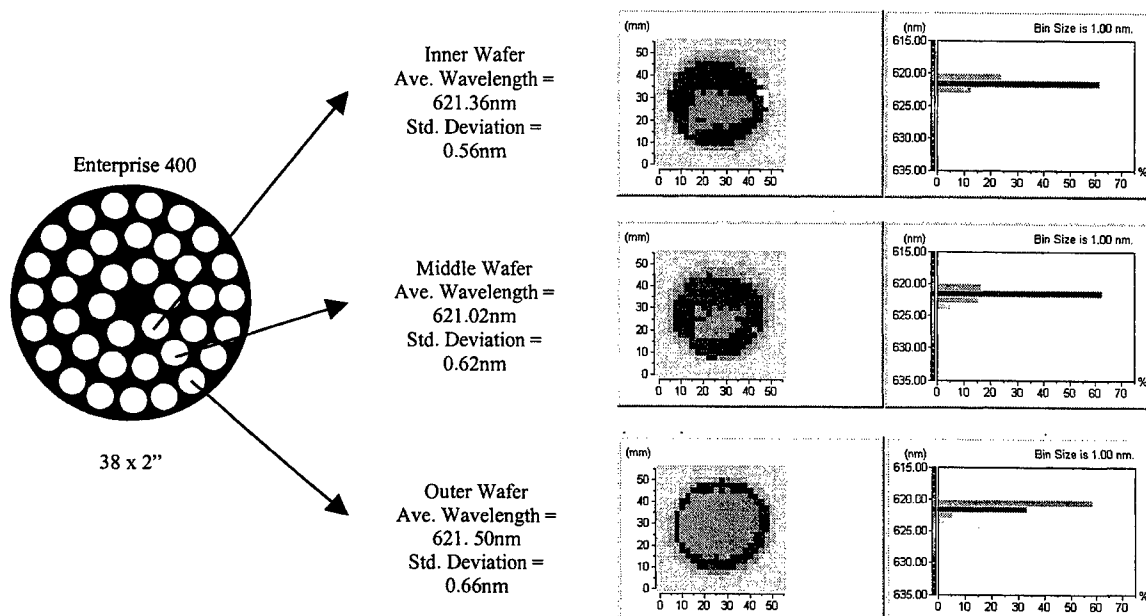


Figure 4. PL wavelength map from inner, middle, and outer ring of a 2" 38 pocket platter run

A common problem with the use of TMIn in MOCVD is the drift in the transport efficiency of TMIn from the bubbler to the reactor over time (Fig. 5). This difficulty is avoided in this work by using a commercially available gas phase alkyl concentration monitor interfaced to the reactor control system for real-time control of the TMIn molar flow into the reactor. There is no compositional change in the growth even though the TMIn bubbler efficiency is unstable. The reproducibility of the LED wavelength uniformity using the closed loop TMIn controller is demonstrated in a series of LED runs, as shown in Fig. 6, where between 3 and 42 wafers from each run were mapped for wavelength uniformity. It should be noted that the PL and EL peak wavelengths of an LED are very closely correlated, so wafer PL uniformity translates to LED device emission wavelength uniformity. A detailed description of TMIn feedback control mechanism used in this work can be found elsewhere<sup>12</sup>.

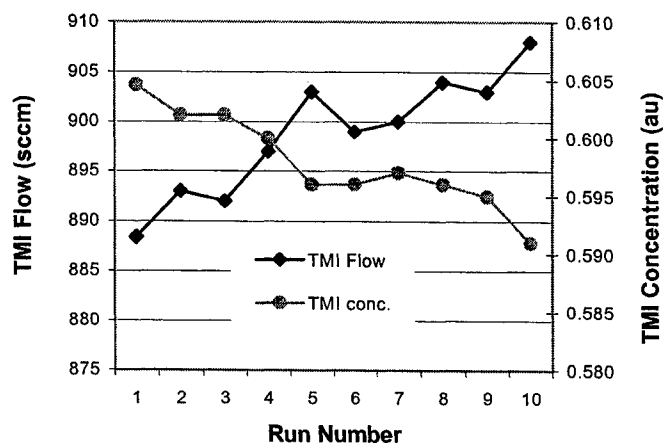


Figure 5. TMI flow and concentration variation with time

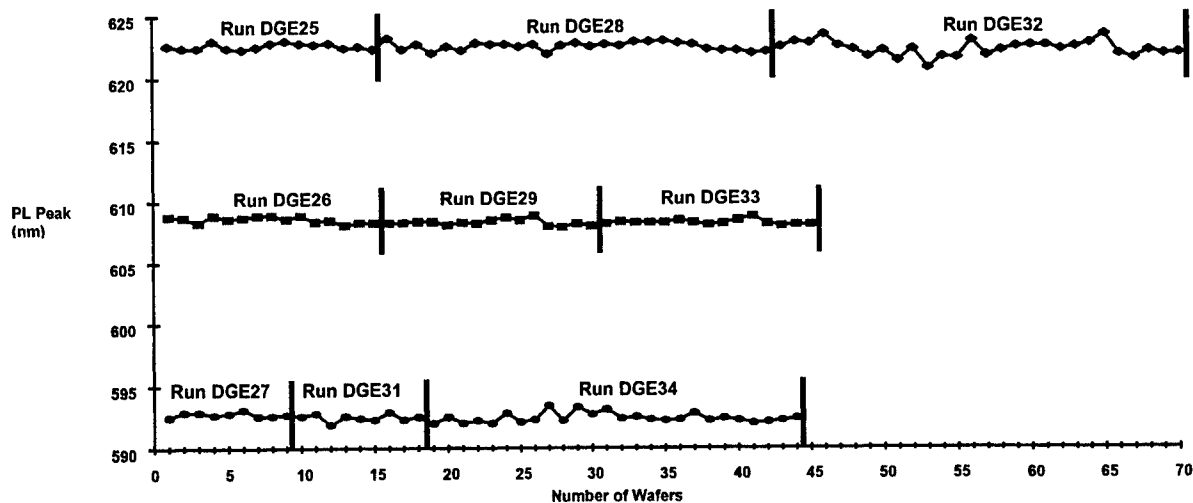


Figure 6. Photoluminescence measurements for 9 consecutive runs at 3 different wavelengths (red, orange, yellow).

### 2.3. LED Performance

With the control of thickness, wavelength and doping uniformity demonstrated, a set of 14 consecutive runs of yellow (593 nm) LEDs with no DBR were conducted in a 42, 2 inch platter following 2 optimization runs. The brightness at 20 mA was analyzed according to a commonly used manufacturing index (Cpk), as shown in Fig. 7. The corresponding operating voltage and the analysis on its moving range are shown in Fig. 8. The statistical study indicates that both the manufacture capability of the HB LED and the reproducibility of the reactor are very promising. Figs. 9 and 10 show typical brightness and operating voltage (20 mA) of selected LED wafers with an AlGaAs DBR grown in 2" 38 pocket platter and 3" 16 pocket platter, respectively. The wafer position in the carrier is indicated with arrows. It is obvious that E-400 production scale reactor is capable of growing HB LEDs with constant high brightness and low forward voltage.

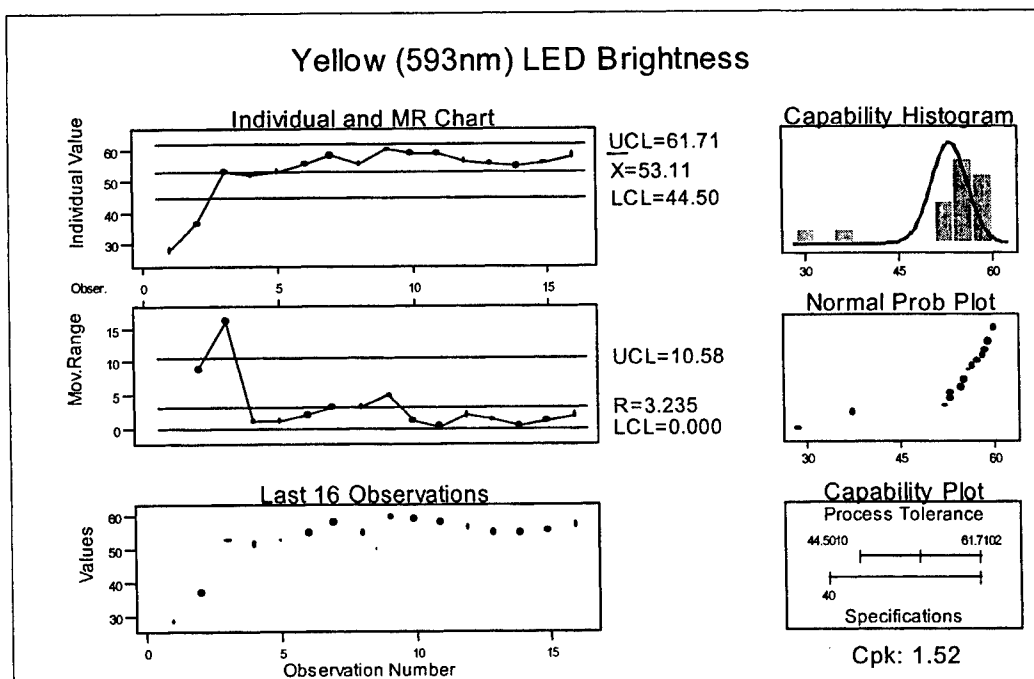


Figure 7. Yellow (593nm) LED brightness @ 20 mA for consecutive runs and analysis on capability for manufacturing.

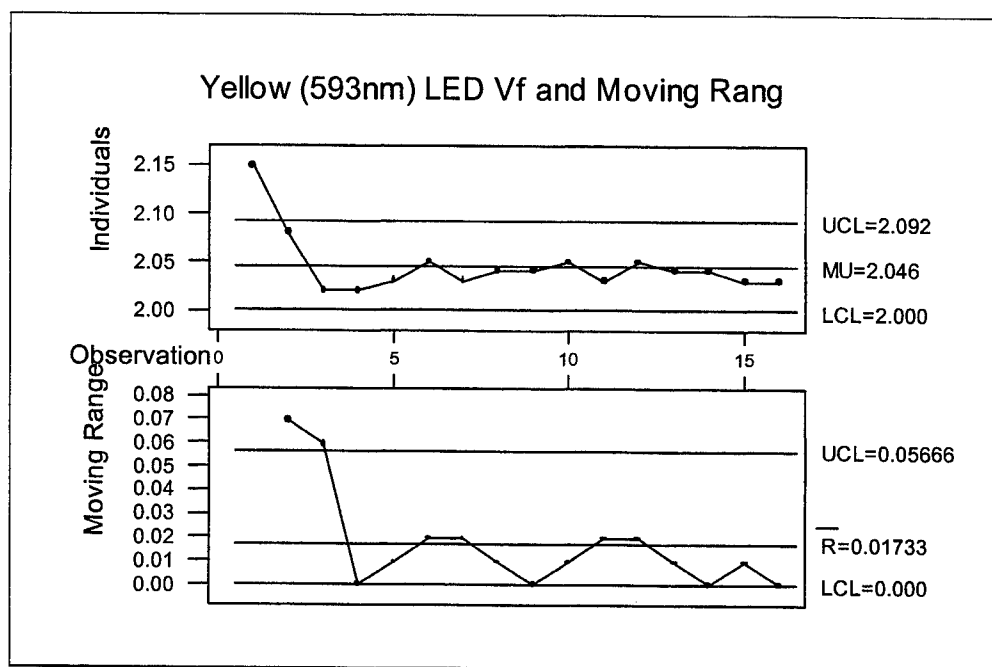


Figure 8. Yellow (593nm) LED forward voltage @ 20mA for consecutive runs and analysis on capability for production.

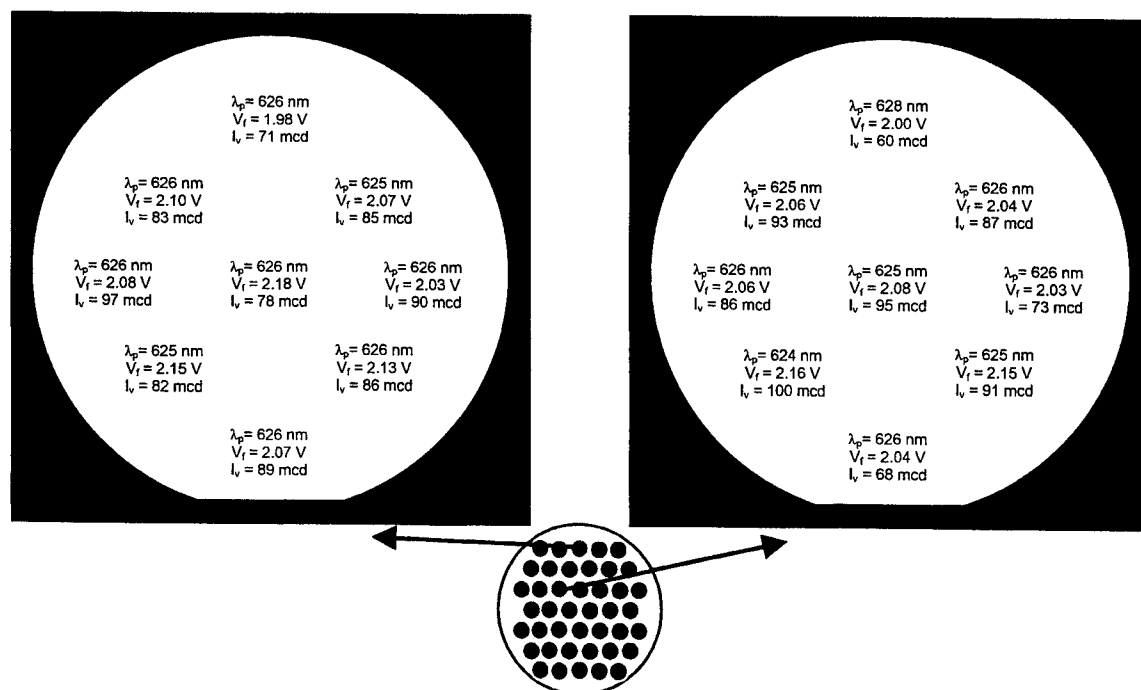


Figure 9. Wavelength, voltage and brightness from a red LED run (outer and inner wafers). Measurements were done after wafer processing.

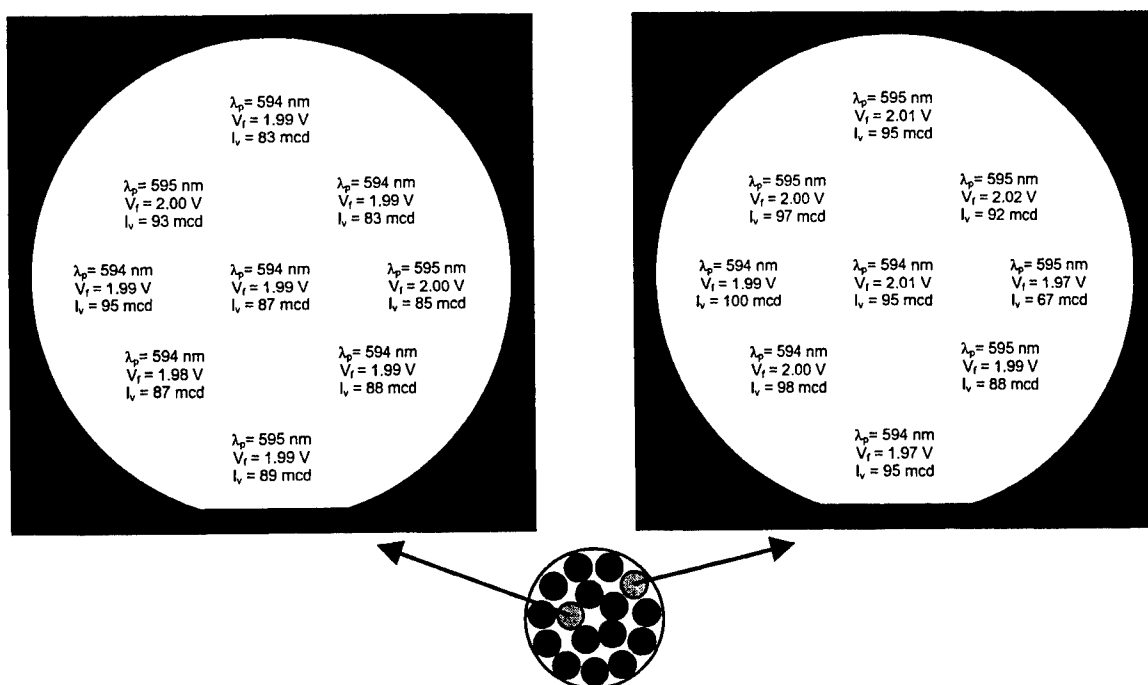


Figure 10. Wavelength, voltage and brightness from a yellow LED run (outer and inner wafers). Measurements were done on fully fabricated LEDs after wafer processing.

In both development and production, it is helpful to monitor the epitaxial growth process as carefully as possible. In addition to the data logging capabilities of the reactor control system, the reactor is equipped with a spectral interferometer (Epimetric) used to measure the growth rate and surface morphology during the growth process. Fig. 11 shows the Epimetric profile of a typical LED grown with an AlGaAs DBR reflector. The data can be used to monitor the growth rate of individual layers and serves as useful monitor during calibration runs or a quality tracking mechanism for production runs. A more detailed description of the use of spectral interferometry for monitoring epitaxial growth can be found elsewhere<sup>13</sup>.

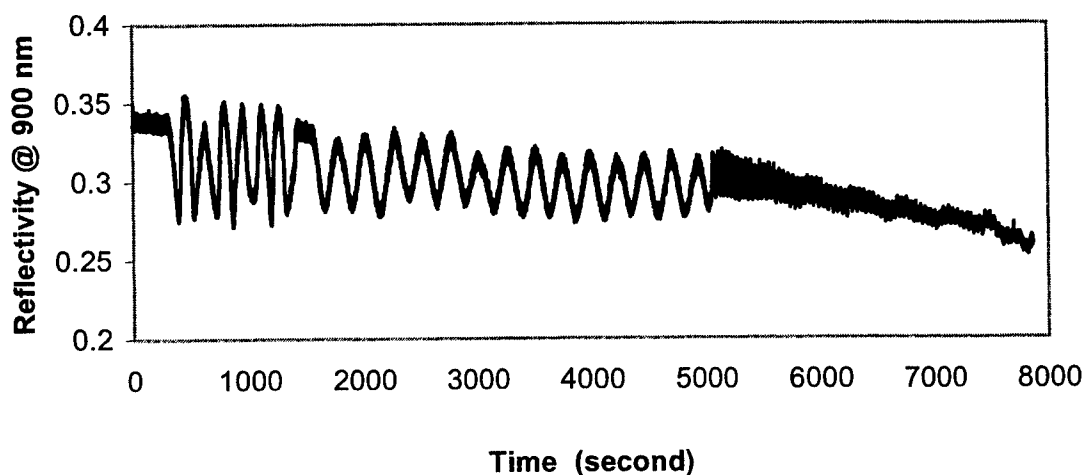


Figure 11. Interferogram of a typical LED growth run recorded at 900 nm used in both LED structure development and for production quality monitoring. The oscillations are used to calculate the growth rate and the average reflectivity is a qualitative measure of the surface morphology.

In addition to MOCVD, a variety of epitaxial growth technologies have been used for HB LEDs. Molecular beam epitaxy<sup>14</sup> (MBE) has been used for HB LEDs, but is not typically used in production environments. Liquid phase epitaxy<sup>15</sup> (LPE) and chloride vapor phase epitaxy<sup>16</sup> (VPE) may also be used for LED manufacturing, but it is rather difficult if not impossible to grow DBR and MQW structures required for high performance by these techniques. The EMCORE E-400 TurboDisc reactor system has opened a new era in HB LED manufacturing with its unique characteristics of good uniformity, good quality control, high stability and reproducibility, low maintenance frequency, low cost, and ease of operation.

## ACKNOWLEDGEMENTS

The authors would like to extend their appreciation to Mr. David Bellina for preparing some of the picture and plots and to Drs. Ian Ferguson and Robert F. Karlicek Jr. for critical review.

## REFERENCES

1. S. J. Chang and C. S. Chang, "AlGaInP-GaInP compressively strained multiquantum-well light-emitting diodes for polymer fiber application," *IEEE Photon. Technol. Lett.* **10**, pp. 772-774, 1998.
2. S. J. Chang, C. S. Chang, Y. K. Su, P. T. Chang, Y. R. Wu, K. H. Hwang, and T. P. Chen, "AlGaInP yellow-green light-emitting diodes with a tensile strain barrier cladding layer," *IEEE Photon. Technol. Lett.* **9**, pp. 1199-1201, 1997.
3. P. S. Zory, Jr., *Quantum Well Lasers*, pp. 423-424, Academic Press, Inc., San Diego, 1993.
4. Y. Ohba, Y. Nishikawa, C. Nozaki, H. Sugawara, and T. Nakanisi, *J. Crystal Growth* **93**, pp. 613, 1988.
5. F. A. Kish, F. M. Steranka, D. C. DeFevere, D. A. Vanderwater, K. G. Park, C. P. Kuo, T. D. Osentowski, M. J. Peanasky, J. G. Yu, R. M. Fletcher, D. A. Steigerwald, M. G. Craford, and V. M. Robbins, "Very high-efficiency semiconductor wafer-bonded transparent-substrate  $(\text{Al}_x\text{Ga}_{1-x})_{0.5}\text{In}_{0.5}\text{P}/\text{GaP}$  light-emitting diodes," *Appl. Phys. Lett.* **64**, pp. 2839-2841, 1994.
6. H. Tanaka, Y. Kawamura, and H. Asahi, "Room-temperature operation of MBE-grown InGaP/InGaAlP MQW visible laser diodes," *Electron. Lett.* **22**, pp. 707, 1986.
7. P. S. Zory, Jr., *Quantum Well Lasers*, pp. 419, Academic Press, Inc., San Diego, 1993.
8. K. H. Huang, J. G. Yu, C. P. Kuo, R. M. Fletcher, T. D. Osentowski, L. J. Stinson, M. G. Craford, and A. S. H. Liao, "Twofold efficiency improvement in high performance AlGaInP light-emitting diodes in the 555-620 nm spectral region using a thick GaP window layer," *Appl. Phys. Lett.* **61** pp. 1045-1047, 1992.
9. G. C. Chi, Y. K. Su, M. J. Jou, and W. C. Hung, "Window layer for current spreading in AlGaInP light-emitting diodes," *J. Appl. Phys.* **76** (5), pp. 2603-2611, 1994.
10. W. G. Breiland, M. E. Coltrin, J. R. Creighton, H. Q. Hou, H. K. Moffat, and J. Y. Tsao, "AlGaAs OMVPE in a rotating-disk reactor: the anatomy of a VCSEL," *Annu. Rev. Mater. Sci.* 1998. Pp. 1-20.
11. P. S. Zory, Jr., *Quantum Well Lasers*, pp. 435-436, Academic Press, Inc., San Diego, 1993.
12. R. Logue, *et al*, "Theory of binary gas concentration determination" LOREX Industries, Inc., *to be published*, 1999.
13. H. Q. Hou, H. C. Chui, K. D. Choquette, B. E. Hammons, W. G. Breiland, and K. M. Geib, "Highly uniform and reproducible vertical-cavity surface-emitting lasers grown by metalorganic vapor phase epitaxy with *in situ* reflectometry," *IEEE Photon. Technol. Lett.*, **8**, pp. 1285-1287.
14. K. Ozasa, M. Yuri, S. Tanaka, and H. Matsunami, *J. Appl. Phys.* **65**, pp. 2711, 1989.
15. Y. K. Su, M. C. Wu, C. Y. Chang, and K. Y. Cheng, *J. Appl. Phys.* **62**, pp. 2541, 1987.
16. M. Hoshino, K. Kitahara, K. Kodama, and M. Ozeki, *J. Cryst. Growth* **96**, pp. 188, 1989.



# Optical Studies of InAs/In(As,Sb) single quantum well (SQW) and strained-layer superlattice (SLS) LED's for the Mid-Infrared (MIR) Region

Harvey Hardaway<sup>a</sup>, Jörg Heber<sup>a</sup>, Peter Möck<sup>b</sup>, Mark Pullin<sup>a</sup>, Tony Stradling<sup>a</sup>,  
Patrick Tang<sup>a</sup>, Chris Phillips<sup>a</sup>.

<sup>a</sup> Solid State Group, Blackett Laboratory, Imperial College, London, UK, SW7 2BZ

<sup>b</sup> IRC for Semiconductor Materials, Imperial College, London, UK, SW7 2AZ

## ABSTRACT

We report on electroluminescence (EL) and photoluminescence (PL) studies of arsenic rich InAs<sub>1-x</sub>Sb<sub>x</sub> heterostructure LED's for the MIR region. Single-quantum-well (SQW) LED's have demonstrated 300K of ~24μW and ~50μW at ~5μm and ~8μm, respectively, with corresponding internal quantum efficiencies of 0.8% and 1.6%. We also demonstrate 4.2μm, 300K emission from strained-layer superlattice (SLS) LED's with AlSb electron confining barriers with output powers > 0.1mW. In reverse bias, these SLS devices exhibit negative luminescence efficiencies of ~14% at 310K.

Keywords: Mid-infrared, LED, Negative luminescence, InAsSb, AlSb.

## 1. INTRODUCTION

Room temperature LED's and LD's are desired for many applications including trace gas analysis. It is feasible that compact, inert, efficient, 'modulatable' solid state devices with emission wavelengths tuned to the strong gas absorption features such as CO<sub>2</sub> (4.2μm), CO (4.9μm), NO<sub>2</sub> (6.3μm) and SO<sub>2</sub> (7.4μm) could replace the black-body thermal emission sources currently employed<sup>1</sup>. The successful application of LED's and LD's depends on their ability to achieve the performance criteria demanded by gas sensing systems which include ambient temperature operation, sufficient spectral brightness, spectral stability and longevity.

In an attempt to achieve high output powers, most research has been focused on the development of laser devices. Of the III-V materials, InAs<sub>1-x</sub>Sb<sub>x</sub> has the narrowest band gap (107meV) which permits interband emission out to λ ~ 12μm. In(As,Sb) LD's have been demonstrated for the 3-4μm region at temperatures up to 175K (cw) at threshold current densities as low as 30 A/cm<sup>2</sup>, and output powers of ~1W<sup>3</sup>. Lasing beyond 3 μm has also been achieved in InAs/(Ga,In)Sb type-II cascade structures up to 286K<sup>4</sup> by pulsed electronic injection. Despite this progress, room temperature, quasi-cw lasing beyond ~3μm from interband devices has yet to be achieved, partially due to the presence of intrinsic non-radiative Auger recombination channels which result in low characteristic temperatures (T<sub>0</sub> ~ 30-50K) for the threshold current density.

Recently, inter-subband (Al,In)As/(In,Ga)As cascade LD's have demonstrated 3-11μm<sup>5,6,7,8</sup> emission at temperatures as high as 320K. The dominant non-radiative channel in these devices is through the emission of optical phonons and as such they are much less sensitive to temperature (T<sub>0</sub> ~ 100K). However, the fundamental loss mechanisms within these devices result in the pulsed (~50ns) threshold current densities of ~0.75kA/cm<sup>2</sup> which are already approaching the theoretical optimum. Lower threshold and hence CW operation still remains a challenge for these devices.

Although LD's offer high powers, the demanding requirements for spectral stability (and hence CW or quasi-CW operation) may prohibit their application in gas sensing systems. Small fluctuations in the dominant lasing mode with varying temperature may reduce the ultimate accuracy of a LD based gas

sensing system. Conversely, the spectral stability of LED's makes them more favourable, and their wide line-width may prove beneficial as the shoulders of the emission which lie away from the absorption feature could be used as reference against which variations in the device brightness and atmospheric scattering losses could be eliminated<sup>1</sup>.

In(As,Sb) LED's have achieved emission beyond 4.2  $\mu\text{m}$  at 300K<sup>9</sup>, with maximum powers of up to 1mW<sup>10</sup>. Longer wavelength,  $\lambda \sim 5.5\mu\text{m}$ <sup>11</sup>, InSb p-i-n LED's have also been demonstrated at room temperature with internal efficiencies of  $\sim 5\%$ , and similar devices have been successfully incorporated into prototype NO<sub>2</sub> gas detection systems<sup>12</sup>.

Under reverse bias, LED's can demonstrate 'negative luminescence' (NL)<sup>13</sup>. The efficient extraction of thermally generated carriers from their active regions reduces the net carrier concentration, specifically the np product therein. Since the thermal equilibrium between the semiconductor and the surrounding thermal radiation is primarily through absorption and emission by the carrier population, this reduction in np results in a net absorption of thermal radiation. From most practical purposes reverse biasing the LED affects its opto-electronic properties as if it had been instantaneously cooled, even though the lattice may still be at or above room temperature. The spectral shape under reverse bias is similar to the forward bias emission spectrum and, since most gas sensing applications require modulated IR signals in any case, NL devices may be equally as useful for gas sensing applications. The strong increase in the available NL device powers with increasing temperature and wavelength may make them the preferred choice for high temperature and/or long wavelength applications.

The 300K performance of these narrow gap devices, as with the lasers, is limited by non-radiative Auger recombination. Various methods of Auger reduction have been proposed, including strain modification of the bandstructure<sup>14</sup>. Theoretical calculations have predicted a reduction in the Auger recombination for type II heterostructure devices<sup>15</sup>, and experimental time resolved pump-probe studies of InAsSb/InAs type II superlattices<sup>16</sup> have shown 10-100 fold reduction in Auger rates compared with InSb samples with comparable band gap.

If these methods of Auger suppression are to be employed successfully then accurate knowledge of the band parameters of InAsSb/InAs heterostructures system is required. Following detailed magneto-absorption<sup>17</sup> and magneto-photoluminescence<sup>18</sup> studies of InAsSb/InAs quantum well (QW) and strained layer superlattice (SLS) samples, we find that a type II<sub>a</sub> (electrons confined in the alloy) exists between the binary and arsenic rich alloys. The QW samples investigated showed preferential recombination in the narrow alloy regions rather than the microns of InAs in which they were embedded, and this initial encouraging result from PL motivated the SQW LED studies presented here.

Previous LED studies have also shown that the incorporation of electron confining barriers improves the high temperature internal conversion efficiencies<sup>13</sup>. Here we report on the development of 4.2 $\mu\text{m}$  SLS LED's for CO<sub>2</sub> detection, and investigate the effectiveness of an electron confining barrier in improving device performance. We also analyse the negative luminescence characteristics of these devices, and consider the effect of the barrier under reverse bias.

## 2. EXPERIMENTAL DETAILS

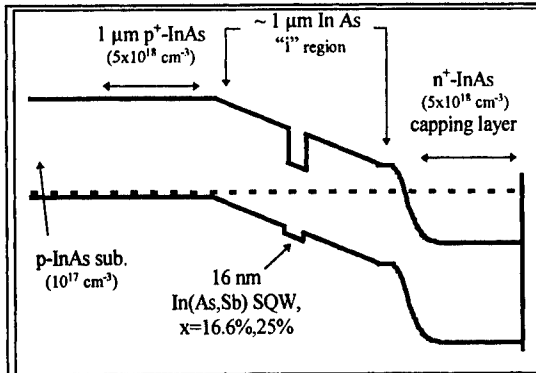


Figure 1. Schematic band profile of SQW LED

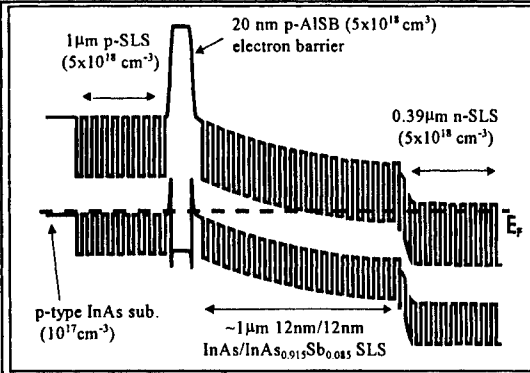


Figure 2. Schematic band profile of SLS LED

### 2.1 Growth

All the samples were grown by molecular beam epitaxy (MBE) in a VG Semicon V80H machine employing uncracked As and Sb sources on p-type InAs [100] substrates zinc doped to  $10^{17} \text{ cm}^{-3}$ , at growth temperatures between 450-465°C. The epilayers were doped p-type and n-type with Beryllium and Silicon, respectively.

The two pseudomorphic SQW samples had the same layer thicknesses and doping concentrations and differed only in the alloy concentrations of the wells. The nominal Sb concentrations of  $x = 0.25$  and  $x = 0.166$  were obtained by varying the As/Sb flux ratio. The device structure was as follows (see figure 1):  $1.8 \mu\text{m}$  of p-type ( $5 \times 10^{18} \text{ cm}^{-3}$ ) InAs;  $0.5 \mu\text{m}$  of undoped InAs;  $16 \text{ nm}$  of undoped  $\text{InAs}_{1-x}\text{Sb}_x$ ;  $0.5 \mu\text{m}$  of undoped InAs;  $1.0 \mu\text{m}$  of n<sup>+</sup>-type InAs.

Two SLS samples were grown, one of which incorporated an AISb electron confining barrier (IC621 in figure 1), and a second sample, with no barrier which acted as a control (IC622). The superlattice period of  $12 \text{ nm}$  InAs/  $12 \text{ nm}$   $\text{InAs}_{0.915}\text{Sb}_{0.085}$  was designed for peak emission at  $4.2 \mu\text{m}$  (at 300K) for CO<sub>2</sub> gas detection. The  $20 \text{ nm}$  AISb barrier is designed to be sufficiently thick to prevent electron tunnelling whilst not exceeding the critical thickness according to Matthews and Blakeslee ( $\sim 60 \text{ nm}$  assuming  $\sim 2\%$  SLS/AISb mismatch). The barrier is p-doped to ensure that the majority of the band offset occurs in the conduction band for maximum electron confinement. The best growth quality was obtained at a growth temperature of 465°C, whilst a 15 sec. pause before and after the AISb growth was sufficient for Sb flux stabilisation.

After growth, high resolution X-ray diffraction (HRXRD) studies were used to evaluate the composition and quality of the samples before they were processed into devices. Fitting the rocking curves to computer predictions confirmed pseudomorphic growth of the SQW wafers, with QW alloy concentrations of  $x=26.0\%$  and  $x=16.6\%$  for IC597 and IC598, respectively, in good agreement with the intended compositions of  $25.0\%$  and  $16.3\%$ .

The HRXRD results for the superlattice samples confirm the superlattice period as  $24 \text{ nm}$ , and the presence of high contrast satellite peaks up to fifth order confirm the high quality of the superlattice. The Sb concentrations within the alloy layers obtained from the X-ray data are  $x=8.2\%$  for IC621 (the "barrier" sample), and  $x=8.6\%$  for IC622 (the "control").

## 2.2 Luminescence Measurements

For electroluminescence measurements, the samples were fabricated into 600  $\mu\text{m}$  diameter mesas using conventional photolithographic wet etch technology, and a non-alloyed Cr/Au top annular contact was evaporated onto the top  $n^+$  InAs epilayers. The back contact was provided by Indium pressing the samples onto T05 headers, the pins of which were connected to the annular metallisation using a 25 $\mu\text{m}$  Au wire wedge bonder. The devices were driven at peak currents of 1.5Amps at 20 kHz (5-50% duty cycle). For the negative luminescence (NL) device studies, the same device processing technique was used but with larger 4mm diameter mesas. For photoluminescence studies, unprocessed samples were excited using a 987nm (InGa)As laser diode capable of providing up to 500mW, modulated at ~20kHz (50% duty cycle).

The samples were mounted in a closed cycle He cryostat (fitted with  $\text{CaF}_2$  windows) and the luminescence was focused using mirror optics into a Bomem DA3.02 Fourier transform infrared spectrometer operating in double modulation mode. The modulated luminescence emerging from the spectrometer was focused onto either an InSb photodiode (cut-off 5.5 $\mu\text{m}$ ) or a CMT photoconductive detector (cut-off 12 $\mu\text{m}$ ).

LED power outputs were measured with a simpler optical arrangement comprising of only a calibrated detector, to eliminate collection efficiency errors. The detector signal was integrated over all forward solid angles, and corrected for detector response and atmospheric absorption features to obtain the total device powers. In calculating the internal quantum efficiencies, it is assumed that the fraction of luminescence escaping from the device is given by<sup>19</sup>  $1/n(n+1)^2$ , which for  $n_{\text{InAs}}=3.6$ , gives  $\eta_{\text{ext.}}/\eta_{\text{int.}}=0.014$ .

## 3. RESULTS AND DISCUSSION

### 3.1 Single Quantum Well LED's

The 9K EL results for IC597 (Sb%=26.0%) and IC598 (Sb%=16.6%) are illustrated in figures 3 and 4, respectively. Under low forward bias, both samples show peaks associated with recombination in the InAs at ~420 meV (and associated defects at 400meV), and lower energy  $\text{InAs}_{1-x}\text{Sb}_x$  QW peaks at 148.3 meV and 235.2 meV for IC597 and IC598, respectively. The later values are much lower than the strained band gaps of the alloys of 269 meV and 312meV. We believe that this emission at energies significantly below the alloy band gaps is due to spatially indirect type II recombination of electrons confined within the alloy and holes residing in the surrounding InAs (see inset in figure 4).

The band offset between the strained binary and the alloy can be described by<sup>17</sup>,

$$Q_{c(v)} = \frac{\Delta E_{c(v)}}{E_{\text{InAs}} - E_{\text{InAsSb}}} \quad (1)$$

where  $E_{\text{mat}}$  is the strained band-gap of the material,  $\Delta E_{c(v)}$  is the conduction (valence) band offset, and  $Q_{c(v)}$  is a constant with a value dependent on the magnitude and sign of the offset. By fitting theoretical absorption curves to experimental magneto-absorption<sup>21</sup> data, a  $Q_c = 2.06 \pm 0.11$  was found. From calculations which include the effects of non-parabolicity and strain, and assuming this value of  $Q_c$ , we calculate transition energies of 151 meV and 234 meV for IC597 and IC598 respectively, in good agreement with the experimental data of figs 3 and 4..

At low temperatures (9K) the overall LED emission spectra are dominated by the InAs related emission at ~420 meV (figures 3 and 4 inset) probably due to radiative recombination at the p-type/v-

type interface. Because of low mobility or carrier freeze-out, the n.p product in the vicinity of the QW is low in these circumstances. At higher excitation densities, the emission from both the SQW LED's shows a blue shift of up to 40meV due to band filling effects.

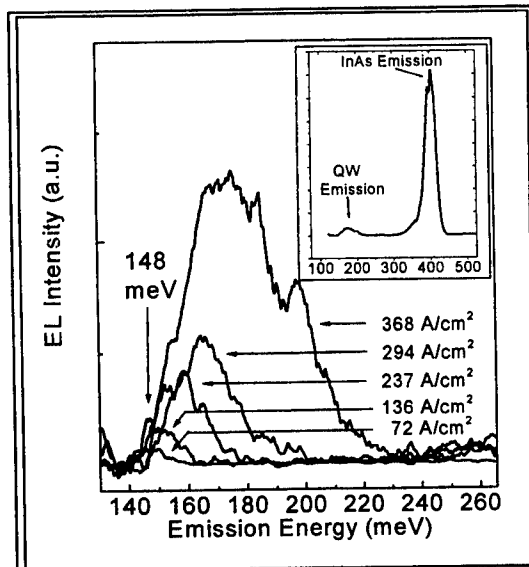


**Figure 3.** 9K emission spectra from a SQW LED from wafer IC597 ( QW alloy concentration 16.6% Sb).

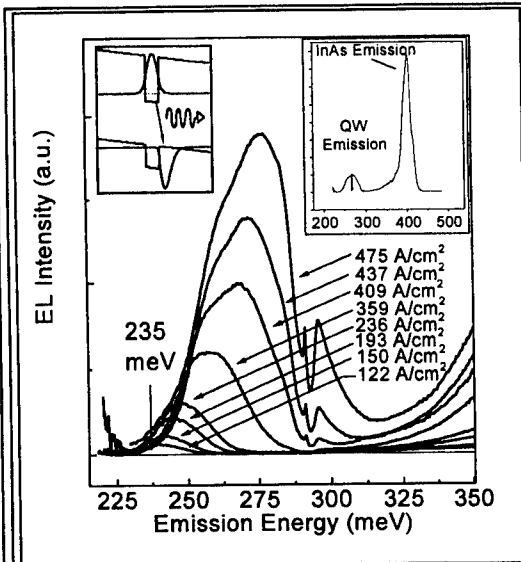


**Figure 4.** 9K emission spectra from a SQW LED from wafer IC598 ( QW alloy concentration 26 % Sb).

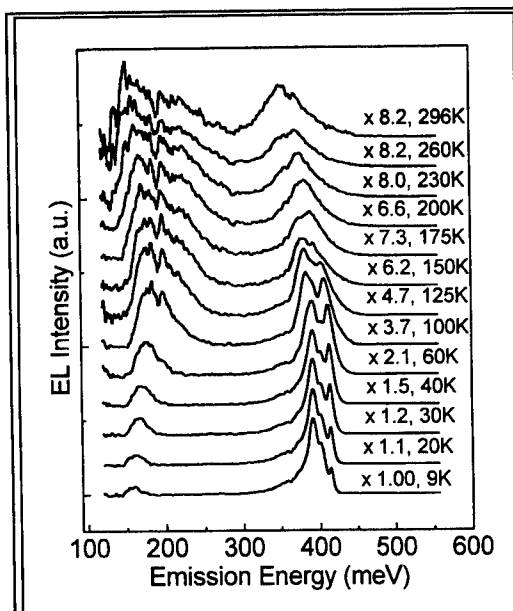


**Figure 5.** Temperature dependent emission spectra from a SQW LED from wafer IC597 ( QW alloy concentration 16.6% Sb).

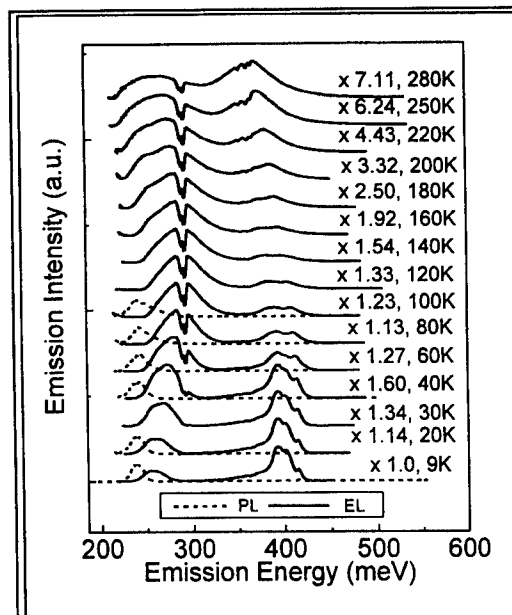


**Figure 6.** Temperature dependent emission spectra from a SQW LED from wafer IC598 ( QW alloy concentration 26% Sb).

The LED spectra also blue shift with increasing temperature (figures 5 and 6). This blue shift is accompanied by an increase in the intensity of the QW emission relative to that of the InAs. In contrast, the temperature dependent PL data for IC598 (dashed spectra in figure 6) at a fixed excitation intensity, show no temperature blue shift. This implies that the temperature dependent spectral shifts and peak intensity changes observed in EL reflect primarily variations in the QW carrier concentrations, and are only weakly affected by temperature dependent band structure changes. As the temperature is further increased, the QW emission intensity relative to the InAs feature goes through a maximum at  $\sim 150\text{K}$  (IC598) and  $\sim 300\text{K}$  (IC597). The difference between these temperatures is probably due to an superior confinement characteristics of the deeper well in IC597.

Room temperature powers of  $24\mu\text{W} \pm 3.6$  and  $50\mu\text{W} \pm 7.5$ , were obtained for IC597 and IC598, respectively, with corresponding internal conversion efficiencies of 0.8% and 1.3%.

### 3.1 SLS Photoluminescence data.

Two peaks are observed in the low temperature PL spectra (figure 7); the high energy peak at 339 meV is associated with the band-to-band SLS transition observed in the LED's from the same wafer. There is also a slightly lower energy peak at 322 meV, the temperature dependence of which suggests recombination from a defect-related state. Assuming a simple hydrogenic model for defect state energies, the 17meV separation between these two peaks suggests an acceptor related transition.

In an attempt to find the origin of this transition, the PL sample was etched down to various depths within the SLS structure and PL measurements repeated. Once etched past the top  $n^+$  region, the low energy peak disappeared (see dashed spectra in figure 7). The presence of a deep level acceptor state within a n-type region may be due to the formation of an acceptor like state by Si due to its amphoteric nature in heavily doped InAs. A red-shift with increasing temperature is observed in the PL under constant excitation conditions.

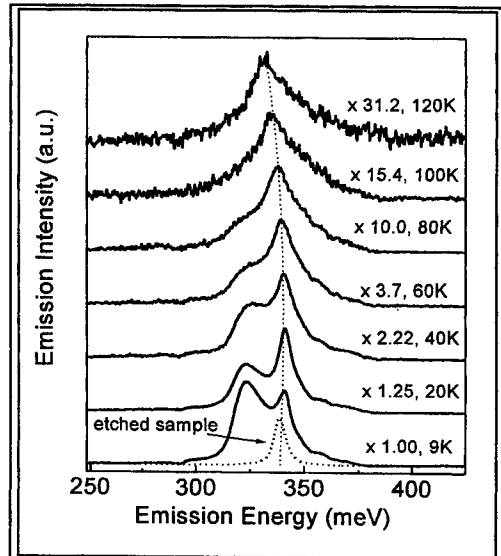


Figure 7. IC621 temperature dependent PL

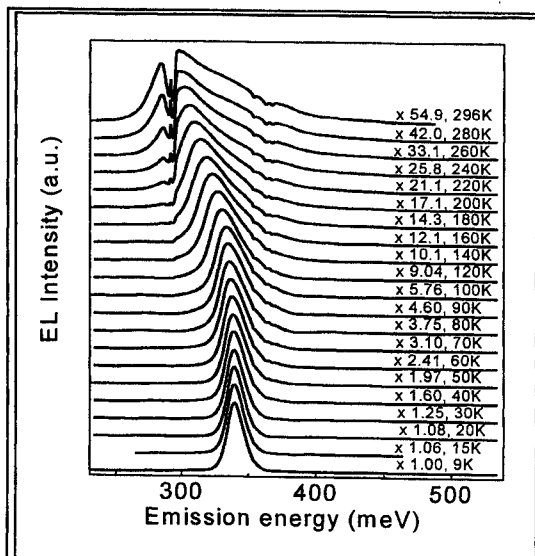


Figure 8. IC621 temperature dependent EL

### 3.2 SLS LED's - The Effect of Electron Confining Barriers

The low temperature (9K) LED spectra for both devices (figure 8) showed strong SLS band-to-band emission at 338meV and 332meV for IC621 and IC622, respectively. The 6meV difference between

the two being due to the slightly higher Sb concentration in IC622, as measured by HRXRD. No significant blue shift in the emission energy of either device was observed at high excitation densities. As in the PL data (figures 7), the LED emission red shifts towards longer wavelengths with increasing temperature.

Although the shape of the LED spectra varies very little between the two devices at a given temperature, figure 9 illustrates the contrast in efficiency between them with increasing temperature. At 9K, the efficiencies of the devices are identical within experimental error but by 300K the “barrier” device is ~3.5 more efficient than the “control” LED. We attribute this improved efficiency to the successful exclusion of electrons from the heavily dislocated p-SLS buffer region where the probability of non-radiative recombination is high.

Figure 10 illustrates the accuracy with which the SLS peak emission energy has been engineered to coincide with the CO<sub>2</sub> absorption feature. The 300K L-I curve for the “barrier” LED is illustrated in the inset of figure 10 from which we obtain powers of 73μW/A ( $\eta_{int} = 2.8\%$ ) up to a maximum output power of 140μW.

### 3.3 Negative Luminescence

In reverse bias, these SLS samples demonstrate “negative luminescence”. Comparison of the forward and reverse bias spectra (figure 11) show very little difference in shape. This is to be expected since no blue shift in the forward bias spectra was observed even at high injection.

The negative luminescence powers, measured at 500mA reverse bias current, were 1.65 and 2.08μW at 300K for IC621 (“barrier”) and IC622 (“control”) respectively. The ratio of the internal efficiencies of the devices ( $\eta_{barrier} / \eta_{control}$ ) under forward bias was 3.5, but in reverse bias it was only  $0.8 \pm 0.1$ .

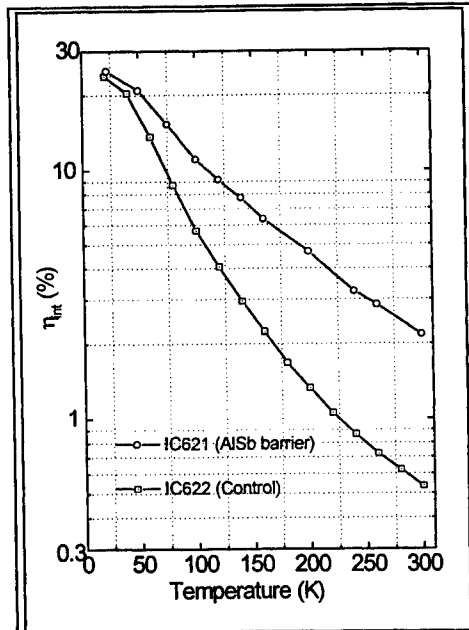


Figure 9. Variation in  $\eta_{int}$  for IC621 & IC622

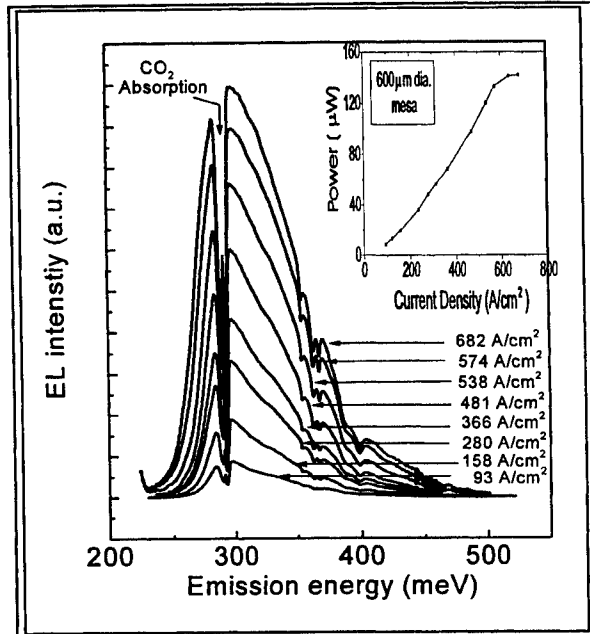
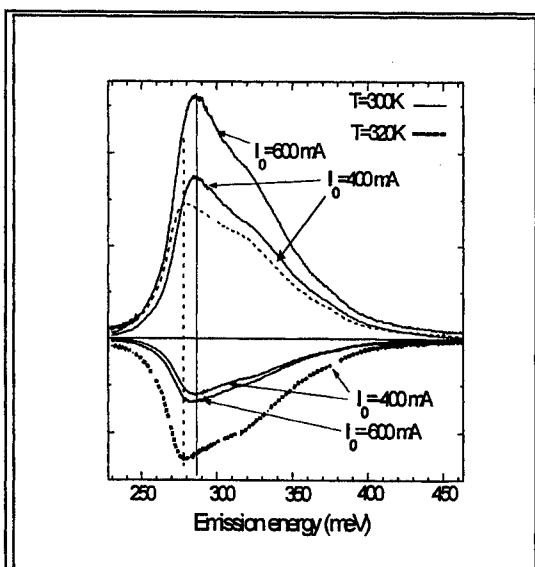


Figure 10. 300K EL (and L-I curve) for IC621

The NL intensity depends on the degree to which the np product in the active region has been reduced by carrier extraction. Auger-generated minority carriers in the n- and p- contacting layers reduce the extraction efficiency. Since our active region is residually n-doped, Auger generated holes in the n-

contact have a larger effect on this np product than do Auger generated electrons in the p-contact. This explains why the electron barrier has a negligible enhancement on the NL efficiency; the observed slight reduction is probably due to slightly inferior growth quality due to the presence of the AlSb layer.

The low duty cycle L-I curves at various temperatures for IC622 large area negative luminescence device are shown in figure 12. As expected, the maximum power obtainable from the devices increases with increasing temperature, ranging from 0.2  $\mu$ W at 250K to 6.0  $\mu$ W at 310K. These curves demonstrate a saturation in the maximum amount of power obtainable at a given temperature, but measuring the RB saturation point accurately is complicated by the effects of device heating with increasing reverse bias current on the NL spectra. From the I-V curves, we have extracted the reverse



**Figure 11.** NL spectra for IC622 at 300K and 320K

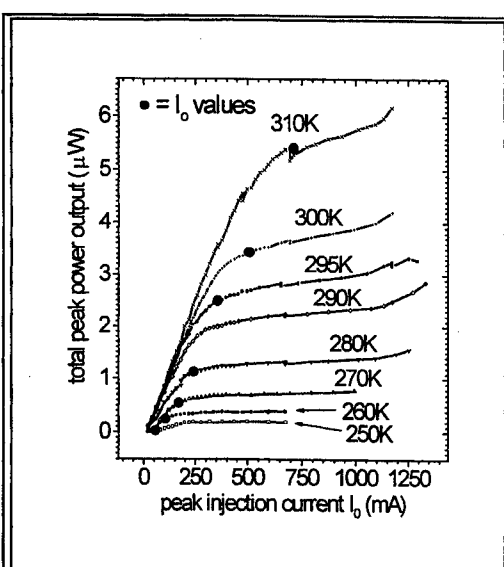


**Figure 12.** NL L-I curves for IC622 at T=250-300K

bias saturation currents,  $I_0$ , and plotted them on the L-I curves in figure 12. As we can see there is a strong correlation between the  $I_0$  values and the reverse bias currents at which the NL power output starts to saturate.

#### 4. CONCLUDING REMARKS

We have demonstrated significant improvements in the 300K performance of  $\text{InAs}_{1-x}\text{Sb}_x$  heterostructure LED's at Mid-IR wavelengths suitable for trace gas detection. SQW LED's have demonstrated excellent capture and confinement characteristics at wavelengths up to 8  $\mu\text{m}$ , with pseudomorphic QW alloy concentrations comfortably within the strain budget imposed by the InAs substrate. SLS LED's have demonstrated improved power outputs at wavelengths suitable for  $\text{CO}_2$  detection at 300K as a result of improved growth, whilst the incorporation of AlSb electron confining barriers has improved device performance by  $\sim 3.5$  fold. The negative luminescence capabilities of these devices are also encouraging, especially at higher temperatures. Despite the progress detailed in this report, the performance of these devices is still thought to be limited by the growth quality of this relatively immature material system, and further improvements in fabrication technology are expected to improve performance to a level more suitable for gas sensing applications.



## ACKNOWLEDGEMENTS

Financial support, from the UK Engineering and Physical Sciences Research Council, and through the 'ASPIRE' project of the UK LINK photonics programme, is gratefully acknowledged. HRH acknowledges financial support from Edinburgh Sensors Ltd. in the form of a CASE studentship and JH acknowledges a European Community Marie Curie Fellowship.

## REFERENCES

1. S.D.Smith, Vass\_A, Bramley\_P, Crowder\_JG, Wang\_CH, "Comparison of IR LED gas sensors with thermal source products.", IEE Proc.-Optoelectron., Vol. 144, No.5, p.266-270, 1997
2. H.K.Choi, G.W.Turner, M.J.Manfra, M.K.Connors, "175K continuous wave operation of InAsSb/InAlAsSb quantum-well diode lasers emitting at 3.5 $\mu$ m", Appl.Phys.Lett., Vol. 68, No. 21, p.2936-2938, 1996
3. B.Lane, D.Wu, A.Rybaltowski, H.Yi, J.Diaz, M.Razeghi, "Compressively strained multiple quantum well InAsSb lasers emitting at 3.6 $\mu$ m grown by metal-organic chemical vapour deposition", Appl.Phys.Lett., Vol. 70, No. 4, p.443-446, 1997
4. L.J.Olafsen, E.H.Aifer, I.Vurgaftman, W.W.Bewley, C.L.Felix, J.R.Meyer, D.Zhang, C.H.Lin, S.S.Pei, "Near-room temperature mid-infrared interband cascade laser", Appl.Phys.Lett. Vol.72, No.19, p.2373, 1998
5. C.Gmachl, A.Tredicucci, F.Capasso, A.Hutchinson, D.L.Sivco, J.N.Baillargeon, A.Y.Chol, "High-power  $\lambda$ ~8 $\mu$ m quantum cascade lasers with near optimum performance", Appl.Phys.Lett., Vol.72, No. 24, p.3130-3132, 1998
6. J.Faist, F.Capasso, D.L.Sivco, A.L.Hutchinson, S.N.G.Chu, A.Y.Cho, "Short wavelength ( $\lambda$ ~3.4 $\mu$ m) quantum cascade laser based on strained compensated InGaAs/AlInAs", Appl. Phys. Lett., Vol. 72, No. 6, p.680-682, 1998
7. J.Faist, C.Sirtori, F.Capasso, D.L.Sivco, J.N.Baillargeon, A.L.Hutchinson, A.Y.Cho, "High-power long-wavelength ( $\lambda$ ~11.5 $\mu$ m) quantum cascade lasers operating above room temperature", IEEE Photonics Technol. Lett., Vol. 10, No. 8, p.1100-1103, 1998
8. J.Faist, A.Tredicucci, F.Capasso, C.Sirtori, D.L.Sivco, J.N.Baillargeon, A.L.Hutchinson, A.Y.Cho, "High-power continuous-wave quantum cascade lasers", IEEE Journal Quantum. Electron., Vol.34, No. 2, p.336-343, 1988
9. A.A.Popov, V.V.Sherstnev, Y.P.Yakovlev, A.N.Baranov, C.Alibert, "Powerful mid-infrared light emitting diodes for pollution monitoring", Electron. Lett., Vol. 33, No. 1, p.86-88, 1997
10. Y.Mao and A.Krier, "Efficient 4.2 $\mu$ m light emitting diodes for detecting CO<sub>2</sub> at room temperature", Vol. 32, No.5, p.479-480, 1997
11. T.Ashley, C.T.Elliott, N.T.Gordon, R.S.Hall, A.D.Johnson, G.J.Pryce, "Uncooled InSb/InAlSb mid-infrared emitter", Appl.Phys.Lett., Vol. 64, No. 18, p.2433-2435, 1994
12. C.H.Wang, J.O.Crowder, V.Mannheim, T.Ashley, D.T.Dutton, A.D.Johnson, G.J.Pryce and S.D.Smith, "Detection of NO<sub>2</sub> using a room temperature operation mid-infrared InSb light emitting diode", Electron. Lett., Vol.34, No.3, p.xxx, 1998
13. T.Ashley, C.T.Elliott, N.T.Gordon, R.S.Hall, A.D.Johnson, G.J.Pryce, "Negative luminescence from InAlSb and CdHgTe diodes", Vol. 36, p.1037-1044, 1995
14. H.P.Hjalmarson and S.R.Kurtz, "Electron Auger processes in mid-infrared InAsSb/InGaAs heterostructures", Appl.Phys.Lett. Vol. 72, No.7, p.949-951, 1996
15. A.D.Andreev and G.G.Zengra, "Mechanism for a suppression of Auger recombination in type-II heterostructures", JETP Lett., Vol. 61, No. 9, p.764-770, 1995
16. C.M.Ciesla, B.N.Muridin, C.R.Pidgeon, R.A.Stradling, C.C.Phillips, D.J.Bain, I.Galbraith, D.A.Jaroszynski, C.J.G.M.Langerak, P.J.P.Tang, M.J.Pullin, "Picosecond free-electron laser studies of Auger recombination in arsenic-rich InAsSb strained layer superlattices", IEE Proc.-Optoelectron., Vol. 144, No. 5, p.331-335, 1997
17. Y.B.Li, D.J.Bain, L.Hart, M.Livingstone, C.M.Ciesla, M.J.Pullin, P.J.P.Tang, Yuen\_WT, I.Galbraith, C.C.Phillips, C.R.Pidgeon, R.A.Stradling, "Band alignments and offsets in InAsSb/InAs superlattices", Phys.Rev.B, Vol.55, No.7, p.4589, 1997.

18. P.J.P.Tang, M.J.Pullin, Y.B.Li, C.CPhillips, R.A.Stradling, S.J.Chung, W.T.Yuen, L.Hart, D.J.Bain, I.Galbraith, "A magneto-photoluminescence investigation of the band offset between InAs and Arsenic-rich InAsSb alloys.", Appl.Phys.Lett., Vol. 69, No. 17, p.2501-2503, 1996 .
19. T.S.Moss, G.J.Burrell, and B.Ellis. "Semiconductor Opto-electronics". (Butterworth, London, 1973)

---

\* Electronic mail: h.hardaway@ic.ac.uk

# Temperature dependence of magneto-optical properties of $\text{Zn}_{1-x}\text{Mn}_x\text{Se}$

Yu-Xiang Zheng, Liang-Yao Chen, Bo Xu, Dong-Liang Qian, Ying-Jun Zhang, Song-You Wang,  
Rong-Jun Zhang, Shi-Ming Zhou, and Ning Dai

Department of Physics, Fudan University, Shanghai 200433, China

Yan-Feng Wei, and Da-Ming Huang

Applied Surface Laboratory, Fudan University, Shanghai 200433, China

## ABSTRACT

This paper reports the temperature dependence of the magneto-optical properties of  $\text{Zn}_{1-x}\text{Mn}_x\text{Se}$  samples prepared by molecular beam epitaxy (MBE) method. In the magneto-optical spectra, there exist several Faraday rotation peaks. The peaks located at  $\sim 2.18$ ,  $\sim 2.36$  and  $2.45\sim 2.57$  eV are attributed to  $\text{Mn}^{2+}$   $d \rightarrow d^*$  transitions. The peak located at  $\sim 2.7$  eV is attributed to the interband transitions and higher order  $\text{Mn}^{2+}$   $d \rightarrow d^*$  transitions, which are blue-shifted with decreasing temperature. The positions of the rotation peaks induced by  $\text{Mn}^{2+}$   $d \rightarrow d^*$  transitions show weak temperature dependence.

**Keywords:** Semiconductor, Farady effect, optical properties

## 1. INTRODUCTION

$\text{Zn}_{1-x}\text{Mn}_x\text{Se}$  is a kind of most common diluted magnetic semiconductors(DMS), which is formed by the random substitution of Mn to Zn in II-VI family semiconductor ZnSe. At low Mn composition (with Mn composition  $x < 0.30$ ), the  $\text{Zn}_{1-x}\text{Mn}_x\text{Se}$  often has the zinc-blende structure. Its optical interband transition gap width can be adjusted by the Mn composition.  $\text{Zn}_{1-x}\text{Mn}_x\text{Se}$  has many interesting properties, such as the giant Faraday effect<sup>[1,2]</sup> and the formation of bound magnetic polarons,<sup>[3-5]</sup> etc. It implies that  $\text{Zn}_{1-x}\text{Mn}_x\text{Se}$  will be a promising material of manufacturing many kinds of optical and magneto-optical devices, such as the magneto-optical switches, light-emitting diodes, magneto-optical isolators, and magnetic sensors, etc.

To understand the properties of this kind of materials better, In this work, we studied the temperature dependence of the magneto-optical properties of  $\text{Zn}_{1-x}\text{Mn}_x\text{Se}$ . In the Faraday spectra, there exist several Faraday rotation peaks, which are due to the  $\text{Mn}^{2+}$   $d \rightarrow d^*$  transitions and interband transition. Experimental results show that the energy of interband transition is blue-shifted with decreasing temperature. But it is seen that the temperature dependence for the peak positions of Faraday rotation induced by the  $\text{Mn}^{2+}$   $d \rightarrow d^*$  transitions is weak.

## 2. EXPERIMENTS

The  $\text{Zn}_{1-x}\text{Mn}_x\text{Se}$  samples were prepared by the MBE method on the (100)-oriented GaAs wafers. The x-ray diffraction technique was used to examine the quality of samples and to determine the Mn composition. The magneto-optical Faraday spectra of the  $\text{Zn}_{1-x}\text{Mn}_x\text{Se}$  samples were measured with a wavelength-scanning and Fourier-transform Faraday spectrometer. A 150-W Xe short-arc lamp was used as a continuum light source to cover the 1.5- to 6.0-eV spectral range. A quasi-homogeneous and computer-controlled magnetic field up to 13 kOe is provided by an electromagnet. A microminiature Joule-Thomson (J-T) refrigerators was used to change the temperature of samples. The sample was mounted onto a clip-on pad contacted by the thermal grease. The clip-on pad is thermally contacted to the J-T refrigerator that is placed into a small vacuum jacket chamber. The sample temperature can be conveniently set and adjusted from -197 to 100 °C. Two  $\text{Zn}_{1-x}\text{Mn}_x\text{Se}$  film samples ( $x=0.14$  and  $0.20$ ) were prepared in the experiment. The results of x-ray diffraction pattern show the perfect crystalline quality of the samples. The Faraday spectra of the samples were measured at temperatures of 80, 100, 150, 200, 250, and 300 °K, respectively, with photon energy scanned from 1.5- to 4.5-eV at an interval of 0.05 eV. The magnetic field was set as 10 kOe.

### 3. RESULTS AND DISCUSSIONS

The band structures of  $A_{1-x}Mn_xB^{VI}$  type DMS are very similar to those of  $A^{II}B^{VI}$  type semiconductors. They have direct band gap with the  $\Gamma_6$  conduction band minimum separated from the  $\Gamma_8$  valence band maximum. As to the  $Mn^{2+}$  ion, it is acted upon by the crystal field of the symmetry of tetrahedral configuration, arising mainly from the four surrounding anions. In the crystal field, the ground state is labeled as  ${}^6A_1$ , the  ${}^4P$  as  ${}^4T_2$ , and the  ${}^4G$  and  ${}^4D$  energy levels of the free atom split as follows:

$${}^4G \rightarrow {}^4T_1 + {}^4T_2 + {}^4A_1 + {}^4E$$

$${}^4D \rightarrow {}^4T_2 + {}^4E$$

Fig. 1 shows the magneto-optical Faraday spectra of  $Zn_{0.86}Mn_{0.14}Se$  at temperature of 80, 100, 150, 200, 250 and 300 °K, respectively. There exists two observed peaks at the energy of  $\sim 2.36$  and  $\sim 2.57$  eV, which are attributed to the  $Mn^{2+} d \rightarrow d^*$  transitions. The peak at  $\sim 2.36$  eV is due to  ${}^6A_1({}^6S) \rightarrow {}^4T_2({}^4G)$ , and the peak at 2.57 eV is due to  ${}^6A_1({}^6S) \rightarrow {}^4A_1({}^4G)$  and  ${}^4E({}^4G)$ . Both peaks at 2.36 and 2.57 eV show weak temperature dependence. The structure around the energy of 2.75 eV is a little complicated, and shifts to the higher energy region with decreasing of temperature. This structure arises from the interband transition  $\Gamma_8 \rightarrow \Gamma_6$ .

The Faraday spectra for sample  $Zn_{0.80}Mn_{0.20}Se$  is shown in Fig. 2. The result is very similar to that of  $Zn_{0.86}Mn_{0.14}Se$ . The peak at 2.17 eV is due to  ${}^6A_1({}^6S) \rightarrow {}^4T_1({}^4G)$ , and the peak at 2.48 eV is due to  ${}^6A_1({}^6S) \rightarrow {}^4A_1({}^4G)$  and  ${}^4E({}^4G)$ . The structure at the vicinity of 2.75 eV is attributed to  $\Gamma_8 \rightarrow \Gamma_6$ .

The magneto-optical properties arising from the interband transition and  $Mn^{2+} d \rightarrow d^*$  transitions have different features as shown by the spectral line shape and have different temperature dependence. The Faraday rotation peaks related to the  $Mn^{2+} d \rightarrow d^*$  transitions are negative in the spectra. The energy peak positions are nearly kept as the same values at different temperature, and the intensities of the peaks increase slightly with decreasing temperature from 300 to 100K, and then the intensity is reduced from 100 to 80 °K. For the Faraday rotation induced by the interband transition, the spectral line shape shows the negative and positive resonance-like peaks. The negative peak increases with decreasing temperature from 300 to 100 °K and then decreases from 100 to 80 °K, just like the situation of the  $Mn^{2+} d \rightarrow d^*$  transitions, but it is blue-shifted clearly. The positive peak increases monotonously with decreasing temperature, and is also blue-shifted. The physical mechanism resulting in the magneto-optical properties, therefore, is different for the  $Mn^{2+} d \rightarrow d^*$  transitions and interband transitions. The higher Faraday rotation effect occurred in the vicinity of the energy gap will be attributed to both of the interband transitions and higher order  $Mn^{2+} d \rightarrow d^*$  transitions. The more detailed mechanism needs to be further studied in the future.

For the  $A_{1-x}Mn_xB^{VI}$  type of DMS, the energy gap  $E_g$  varies with temperature as the following experiential formula: [6]

$$E_g(T) = E_0 - \frac{aT^2}{T+b},$$

where,  $E_0$  is the energy gap at  $T=0$  °K, and  $a$  and  $b$  are constants. This formula is used to fit the dependence of the magneto-optical property induced by the interband transition with the temperature. The fitting results are shown in Figs. 3 and 4. The constants used in fitting are tabled as following:

x	$E_0$ (eV)	a(K <sup>-1</sup> )	B(K)
0.14	2.76	0.00045	196.8
0.20	2.78	0.00046	76.5

### 4. CONCLUSION

The magneto-optical properties of MBE-prepared  $Zn_{1-x}Mn_xSe$  were measured at different temperature. In the magneto-optical spectra, there are several Faraday rotation peaks. The peaks located at 2.18, 2.36, 2.45~2.57 eV are attributed to  ${}^6A_1({}^6S) \rightarrow {}^4T_1({}^4G)$ ,  ${}^6A_1({}^6S) \rightarrow {}^4T_2({}^4G)$ ,  ${}^6A_1({}^6S) \rightarrow {}^4A_1({}^4G)$  and  ${}^4E({}^4G)$ , respectively. The peak located at 2.7 eV is attributed to the interband transitions and higher order  $Mn^{2+} d \rightarrow d^*$  transitions. The intensities of the peaks increase slightly with decreasing temperature from 300 to 100 °K, and decrease with decreasing temperature from 100 to 80 °K. The peak positions show weak dependence on temperature. The Faraday rotation induced by the interband transitions has

resonance-like negative and positive peaks. The negative peak increases with decreasing temperature from 300 to 100 °K and then decreases from 100 to 80 °K. The positive peak increases monotonously with the decreasing temperature. Both negative and positive peaks are blue-shifted with decreasing temperature.

### ACKNOWLEDGMENTS

This work is supported by NSFC and SRCAP of China.

### REFERENCES

1. J. A. Gaj, R. R. Galazka, and M. Nawrocki, Solid State Commun. **25**, 193 (1978).
2. D. U. Bartholomew, J. K. Furdyna and A. K. Ramdas, Phys. Rev. **B 34**, 6943 (1986).
3. J. K. Furdyna, J. Appl. Phys. **64**, R29 (1988).
4. S. M. Ryabchenko and Yu. G. Semenov, Sov. Phys. JETP **57**, 825 (1983).
5. I. A. Merkulov, et al., Phys. Rev. **B 54**, 5727 (1996).
6. Y. P. Varshni, Physica **34**, 149 (1967).

### Figure Captions

Figure 1. Faraday spectra of  $\text{Zn}_{0.86}\text{Mn}_{0.14}\text{Se}$  measured at temperature of 80, 100, 150, 200, 250 and 300 °K, respectively, and at the magnetic field of 10 KOe.

Figure 2. Faraday spectra of  $\text{Zn}_{0.80}\text{Mn}_{0.20}\text{Se}$  measured at temperature of 80, 100, 150, 200, 250 and 300 °K, respectively, and at the magnetic field of 10 KOe.

Figure 3. Fitting results of energy gap vs. temperature for  $\text{Zn}_{0.86}\text{Mn}_{0.14}\text{Se}$ .

Figure 4. Fitting results of energy gap vs. temperature for  $\text{Zn}_{0.80}\text{Mn}_{0.20}\text{Se}$ .

---

\* Correspondence: Email: lychen@fudan.ac.cn; Telephone: 086-21-6564-6068

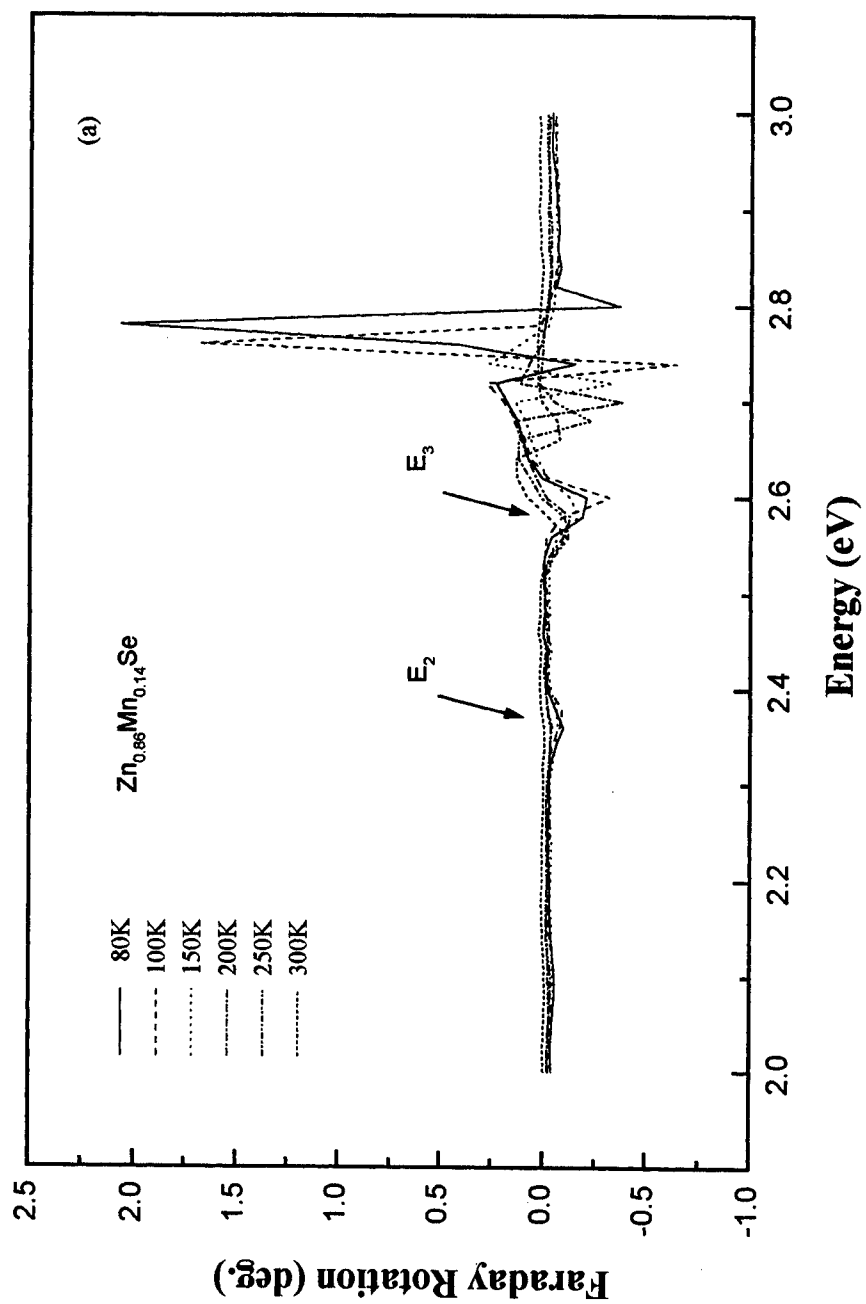


Fig. 1(a)

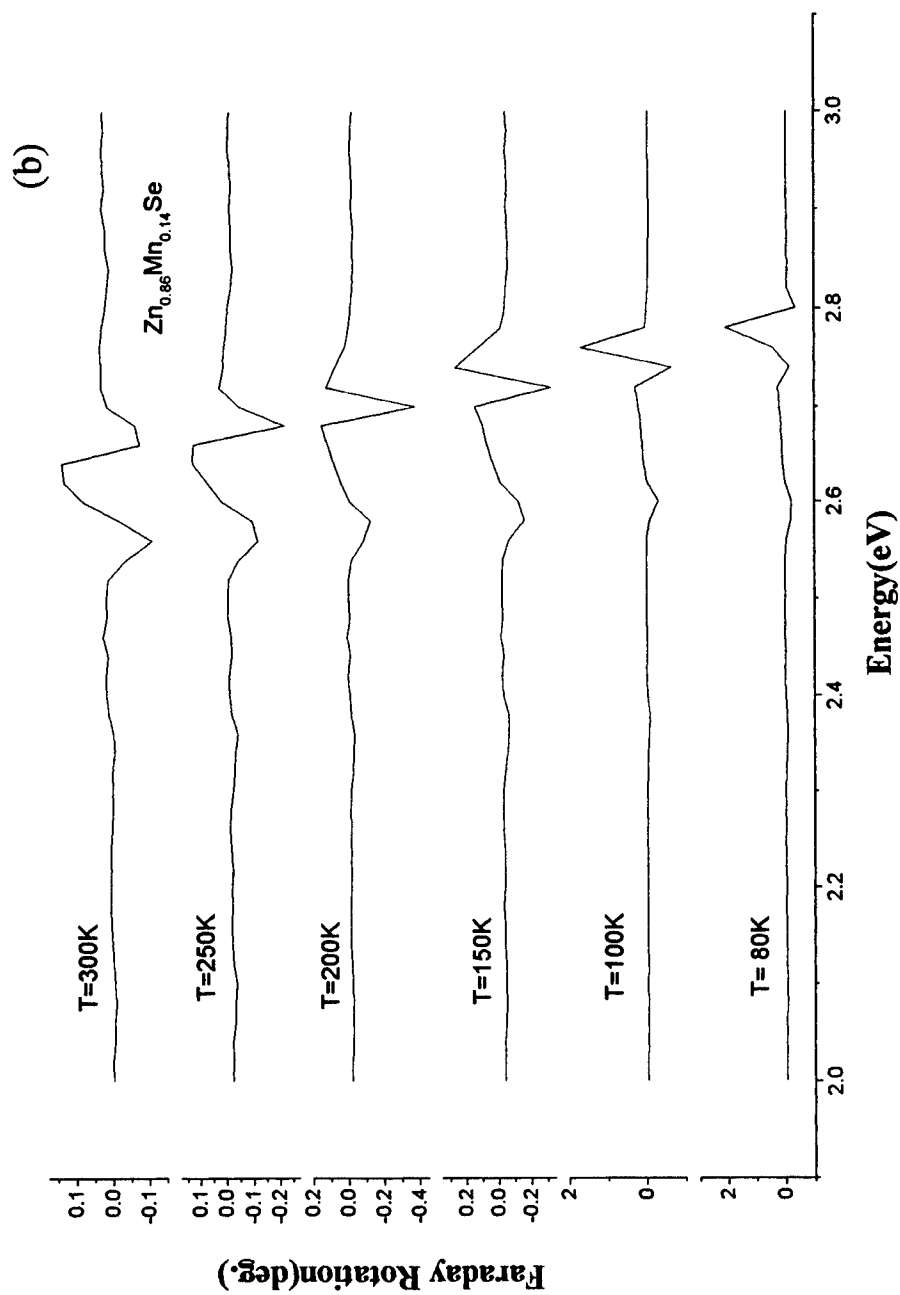


Fig. 1(b)

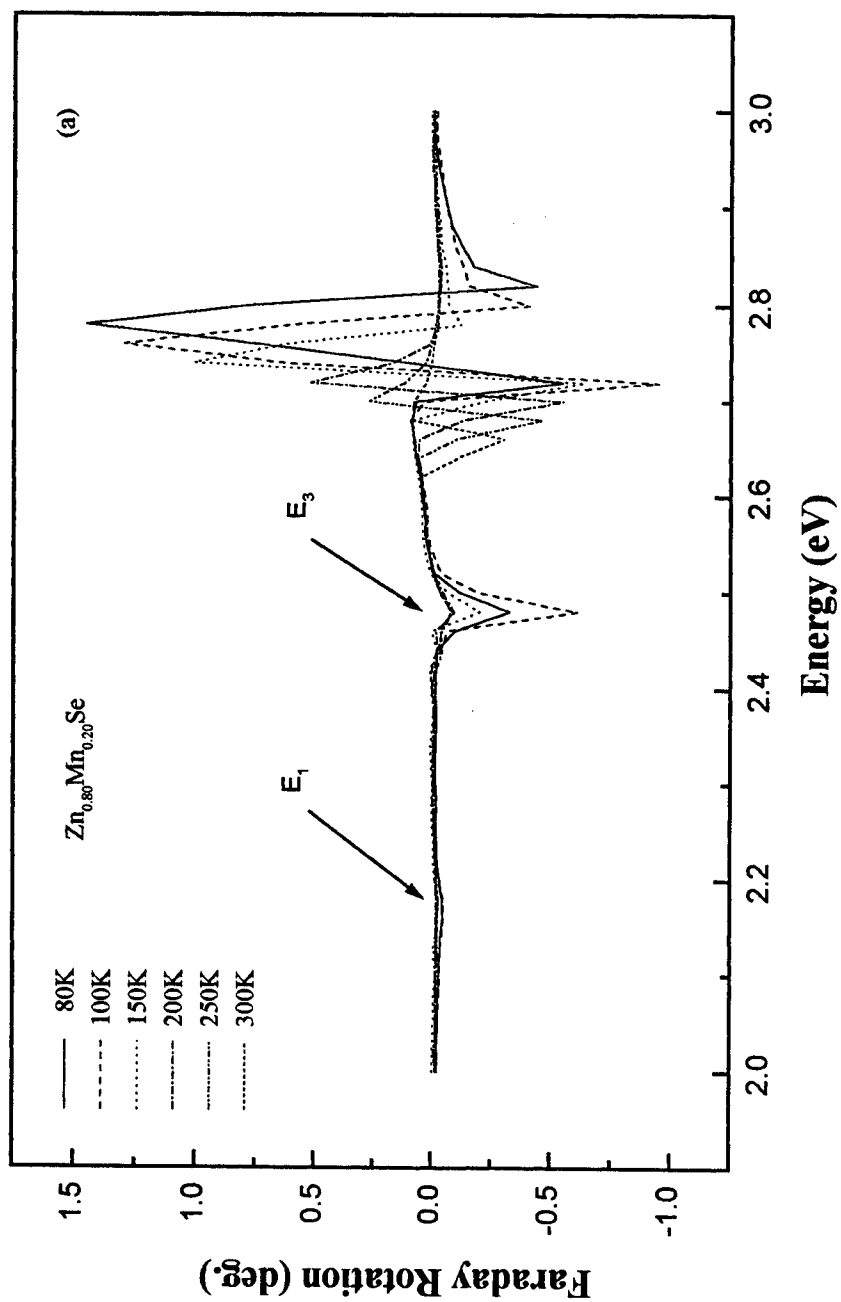


Fig. 2(a)



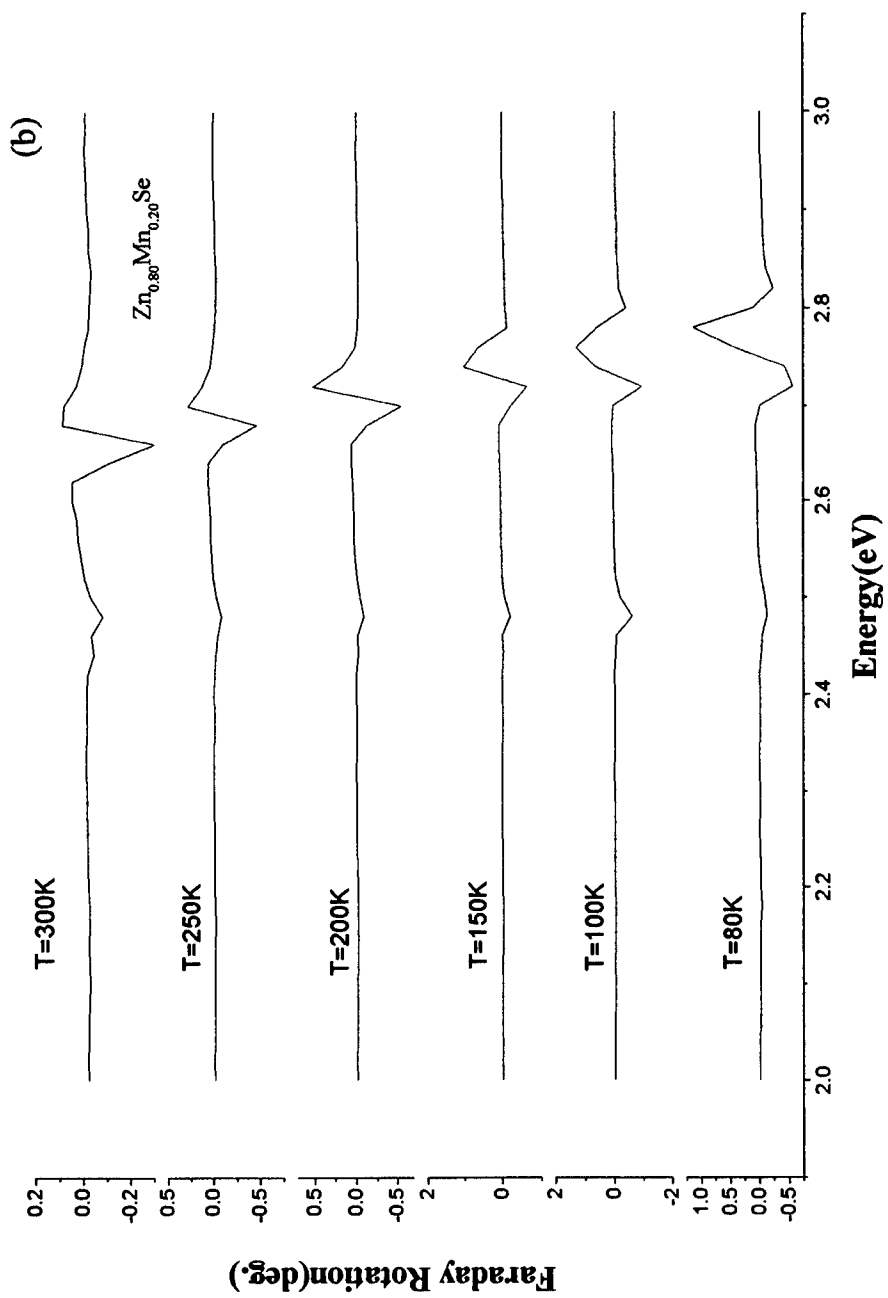


Fig. 2(b)

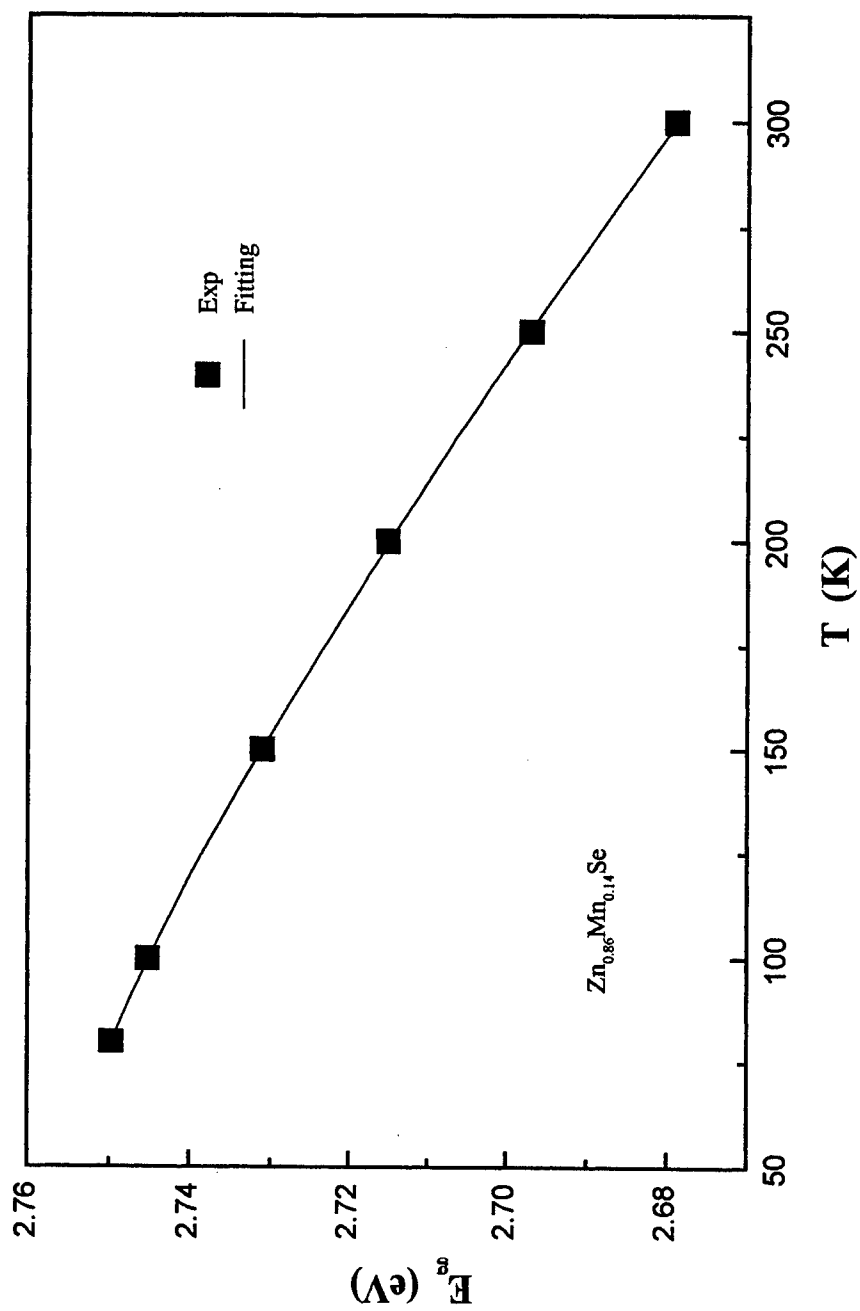


Fig. 3

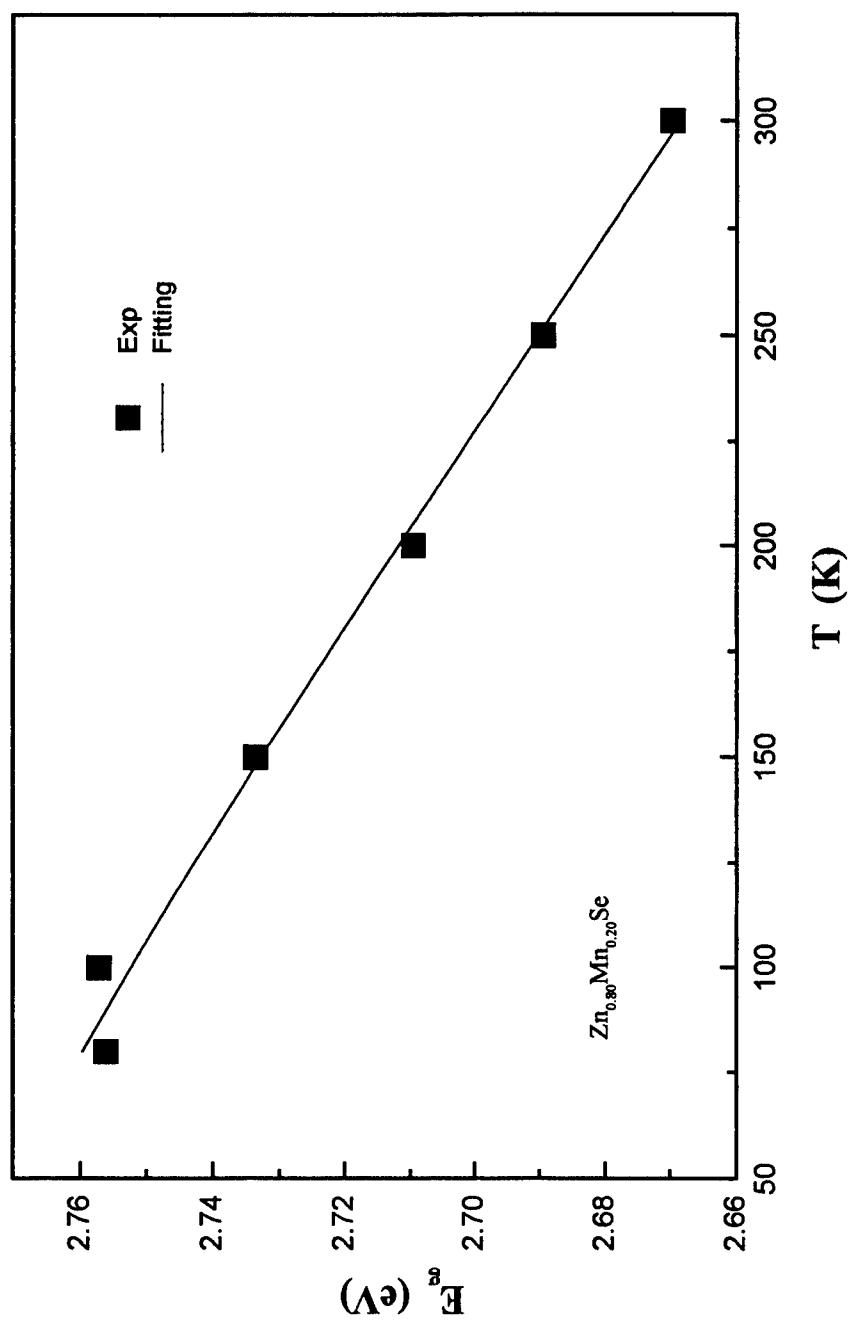


Fig. 4

## White LED

Georg Bogner<sup>a</sup>, Alexandra Debray<sup>a</sup>, Günther Heidel<sup>a</sup>, Dr. Klaus Höhn<sup>b</sup>, Ulrich Müller<sup>c</sup>, Dr. Peter Schlotter<sup>d</sup>

<sup>a</sup>OSRAM Opto Semiconductor GmbH, Germany, <sup>b</sup>Siemens AG, Germany, <sup>c</sup>OSRAM GmbH, Germany,  
<sup>d</sup>Fraunhofer IAF, Germany

### Abstract

Since several years light emitting diodes are in use to generate white light. Pixels with green, red and blue LED's are arranged to get any coordinate in the CIE - diagram with matched current for each diode. For instance Siemens Opto Semiconductor (OS) now OSRAM Opto Semiconductor offers multi chip LED's (LHGB T676) especially for the application above.

A far better solution for producing white light represents luminescence conversion. The emitted light of blue diodes is used as a primary source for exciting organic or inorganic fluorescent.

By conversion, "Stokes Shift", red, green, yellow and mixed colored light can be generated.

After first studies of Fraunhofer IAF Freiburg Siemens OS selected in cooperation with OSRAM an especially qualified converter, a yellow light emitting phosphor. This phosphor is used since several years for production of fluorescent lamps and can be produced in high quality. The fluorescent is distinguished by high thermic and chemical resistance. Very good spectral characteristics and quantum efficiency of nearly 100% are typical. By additive mixing of color the yellow radiation of the fluorescent and the incomplete absorbed blue light of the LED make the assembly of single-chip-white-LED's near the white color point possible.

In established technology Siemens OS developed a casting resin which contains the fluorescent and his production procedure. Patents are taken out. This casting resin can be used in mass production for assembly of SMT-LED's. The start of ramp up was in 6/98.

Further activities for development of fluorescent for different tendencies near the white color point. By changing doping material and use of new producing methods a shift to the red or green sector of CIE-diagram can be reached. This makes single-chip-white-LED's for common illumination possible. Additional advantages in stability of color and efficiency are to expect by luminescence of UV-light emitting diodes.

**Keywords:** Blue LED, luminescence conversion, fluorescent, casting resin, high volume production of SMT-LED's

### 1. Introduction

To build a full color video screen three basic colors are needed. Red green and blue pixels can be arranged to get any coordinate in the CIE-diagram with matched brightness of each color. Each hue and also white can be generated. For big screens e.g. for a telltale board in a football stage or in open air concerts for one picture point 3 single LED's can be used. Due to the long viewing distance to the onlooker the resolution is not so important. Usually 5mm LED's are applied. Their radiation characteristic is very narrow to reach a high luminous intensity. For indoor applications with only a few meter to the observer a high resolution and high pixel density is necessary. 60000 picture points on one square meter are not unusual. Therefore the 3 colors have to be mounted very narrow. For such applications Siemens OS (Osram OS) offers a so called RGB Multi-TOPLED<sup>®</sup> which is shown in fig.1.

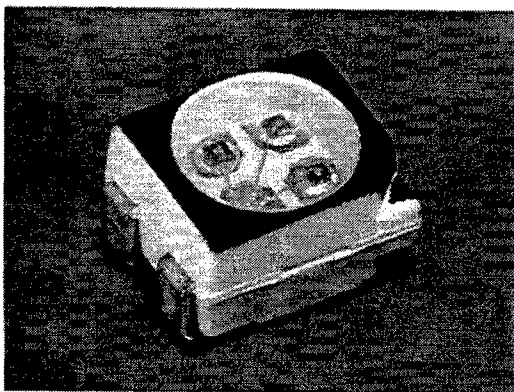


Fig.1: Siemens RGB Multi-TOPLED<sup>®</sup>

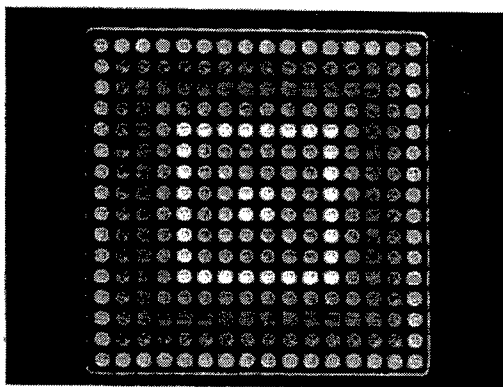


Fig.2: 16 x 16 Full Color Display

This package contains the 3 chips, red, green and blue in a TOPLED® sized package. For contrast enhancement the top surface of the LED can be supplied black. Fig.2. shows a 16 x 16 matrix full color display. Each hue can be reached by tuning of the proper current of the single chips.

For other applications like interior lighting in cars, instruments, courtesy lights, or general illumination only white light is requested.

A far better and simpler solution for production of only white light represents luminescence conversion. The emitted light of a blue diode is used as primary source for exciting organic or inorganic fluorescent which is embedded in the epoxy resin. This technique allows to generate bright white light with only one blue chip. With the production start in June 98 Siemens OS was worldwide one of the first supplier for a single chip white LED in SMT technology. The so called "Single Chip White LED" from Siemens is shown in fig.3.

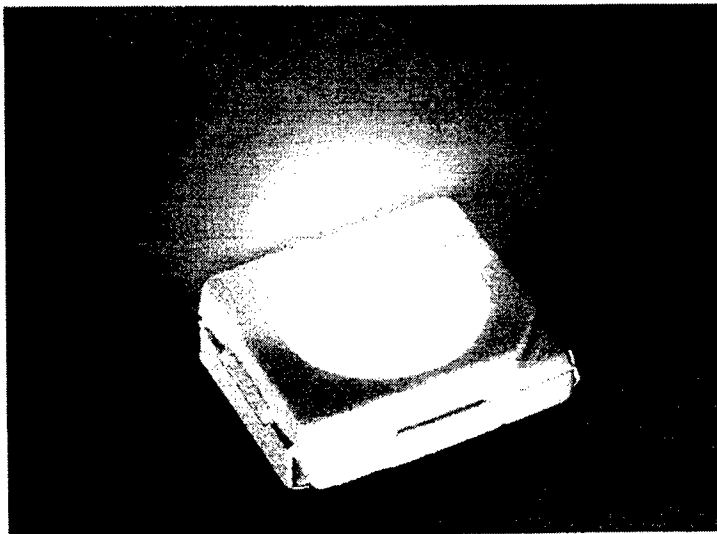


Fig.3: LW T676, the "Single Chip White LED" from Siemens

## 2. Principle of luminescence conversion

For white LED high brightness blue light emitting diodes based on gallium nitride (GaN) or indium gallium nitride (InGaN) are used. This light source works as an efficient pump exciting the luminescent material to higher energy levels. The lifetime of these levels is only a few nanoseconds. The luminescent molecules come back to their ground state by radiation of surplus energy as green, yellow or red light.

The principle of conversion is well-founded in the pronounced "Stokes-Shift" (electron – phonon coupling) between absorption and emission of electromagnetic radiation.

A similar situation is given for fluorescent lamps. By high voltage excited mercury atoms emit UV – light with a wavelength of 253.7nm. The down conversion of the UV-photons to the visible white light happens by an inorganic fluorescent coated on the inner side of the tube.

After first studies of Fraunhofer IAF Freiburg, Siemens OS selected in cooperation with OSRAM GmbH an especially qualified converter, a yellow light emitting phosphor. The luminescent material from OSRAM called L175 is used since several years for the lamp production and can be produced in high quality. The fluorescent is distinguished by high thermal and chemical resistance. Further advantages are the low corrosive potential and the defect free structure of the high pure material. A very good spectral characteristic and quantum efficiency of nearly 100% are typical. The phosphor is produced by a classical melting process out of oxides at a typical temperature of 1600°C.

Fig.4 shows the emission spectra of a GaN and InGaN LED and the absorption spectrum of L175. On the basis of the overlap of the spectra high absorption efficiency of the blue LED light is possible. L175 is a cerium doped yttrium aluminum garnet with the formula  $Y_3Al_5O_{12} : Ce^{3+}(4f^1)$  in short: YAG:Ce.

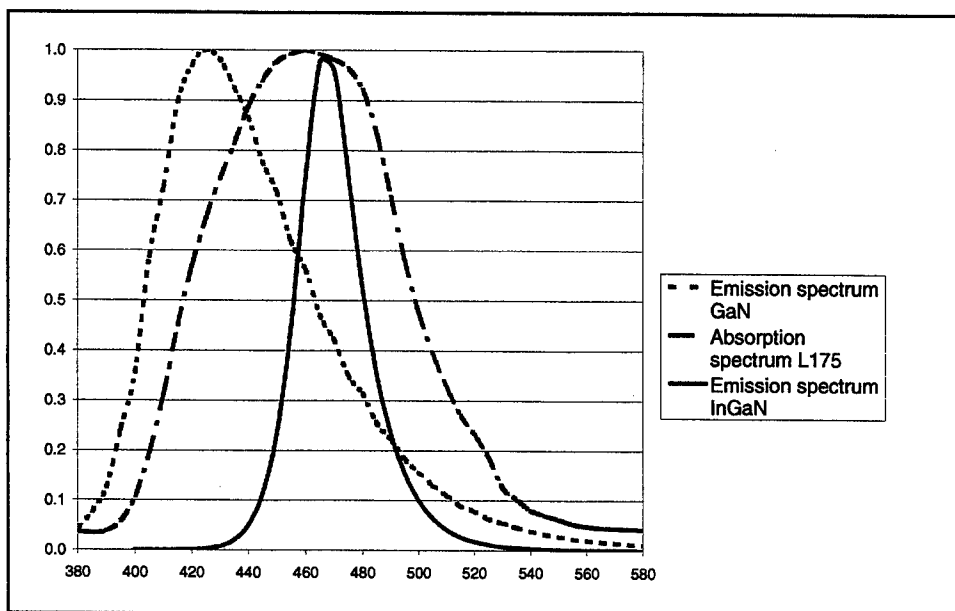


Fig. 4: Emission spectra of GaN and InGaN LED and absorption spectrum of phosphor L175

The blue LED excites the  $\text{Ce}^{3+}$ -ion from  $4f^1$  ground state to the  $5d^1$  level. The down conversion  $5d \rightarrow 4f$  exhibit the Stokes Shift, caused by vibronic coupling of the excited  $5d$  level. A further red shift of the emission is caused by spin orbit splitting of the ground state. The resulting energy level is illustrated in fig.5. The emission spectrum of L175 is shown in fig.6.

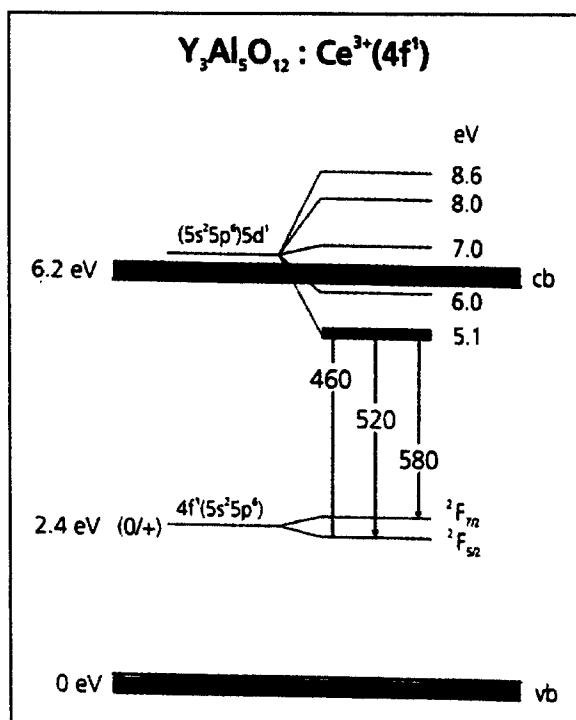


Fig.5: Energy level of cerium doped yttrium aluminum garnet  $\text{Y}_3\text{Al}_5\text{O}_{12} : \text{Ce}^{3+}(4f^1)$

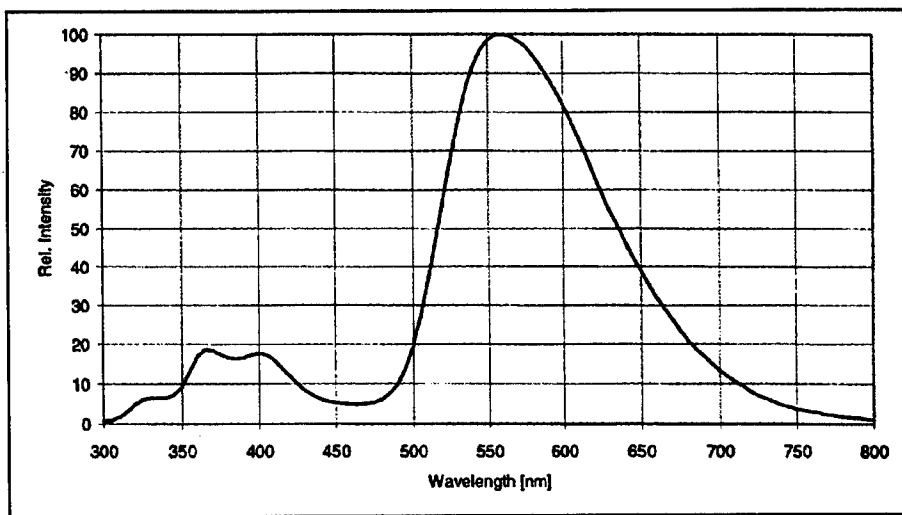


Fig.6: Emission spectrum of L175 (Chromaticity  $x = 0.462$ ,  $y = 0.517$ )

The low emission in the UV-area is not relevant for exciting with blue light. For white LED's the yellow light emitting phosphor is ideally suited, since blue and yellow light are complementary colors, adding to white light after proper additive mixing. A representative spectrum of a single chip white LED you see in fig.7. Because of the wide spectral distribution of the phosphor white LED's present a good color fidelity ( $R_a = 85$ ). An object illuminated with this light can be seen from the human eye nearly correct in color.

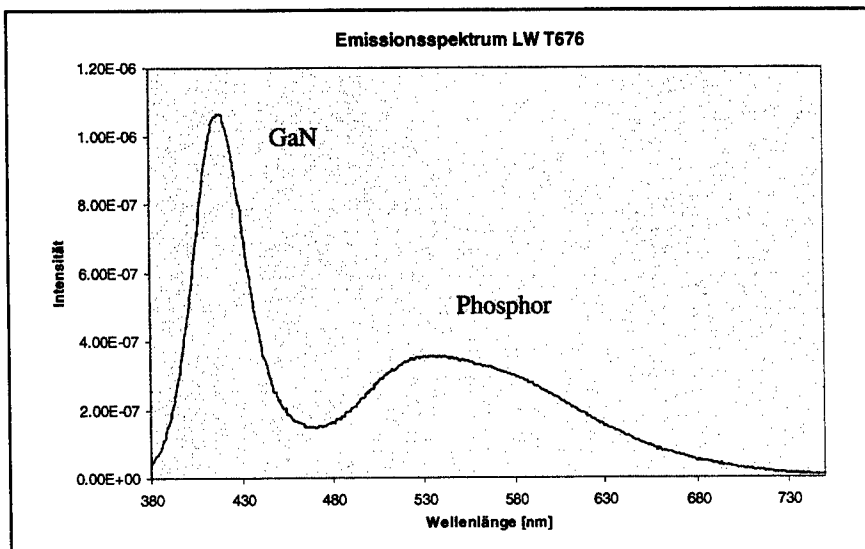


Fig.7: Representative spectrum of a single chip white LED

### 3. Production

For the production of a white LED with luminescence converter different methods can be used. One possibility is to coat the blue chip with a thin high concentrate mixture of resin and converter. A adequate layer can also be brought up like a window on the top surface of the plastic. In this way converter concentration and thickness of the layer have to be very exact to get the wished hue. A further method used also for the production of the Siemens Single Chip White LED is to mix the phosphor in the whole plastic volume. Patents for this method are taken out. Fig.8 shows a cross

section of white TOPLED®. The chip is mounted on a premolded leadframe and embedded in the resin including the fluorescent.

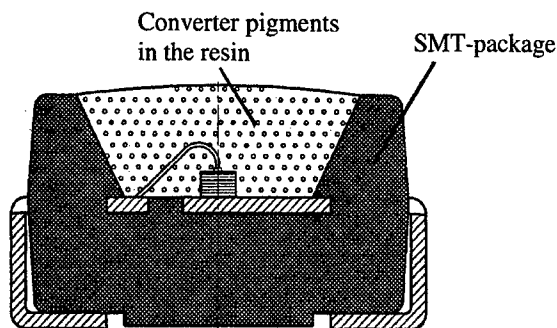


Fig.8: Cross section of white TOPLED®

For the development it was very important to find a resin which has the same quality level as used for the other products, released for automotive applications. A lifetime up to 100000h and cycle stability from  $-40^{\circ}\text{C}$  to  $100^{\circ}\text{C}$  is requested. Faultless operating at  $85^{\circ}\text{C}/85\%$  relative humidity and solderability for different soldering procedures like infrared and through the wave soldering is assumed.

Characteristics of the resin like high transparency and color stability of the emitted light even under high temperature and temperature / humidity stresses have to be considered. Last but not least the possibility for a use in a high volume production with more than a billion parts a year has been given.

For above reasons Siemens OS developed a casting resin including the luminescent material in a established way. Well known epoxy resin base materials were used. In this way technical risks for fabrication of the filled resin were minimized and the quality of the LED product were maximized.

The inorganic phosphor shows a strong abrasive character. Its density is much higher as the density of the of the epoxy resin. For the production of the new casting material problems like abrasion, sedimentation and the wetting of the phosphor with the resin has to be solved. A storage stable dispersion free from agglomerates is to guarantee. Only fine grained fluorescent powder can be used in the resin. Particle sizes below  $20\mu\text{m}$  microns and a main grain diameter  $d_{50} \leq 5\mu\text{m}$  are necessary. In production particle size and agglomerate free morphology is investigated by REM. Only converter powder which meets our targets can be used for fabrication of the resin. Fig.9 shows a picture of the yellow phosphor powder. In fig 10 a REM picture of converter pigments with an enlargement of 5000 is to see.

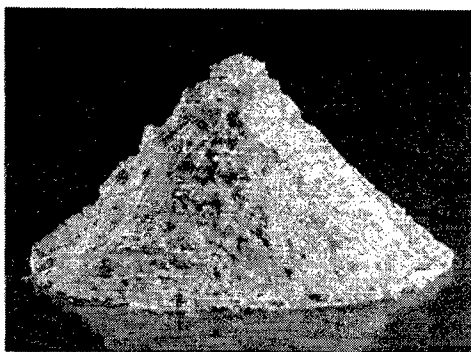


Fig.9: Yellow phoshor powder

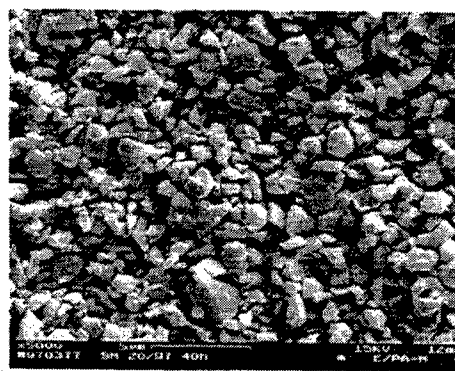


Fig.10: REM picture of converter pigments

For dispersion of the converter normal stainless steel plates can be used. Investigations have shown that at existing dispersion conditions the abrasion is below 13ppm. In this way the converter get not contaminated by the plate material.

The wetting of the pigments to the plastic and the homogenous distribution in the fluid resin is improved by alcoholic prepreparation.



Investigations have shown that the resin mixed with the hardener does not change the behavior after storage of several hours. The viscosity is adjusted to around 1000 mPas. The dispensing system in the production line was adapted to the abrasive character of the converter resin. Also  $T_G$ -measurement after curing showed nearly same results as for other SMT - packages. So the normal SMT- line can be used for the production of the white SMT-LED.

#### 4. Spectral characteristics

The optical spectrum of a white LED was already shown in fig.6. The spectrum is a mixture of the blue radiation of a GaN chip and the yellow radiation of the phosphor L175. The typical CIE coordinates of a LW T676 are  $x = 0.29$  and  $y = 0.31$  equivalent to 7500 K color temperature. The theoretical white point, with an equal distribution of all colors has the xy chromaticity coordinates (0.33,0.33). Fig.11 illustrates the CIE-diagram (DIN 5033) with the blue, green, yellow, red and white area. Also included are the color points of the GaN - chip and the color point of the converter. With different concentrations of the phosphor powder in the resin all different hues in the hatched area can be produced.

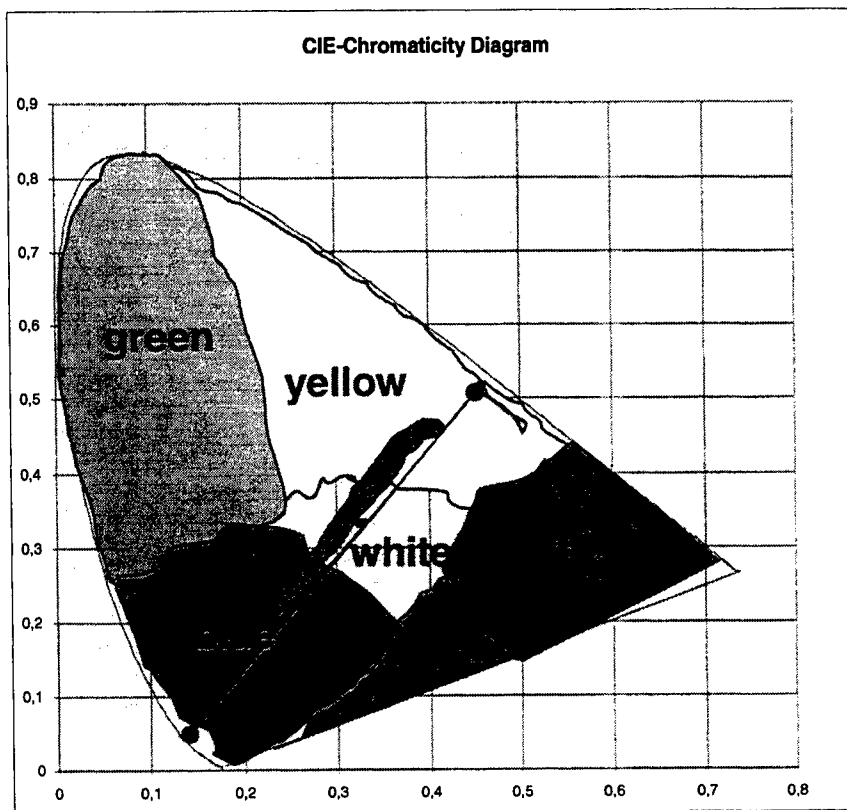


Fig. 11: CIE-diagram with blue, green yellow, red and white area. The hatched zone shows the coordinates reachable by conversion.

In many applications e. g. for backlighting of dashboards or LCD – displays in the automotive area on pcb mounted LED's are covered by a scattering foil or other light guiding materials which can shift the aimed color point. These shifts can be equalized by changing the converter concentration to reach the adapted white color.

The human eye is very sensitive in the white area. Hues with only 0.01 distance in the coordinates can be resolved. Therefore a narrow tolerance of the aimed color point is very important. Previous spectrometer have shown different sensitivity for the blue and yellow-red area and didn't allow to measure with the necessary accuracy. Novel testheads with special filter systems were developed. So narrow tolerances at high speed measurements in a volume production could be reached.

In the same way as the converter concentration the dosed resin volume can shift the xy coordinates in the CIE – diagram. But because the phosphor proportion in the resin is low in comparison to other assembly methods where the chip is only coated with the converter resin the existing dosage accuracy was qualified for the production of the white LED.

## 5. Further activities

With the introduction of InGaN – technology further development of the converter technology was necessary. The usual peak wavelength  $\lambda_{\text{peak}}$  for blue InGaN chips is at 470nm. The peak wavelength for GaN chips is at 430nm. Therefore the absorption behavior of the new phosphor had to be optimized for  $\lambda_{\text{peak}}$  470nm. For better adjustment of the white point an additional red shift in the emission spectrum was aimed.

Fig.12 shows the emission spectrum of the new developed fluorescent KF776 from OSRAM. In comparison to L175 the spectrum is shifted 20nm to longer wavelengths. The maximum of absorption is at 470nm with a quantum efficiency of nearly 100%. This result could be reached by substitution of the cerium doped yttrium aluminum garnet by gadolinium (Gd). The xy- coordinates of the CIE-diagram are  $x = 0.506$  and  $y = 0.488$ . Fig.13 illustrates the CIE-diagram with the color points of a blue InGaN and GaN chip and from the luminescence converter L175 and KF 776. The lines between converter and chip hue symbolize all coordinates in the CIE-diagram which are possible by adequate tuning of the converter pigments in the resin.

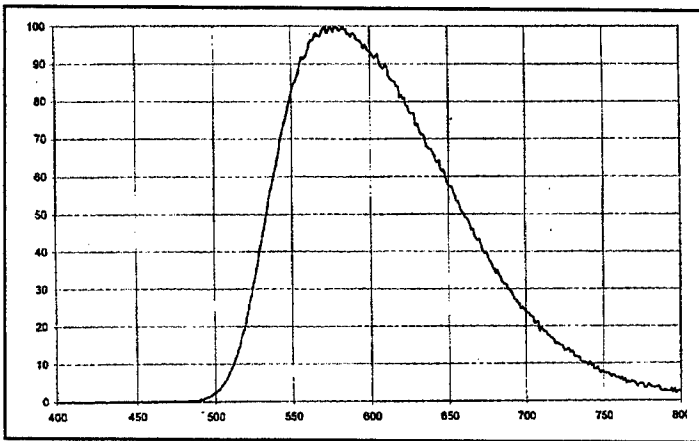


Fig.12: Emission spectrum of the fluorescent KF776 from OSRAM  
Chromaticity:  $x = 0.506$  /  $y = 0.488$

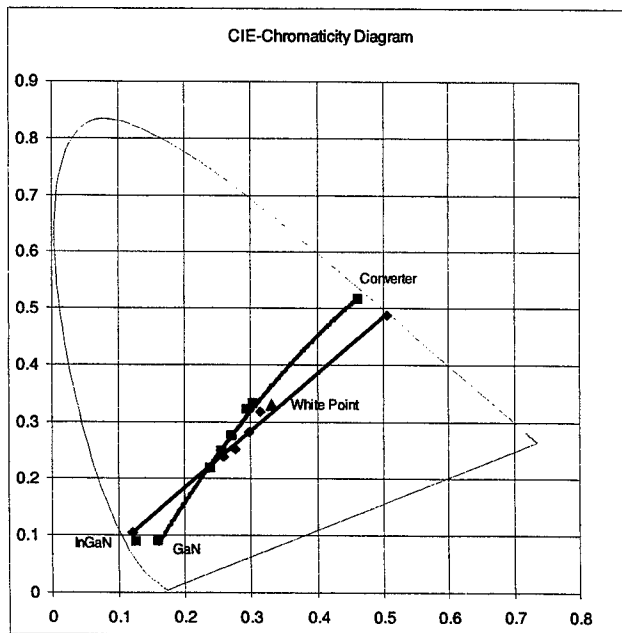


Fig.13: CIE-diagram with the color points of a blue InGaN and GaN chip and the color points of the luminescence converter L175 and KF 776

With the InGaN technology it is possible to shift the wavelengths over a wide range. Theoretical wavelength from UV- to the red - area are possible. Due to the semiconductor structure the wavelength distribution over one wafer is also wider as the distribution over one GaN wafer where the wavelength is relatively fixed due to the acceptor and donator levels.

To reach the certain xy- color coordinates, necessary for the respective application, a narrow wavelength distribution of the blue diodes is very important. In experiments the influence of the blue wavelength on the xy coordinates of the converted light was investigated. Fig 14 and 15 show the results of these experiments. The diagrams show the color coordinate of the bare chip (lower curve) and the coordinate of the casted chip (upper line). The converter concentration was fixed. As already expected from the CIE-diagram the y coordinate is strongly influenced by the blue chip. A nearly linear behavior is recognized. Whereas the influence on the x coordinate is much lower as shown in fig.14.

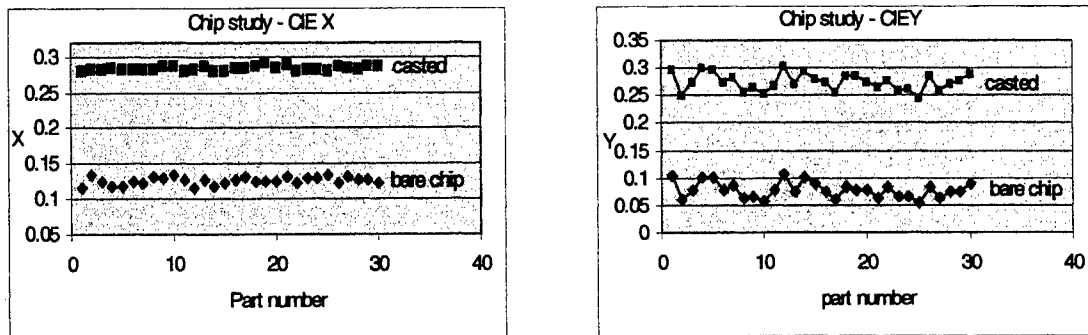


Fig.14/15: Influence of the color coordinates of a bare chip on the coordinates of a casted chip

## 6. Conclusion

Luminescence conversion is a very promising method for production of white LED's. An efficiency of more than 10lm/W is already possible which is higher as the efficiency of a normal incandescent lamp. First volume projects with white LED's for backlighting of dashboard and indicator instruments in the automotive area are running. By supplying more powerful blue diodes more and more incandescent lamps can be replaced by LED products. A further step is the introduction of UV - emitters as a primary light source. By absorption of 100% of the UV - light only the emission spectrum of the fluorescent is responsible for the final LED color coordinates. Wavelength variations of the diode do not longer influence the color point. This technology and further developments to increase the chip brightness make common illumination with LED's possible.

## 7. References

1. Dr. Klaus Höhn, Siemens AG Munich, white lighting single chip luminescence diode, 17.06.98, Munich
2. Alexandra Debray, OSRAM Opto Semiconductor GmbH, Regensburg, Dr. Klaus Höhn, Siemens AG Munich, "Die Beleuchtung von Morgen",
3. OSRAM GmbH, collection of technical datasheets, "Fertigungsleuchtstoffe des Werks Schwabmünchen", 12/1996
4. Siemens AG, Patent: DE 19625622.4, 26.06.1996
5. J. Baur, Fraunhofer IAF Freiburg, presentation, 23.01.1997, Munich
6. J. Baur, P. Schlotter, J. Schneider, Fraunhofer IAF Freiburg, white light emitting diodes, Solid State Physics Vol. 37, 1997
7. F. Wells, Structural Inorganic Chemistry, 4<sup>th</sup> edition, Oxford University Press, Oxford, 1975

# High efficiency top-emitting microcavity light-emitting diodes

P. Royo \*<sup>a</sup>, J. F. Carlin<sup>a</sup>, J. Spicher<sup>a</sup>, R. Stanley<sup>a</sup>, R. Houdré<sup>a</sup>,

V. Bardinal<sup>b</sup>, U. Oesterle<sup>a</sup> and M. Illegems<sup>a</sup>

<sup>a</sup>Institut de micro- et optoélectronique, Département de Physique, Ecole Polytechnique  
Fédérale de Lausanne, CH-1015 Lausanne, Switzerland

<sup>b</sup>LAAS-CNRS, 7 av. du Colonel Roche, F-31077 Toulouse, France

## ABSTRACT

Microcavity light emitting diodes (MCLEDs) present several interesting features compared to conventional LEDs such as narrow linewidth, improved directionality and high efficiency. We report here on MCLEDs with a top emitting geometry. The MCLED layers were grown using molecular beam epitaxy on GaAs substrates. They consist of a 3-period Be-doped distributed Bragg reflector (DBR) centered at 950 nm wavelength, a cavity containing three InGaAs quantum wells and a 15-periods Si-doped DBR. Different values for the wavelength detuning between spontaneous emission line and Fabry-Perot cavity mode were explored, between -40 nm and +10 nm. Devices sizes ranged from  $420 \times 420 \mu\text{m}^2$  to  $22 \times 22 \mu\text{m}^2$ . As expected from simulations, the higher efficiencies are obtained when the detuning is in the -20 to 0 nm range. The devices exhibit then up to 10% external quantum efficiency, measured for a  $62^\circ$  collection half-angle. After correction for the surface shadowing due to the grid p-contact, the efficiency increases to 14% and is practically independent of device size.

**Keywords:** top emission microcavity light emitting device

## 1. INTRODUCTION

There is a growing interest in microcavity light emitting diodes (MCLEDs) as they present several advantages compared to conventional LEDs such as narrow linewidth, improved directionality, high brightness, and high efficiency<sup>1</sup>. These enhancements result essentially from the ability to tailor the emission pattern and to redirect the modes into the escape cone defined by the dielectric interface between the device and the outside medium (usually air). These features translate into improved performance and lower overall fabrication costs compared to other types of LEDs. High efficiencies can also be obtained from non-microcavity LEDs by using a transparent substrate coated with a metal back reflector and by collecting the light from all six facets of the LED<sup>2</sup>. This approach requires the growth of a thick epitaxial high-bandgap layer or of epitaxial film lift-off and wafer fusion steps, and is only feasible for individually packaged devices, excluding all forms of integration. Other approaches, based on nanotexturing the surface of the LED deposited by the lift-off and bonding technique on a metal reflector, have demonstrated external efficiencies of up to 30 %, which represents the highest values reported to date<sup>3</sup>. However these have not yet found large-scale application because of the non-standard technology steps involved. In the case of a MCLED, the highest external quantum efficiencies reported stand at 22% for large-area substrate-emitting diodes<sup>4</sup>. The fact that the light is emitted from a single facet leads to inherently higher brightness, reduces the packaging

constraints, and allows the monolithic integration of MCLEDs with other electronic components or in the form of surface emitting diode arrays. Highest efficiency MCLEDs have only been reported for the case of substrate emission geometry, which limits the wavelengths to those where the substrate is transparent. We report here results on MBE-grown top-emitting MCLEDs (TE-MCLEDs) realized in the Ga(In)As/AlAs materials system and emitting between 920 nm and 960 nm, but the extension to shorter wavelengths more compatible with Si detectors is straightforward.

## 2. OPTICAL DESIGN OF THE TE-MCLED STRUCTURES

### 2.1. DESIGN PROCEDURE

The basic layers sequence of the TE-MCLEDs is shown on figure 1. Light is generated by radiative recombination of carriers injected into three 7.5 nm thick strained GaInAs quantum wells (QWs) situated at the antinode positions of a  $\lambda$ -size Ga<sub>0.9</sub>Al<sub>0.1</sub>As planar Fabry-Perot cavity. The cavity is surrounded by top and bottom distributed Bragg reflectors (DBRs) centered at  $\lambda_{FP}$ . The top DBR is doped with Beryllium and has three GaAs/AlAs pairs, the bottom DBR is Si-doped and is made of 15.5 pairs. 150 Å-thick Ga<sub>0.5</sub>Al<sub>0.5</sub>As layers are inserted at each GaAs/AlAs interface to reduce the series resistance associated with the band discontinuity at interfaces.

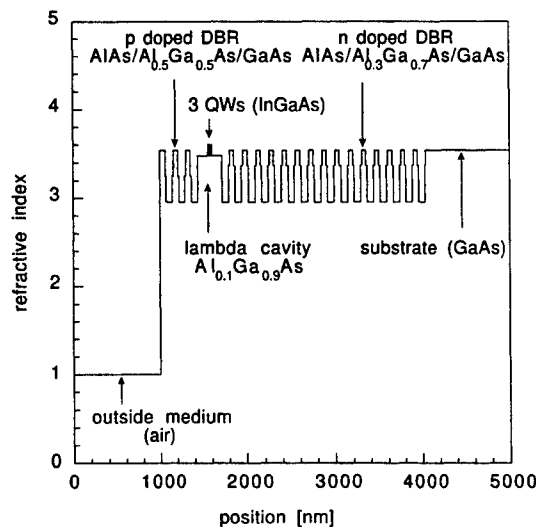


Figure 1: Structure of the MCLED

We used a program based on the model proposed by H. Benisti et al.<sup>5</sup> to calculate the optical characteristics of this structure. With this formalism the source is described by a distribution of oscillating dipoles. In a first step the parameters of interest (extraction efficiency, patterns of emission) were calculated for a monochromatic source. These results were then averaged to describe the emission of a broad spectrum source. The source spectrum shape was taken gaussian with a full width at half maximum (FWHM)  $\sigma$  of 40 nm in order to take into account for the experimental spectra of the QW layers. Indeed, room temperature electroluminescence spectra measurements on test LEDs having identical active QWs showed 20 to 40 nm

FWHM emission lines for current injection below  $100 \text{ A/cm}^2$  and  $\sigma$  increased to over  $70 \text{ nm}$  for current densities higher than  $500 \text{ A/cm}^2$ . Thus  $\sigma = 40 \text{ nm}$  in the simulations is a good assumption for the TE-MCLEDs driven at a typical current density of a few hundred  $\text{A/cm}^2$ . The TE-MCLED structure was designed in order to maximize light extraction efficiency (LEE). LEE is defined as the amount of optical power emitted by the source which can be extracted outside the structure within a given collection half-angle  $\alpha$ ; this coefficient must be multiplied by the internal quantum efficiency of the InGaAs QWs to get the external quantum efficiency. Depending on the device application LEE should be optimized for different collection half-angles: if the goal is to extract maximum light without geometrical constraints LEE must be optimized for  $\alpha = 90^\circ$ , while for applications such as direct coupling of light into optical fibers,  $\alpha$  should equal the fiber acceptance cone, around  $15^\circ$  for silica fibers and  $45^\circ$  for plastic optical fibers. The simulations showed that LEE depends mainly on the wavelength detuning,  $\Delta\lambda = \lambda_{\text{QW}} - \lambda_{\text{FP}}$ , between the QW emission peak and the Fabry-Perot mode and on the back and front mirrors reflectivities (numbers of DBR pairs). The optimization of the DBR number of pairs is described elsewhere<sup>6</sup>. The results gave the structure presented above (figure 1).

## 2.2. DETUNING OPTIMIZATION

The light extraction efficiency was calculated with respect to the detuning for the structure presented on the figure 1. We assumed that the Fabry-Perot mode wavelength was  $960 \text{ nm}$  and we changed the QW emission peak to vary the detuning.

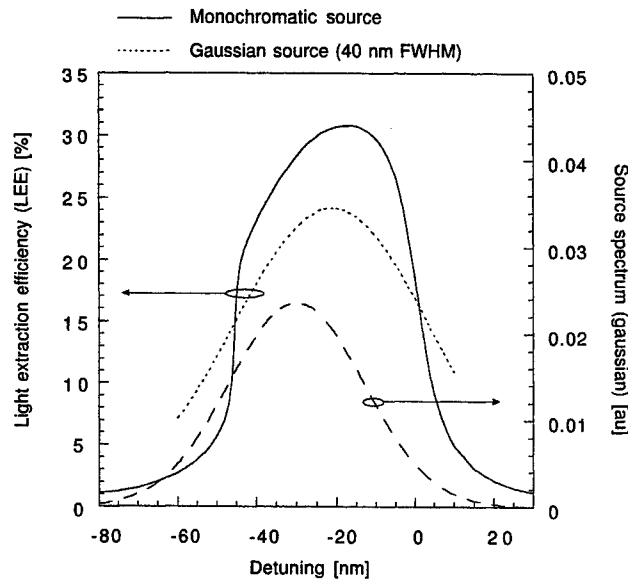
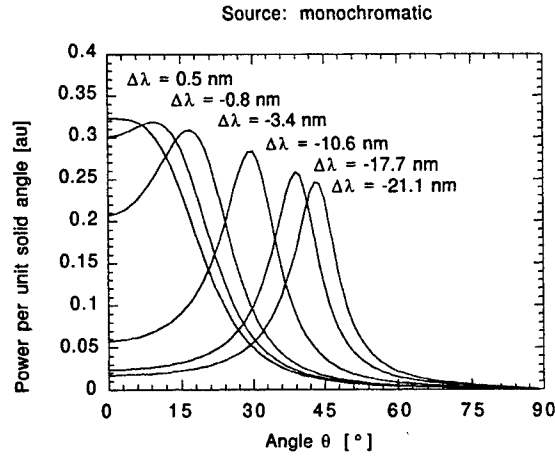


Figure 2: Light extraction efficiency (monochromatic and broad spectrum sources)

The collection half-angle  $\alpha$  was set to  $90^\circ$  (figure 2) meaning that all the light emitted outside the structure is supposed to be collected. We first calculated the LEE for a monochromatic source which gave us a maximum of extraction of 30.8% for a negative detuning of  $-17.2 \text{ nm}$ . Using a gaussian function which was shifted over the detuning axis, we averaged the previous LEE curve to get a maximum of extraction of 24.1% corresponding to a detuning of  $-21.1 \text{ nm}$ . The effect of the

averaging is to modify the optimal detuning value and to lower the extraction efficiency. The narrower is the source linewidth and the higher is the extraction efficiency. The dependence of the light extraction efficiency with the detuning comes mainly from a mode redirection effect as explained in details elsewhere<sup>7</sup>. We can illustrate this effect by plotting the emission patterns for various detuning values in the case of a monochromatic source (figure 3) or in the case of a gaussian spectrum (figure 4).



**Figure 3:** Patterns of emission for various detuning values (monochromatic source)

The angle  $\theta$  is defined as the angle between the growth axis and the direction of observation. For emission wavelengths lower than the cavity mode (negative detuning), the maximum of the emission occurs for a direction different from the normal. The angle corresponding to the maximum of emission increases when the detuning becomes more and more negative. For a positive detuning we get a single lobe centered around the normal direction, but the increase of the source directionality is at the expense of the light extraction efficiency which decreases. A trade-off thus exists between directionality and efficiency.

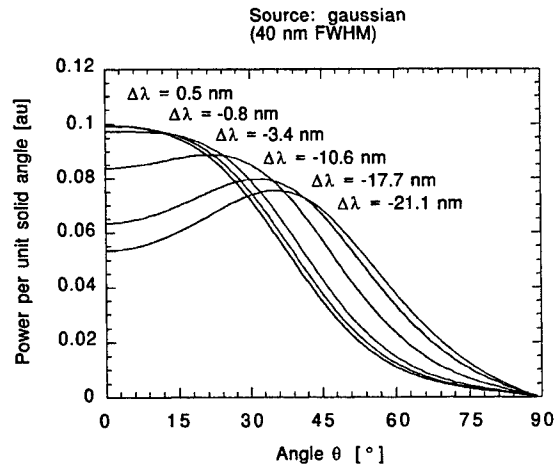


**Figure 4:** Patterns of emission for various detuning values (broad spectrum source)

### 3. EXPERIMENTAL RESULTS

#### 3.1. DEVICE PROCESSING

TE-MCLED layers as described in figure 1 were grown on GaAs substrates by conventional MBE using standard Al, Ga, In and valved-cracker  $\text{As}_2$  sources. InGaAs QWs indium content was varied between 12% and 18% in order to explore detuning values from -30 to +10 nm; detuning was checked after growth by comparing the reflectivity curve with the photoluminescence spectrum taken from a cleaved edge of samples. Samples were then processed into devices with sizes ranging from  $420 \times 420 \mu\text{m}^2$  to  $24 \times 24 \mu\text{m}^2$  by conventional photolithography and wet-etching procedures. The current was injected through an alloyed Ti-Pt-Au grid connected to a  $50 \times 50 \mu\text{m}^2$  contact pad; Ni-Ge-Au contacts were alloyed on the top of the n-DBR and a polyimide planarization layer provided electrical insulation between the contact pads and the bonding leads (figure 5).

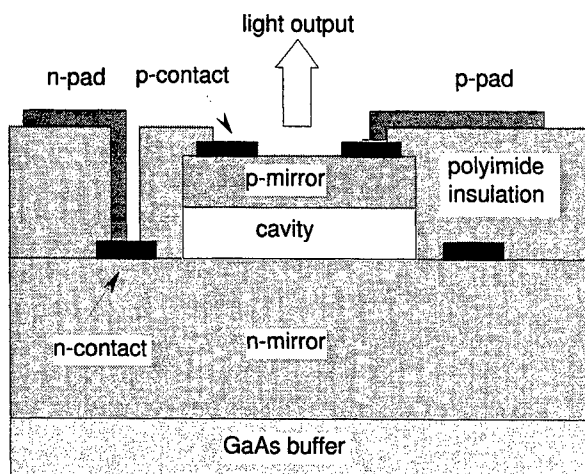
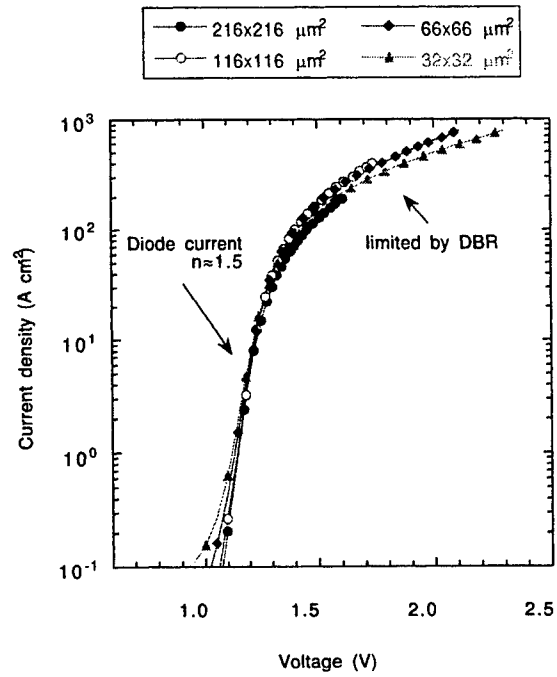


Figure 5: Processed structure

#### 3.2. CURRENT-VOLTAGE CURVES

The current density versus voltage curves for the different device sizes are presented on the figure 6. The turn-on voltage defined here for a current density of  $100 \text{ mA/cm}^2$  lies below 1.1 V for all device sizes. For current injection below  $100 \text{ A/cm}^2$  we measure an exponential dependence with an ideality coefficient of 1.5. At higher injection, the current is limited by the series resistance of the p-DBR mirror which is of the order of  $10^{-3} \Omega\text{cm}^2$ . Under the typical driving current density of  $100 \text{ A/cm}^2$  the voltage drop is 1.3 V so the external quantum efficiency and wall-plug efficiency are quasi-equal.





**Figure 6:** Current-voltage characteristics for several device sizes

### 3.3. OPTICAL EFFICIENCY OVER LARGE COLLECTION ANGLE

A  $10 \times 10 \text{ mm}^2$  calibrated Si photodiode was positioned at 3 mm of the TE-MCLEDs surface for light output power measurements under a large ( $62^\circ$ ) collection half-angle. The light output power versus current (L-I) curve of a  $420 \times 420 \text{ }\mu\text{m}^2$  device is presented on figure 7. The detuning is -18 nm on this sample. A 10.2 % external quantum efficiency was obtained at a current density of  $10 \text{ A/cm}^2$ . For smaller diodes, we find very similar L-I curves; however, the efficiency is progressively reduced and the maximum efficiency shifts to higher current density as the diode size is reduced, for instance to 4.1% at  $200 \text{ A/cm}^2$  for the  $24 \times 24 \text{ }\mu\text{m}^2$  device. The decrease in efficiency for smaller devices is mainly due to the fact that the contact grid shadows an increasing fraction of the emitted light. We verify on figure 8 that the external quantum efficiency increases linearly with the ratio of the uncovered surface to the total device area. An extrapolation of this linear relationship yields an external efficiency, corrected for the p-contact shadowing, of 13 % for devices with a -18 nm detuning; The improvement of the p-contact processing, using for instance transparent contacts, should bring the experimental results close to this extrapolated value. We mention that photon recycling does not appear to play a significant role in these devices as the efficiencies appear to be practically independent of device size after correcting for contact shadowing.

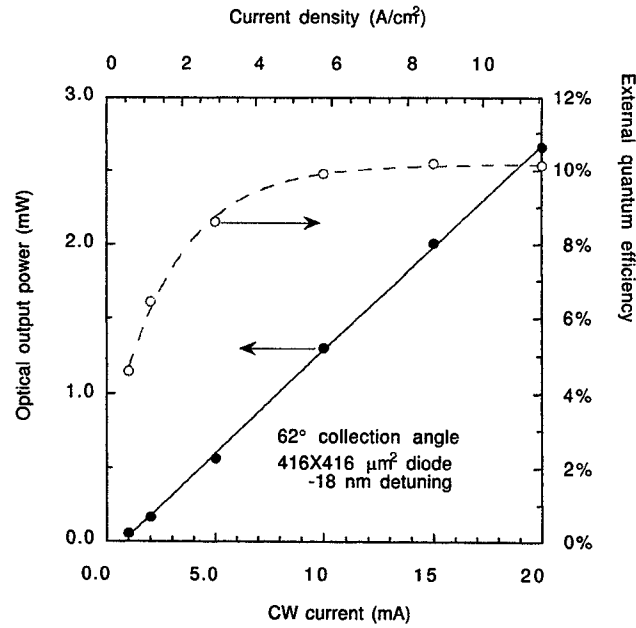


**Figure 7:** Emitted power and corresponding external quantum efficiency of a large diode with a -18 nm detuning

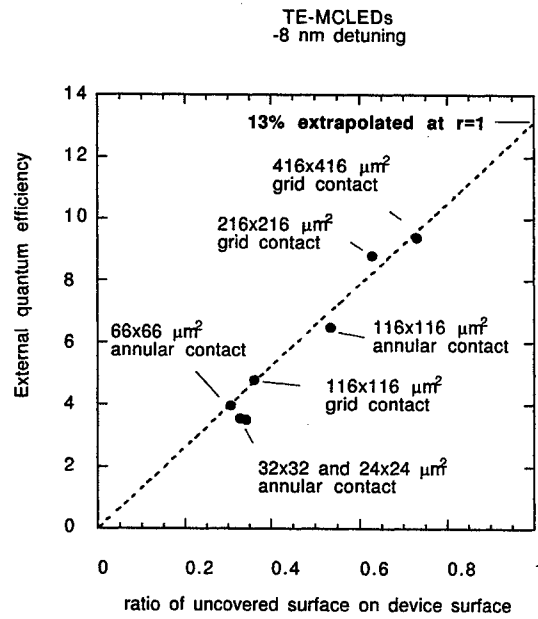


**Figure 8:** Effect of the shadowing on the external quantum efficiency

The external efficiencies corrected for contact shadowing for devices processed from different growth runs are displayed in figure 9 as a function of the detuning and compared with the simulated light extraction efficiencies calculated assuming a

100 % internal quantum efficiency. The experimental curve is in quite good agreement with the simulations and confirms the optimum detuning around -18 nm. In addition, we can estimate from this figure the internal quantum efficiency of the QW emission by taking the ratio between the external quantum efficiency (corrected for shadowing) and the light extraction efficiency. The resulting value of 70 % gives a good indication of the quality of the MBE-grown material. We estimate that this value is limited by carrier diffusion out of the quantum wells, rather than by the presence of non-radiative recombination channels, and that further improvement is possible by a more careful design of the quantum well environment.

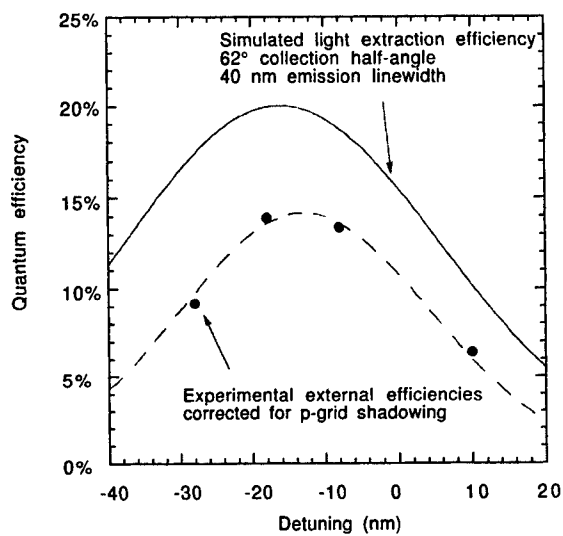


**Figure 9:** Comparison of the measured and simulated external quantum efficiencies for various detuning values

#### 4. CONCLUSION

We designed and fabricated high efficiency SE-MCLEDs, efficient for large angle emission. We showed that the experimental external efficiencies are in very good agreement with the simulated light extraction efficiency if we take into account the p-contact shadowing and a 70% internal quantum efficiency.

#### ACKNOWLEDGMENTS

This work was carried out in the framework of the ESPRIT-Monolith project and has been supported by the Swiss Federal Office for Education and Science.

## REFERENCES

1. E. F. Schubert, Y. H. Wang, A. Y. Cho, L. W. Tu, G. J. Zydzik, "Resonant cavity light-emitting diode", Appl. Phys. Lett., vol. 60, no. 8, pp. 921-923, 1992.
2. M. G. Craford, "Commercial light emitting diode technology: Status, trends and possible future performances", in Microcavities and Photonic Bandgaps: Physics and Application, J. Rarity and C. Weisbuch, pp. 323-332, Eds. Dordrecht, The Netherlands: Kluwer, 1996.
3. I. Schnitzer, E. Yablonovitch, C. Caneau, T. J. Gmitter, and A. Scherer, "30-percent external quantum efficiency from surface textured, thin-film light-emitting-diodes", Appl. Phys. Lett., vol. 63, pp. 2174-2176, 1993.
4. J. Blondelle, H. De Neve, G. Borghs, P. Vandaele, P. Demeester, and R. Baets, "High efficiency (>20%) microcavity LED's", in IEE Colloquium on Semiconductor Optical Microcavity Devices and Photonic Bandgaps, London, U. K., 1996.
5. H. Benisty, M. Mayer, and R. Stanley, "A method of source terms for dipole emission modification in modes of arbitrary planar structures", J. Opt. Soc. Amer. A, vol. 15, pp. 1192-1201, 1998.
6. J.F. Carlin, P. Royo, R. Stanley, R. Houdre, J. Spicher, U. Oesterle and M. Ilegems, unpublished.
7. H. Benisty, H. De Neve, and C. Weisbuch, "Impact of Planar Microcavity Effects on Light Extraction", IEEE Journal of Quantum Electronics, vol. 34, no. 9, pp. 1612-1643, 1998.

---

\* Correspondence: Email: royo@imo.dp.epfl.ch; Telephone: +41 (21) 693 34 46; Fax: +41 (21) 693 54 90

# 16.8 % external quantum efficiency from a planar LED

C. Dill<sup>\*</sup>, R. P. Stanley, U. Oesterle, M. Illegems

Institut de micro- et optoélectronique, Département de Physique, Ecole Polytechnique  
Fédérale de Lausanne, CH-1015 Lausanne, Switzerland

## ABSTRACT

Efficient, cheap, and simple, LEDs are used in many applications and make up the bulk of the opto-electronic component market. Due to the small critical angle at the semiconductor-air interface, relatively little light escapes per facet. The conventional route is to collect light from all six facets and redirect it, using external reflectors into a useful direction. While this increases external quantum efficiency it does little to increase brightness. In the last few years the microcavity approach has been used to persuade the light to leave by just one facet, thus increasing the brightness considerably. Although remarkable efficiencies have been achieved, microcavity LEDs (MCLEDs) have yet to surpass conventional LEDs.

We present here a single mirror LED (SMLED), grown by MBE, which falls between the conventional LED and the planar MCLED. The top mirror is a non-alloyed Au layer deposited on a highly doped GaAs phase-match-layer. This is followed by a single Bragg pair of GaAs/Al(0.6)Ga(0.4)As p-doped. The active region is comprised of one InGaAs 7 nm wide QW embedded in a lambda thickness of Al<sub>0.1</sub>Ga<sub>0.9</sub>As. On the substrate side carrier confinement is given by a  $\lambda/2$  AlAs layer n-doped on an n<sup>+</sup>-GaAs substrate.

The emission reflected by the p-side mirror interferes constructively with the emission through the substrate, giving a 4-fold increase in power per facet. The actual device performance is 16.8 % external quantum efficiency and this exceeds expectations and can be accounted for by significant photon recycling.

**Keywords:** microcavity, substrate emitting, planar LED, photon recycling, high efficiency

## 1. INTRODUCTION

There is a great interest for vertical light emitters, as laser diodes and light emitting diodes (LEDs), in the near infrared for many applications in optoelectronic systems. Light emitting diodes are used in displays, as indicator lights, as emitters for remote free-space functions, and to a lesser extent, for short distance communication and optical interconnects. The interest in LEDs for these applications lies in their simple design and low fabrication costs. In addition, LEDs are inherently more reliable than laser diodes, have a lower temperature sensitivity, operate without threshold and are better in terms of eye-safety.

---

<sup>\*</sup> Correspondence: Email: dill@dpmail.epfl.ch; Telephone: +41-21-693 44 22; Fax: +41-21-693 44 22

Despite these advantages, light emitting diodes suffer from some major limitations such as the poor extraction efficiency of light (typically below 2% per facet for a simple planar design), the wide spectral width, and the large divergence of the output beam.

Apart from the external methods to improve the LED's light extraction efficiency, such as the use of transparent substrates and external mirrors to collect the light emerging from all sides<sup>1</sup>, a second avenue for the improvement of the LED performance is to control the internal spontaneous emission process in order to direct the light within the "escape cone" defined by the critical angle for total internal reflection at the interface between the semiconductor and the outside medium.

In the last 5 to 6 years, the concept of microcavity light emitting diodes (MCLED) has been used<sup>2</sup> to overcome some of the limitations of conventional LEDs. The presence of the microcavity modifies the spontaneous emission characteristics of the source and can lead to narrower linewidths, improved directionality, and higher efficiencies<sup>3</sup>. The fact that the light is emitted from a single facet leads to an inherently higher brightness, reduces the packaging constraints, and allows the monolithic integration of these diodes with other electronic devices.

However, one drawback of the MCLED is the fact that its device performance is sensitive to the operating conditions, since its light extraction is critically dependent on spectral overlap between the spontaneous emission spectrum from the active layer and the cavity resonance<sup>4</sup>, and both change with the injected current. In this paper we present an LED based on the same principle of spontaneous emission control as the MCLED, the single mirror LED (SMLED). Instead of a cavity the emission characteristic is modified by only one closely spaced mirror. The optical performance of this device is fairly independent on operating conditions, while achieving a high efficiency for emission from a single facet which represents a clear advantage for a number of industrial applications.

## 2. DESIGN AND FABRICATION

### 2.1. Design

The vertical layer sequence of the SMLED is shown in Figure 1. Light is generated by radiative recombination of carriers injected into a strained InGaAs quantum well (QW) embedded in the center of an undoped  $\lambda$ -cavity ( $\text{Al}_{0.1}\text{Ga}_{0.9}\text{As}$ ). To provide a better carrier confinement and to improve the interface quality, the  $\text{In}_{0.17}\text{Ga}_{0.83}\text{As}$  QW with a thickness of 7 nm is separated by 2 nm GaAs spacers from the  $\text{Al}_{0.1}\text{Ga}_{0.9}\text{As}$ .

The undoped region is surrounded by a top mirror, consisting of one  $\lambda/4$  mirror pair of  $\text{Al}_{0.6}\text{Ga}_{0.4}\text{As}/\text{GaAs}$ , a phase match layer and a gold mirror, is added. The  $\text{Al}_{0.6}\text{Ga}_{0.4}\text{As}$  layer and GaAs layer have thicknesses of 76 nm and 68 nm, respectively, and both are p-(Be)-doped at a level of  $5 \cdot 10^{18} \text{ cm}^{-3}$ . The GaAs phase-match-layer has a thickness of 45 nm. The first 36 nm is doped  $5 \cdot 10^{18} \text{ cm}^{-3}$ , whereas the upper part of this layer - the cap - is doped with an increasing step profile. An intermediate step with a thickness of 3 nm is doped  $1.4 \cdot 10^{19} \text{ cm}^{-3}$ ; the last part of the cap, i.e. 6 nm is doped  $5 \cdot 10^{19} \text{ cm}^{-3}$  to allow non-alloyed ohmic contacting.

Between the  $n^+$ -GaAs-substrate, n-(Si)-doped at a level of  $2 \cdot 10^{18} \text{ cm}^{-3}$ , and the undoped region a  $\lambda/2$  AlAs layer (n-(Si)-doped:  $2 \cdot 10^{18} \text{ cm}^{-3}$ ) is inserted which serves as a barrier for carrier confinement, while keeping the structure optically transparent.

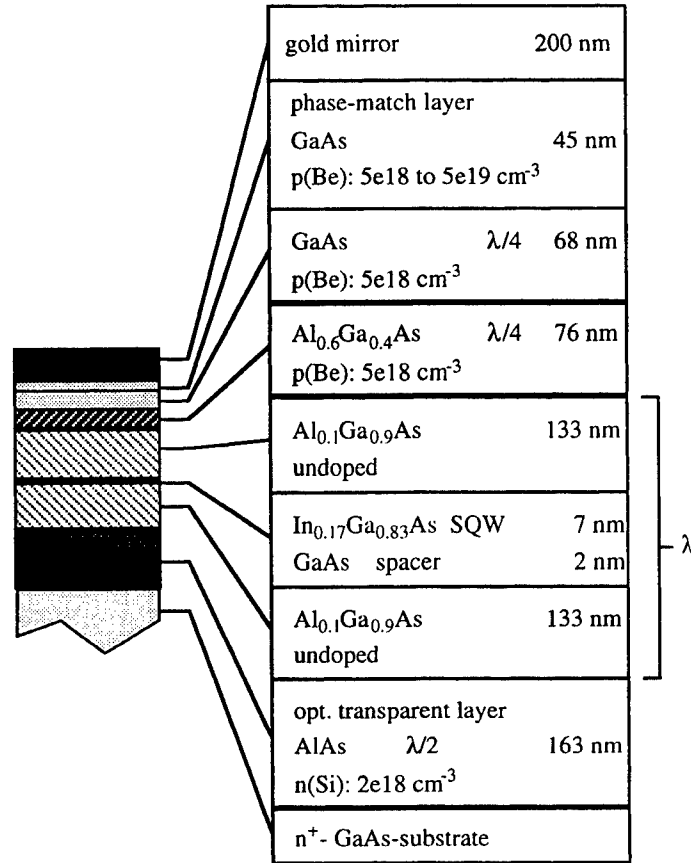


Figure 1: Vertical structure of the SMLED

## 2.2. Simulation of the emission properties

We used a program based on the model proposed by H. Benisti et al.<sup>5</sup> to compute the emission properties of this structure.

The model is based on the plane wave expansion of an electrical dipole emitter inside a multilayer structure, assuming that the recombination of electrons and holes inside a semiconductor is an electrical dipole transition.

The extraction efficiency and the angular emission pattern were simulated as a function of the spectral position of the emitting source. The values are calculated for a monochromatic source emitting into air without anti-reflection coating, neglecting recycling effects and are not corrected for substrate absorption.

Figure 2 shows that the efficiency is fairly wavelength independent over a wide spectral range. The calculated efficiency is greater than 7 % over a spectral range of more than 100 nm. Since the spectral peak position of the source shifts with injection level, this means essentially that the optical performance of the device is expected to be nearly independent on the injected current. Figure 3 shows the calculated radiation pattern for different wavelengths as a function of the angle between the growth axis and the direction of observation. The emission profiles are large and similar for the three wavelengths, showing maximum emission in the normal direction.

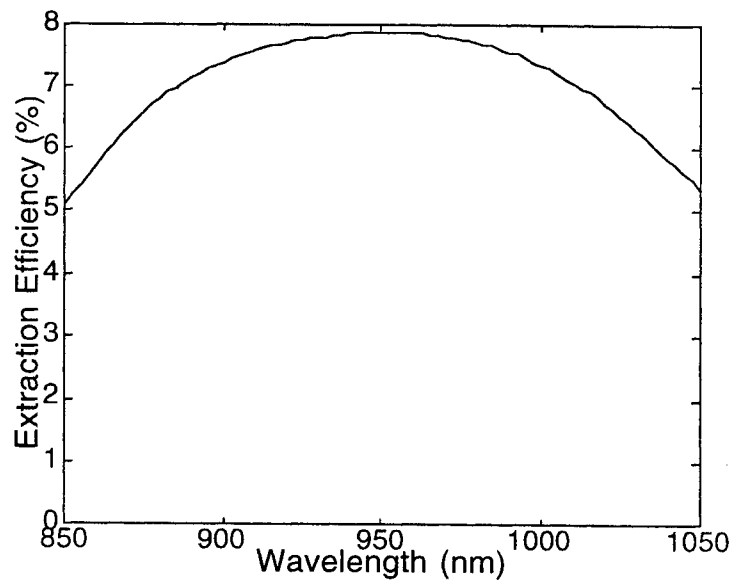


Figure 2: Calculated light extraction efficiency (monochromatic source)

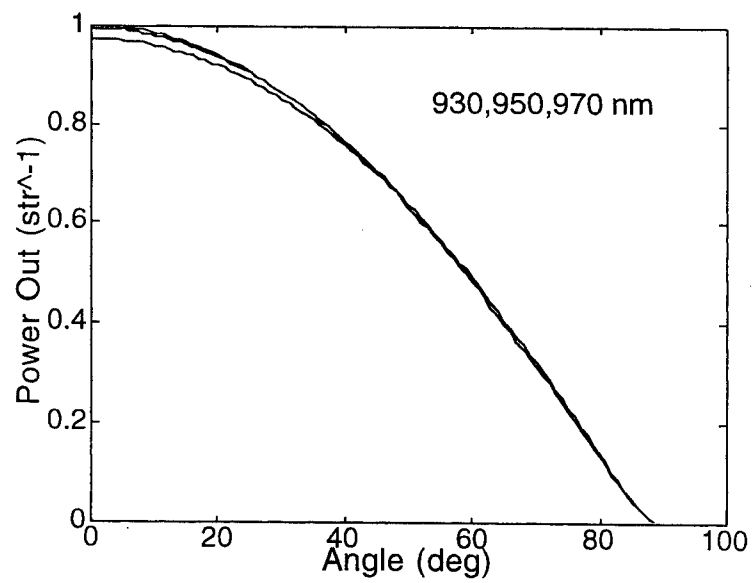


Figure 3: Calculated angular emission pattern for different wavelengths (monochromatic source)



### 2.3. Devices processing

The diodes are prepared using standard lithography and wet-chemical etching technique. In the first process step a large mesa is defined with standard photoresist and etched down into the  $n^+$ -substrate. The metals for the bottom ohmic n-contact (Ni/Ge/Au) are deposited by e-beam evaporation and alloyed. The gold p-contact acts both as a metallic mirror and as an ohmic contact. In order to maintain its high reflectivity the p-contact is non-alloyed. These non-alloyed contacts fabricated on the  $1 \cdot 10^{20} \text{ cm}^{-3}$  p-doped layer have a specific resistance of  $5 \cdot 10^{-5} \Omega \text{ cm}^2$ . Finally the mesas are etched down around the p-contact dots (50 to 400  $\mu\text{m}$  diameter) into the active region, to prevent leakage current across the p-i-n-junction perimeter. The substrate is thinned down to 60  $\mu\text{m}$  to reduce absorption losses for substrate emission. Finally the substrate side is anti-reflection coated.

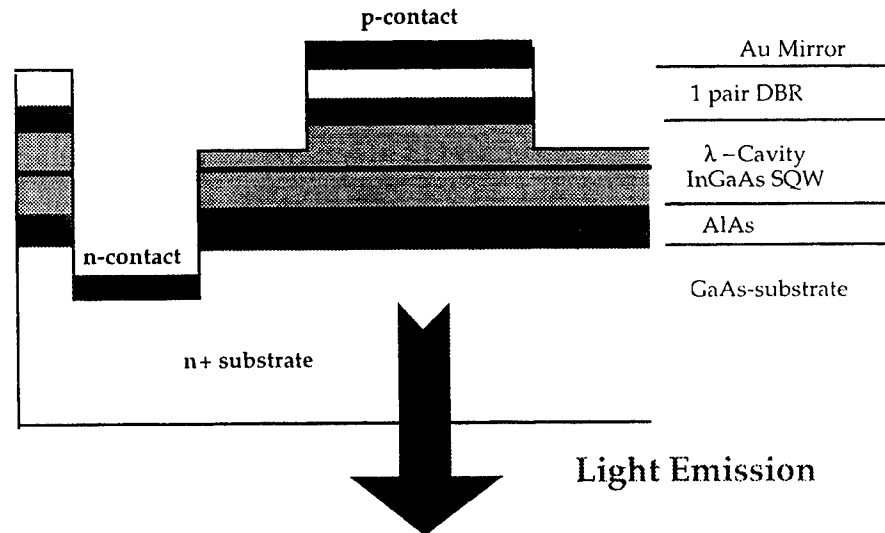


Figure 4: Processed structure

## 3. EXPERIMENTAL RESULTS

### 3.1. Voltage-Current-Characteristic

Figure 5 shows the voltage versus current (V-I) characteristic of diodes with different sizes in the forward bias region. The largest diode has a turn-on-voltage, defined here for a current of 1 mA, of 1.1 V, a voltage of 1.3 V at a current of 100 mA and a differential resistance of less than 1  $\Omega$  at 100 mA. With decreasing diameter the turn-on voltage increases slightly and the differential resistance increases from 0.5  $\Omega$  at 100 mA for the 400  $\mu\text{m}$  device to 1.5  $\Omega$  for the 50  $\mu\text{m}$  device. For the 400  $\mu\text{m}$  diode, a series resistance  $R_s$  of 0.4  $\Omega$  was determined in a differential measurement. At current density injection

below  $100 \text{ A/cm}^2$  we measure an exponential dependence with an ideality factor of 1.5. For the smaller devices, a slight roll over at high injection level, indicating the increasing influence of ohmic resistance, can be observed.

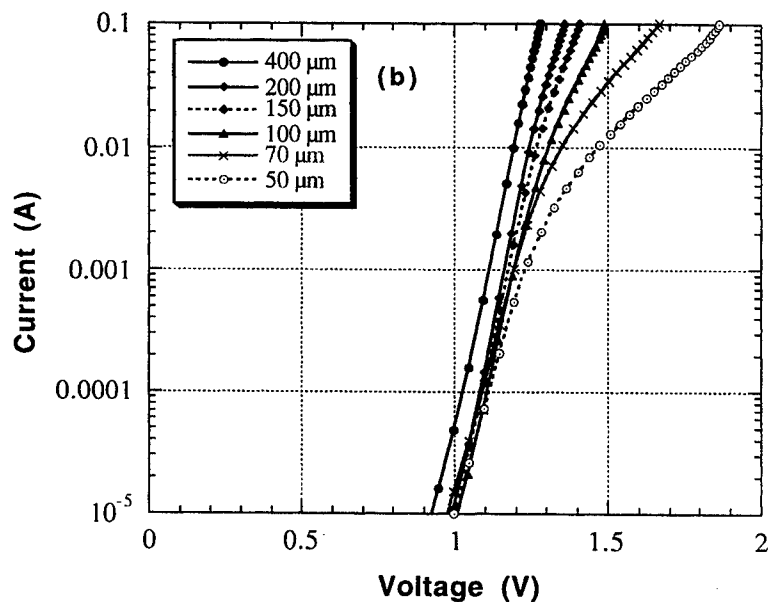


Figure 5: Voltage-current characteristics for several device sizes

### 3.2. Optical Power

In order to determine the total light output and the overall external efficiency of the SMLDs we use the measurement scheme, as shown in Figure 6. The samples are placed on a copper plate, into which a highly polished conic hole with a  $60^\circ$  full angle was drilled. By coating this cone with a high reflection gold film, emission emerging at all angles up to  $180^\circ$  is captured and directed into the integrating sphere with a single reflection.

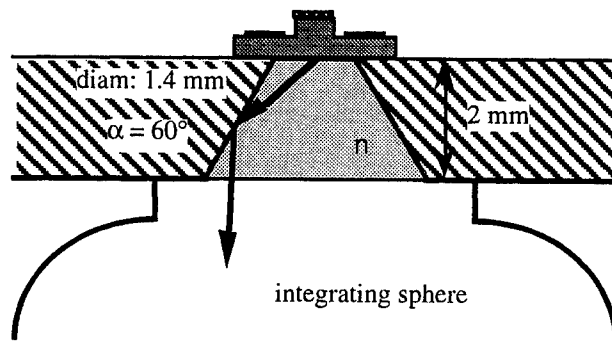


Figure 6: Cross section of the light measurement configuration using a high reflection cone (full angle  $\alpha = 60^\circ$ ) and an integrating sphere; the cone can be filled with a medium of refractive index  $n$

By encapsulating the LEDs in a transparent high refraction index medium (glycerine), the critical angle of internal reflection increases from about  $16^\circ$  to  $25^\circ$  resulting in an increase in extraction efficiency by almost a factor of two.

The light output versus current (L-I) characteristics of the same  $400\ \mu\text{m}$  diameter diode without anti-reflection coating into air, with the added anti-reflection coating into air, and with anti-reflection coating into glycerine are shown in Figure 7. The light output of the diode is very linear with drive current showing output powers of 10.5 mW, 12.2 mW, and 21 mW, respectively, at a current of 100 mA.

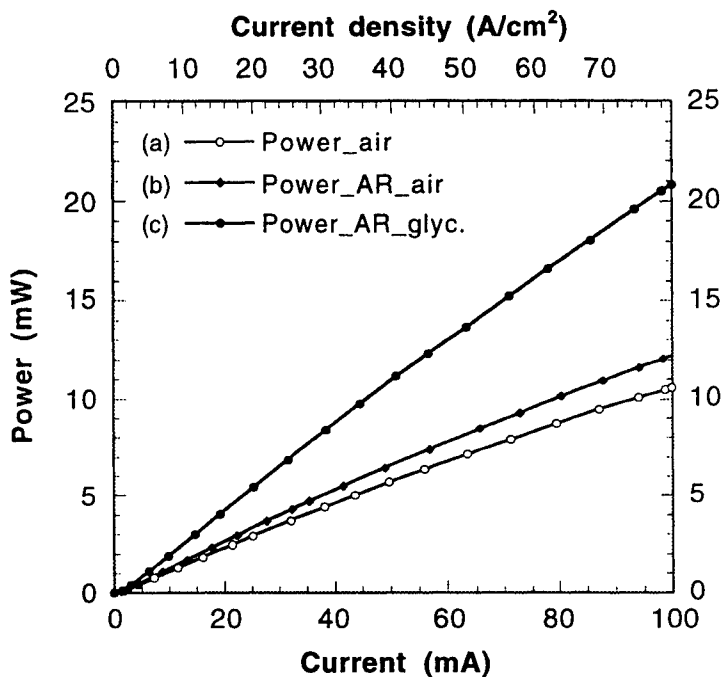


Figure 7: Light output versus current characteristic of a  $400\ \mu\text{m}$  diameter diode (a) without anti-reflection coating into air, (b) with anti-reflection into air and (c) with anti-reflection coating into glycerine.

### 3.3. Efficiency

The corresponding external quantum efficiencies of the SMLED emitting into the different media are shown in Figure 8. Maximum external quantum efficiencies of 8.9 %, 10.2 % and a record value of 16.8 % into glycerine could be achieved. In Table I the measured maximum external quantum efficiencies are compared to the model predictions calculated with our simulation tool, assuming a linewidth of 32 nm, as found for the electroluminescence spectrum at a current of about 30 mA.

Table I: Measured external quantum efficiencies compared to calculated extraction efficiencies obtained by modeling.

	meas. QE	calcul. QE	meas. $\eta/\eta_{\text{air}}$	calcul. $\eta/\eta_{\text{air}}$
into air	8.9 %	7.1 %	1	1
with AR+glycerine	16.8 %	14.1 %	1.89	1.92

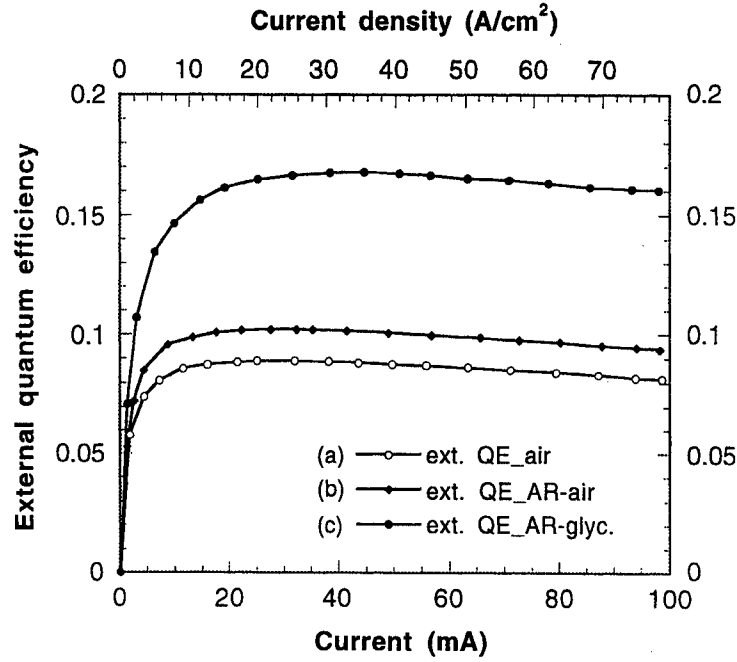


Figure 8: External quantum efficiency versus current characteristic of a 400  $\mu\text{m}$  diameter diode (a) without anti-reflection coating into air, (b) with anti-reflection coating into air and (c) with anti-reflection coating into glycerine.

The measured external quantum efficiencies are significantly higher than the calculated extraction efficiencies. It is important to note that the factor gained by depositing an anti-reflecting coating and by emitting into glycerine is in very good agreement with the theoretical predictions. The improvement in efficiency and light output of almost a factor of two (1.89), attaining an external quantum efficiency of 16.8 %, shows that the technique of immersing the sample into glycerine works. Furthermore it demonstrates that an industrially applied epoxy dome could lead to very high efficiencies for a device emitting through a single facet.

The measured external quantum efficiency of 8.9 % into air compared to the calculated efficiency of 7.1 % suggests the presence of considerable photon recycling, i.e. photons travelling in a non-useful direction are absorbed and re-emitted. The fraction of re-emitted photons that are useful will be given by the extraction efficiency. This increases the efficiency of the device by the recycling factor  $R$ :

$$R = \frac{\eta_{\text{int}}}{1 - g\eta_{\text{int}}}$$

where  $g$  is the fraction absorbed and  $\eta_{\text{int}}$  is the internal quantum efficiency of the quantum well emission. The ratio between the external quantum efficiency (8.9 %) and the light extraction efficiency, corrected for current spreading (6.75 %), results in an recycling factor of 1.32. To give a lower limit for the internal quantum efficiency we assume maximum recycling, i.e. 40 % reabsorption which is maximum of the guided mode power, which would imply an internal quantum efficiency of 86 %. On the other hand, assuming 100 % internal quantum efficiency gives a reabsorption fraction of at least 24 %, which represents the lower limit. This range of possible values can be further reduced by means of temperature

measurements (section 3.4). This simple analysis allows us to conclude that a large fraction of the radiation emitted into guided modes is recycled and contributes to the extraordinary high light output of this SMLED. Previous work on very large microcavity LEDs suggested also g-factors of about 30 %<sup>6</sup>.

### 3.4. Influence of temperature

First, the diode was measured over all emitting angles at room temperature, showing a maximum external quantum efficiency of 8.0 %. Then the measurements were carried out in the temperature range between  $-30^{\circ}\text{C}$  and  $+100^{\circ}\text{C}$ . Considering the corrected extraction efficiency of 6.75 %, the apparent internal quantum efficiency of this diode is 117 %. We assume that the reabsorption fraction  $g$  stays constant across the temperature range investigated and only the internal quantum efficiency changes with temperature. By using the equation given above we can extrapolate the internal quantum efficiency. In Figure 9 we consider the two boundary cases: i) maximum photon recycling, i.e. a reabsorption fraction of 40 % which leads for this diode at  $-30^{\circ}\text{C}$  to an internal quantum efficiency of 92 %; ii) since the internal quantum efficiency cannot be greater than 100 % at very low temperatures, we assume this upper limit at  $-30^{\circ}\text{C}$  which requires a reabsorption fraction of 31 %.

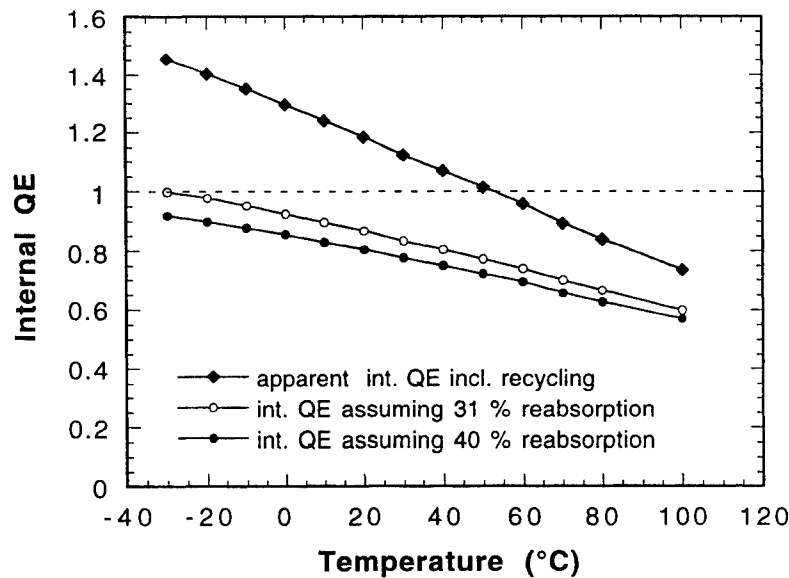


Figure 9: Internal quantum efficiency as a function of temperature, extrapolated from a  $400\text{ }\mu\text{m}$  diameter diode measured under pulsed conditions ( $2\text{ }\mu\text{s}$ ,  $1\text{ kHz}$ ) at temperatures ranging from  $-30^{\circ}\text{C}$  to  $+100^{\circ}\text{C}$  at a current density of  $50\text{ A/cm}^2$ .

This result allows us to further reduce the range of possible values for the internal quantum efficiency. For the diode studied above, measured at room temperature, we determined the internal quantum efficiencies to be bounded by 86 and 100 % which balances with g-factors from 24 to 40 %. Considering the determined reabsorption fractions ( $31\% \leq g \leq 40\%$ ), the internal quantum efficiency of this diode should lie in the range between 86 and 94 %.

#### 4. CONCLUSION

We reported the fabrication of an MBE grown high efficiency, substrate emitting planar LED using one hybrid mirror. By immersing the device into a high refractive index film, a maximum external efficiency of 16.8 % could be achieved. In addition, the data presented demonstrate the occurrence of a significant photon recycling mechanism and allowed us to determine the upper and lower limits for the internal quantum efficiency of the quantum well emission.

#### ACKNOWLEDGMENTS

This work was supported by the European Commission within the framework of the ESPRIT-SMILED program.

#### REFERENCES

1. M. G. Craford, "Commercial light emitting diode technology: Status, trends and possible future performances", in *Microcavities and Photonic Bandgaps: Physics and Application*, J. Rarity and C. Weisbuch, pp. 323-332, Eds. Dordrecht, The Netherlands: Kluwer, 1996.
2. E. F. Schubert, Y. H. Wang, A. Y. Cho, L. W. Tu, G. J. Zyzdik, "Resonant cavity light-emitting diode", *Appl. Phys. Lett.*, vol. 60, no. 8, pp. 921-923, 1992.
3. J. Blondelle, H. De Neve, G. Borghs, P. Vandaele, P. Demeester, and R. Baets, "High efficiency (>20%) microcavity LED's", in *IEEE Colloquium on Semiconductor Optical Microcavity Devices and Photonic Bandgaps*, London, U. K., 1996.
4. J. Blondelle, H. De Neve, P. Demeester, P. Van Daele, G. Borghs, and R. Baets, "16 % external quantum efficiency from planar microcavity LEDs at 940 nm by precise matching of cavity wavelength," *Electron. Lett.*, vol. 31, pp. 1286-1287, 1995.
5. H. Benisty, M. Mayer, and R. Stanley, "A method of source terms for dipole emission modification in modes of arbitrary planar structures", *J. Opt. Soc. Amer. A*, vol. 15, pp. 1192-1201, 1998.
6. H. De Neve, J. Blondelle, P. Van Daele, P. Demeester, R. Baets, and G. Borghs, "Recycling of Guided Mode Light-Emission in Planar Microcavity Light-Emitting-Diodes," *Appl. Phys. Lett.* vol. 70, pp. 799-801, 1997.

# Uniformity of GaInAsP/GaInAsP Multiquantum Well Structures Grown in Multiwafer Reactors

Markus Deufel, Michael Heuken, Rainer Beccard, Holger Juergensen  
AIXTRON AG, Kackertstr. 15-17, D-52072 Aachen, Germany  
Tel: + 49 (241) 8909-0, Fax: + 49 (241) 8909-40, E-mail: heu@aixtron.com

E. Woelk  
AIXTRON Inc., 1670 Barclay Blvd., Buffalo Grove, IL 60089, USA  
Tel: + 1 (847) 215-7335, Fax: + 1 (847) 215-7341, E-mail: woe@aixtron.com

The increasing demand for sophisticated laser devices for high speed telecommunication systems, CATV, multimedia or printing markets requires the application of multiwafer MOVPE systems. To meet the targets of these markets, the Planetary Reactor<sup>®</sup> as well proven production tool was used to fabricate InGaAsP single and multilayer test structures with outstanding uniformity. Up to 35 x 2" wafer can be processed simultaneously in the AIX 2600G3 system. GaInAsP single layers on 2" InP substrates emit at a wavelength of 1350.44 nm with a standard deviation of 1.77 nm which is 0.25 %. Adjusting the gas flow parameter to an emission wavelength of 1.024 nm results in a uniformity of 1.07 nm. In the active region of high performance laser structures MQW structures are needed to achieve lasers with superior device characteristics. To prove the ability of our Planetary Reactor<sup>®</sup> to grow this kind of structure we demonstrate GaInAsP/GaInAsP MQW structures emitting light at 1392.61 nm. A full wafer photoluminescence mapping across a 2" wafer shows a standard deviation of the wavelength of 1.77 nm. Temperature management in the reactor, gas flow dynamics and rotation of the wafer will be discussed to understand the physical mechanisms to achieve this highly uniform layers from wafer to wafer and run to run in combination with a low cost of ownership.

**Keywords:** MOVPE, multiwafer growth, InGaAsP, uniformity laser, LED

## 1. Introduction

AlInGaP and InGaP are the key materials to produce optoelectronic devices such as light emitting diodes and lasers. LEDs with 50 lm/W have already been demonstrated [1]. These highly efficient light emitters open new market areas for semiconductor based illumination technology. Since these devices are fabricated by mass production processes, it is necessary to perform the epitaxial growth in multiwafer MOVPE reactors. It is expected that in the near future up to 50% of all III-V substrates will be used to produce ultra high brightness LED grown by MOVPE. The requirements for a production machine are high throughput, high efficiency and a good uniformity of composition, layer thickness and doping. These requirements are met by AIXTRON Planetary Reactors<sup>®</sup> due to their unique design which offers real multiwafer capability at a high degree of flexibility. Depending on the chosen setup, up to 95x2" wafers can be grown simultaneously in one run. Recently, a new fully automated 35x2" or 5x6" type has been introduced.

## 2. Experimental

The AIXTRON Planetary Reactor® is a tool for the mass production of various III-V compounds [2,3,4,5,6,7]. The principle is based on a horizontal reactor shown in Fig. 1.

The main carrier gas ( $N_2$  and  $H_2$ ) and the standard group III elements (TMGa, TMAI, TMIn) and dopants ( $DEZn$ ,  $SiH_4$ ) were injected in the center of the susceptor with a rotational symmetry. The second carrier gas and the standard group V elements ( $AsH_3$ ,  $PH_3$ ) were also injected in the center but separated from the group III elements. This special design of the inlet geometry avoids pre-reactions and allows a very good run-to-run reproducibility and an excellent uniformity. To achieve the good uniformity a precise temperature management of the reactor is necessary. There are several hardware options available to optimize the temperature profile in the reactor for each customer requirement. Absolute growth temperature, gas flow distribution, rotation speed of the main plate and the gas foil rotation of each wafer as well as the gas phase composition are the common parameters which need to be controlled to optimize the layer properties.

In this study we discuss results obtained in various types of Planetary Reactors® used for the growth of InGaP based materials. Standard growth parameters used in this study are low total gas flows between 20 and 30 l/min (depending on the reactor size) and a total pressure around 100 mbar. InGaP has been grown both with phosphine and tertiary-butyl-phosphine as the group V precursor. AlInGaP with various Al concentrations up to AlInP have been grown. Typical growth temperatures used were between 675°C and 750°C.

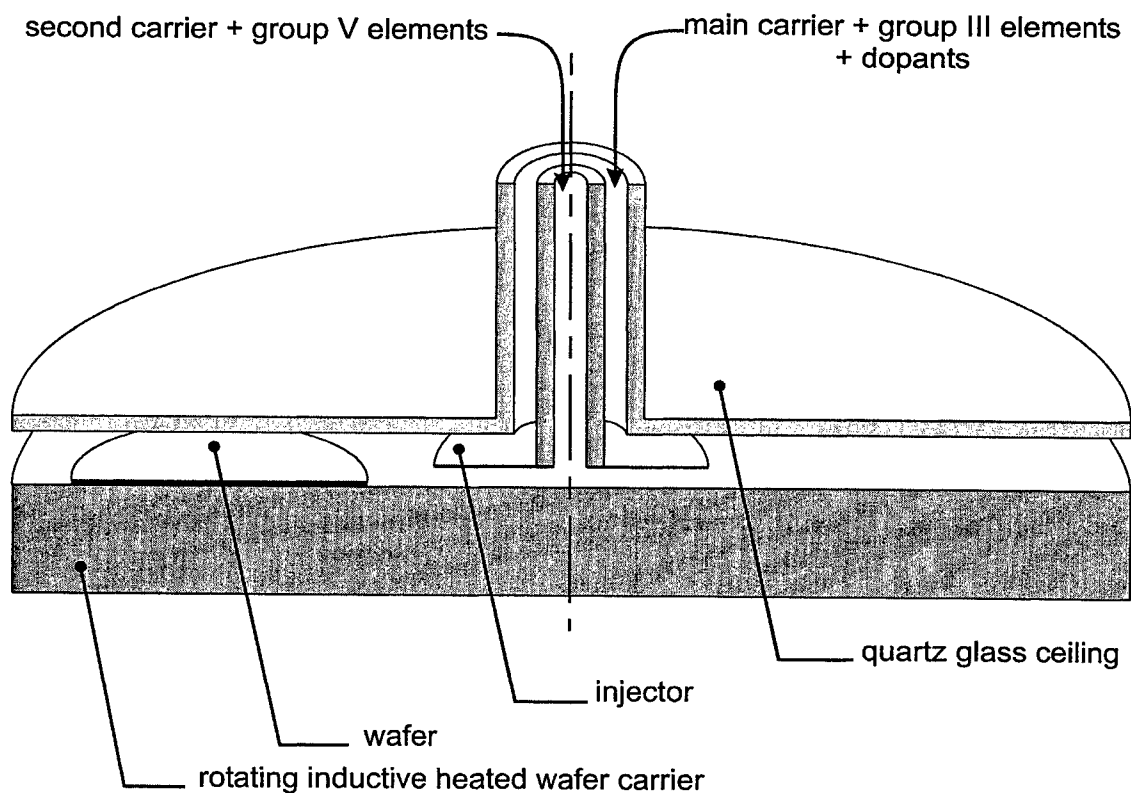


Fig. 1: Planetary Reactor® principle



### 3. Results and Discussion

#### 3.1. Evaluation of AlGaInP

To demonstrate the capabilities of the AIX 2400 reactor we loaded 15x2" wafer in the reactor to grow AlInGaP on GaAs substrates. Room temperature photoluminescence mapping was carried out and the obtained wavelength distribution across one 2" wafer is shown in Fig. 2. The obtained average wavelength is 590.78 nm with a standard deviation of 0.80 nm which is 0.13%. Basically little variation of composition is observed across the wafer except at the edges.

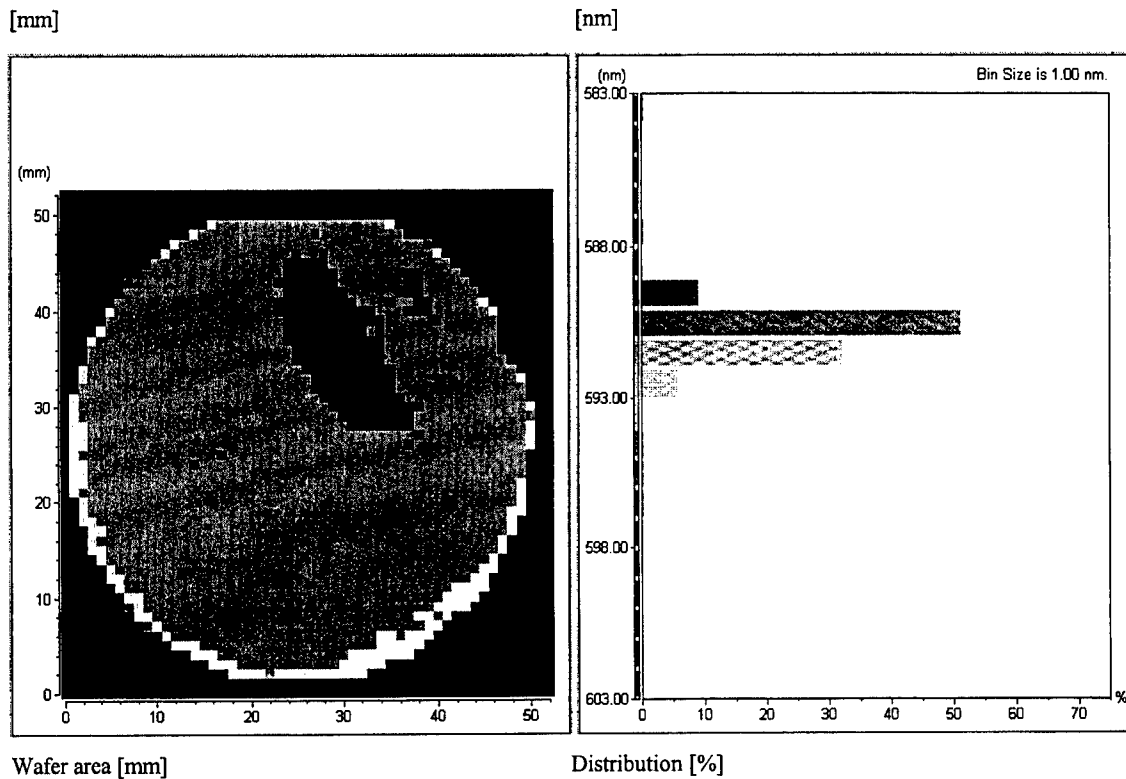


Fig. 2: Uniformity of wavelength of AlInGaP on 2'' GaAs

Wavelength	- Average:	590.78 nm
	- Std. Dev.:	0.80 nm
		= 0.13 %

#### 3.2. Properties of GaInP

The composition uniformity of GaInP has been demonstrated on 4" GaAs substrates grown in the AIX 2400 reactor loaded with 5 wafer. The wavelength distributions obtained from automatically performed room temperature photoluminescence measurements are shown in Fig. 3. The average wavelength is 665.99 nm with a standard deviation of 1.68 nm which is 0.25%. Similar values were obtained in the AIX 2600G3 reactor loaded with 9x4" wafer. As an example we demonstrate a good layer thickness homogeneity, represented by a standard deviation of only 0.24%, as shown in Fig. 4. The average layer thickness is 4135 nm with a standard deviation of 9.8 nm. One can observe a rotational symmetry to the thickness distribution which corresponds to the reactor configuration including the very homogeneous temperature profile together with the well adapted rotation speed of the wafer. The rotational symmetry of the film thickness distribution represents a characteristic of the Planetary Reactor® with individual rotating substrates. The very low number of standard deviation in all important properties (layer thickness as shown, but also composition and PL-intensity) indicate the proper adjustment of the corresponding process parameters. These parameters are temperature and flow profile as well as rotation speed of main plate and wafers.

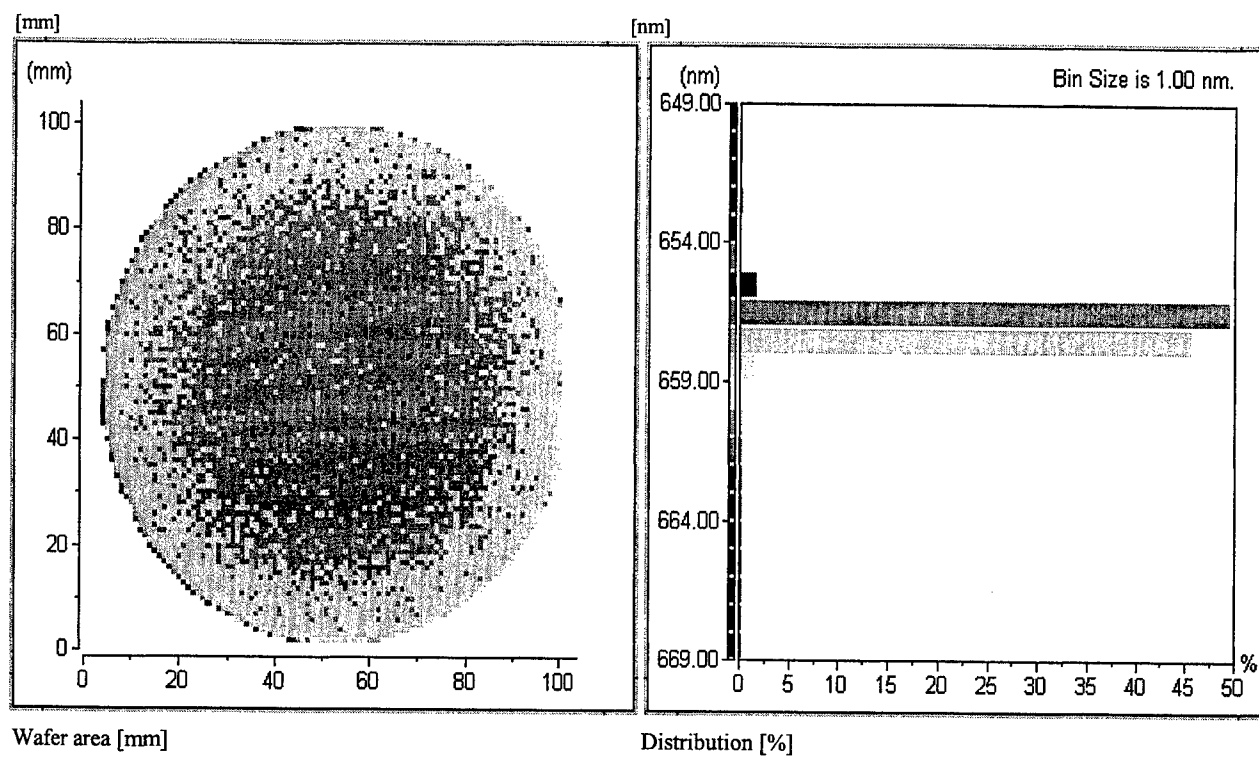


Fig. 3: Uniformity of wavelength of GaInP on 4'' GaAs

Wavelength	- Average:	665.99 nm
	- Std. Dev.:	1.68 nm
		= 0.25 %

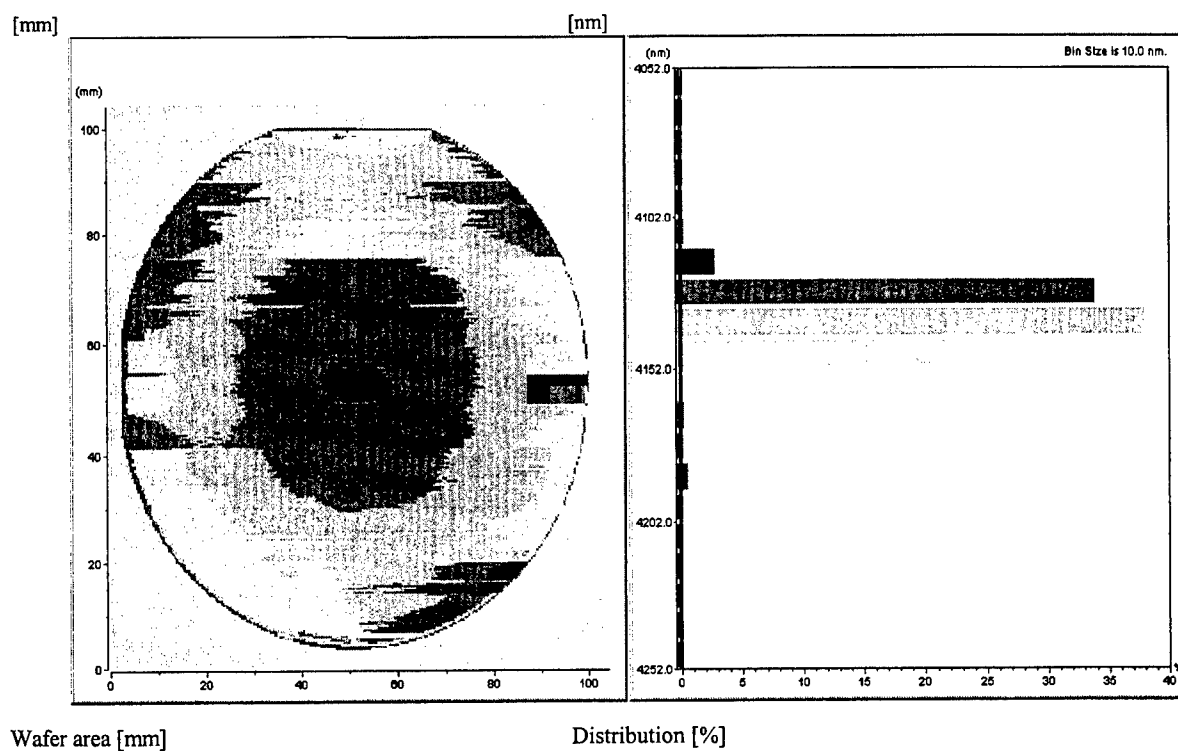


Fig. 4: Homogeneity of layer thickness of GaInP grown on 4'' GaAs substrates

Layer thickness

- Average: 4135.0 nm
- Std. Dev.: 9.8 nm
- = 0.24 %

Another important point to increase the device yield is the homogeneity of photoluminescence intensity. Again we will discuss a GaInP layer grown on 4" GaAs substrates in an AIX 2400 reactor in the 5x4" configuration. The room temperature PL intensity distribution is shown in Fig. 5. An average of 919 counts was obtained with a standard deviation of 112 counts (12%) which is an excellent value and would permit the use of nearly the whole wafer area to fabricate optoelectronic devices.

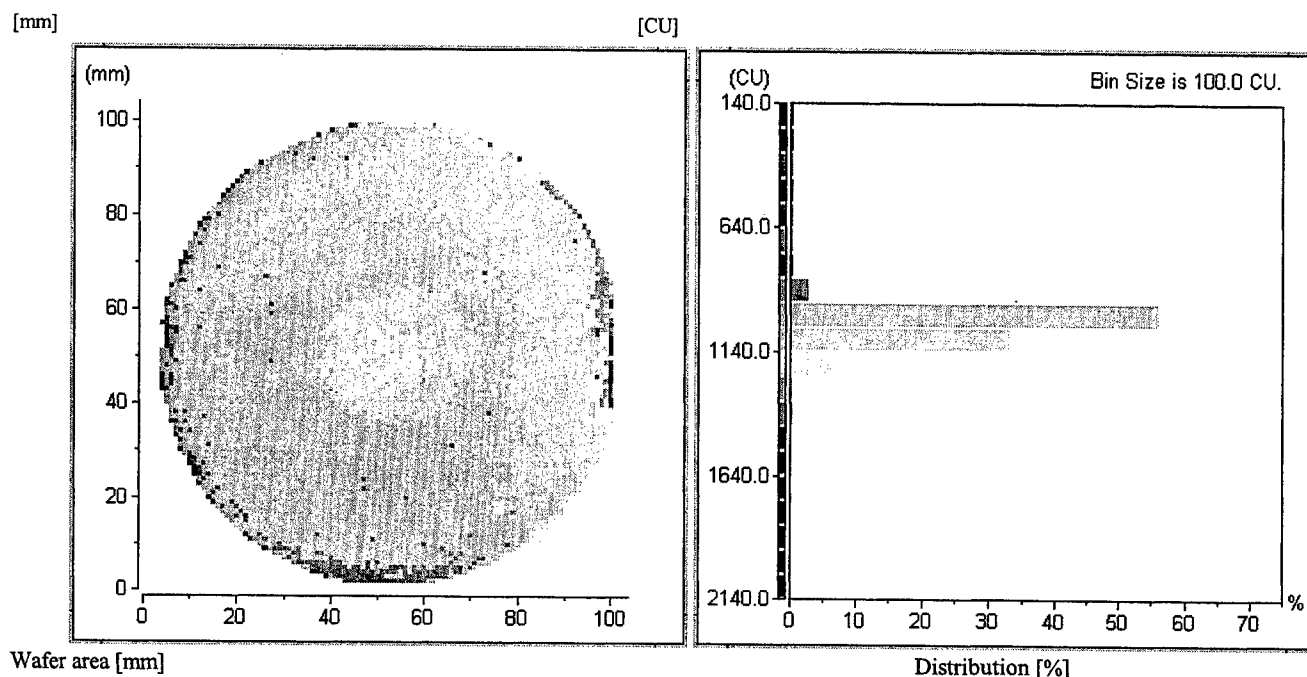


Fig.5: Homogeneity of intensity of GaInP grown on 4" GaAs substrates

Intensity	- Average:	919 CU
	- Std. Dev.:	112 CU
		= 12 %

### 3.3. Growth of GaInAsP Single Layers and GaInAsP/GaInAsP Multiquantum Well Structures

Since no 4" InP wafers are currently available on a commercial base, GaInAsP was grown on 2" InP. Since this material is very temperature sensitive, this is the ultimate homogeneity proof. The wavelength distribution of GaInAsP with an average wavelength of 1350.44 nm is shown in Fig. 6. The standard deviation is 1.77 nm which is 0.25%. This result demonstrates the very good uniformity obtainable in this kind of reactors.

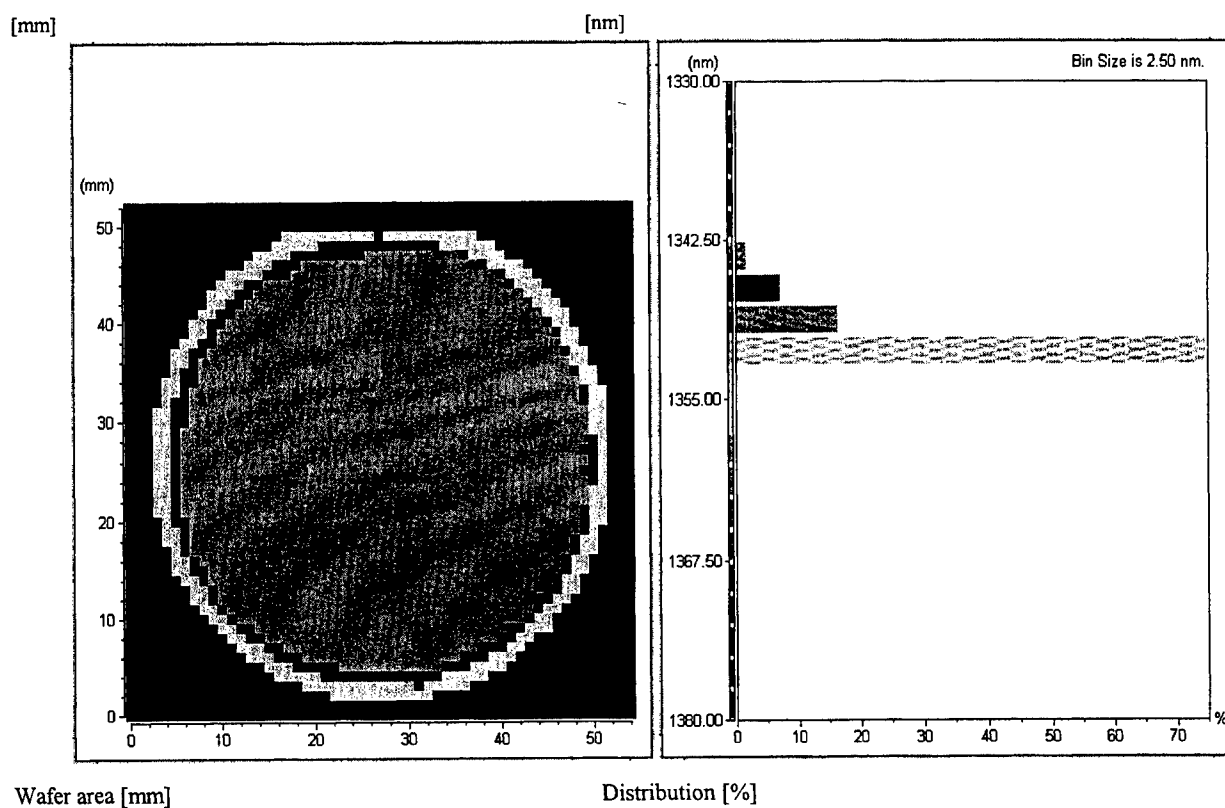


Fig. 6: Wavelength uniformity of GaInAsP grown on 2" InP substrates

Wavelength

- Average: 1350.44 nm
- Std. Dev.: 1.77 nm
- = 0.25 %

Since optoelectronic devices such as laser and optical modulator rely on quantum well structures we studied the quality and uniformity of multiquantum well structures. To avoid the well known carry over of group V elements in InGaAs/InP quantum wells we studied InGaAsP/InGaAsP quaternary layer stacks with an average emission wavelength of 1392nm. X-ray measurements taken across the wafer shows multiple satellite peaks indicating the sharp interfaces between the layers qualifying the periodicity of the layer stack. The room temperatures PL mapping of these wafer show a standard deviation of only 1.77 nm. This is a clear proof that complicated multiquantum well structures can be grown in multiwafer reactors maintaining the excellent uniformity known from single layers.

Increasing need of single devices and larger chip size of optoelectronic circuits based on InP substrates as well as the market pressure to lower prices makes the growth of 3 inch InP substrates interesting. To demonstrate the performance of the AIX 2400 reactor we let the reactor run in a 8x3 inch configuration for InGaAsP on 3 inch InP. The room temperature PL mapping shown in Fig. 7 shows a standard deviation of 2.46 nm with an average wavelength of 1326 nm. These results are very promising to establish a 3 inch InP technology based on production proven multiwafer MOVPE reactors.

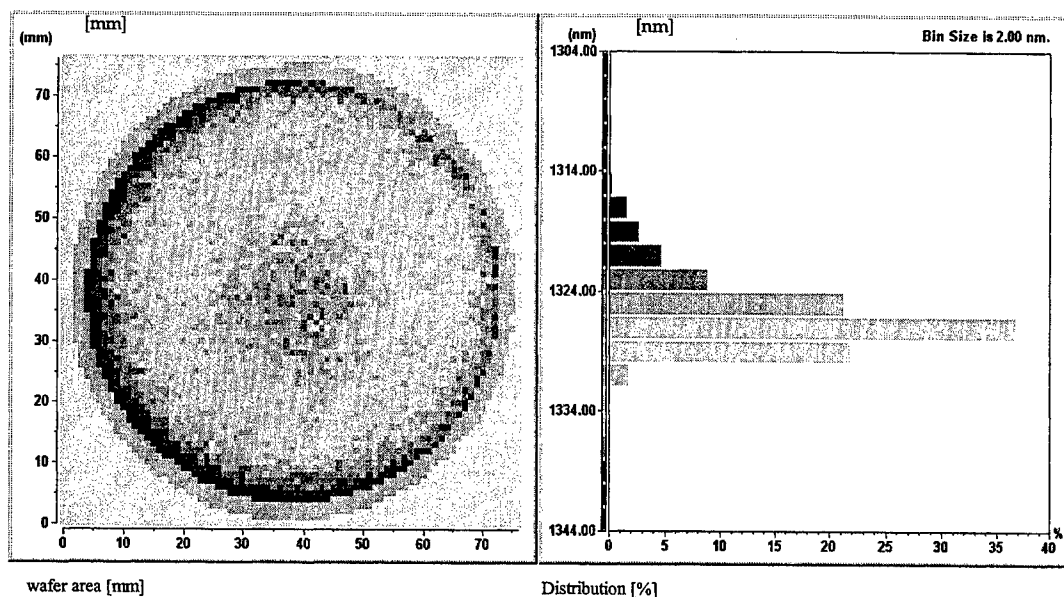


Fig. 7 Wavelength uniformity of GaInAsP grown on 3 inch substrates

Wavelength      -Average : 1325.93 nm  
                      -Std. Dev. : 2.70 nm  
                      -Laser : HeNe

### 3.4. Growth of AlGaAs and GaAs for Electronic Application

Since the market for low power and high speed electronics based on GaAs is rapidly increasing we will demonstrate typical material systems in a large scale dimension. The growth of the corresponding layers is performed in the AIX 2600 9x4" configuration. Here we will focus on typical layers used for the design of a AlGaAs based heterobipolar transistors (HBT). The resistivity distribution of a  $\text{Al}_{0.3}\text{Ga}_{0.7}\text{As}:\text{Si}$  layer on 4" GaAs wafer without edge exclusion was measured and evaluated. Hall measurements show an electron concentration of  $3 \times 10^{17} \text{cm}^{-3}$  and a mobility of  $1600 \text{cm}^2/\text{Vs}$ . These data fit to the theoretically expected values for  $\text{Al}_{0.3}\text{Ga}_{0.7}\text{As}$  to conclude that sufficient low oxygen and carbon levels are present in the sample [8]. In accordance with the Hall data non destructive sheet resistivity measurements with a sheet resistance of  $139 \Omega/\square$  were measured. The standard deviation is only 1.4%. The thickness uniformity of this  $2 \mu\text{m}$  thick 30% Al containing layer is below 0.25%. The rapid heating and cooling cycle of the G3 system allows to grow the p-type material at significant lower temperatures than the undoped and n-doped layers. The resistivity distribution of a GaAs:C layer grown below  $550^\circ\text{C}$  on a 4" substrate was used to evaluate the doping uniformity. Using this doping technique we make use of the intrinsic carbon uptake from metalorganic precursors. The high hole concentration of  $4 \times 10^{19} \text{cm}^{-3}$  with a mobility of  $99 \text{cm}^2/\text{Vs}$  and the sheet resistivity distribution with a standard deviation of only 0.9% proves the ability of this reactor concept to provide excellent doping uniformity in the temperature range lower than  $800^\circ\text{C}$  and down to lower than  $550^\circ\text{C}$  simultaneously without hardware change. These are the temperature intervalls usually employed in HBT growth. These high uniformities in dopant distribution demonstrate the high potential for maximum yield in device fabrication.

## 4. Conclusion

We presented comprehensive data concerning the growth of GaInAsP, GaInP, AlGaAs, AlGaInP and other III-V materials. Special focus was put on uniformity (typical data: 1% thickness uniformity and 1nm wavelength uniformity for most of the materials) and electrical and optical characteristics of films grown in these machines. The data prove that the G3 systems are the most flexible and efficient reactors to meet the demands of III-V manufacturing for the next decade.

## 5. References

- [1] R.L. Moon, "MOVPE: Is there any other technology for optoelectronics?", *Journal of Crystal Growth*, Vol 170, pp. 1-10, (1997)
- [2] R. Beccard, O. Schoen, B. Schineller, D. Schmitz, M. Heuken and H. Juergensen, "Multiwafer MOVPE of III-Nitrides Films for LED and Laser Applications", to be published in the proceedings of the MRS 1997 Fall Meeting, Boston, Massachusetts, USA, December 1-5, 1997
- [3] I. Rechenberg, A. Knauer, F. Bugge, U. Richter, G. Erbert, K. Vogel, A. Klein, U. Zeimer and M. Weyers, "Crystalline Perfection in GaInAsP/GaAs Laser Structures with GaInP or AlGaAs Cladding Layers", *Materials Science and Engineering*, Vol. B44, pp. 368-372, (1997)
- [4] R. Beccard, H. Juergensen and E. Woelk, "Large Area Production of Indium Antimonide for Position Sensors in Automobile Engines", to be published in the proceedings MRS 1997 Fall Meeting, Boston, Massachusetts, USA, December 1-5, 1997
- [5] M. Deschler, R. Beccard, R. Niebuhr, B. Wachtendorf, H. Juergensen, "MOVPE Technology for Multiwafer Production: Ga-Al-In-N Heterostructures and Optical and Electrical Properties of Deposited Layers", to be published in the proceedings of the Workshop on Heterostructure Epitaxy and Devices, Smolenice, October 13-17, 1997
- [6] R. Beccard, R. Niebuhr, B. Wachtendorf, D. Schmitz and H. Juergensen, "Multiwafer MOVPE Technology for Low Dimensional Ga-Al-In-N Structures", to be published in the proceedings of the LDS '97, Lisbon, May 19-21, 1997
- [7] David L. Evans "High Luminance LEDs Replace Incandescence Lamps in New Applications", *Proceedings of SPIE*, Vol. 3002, pp. 142-153, San Jose, California, February 13-14, 1997
- [8] G.B. Springfellow: "MOVPE Growth of  $\text{Al}_x\text{Ga}_{1-x}\text{As}$ ", *Journal of Crystal Growth* 53, (1981), 42-52

# Engineering high-quality $\text{In}_x\text{Ga}_{1-x}\text{P}$ Graded composition buffers on GaP for transparent substrate light-emitting diodes

Andrew Y. Kim and Eugene A. Fitzgerald

Massachusetts Institute of Technology, Cambridge, MA 02139

## ABSTRACT

We present the development of high-quality  $\text{In}_x\text{Ga}_{1-x}\text{P}$  graded buffers on GaP substrates ( $\text{In}_x\text{Ga}_{1-x}\text{P}/\text{GaP}$ ) for use in epitaxial transparent-substrate light-emitting diodes (ETS-LEDs). The evolution of microstructure and dislocation dynamics of these materials has been explored as a function of growth conditions. The primarily limiting factor in obtaining high-quality  $\text{In}_x\text{Ga}_{1-x}\text{P}/\text{GaP}$  is a new defect microstructure that we call branch defects. Branch defects pin dislocations and result in dislocation pileups that cause an escalation in threading dislocation density with continued grading. The morphology of branch defects is dominated by growth temperature, which can be used to control the strength and density of branch defects. In the absence of branch defects, we observe nearly ideal dislocation dynamics that are controlled by the kinetics of dislocation glide. This new understanding results in two primary design rules for achieving high-quality materials: 1) control branch defects, and 2) maximize dislocation glide kinetics. Combining these design rules into optimization strategies, we develop and demonstrate processes based on single and multiple growth temperatures. With optimization, threading dislocation densities below  $5 \times 10^6 \text{ cm}^{-2}$  are achieved out to  $x = 0.39$  and a nearly steady-state relaxation process is recovered. Having controlled the severe material degradation with continued grading that stopped earlier  $\text{In}_x\text{Ga}_{1-x}\text{P}/\text{GaP}$  efforts, we describe the basic device design and process for ETS-LEDs. The ETS-LED technology promises significantly reduced processing requirements, higher yield, lower cost, and enhanced design flexibility over existing LED technologies.

**Keywords:** InGaP, InAlGaP, GaP, transparent substrate, light-emitting diode, dislocation dynamics, graded composition buffers, branch defects, metal-organic vapor phase epitaxy, ETS-LED

## 1. INTRODUCTION

### 1.1. Current Light-Emitting Diode Technology

Light-emitting diodes (LEDs) based on  $\text{In}_{0.5}(\text{Ga}_y\text{Al}_{1-y})_{0.5}\text{P}$  alloys grown on GaAs substrates by metal-organic vapor phase epitaxy (MOVPE) have emerged as the dominant technology for bright and efficient devices in the green to red visible wavelengths. The novel application of highly-mismatched GaP window layers for improved current spreading and light extraction provided improved efficiency for devices on GaAs absorbing-substrate<sup>1,2</sup>. Recently, transparent-substrate LEDs (TS-LEDs) were developed where the absorbing GaAs substrate is removed and replaced by a transparent GaP substrate, resulting in a roughly two-fold improvement in external quantum efficiency over absorbing-substrate LEDs (AS-LEDs)<sup>3</sup>.

The current TS-LED technology has evolved into a series of commercially successful products. A general schematic of the process is shown in Figure 1 and goes as follows: a normal  $\text{In}_{0.5}(\text{Ga}_y\text{Al}_{1-y})_{0.5}\text{P}$  double heterostructure LED is grown on GaAs by MOVPE, a thick GaP window layer is grown on the LED structure by hydride vapor-phase epitaxy (HVPE), the GaAs substrate is etched away, and the LED structure with the thick GaP window layer is wafer-bonded to a GaP substrate<sup>3</sup>. The processing demands of TS-LEDs are much more extensive than for AS-LEDs, but the improved performance justifies the added cost in many applications.

### 1.2. $\text{In}_x\text{Ga}_{1-x}\text{P}/\text{GaP}$ Graded Composition Buffers

Graded composition buffers (graded buffers) of  $\text{In}_x\text{Ga}_{1-x}\text{P}$  grown on GaP ( $\text{In}_x\text{Ga}_{1-x}\text{P}/\text{GaP}$ ) could also be used as transparent substrates without any of the additional processing necessary in current TS-LEDs. Since the bandgap of  $\text{In}_x\text{Ga}_{1-x}\text{P}$  decreases steadily with increasing indium content, the GaP wafer and most of the  $\text{In}_x\text{Ga}_{1-x}\text{P}$  graded buffer is always transparent to the final  $\text{In}_x\text{Ga}_{1-x}\text{P}$  composition, resulting in a transparent virtual substrate. LEDs or other optoelectronic devices can be grown immediately in the same reactor and the resulting device structure can be processed like an AS-LED.



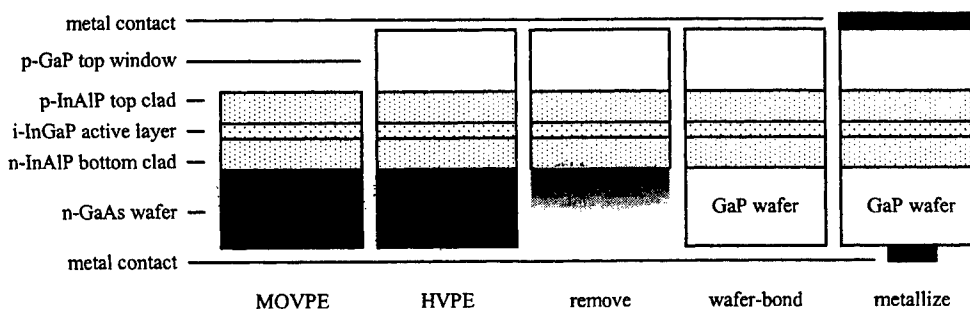


**Figure 1.** Schematic diagram of the structure of a TS-LED through the various processing steps necessary with the current technology. Layer thicknesses are not to scale.

Some of the advantages of  $\text{In}_x\text{Ga}_{1-x}\text{P}/\text{GaP}$  were recognized by earlier workers, but severe material degradation during growth limited device applications. Stinson *et al* grew a series of  $\text{In}_x\text{Ga}_{1-x}\text{P}/\text{GaP}$  LEDs by HVPE and found that efficiency degraded sharply as the emission wavelength was increased past 600nm, which corresponds to  $\text{In}_x\text{Ga}_{1-x}\text{P}$  compositions of  $x > 0.35^4$ . Chin *et al* grew  $\text{In}_x\text{Ga}_{1-x}\text{P}/\text{GaP}$  by gas-source molecular beam epitaxy (GSMBE) and observed degradation for compositions of  $x > 0.32^5$ , in agreement with the results of Stinson *et al*. Both groups attributed the degradation beyond  $x \sim 0.3$  to increasing dislocation density in  $\text{In}_x\text{Ga}_{1-x}\text{P}/\text{GaP}$  due to the increasing mismatch with GaP with continued grading<sup>4,5</sup>.

The belief that dislocation density should increase with continued grading is based on a static interpretation of the relaxation process. Early work with graded buffers indicated a steady-state dynamic process that should actually feature a nearly constant dislocation density<sup>6,7</sup>. Advances in  $\text{Ge}_x\text{Si}_{1-x}/\text{Si}$  have demonstrated that dislocation density escalation with continued grading is caused by the formation of pileups, predominantly due to a recursive and escalating interaction between dislocations and evolving surface roughness. Related work with  $\text{In}_x\text{Ga}_{1-x}\text{As}/\text{GaAs}$  showed that the roughness and material properties of  $\text{In}_x\text{Ga}_{1-x}\text{As}/\text{GaAs}$  are heavily dependent on growth temperature<sup>8,9</sup>, suggesting an opportunity for improving the quality of  $\text{In}_x\text{Ga}_{1-x}\text{P}/\text{GaP}$  by optimizing growth conditions.

### 1.3. Our Work

We recently optimized growth conditions for  $\text{In}_x\text{Ga}_{1-x}\text{P}/\text{GaP}$  grown by MOVPE and obtained a nearly steady state dislocation density of  $\sim 5 \times 10^6 \text{ cm}^{-2}$  for the composition range of  $x = 0.26$  to  $x = 0.40^{10,11}$ . A new defect microstructure that we called branch defects was identified and demonstrated to control the microstructure of  $\text{In}_x\text{Ga}_{1-x}\text{P}$  in the temperature range of 650°C to 810°C<sup>11</sup>. Furthermore, we showed the first experimental verification of a kinetic model for relaxation proposed by Fitzgerald *et al*<sup>12</sup>. Examining the literature, we proposed a picture of the evolution of microstructure in  $\text{In}_x\text{Ga}_{1-x}\text{P}$  ranging from roughly 300°C to 800°C. These findings were condensed into a series of design rules and an optimization strategy for producing device-quality  $\text{In}_x\text{Ga}_{1-x}\text{P}/\text{GaP}$ , which resulted in the recovery of a steady-state dislocation density<sup>11</sup>.

In this paper, we will explain and condense the understanding of the evolution of microstructure and dislocation dynamics in  $\text{In}_x\text{Ga}_{1-x}\text{P}/\text{GaP}$  into a set of design rules for achieving high-quality materials. We will present our current optimization strategy that achieves a nearly steady state dislocation density of  $\sim 5 \times 10^6 \text{ cm}^{-2}$  for the composition range of  $x = 0.26$  to  $x = 0.40$ . Finally, we will discuss device design and processing advantages for these entirely epitaxial transparent-substrate (ETS) materials.

## 2. EXPERIMENT

Undoped  $\text{In}_x\text{Ga}_{1-x}\text{P}$  graded buffers were grown on (001) GaP off-cut 10° towards a {011}. A Thomas Swan atmospheric pressure MOVPE reactor was used with trimethylgallium, solution trimethylindium, and  $\text{PH}_3$  source gases carried in  $\text{H}_2$  flowing at 5 slpm. Substrates were placed on a graphite susceptor in a horizontal, rectangular quartz reactor. Growth temperature was controlled by a halogen lamp under the reactor and a thermocouple inside the susceptor.

Samples began with a 0.5  $\mu\text{m}$  GaP homoepitaxial buffer, followed by a graded composition buffer, and finished with a 4  $\mu\text{m}$  uniform composition layer. An average grading rate of 0.4% strain/ $\mu\text{m}$ , which corresponds to 5% indium/ $\mu\text{m}$ , was used in all samples. Growth temperatures ranged from 650°C to 810°C. Additional details are available in prior reports<sup>10,11</sup>.

### 3. RESULTS AND DISCUSSION

#### 3.1. Evolution of Microstructure and Dislocation Dynamics

In  $\text{In}_x\text{Ga}_{1-x}\text{P}/\text{GaP}$ , the primary cause of escalating defect density with continued grading is the formation of dislocation pileups<sup>10</sup>. Dislocations become immobilized through interaction with other defects in the microstructure, forcing the nucleation of new dislocations to continue relieving strain. As pileups grow stronger and more frequent, dislocation density continues to escalate with grading.

For high growth temperature roughly above 600°C, the primary cause of dislocation pileups in  $\text{In}_x\text{Ga}_{1-x}\text{P}/\text{GaP}$  is the formation of  $\langle 110 \rangle$  branch-like defects with sharp local strain fields<sup>11</sup>, which we call branch defects. Branch defects hinder or pin gliding dislocations, resulting in dislocation pileups. Figure 2 shows branch defects and dislocation pinning, as seen in plan-view transmission electron microscopy (PVTEM).

Branch defect morphology and evolution are dominated by growth temperature. The density of branch defects,  $\rho_{\text{branch}}$ , decays exponentially with temperature, as shown in Figure 3. Typical dislocation pileup densities,  $\rho_{\text{pileup}}$ , in these samples range from 50  $\text{cm}^{-1}$  to 2000  $\text{cm}^{-1}$ , so clearly not all branch defects result in dislocation pileups. Figure 4 shows the trends in  $\rho_{\text{thread}}$  and  $\rho_{\text{pileup}}$ , which clearly indicate that more dislocation pileups occur with increasing temperature. Therefore, since  $\rho_{\text{branch}}$  decays exponentially and  $\rho_{\text{pileup}}$  increases exponentially with increasing temperature, the ability of branch defects to pin dislocations must increase dramatically with increasing growth temperature.

Branch defects indeed look sharper and stronger with increasing growth temperature in PVTEM images. Furthermore, branch defects at high temperatures turn bend contours in PVTEM images much more sharply than at low temperatures, suggesting that the branch defects possess much more strain at high temperatures. It is reasonable to assume that dislocation pinning ability depends on the strength of the branch defects.

Additional experiments show that branch defects have an evolution, appearing only after some amount of grading. The onset of branch defect formation is dependent on temperature, hence a phase diagram can be developed, as shown in Figure 5. Since all samples were grown with the same grading rate, it is impossible to deconvolute the dependencies on total film thickness and composition in the current data set.

Figure 5 suggests an interesting possibility: at low compositions, branch defects are absent and nearly ideal dislocation

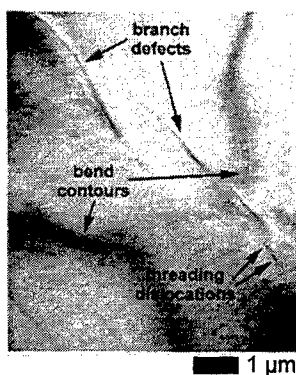


**Figure 2.** PVTEM image of branch defects in  $\text{In}_x\text{Ga}_{1-x}\text{P}/\text{GaP}$  graded to  $x = 0.26$ . The branch defects pin dislocations and sharply turn bend contours.

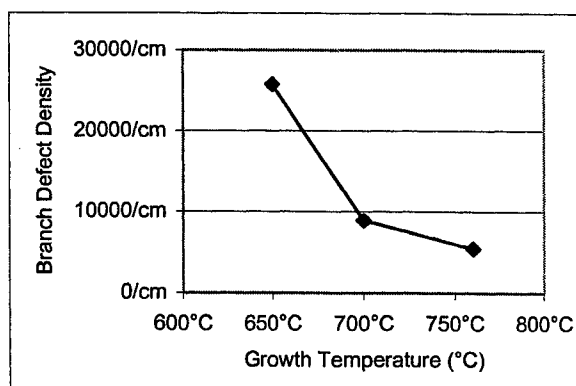


**Figure 3.** Average branch defect density plotted against growth temperature for  $\text{In}_x\text{Ga}_{1-x}\text{P}/\text{GaP}$ .

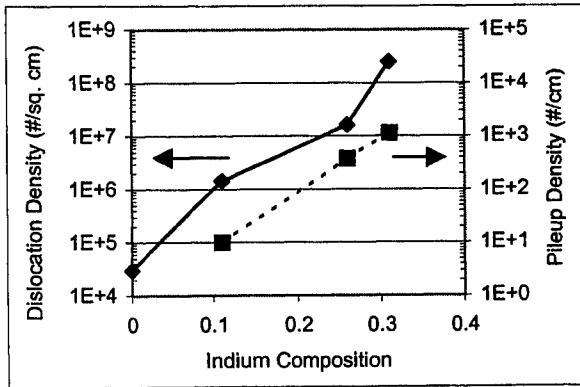


**Figure 4.** Threading dislocation density and dislocation pileup density versus final graded buffer composition.

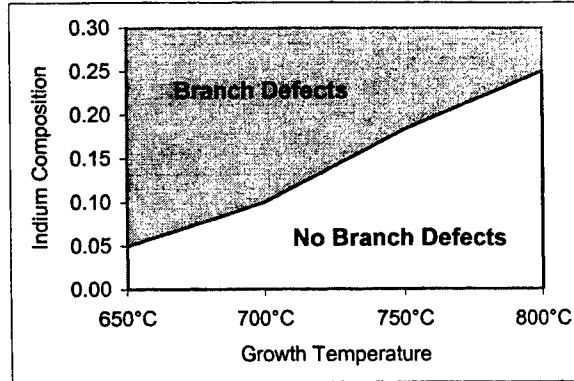


**Figure 5.** Phase diagram for branch defects at  $x \sim 0.3$ .

dynamics should be observed. At  $x \sim 0.1$ , Figure 6 shows that  $\rho_{thread}$  decays exponentially with temperature, the opposite of the trend observed in Figure 4. Clearly, the limiting phenomena for relaxation are very different in the absence of branch defects.

Figure 6 shows that relaxation becomes more efficient with increasing temperature, requiring fewer dislocations to relieve strain. The exponential temperature dependence of  $\rho_{thread}$  suggests that a kinetic mechanism limits dislocation dynamics in the absence of branch defects. If relaxation is envisioned as a process of dislocation nucleation and subsequent glide to relieve strain, it is apparent that if nucleation were rate limiting, then  $\rho_{thread}$  would increase exponentially with temperature. The observed trend is the exact opposite, therefore dislocation glide kinetics must limit relaxation in  $\text{In}_x\text{Ga}_{1-x}\text{P}/\text{GaP}$  in the absence of branch defects.

The change in surface morphology shown in Figure 7 also suggests an improvement of dislocation dynamics at higher temperatures. The transition from a rough, cellular surface at low temperatures to a smooth, ordered crosshatch surface at higher temperatures is indicative of increasingly efficient strain relaxation in low-mismatch systems by dislocation glide<sup>13</sup>.

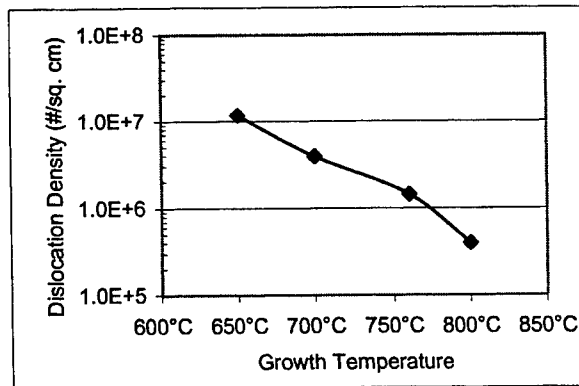


**Figure 6.** Threading dislocation density versus growth temperature  $x \sim 0.1$ , in the absence of branch defects.

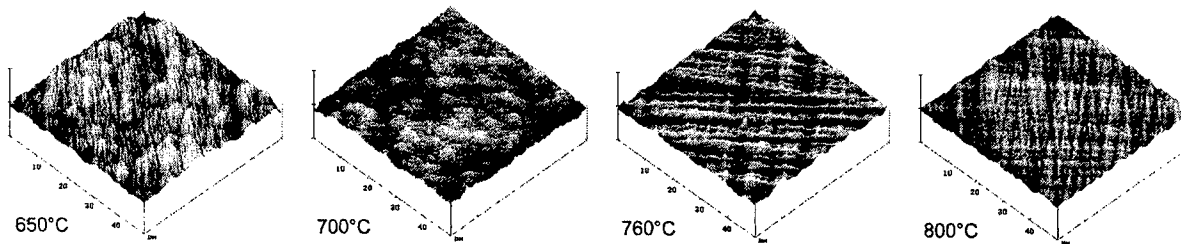


Figure 7. Atomic force microscopy images of surface morphology versus growth temperature at  $x \sim 0.1$ .

### 3.2. Process Design Rules and Optimization

The new understanding of branch defect evolution and ideal dislocation dynamics in  $\text{In}_x\text{Ga}_{1-x}\text{P}/\text{GaP}$  is critical for process optimization. It is desirable to condense the details of the observed evolution into simple design rules and an optimization strategy.

The simplest approach is to consolidate the data into one graph, as shown in Figure 8. At  $x > 0.3$ , increasing branch defect strength with temperature limits material quality, so a low growth temperature is preferable. At low compositions, dislocation glide kinetics limit material quality and a high growth temperature is desirable. Unless substrates are patterned or significant dislocation annihilation can be induced<sup>13</sup>, dislocations generated at a low composition are retained with further grading. Therefore, the temperature dependencies of branch defect strength and dislocation glide kinetics combine to form a process window near 700°C for the growth of high-quality  $\text{In}_x\text{Ga}_{1-x}\text{P}/\text{GaP}$  with compositions of  $x > 0.3$  at a single temperature.

Experimentally, a growth temperature of 700°C indeed resulted in the best material quality among samples grown at a single temperature<sup>10,11</sup>. Unfortunately, the process window at 700°C is narrow and dislocation density increases exponentially in either direction. A more robust process is desirable for consistent commercial production. Clearly, there are two imperatives for any optimization strategy intended to open up the process window: control branch defects and maximize dislocation glide kinetics. Our current optimization strategy incorporates both design rules into a two-step process.

First, the highest possible temperature is used initially. High temperatures maximize dislocation glide kinetics, resulting in low values of  $\rho_{\text{thread}}$ . Extrapolation of Figure 6 shows that  $\rho_{\text{thread}} = 3 \times 10^4 \text{ cm}^{-2}$  at 926°C, which is equal to the measured  $\rho_{\text{thread}}$  of the GaP substrates, thus setting an upper bound for useful growth temperature. Furthermore, Figure 5 shows that the onset of branch defect formation occurs later at higher temperatures, therefore a high growth temperature avoids the formation of branch defects for as long as possible.

Then, just before the onset of branch defect formation at the initial high temperature, the growth temperature is dropped sharply. Since branch defects are inevitable at this point, the temperature is lowered to suppress branch defect strength. PVTEM images of branch defects and quantitative  $\rho_{\text{thread}}$  and  $\rho_{\text{branch}}$  data show that this strategy effectively suppresses branch defect strength.

Figure 6 suggests that a sharp temperature drop should slow dislocation glide kinetics and result in higher  $\rho_{\text{thread}}$ . This does not occur in practice because dislocation glide kinetics increase with grading. While dislocation glide kinetics data is not available for  $\text{In}_x\text{Ga}_{1-x}\text{P}$ , it can be estimated from existing data. Dislocation glide kinetics have been measured to be orders of magnitude faster in  $\text{InP}$ <sup>14</sup> than in  $\text{GaP}$ <sup>15</sup>. The equilibrium phase diagram for  $\text{In}_x\text{Ga}_{1-x}\text{P}$  in Figure 9<sup>16</sup> shows that most of the change in solidus temperature occurs between  $x = 0$  to  $x \sim 0.3$ , so most of the change in materials properties between GaP and InP should occur in that range. Therefore, dislocation glide kinetics should increase orders of magnitude when grading  $\text{In}_x\text{Ga}_{1-x}\text{P}$  on GaP substrates, allowing a sharp temperature drop without increasing  $\rho_{\text{thread}}$  if the resulting dislocation glide kinetics are as fast as those at the beginning of the graded buffer.

The largest allowable temperature drop can be calculated by estimating the change in dislocation glide kinetics with composition, as shown in Figure 10. A temperature drop of roughly 100°C to 150°C is possible at  $x = 0.2$  without increasing  $\rho_{\text{thread}}$  due to slow dislocation glide kinetics.

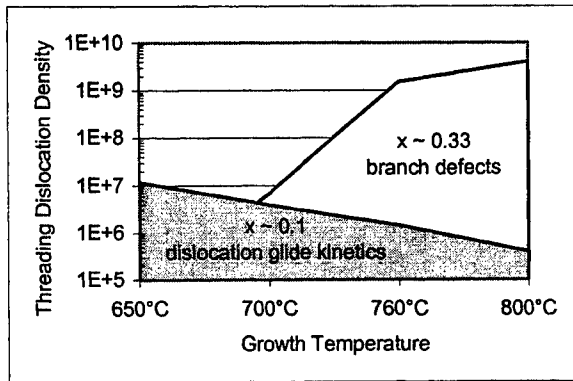


Figure 8. Consolidated graph of threading dislocation density versus growth temperature for  $\text{In}_x\text{Ga}_{1-x}\text{P}/\text{GaP}$ .

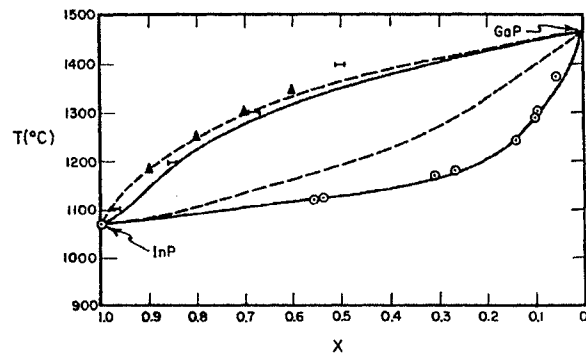


Figure 9. Equilibrium phase diagram for  $\text{In}_x\text{Ga}_{1-x}\text{P}$ . Taken from Ref. 14 and digitally edited.

An early optimized sample grown by a three-step process (760°C, 700°C, and 650°C) resulted in  $\rho_{\text{thread}} = 4.7 \times 10^6 \text{ cm}^{-2}$  at  $x = 0.39$ , compared to  $\rho_{\text{thread}} = 6.8 \times 10^6 \text{ cm}^{-2}$  at  $x = 0.34$  in the best sample grown at a single growth temperature of 700°C. Optimization both decreases overall defect density and extends the useful range of indium compositions, compared to samples grown at a single temperature. Since branch defect strength dominates dislocation dynamics, a two-step process is likely to produce better results. Figure 11 compares the escalation of  $\rho_{\text{thread}}$  with grading shown earlier in Figure 4 with results from optimized samples. The optimized samples appear to recover nearly steady-state behavior at  $\rho_{\text{thread}} \sim 10^6 \text{ cm}^{-2}$  and further optimization may achieve  $\rho_{\text{thread}} < 10^6 \text{ cm}^{-2}$ .

### 3.3. Development of Device Structure and Process

LED heterostructures can be grown immediately after the uniform composition layers in the same MOVPE reactor. With defect densities of  $\rho_{\text{thread}} < 5 \times 10^6 \text{ cm}^{-2}$  over a wide range of compositions in our  $\text{In}_x\text{Ga}_{1-x}\text{P}/\text{GaP}$ , efficient and reliable epitaxial transparent-substrate LEDs (ETS-LEDs) are a possibility. A discussion of device designs will show significant design and processing advantages to the ETS-LED technology.

Our basic device structure is shown schematically in Figure 12. Beginning with an n-type GaP substrate, an n-type GaP homoepitaxial buffer layer is grown. An n-type  $\text{In}_x\text{Ga}_{1-x}\text{P}$  graded buffer is then grown at roughly 5%  $\text{In}/\mu\text{m}$ . Either at the indirect-direct bandgap transition near  $x = 0.27$  or at some composition slightly before the desired active layer composition, a percentage of the gallium is replaced with aluminum and grading is continued with  $\text{In}_x(\text{Ga}_y\text{Al}_{1-y})_{1-x}\text{P}$ . When the final desired lattice constant is achieved with  $\text{In}_x(\text{Ga}_y\text{Al}_{1-y})_{1-x}\text{P}$ , grading is stopped and a uniform composition layer is grown. At this

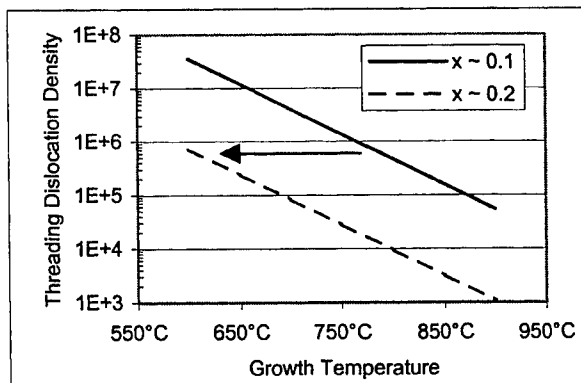


Figure 10. Plot used to estimate maximum allowable growth temperature drop for optimization.

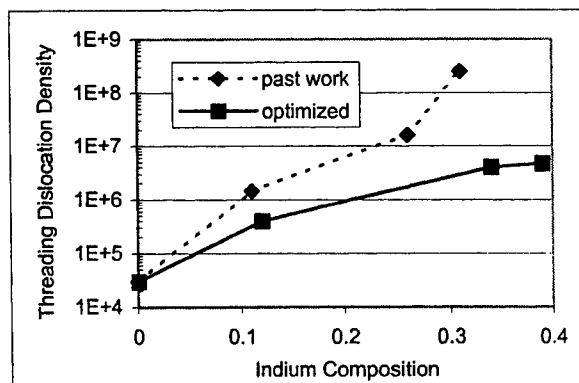
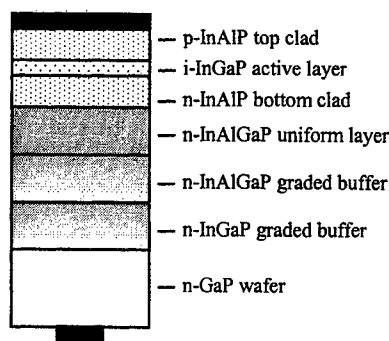


Figure 11. Comparison of threading dislocation density versus grading before and after optimization.



**Figure 12.** Schematic diagram of an ETS-LED based on  $\text{In}_x(\text{Ga}_{1-x}\text{Al}_{1-y})_{1-x}\text{P}/\text{GaP}$ . The black layers on the top and bottom are metal contacts. Layer thicknesses are not to scale.

point, a standard LED double-heterostructure is grown. The resulting device structure can then be removed from the reactor and processed like a standard AS-LED structure.

The ETS-LED device structure is entirely transparent to light emitted from the active layer of the LED. Aluminum is added to the graded buffer to ensure that the entire graded buffer and the uniform composition layer are transparent. Alternatively, the active layer can be implemented as a strained quantum well or grown with aluminum to shift emission to wavelengths beyond the absorption edge of  $\text{In}_x\text{Ga}_{1-x}\text{P}$ . Adding aluminum to the graded buffer is preferable, because it is prudent to avoid aluminum in the active layer to maximize both material quality and heterostructure band offsets and high power LEDs typically require relatively thick active layers.

The thick GaP substrate acts as both a current spreading layer and a light-extraction window. A small patterned contact on the substrate combined with a fully metallized top contact should provide full current spreading within the device. Mounted top-side down on a standard header, the small patterned back contact minimizes reflection back into the device. Furthermore, earlier work with AS-LEDs has shown that thicker GaP window layers continuously improve light extraction efficiency<sup>1,2</sup> and a typical 200  $\mu\text{m}$  thick GaP substrate is far thicker than any practical epitaxial GaP window layer.

The device schematic of the ETS-LED is very similar to the current TS-LED shown in Figure 1, except for the presence of the graded buffer and the absence of a GaP top window layer in the ETS-LED. The GaP top window layer is necessary to support the LED heterostructure when the original GaAs substrate is etched<sup>3</sup>. Otherwise, with the wafer-bonded GaP substrate acting as a current-spreading and light-extraction layer, the epitaxial GaP top window layer appears to be superfluous in the TS-LED device structure. The GaP top window layers in TS-LEDs are typically  $\sim 50 \mu\text{m}^3$ , while the graded buffer of an ETS-LED is typically  $\sim 5\text{-}10 \mu\text{m}$ , therefore less total epitaxy is required in the ETS-LED technology and series resistance may be smaller.

Another device design advantage of the ETS-LED is that emission wavelength may be varied without adding aluminum to the active layer simply by grading to different compositions. The added freedom of bandgap and lattice constant engineering provided by graded buffers opens up new device design possibilities.

There are significant processing advantages to the ETS-LED technology. The substrate removal and wafer-bonding processing steps of the current TS-LED technology are eliminated. A thick GaP top window layer is unnecessary in ETS-LEDs, therefore all of the epitaxy can be performed in a single MOVPE reactor.

Another important benefit is that thermal expansion coefficient mismatch is minimized in the ETS-LED technology. The thermal mismatch between GaP and GaAs is 11%<sup>17</sup>, so wafers must suffer from severe curvature after the  $\sim 50 \mu\text{m}$  thick GaP top window is grown in the current TS-LED technology. Wafer curvature makes processing difficult, especially since the GaAs substrate must be removed in TS-LEDs. The thermal mismatch with GaP is 4% for  $\text{In}_{0.3}\text{Ga}_{0.7}\text{P}$  (565 nm) and 10% for  $\text{In}_{0.5}\text{Ga}_{0.5}\text{P}$  (660 nm)<sup>17</sup>, plus the total epitaxial thickness is  $\sim 10 \mu\text{m}$  rather than  $\sim 50 \mu\text{m}$ , so ETS-LED wafers should have much less curvature and better yield than TS-LED wafers.

Overall, the ETS-LED technology has significant potential benefits over existing LED technologies. The graded buffer provides new design flexibility, providing another dimension to bandgap engineering. The simpler processing is the major improvement in ETS-LEDs over current TS-LEDs: less wafer curvature and fewer processing steps should lead to higher yield and consistency and lower costs.

#### 4. CONCLUSIONS

In this paper, we present a summary of the evolution of a new defect microstructure that we call branch defects. Branch defects have been identified as the primary cause of material degradation in  $\text{In}_x\text{Ga}_{1-x}\text{P}/\text{GaP}$ . The evolution of branch defects was mapped as a function of growth temperature and composition and the resulting branch defect phase diagram lead to the exploration of ideal dislocation dynamics at low indium compositions. Dislocation glide kinetics were identified as the limiting mechanism for relaxation in the absence of branch defects.

The new understanding of the evolution of microstructure and dislocation dynamics in  $\text{In}_x\text{Ga}_{1-x}\text{P}/\text{GaP}$  was condensed into design rules for achieving high-quality materials: 1) control branch defects and 2) maximize dislocation glide. For materials grown at a single growth temperature in our system, the two design rules combine to form a sharp process window near 700°C. More sophisticated optimization involves changes in growth temperature to open up the process window and we proposed a two-step optimization strategy. Early results show reduced defect densities of  $\rho_{\text{thread}} < 5 \times 10^6 \text{ cm}^{-2}$  over a wide range of composition from  $x = 0.1$  to  $x = 0.4$ .

Device and process schematics for a new ETS-LED technology were developed and discussed in comparison to existing technologies. Overall, the benefits of the ETS-LED technology are significant: new design flexibility, less epitaxy, less wafer curvature, elimination of substrate removal and wafer bonding steps. If the ETS-LED technology can be commercialized, the resulting products should feature higher yields and significantly lower costs.

We are currently working on better optimization of growth processes to further improve material quality. Estimates made with our dislocation dynamics models suggest that values of  $\rho_{\text{thread}} < 10^6 \text{ cm}^{-2}$  should be achievable in  $\text{In}_x\text{Ga}_{1-x}\text{P}/\text{GaP}$ . Even in the current range of defect densities, high-quality LED operation should be possible and we have begun to test devices grown on  $\text{In}_x\text{Ga}_{1-x}\text{P}/\text{GaP}$ . With further development, the promise of efficient ETS-LEDs based on  $\text{In}_x\text{Ga}_{1-x}\text{P}/\text{GaP}$  substrates should be fulfilled.

#### ACKNOWLEDGEMENTS

The authors would like to thank Steve Stockman of Hewlett-Packard for the generous donation of GaP wafers. Partial funding for this work was provided by ARO Contract No. DAAG55-97-1-0111 and by a Department of Defense NDSEG Fellowship. This work made use of the MRSEC Shared Facilities supported by the National Science Foundation under Award No. DMR-940034.

## REFERENCES

1. K.H. Huang, J.G. Yu, C.P. Kuo, R.M. Fletcher, T.D. Osentowski, L.J. Stinson, A.S.H. Liao, "Twofold efficiency improvement in high performance AlGaInP light-emitting diodes in the 555-620 nm spectral region using a thick GaP window layer", *Appl. Phys. Lett.* **61**, pp. 1045-1047, 1992.
2. R.M. Fletcher, C.P. Kuo, T.D. Osentowski, K.H. Huang, M.G. Craford, "The Growth and Properties of High Performance AlGaInP Emitters Using a Lattice Mismatched GaP Window Layer", *J. Elec. Mater.* **20**, pp. 1125-1130, 1991.
3. F.A. Kish, F.M. Steranka, D.C. DeFevere, D.A. Vandewater, K.G. Park, C.P. Kuo, T.D. Osentowski, M.J. Peanasky, J.G. Yu, R.M. Fletcher, D.A. Steigerwald, M.G. Craford, V.M. Robbins, "Very high-efficiency semiconductor wafer-bonded transparent-substrate  $(\text{Al}_x\text{Ga}_{1-x})_{0.5}\text{In}_{0.5}\text{P}/\text{GaP}$  light-emitting diodes", *Appl. Phys. Lett.* **64**, pp. 2839-2841, 1994.
4. L.J. Stinson, J.G. Yu, S.D. Lester, M.J. Peanasky, K. Park, "High-efficiency InGaP light-emitting diodes on GaP substrates", *Appl. Phys. Lett.* **58**, pp. 2012-2014, 1991.
5. T.P. Chin, J.C.P. Chang, K.L. Kavanagh, C.W. Tu, P.D. Kirchner, J.M. Woodall, "Gas-source molecular beam epitaxial growth, characterization, and light-emitting diode application of  $\text{In}_x\text{Ga}_{1-x}\text{P}$  on GaP(100)", *Appl. Phys. Lett.* **62**, pp. 2369-2371, 1993.
6. M.S. Abrahams, C.J. Buiocchi, G.H. Olsen, "Dislocations in vapor-grown compositionally graded (In,Ga)P", *J. Appl. Phys.* **46**, pp. 4259-4270, 1975.
7. M.S. Abrahams, L.R. Weisberg, C.J. Buiocchi, J. Blanc, "Dislocation Morphology in Graded Heterojunctions:  $\text{GaAs}_{1-x}\text{P}_x$ ", *J. Mat. Sci.* **4**, pp. 223-235, 1969.
8. M.T. Bulsara, V. Yang, A. Thilderkvist, E.A. Fitzgerald, K. Häusler, K. Eberl, "Graded  $\text{In}_x\text{Ga}_{1-x}\text{As}/\text{GaAs}$  1.3  $\mu\text{m}$  wavelength light-emitting diode structures grown with molecular beam epitaxy", *J. Appl. Phys.* **83**, pp. 592-599, 1998.
9. M.T. Bulsara, C. Leitz, E.A. Fitzgerald, "Relaxed  $\text{In}_x\text{Ga}_{1-x}\text{As}$  graded buffers grown with organometallic vapor phase epitaxy on GaAs", *Appl. Phys. Lett.* **72**, pp. 1608-1610, 1998.
10. A.Y. Kim, E.A. Fitzgerald, "Engineering Dislocation Dynamics in  $\text{In}_x(\text{Al}_y\text{Ga}_{1-y})_{1-x}\text{P}$  Graded Buffers Grown on GaP by MOVPE", *Mat. Res. Soc. Symp. Proc.* **510**, pp. 131-136, 1998.
11. A.Y. Kim, W.S. McCullough, E.A. Fitzgerald, submitted for publication.
12. E.A. Fitzgerald, Y.H. Xie, D. Monroe, P.J. Silverman, J.M. Kuo, A.R. Kortan, F.A. Thiel, B.E. Weir, "Relaxed  $\text{Ge}_x\text{Si}_{1-x}$  structures for III-V integration with Si and high mobility two-dimensional electron gases in Si", *J. Vac. Sci. Technol. B* **10**, pp. 1807-1819, 1992.
13. E.A. Fitzgerald, "Dislocations in Strain-Layer Epitaxy: Theory, Experiment, and Applications", *Mat. Sci. Rep.* **7**, pp. 87-142, 1991.
14. I. Yonenaga, K. Sumino, "Dislocation velocity in indium phosphide", *Appl. Phys. Lett.* **58**, pp. 48-50, 1991.
15. I. Yonenaga, K. Sumino, "Dynamic activity of dislocations in gallium phosphide", *J. Appl. Phys.* **73**, pp. 1681-1685, 1993.
16. G. Stringfellow, *Organometallic Vapor-Phase Epitaxy*, Academic Press, Boston, 1989.
17. I. Kudman, R.J. Paff, "Thermal expansion of  $\text{In}_x\text{Ga}_{1-x}\text{P}$  alloys", *J. Appl. Phys.* **43**, pp. 3760-3762, 1972.





---

## **SESSION 5**

### **Novel Structures and Materials**

# Control of spontaneous emission in photonic crystals

Misha Boroditsky<sup>a</sup>, Rutger Vrijen<sup>a</sup>, Thomas Krauss<sup>b</sup>, Roberto Coccioli<sup>a</sup>, Raj Bhat<sup>c</sup>, Eli Yablonovitch<sup>a</sup>

<sup>a</sup>Electrical Engineering Department, UCLA

<sup>b</sup>Electrical Engineering Department, Glasgow University

<sup>c</sup>Corning

## ABSTRACT

We studied enhancement and suppression of spontaneous emission in thin-film InGaAs/InP photonic crystal at room temperature. Angular resolved photoluminescence measurements were used to determine experimentally the band structure of conduction band of such a photonic crystal and overall enhancement of spontaneous emission. We demonstrated spontaneous emission enhancement in thin slab photonic crystals. It was shown that emission into the leaky conduction bands of the crystal has the same effect as cavity-enhanced spontaneous emission provided these bands are flat enough relative to the emission band of the material.

**Keywords:** Photonic crystals, Purcell effect, resonant enhancement, spontaneous emission.

## 1. INTRODUCTION

For a long time the spontaneous emission rates were believed to be an intrinsic property of a material. It was later understood that spontaneous emission also depends strongly on the surrounding environment through the density of states and local strength of the electromagnetic modes<sup>1</sup>. The first work on enhancement and suppression of spontaneous emission in the microwave regime were performed in 1980's by Haroche and Kleppner<sup>2</sup>. It was predicted by Purcell<sup>3</sup> that an atom in a wavelength-size cavity can radiate much faster than in the free space. This effect was measured in a cavity formed by two parallel mirrors by Haroche *et al.*<sup>4</sup>. All these measurements were performed on single atoms. A similar effect can be observed in semiconductor materials, even though the smallest chunk of the semiconductor we can imagine consists of thousands of atoms. Enhancement of the spontaneous emission rate was recently observed at low temperatures in Vertical Cavity Surface Emitting Laser type structures of small lateral dimensions<sup>5</sup>.

Photonic crystals, artificially created, multi-dimensionally periodic structures are known for a forbidden electromagnetic bandgap. For that reason, they can be used to modify spontaneous emission. Initially, it was proposed to use photonic crystals to inhibit spontaneous emission<sup>6</sup>, but they can be employed to enhance it as well.

Enhancement and suppression of spontaneous emission in thin film photonic crystals at room temperature is the subject of this paper.

We used angular resolved photoluminescence (PL) measurements to experimentally measure the band structure of the conduction band of such a photonic crystal and the overall enhancement of spontaneous emission. It will be shown below that emission into the leaky conduction bands of the crystal can be enhanced just like emission into a cavity mode provided these bands are flat enough relative to the emission band of the material.

An MOCVD-grown In<sub>0.47</sub>Ga<sub>0.53</sub>As/InP single quantum well

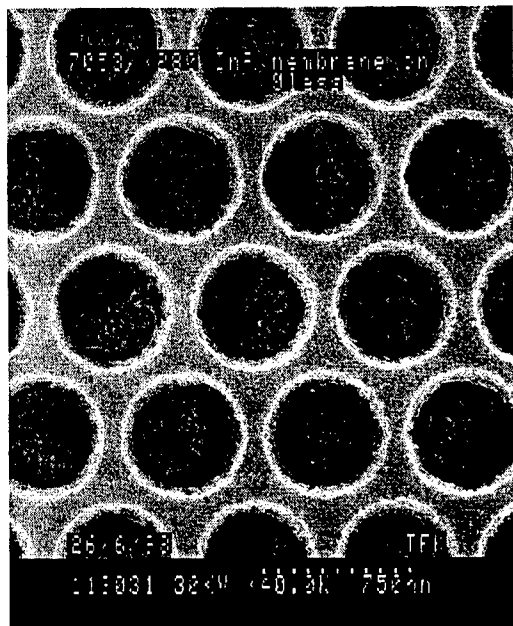
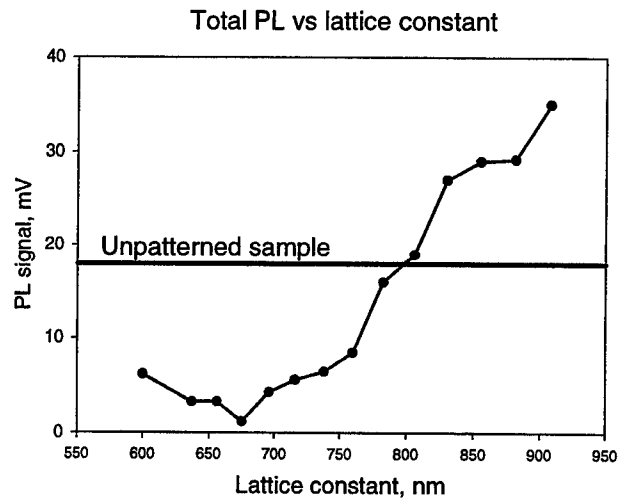
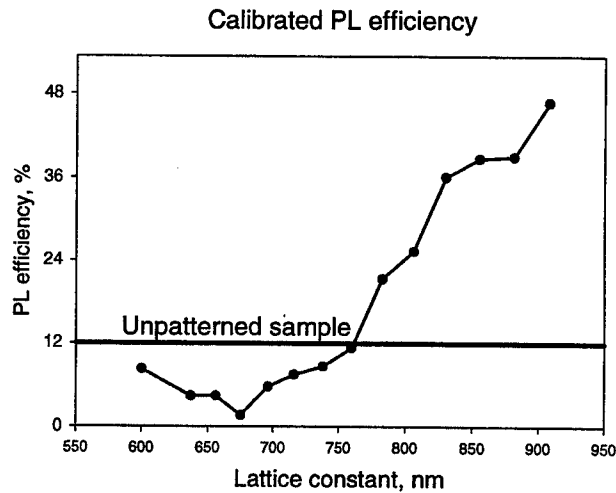


Figure 1. A triangular array of holes in the thin film on InGaAs/InP double hetero-structure. The spongy gray substance inside the holes is the optical glue. Lattice spacing is 720nm, film thickness is 240nm and hole diameter is 550nm.

<sup>a</sup> Corresponding author - Misha Boroditsky, Email: [misha@physics.ucla.edu](mailto:misha@physics.ucla.edu); tel: (310)206-3724; fax: (310)206-2596



(a)



(b)

Figure 2. (a) Photoluminescence from a thin slab photonic crystal with a triangular lattice (raw data). Thickness of the photonic crystal is  $t=240\text{nm}$ . b) the same with efficiency calibrated to the reference sample

double hetero-structure (see Table 1) was used for these experiments.

InP top cladding layer	90nm
$\text{In}_{0.47}\text{Ga}_{0.53}\text{As}$ , $n=10^{18}\text{cm}^{-3}$ , active region	60nm
InP bottom cladding layer	90nm
Glass slide	

Table 1. Sample structure.

Thin films for the photoluminescence experiments were fabricated using a substrate removal technique and bonded to a glass slide. A set of photonic crystal structures were etched into the thin film samples using electron-beam lithography and ion beam etching. Each sample had numerous triangular lattice structures spanning a lattice constant range sufficient for the spontaneous emission band to overlap with both the photonic bandgap and with conduction band modes. In our case of emission wavelength centered at  $\lambda=1650\text{nm}$ , the photonic crystal's lattice constant was made to vary from  $a=550\text{nm}$  to  $a=910\text{nm}$ . Correspondingly, the center of the photonic band gap varied from  $\lambda=1300\text{nm}$  to  $\lambda=1900\text{nm}$  (all wavelength  $\lambda$  are

vacuum wavelength). An SEM picture of a typical structure with  $a=720\text{nm}$  and  $r/a=0.37$ , where  $r$  is the radius of the holes, is shown in Figure 1.

## 2. ANGLE INTEGRATED PHOTOLUMINESCENCE MEASUREMENTS

All examples of a thin slab photonic crystal were measured using a standard PL setup with a 780nm AlGaAs pump laser. This gave a quick way of estimating overall photoluminescence efficiency. The results of measurements for these lattices are shown in Figure 2. As one can see from Figure 2, the photoluminescence efficiency increases with lattice constant. The pumping conditions were fixed and the results did not depend on orientation of the pumping beam with respect to the samples. The dependence in Figure 2 represents exactly the behavior one would expect for emission into leaking conduction band modes<sup>8</sup>. Indeed, at small lattice constant, the semiconductor emission falls into the forbidden TE gap of the photonic crystal. The light is emitted into the TM guided modes and lost. When the spontaneous emission band overlaps with the forbidden TE gap for guided modes, emission rate is small. However, as the lattice constant of a photonic crystal becomes larger, the frequency of the photonic bandgap slides down and the emission band starts to overlap with leaking conduction band modes. Most of the photons are emitted into these guided modes of the crystal and then leak into the free space. The behavior of such photonic crystals was predicted by S.Fan *et al.*<sup>7</sup> for larger lattice constants but the influence of non-radiative recombination, a factor crucial for the analyses at small lattice constants, was not taken into account in their work.

## 3. BAND STRUCTURE MEASUREMENTS ON PHOTONIC CRYSTALS.

The angular resolved emission allows for measurements of the dispersion diagram of a photonic crystal's leaky modes, that is modes with frequencies lying above the light cone in glass. Indeed, as discussed above, any eigenmode of a thin slab photonic crystal with the in-plane wave vector  $\mathbf{k}_{\parallel}$  must satisfy Bloch condition for in-plane propagation

$$\mathbf{E}(\mathbf{r}, t) = \mathbf{U}(\mathbf{r}, t) e^{-i\mathbf{k}_{\parallel} \cdot \mathbf{R}}, \quad (1)$$

where  $\mathbf{U}(\mathbf{r})$  has the periodicity of a crystal. On the other hand, the wave function of the mode outside of the slab, in the air or in the glass must be a plane wave asymptotically.

$$\mathbf{E}(\mathbf{r}, t) \sim e^{-i(\mathbf{k}_{\parallel} \cdot \mathbf{R} + \mathbf{k}_{\perp} \cdot \mathbf{R})}, \quad (2)$$

where  $\mathbf{k}_{\perp}$  is the out-of-plane component of the wavevector, so that the propagation angle is  $\alpha = \arctan(k_{\parallel}/k_{\perp})$ . Then, keeping in mind that for the modes above the line light  $\omega(\mathbf{k}_{\parallel}) > k_{\parallel}c/n$ , we conclude that relation

$$\left( \frac{\omega(\mathbf{k}_{\parallel})n}{c} \right)^2 > k_{\parallel}^2 + k_{\perp}^2 \quad (3)$$

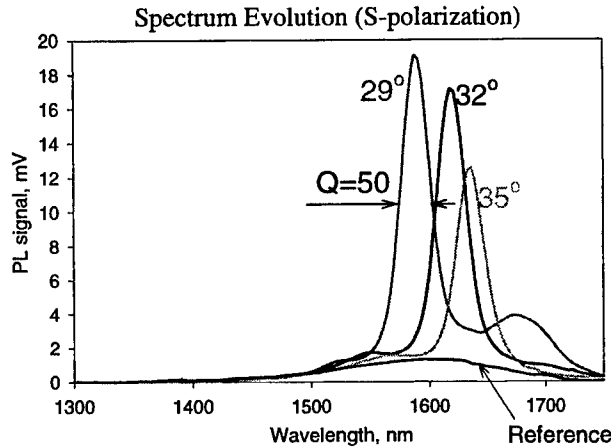


Figure 3. Measured angular resolved emission with respect to the normal axis spectra have relatively high Q between 30 and 100 and peak to background ratio about 15.

can not be satisfied for real  $\omega$  and  $\mathbf{k}$ . Thus the modes in the region above the light line have to be leaking and hence detectable. From the information on frequency versus emission angle we are able to reconstruct the band structure of the leaking modes. We used the spontaneous emission spectral peaks versus angle to study the bandstructure of the photonic crystal. A typical sequence of spectra corresponding to the various angles of is shown in Figure 3 for 29, 32 and 35 degrees. A smooth evolution of the peaks is clearly visible. Our spectral data in Figure 4 showed also, that, even though the modes of a thin film photonic crystal can not be classified as pure TE or pure TM, some of them have strongly dominating TE or TM components, while others are more mixed. If so, the photoluminescence at large angles must be polarized depending on the dominant polarization of a corresponding leaky mode. We used a polarizing beam-splitter to select the different polarizations. As can be seen from the Figure 4, the broad background turned out to consist of a few clearly polarized (or

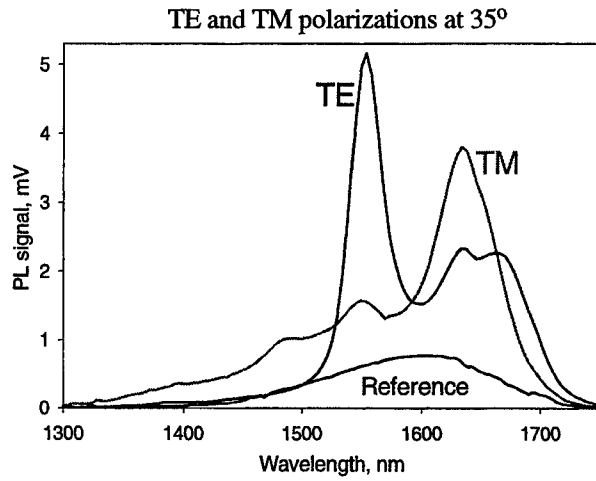


Figure 4. Some modes are well polarized while others are of mixed polarization.

computed using the Finite Difference in Time Domain technique<sup>8</sup>, we see a good agreement in the shape of the curves as well as in their polarization. A triangle formed by the crossing of the lowest TE and TM conduction bands in Figure 5 is a typical and repeatable feature in several samples with different lattice constants. This is the first, to our knowledge, demonstration of spontaneous emission directly into the photonic bands and the first measurement thereof. Angular resolved spectra on thin film photonic crystals reveal some very sharp peaks (compared to the emission linewidth of InGaAs), with a  $Q$  between 100 and 30, a feature that was not present in previous experiments on thicker films. Besides the high  $Q$ , another important feature of the figure is a very high peak to background ratio, around 15, as can be seen from Figure 3. In the following section we will argue that these are signatures of the Purcell enhancement realized without a cavity.

#### 4. RESONANT ENHANCEMENT IN THIN-SLAB PHOTONIC CRYSTALS

It was shown<sup>9</sup> that spontaneous emission in a small cavity is faster than in the bulk material. Crucial parameters for the speedup were cavity  $Q$  and effective volume  $V_{\text{eff}}$  of the resonant mode:

$$\frac{\Gamma}{\Gamma_0} = \frac{3Q_m g (\lambda / 2n)^3}{2\pi V_{\text{eff}}} \quad (4)$$

In the photonic crystals studied in the previous section, the measured  $Q$ 's of modes were comparable to that of a dielectric cavity. Since these modes are large in volume, local field enhancement is much smaller. But since the band structure of upper modes is nearly flat as can be seen from both theoretical and experimental results (Figure 5), these modes pick up a large degeneracy factor,  $g$ , compensating the loss in the local field enhancement.

Now we will derive the enhancement of spontaneous emission in a particular direction:

Suppose we have selected a narrow solid angle  $\sin\theta d\theta d\phi$  and a frequency range  $d\omega$ . Then, similarly to the derivation in Ref 9, we have to compare the density of modes and local fields of the emission into a 3-d continuum of modes to that of the emission into the leaky guided modes.

The spontaneous emission rate is proportional to square of the local field of the mode  $E^2(\mathbf{r})$  (normalized to  $h\nu/2$ ) and to the number of modes  $\Delta N$  emitting into the given solid angle in given frequency range.

sometimes mixed) peaks.

Plotting values of the spectral peak positions versus angle allows us to re-plot the graph (see Figure 5) on the frequency versus in-plane  $k_{\parallel}$  using expressions derived earlier in the section. All detectable bands above the light line correspond to leaky modes, and that permits us to measure them. The recorded spectrum of the photoluminescence consists of peaks corresponding to the leaky modes and a broad bell-shaped background corresponding to the emission into the 3D continuum of extended modes. The coupling overlap of the leaky modes with the active region of the photonic crystal is determined by the internal structure of the mode. The farther the mode is from the light line the easier it is to detect. Also, some of the conduction band modes of the photonic crystal have their electric field concentrated in the air regions. Thus, electron-hole pairs can not emit efficiently into these modes and it is difficult to observe them.

Comparing the measured band structure in Figure 5 with the overlaid dispersion diagram

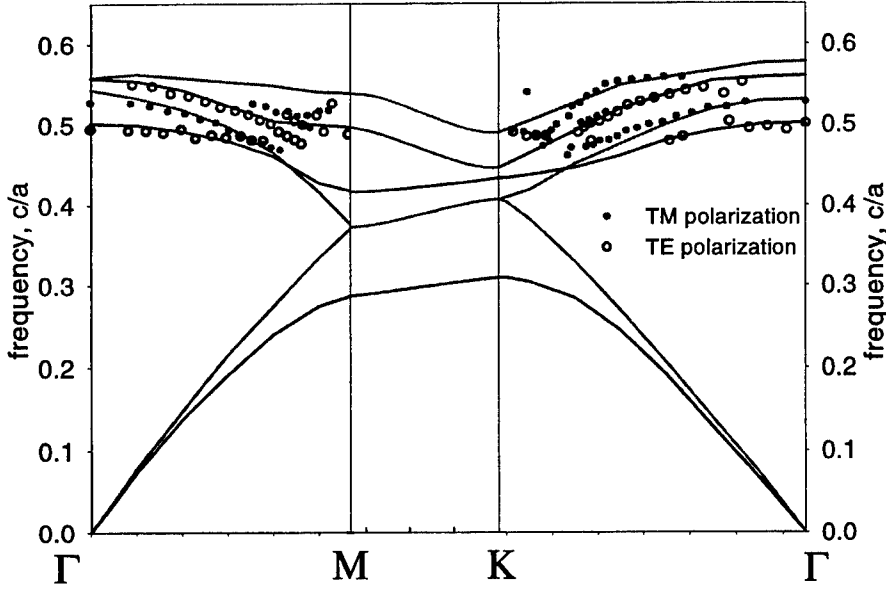


Figure 5. Theoretical and experimental bands for the photonic crystal from Figure 1. Red lines correspond to TM-like modes, blue lines are TE like modes.

For emission into the 3-d continuum of modes,

$$\mathbf{E}^2(\mathbf{r}) = \frac{\hbar\omega}{2nV}, \quad (5)$$

And number of modes emitting into the given solid angle is given by

$$\Delta N_{3d} = 2 \frac{k^2 \sin\theta dk d\theta d\phi}{(2\pi)^3} V, \quad (6)$$

where  $k=\omega/c$  is a corresponding wavevector and  $V=L^3$  is the quantization volume.

For the case of emission into the leaky modes, the local field depends on the position of the emission dipole in the active region. We can assume that vertical distribution of the electric field is concentrated in a slab waveguide. Then, the average square of the electric field normalized by a single quantum in a given point is given by

$$\mathbf{E}^2(\mathbf{r}) = \frac{\hbar\omega}{2 \int_{slab} \epsilon(\mathbf{r}') \mathbf{E}_0^2(\mathbf{r}') d^3\mathbf{r}'} \mathbf{E}_0^2(\mathbf{r}) \approx \frac{\hbar\omega}{2(t/2) \int_{slab} \epsilon(\mathbf{r}') \mathbf{E}_0^2(\mathbf{r}') d^2\mathbf{r}'} \mathbf{E}_0^2(\mathbf{r}), \quad (7)$$

where  $t$  is the slab's effective thickness and  $\mathbf{E}_0$  is the non-normalized electric field distribution of the mode. Integration in the last expression is performed over the center plane of the slab.

The number of modes emitting at this angle is given by a projection of the three-dimensional  $k$ -space onto the plane of guided mode wave vectors:

$$\Delta N_{3d} = 2 \frac{k_{\parallel} dk_{\parallel} d\phi}{(2\pi)^2} A, \quad (8)$$

where  $k_{\parallel}=k\sin\theta$ ,  $dk_{\parallel}=k\cos\theta d\theta$  and  $A=L^2$  is the area of the slab.

Averaging over the active region  $A_{\text{active}}$  in a unit cell would give the total radiation rate in a given direction.

However, since the line width of the leaky mode  $\Delta\omega$  is much larger than specified spectral resolution  $d\omega$ , only  $\frac{2}{\pi} \frac{d\omega}{\Delta\omega}$  of the

radiation will be in the spectral range. The  $2/\pi$  pre-factor comes from the Lorentzian lineshape of the leaky mode, similar to the derivation in Chapter 3.

Thus, the rate of background radiation would be given by

$$\Gamma_{3d} \propto \int_{active} \mathbf{E}^2(\mathbf{r}) \Delta N_{3d} d^2 r = 2 \frac{k^2 \sin \theta dk d\theta d\phi}{(2\pi)^3} V \cdot \frac{\hbar \omega}{2nV} \cdot A_{active} \quad (9)$$

And, in the same way, emission into the leaky modes is

$$\Gamma_{2d} \propto \int_{active} \mathbf{E}^2(\mathbf{r}) \Delta N_{2d} d^2 r = \frac{\hbar \omega}{2(t/2) \int_{slab} \epsilon(\mathbf{r}') \mathbf{E}_0^2(\mathbf{r}') d^2 \mathbf{r}'} \cdot \frac{2d\omega}{\pi \Delta \omega} \frac{(k \sin \theta)(k \cos \theta d\theta) d\phi}{(2\pi)^2} \int_{active} A \mathbf{E}_0^2(\mathbf{r}) d^2 r \quad (10)$$

Taking a ratio and simplifying we get:

$$\frac{\Gamma_{2d}}{\Gamma_{3d}} = \frac{1}{\pi} \frac{A_{slab}}{\int_{slab} \epsilon(\mathbf{r}') \mathbf{E}_0^2(\mathbf{r}') d^2 \mathbf{r}'} \cdot \frac{\int_{active} \epsilon \mathbf{E}_0^2(\mathbf{r}) d^2 r}{A_{active}} \cdot \frac{\omega}{\Delta \omega} \cdot \frac{\lambda}{nt} \cos \theta \quad (11)$$

Introducing mode's  $Q = \omega / \Delta \omega$ , and a parameter  $\gamma$  to characterize electric energy overlap with the active region:

$$\gamma = \frac{A_{slab}}{\int_{slab} \epsilon(\mathbf{r}') \mathbf{E}_0^2(\mathbf{r}') d^2 \mathbf{r}'} \cdot \frac{\int_{active} \epsilon \mathbf{E}_0^2(\mathbf{r}) d^2 r}{A_{active}} \quad (12)$$

enhancement of spontaneous emission rate at a given frequency can be transformed into a familiar structure of a Purcell number in 1 dimension:

$$\frac{\Gamma_{2d}(\omega)}{\Gamma_{3d}} = \frac{2\gamma}{\pi} Q \cdot \frac{\lambda}{2nt} \cos \theta \quad (13)$$

In semiconductors, the emission band is normally wider than the cavity linewidth. For that reason the Lorentzian in Equation (13) has to be convoluted with the semiconductor emission spectrum, as it is done in derivation of Purcell factor. This integrates out the  $2/\pi$  in the Lorentzian and substitutes  $Q$  with the material's  $Q_m$  (10 for InGaAs in our case). Then the spectrally integrated enhancement in a given direction becomes

$$\frac{\Gamma_{2d}}{\Gamma_{3d}} = \gamma Q_m \cdot \frac{\lambda}{2nt} \cos \theta \quad (14)$$

In the structure we have studied, the active region covers approximately half of the sample area. In the optimal case, when all electric energy of the mode is concentrated in the semiconductor, the overlap parameter is simply  $\gamma=2$ . This happens close to the  $\Gamma$  point of the Brillouin zone, as can be seen from the computed energy distribution plot in Figure 6. Then, expected peak enhancement, i.e the peak to background ratio of the spectra in Figure 2, in a direction close to the normal would be  $\frac{\Gamma_{2d}}{\Gamma_{3d}} \leq 2 \cdot \frac{2}{\pi} Q \cdot \frac{1650}{7 \cdot 240} \approx Q$ , i.e. approximately the modal  $Q$ . The observed peak to background ratio is smaller, about 15 to

20. We attribute this discrepancy to two factors: First, the background may be higher due to the contribution of other modal peaks, and, second, the structure imperfections may cause some additional scattering of the mode.

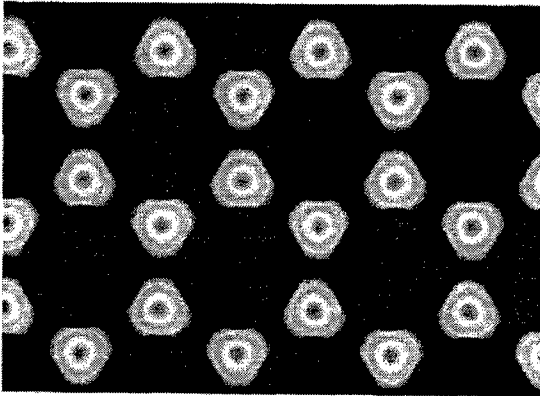


Figure 6. Electric energy distribution in the  $\Gamma$  point of the Brillouin zone. All energy is concentrated in the dielectric veins.

If the photonic bands could be engineered to be relatively flat compared to the emission spectrum, this enhancement would be achieved for all directions. As can be seen from the experimental and theoretical band structures of the photonic crystal that we considered, the spectral variation of the lowest "conduction" band is approximately twice the spontaneous emission band. Then, the enhancement integrated over all the angles becomes somewhat smaller, between 3 and 5. If the band can be made flat, the radiative lifetime can be made influenced by Purcell effect.

In the best of the thin slab photonic crystals, the photoluminescence efficiency was considerably greater than in unpatterned samples. Absolute efficiency calibration can be made by referencing the emission to the reflection (100%) from a white surface. Such calibration generally shows that InGaAs double hetero-structures grown by Raj Bhat, have an internal quantum efficiency near 100%.



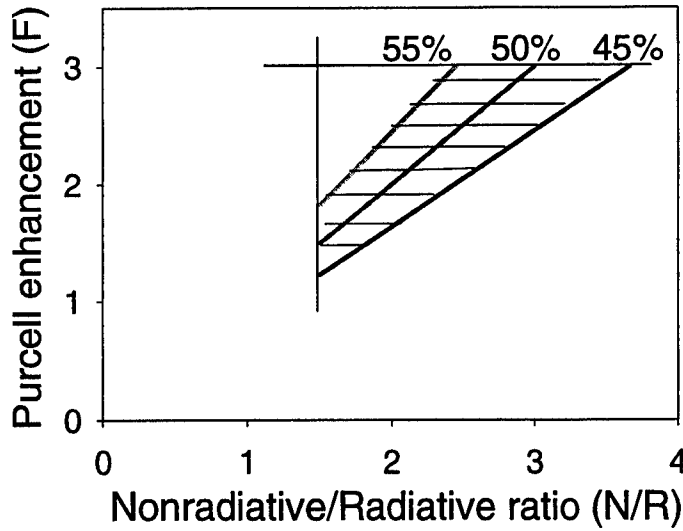


Figure 7. Dependence of the Purcell enhancement factor on the value of the non-radiative recombination rate  $N/R$  for different values external efficiency  $\eta=45, 50, 55\%$ . The shaded area limits the possible values of the Purcell enhancement factor. The Purcell factor is constrained by the lower limit on  $N/R=1.5$  from the left, and by the maximum Purcell factor 3 in this kind of structure from the top.

account that there is only half as much surface area in the patterned PBG samples to absorb light (at least in the geometrical optics approximation), this gives the external efficiency of  $4 \times 12 = 48\%$ . There are three factors influencing the measured external quantum efficiency of photonic crystal samples:

1. In principle, the extraction efficiency can be unity since all modes are leaky.
2. By drilling the holes through the active region, we introduce non-radiative recombination. We will show below that non-radiative recombination rate  $N$  is comparable to the radiative emission rate  $R$ :  $N/R \sim 1$ , where  $R$  is the radiative emission rate in bulk semiconductor material in which there is no Purcell effect.
3. The radiative emission rate in the patterned film is enhanced by the Purcell factor  $F$ , a quantity we would like to determine:  $R \rightarrow FR$ .

Then, the external quantum efficiency of the sample emitting into the conduction band modes of the photonic crystal would be given by the fractional rates:

$$\eta = \frac{FR}{FR + N} = \frac{F}{F + N/R}, \quad (15)$$

which can be solved for the Purcell enhancement factor  $F$ :

$$F = \frac{\eta}{1-\eta} \cdot \frac{N}{R} \quad (16)$$

It follows from the Equation (16) that the knowledge of relative non-radiative recombination rate ( $N/R$ ) is necessary to determine the Purcell factor.

We can use the  $a=600-700\text{nm}$  samples in Figure 2b emitting into the forbidden photonic bandgap to estimate the non-radiative recombination rate. Indeed, as can be seen from the Figure 2b, the total photoluminescence signal in those samples is 5 times lower than in the unpatterned sample. Correcting for pumped area ratio, a factor of 2 as before, gives us a 2.5 times drop in the external efficiency compared to the unpatterned continuous film, as shown in Fig 2a. Using a conservative assumption that the escape probability is the same as in unpatterned film, we obtain an estimate on non-radiative recombination rate  $N$  in terms of the radiation recombination rate  $R$ :

$$\frac{R}{R + N} < 0.4 \quad (17)$$

from which follows  $N/R > 1.5$ .

An unpatterned thin film between two glass hemispheres has an optical escape probability of  $2 \frac{1}{4(n_f/n_g)^2} \sim 0.11$ , where  $n_f=3.2$  and

$n_g=1.5$  are refractive indices of the semiconductor film and glass correspondingly. In our ultra-thin films, the effective refractive index is probably slightly smaller than that of the bulk material. Also, the high internal efficiency of the InGaAs active layer allows the photon recycling to boost the external efficiency of the film even higher. With all these benefits combined, we conservatively estimate that a thin film, when encapsulated in glass or epoxy, can have a double sided 12% external efficiency. This sets an absolute efficiency scale for the photonic crystal samples shown in the Figure 2b, (which were all measured under identical pump and collection conditions). The calibrated photoluminescence signal versus lattice spacing is shown in Figure 2a. As can be seen from the graph, the PL strength from the photonic crystal samples with lattice constant  $\sim 900\text{nm}$ , where conduction band modes match the InGaAs emission frequency, is twice as large as that from an unpatterned sample. Taking into

The factor 1.5 is a lower limit on the non-radiative/radiative recombination rate because the extraction efficiency of the sample with holes is more likely to increase due to the presence of additional surfaces. Plotted in Figure 7, is a family of curves showing the dependence of Purcell enhancement factor versus  $(N/R)$  for different efficiencies from Eqn. (16). As one can see from the Figure 7, the Purcell factor is constrained by our measurements to be above 1.5 but probably less than the  $F=3$  which would occur in the ideal case at room temperature in InGaAs. Certainly, we will need to perform lifetime measurements on our samples to verify the exact value of the Purcell factor for spontaneous emission into conduction band modes.

## 5. SUMMARY

The results of photoluminescence measurements on thin slab photonic crystals were presented in this paper. The angle dependence of the PL spectral peaks was shown to follow the photonic bands of the photonic crystals. The band structure of the conduction bands was measured using the angular resolved spectra. Up to a 15-fold enhancement of the emission in a given direction was observed and explained in terms of the Purcell enhancement.

## REFERENCES

1. P. Selenyi, *Phys. Rev.* **56**, 477-480 (1939)
2. R.G.Hulet, E.S. Hilfer, D. Kleppner, *Phys. Rev. Lett.* **59**, 2955 (1955)
3. E.M. Purcell, *Phys. Rev.* **69**, 681(1946)
4. P. Goy, J.M. Raimond, M. Gross, S. Haroche, *Phys. Rev. Lett.* **50**, 1903 (1983)
5. J. Gérard, B. Sermage, B. Gayral, B. Legrand, E. Costard, V. Thierry-Mieg, "Enhanced spontaneous emission by quantum boxes in a monolithic optical microcavity," *Phys. Rev. Lett.*, 1998, 91(5), pp. 1110-1113.
6. E. Yablonovitch, 'Inhibited spontaneous emission in solid-state physics and electronics,' *Phys. Rev. Lett.*, 1987, **58** (20), pp. 2059-2062.
7. S. Fan, P. Villeneuve, J. Joannopoulos, E.F. Schubert, *Phys. Rev. Lett.* **78**, 3295, (1997)
8. M. Boroditsky, R. Coccioli, E. Yablonovitch, "Analysis of photonic crystals for light-emitting diodes using the finite difference time domain technique", *Proc. Photonics West '98*, San Jose, CA, 26-30 Jan. 1998, vol. **3283**, p.184-90.
9. R. Coccioli, M. Boroditsky, K. Kim, Y. Rahmat-Samii, E. Yablonovitch, "What is the Smallest Possible Electromagnetic Mode Volume in a Dielectric Cavity?" to be published in *IEE Proceedings - Optoelectronics*.

# Infrared Light-Emitting Diodes with Lateral Outcoupling Taper for High Extraction Efficiency

W. Schmid, F. Eberhard, M. Schauler, M. Grabherr, R. King, M. Miller, E. Deichsel,  
G. Stareev, U. Martin, R. Jäger, J. Joos, R. Michalzik, and K.J. Ebeling

Department of Optoelectronics, University of Ulm, D-89069 Ulm, Germany

## ABSTRACT

We present a non-resonant light emitting diode with a novel concept of light outcoupling. Light is generated in the center of a radially symmetric structure and propagates between two mirrors to a tapered region where outcoupling occurs. Principles of outcoupling are given using a simple ray tracing model. Different process routes are developed resulting in on-substrate as well as substratless devices. Not yet optimized devices show quantum efficiencies of 12 % and 15 %, respectively.

**Keywords:** Light-emitting diodes, High-efficiency

## 1. INTRODUCTION

One of the cardinal problems limiting the performance of light emitting diodes (LEDs) is their low efficiency caused by total internal reflection (TIR). Different approaches already exist to overcome this problem. Among those are resonant cavity LEDs with their modified internal direction of spontaneous emission,<sup>1,2</sup> surface textured devices with a back side mirror where photons repeatedly try to escape,<sup>3,4</sup> or the use of transparent substrate.<sup>5</sup> We introduce a new concept of efficient outcoupling for both top and bottom emitting devices. While top emitters have the advantage of remaining on the original substrate, substrateless bottom emitters require no distributed Bragg reflector (DBR) allowing an easy process transfer to other materials and wavelengths. In both devices the light is generated in a central area of a radially symmetric structure and the total internally reflected part of light propagates between a high reflecting mirror and the surface of the semiconductor to a laterally tapered region. Here light is coupled out by successively decreasing the incident angle of the light to the tapered surface until it overcomes the condition of TIR. Because light is redirected in a more systematical rather than random way compared to surface textured devices only a few reflections are required. This relaxes the requirements to be met by the mirror which is realized in the top emitting device as an AlGaAs/GaAs DBR combined with a thick wet oxidized AlAs layer. In the bottom emitter the reflector consists of a Au layer deposited on a passivation layer.

## 2. LED STRUCTURE AND PROCESSING OF TOP-EMITTING DEVICES

Fig. 1 shows a schematic cross-section of a processed LED. The layers are MBE grown on GaAs substrate. The lowest layer stack consists of an AlGaAs/GaAs DBR with an additional thick ( $\approx 160$  nm) AlAs layer which is completely wet oxidized. A following  $1.5\ \mu\text{m}$  thick n-GaAs layer offers lateral optical confinement and is employed to create an n-short to substrate. The  $\text{In}_{0.15}\text{Ga}_{0.85}\text{As}$  quantum well based active region includes a 30 nm thick  $\text{Al}_{0.97}\text{Ga}_{0.03}\text{As}$  layer to be partially oxidized to concentrate light generation to the center of the device. A several hundred nm thick GaAs layer serves as p-region and contributes to lateral optical guiding.

The processing is as follows. After MBE growth a few hundred nm thick pedestal with the outer diameter of the later device is wet etched. A photo resist is deposited and circularly structured with a slightly smaller size. In a reactor with a well defined temperature and organic solvent concentration the photo resist reflows to the edge of the pedestal and assumes a lensed shape due to surface tension.<sup>6</sup> Using ion beam etching with low selectivity the structure is partially transferred into the semiconductor. After removing the photo resist both AlGaAs layers with 97 and 100 % Al contents are simultaneously wet oxidized. A lower oxidation rate of the thin layer is ensured by adding a few percent Ga. This enables a partial oxidation of the current confining layer while the optical guiding layer is completely converted to  $\text{Al}_x\text{O}_y$  despite of its larger diameter. To overcome the resulting electrical isolation a metal contact between the tapered n-region and the substrate is required which is realized as quarter ring shaped contact to limit the shaded area. For the p-contact we use a small circular Ti/Pt/Au metalization on the flat top surface. Finally, a bond pad is deposited on a passivation layer.

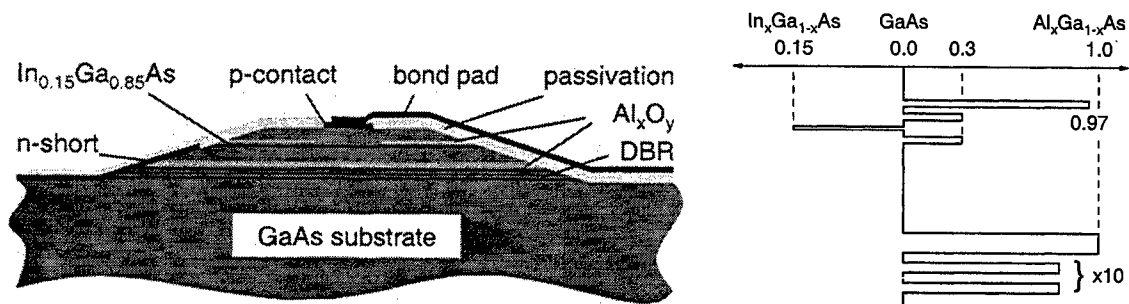


**Figure 1.** Schematic cross-section of an LED with a lateral taper. The upper and lower  $\text{Al}_x\text{O}_y$  layers serve for current confinement and light guiding to the tapered region, respectively. The right hand part indicates layer composition.

### 3. CHARACTERISTICS OF TOP-EMITTING DEVICES

The left and right parts of Fig. 2 show CCD images of a fully processed device under external illumination and in LED operation, respectively. The bright emission ring clearly demonstrates an efficient outcoupling in the tapered area. A more detailed intensity scan is taken in Fig. 3 from a semi-processed device without shading p-contact. The integrated intensity of the ring is three times higher than the emission from the flat surface above the active area.

Output and voltage characteristics of a  $100\text{ }\mu\text{m}$  device with an active diameter of about  $35\text{ }\mu\text{m}$  and a taper angle of  $20^\circ$  are displayed in Fig. 4. The optical output power is measured with an integrating sphere. For calibration an average emission wavelength of  $930\text{ nm}$  is estimated from the measured spectrum taken at a current of  $4\text{ mA}$  as shown in the inset of Fig. 4. The LED is driven up to  $4\text{ mA}$  where the output power reaches  $460\text{ }\mu\text{W}$ . A maximum quantum efficiency  $\eta_q = 12\%$  is obtained in the current range between  $0.6$  and  $0.8\text{ mA}$  corresponding to a current density of about  $70\text{ A/cm}^2$ . Conversion efficiency  $\eta$  is up to  $10\%$ . Fig. 5 shows optical output power versus temperature for a constant current of  $1\text{ mA}$ . For decreasing temperature the output power increases but saturates at  $50\%$  above the room temperature value. Considering an upper limit of  $100\%$  for the internal quantum efficiency  $\eta_i$ <sup>7</sup> and neglecting the temperature dependence of the lower mirror characteristics leads to  $\eta_i \leq 67\%$  at room temperature and therefore extraction efficiency can roughly be estimated to be about  $18\%$ .

Fig. 6 shows the dynamic behavior of a bonded  $95\text{ }\mu\text{m}$  diameter device biased at a current of  $1\text{ mA}$ . The transfer function is limited to a relatively low  $3\text{ dB}$  frequency  $f_{3\text{dB}} = 50\text{ MHz}$  independently on bias currents in a range from  $0.1$  to  $2.0\text{ mA}$ . To estimate the RC time constant of the device we assume a capacity of the current confining oxide of

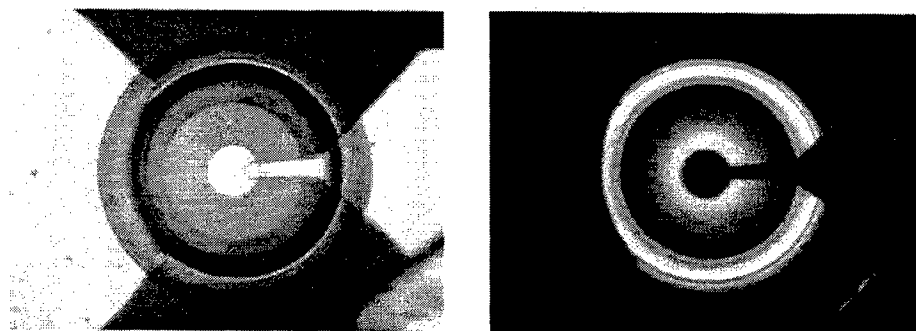


**Figure 2.** CCD images of a completely processed device of  $100\text{ }\mu\text{m}$  diameter. In the top view of the left hand side we can see the quarter ring shaped n-contact and the circular p-contact deposited on the top and connected to a bond pad. The right hand side picture shows the near field emission pattern of the device at a current of  $1\text{ mA}$ .

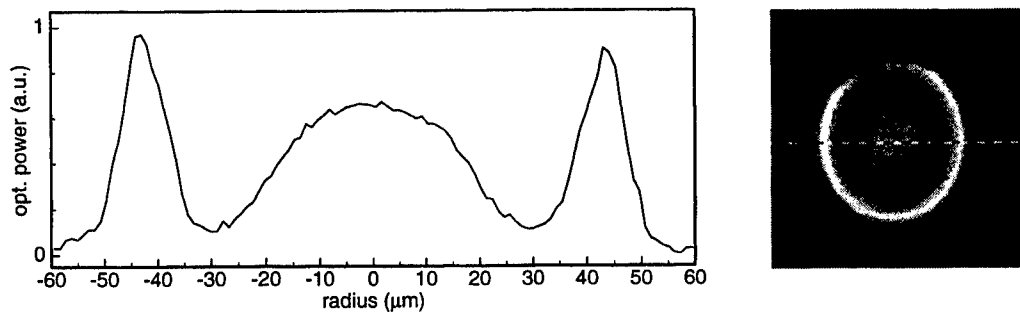


**Figure 3.** Intensity scan of an active LED before processing the p-contact. Driving current of 1 mA is supplied with a tungsten probe tip. The curve corresponds to the dashed line in the CCD image in the right hand picture.

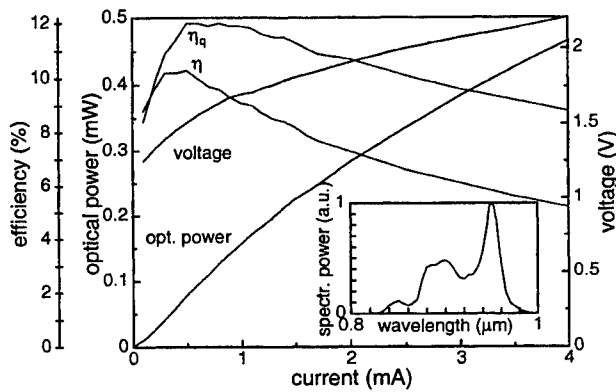


**Figure 4.** Power and voltage characteristics of a 100  $\mu\text{m}$  device with an active diameter of about 35  $\mu\text{m}$  and a taper angle of 20  $^\circ$ . Also shown are quantum and conversion efficiencies and the optical spectrum at 4 mA.

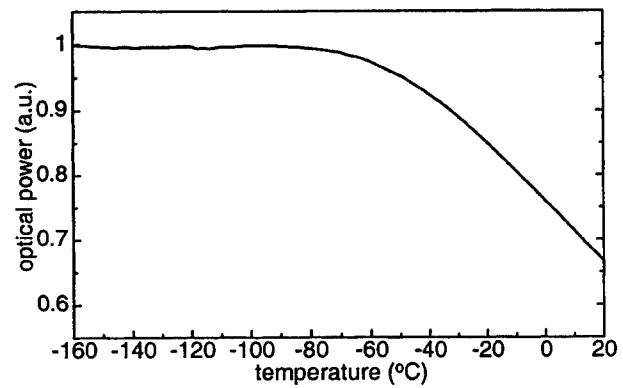


**Figure 5.** Optical output power versus temperature of a 100  $\mu\text{m}$  diameter device at a current of 1 mA.

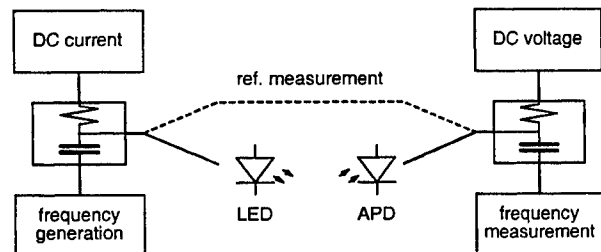
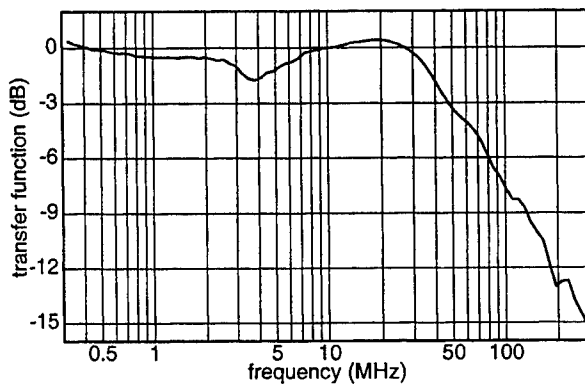


**Figure 6.** Transfer function of a top-emitting LED and measurement setup.

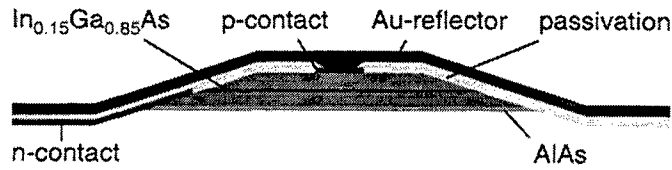


**Figure 7.** Schematic cross-section of a substrateless LED with a lateral taper.

$C_{ox} = \epsilon_0 \epsilon_{AlO} A_{ox} / d_{ox} \approx 8 pF$  where we use the oxide ring area  $A_{ox} \approx \pi \cdot (35^2 - 15^2) \mu m^2$ , the thickness  $d_{ox} = 30$  nm, and the relative dielectric constant  $\epsilon_{AlO} = 8$ .<sup>8</sup> The capacity of the bond pad is estimated to about 4 pF and the measured series resistance is  $R = 100 \Omega$ . The resulting time constant  $\tau = R(C_{ox} + C_{bond pad}) = 1.2$  ns leads to a 3-dB frequency  $f_{3dB} = 1/(2\pi\tau) = 130$  MHz which deviates from the measured value. The discrepancy might origin from additional distributed parasitics as well as a not optimized active region. Nevertheless, reducing series resistances will improve dynamics.

#### 4. SUBSTRATELESS LED STRUCTURE AND PROCESSING

Since an effective DBR cannot be easily manufactured in all material systems we have also investigated an alternative processing route which results in a substrateless bottom-emitting device as shown in Fig. 7. The lowermost layer used as an etch stop consists of 200 nm thick AlAs. Active region as well as n- and p-type layers are similar to those in the top-emitting devices. Also, the first processing steps are the same except that no oxidation step is applied. Light generation is restricted to the central region by the relatively high resistance in the p-type material and the small diameter p-contact. The p-bond pad of the top-emitting devices is provided by a homogeneous Au layer which simultaneously serves as a reflector. For substrate removal additional processing steps are required. The Au layer thickness is galvanically increased to about 1  $\mu m$ . After glueing the wafer upside down on a glass carrier, the substrate is chemo-mechanically thinned down to 50  $\mu m$ . Finally the substrate is selectively etched with an  $H_2O_2:NH_4OH$  solution where the pH is adjusted to 8.1.<sup>9</sup> In this way the quarter ring n-contact appears at the surface and can be used for independent addressing current supply.

#### 5. CHARACTERISTICS OF SUBSTRATELESS DEVICES

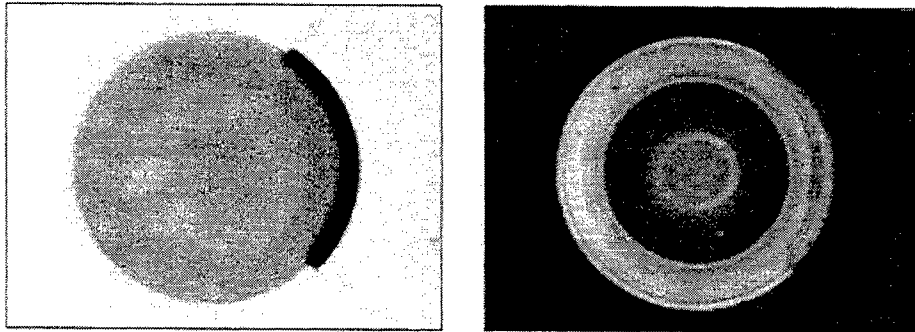


**Figure 8.** CCD images of a 95  $\mu m$  diameter device, on the left hand side illuminated, on the right hand side driven at a current of 1 mA.

Fig. 8 shows CCD images of a substrateless device. Since the remaining semiconductor has a thickness of only 4  $\mu m$ , the back side is visible in the illuminated device. The p-contact is surrounded by the flat surface which is somewhat brighter due to higher reflectivity of the Au layer. The outer dark ring corresponds to the tapered area.

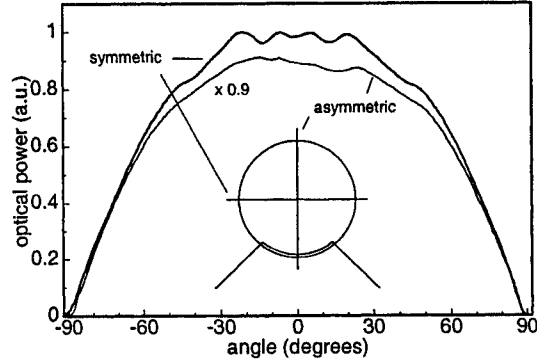


**Figure 9.** Lambertian far field patterns both along and perpendicular to the symmetry axis of the device.

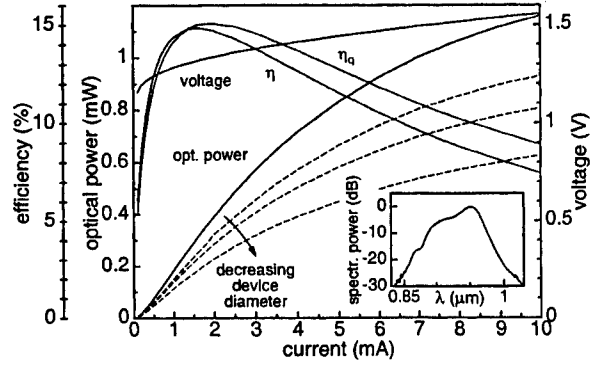


**Figure 10.** Voltage and output characteristics of a 95  $\mu\text{m}$  device. For calibration we have used the sensitivity at the 950 nm peak in the inset spectrum.

In the active device emission occurs in the p-contact area and in the taper region while the flat surface area is dark because of total internal reflection.

Far field patterns are depicted in Fig. 9 both along and perpendicular to the symmetry axis of the device. Since the n-contact metal has a lower reflectivity compared to the pure Au reflector the pattern along the symmetry axis is somewhat attenuated in the direction of the contact. In contrast, the off-axis pattern is highly symmetric and approximately of a Lambertian shape.

Voltage and output characteristics of a device with a 95  $\mu\text{m}$  outer diameter are shown in Fig. 10. An optical power of 1 mW is obtained at a current of 7 mA. Quantum efficiency  $\eta_q$  as well as conversion efficiency  $\eta$  are about 15 % at currents in the 1.5 to 2.5 mA range. The decrease of efficiency at higher currents can be related to heating and current spreading effects. The applied voltage corresponds to the bandgap energy. The series resistance of about 25 to 30  $\Omega$  is mainly due to the small area of the n-contact and the high p-layer resistance required for current confinement.

Optical characteristics of smaller devices with the same p-contact area are additionally plotted in the diagram and show inferior characteristics as will be discussed below. This clearly indicates that we have not yet achieved an optimum device design where gain due to improved outcoupling is in the same range as losses due to absorption.

## 6. DISCUSSION AND MODELLING

Fig. 11 shows the general structure of the devices studied. Central light generating area and tapered region are indicated. To understand the principle of operation some ray traces are discussed.

(a) When light is generated without an azimuthal component of the wave vector  $\vec{k} = (k_r, k_\phi, k_\vartheta)$ , i.e. with  $k_\phi = 0$  and with polar angle  $\vartheta$  larger than the critical angle for TIR, rays propagate between upper surface and lower mirror. Every reflection at the tapered surface reduces  $\vartheta$  by  $2\tau$  where  $\tau$  is the taper angle. After a few reflections  $\vartheta$  is too small for TIR and light can escape. If a single redirection is larger than twice the angle of TIR a subset of initial polar angles exists which does not meet the condition for transmission. This leads to a first design rule

$$\bar{n} \sin \tau \leq 1 \quad , \quad (1)$$

where  $\bar{n}$  is the refractive index of the semiconductor.

(b) For light excentrically generated at point  $r_0$  the behavior is somewhat more complicated. The  $k$ -vector has an initial azimuthal component of  $k_{\phi,0} = 2\pi\bar{n}\lambda^{-1} \sin \varphi_0 \sin \vartheta_0$ , where  $\lambda$  is the vacuum wavelength and  $\varphi_0$  and  $\vartheta_0$  are the initial azimuthal and polar angles, respectively. With radial distance  $r$  from the center, the product  $k_\phi \cdot r = k_{\phi,0} \cdot r_0$  remains constant (as can easily be seen by applying the sine theorem). Also no reflection will affect

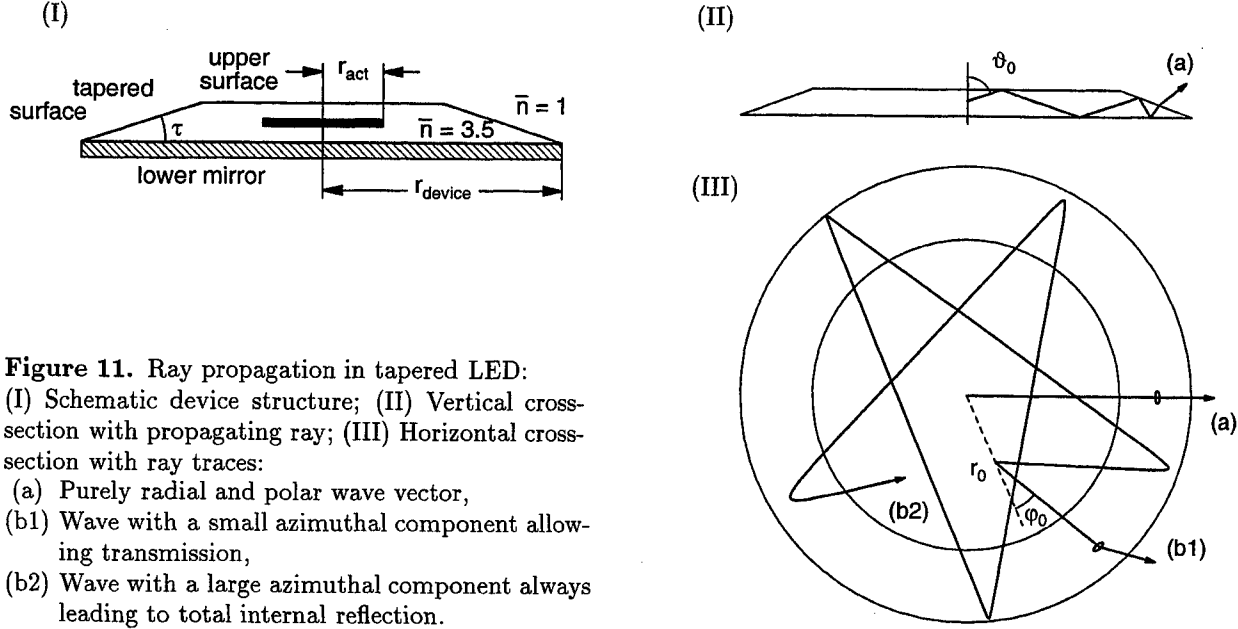


**Figure 11.** Ray propagation in tapered LED:

(I) Schematic device structure; (II) Vertical cross-section with propagating ray; (III) Horizontal cross-section with ray traces:

- (a) Purely radial and polar wave vector,
- (b1) Wave with a small azimuthal component allowing transmission,
- (b2) Wave with a large azimuthal component always leading to total internal reflection.

this value because the normal vectors of the lower mirror as well as both surfaces have no azimuthal component in the circularly symmetric structure. Therefore the azimuthal component reaches its lower limit of

$$k_{\varphi, \min} = \frac{2\pi\bar{n}}{\lambda} \sin \varphi_0 \sin \vartheta_0 \cdot \frac{r_0}{r_{\text{device}}}$$

only at the tapered edge of a device with radius  $r_{\text{device}}$ . Depending on the position of light generation and direction of light propagation this limit can be smaller (b1) or larger (b2) than the vacuum wave vector. In the latter case light is prevented to escape due to TIR and forced in a ray trace similar to whispering gallery modes. To avoid such traces one has to ensure all light being generated in a central area of the structure, i.e.  $0 \leq r_0 \leq r_{\text{act}}$  with the active radius  $r_{\text{act}}$ . This gives us a second design rule

$$\bar{n} \cdot r_{\text{act}} \leq r_{\text{device}} \quad (2)$$

resulting from examination of azimuthal ray propagation.

At this point some remarks are in order:

- Breaking circular symmetry, for example in elliptical structures, modifies design rules and may lead to enhanced outcoupling efficiency.
- The first and second design rules specify upper limits for  $\tau$  and  $r_{\text{act}}$  which are strictly valid only for the extreme cases  $r_{\text{act}} = 0$  and  $\tau = 0$ , respectively. Increasing one quantity the other has to be reduced.
- Light will be redirected before reaching the outer perimeter of the device at  $r_{\text{device}}$  (see ray (b2) in Fig. 11) which requires a further reduction of  $r_{\text{act}}$ .

For obtaining more detailed information particularly on top-emitting devices we have implemented a ray tracing model in order to estimate the influences of parameters like reflectivity of the lower mirror, taper angle, active and device diameter on extraction efficiency. In this model we use reflectivities of transverse electric (TE) and magnetic (TM) waves calculated with the transfer matrix method.<sup>10</sup> Rays start in the active layer within the active diameter. On their zigzag way to the tapered region the lossy bulk material as well as strong absorption in the unpumped quantum well is taken into account. Both TE- and TM-polarized light are considered because of the polarization dependent reflectivity. For rays including an azimuthal component we consider different orientations of the TE-



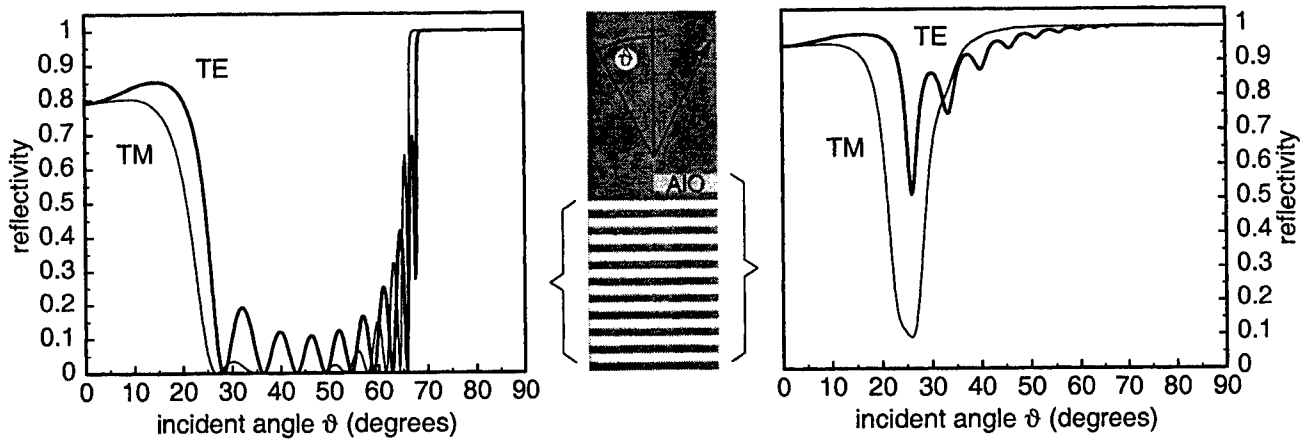


**Figure 12.** Angle dependent reflectivity of TE- and TM-waves for a pure 10 period  $\text{Al}_{0.87}\text{Ga}_{0.13}\text{As}/\text{GaAs}$  DBR (left) and for the same DBR with an additional 160 nm thick  $\text{Al}_x\text{O}_y$  layer (right).

and TM-polarizations related to the lower mirror or the taper surface. Since incoherent light generation and phase shifting reflection at the lower mirror prevent a well defined phase between TE- and TM-polarized light we use an average mixing between both states. When a ray reaches a negligible fraction of initial power the trace is discarded and another is started. A weighted integration over all solid angles and starting points yields the extraction efficiency.

For calculating the reflectivity of the lower mirror we use the layer sequence of the actually employed structure (Fig. 1) with 10 periods  $\text{Al}_{0.87}\text{Ga}_{0.13}\text{As}/\text{GaAs}$  and a 160 nm thick  $\text{Al}_x\text{O}_y$  layer. The dependences on both incident angle and polarization are shown in the right hand part of Fig. 12. To illustrate the importance of the  $\text{Al}_x\text{O}_y$  layer the left hand part of Fig. 12 shows the corresponding characteristics for a similar DBR without  $\text{Al}_x\text{O}_y$  top layer. Without the oxide layer a high reflectivity is observed only for very small and large incident angles where the layers work either as a DBR or a bulk material with an average refractive index lower than the surrounding semiconductor leading to frustrated TIR. For a broad range of incident angles reflectivity is very low which is not tolerable for high efficiency. With the  $\text{Al}_x\text{O}_y$  layer of low refractive index  $\bar{n} \approx 1.6$  included frustrated TIR already occurs at low incident angles of about  $30^\circ$  which gives high TE-reflectivities for all incident angles. For TM-waves one has to accept an unavoidable low-reflectivity dip due to the Brewster angle.

We have simulated the extraction efficiency for monochromatic light at a wavelength of 950 nm using the parameters given in Fig. 13. The observed influence of the slope of the taper on the device can be explained as follows. Since a minor change in light direction increases the number of reflections at the lossy mirror, efficiency is reduced for very low taper angles. On the other hand a steep taper prevents some light from escaping (i.e.  $\tau$  larger than the critical angle of TIR) leading to an optimum taper angle at around  $10^\circ$ . Since the reflectivity of the lower mirror is wavelength dependent the simulation is done in a wavelength range from 880 to 960 nm leading to extraction efficiencies from 25 to 33 % for a taper angle  $\tau = 10^\circ$ . Therefore the external efficiency is expected to decrease with increasing injection current due to spontaneous emission broadening. Nevertheless because no feedback of reflectivity on spontaneous emission is intentionally used in our device this effect should be of minor importance compared to resonant-cavity LEDs.

## 7. CONCLUSION

We have presented a new concept for efficient light outcoupling from LEDs applying a radial taper combined with spot-like central light generation. For material systems with efficient DBRs we have developed a processing route resulting in efficient devices without the requirement of epitaxial lift-off. First test structures show a quantum-efficiency of 12 %. Using substrate removal devices with efficiencies of about 15 % have been fabricated which can easily be transferred to material systems where effective DBRs cannot be realized. Finally we have illustrated the principles of outcoupling using a simple ray tracing model. The results clearly demonstrate that LEDs with lateral taper can be extremely attractive for achieving high light outcoupling efficiencies.

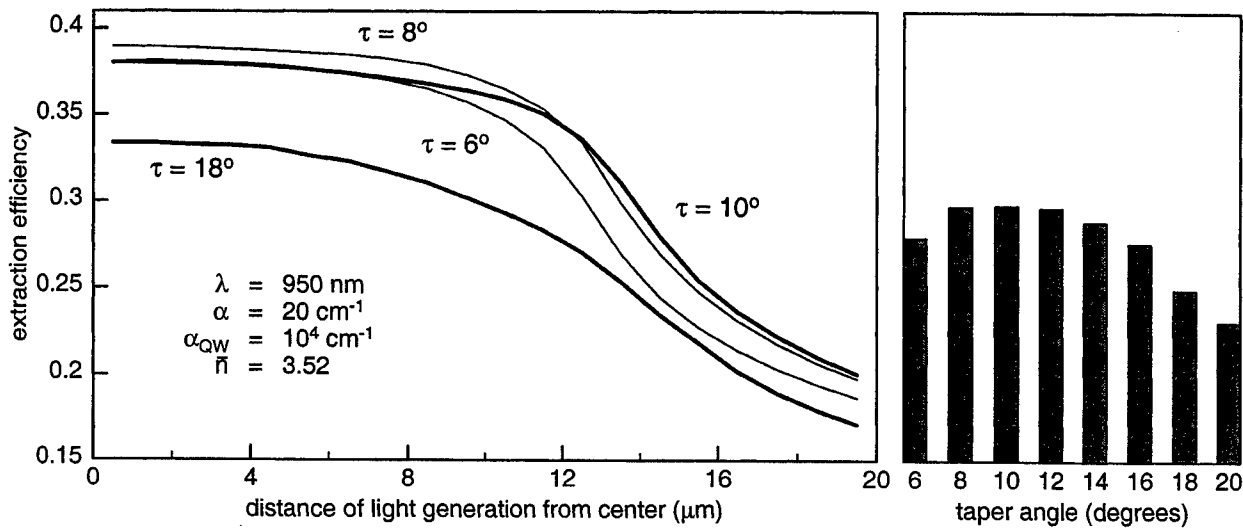


**Figure 13.** Calculated extraction efficiency as a function of the position of light generation for different taper angles (left diagram). Overall extraction efficiency resulting from  $r$ -weighted integration of the left curves (right diagram). Parameters for simulation are  $r_{\text{device}} = 50 \text{ } \mu\text{m}$ ,  $r_{\text{act}} = 20 \text{ } \mu\text{m}$  and  $n$ - and  $p$ -layers with  $2 \text{ } \mu\text{m}$  and  $0.5 \text{ } \mu\text{m}$  thicknesses, respectively.

### ACKNOWLEDGMENT

This work is supported by the "Deutsche Forschungsgemeinschaft" under contract No. EB 83/10-1.

### REFERENCES

1. E. F. Schubert, N. E. J. Hunt, M. Micovic, R. J. Malik, D. L. Sivco, A. Y. Cho, and G. J. Zydzik, "Highly efficient light-emitting diodes with microcavities," *Science* **265**, pp. 943-945, 1994.
2. H. D. Neve, J. Blondelle, P. van Daele, P. Demeester, and R. Baets, "Recycling of guided mode light emission in planar microcavity light emitting diodes," *Appl. Phys. Lett.* **70**, pp. 799-801, 1997.
3. I. Schnitzer, C. Caneau, T. J. Gmitter, A. Scherer, and E. Yablonovitch, "30 % external quantum efficiency from surface textured, thin-film light-emitting diodes," *Appl. Phys. Lett.* **63**, pp. 2174-2176, 1993.
4. R. Windisch, P. Heremans, B. Dutta, M. Kuijk, S. Schoberth, P. Kiesel, G. H. Döhler, and G. Borghs, "High-efficiency non-resonant cavity light-emitting diodes," *Electron. Lett.* **34**, pp. 1153-1154, 1998.
5. D. A. Vanderwater, I.-H. Tan, G. E. Höfler, D. C. Defever, and F. A. Kish, "High-brightness AlGaInP light emitting diodes," *Proc. IEEE* **85**, pp. 1752-1763, 1997.
6. L. Erdmann and D. Efferenn, "Technique for monolithic fabrication of silicon microlenses with selectable rim angles," *Opt. Eng.* **36**, pp. 1094-1098, 1997.
7. G. B. Stringfellow and M. G. Craford, eds., *Semiconductors and semimetals*, vol. 48, ch. "AlGaAs red light-emitting diodes". Academic Press, San Diego, 1997.
8. C. I. H. Ashby, J. P. Sullivan, P. P. Newcomer, N. A. Missert, H. Q. Hou, B. E. Hammons, M. J. Hafich, and A. G. Baca, "Wet oxidation of  $\text{Al}_x\text{Ga}_{1-x}\text{As}$ : Temporal evolution of composition and microstructure and the implications for metal-insulator-semiconductor applications," *J. Appl. Phys.* **70**, pp. 2443-2445, 1997.
9. J. LePore, "An improved technique for selective etching of GaAs and  $\text{Ga}_{1-x}\text{Al}_x\text{As}$ ," *J. Appl. Phys.* **51**, pp. 6441-6442, 1980.
10. P. Yeh, *Optical waves in layered media*, J. Wiley & Sons, New York, 1988.

# Frequency limits of high-efficiency non-resonant cavity light-emitting diodes

P. Heremans\*, R. Windisch, A. Knobloch\*, J. Potemans, B. Dutta, G. H. Döhler\*, G. Borghs

IMEC, Kapeldreef 75, B-3001 Leuven, Belgium

\* Institute for Technical Physics, University of Erlangen-Nürnberg, Erwin-Rommel-Str. 1, D-91058 Erlangen, Germany

## ABSTRACT

In this paper, we present measurements of the switch-on times and of the switch-off times of non-resonant cavity light-emitting diodes, compared to those of conventional reference diodes. From this comparison, we infer that the high quantum efficiency of NRC-LED's is not achieved by photon recycling, but purely by efficient extraction of generated photons. This is further corroborated by the good matching that is achieved between the measured switch-on times and theoretical predictions of the switch-on times. The latter are calculated with a model that includes only the electrical charging of the active layer and assumes that photon recycling does not occur. It is furthermore shown that the switch-on can be made faster by switching the diode between a non-zero low-state and the required high state. Doing so, an open eye diagram is achieved at 622 Mbit/s for a NRC-LED having an external quantum efficiency of 17%.

**Keywords:** Non-resonant cavity light-emitting diode, high-speed LED, eye diagram, switch-on, turn-on, high-efficiency LED

## 1. INTRODUCTION

High external quantum efficiencies of more than 30% can be obtained with non-resonant cavity light-emitting diodes (NRC-LED's)<sup>1</sup>. After the standard processing of the p-n LED structure, the fabrication of these LED's requires two additional processing steps: First, the substrate is removed by epitaxial lift-off and the devices are Van der Waals bonded onto a metal mirror, then the optical window of the device is textured.

The improvement in the extraction of the light in NRC-LED's compared to standard LED's could be due to a combination of two scattering processes, namely scattering at the textured surface and photon recycling. Photon recycling is a relatively slow mechanism, and therefore unwanted for high-speed LED's.

In this work, we present a study of the dynamic operation of NRC-LED's. We compare the theoretically expected optical rise time to the rise times measured on various types of LED's: un-textured on substrate, un-textured on mirror, textured on substrate and textured on mirror. From this comparison, we infer that no photon recycling is occurring.

---

\* E-mail: [heremans@imec.be](mailto:heremans@imec.be), Tel:++32-16-281521,Fax: ++32-16-281501

## 2. THEORETICAL CONSIDERATIONS ABOUT SWITCHING OF DOUBLE-HETEROJUNCTION DIODES

### 2.1 Switch-on of a double-heterojunction diode

When switching on a diode with a voltage source biased at  $V_o$ , the current first rises to  $I_o = V_o/R$  with  $R$  the series resistance of the circuit. Then, the current gradually evolves to the quasi-static current  $I_{qs}$ , the value of which is determined by the diode. The duration of the current transient between the initial  $I_o$  and the final quasi-static  $I_{qs}$  is determined essentially by the charging of the junction capacitance of the diode. For an average diode having an area of  $20 \times 20 \mu\text{m}^2$ , an active layer thickness (or depletion-layer thickness, in case of a quantum-well diode) of 100 nm and a relative permittivity of 13, the junction capacitance is of the order of 0.5 pF. When switched with a series resistance of 50 to 1000 Ohm, the corresponding time constant is 25 to 500 ps.

After this time, the current through the diode is roughly constant and equal to the quasi-static current. Initially, part of this constant current is used to charge the diffusion capacitance, i.e., it serves to increase the minority-carrier concentration in the central region. In a double-heterojunction diode made from a direct-bandgap semiconductor, this process corresponds to filling the central diode region, i.e. the active layer and eventually the quantum-wells, with both types of carriers. In a direct-bandgap semiconductor, the rate of recombination is dominantly determined by radiative recombination. It is the balance between the filling rate – by a current that can be considered constant – and the recombination rate that determines the speed with which the carriers reach their quasi-static concentration, and hence the optical turn-on speed of the diode. The rate equation is:

$$\frac{dp}{dt} = \frac{J}{ql} - R(p) \quad (1)$$

$p$  is the hole concentration,  $t$  is the time,  $J$  is the current density,  $q$  is the elementary charge,  $l$  is the active layer thickness, and  $R(p)$  is the recombination rate as a function of the hole concentration.

Once this equation is solved, the light emission as a function of time can be written as:

$$P_l(t) = R(p(t)) \cdot q \cdot l \quad (2)$$

Assuming bi-molecular recombination:

$$R(p) = Bpn \quad (3)$$

We assume that the layer where the recombination takes place has an n-type doping with concentration  $N$ . Detailed simulations using MEDICI show that the active layer remains approximately neutral during its filling with electrons and holes (after the junction capacitance has been charged). Hence, the following relationship holds between  $n$  and  $p$  during the filling process:

$$n = p + N \quad (4)$$

and therefore:

$$\frac{dp}{dt} = \frac{J}{ql} - Bp(N + p) \quad (5)$$

Using as boundary condition that the starting value for  $p$  is zero, the solution for the differential equation (5) is:

$$p(t) = \frac{1}{2} \left\{ -N + \frac{1}{\sqrt{B}} \left[ \sqrt{-4 \frac{J}{ql} - BN^2} \cdot \tan \left[ \frac{1}{2} \left( -\sqrt{B} \sqrt{-4 \frac{J}{ql} - BN^2} \cdot t + 2 \arctan \left\{ \frac{N\sqrt{B}}{\sqrt{-4 \frac{J}{ql} - BN^2}} \right\}} \right) \right] \right\} \quad (6)$$

In Figure 1, we compare the normalized transient optical output (Eqs 2+3+4) calculated from the analytical solution (6) of equation (5), using for the constant  $B$  the value of  $10^{-10} \text{ cm}^3/\text{s}$  (see e.g. ref 2). The doping level  $N$  was taken  $5 \times 10^{17} \text{ cm}^{-3}$ , the active layer thickness was assumed  $l = 30 \text{ nm}$  and the current density  $J$  was varied from  $30 \text{ A/cm}^2$  to  $3000 \text{ A/cm}^2$ .

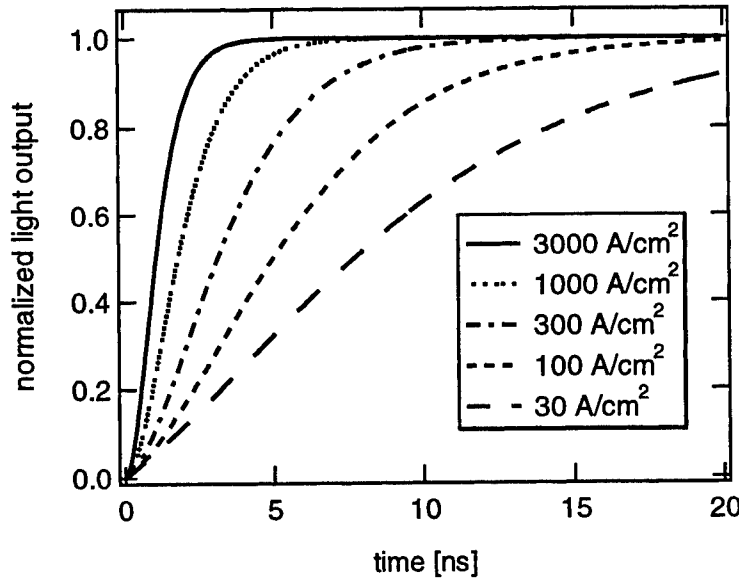


FIGURE 1: Calculated normalized transient optical output for various current densities; the active layer thickness is 30 nm.

## 2.2 The effect of photon recycling

Photon recycling is a phenomenon by which photons that are not emitted to air are re-absorbed and re-emitted. The condition for this to occur is that the photons are re-absorbed in the active layer of the material, and the generated electron-hole pair subsequently recombines radiatively<sup>3</sup>. If this process occurs, the switch-on time is slowed down. Indeed, the quasi-static electron and hole population is only obtained after a cascade of radiative recombination events have taken place.

## 2.3 Switch-off of a double-heterojunction diode

When switching off a light-emitting diode by returning to zero (or small) voltage, the mechanism for removal of the carriers from the active layer is extraction by a reverse current forced through the diode rather than radiative decay<sup>4</sup>. Indeed, the reverse current expected is:  $I_{off} = -V_F/R$  with  $R$  the series resistance of the circuit and  $V_F$  the forward voltage over the diode junction. Because of this forced carrier extraction, the switch-off time is typically faster than the switch-on time and faster than the radiative decay time. It is mostly determined by the series resistance of the device.

### 3. MEASUREMENTS OF SWITCHING TRANSIENTS OF NRC-LEDs AND OF NON-NRC-LEDs

The LEDs discussed in this paragraph have an active layer thickness of 30 nm. The structure is shown in Fig. 2. The mesa has a diameter of 54 micron, and the top contact is ring-shaped. An  $\text{Al}_{0.98}\text{Ga}_{0.02}\text{As}$  layer is oxidized laterally to produce a current aperture. In this paragraph, all LEDs had an aperture size of 15 to 17 micron in diameter. Four LEDs are compared, listed in Table 1.

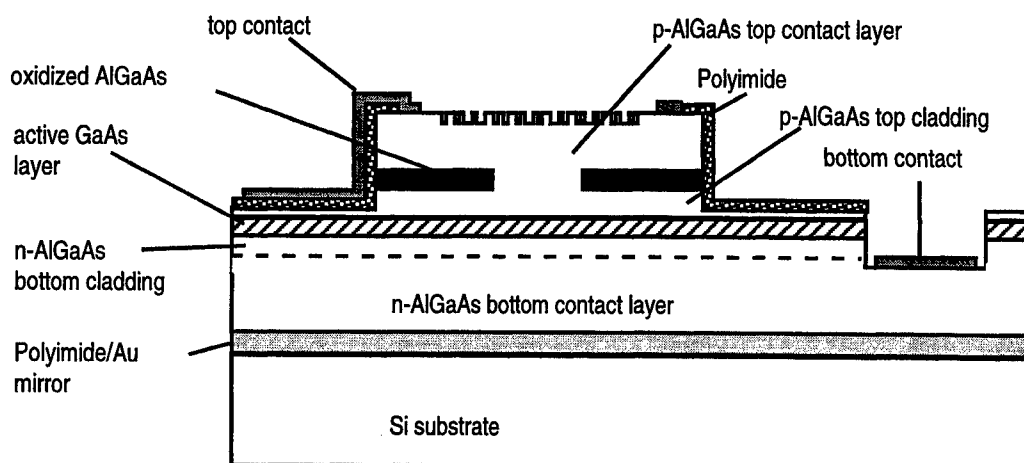


FIGURE 2: Cross-section of NRC-LED

LED type	surface texturing	on mirror
A: "NRC-LED"	yes	yes
B: "flat on mirror"	no	yes
C: "textured on substrate"	yes	no
D: "flat on substrate"	no	no

TABLE 1: Overview of tested LEDs

These LED's were pulsed to a constant voltage, in a 50-Ohm terminated circuit. The pulse generator has a rise time and fall time of approximately 400 ns. The optical output was measured with a high-speed photodiode the output of which was connected to a 1 GHz oscilloscope. The 10-to-90 percent switch-on times and switch-off times of two of each of these 4 LED types are compared in Table 2, for comparable quasi-static current densities of 1200 to 1500  $\text{A}/\text{cm}^2$ .

From Table 2, it is clear that within the margin of experimental error, the switch-on times are equal in all cases. There is, in other words, no measurable slow-down of NRC-LED's compared to LED's which are flat on substrate, despite the more than 1 order of magnitude higher efficiency. From this and from the discussion in paragraph 2.2, we infer that no photon recycling is occurring in our samples. The efficiency increase observed for the NRC-LED's is entirely due to a larger extraction efficiency of generated photons, and not to photon recycling.

It is further clear from Table 2 that the turn-off speed is high compared to the turn-on speed, as predicted in paragraph 2.3.

LED type	10%-90% rise time ns	90%-10% fall time ns	Maximum external quantum efficiency (%)
A: "NRC-LED"	4.00 3.21	0.78 0.76	approx. 17
B: "flat on mirror"	4.42 3.64	0.77 0.75	
C: "textured on substrate"	3.97 3.98	0.73 0.84	
D: "flat on substrate"	4.11 3.91	0.73 0.76	approx. 1.5

TABLE 2: Comparison of rise and fall times and external quantum efficiency of tested LEDs, at current densities of 1200 to 1500 A/cm<sup>2</sup>

#### 4. COMPARISON OF SWITCH-ON TIMES OF NRC-LEDs WITH THEORY

Since we conclude that no photon recycling occurs in the NRC-LED's presented in this study, it should be possible to model the switch-on time using the theory presented in paragraph 2.1.

Figure 3 shows the measured optical switch-on and switch-off transient, for a NRC-LED pulsed at constant voltage. The quasi-static current density corresponding to this constant voltage is 865 A/cm<sup>2</sup>. For comparison, the switch-on transient calculated for switching from zero to a constant current density of 865 A/cm<sup>2</sup> using Eq. 6 is also shown in Figure 3. It can be seen that the calculation is in fair agreement with the measurements. It can, furthermore, be observed that the theory actually tends to predict a slower turn-on transient than the measured transient. This confirms the finding in the previous paragraph that no photon recycling is observed in the measurement.

The main factor in equation (5) and its solution (6) is the ratio  $J/l$ , i.e., the ratio of the current density to the active layer thickness. Figure 4 shows a comparison of the measured (symbols) and calculated 10-to-90 percent rise times as a function of quasi-static current density for an NRC-LED with an active layer of 30 nm. It can be seen that 10-to-90 percent switch-on times of 2 ns can be achieved with approximately 2000 A/cm<sup>2</sup> for an active layer thickness of 30 nm.

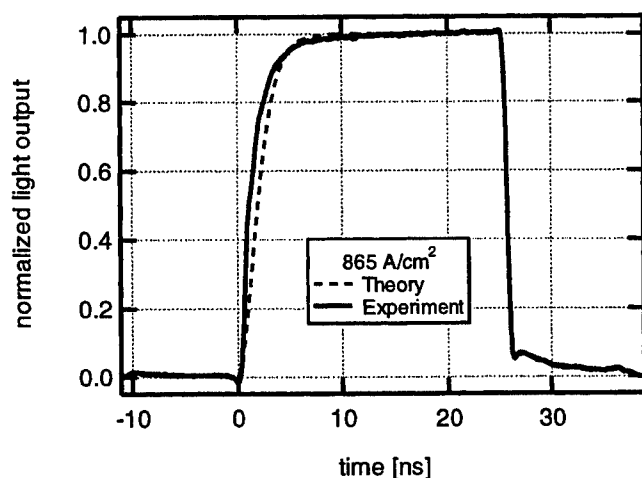


FIGURE 3: Measured switch-on and switch-off for NRC-LED pulsed at constant voltage, and calculated switch-on time for corresponding current density.

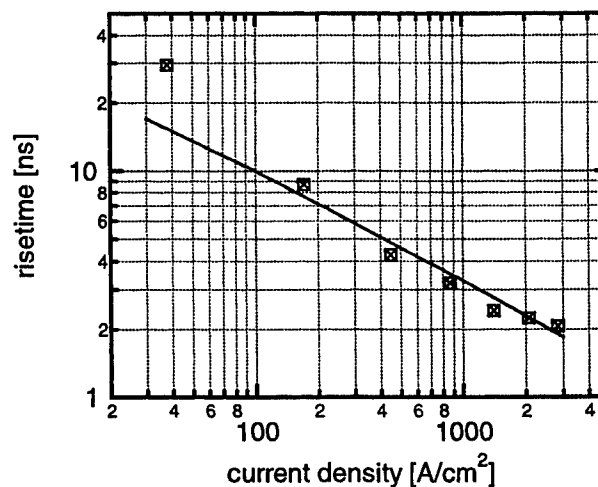


FIGURE 4: Comparison of measured (symbols) calculated (line) 10-to-90 percent switch-on times as a function of current density.

The agreement between measurement and calculation is remarkable for current densities larger than about  $100 \text{ A/cm}^2$ . For smaller current densities, the measured transient is slower than the theory would predict. We attribute this discrepancy to the fact that Eq. 1 is based on the assumption that the carrier density is constant over the thickness of the active layer, and that this assumption may be invalid when the carrier injection into the active layer is too small.

## 5. SWITCHING FROM NON-ZERO LOW-STATE VOLTAGE

A way to decrease the switch-on time to values smaller than achieved in Fig. 4 is to switch the LED from a non-zero low-state voltage. This comes down to altering the boundary condition of Eq. 5 such as to include a charge offset at time zero.

The NRC-LED's used for this study had a square current aperture with sides of 22 microns, larger than those of the previous paragraph. Figure 5 shows the measured 10-to-90 percent switch-on times (closed circles) and switch-off times (open circles) when pulsed from 0 V to various high-state voltages, as a function of the current density  $J_{\text{high}}$  reached at these high-state voltages. When increasing the low-state voltage above 0 V, the switch-on time decreases, while the switch-off time increases. For every high-state current density, there is a low-state current density such that rise and fall times become equal. The solid line in Fig. 5 is the fall time and rise time for this condition. The low-state current density used to achieve equal rise and fall time is written along the curve.

From Figure 5, sub-2 ns equal rise and fall times can be achieved at  $800 \text{ A/cm}^2$ . An eye diagram taken at 622 Mbit/s with a pseudo-random bitstream of  $2^{23} - 1$  bits for a high-state current of 3.9 mA ( $800 \text{ A/cm}^2$ ) is shown in Fig. 6. Thanks to the equal rise and fall times, the eye opening is symmetric. The external quantum efficiency of this NRC-LED at the current of 3.9 mA is 17%. To our knowledge, the combination of 2 ns rise and fall times with 17% external quantum efficiency results in the LED with the largest speed  $\times$  efficiency product published so far<sup>5</sup>, even compared to edge-emitting diodes<sup>6</sup> and high-speed field-effect light-emitting triodes<sup>7</sup>.

We conclude that switching from a non-zero low voltage has two benefits. Firstly, it allows to decrease the high-state current density. This is favorable for the long-term reliability of the LED and at the same time for the power consumption. Secondly, by simultaneously increasing the fall time and decreasing the rise time, it makes the optical pulse shape symmetric, and this is beneficial for the detector system.

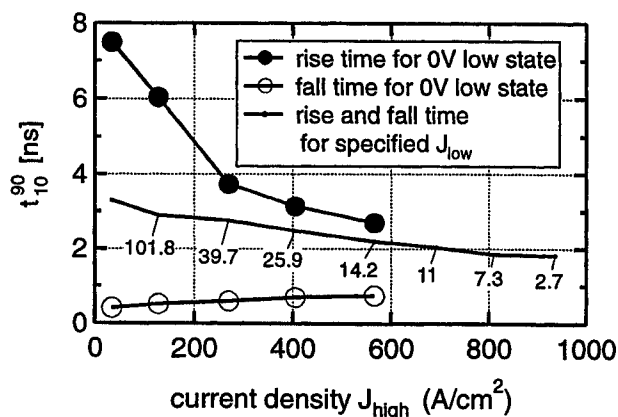


**FIGURE 5:** Symbols: optical rise (full circles) and fall times (open circles) for NRC-LEDs switched from 0 V to the constant voltage that results in the values of  $J_{\text{high}}$  labeled on the bottom axis.  
Line: optical rise time and fall time vs.  $J_{\text{high}}$  when switched to a low-state voltage (corresponding to indicated  $J_{\text{low}}$ ) such that rise and fall times are equal

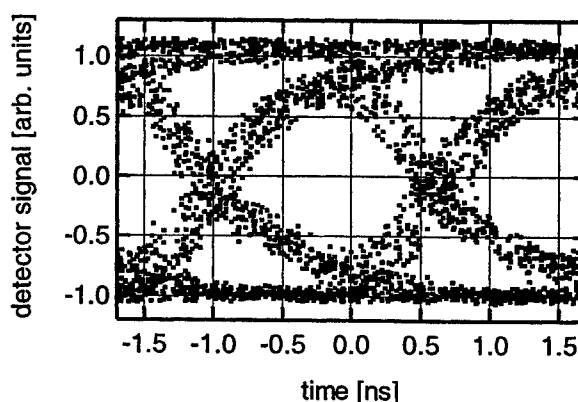


**FIGURE 6:** Eye diagram measured at 622 Mbit/s using a pseudo-random bitstream of  $2^{23} - 1$  bits.



## 6. CONCLUSIONS

In this paper, we prove that the high external quantum efficiency of the studied NRC-LED's is not achieved by photon recycling and that therefore the speed is determined by the same factors as govern the speed of conventional planar LEDs. Both theoretically and experimentally, we show that the main factor determining the switch-on speed is the ratio of the current density to active layer thickness. Furthermore, we show that the NRC-LED can be speeded up by having it switched from a larger-than-zero low-state voltage.

From all known LED types, NRC-LED's prove to have the largest speed  $\times$  efficiency product, known to be an important parameter for high-speed LEDs. We have demonstrated a combined 17% external quantum efficiency with 2-ns 10-to-90 percent optical rise and fall times, allowing operation at 622 Mbit/s.

## ACKNOWLEDGEMENTS

The authors thank W. Van de Graaf for the MBE growth of the samples and S. Peeters for help with device processing. This work was in part funded by the EC under contract No. 22641 (OIIC). R. Windisch acknowledges the EC for his Marie Curie Fellowship (TMR grant No. ERBFMCT972046).

## REFERENCES

1. R. Windisch, P. Heremans, J. Potemans, A. Knobloch, B. Dutta, G. Dohler, G. Borghs, "31% absolute external quantum efficiency 850-nm LEDs and their modulation behavior", *IEDM technical digest*, pp. 1026-1028, 1998.
2. S. M. Sze, *Physics of Semiconductor Devices*, 2<sup>nd</sup> Ed., Wiley, 1981
3. H. De Neve, J. Blondelle, P. Van Daele, P. Demeester, R. Baets and G. Borghs, "Recycling of guided mode light emission in planar microcavity light emitting diodes", *Applied Physics Letters* Vol. 70, p. 799, 1997
4. E. F. Schubert, N. E. J. Hunt, R. J. Malik, M. Micovic and D. L. Miller, "Temperature and modulation characteristics of resonant-cavity light-emitting diodes", *IEEE Journal of Lightwave Technology*, Vol. 14, p. 1721-1729, 1996
5. T. J. de Lyon, J. M. Woodall, D. T. McInturff, R. J. S. Bates, J. A. Kash, P. D. Kirchner and F. Cardone, "Doping concentration dependence of radiation and optical modulation bandwidth in carbon-doped Ga<sub>0.51</sub>In<sub>0.49</sub>P/GaAs light-emitting diodes grown by gas source molecular beam epitaxy", *Applied Physics Letters* Vol. 60, p. 353, 1992.
6. M. Ettenberg, M. G. Harvey and D. R. Patterson, "Linear, high-speed, high-power strained quantum-well LEDs", *IEEE Photon. Techn. Lett.*, Vol. 4, p. 27, 1992
7. T. Ohnishi, K. Mukaiyama, M. Yamanishi, N. Ochi, Y. Ono, Y. Kan, H. Ishikawa and I. Suemune, "300 ps switching of spontaneous emission by quantum confined field effect in a light emitting diode", *IEEE Photon. Techn. Lett.*, Vol. 2, p. 546, 1990.

# Size dependence of record-efficiency non-resonant cavity light-emitting diodes

R. Windisch\*, P. Heremans, B. Dutta, S. Nemeth, A. Knobloch†, G. H. Döhler†, and G. Borghs

IMEC, Kapeldreef 75, 3001 Leuven, Belgium

† Institute for Technical Physics I, University of Erlangen-Nürnberg, Erwin-Rommel-Str.1,  
91058 Erlangen, Germany

## ABSTRACT

Non-resonant cavity light-emitting diodes (NRC-LED's) are based on the combination of surface texturing and the application of a back mirror. With this concept, the extraction efficiency of LED's can be enhanced considerably. We fabricated NRC-LED's with a more sophisticated design employing an oxidized current aperture, which is similar to that commonly used for vertical-cavity surface-emitting lasers. In our NRC-LED's, it confines the injection current to the center of the device in order to reduce light generation below the top contact. We analyze the impact of the aperture size on the device performance, and we show that both the maximum efficiency and the injection current where it is reached are strongly dependent on the device size. Its correlation with the temperature in the active region and the current density is discussed. In addition, we demonstrate that a considerable fraction of the light can be extracted from lateral guided modes in the LED structure by extending the surface texturing beyond the device mesa. Devices fabricated by applying all of the above techniques result in record external quantum efficiencies of 31%.

**Keywords:** Non-resonant cavity light-emitting diode, surface texturing, oxidized aperture, outcoupling of guided modes

## 1. INTRODUCTION

The external efficiency of conventional LED's is limited by total internal reflection due to the large difference in the refractive index between the semiconductor and air. In single LED's made for illumination purposes, this problem can in part be overcome by intelligent packaging. This, however, is not a viable solution for LED arrays required for parallel optical interconnects. One way to increase the external efficiency of planar LED's is to incorporate the LED in a resonant cavity. With this approach, external quantum efficiencies of more than 20% have been reached. However, such high efficiencies can only be achieved for large-area devices, because photon recycling is required<sup>1</sup>. This makes the use of microcavity LED's unattractive for optical interconnects, since the dynamic characteristics of large devices are poor.

Another approach which allows to increase the external efficiency is to make use of a non-resonant cavity, i.e. a cavity formed between a backside mirror and a textured top surface. The light which is internally reflected at the semiconductor-air interface is scattered due to the surface texturing, and gets a second chance to escape from the semiconductor after being reflected at the back mirror (see Fig. 1)<sup>2</sup>. Recently, we have shown that this effect allows the fabrication of small and highly efficient LED's, which have remarkable external quantum efficiencies at very low currents<sup>3</sup>. This is only possible if the current confinement in the LED does not depend on current crowding. For this reason, we have incorporated a current aperture fabricated by selective wet oxidation of an  $\text{Al}_{0.98}\text{Ga}_{0.02}\text{As}$  layer, which defines the effective device size. In order to determine the minimum LED size that is possible without paying a penalty in efficiency, we investigate the dependence of the external quantum efficiency on the aperture size.

---

\* Email: windisch@imec.be

## 2. DEVICE FABRICATION

### 2.1. LED Structure

The LED layers are grown by MBE on a GaAs substrate. Following the buffer layer, a 50 nm thick sacrificial AlAs layer is grown to perform epitaxial lift-off. The actual LED structure consists of a 120 nm thick active GaAs layer embedded between AlGaAs cladding layers. In the top cladding, a 130 nm thick  $\text{Al}_{0.98}\text{Ga}_{0.02}\text{As}$  layer is introduced for selective lateral oxidation. Mesas with a diameter of 60  $\mu\text{m}$  are structured by wet chemical etching, which is stopped between the  $\text{Al}_{0.98}\text{Ga}_{0.02}\text{As}$  layer and the active layer. Subsequently, the oxidation of the  $\text{Al}_{0.98}\text{Ga}_{0.02}\text{As}$  layer is performed in an  $\text{N}_2/\text{H}_2\text{O}$  atmosphere at temperatures between 370°C and 390°C for 10 min. The temperature used during the oxidation determines the diameter of the current aperture.

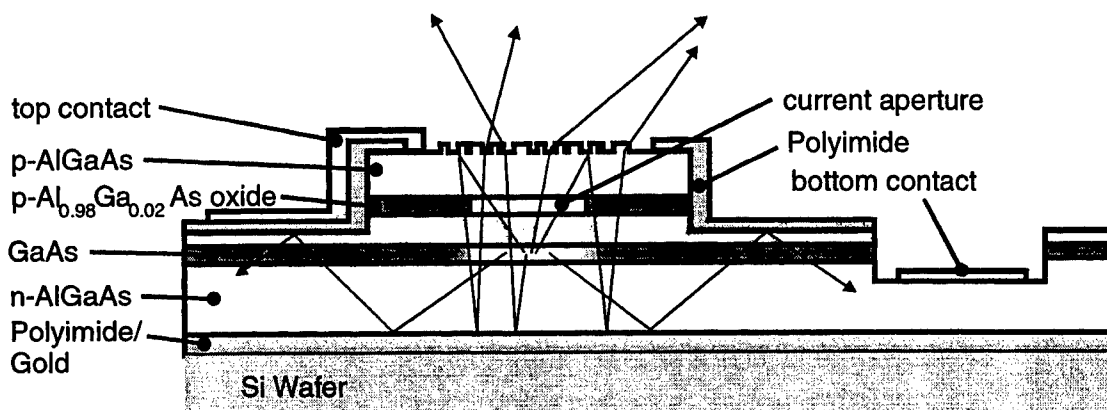


Fig. 1: Schematic drawing of our non-resonant cavity LED structure. Typical trajectories of the light emitted in the active GaAs region underneath the current aperture are also shown.

After oxidation, a polyimide surface passivation layer is applied and opened on the mesa top and for the bottom contact. After etching down to the n-doped bottom layer, the bottom contact is evaporated and annealed. The top contact consists of a non-alloyed TiW/Au contact, which contacts the mesa top only above the oxide layer and extends over the mesa edge for probing. In this way, the generation of light below the top contact is avoided. The devices processed up to this stage are still conventional LED's and exhibit external quantum efficiencies between 1.5 and 2%. In order to fabricate NRC-LED's, two additional processing steps are necessary: Surface texturing and the application of a back mirror.

### 2.2. Surface Texturing

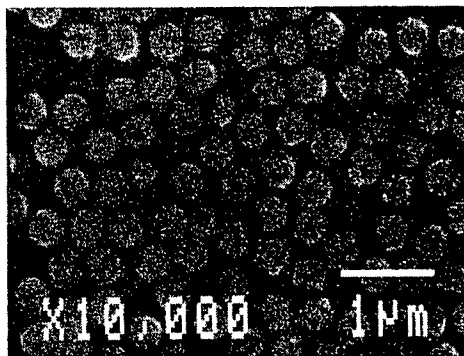


Fig. 2: Distribution of the polystyrene spheres on the surface after size reduction in oxygen plasma.

The surface texturing is performed using a technique which is often called natural lithography<sup>4</sup>. In this technique, a monolayer of randomly distributed polystyrene spheres is used as a mask for dry etching.

In the first step, a monolayer of polystyrene spheres is formed on a water surface and transferred onto the sample surface, which is treated to be hydrophilic. The result is a densely packed monolayer of polystyrene spheres. In a previous study<sup>5</sup>, we have shown that the optimum sphere size for GaAs LED's is about 300 nm, if this layer is used as a mask for dry etching. However, the scattering efficiency of the surface fabricated in this way is not optimum, as the pillars formed by the dry etching are not single, but are in contact with each other. In order to avoid this, the spheres would have to be deposited with a lower packing density, but still homogeneously. This is not easily possible with the current technique. As an alternative, we deposit larger spheres of 400 nm diameter and

reduce their size in an oxygen plasma to approximately 300 nm. The resulting coverage of the surface is shown in Fig. 2.

In the next step, Cl-assisted Ar etching is used to etch the top of the devices using the spheres as a mask to an etch depth of 170 nm. The resulting surface is shown in Fig. 3. After etching, the spheres are removed from the sample.

### 2.3. Application of a Back Mirror

The final step in the processing of NRC-LED's is the application of a back mirror. This is done by performing epitaxial lift-off on LED arrays of a few millimeters in size. After epitaxial lift-off, the LED's are Van der Waals bonded onto a polyimide coated gold mirror evaporated on a silicon wafer. Fig. 1 shows a schematic cross-section of a completely processed NRC-LED.

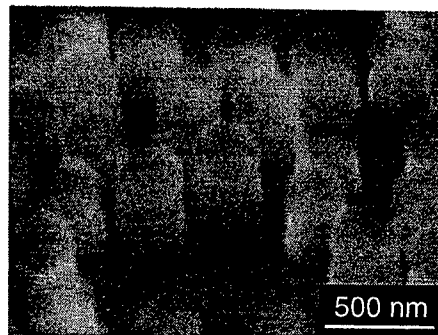


Fig. 3: The surface after dry etching. The polystyrene spheres are still present.

## 3. APERTURE SIZE DEPENDENCE

### 3.1. Device Characteristics

The emitted optical power is measured with a calibrated photodetector with a radius  $r = 5.65$  mm, which is positioned at a distance of approximately 4 cm above the device. The setup is calibrated such that the calculated total light output is independent from the measuring distance. In order to do this, the distance between the sample holder and the housing of the detector is determined with a precision better than 0.05 mm using a calliper. An offset between this measured distance and the precise distance  $d$  between the device and the detector arises from the detector housing geometry and the sample thickness. This offset can be determined by measuring the output power for varying distances between the sample and the detector.

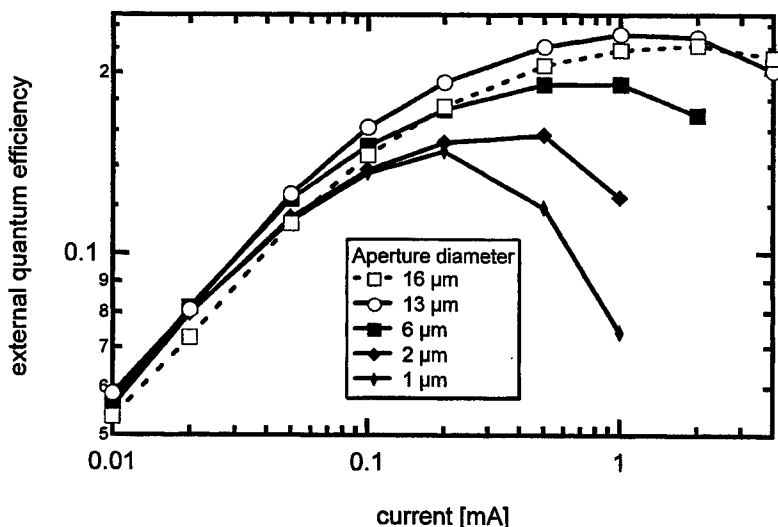


Fig. 4: External quantum efficiency of NRC-LED's versus device current for various current apertures.

In addition, the angular light output was measured and found to be Lambertian. Using this information, the total light output  $P_{opt}$  of the LED can be calculated from the measured power  $P_{meas}$  with the formula

$$P_{opt} = P_{meas} \cdot \frac{d^2}{r^2},$$

which assumes that the distance between the detector and the device is large enough such that only the light emitted into a small angle is measured. This assumption is justified for all our measurements. Finally, the external quantum efficiency is calculated using the formula

$$\eta = \frac{P_{opt} / E_{phot}}{I / q}$$

with  $E_{phot}$  being the energy of the emitted photons,  $q$  being the elementary charge, and  $I$  being the device current.

Fig. 4 shows the external quantum efficiency of our NRC-LED's for various aperture sizes. The maximum external quantum efficiency obtained with NRC-LED's textured only on the top of the device is 23%. This efficiency is reached as soon as the current aperture is at least 12  $\mu\text{m}$  in diameter for currents of 1 mA and higher. For smaller aperture sizes, the efficiencies are still identical for low currents, but start dropping already at currents below 1 mA, and thus the devices do not reach the highest efficiencies.

The drop in efficiency at low currents is due to nonradiative recombination, while the drop at high currents is often believed to be due to simple heating effects<sup>2</sup>. The latter can be studied in detail by investigations of the temperature dependence of the light output and of the influence of the injection current on the LED spectra, which allows conclusions on bandfilling effects. These studies will be described in the following sections.

### 3.2. Temperature Dependence

The temperature dependence of the devices is characterized by measuring the spectra and the total light output power with the sample placed on a hotplate. The results of the measurements are shown in Fig. 5 and Fig. 6, respectively. It is not only important for the physical explanation of the decrease in efficiency for high currents, but the temperature dependence shown in Fig. 6 is also an important aspect of the device performance, especially for the application in optical communication systems. Hence, it is important to note that the observed decrease of 0.36% per degree is much smaller than for any other high efficiency light sources. The small decrease of the efficiency in NRC-LED's is due to their independence from a resonance.

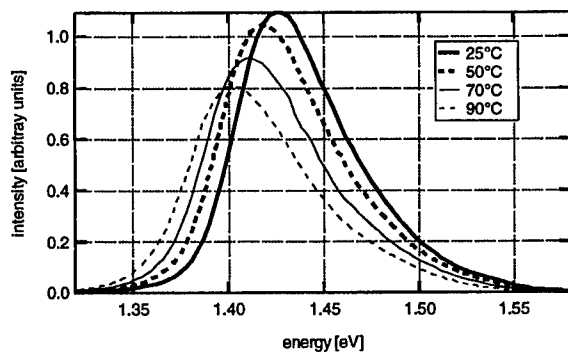


Fig. 5: Spectrum emitted from NRC-LED's for various temperatures. The device current is uniformly 0.1 mA, the aperture size is 16  $\mu\text{m}$ .

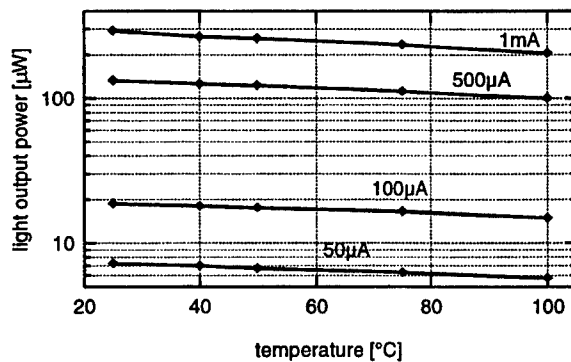


Fig. 6: Temperature dependence of the light output. The emitted optical power decreases only by 0.36% per degree.

The spectra from Fig. 5 show two important features. As expected, the maximum of the spectrum moves to lower energies with increasing temperature, which is due to the temperature dependence of the GaAs bandgap energy. Besides this, only the intensity decreases, as also shown in Fig. 6, while the linewidth remains almost constant. This behaviour has to be compared with the dependence of the spectrum on the device current.

### 3.3. Current Dependence

The current dependence of the spectrum of a device which is 5  $\mu\text{m}$  in diameter is shown in Fig. 7. This device reaches its maximum efficiency at currents around 0.7 mA, as can be seen from Fig. 4. At a current of 1 mA, the efficiency starts decreasing rapidly.

This behaviour is correlated to a change in the emitted spectrum. For currents below 0.5 mA, the spectrum does not change considerably. At 1 mA, however, the spectrum is clearly broadened. In addition, it is slightly shifted to lower energies, indicating heating of the GaAs lattice. The corresponding device temperature is 45°C.

From the measurement of the temperature dependence, however, it is known that heating the device by 20°C only results in a decrease in efficiency by 7%, which is less than observed when comparing the 5  $\mu\text{m}$  aperture device with a device which reaches its highest efficiency of 23% at 1 mA.

In addition, the comparison of the spectrum measured at low currents and elevated temperatures with the spectrum measured at higher currents indicates that the decrease in efficiency at high currents is not purely due to heating of the device. The considerable high energy tail of the spectrum suggests a combination of bandfilling effects and an increase in the electron temperature above the lattice temperature. The electron temperature can be extracted from the high energy decay of the spectrum as shown in Fig. 7. For the evaluation, only the energy range between 1.47 and 1.54 eV is useful, as the absorption in the AlGaAs layers in the LED structure cuts off higher photon energies. The result of this evaluation is shown in Fig. 8.

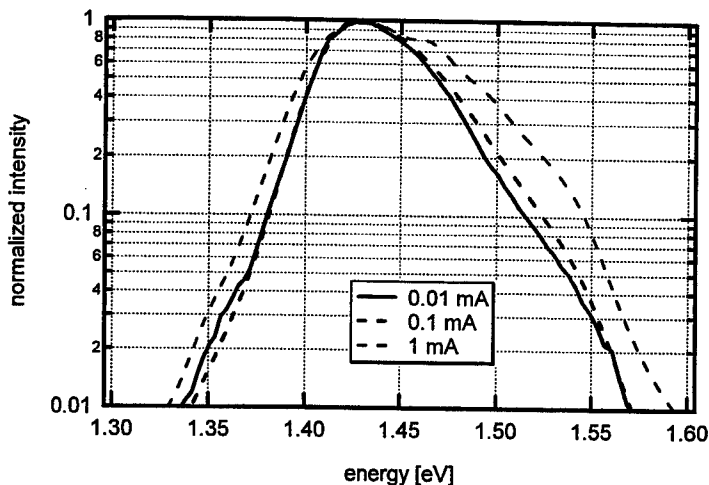


Fig. 7: Normalized spectra emitted from an NRC-LED with 5  $\mu\text{m}$  aperture diameter for various currents at room temperature.

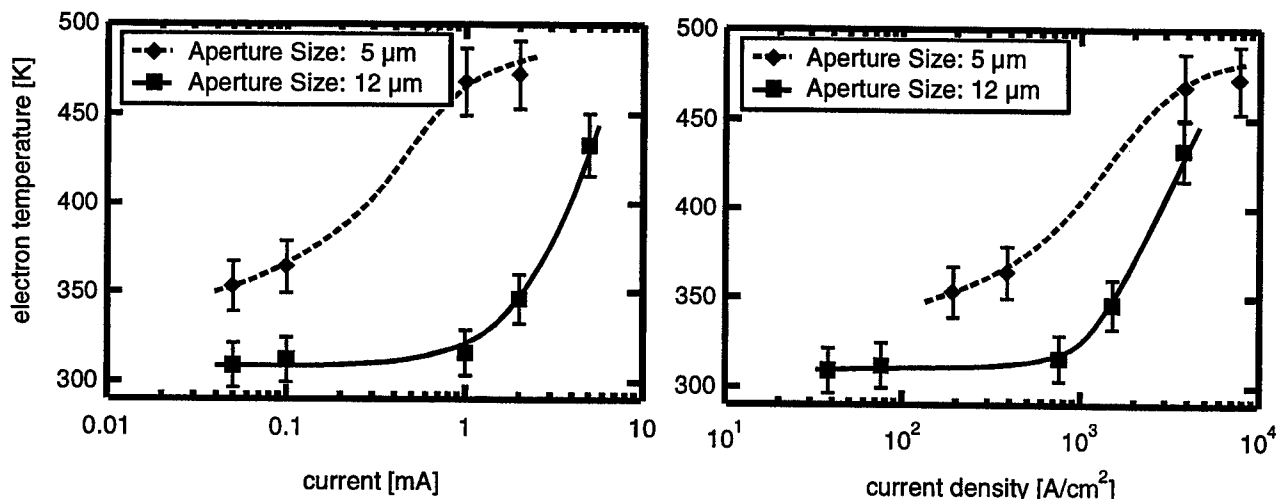


Fig. 8: The electron temperature as determined from the high energy tail of the measured spectra for two different aperture sizes. The spectra for the 5  $\mu\text{m}$  aperture device are shown in Fig. 7. The left graph shows the dependence on the current, the right graph displays the current density dependence of the electron temperature.

For low currents, the electron temperature is close to the sample temperature, as expected. In the high current regime, the electron temperature appears to be more than 100°C above the lattice temperature. This explains the fast decrease in efficiency for high currents: Due to the high electron temperature, which is in addition combined with bandfilling, the carriers have a larger probability to escape from the active layer by thermal excitation across the AlGaAs barrier. In the AlGaAs, the carriers either recombine non-radiatively due to the relatively low minority carrier concentration, or drift all the way to the contact.

The comparison between various aperture sizes shows that considerable heating of the carriers occurs typically at current densities above about 2000  $\text{A}/\text{cm}^2$  (see right graph in Fig. 8). In other words, for current densities above approximately

2000 A/cm<sup>2</sup> the efficiency is mainly limited by carrier spill-over into the AlGaAs layers. Thus higher the current density, the stronger the limitation. This is represented qualitatively by the dotted line in Fig. 9, which shows the external quantum efficiency for various aperture sizes as a function of the current density.

### 3.4. Large Apertures

In the previous sections the discussion concerns the behaviour of devices with an aperture size smaller than 12  $\mu\text{m}$ , where the maximum external efficiency is lower than for larger apertures. Now, we will briefly discuss the aperture size dependence of larger devices. In figures 4 and 9, the efficiency is also shown for a device with an aperture of 16  $\mu\text{m}$ . One can observe that a further increase in efficiency is not possible anymore. As the same external efficiencies have also been obtained from other samples with apertures as large as 35  $\mu\text{m}$ , we conclude that the slightly smaller efficiency of the 16  $\mu\text{m}$  sample is mainly due to local variations in the layer quality.

In Fig. 4 it can be seen that the efficiency-current curve for the 16  $\mu\text{m}$  device appears to be shifted to higher currents. For devices which are large enough such that edge effects do not play an important role anymore, it can be assumed that the current density is the parameter of interest, instead of the total current. This is confirmed in Fig. 9, where the curves for 13  $\mu\text{m}$  and 16  $\mu\text{m}$  aperture size are identical within typical deviations between different devices. Thus, for larger apertures than 13  $\mu\text{m}$ , the current where the maximum quantum efficiency is reached increases with the aperture size.

We conclude that for low power applications like short-range optical interconnects the optimum aperture size of NRC-LEDs of the presented design is approximately 13  $\mu\text{m}$ . Smaller apertures result in lower efficiency devices, while larger apertures reach the maximum efficiency at higher current levels. In contrast, for applications where high luminosity is a requirement, obviously large area LED's are the devices of choice.

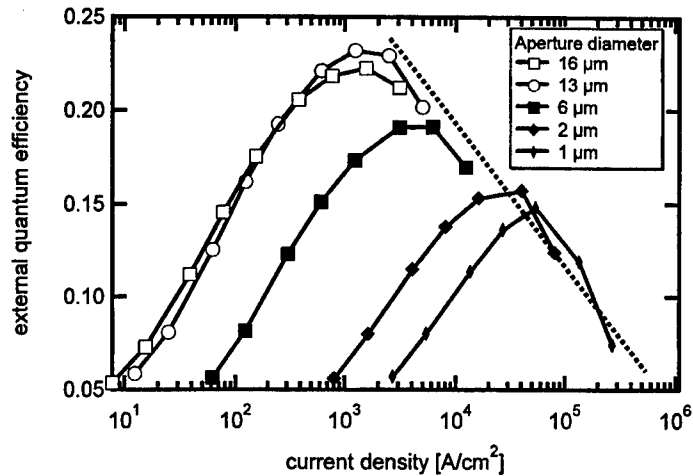


Fig. 9: External quantum efficiency of NRC-LED's with various aperture sizes as a function of the current density. The dotted line represents the upper limit for the efficiency at high current densities. Note that the precise determination of the aperture size is difficult for small apertures, so the curves for 1 and 2  $\mu\text{m}$  apertures might be shifted slightly too far to high current densities.

## 4. OUTCOUPLING OF GUIDED MODES

The above described study on the aperture size dependence was performed on devices which were textured on top of the device mesa, as shown in Fig. 1. In this figure it is also shown that a fraction of the emitted light is also coupled into a waveguide structure which is formed between the back mirror and the flat top surface next to the actual device. In addition, a wave-guide is also formed within the active layer of the LED structure itself, as it is a GaAs layer embedded in between two AlGaAs layers of a lower refractive index (not shown in Fig. 1).

A simple estimation of the angle of total internal reflection between GaAs and Al<sub>0.25</sub>Ga<sub>0.75</sub>As shows that around 30% of the emitted light can be expected to be coupled only into the latter waveguide. Hence, the external efficiency of NRC-LED's can be further improved by outcoupling of these guided modes.

In order to achieve this, the processing of the NRC-LED's is varied slightly. The polyimide passivation layer is now removed from the complete surface, except for the area under the probing pad of the top contact, where it serves as insulation layer. The surface texturing step is performed on the complete sample surface, instead of only texturing the top of the devices. As the metal contacts are hardly etched during the dry etching, it is not necessary to protect the contact area from being textured. The top panel of Fig. 10 shows microscope photographs of the two types of devices.

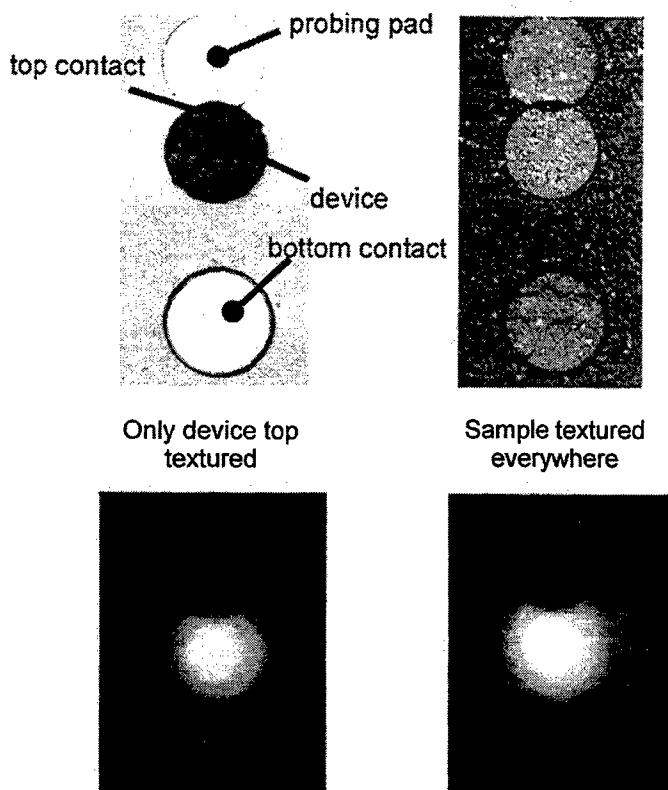


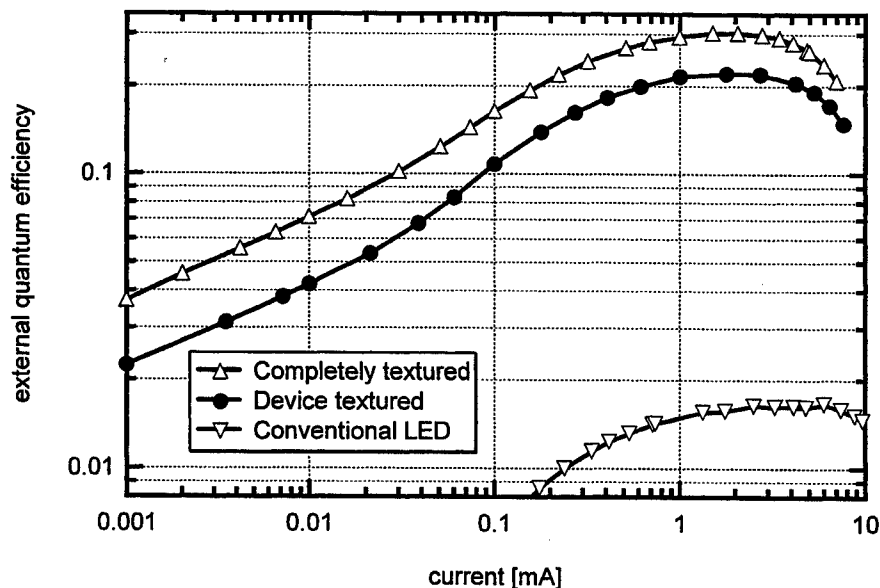
Fig. 10: Microscope photographs of NRC-LED's which are textured only on top of the device mesas (left side) and everywhere (right side). The top panel shows a top view of the devices. The textured regions appear dark, as their reflectivity is reduced. The bottom panel shows the LED's under operation. The aperture size of the LED's displayed in this figure is 32  $\mu\text{m}$ .

The bottom panel shows the respective LED's under operation. The device textured only on the mesa top shows bright emission from the center, which corresponds to the current aperture, and a weaker emission from the edge, which corresponds to the oxidized area. The latter is due to photon diffusion within the LED structure, as already indicated in Fig. 1.

In contrast to this, the LED textured everywhere shows an additional emission from the area around the device, which decays homogenously with the distance from the device center. The light emitted here is coupled out from the above described waveguides. As the etching performed for texturing proceeds to a depth of 170 nm, also the active layer itself is textured, such that also light from the intrinsic waveguide in this GaAs layer can be coupled out. Although the area around the device appears to be relatively dark, a considerable amount of light is emitted there, as the area is considerably larger than the device itself.

The external quantum efficiency of this completely textured LED is shown in Fig. 11. It can be seen that the light output is homogenously increased by approximately 50% throughout the whole current range when compared to the device textured only on the mesa top. This results in a record external quantum efficiency of 31% achieved by outcoupling of these guided modes.

Fig. 11: External quantum efficiency of the NRC-LED's taken from the same processing run with and without the outcoupling of guided modes by texturing the complete sample surface. The aperture size is 16  $\mu\text{m}$ . Their efficiencies are also compared with a conventional LED, i.e. the LED with an untextured surface on the original GaAs substrate. The completely textured LED reaches a record efficiency of 31%.





The effective device size of these LED's is larger than the aperture size. However, in case a small device is desired, it should be feasible to break the waveguide also with a mirror placed under a tilted angle at the mesa edge. In this way, the light from the waveguide can be reflected back into the device, where it can be extracted.

## 5. CONCLUSIONS

We have presented non-resonant cavity GaAs LED's with record external quantum efficiencies. These efficiencies are obtained with an LED design that employs an oxidized current aperture to avoid light generation below the top contact. Thus, the effective device size is defined by the aperture size. We have studied the effect of the aperture size on the performance of the device. The maximum efficiency is reached for aperture diameters of 12  $\mu\text{m}$  and more. The decrease in efficiency for lower aperture sizes, and correspondingly for higher current densities, is demonstrated to be due to carrier spill-over into the AlGaAs cladding layers, due to a combination of bandfilling and an increase in the electron temperature. In the context of this study, we have also shown that the decrease of the light output with increasing temperature is as small as 0.36%/°C.

In addition, we have demonstrated the outcoupling of light which is trapped in the lateral guided modes in the LED structure, which results in an external quantum efficiency of 31%, corresponding to 0.44 mW/mA. The extraction of light from guided modes by surface texturing is not only applicable for NRC-LED's, but also for other LED structures like microcavity LED's.

## ACKNOWLEDGEMENTS

The authors thank W. Van de Graaf for the MBE growth of the samples and S. Peeters for help in processing. This work was in part funded by the EC under contract No. 22641 (OIIC). R. Windisch acknowledges the EC for his Marie Curie Fellowship (TMR grant No. ERBFMICT972046).

## REFERENCES

1. H. De Neve, J. Blondelle, P. Van Daele, P. Demeester, R. Baets, and G. Borghs, "Recycling of guided mode light emission in planar microcavity light emitting diodes", *Appl. Phys. Lett.* **70**, pp. 799-801, 1997
2. I. Schnitzer, E. Yablonovitch, C. Caneau, T. J. Gmitter, and A. Scherer, "30% external quantum efficiency from surface textured, thin-film light-emitting diodes", *Appl. Phys. Lett.* **63**, pp. 2174-2176, 1993
3. R. Windisch, P. Heremans, B. Dutta, M. Kuijk, S. Schoberth, P. Kiesel, G. H. Döhler, and G. Borghs, "High-efficiency non-resonant cavity light-emitting diodes", *Electronics Lett.* **34**, pp. 1153-1155, 1998
4. H. W. Deckman and J. H. Dunsmuir, "Natural lithography", *Appl. Phys. Lett.* **41**, pp. 377-379, 1982
5. R. Windisch, P. Heremans, B. Dutta, S. Schoberth, J. Genoe, M. Kuijk, P. Kiesel, G. H. Döhler, and G. Borghs, "Systematic photoluminescence and electroluminescence study of high efficiency surface-textured thin-film light-emitting structures", *Proc. SPIE* **3279**, pp. 94-103, 1998

# Realisation of highly efficient and high-speed Resonant Cavity LED for coupling to Plastic Optical Fibres.

Ronny Bockstaele, Thierry Coosemans, Carl Sys, Luc Vanwassenhove, An Van Hove,  
Bart Dhoedt, Ingrid Moerman, Peter Van Daele, Roel Baets

University of Gent, INTEC - Department of Information Technology - IMEC  
St-Pietersnieuwstraat 41, B-9000 Gent, Belgium  
tel. : +32 9 264 3316, fax. : +32 9 264 3593  
email : ronny.bockstaele@intec.rug.ac.be

## Abstract

Planar Resonant Cavity LEDs (RCLEDs) are suitable light sources for parallel interchip interconnect links, due to their high efficiency, zero-threshold, low voltage, high reliability and high speed characteristics. The through-substrate emitting RCLEDs, optimised for Polymer Optical Fibre (POF) coupling, consist of an InGaAs quantum sandwiched between a metal mirror and a distributed Bragg reflector. The RCLEDs are arranged in 8x8 arrays with 250  $\mu\text{m}$  pitch. The arrays have been mounted onto glass carriers, and the coupling efficiency into POF, the far-field pattern and the modulation characteristics are measured. The overall quantum efficiency of the devices with 50  $\mu\text{m}$  diameter was found to be 13.4%, the QE into POF was 3.7%. The large-signal transient behaviour of the devices has been investigated. Using a high-speed pulse source, nanosecond rise and fall times have been measured. Wide open eye diagrams at 1 Gbit/s were obtained using voltage pulse drivers. These data were compared to theoretical results based on a non-linear rate equations model.

## 1. Introduction

Due to the increasing component density, chip size and clock frequencies, the electrical interconnections in and between chips may present a bottleneck in the next years [1]. Parallel optical interconnect with direct access to any location within a CMOS chip, has been proposed as a solution to the problems inherent to the electrical interconnect. The light sources in these applications must meet specific requirements, as high efficiency, low beam divergence, low thermal dissipation, electrical compatibility with standard CMOS-circuitry (e.g. drive voltage < 3.3 V), high yield, possibility of realisation of large arrays and flip-chip mounting compatibility (i.e. through-substrate emitting devices). Resonant Cavity LEDs are suitable light sources for such interconnect systems, due to their high efficiency, vertical light emission, potential for integration into large 2D arrays, low thermal and electrical resistance, high speed and absence of a threshold current (implying efficient light emission down to very low currents). Although 2D arrays of high-performance VCSELs (Vertical Cavity Surface Emitting Lasers) for optical interconnect applications have been reported recently [2-4], we believe that RCLED based interconnect may present a better solution if reliability, price and low power consumption become important. Eye-safety issues demand small optical power. The lack of any threshold allows the emission of light down to very small currents, whereas VCSELs need to be driven above threshold (implying a relative large current, even if only little light power is required). Moreover, VCSELs need a larger voltage drop, because they operate at higher current densities through smaller circuit apertures, implying larger series resistances. On the other hand, VCSELs are inherently faster (due to the fast stimulated emission), emit low-divergent beams (even diffraction limited for single mode VCSELs) and are more efficient at higher current densities.

Standard planar LEDs suffer from a low efficiency due to the total internal reflection at the semiconductor-air interface. However, if the active layer is sandwiched between 2 mirrors, the microcavity effect alters the radiation pattern, resulting in a more directed beam and smaller emission spectra [5-7]. More power is emitted

within the solid angle of escape, resulting in an increased extraction efficiency. This effect has been used to increase the total extraction efficiency, up to record values of 22 % [8] (this overall quantum efficiency is the combination of the microcavity effect and the photon recycling effect). RCLEDs have been used as tunable light sources [9], are integrated with GaAs driver to built smart pixels [10]. The realisation of 8x8 arrays of RCLED have been reported, as a grayscale image display [11]. However, these RCLEDs had an absorbing metal outcoupling mirror, reducing the overall efficiency of the devices. There are several ways to increase the extraction efficiency of LEDs. In single devices, it is possible to extract the light from the sidewalls [12]. However, this approach is not compatible with the integration in arrays. Another technique uses the reabsorption of the light by the active layer, followed by re-emission, with a new chance to escape the device [13]. However, this process slows down the emission dynamics. LEDs with roughened surfaces also show high extraction efficiencies, as the light is reflected at the irregular interface until it intercepts the boundary at a small angle and escapes the cavity [14,15]. However, this technique requires substrate removal and a non-trivial roughening technology.

In this paper, the DC and modulation characteristics of 8x8 arrays of 980 nm RCLEDs, are reported. The devices are part of a system demonstrator, built in the framework of the ESPRIT OIIC project [16]. This demonstrator consists of several optically interconnected FPGA (Field Programmable Gate Arrays), resulting in a 3D stack of interconnected gates with a low latency. The 8x8 RCLED array is mounted onto a CMOS chip, containing the FPGA cells and the analog circuitry to drive the RCLEDs. The emitted light is coupled into a waveguide system, and detected by InGaAs detectors, flip-chip mounted on another CMOS chip. The waveguide system is based on Plastic Optical Fibre arrays (POF). The POF is cheap, flexible, easily connectable and it has very small bending losses [17]. Moreover, it has a large NA (0.5), allowing much light to be captured in the fibre. Its disadvantages are the high losses (about 12 dB/m at 980 nm). Although red emitting (InGaP-based) or green emitting (InGaN-based) LEDs seem to be more suitable for POF links [18], InGaAs based RCLEDs are used, because of their intrinsic high internal quantum efficiency. The fibre losses becomes negligible when short (few ten's cm) interconnect links are used. Moreover, the GaAs substrate is transparent at this wavelength, allowing the monolithic realisation of substrate emitting devices.

## ***II. Design and realization of RCLED optimised for coupling in NA.***

The microcavity effect has been shown to influence the spontaneous emission process such that extraction efficiencies up to 10 times higher than in conventional planar LEDs are obtained [5,8]. The microcavity effect provides a redistribution of emitted light through enhancement or inhibition of spontaneous emission, depending on the position of the emission dipole with respect to the cavity standing wave pattern. This effect is used to influence the overall quantum efficiency (QE), the far field pattern and/or the spectral width of the emitted light. The influence of the design parameters (mirror reflectivity, cavity thickness) onto the extraction efficiency was investigated using a numerical tool. The spontaneous emission in the InGaAs quantum well is presented by horizontally oriented electric dipoles [19]. The emission pattern of the dipoles is calculated by expanding the field of the dipoles into a set of planer waves. This tool takes also the photon recycling into account: a part of the emitted light is captured in a lateral waveguide, defined by the metal mirror, the cavity and the DBR. This light can be reabsorbed by the active layer, and again be emitted. This effect increases the apparent internal QE, as an electron has more change to escape the cavity. However, this effect is negligible at high current densities (as the reabsorption of the active layer decreases [20]), and for small diameter LEDs (as most of the light escapes the cavity laterally before it is reabsorbed). RCLEDs for parallel interconnect applications are typically small (to capture all the external emitted light in the fibre) and driven at relatively high current densities (to increase the modulation speed). The results are summarised in fig 1, where the extraction efficiency into NA=0.5 is plotted as a function of the thickness of the GaAs phase matching layer and the number of DBR pairs.

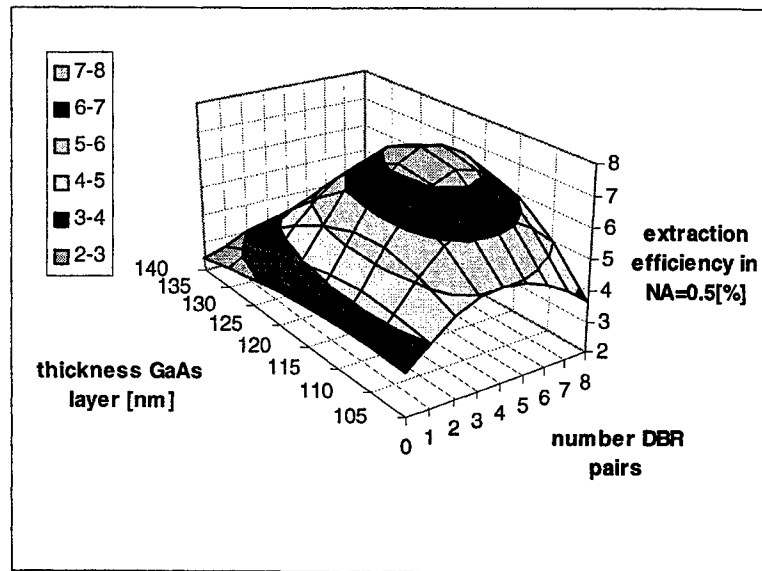


**Figure 1: simulated extraction efficiency as function of the thickness of the phase matching GaAs layer and of the outcoupling mirror reflectivity**

The intrinsic spontaneous emission spectrum is assumed to be Gaussian-like, with a FWHM of 30 nm (corresponding to a current density in the order of 100 A/cm<sup>2</sup>) and peak wavelength at 980 nm. The optimal GaAs layer thickness was found to be 121 nm, the corresponding cavity resonance wavelength is 981 nm. This cavity is slightly overtuned : the design results in an optimised extraction efficiency into NA=0.5, whereas a perfect tuned cavity (resonance wavelength is 980 nm) maximises the overlap in perpendicular direction [21]. The optimal reflection of the DBR (at an intrinsic spontaneous emission spectral width of 30 nm), is 70.8% amplitude reflection (50.2% power reflection), corresponding to a 5 pairs GaAs/AlAs DBR. For the given device structure, the maximal extraction efficiency into NA=0.5 is found to be 7.8%. In that case, the total extraction efficiency is 19.7%.

The designed layer structure is grown in a horizontal MOCVD-reactor at low pressure (76 Torr). N-dopant is Si, p-dopant is Zn. After growing a 200 nm thick buffer layer, a 5 pair Si doped ( $n=5 \cdot 10^{17}$ ) AlAs/GaAs DBR was grown, followed by a 50.6 nm thick Al<sub>40</sub>Ga<sub>60</sub>As spacer, of which 40 nm was n-doped. The active layer consists of 3 In<sub>20</sub>Ga<sub>80</sub>As quantum wells (thickness is 6 nm) and 6 nm Al<sub>20</sub>Ga<sub>80</sub>As barriers. To obtain better interfaces, a 2 nm thick GaAs layer was inserted between the well and the barrier material. The growth temperature of the active layer (650 C) was optimised to maximise the photo current peak [22]. Above the active layer, a 50.6 nm thick Al<sub>40</sub>Ga<sub>60</sub>As upper spacer was grown, of which 20 nm was undoped, and the remaining 30.6 nm Zn doped ( $p=5 \cdot 10^{17}$ ). Finally, a 120 nm thick p-doped GaAs phase matching layer was grown, of which the upper 40 nm was p++ ( $p=2 \cdot 10^{19}$ ) doped.

Several RCLED arrays, compatible with gold bump flip-chip mounting, were realised. A cross-section of the RCLED is schematically represented in fig 2. The processing starts with the (wet) mesa etching. The n-metallisation (Au/Ge/Ni) is deposited in the moat, followed by an alloy step to reduce the ohmic resistance of the contact. Then the Au p-metal, also serving as highly reflecting mirror, is deposited. After that step, no high-temperature steps are allowed, because this degrades the highly reflecting GaAs-Au interface. Afterwards, a first isolation (120 nm Al<sub>2</sub>O<sub>3</sub>) is deposited at room temperature, followed by the interconnect wiring (Ti/Au). Three different mesas and mirror diameters are available: 70 μm mesa (with 50 μm mirror), 52 μm mesa (with 32 μm diameter) and 40 μm mesa (with 20 μm mesa). The mirror diameter is 20 μm smaller than the mesa to reduce the non-radiative surface recombination by reducing the current density at the border of the device. This

also influences the injection efficiency, since a part of the current flows next to the mirror. Fig 2 shows the 70  $\mu\text{m}$  mesa (50  $\mu\text{m}$  mirror) devices.

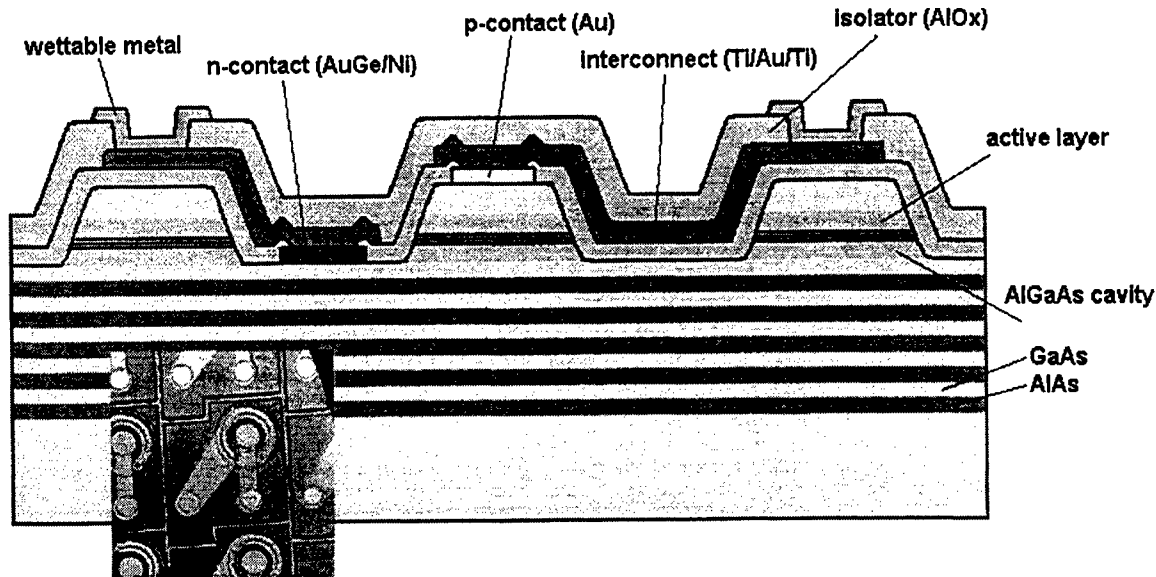


**Figure 2: Sectional view of processed RCLED. (Inset: photograph of RCLED)**

### ***III. Characterisation of the RCLED.***

The (P, I) and (V, I) characteristics for the 3 different mesa diameters are shown in fig 3. The quantum efficiency at 3 mA is 13.4 % for the 70  $\mu\text{m}$  mesa RCLED, 11.8 % for the 52  $\mu\text{m}$  mesa RCLED and 8.6 % for the 40  $\mu\text{m}$  mesa RCLED. The efficiency decreases as function of decreasing RCLED diameter. This is explained by the higher current density, resulting in a broader intrinsic spontaneous emission spectrum (and thus decreased overlap with the cavity enhancement). This effect results in a saturation of the output power at higher current densities, where the thermal effects become important. The internal heating results in a shift of the cavity resonance, and a decreased overlap. The efficiency decreases at very low current densities, due to the current spreading effects in the mesa.

The differential resistance at 3mA is 30 ohm for the 70  $\mu\text{m}$  mesa RCLED, 35 ohm for the 52  $\mu\text{m}$  mesa RCLED and 48 ohm for the 40  $\mu\text{m}$  mesa RCLED. The voltage drop across the devices is small. The emission spectrum of the RCLED has a peak at 984 nm, and its width is 21 nm. The spectral width does not depend on the current level or RCLED diameter, indicating the filter effect of the microcavity on the intrinsic spectrum.

The far field pattern of the 70  $\mu\text{m}$  mesa RCLED is shown in fig 4. The lobe shows a small extra peak at the top, which is explained by the current spreading. A part of the current flows next to the mirror, but still within the mesa. The cavity resonance next to the mirror is at shorter wavelengths, due to the absence of the phase shift of the metal mirror. The resulting light emission is more perpendicular but not as efficient as the metal covered part of the device.

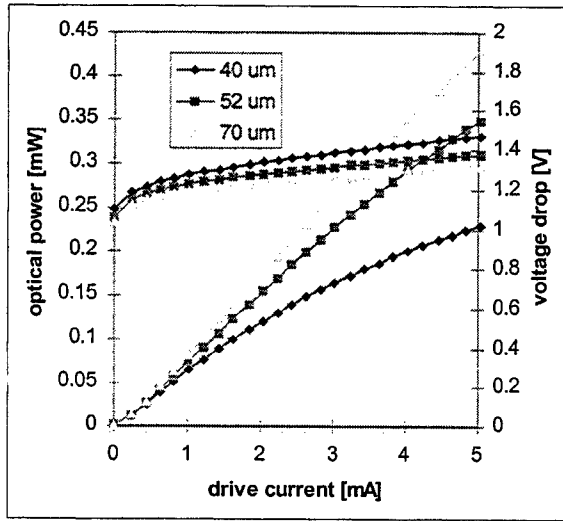


**Figure 3: measured (P, I, V) characteristics of 3 different diameter RCLEDs.**

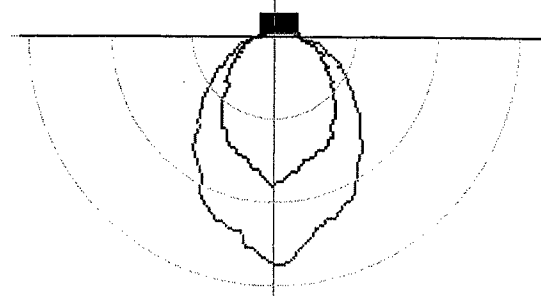


**Figure 4: Far field pattern as function of current.**

The coupling efficiency of RCLEDs to POF was investigated experimentally. First, the absorption of the POF at 980 nm was measured using the cut-back method. The resulting absorption is about 12 dB/m, independent of the diameter of the fibre. To measure the coupling from RCLED to POF, the RCLEDs were flip-chip mounted onto a glass substrate and the POF was aligned to the RCLED using a XYZ-translation stage. Using this set-up, we measured the coupling as a function of POF-diameter and current. A difficulty in the coupling experiments with the POF's is the repeatability of the fibre facet quality. We used a hot knife technique, followed by a very short polishing step, to obtain smooth POF surfaces [23]. The measured overall quantum efficiency at 2 mA drive current into a 125 μm diameter POF is 2.8%. A value of 3.7% was expected from the numerical integration of the measured far-field pattern. The difference can be explained by the reflectivity and scattering at the non-polished fibre facet.

#### **IV. High speed characteristics.**

The dynamics of the MCLED can be described by the following rate equation :

$$\frac{dn}{dt} = \frac{I}{qV} - \frac{n}{\tau_{nr}} - Bn^2 \quad (1)$$

$$P = h\nu \cdot \eta_{extr} \cdot Bn^2 \cdot V$$

$n$  is the carrier concentration in the active layer,  $I$  is the injected current,  $q$  is the elementary charge,  $V$  the volume of the active layer,  $\tau_{nr}$  is the non-radiative lifetime,  $B$  is the bimolecular recombination coefficient (representing the radiative recombination),  $h\nu$  is the photon energy and  $\eta_{ex}$  is the extraction efficiency. The first equation describes the change in carrier concentration, which is given by the difference of the injected carriers and the recombining carriers, which contain the non-radiative recombination (described by  $\tau_{nr}$ , typically 10 to a few 100 ns, depending on the quality of the active layer) and the (important) radiative recombination (described by the bimolecular recombination coefficient).

The microcavity effect influences both the bimolecular recombination coefficient  $B$  and the extraction efficiency. This bimolecular recombination coefficient is proportional to the emission lifetime. The microcavity effect predicts that the spontaneous emission lifetime is inverse proportional to the total emitted power in the active layer, (described by the Purcell factor [24]). Ideal planar microcavities have a maximum decrease of the lifetime of a factor of 3, this corresponds to a  $\lambda/2$  cavity with perfect reflecting mirrors at the resonance

wavelength [25]. However, this factor is close to one for one dimensional cavities with one or two DBR's. This is due to the broad intrinsic emission and the broad cavity bandwidth (due to the rather low reflection of the outcoupling mirror). This makes that the bimolecular recombination coefficient and thus the intrinsic speed characteristics of planar MCLEDs similar to conventional LEDs.

The rise times of a step current driven RCLED can be expressed analytically when an uniform current injection and no non-radiative recombination are assumed :

$$t_{rise} \approx 1.49 \sqrt{\frac{qV}{BI_{on}}} \quad (2)$$

This leads to a rise time of 5.5 ns for a 50 $\mu$ m diameter RCLED driven at 3 mA and 2.2 ns for 20 $\mu$ m RCLEDs driven at the same current level. The transient of the current driven LED is determined by the time to fill the active layer. Smaller active regions or larger drive currents will decrease the rise time of the RCLED.

Step voltage driven diodes show shorter rise times, as the current transient during switching is strongly peaked. The active layer is filled faster, and the rise time decreases. Rise times under 1.5 ns are measured (see figure 6). The fall time is determined by the carrier sweep-out effect : at the off-transient, the RCLED is connected to the ground by a small resistor (quasi a short-circuit) and accumulated carriers are swept out the active regions of the device [5].

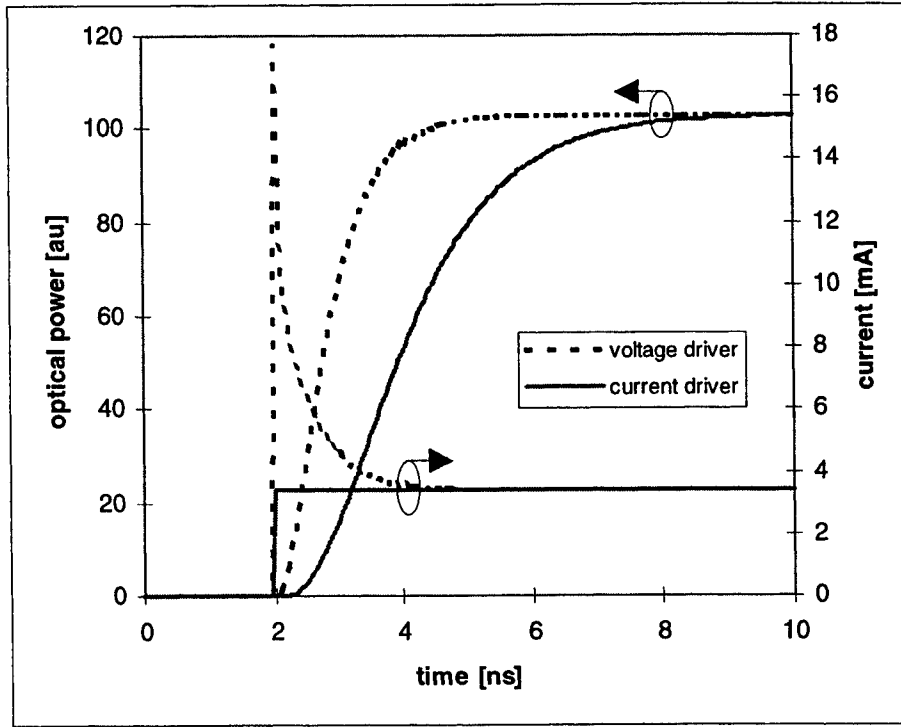


**Figure 5 : Calculated transient of current driven and voltage driven LED.**

A simple model was used to investigate the behaviour of voltage driven RCLED's. The rate equations were extended with a non-linear relation between the carrier density in the active layer and the voltage drop. In case of a quantum well active layer, this relation is given by :

$$V_j = \frac{E_{g,qw}}{q} + \frac{kT}{q} \ln \left[ \left( \exp \left( \frac{n}{N_c} \right) - 1 \right) \left( \exp \left( \frac{n}{N_v} \right) - 1 \right) \right] \quad (3)$$

The injected current into the active layer is given by :

$$I = \frac{V_{source} - V_j}{R_{series}} \quad (4)$$

This current consists of a current to fill up the depletion capacitance and a current to fill up the active layer. The resulting nonlinear differential equation was solved numerically, using MathCad. Fig 7 shows the calculated optical signal of the voltage driven RCLED and current driven RCLED (assuming a constant current, equal to the regime current of the voltage driven RCLED). The RCLED diameter was 30  $\mu\text{m}$ , the driving voltage 2 V, and the series resistance was assumed to be 70 Ohm (this is the 50 Ohm internal impedance of the voltage source and 20 Ohm extra series resistance of the connectors). The filling of the depletion capacitance results in a short delay (<100ps) of the optical signal. After that delay, the carrier density in the active layer increases linearly with time, and the output optical signal increases quadratically, due to the bimolecular recombination involved. The voltage driven RCLED clearly shows a shorter rise time (1.5 ns compared to 3.3 ns), due to the peaked current. This reduction depends on the series resistance of the driver circuit : the smaller this resistance, the larger the initial peak current and the shorter the rise time. However, these current peaks can induce large variations on the voltage supply, and thereby disturb the nearby electronic circuitry.

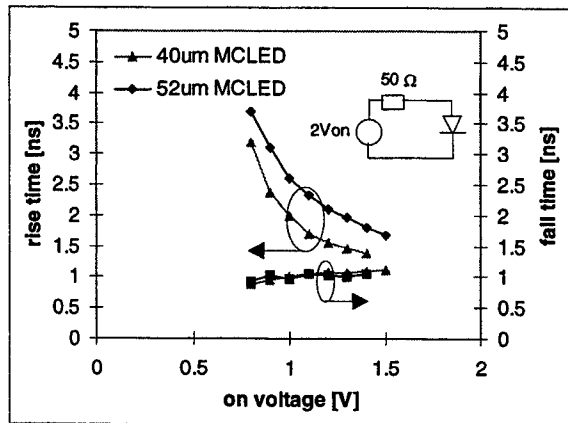


Figure 6 : Measured rise and fall time of 2 different diameter RCLEDs.

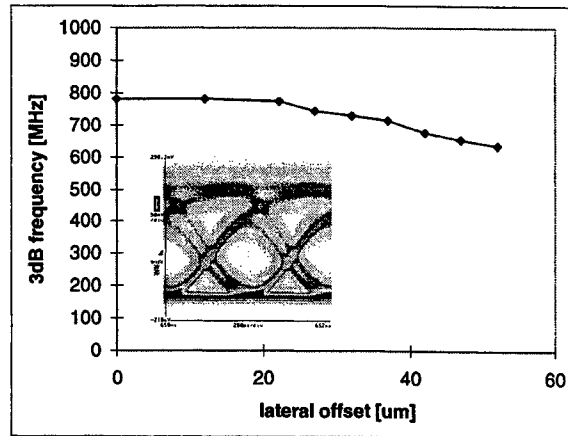


Figure 7 : Measured bandwidth of 50 $\mu\text{m}$  RCLED coupled to 125 $\mu\text{m}$  POF as function of lateral offset. Inset : eyediagram of 50  $\mu\text{m}$  RCLED at 1-Gbit/s.

The transient behaviour of the flip-chip mounted RCLEDs was evaluated using a high-speed voltage pulse generator (HP 8133A). The light was detected using a high-speed Hamamatsu APD-receiver combination (C5658). The detector was placed as close as possible to the RCLEDs. However, there was a rather large electrical crosstalk, due to interference with the probe needles carrying the high-speed signal. In a second approach, the light was coupled to a POF (diameter 125  $\mu\text{m}$ ) and guided to the detector. Fig 6 shows the measured rise and fall times as function of the on-voltage for 2 different RCLED diameters. The on-voltage is defined in a 50 Ohm environment, as shown in the equivalent circuit on the inset. Fig 7 shows the measured bandwidth (defined as the maximal square wave frequency at which the measured peak to peak signal is the half of the DC-signal) as function of the lateral misalignment of a voltage driven RCLED. For perfect alignment, a bandwidth of about 800 MHz. Is obtained, which enables digital transmission of at least 1 Gbit./s, as demonstrated by the eye pattern in fig 7. The decreasing trend as function of the misalignment is explained by the current spreading effect in the mesa. The current density outside the metal mirror is smaller, resulting in larger rise and fall times. For increasing misalignments, the POF captures relatively more light emitted next to the metal mirror (but still within the mesa), implying larger rise and fall times.



## V. Conclusion

We have realised an 8x8 RCLED array flipchip mounted onto a glass test carrier. The RCLEDs were optimised for coupling to POF, and the calculated maximal extraction efficiency into the numerical aperture of a standard POF (NA=0.5) was found to be 7.6 %. In this design, a modestly reflecting outcoupling mirror (5 pairs AlAs/GaAs DBR) was used, in order to enhance the whole intrinsic spectrum by the microcavity effect. The cavity resonance wavelength was found to be slightly larger than the peak intrinsic emission wavelength. The RCLED arrays were realised and characterised, and unmounted devices showed overall quantum efficiencies of 14% and voltage drop under 1,5 V at 3mA drive current. The high speed characteristics of the devices were determined experimentally. Very short rise and fall times (<1.5 ns) were measured using a voltage pulse source, enabling digital transmission of up to 1 Gbit/s. However, it was demonstrated by numerical calculations that the devices will be slower if they are driven by a current source..

## Acknowledgement

This work was partially funded by the European Community ESPRIT project "OIIC" as well as by the Belgian DWTC-project "IUAP-13". Ronny Bockstaele, Bart Dhoedt and Carl Sys acknowledge the IWT, Vlaams Instituut voor de bevordering van het Wetenschappelijk-Technologisch onderzoek in de industrie

## References

- [1] D. A. B. Miller and H. M. Ozaktas : Limit to the bit-rate capacity of electrical interconnects from the aspect ratio of the system architecture, *J. Parallel Dist. Computing* Vol. 41-1 (1997) pp. 42-52
- [2] R. King, R. Michalzik, C. Jung, M. Grabherr, F. Eberhard, R. Jsigmager, P. Schnitzer and K. J. Ebeling : Oxide confined 2D VCSEL arrays for high-density inter/intra-chip interconnects, *Proc. SPIE* 3286 Vol. (1998) pp. 64-71
- [3] C.L. Chua, R.L. Thornton, D.W. Treat, and R.M. Donaldson : Independently addressable VCSEL arrays on 3- $\mu$ m Pitch, *IEEE-PTL* Vol. 10 (1998) pp. 917-919
- [4] G. Giaretta, M.Y. Li., G.S. Li, W. Yuen, and C.J. Chang-Hasnain : A novel 4 x 8 single-mode independently addressable oxide-isolated VCSEL array, *IEEE-PTL* Vol. 9 (1997) pp. 1196-1198
- [5] E. F. Schubert, N. E. J. Hunt, R. J. Malik, M. Micovic and D. L. Miller : Temperature and Modulation Characteristics of Resonant-Cavity Light-Emitting Diodes, *J. Lightw. Techn.* Vol. 14-7 (1996) pp. 1721-1728
- [6] D.L. Huffaker, C. C. Lin, J. Shin and D. G. Deppe : Resonant Cavity light-emitting Diode with an AlOx/GaAs reflector, *Appl. Phys. Lett.* Vol. 66-23 (1995) pp. 3096-3098
- [7] R. Bockstaele, C. Sys, J. Blondelle, H. De Neve, B. Dhoedt, I. Moerman, P. Van Daele and R. Baets : Microcavity LEDs with an Overall Efficiency of 4 % into a numerical aperture of 0.5, *LEOS Summer Topicals* Vol. (1997) pp. 69-70
- [8] H. De Neve, J. Blondelle, P. Van Daele, P. Demeester, R. Baets and G. Borghs : Recycling of Guided Mode Light Emission in Planar Microcavity Light Emitting Diodes, *Appl. Phys. Lett.* Vol. 70-7 (1997) pp. 799-801
- [9] M. C. Larson and J. S. Harris : Broadly-Tunable Resonant-Cavity Light-Emitting Diode, *IEEE-PTL* Vol. 36106 (1995) pp. 1267-1269
- [10] C. Wheeler, S. Daryanani, D. L. Mathine, G.. N. Maracas and D. R. Allee : Monolithic Integration of a GaAs MESFET with a Resonant Cavity LED using a Buried Oxide Layer, *IEEE-PTL* Vol. 35835 (1997) pp. 194-196
- [11] S. T. Wilkinson, J. Tabler, N. M. Jokerst, M. Brooke and R. P. Leavitt : An 8x8 Array of Resonant Cavity Enhanced Light Emitting Diodes Integrated Onto Silicon Grayscale (32 Level) Driver Circuitry, *LEOS Annual Meeting* Vol. Vol 1 (1996) pp. 277
- [12] F. Kish, D. Vanderwater, D. Defever, D. Steigerwald, G. Hofler, K. Park and F. Steranka : Highly reliable and efficient semiconductor wafer-bonded AlGaInP/GaP light-emitting diodes, *Electr. Lett.* Vol. 32-2 (1996) pp. 132-133

- [13] I. Schitzer, E. Yablonovitch, C. Caneau and T. J. Gmitter : Ultrahigh spontaneous emission quantum efficiency, 99.7% internally and 72% externally, from AlGaAs/GaAs/AlGaAs double heterostructures, Appl. Phys. Lett. Vol. 62-2 (1993) pp. 131-133
- [14] I. Schitzer, E. Yablonovitch, C. Caneau, T. J. Gmitter and A. Scherer : 30 % external quantum efficiency from surface textured, thin-film light-emitting diodes, Appl. Phys. Lett. Vol. 63-16 (1993) pp. 2174-2176
- [15] R. Windisch, P. Heremans, B. Dutta, M. Kuijk, S. Schoberth, P. Kiesel, G. H. Dohler and G. Borghs : High-efficiency non-resonant cavity light-emitting diodes, Electr. Lett. Vol. 34-11 (1998) pp. 1153-1154
- [16] B. Dhoedt : Optically Interconnected Integrated Circuits to solve the CMOS Interconnect Bottleneck, ECTC Vol. (1998) pp.
- [17] Y. Koike : POF - From past to the future, POF '98 Vol. Berlin (1998) pp. 1-7
- [18] O. Ziemann, J. Krauser : The Use of Polymer Optical Fibers for In-House-Networks, Advantages of 520 nm LED transmission Systems, ECOC '98 Vol. Madrid (1998) pp.
- [19] M. Yamanishi and I. Suemune : Comment on the polarisation dependent momentum matrix elements in quantum well lasers, Jpn. J. Appl. Phys. Vol. 23 (1984) pp. L35-L36
- [20] T. Baba, R. Watanabe, K. Asano, F. Koyama and K. Iga : Theoretical and Experimental Estimations of Photon Recycling Effect in Light Emitting Devices with a Metal Mirror, Jpn. J. Appl. Phys. Vol. 35 (1996) pp. 97-100
- [21] R. Bockstaele, T. Coosemans, C. Sys, L. Vanwassenhove, A. Van Hove, B. Dhoedt, I. Moerman, P. Van Daele, R. Baets, R. Annen, H. Melchior, J. Hall, P. Heremans, M. Brunfaut and J. Van Campenhout : Realisation and Characterisation of 8x8 Resonant Cavity LED arrays mounted onto CMOS drivers for POF based interchip interconnections., submitted to IEEE JSTQE, 1999.
- [22] Luc Buydens : Growth and characterisation of InAlGaAs/AlGaAs quantum well opto-electronic components, Doctoral Thesis (in Dutch), University of Ghent, INTEC, 1993-1994
- [23] A. Van Hove, T. Coosemans, B. Dhoedt, P. Van Daele, R. Baets : Termination of Small Diameter (125 micrometer) Plastic Optical Fiber for 1 x 12 Datacommunication, ECTC '98 Vol. Seattle (1998) pp. 783-798
- [24] I. Abram, I. Robert and R. Kuszelewicz : Spontaneous Emission Control in Semiconductor Microcavities with Metallic or Bragg Mirrors, IEEE-JQE Vol. 34-1 (1998) pp. 71-76
- [25] S. D. Brorson, H. Yokoyama and E. P. Ippen : Spontaneous Emission Rate Alteration in Optical Waveguide Structures, IEEE-JQE Vol. 26-9 (1990) pp. 1492-1499

# Solid source molecular beam epitaxy growth and characteristics of resonant cavity light-emitting diodes

Mika Saarinen\*, Seppo Orsila, Mika Toivonen, Pekka Savolainen, Tiina Kuuslahti, Ville Vilokkinen, Petri Melanen, Pekko Sipilä, and Markus Pessa

Tampere University of Technology, Department of Physics, P.O. Box 692, FIN-33101 Tampere, Finland

## ABSTRACT

We report on resonant cavity light-emitting diodes (RCLED), operating at 660, 880, and 1300 nm wavelengths. Some of the characteristic features of these devices will be discussed. The devices were grown by all-solid-source molecular beam epitaxy (SSMBE). The results provide clear-cut evidence that SSMBE is a viable method to growth of phosphorous containing semiconductors.

**Keywords:** SSMBE, RCLED, IR, VISIBLE, DBR

## 1. INTRODUCTION

One remarkable consequence of the theory of cavity quantum electrodynamics is that an excited atom can be induced to emit a photon by placing it in a small cavity with boundary conditions on the electromagnetic field. If the space within this cavity is resonant, resulting emission takes place very fast and is highly directional. The same physical principle applies to semiconductor microcavities having spontaneous light-emitting quantum-wells placed strategically in the anti-node positions of the Fabry-Perot mode. Such a device — resonant cavity light-emitting diode (RCLED) — has a high speed, narrow spectrum, circular cross-section of the far field, and high brightness. RCLED's are predicted to have many applications, including transmitters in plastic optical fiber local area networks and very bright light-sources for monochromatic two-dimensional arrays and high-resolution printing. Apart from crystal growth, the RCLED manufacturing process is comparable to that of a conventional LED. They are not yet commercially available.

To date, RCLED layer structures have been primarily grown by metal organic chemical vapor deposition (MOCVD).<sup>1, 2, 3</sup> We present in this paper one of the first attempts to prepare RCLEDs by all-solid-source molecular beam epitaxy (SSMBE),<sup>4, 5</sup> and discuss the performance characteristics of these devices.

SSMBE is a toxic-gas-free method that uses multi-zone solid phosphorus (and arsenic) valved cracking cells.<sup>6, 7</sup> It has become clear through many recent experiments that environmentally friendly SSMBE is capable of growing state-of-the-art phosphorus containing semiconductors over a spectral range of technological importance.

---

\* Correspondence: Email: [misa@ee.tut.fi](mailto:misa@ee.tut.fi), Telephone: +358 3 3652552; Fax: +358 3 357 9155

## 2. DESIGN OF DEVICES

Our design of RCLED's aimed at preparing monolithic top-emitting devices. We modelled them using a LASTIP / PICS3D™ simulation package from CrossLight Software Inc. (Canada) in conjunction with our own programs, which were based on the Transfer Matrix formalism. All the structures designed for 660-nm, 880-nm, and 1300-nm wavelengths contained  $1\text{-}\lambda$  microcavities as resonators. Though each anti-node can only accommodate one quantum-well, we considered a stack of three quantum-wells (compressively strained) which were placed symmetrically at the anti-node in the centre of the cavity. The experiments, too, were carried out with such cavity structures.

Once the cavity was defined, the bottom and top distributed Bragg reflectors (DBR's) were designed. The refractive index step  $\Delta n$  between the adjacent layers and the number of layers were calculated using the Transfer Matrix based programs. To find reasonable values for  $n_i$  of each layer we compared calculated reflectivities with measured ones.

There are several issues that must be taken into account when designing RCLED's. Besides a desired large contrast  $\Delta n$ , one should also consider achieving low photon absorption and small potential barriers between individual layers. Bearing in mind these main requirements we chose pairs of layers that could be grown monolithically and then calculated the reflection coefficients. Fig. 1 shows the reflection coefficient for a 30-pair  $\text{Al}_{0.95}\text{Ga}_{0.05}\text{As} / \text{Al}_x\text{Ga}_{1-x}\text{As}$  DBR as a function of  $\Delta n = n_{\text{high}} - n_{\text{low}}$  at  $\lambda = 660$  nm. One can see that  $\Delta n > 0.33$  should be achieved in order to attain reasonable reflectivity. Fig. 2 shows reflectivity of an 880-nm  $\text{Al}_{0.9}\text{Ga}_{0.1}\text{As} / \text{Al}_{0.2}\text{Ga}_{0.8}\text{As}$  DBR, as the number of pairs were varied. At least 20 periods are needed in this case. Consequently, a relatively thick DBR must be grown to obtain high reflectivity for the bottom part of a RCLED.

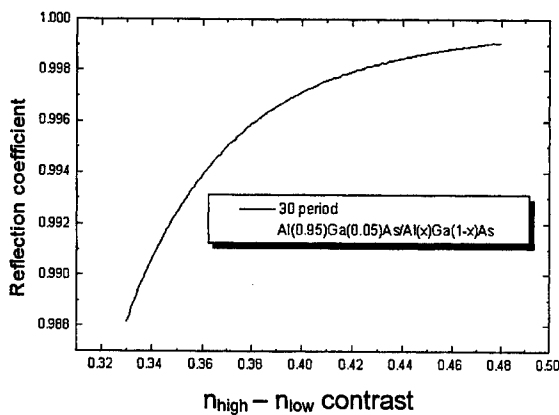


Figure 1. 30-period  $\text{Al}_{0.95}\text{Ga}_{0.05}\text{As} / \text{Al}_x\text{Ga}_{1-x}\text{As}$  DBR mirror reflectivity dependence upon compositionally determined contrast at wavelength 660 nm.

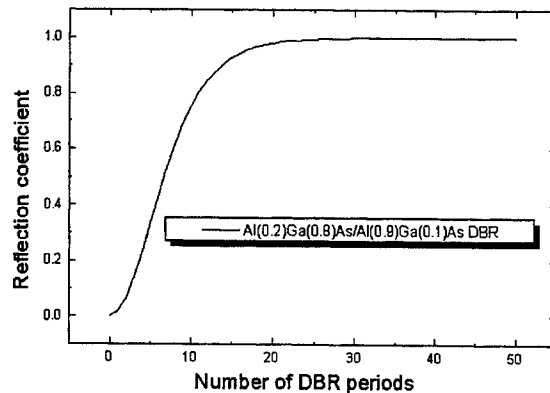


Figure 2.  $\text{Al}_{0.9}\text{Ga}_{0.1}\text{As} / \text{Al}_{0.2}\text{Ga}_{0.8}\text{As}$  DBR mirror reflectivity dependence upon the number of periods at  $\lambda = 880$  nm.

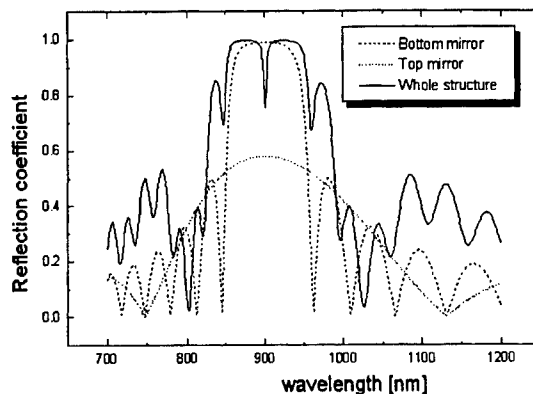


Figure 3. Spectral reflectivity of the top and bottom Bragg mirrors and of complete RCLED at emission wavelength of 880 nm. Detuning of the Bragg mirror and the cavity is about 20 nm. Reflectivities of the top and bottom DBR's are 55 % and 98 %, respectively.

The top mirror of lower reflectivity and the cavity must be detuned appropriately to enhance the extraction efficiency. Large extraction efficiency is contradictory to good directionality of emission. Therefore, in our design, a trade-off between the extraction efficiency and directionality was considered to yield a “rabbit ear -like” far-field pattern. This far-field pattern was achieved by red-shifting the DBR stop-band and the cavity about 15 – 20 nm relative to the photon wavelength.

Fig. 3 gives an example of spectral reflectivity calculated separately for the top (8 pairs) and bottom (32.5 pairs) DBR's of an 880-nm RCLED, detuned by 20 nm. Also shown is the reflection coefficient of a complete 1- $\lambda$  3-QW RCLED structure.

### 3. GROWTH AND PROCESSING

The SSMBE reactor used in this work (VG Semicon V-80H) was equipped with valved cracker cells for arsenic and phosphorous. Aluminium and indium were produced from conventional effusion cells. Gallium was produced from an EPI SUMO<sup>TM</sup> cell.<sup>8</sup> Silicon and beryllium were used as *n*-type and *p*-type dopants, respectively. All the sources exhibited negligible overshooting.

Cracking zone temperatures were 950°C for P<sub>2</sub> and 650°C for As<sub>4</sub>. Contrary to suggestions made by other researchers<sup>9</sup>, we observed no particular advantage of using As<sub>2</sub> over As<sub>4</sub>. The higher cracking zone temperature (920 °C), attempted in some of our experiments to obtain As<sub>2</sub>, introduced unintentional impurities which, according to our observations, counterbalanced advantages possibly gained by easier dissociation of As<sub>2</sub> on the growing front.

Prior to growth of the devices, test samples were prepared. Undoped pairs of  $\lambda/4n$  layers were grown, and spectral reflectance was measured to adjust the stop-band. A few samples were also prepared for photoluminescence (PL) studies.

Figs 4 and 5 illustrate the experiments on the basis of which the beam pressure of phosphorus and the substrate (growth) temperature were attempted to be optimised for the 660-nm RCLED's. Similar experiments were made for the 880-nm and 1300-nm RCLED's to optimise the growth conditions. Fig. 6 shows structures of the 660-nm, 880-nm, and 1300-nm devices prepared. Each device consisted of a 1- $\lambda$  cavity and three quantum-wells.

The 660-nm RCLED had three 50-Å GaInP quantum-wells, separated by 60-Å  $(\text{Al}_{0.3}\text{Ga}_{0.7})_{0.51}\text{In}_{0.49}\text{P}$  barriers. The active region was surrounded by  $\lambda/4n$   $(\text{Al}_{0.7}\text{Ga}_{0.3})_{0.51}\text{In}_{0.49}\text{P}$  spacers. The bottom DBR was made of 32.5 pairs of  $n\text{-AlAs}$  and  $n\text{-Al}_{0.5}\text{Ga}_{0.5}\text{As}$   $\lambda/4n$  layers giving reflectivity of 99 %. In addition, 100-Å  $n\text{-Al}_{0.75}\text{Ga}_{0.25}\text{As}$  was inserted into each interface to reduce potential barriers. The top DBR consisted of 8 pairs of  $p\text{-Al}_{0.9}\text{Ga}_{0.1}\text{As}$  /  $p\text{-Al}_{0.5}\text{Ga}_{0.5}\text{As}$   $\lambda/4n$  layers with reflectivity of 80 %. The doping con-

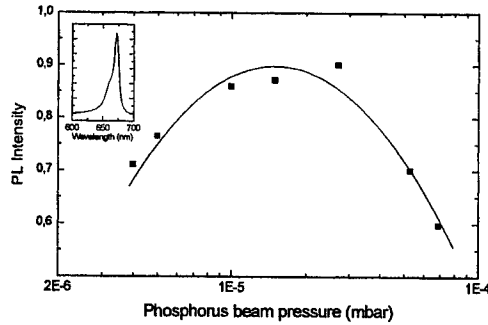


Figure 4. Photoluminescence peak intensity at  $\lambda = 660$  nm as a function of phosphorus beam pressure. This data was used, in part, to optimisation of the growth conditions. The inset shows a PL spectrum at room temperature.

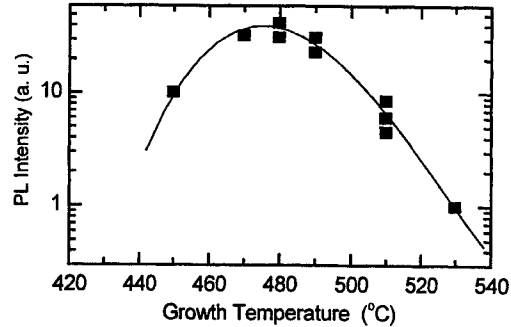


Figure 5. Photoluminescence peak intensity as a function of substrate (growth) temperature. This data was used, in part, to optimise growth temperature.  $\lambda = 660$  nm.

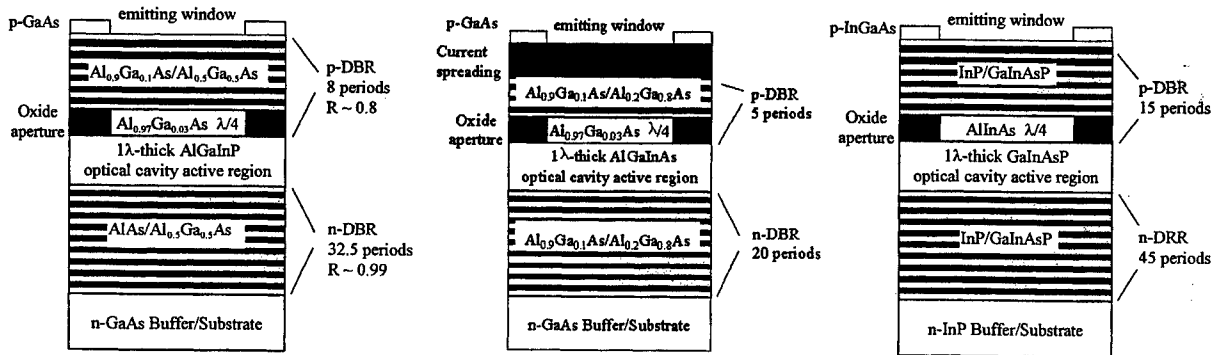


Figure 6. Layer structures of monolithic top-emitting RCLED's at 660 nm (left panel), 880 nm (middle panel), and 1300 nm.

centration of this DBR was linearly graded from  $p = 5 \times 10^{17} \text{ cm}^{-3}$  to  $p = 1 \times 10^{19} \text{ cm}^{-3}$  towards the  $p$ -type contact layer. A  $p\text{-Al}_{0.97}\text{Ga}_{0.03}\text{As}$  layer grown on top of the cavity was used as a lateral current aperture, which was formed by post-growth selective wet thermal oxidation process.<sup>10</sup>

The 880 nm RCLED had three 90-Å  $\text{In}_{0.04}\text{Ga}_{0.96}\text{As}$  quantum-wells separated by 120-Å  $\text{Al}_{0.2}\text{Ga}_{0.8}\text{As}$  barriers. The  $\text{Al}_{0.2}\text{Ga}_{0.8}\text{As}$   $\lambda/4n$  spacers were placed on both sides of the cavity, and a current aperture layer

was grown. On top of the structure a thick current spreading layer was deposited. The DBR's in this case were  $\text{Al}_{0.9}\text{Ga}_{0.1}\text{As}/\text{Al}_{0.2}\text{Ga}_{0.8}\text{As}$  with reflectivities of  $\sim 55\%$  and  $\sim 98\%$

The 1300 nm RCLED consisted of three InAsP ( $80\text{\AA}$ ) quantum-wells sandwiched between 120- $\text{\AA}$  GaInAsP ( $\lambda_{\text{gap}} = 1.1\text{ }\mu\text{m}$ ) barriers. The DBR's had 45 and 15 periods of GaInAsP ( $\lambda_{\text{gap}} = 1.2\text{ }\mu\text{m}$ ) / InP yielding over 95 % and 70 % reflectivities for the bottom and top mirrors, respectively. The bottom DBR was doped at  $n = 2 \times 10^{18}\text{ cm}^{-3}$ . Doping of the top DBR was linearly graded from  $p = 5 \times 10^{17}\text{ cm}^{-3}$  to  $(1.5) \times 10^{19}\text{ cm}^{-3}$  towards the  $p$ -GaInAs contact ( $p > 1 \times 10^{19}\text{ cm}^{-3}$ ). Again,  $\text{Al}_{0.475}\text{In}_{0.525}\text{As}$  was grown for a lateral current confinement.

The 660-nm and 880-nm RCLED's were grown on exactly cut 2-inch (100)  $n$ -GaAs wafers. The 1300-nm RCLED was grown on a 2-inch  $n$ -type InP (100) wafer deliberately misoriented  $2^\circ$  towards (110).<sup>11</sup>

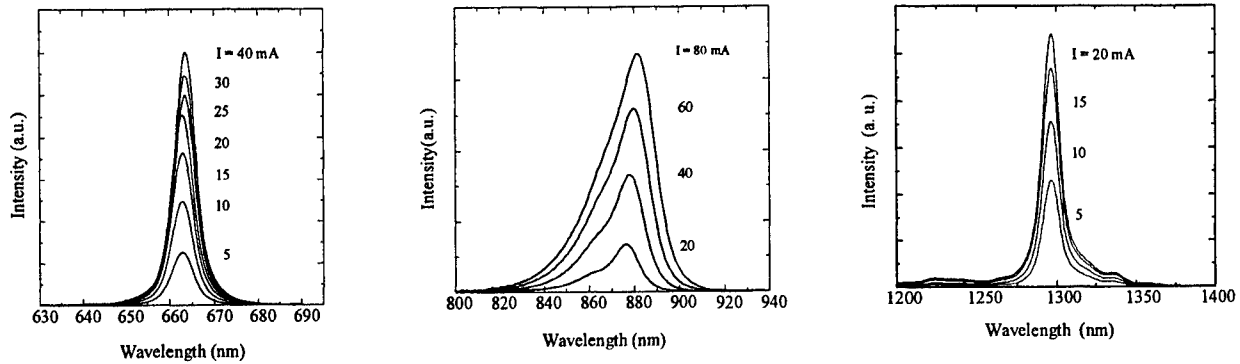


Figure 7. Emission from 660-nm RCLED (left panel), 880-nm RCLED (middle panel), and 1300-nm RCLED at different drive currents.

Upon deposition of  $\text{SiO}_2$ , rapid thermal annealing (RTA) at  $850^\circ\text{C}$  for one second was applied to all devices. This RTA reduced the density of non-radiative recombination centres.<sup>12</sup> The mesas were fabricated by etching through the top DBR and the oxidation layer using  $\text{H}_3\text{PO}_4:\text{H}_2\text{O}_2:\text{H}_2\text{O}$  and  $\text{H}_2\text{SO}_4:\text{H}_2\text{O}_2:\text{H}_2\text{O}$  solutions. Circular 10- $\mu\text{m}$ -wide metal  $p$ -contacts (Ti/Pt/Au) with 5- $\mu\text{m}$ -wide current spreading stripes were made across the windows. The bonding pads were formed on the  $p$ -side of the device array. After polishing the backside,  $n$ -type contact metal (Ni/Au/Ge/Au) was made.

The processed wafers were cut into single devices or small arrays of devices and were bonded on submounts with conducting epoxy. Some of the devices were coated with transparent epoxy, which protected the surfaces and improved extraction of light from the device.

#### 4. RESULTS AND DISCUSSION

Electroluminescent spectra were measured at various drive currents. The spectra recorded at room temperature are displayed in Fig. 7. The first thing to note is that the line widths (FWHM) are narrow, as expected from theory. The line widths are 5 nm, 15 nm, and 18 nm for the 660-nm, 880-nm, and 1300-nm RCLED's, considerably narrower than usual LED's, which exhibit FWHM of typically  $1.8\text{ }kT \approx 45\text{ meV}$  at room temperature. Secondly, the temperature rise, due to an increase in drive current, appeared

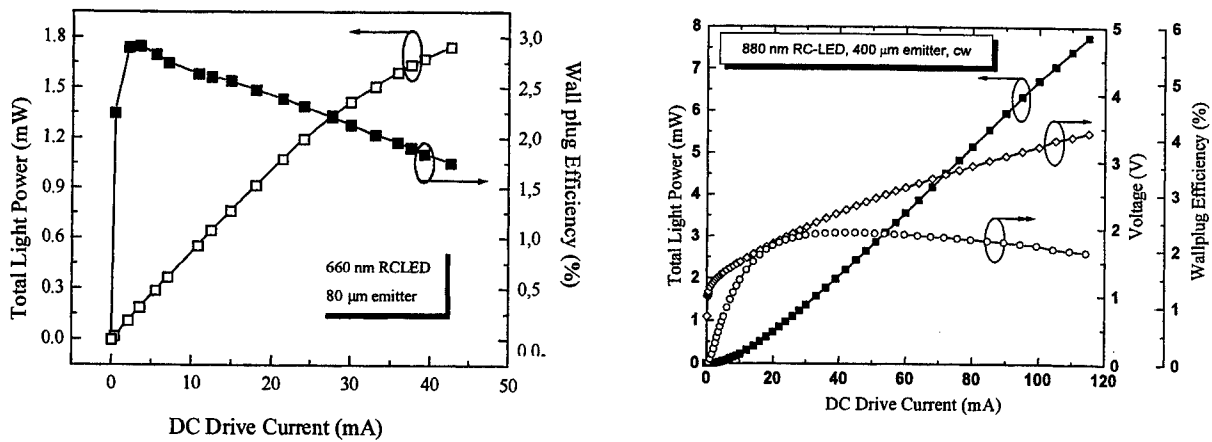


Figure 8. Light current curves for a 660-nm RCLED with an 80-μm window (left panel) and an 880-nm RCLED with a 400-μm window.

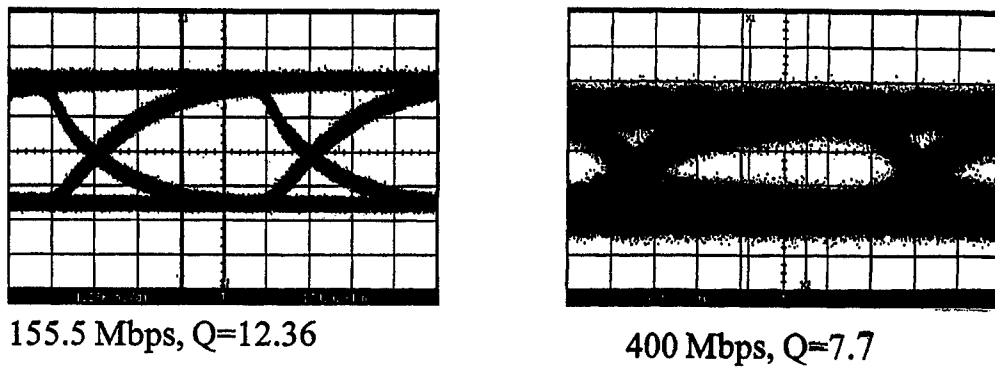


Figure 9. Modulation of 660-nm RCLED at 155.5 and 400 Mbit/s.  $I = \pm 20$  mA, plastic optical fibre = 1 mm / 1 m (measured at Mitel Semiconductor).

to only little affect emission and left the line width almost unchanged. This is because the emission wavelength of a RCLED is primarily determined by the cavity, which is not very sensitive to temperature variations.

The light – current curves of 660-nm and 880-nm devices of 80 μm in diameter are shown in Fig. 8. This RCLED has a turn-on-voltage of 1.7 V and a series resistance of 15 Ω at 30 mA drive current. Previously, we reported  $V = 2.0$  V and  $R = 30$  Ω for a similar device. This improvement in electrical properties of the present *p*-DBR is likely due to the use of the graded doping profile. Since a lower series resistance translates into reduced thermal load, we believe that our new devices exhibit improved lifetime (not yet examined). The 880-nm RCLED's are not optimised, and they exhibit a higher series resistance since no graded doping was used in this case. The light – current characteristics of the 1300-nm devices could not be measured because of a lack of a suitable detector available to us. The maximum output power for the 80-μm 660-nm device was 1.8 mW and for the 400-μm 880-nm device 8 mW. The maxi-



lum wall plug efficiencies was 3 % and 2.3 %, respectively.

Dynamic properties have been investigated in very preliminary experiments for a 660-nm RCLED in a non-optimised package. Fig. 9 shows eye patterns taken at transmission rates of 155.5 Mbit/s at BER <  $10^{-9}$  measured from the exit of a 1-mm / 1-m plastic optical fibre. The eyes remain relatively open at 155.5 Mbit/s.

## 5. CONCLUSION

Monolithic top-emitting RCLED's at  $\lambda = 660$  nm, 880 nm, and 1300 nm have been designed, grown, processed, and characterised. Preliminary results of their optoelectronic features have been discussed. Though not yet fully optimised, they are very promising for a number of low-cost, high-brightness applications where monochromatic light, circular far-field pattern, and high speed are required. This work also indicates that they can be prepared to desired structural perfection by the toxic-gas-free solid-source MBE method.

## ACKNOWLEDGEMENTS

This research was carried out within the framework of EU SMILED Project #24997, EPI-2 Project #56085/97 of the Academy of Finland, and SUPREME-2 Project #40861/97 of the Technology Development Centre (TEKES, Finland). The authors wish to thank their EU SMILED partners for many fruitful discussions.

## REFERENCES

1. J.A. Lott, R.P. Schneider, Jr., J. C. Zolper, and K. J. Malloy: 'AlGaInP visible resonant cavity light-emitting diodes', IEEE Photonics Tech. Lett. Vol. 5, NO. 6, June 1993
2. H. De Neve, J. Blondelle, P. Van Daele, P. Demeester, and R. Baets: 'Recycling of guided mode light emission in planar microcavity light emitting diodes', Appl. Phys. Lett. 70 (7), 17 Feb. 1997
- 3 K. Streubel, U. Helin, V. Oskarsson, E. Bäcklin, and Å. Johansson, 'High brightness visible (660 nm) Resonant-Cavity Light-Emitting Diode', Photon Tech. Lett., Vol. 10, No 12, 1998, pp. 1685-1687
- 4 E.F. Shubert, Y.H. Wang, A.Y. Cho, L.W. Tu, and G.J. Zydzik: "Resonant cavity light-emitting diode", Appl. Phys. Lett. 60, pp. 921-923, 1992
- 5 M. Jalonen, M. Toivonen, J. Kōngäs, A. Salokatve, and M. Pessa, 'Oxide-confined resonant cavity red light-emitting diode grown by solid source molecular beam epitaxy', Electron. Lett., vol. 33, pp. 1989-1990, 1997
6. EPI MBE Products Group: 'Advances in phosphorous valved cracker technology', EPI MBE Products Group Application Note, May., 1997
7. M. Pessa, M. Toivonen, M. Jalonen, P. Savolainen, and A. Salokatve, 'All-solid-source molecular beam epitaxy for growth of III-V compound semiconductors', Thin Solid Films 306, 237, 1997
8. EPI MBE Products Group: 'A revolutionary group III source', EPI MBE Products Group Application Note, Feb., 1996
9. N. Chand, T.D. Harris, S.N.G. Chu, E.A. Fitzgerald, J. Lopata, M. Schnoes, N.K. Dutta, 'Performance of a valved arsenic cracker source for MBE growth', J. Crystal Growth 126, pp. 530-538, 1993
10. K. M. Geib, K. D. Choquette, H.Q. Hou, and B. E. Hammons, "Fabrication issues of oxide-confined VCSEL's," Proc. SPIE, vol. 3003, 1997, pp. 69-74.
11. K. Rakennus, T. Hakkarainen, K. Tappura, H. Asonen, and M. Pessa, "Morphological defects in InP layers grown by gas-source molecular beam epitaxy", Proc. of InP and Related Materials, 4<sup>th</sup> Int. Conf., Rhode Island USA, April 21<sup>st</sup>-24<sup>th</sup>, 1992
12. M. Jalonen, M. Toivonen, P. Savolainen, J. Kōngäs, and M. Pessa, "Effects of rapid thermal annealing on GaInP/AlGaInP lasers grown by all-solid-source-molecular beam epitaxy," Appl. Phys. Lett., vol. 71, pp. 479-481, 1997.

# Efficiency improvement in light-emitting diodes based on geometrically deformed chips

Song Jae Lee and Seok Won Song

Electronics Engineering Department, Chungnam National University  
Yusung-gu Koong-dong 220, Taejon, 305-764, Korea

## ABSTRACT

We propose LEDs based on geometrically deformed chips of which the horizontal cross-section is either rhomboidal or triangular and, in addition, side walls may also be slanted. In such deformed chips, the photon trajectory changes with each reflection off the wall and, as a result, the continued total internal reflections as observed in conventional rectangular cubic chips are suppressed. Monte Carlo photon simulation that has been developed for this study shows that the photon output coupling or extraction efficiency in the proposed design is improved by about 100 to 120 % over that in conventional LEDs. Improved photon emission has also been experimentally observed in LED lamps that have been deformed by filing away a portion of the chip and encapsulant epoxy as well. The rhomboidal or triangular chips, in addition, may be integrated into super-bright LED lamps, in which the chips are arrayed such that the side walls of neighboring chips face each other obliquely, virtually eliminating the optical coupling between neighboring chips. The minimized optical coupling would prevent the efficiency of the integrated lamps from degrading significantly below that in single chip LED lamps.

**Keywords:** Light-emitting diodes (LEDs), super-bright LEDs, external quantum efficiency, photon output coupling efficiency, textured surface, photon trajectory randomization, Monte Carlo photon simulation

## 1. INTRODUCTION

With brightness of light-emitting diodes (LEDs) increasing very rapidly, it is more realistic than ever for LEDs to replace incandescent lamps in many applications such as traffic lights. Over the years researches on LEDs may have been focused on growth of various light-emitting materials.<sup>1</sup> In order to achieve high brightness, however, the development of LED structures with maximized efficiency as well is equally important. In this presentation, we will describe a new LED chip geometry that would significantly improve the photon output coupling or extraction efficiency.

Typical LED structures are based on rectangular cubic chips as shown in Fig. 1. The most serious problem with rectangular cubic chips may be that the photons emitted outside the escape cones are trapped inside the chip, due to continued total internal reflections off the chip wall as illustrated in Fig. 2(a). An escape cone with critical angle  $\theta_c$

$$\theta_c = \sin^{-1}(n_e / n_s) \quad (1)$$

will have a solid angle  $\Omega_c$

$$\Omega_c(n_s, n_e) = \int_{\varphi=0}^{2\pi} \int_{\theta=0}^{\theta_c} \sin \theta d\theta d\varphi = 2\pi \left( 1 - \sqrt{1 - (n_e/n_s)^2} \right) \quad (2)$$

where we assume the chip has an average refractive index  $n_s$  and is encapsulated with epoxy of refractive index  $n_e$ .<sup>2</sup> In

this case, the fraction of trapped photons  $\eta_{trap}$  may be estimated by

$$\eta_{trap} = \frac{4\pi - 6\Omega_c}{4\pi} = 3\sqrt{1 - (n_e/n_s)^2} - 2 \quad (3)$$

which is evaluated to about 70 % in AlGaAs or InGaAlP system with  $n_e \approx 1.5$ ,  $n_s \approx 3.5$ . With such a large fraction of trapped photons to be eventually absorbed inside the chip, the external quantum efficiency should be seriously limited.

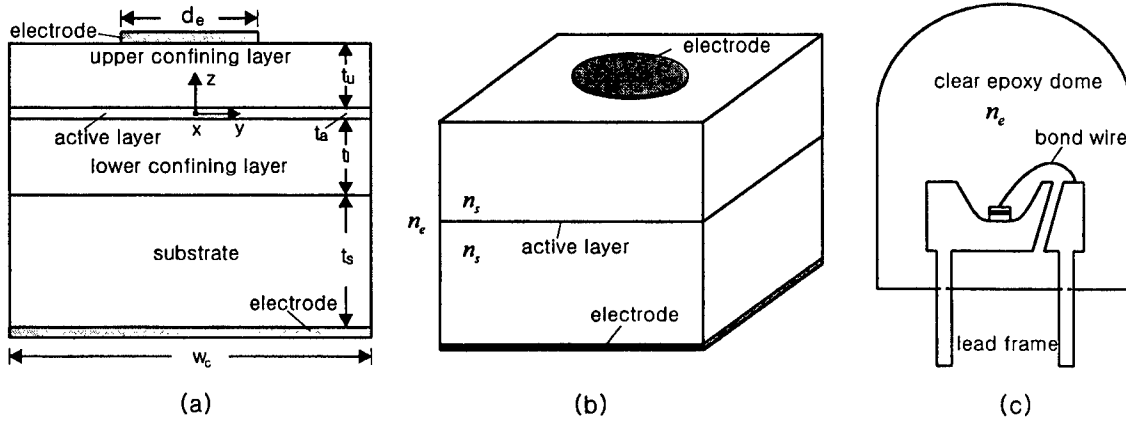


Fig. 1. Typical LED structures and lamps

An approach to extract the photons emitted outside the escape cones has been known to employ textured surfaces as illustrated in Fig. 2(b).<sup>3</sup> Textured surfaces would randomize the photon trajectories and enable some of the photons outside the escape cones to couple out of the chip either directly or in subsequent flights.

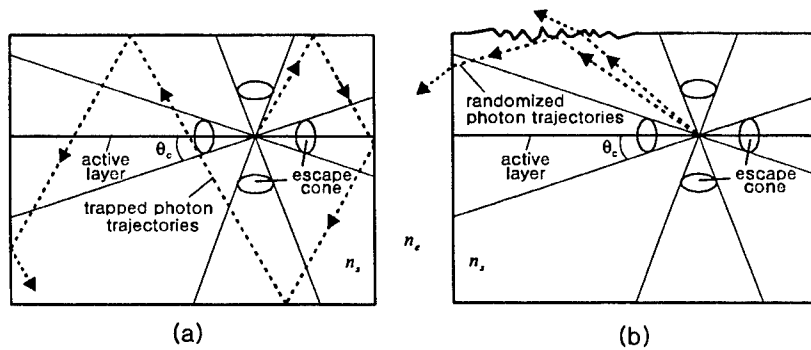


Fig. 2. Photon trajectories inside the chips

## 2. GEOMETRICALLY DEFORMED CHIPS

In this report, we propose LEDs based on geometrically deformed chips of which the horizontal cross-section is either rhomboidal or triangular and, in addition, side walls may also be slanted as shown in Fig. 3.<sup>4</sup> If the horizontal plane of the chip is deformed such that the horizontal plane deformation angle  $\alpha_h$  is chosen to satisfy approximately the condition

$$\alpha_h = 2\theta_c(n_s, n_e) \quad (4)$$

most of the photons travelling parallel to horizontal plane will find escape cones in a couple of flights as illustrated in Fig 3(b) and 3(c). Without deforming the vertical plane, however, significant fraction of the photons travelling parallel to the vertical plane will still be trapped because of the structural symmetry remained in the vertical plane. If the vertical plane is deformed as well by slanting the side walls off by an angle  $\alpha_v$ , most photons generated, regardless of their travelling directions, would find escape cones in a couple of flights, significantly enhancing the photon output coupling efficiency.

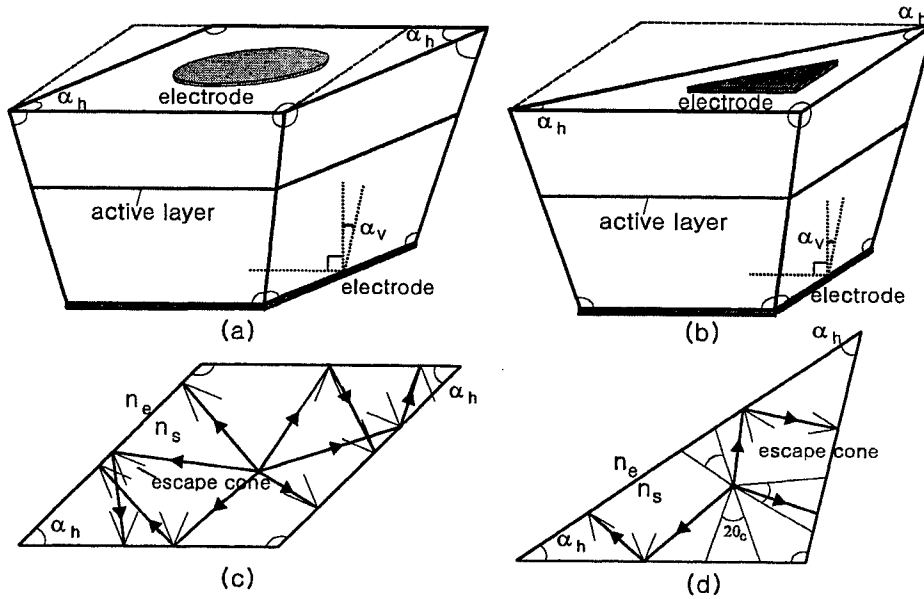


Fig. 3. Geometrically deformed chips and photon trajectories in the horizontal planes

The LED cavity obtained by deforming both the horizontal and vertical plane is non-resonant and therefore the surface-texturing processes required in rectangular cubic chips may not be necessary. In terms of photon trajectory changes, the geometrically deformed chips may have significant advantages over the rectangular cubic chips employing textured surfaces. In surface-textured chips, photon trajectories are randomized and therefore it is equally possible that even the photons incident perpendicularly to the textured surfaces would be randomized to be reflected total-internally off the textured surfaces. In geometrically deformed chips, however, the photon trajectories can rather be controlled by chip deformation angles,  $\alpha_h$  and  $\alpha_v$  and in general the improvement of the photon output coupling efficiency would be more significant.

### 3. MONTE CARLO PHOTON SIMULATION

Conventionally LEDs have been analyzed usually by using the escape cone method.<sup>5</sup> However, the method may involve significant errors in LEDs utilizing non-resonant cavities based on such as textured surfaces or geometrically deformed chips proposed in this study. In non-resonant cavity LEDs, the photon trajectory changes quite randomly and thus the escape cones may not even be defined simply.

Photons generated at a point in the active region will take free flights along random directions until they are interrupted by various flight intervening events. Important among them may be scattering, absorption and reemission in the active layer, absorption inside the other crystal layers, and reflection or transmission at interfaces between mediums of different refractive indices. Basically, in Monte Carlo simulation, the flights of the photons are statistically traced by using random numbers generated to have the same probability as the particular flight intervening events. In this study, we will consider only the effect of internal photon absorption either in semiconductor crystal layers or ohmic electrodes and the effect of photon reflection or transmission at interface.

First we assume a photon generated in active region has photon strength  $P$

$$P = 1 \quad (5).$$

In this notation, the other status  $P = 0$  will imply that the photon has been absorbed. The flight starting position  $r_o$  and velocity  $v_o$  are specified, respectively by

$$r_o = \hat{x}x_o + \hat{y}y_o + \hat{z}z_o \quad (6)$$

$$v_o = \frac{c}{n} (\hat{x} \sin \theta_o \cos \varphi_o + \hat{y} \sin \theta_o \sin \varphi_o + \hat{z} \cos \varphi_o) \quad (7)$$

where  $\hat{x}$ ,  $\hat{y}$ ,  $\hat{z}$  are unit vectors in rectangular coordinates,  $x_o$ ,  $y_o$ , and  $z_o$  are the coordinates of the photon generation position,  $c$  is the speed of light,  $n$  is the refractive index of the layer in which the photon is flying, and  $\theta_o$  and  $\varphi_o$  are the elevation and azimuth angles of the photon direction that should be chosen such that the photons be directed uniformly over all angles when enough number of photons are generated at the same location  $r_o$ .

At the end of a flight, the fate of the photon - either being absorbed or alive - should be determined first. If a number of photons would take a flight of path length  $l_n$  simultaneously, the photon intensity would drop by a factor  $A_n$

$$A_n = \exp(-\alpha_n l_n) \quad (8)$$

where  $\alpha_n$  is the absorption coefficient in the medium in which the flight takes place. In the case of the flight by a single photon as in Monte Carlo simulation, however,  $A_n$  may be interpreted as the probability for the photon to survive in the  $n$ -th flight. Thus, the mutually exclusive events of either being absorbed or alive are predicted by a random number  $\rho_p$  with uniform probability density between 0 and 1 using the conditions

$$P = 1 \text{ when } \rho_p < A_n : \text{photon alive} \quad (9)$$

$$P = 0 \text{ when } \rho_p > A_n : \text{photon absorbed} \quad (10).$$

If the photon survives in the  $n$ -th flight by the random number event in equation (9), the photon will take another flight

with new velocity  $v_{n+1}$  which would be either the Fresnel reflection velocity  $v_{ref}$  or transmission velocity  $v_{tr}$ . The event of either being reflected or transmitted would be predicted by a random number  $\rho_f$  using the conditions

$$v_{n+1} = v_{ref} \text{ when } \rho_f < R_{avg} : \text{photon reflected} \quad (11)$$

$$v_{n+1} = v_{tr} \text{ when } \rho_f > R_{avg} : \text{photon transmitted} \quad (12)$$

where  $R_{avg}$  is the average reflectivity for photons that is assumed to be the mean of the reflectivity for TE photon and that for TM photon.<sup>2</sup>

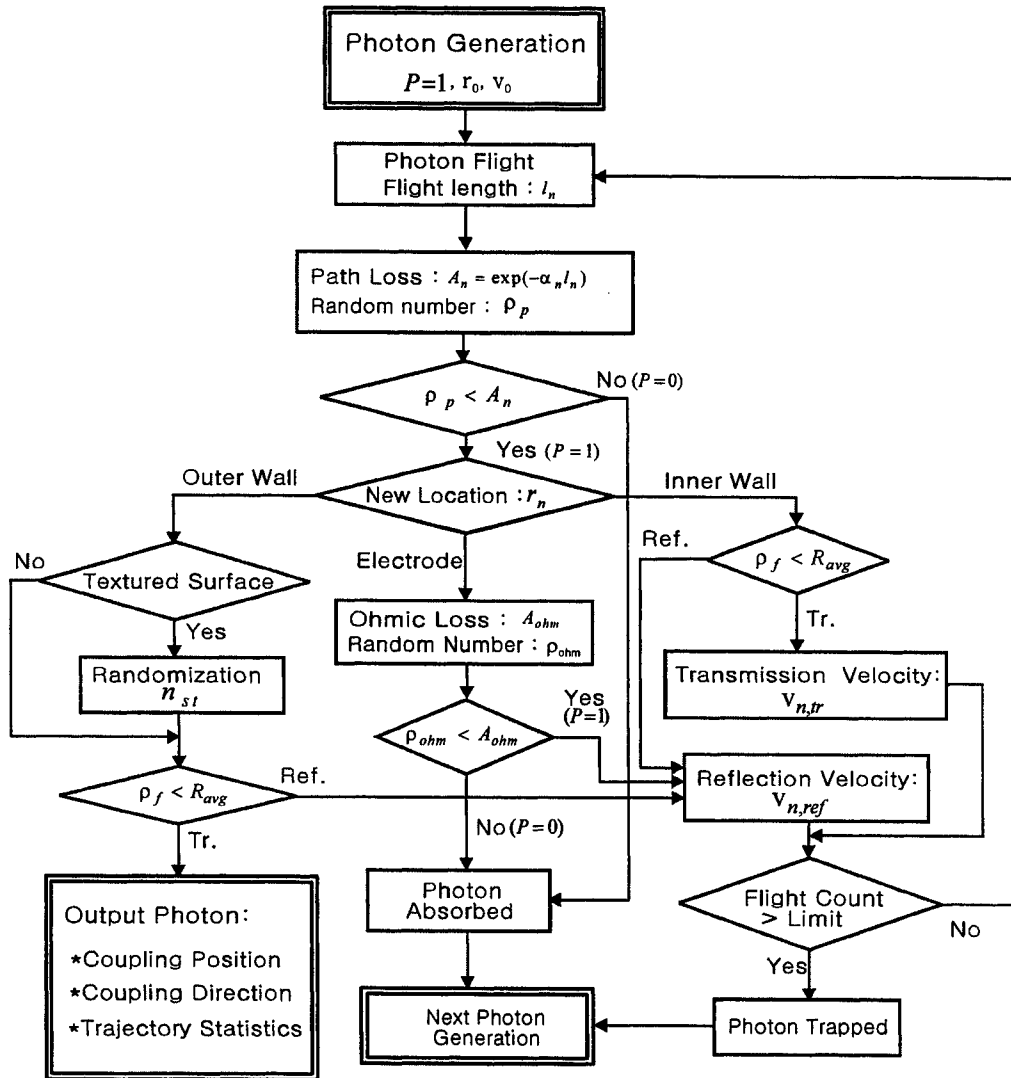


Fig. 4. Flow chart for Monte Carlo simulation for a single photon.

If a flight ends at a point in interface at ohmic electrode, the photon will experience absorption due to the amorphous nature of the ohmic region. The absorption in ohmic region may be a very complicated phenomenon and it may depend strongly on material system. If both the depth of the ohmic region and absorption coefficient is known, the ohmic region may be treated as an extra lossy layer and basically the same procedures in equations (9) and (10) would be used. Since ohmic region is usually very shallow, however, we may use a model of lumped absorption instead the distributed absorption as in semiconductor layers. It is assumed, in the lumped absorption model, that the photon is absorbed at a single point in ohmic region with a net absorption factor  $A_{ohm}$ . Thus, the mutually exclusive events of either being absorbed or alive in ohmic region would be predicted by a random number  $\rho_{ohm}$  using the conditions

$$P = 1 \text{ when } \rho_{ohm} < A_{ohm} : \text{photon survived} \quad (13)$$

$$P = 0 \text{ when } \rho_{ohm} > A_{ohm} : \text{photon absorbed} \quad (14).$$

Fig. 4 shows the flowchart for tracing a single photon generated at a point in the active region. In Monte Carlo simulation, enough number of photons would be generated at the same point such that the photons be directed uniformly over all angles. The photon output coupling efficiency  $\eta_c(x_o, y_o, z_o)$  at location  $r_o = \hat{x}x_o + \hat{y}y_o + \hat{z}z_o$  is then evaluated as the ratio of the photons that couple out of the chip to the total number of photons generated at the point.

#### 4. TEXTURED SURFACE MODELING

In textured surface, the direction normal to local surface area  $dS$  may be randomly distributed about an average direction. Since the incident angle of the photons incident on  $dS$  is decided by the normal direction of  $dS$ , the next flight direction off  $dS$  would be accordingly distributed. In this study, we assume the direction normal to  $dS$  is distributed with some probability density function  $N(\theta_i)$ . Here  $\theta_i$  is the angle by which the normal direction of  $dS$  is off from a reference direction. A reasonable choice for the reference direction may be the direction normal to non-textured flat surface.

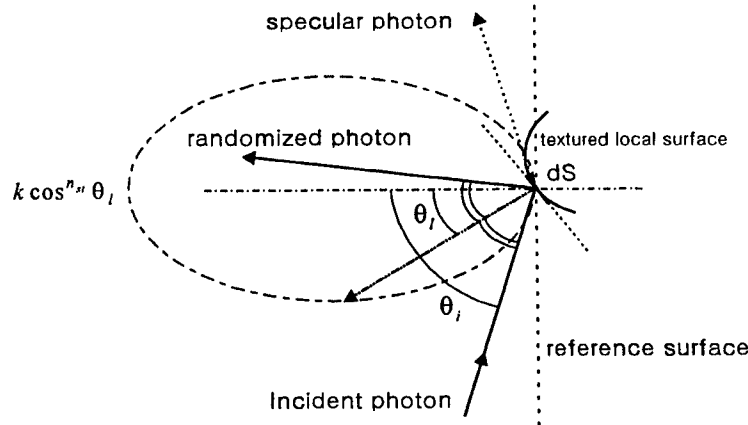


Fig. 5. Modeling of the photon reflection off textured surfaces

Fig. 5 shows a case in which a photon is incident on a local surface area  $dS$  whose normal direction is off by an angle

$\theta_i$  with respect to the reference normal. In reality, there exist two degree of freedoms in the local surface direction angle  $\theta_i$ . Thus, the angle  $\theta_i$  may be divided into two angles,  $\theta_{li}$  and  $\theta_{li}$ , i.e., the angles measured in the incidence plane and the plane perpendicular to the incidence plane, respectively. Here the incidence plane is defined by both the reference normal and photon incidence direction. In this study, we introduce probability density functions  $P_i(\theta_{li})$  and  $P_i(\theta_{li})$  for photons to be incident on  $dS$  specified by  $\theta_{li}$  and  $\theta_{li}$ , which are expressed, respectively by

$$P_i(\theta_{li}) = k_i \cos^{n_{st}} \theta_{li} \cdot \cos(\theta_i - \theta_{li}), \quad \theta_i - \pi/2 < \theta_{li} < \pi/2 \quad (14)$$

$$k_i = 1 / \int_{\theta_{li}-\pi/2}^{\pi/2} \cos^{n_{st}} \theta_{li} \cdot \cos(\theta_i - \theta_{li}) d\theta_{li} \quad (15)$$

$$P_i(\theta_{li}) = k_i \cos^{n_{st}} \theta_{li} \cdot \cos \theta_{li}, \quad -\pi/2 < \theta_{li} < \pi/2 \quad (16)$$

$$k_i = 1 / \int_{-\pi/2}^{\pi/2} \cos^{n_{st}+1} \theta_{li} d\theta_{li} \quad (17)$$

where  $k_i$  and  $k_i$  are normalization constants and  $n_{st}$  is a parameter related with the randomness of the surface topography. The surface would become flatter as  $n_{st}$  increases and, for instance, the case  $n_{st} = \infty$  would correspond to the non-textured flat surface.

In Monte Carlo simulation, the normal direction angles of  $dS$ ,  $\theta_{li}$  and  $\theta_{li}$  are determined by two random numbers,  $\rho_{li}$  and  $\rho_{li}$  such that the conditions

$$\rho_{li} = \int_{\theta_{li}-\pi/2}^{\theta_{li}} P_i(\tau) d\tau \quad (18)$$

$$\rho_{li} = \int_{-\pi/2}^{\theta_{li}} P_i(\tau) d\tau \quad (19)$$

should be satisfied. Once the normal direction of  $dS$  is specified by the angles  $\theta_{li}$  and  $\theta_{li}$ , either the photon reflection velocity  $v_{ref}$  or transmission velocity  $v_{tr}$  off the local surface area  $dS$  would be similarly found as in the regular reflection off flat-surfaced walls.

## 5. SIMULATION RESULTS

For computer simulation, parameters such as the absorption coefficient  $\alpha$  in crystal layers and the net absorption factor in ohmic electrode  $A_{ohm}$  should be specified. In the case of absorption coefficient, we assume  $\alpha = 8 \text{ cm}^{-1}$  for confining layers,  $\alpha = 200 \text{ cm}^{-1}$  for active layer, and  $\alpha = 8000 \text{ cm}^{-1}$  for absorbing substrate. However, absorption coefficients in ohmic region are rarely known and thus, in this study, we presume  $A_{ohm} = 0.5$  for AlGaAs or InGaAlP systems and  $A_{ohm} = 0.1$  for InGaN systems. It is noted that ohmic absorption in a wide bandgap semiconductor such as GaN may be significantly smaller than in AlGaAs or InGaAlP systems.



Fig. 6 shows the variation of the photon output coupling efficiency  $\eta_c(x_o, y_o, z_o)$  as a function of photon generation position, in a typical rectangular cubic structures utilizing a transparent substrate (TS). In general, the photon output coupling efficiency  $\eta_c$  will be smaller in the region under the top ohmic electrode because of the severe photon shielding by the top electrode. In this study, the average photon output coupling efficiency  $\eta_{avg}$  is estimated by averaging the photon output coupling efficiencies at multiple points around the perimeter of the top electrode image projected into the active layer.

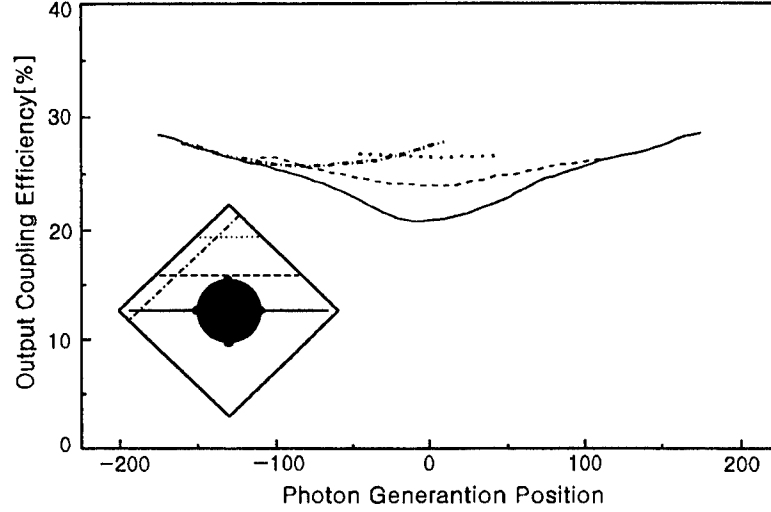


Fig. 6. Photon output coupling efficiency depending on the position in the active layer

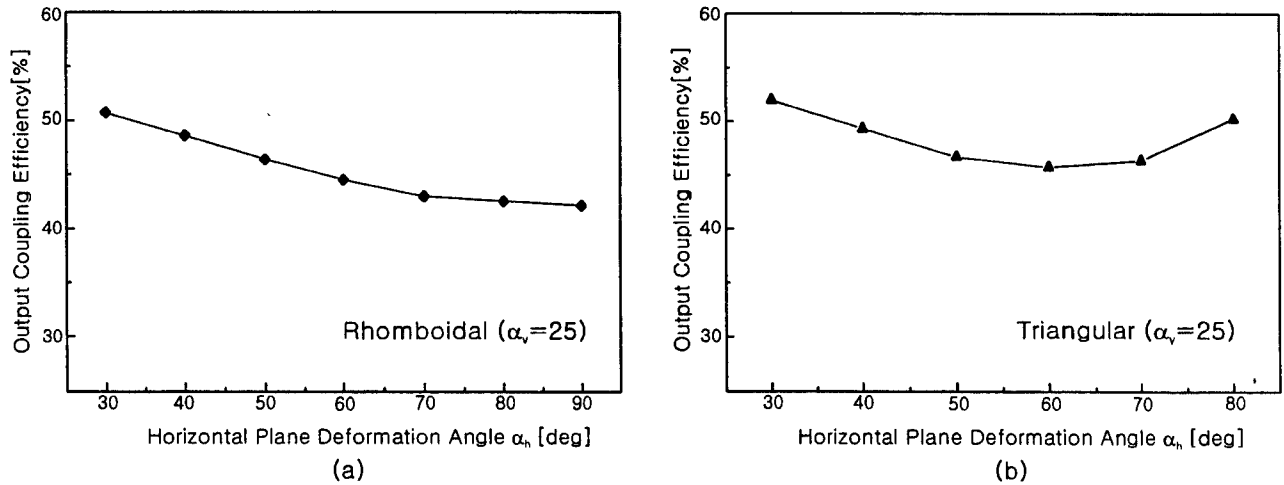


Fig. 7. Photon output coupling efficiency depending on the horizontal deformation angle

The most important design parameters in the geometrically deformed chips would be the horizontal plane deformation angle  $\alpha_h$  and the vertical plane deformation angle  $\alpha_v$ . It is noted that the rhomboidal chip with  $\alpha_h = 90^\circ$  and  $\alpha_v = 0^\circ$

corresponds to the conventional rectangular cubic chips. Fig. 7(a) and 7(b) show the average photon output coupling efficiency as a function of  $\alpha_h$  in the rhomboidal and triangular chips, respectively. In rhomboidal chips, the photon output coupling efficiency increases as  $\alpha_h$  decreases. However, in triangular chips, the output coupling efficiency increases as  $\alpha_h$  is being far off from  $60^\circ$ . It is noted that when  $\alpha_h = 60^\circ$ , there exists some symmetry in horizontal plane. The photon output coupling efficiency also shows a sensitive dependence on the vertical plane deformation angle  $\alpha_v$ , as shown in Fig. 8 (a) and (b). In general, as  $\alpha_v$  increases, the photons reflected off the walls would be directed more toward the upper region and, as a result, the photon interaction with the substrate would be minimized. Thus, as shown in Fig. 9, the improvement by patterned bottom electrode becomes minimal as  $\alpha_v$  increases.

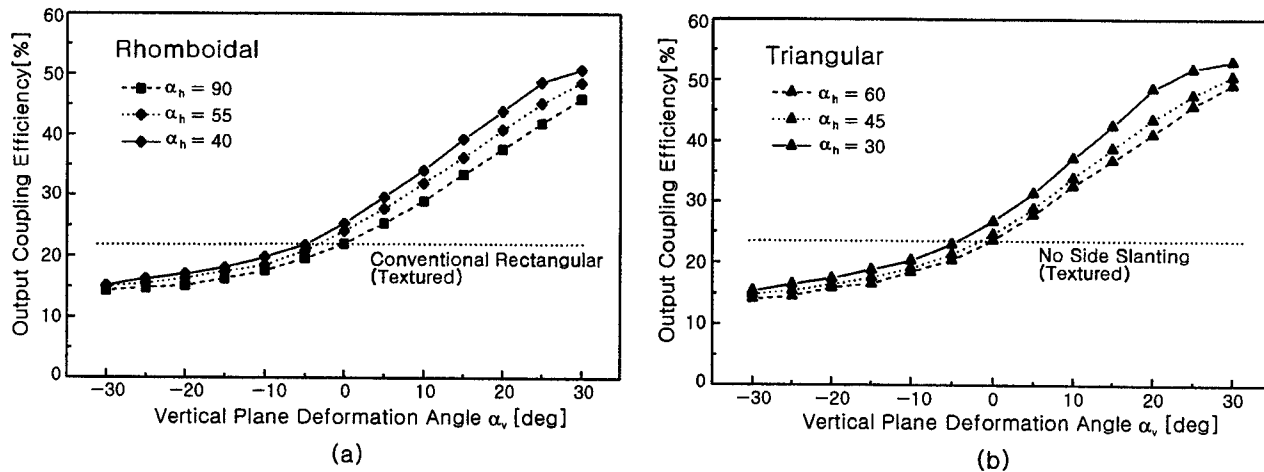


Fig. 8. Photon output coupling efficiency depending on the vertical plane deformation angle

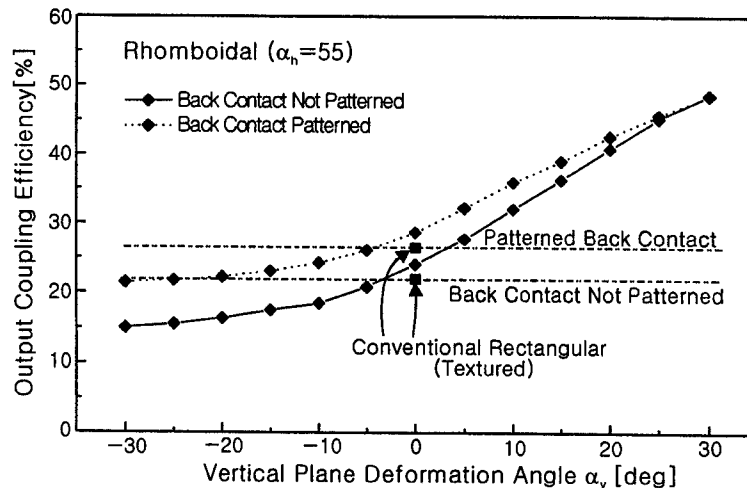


Fig. 9. The effect of patterned bottom ohmic contact on the photon output coupling efficiency

Fig. 10 shows the effect of the surface texturing both in the rectangular cubic chips and the geometrically deformed chips. In rectangular cubic chips, the photon output coupling efficiency increases rather sensitively as the surface texturing index  $n_{st}$  decreases. In geometrically deformed chips, however, the photon output coupling efficiency that is significantly improved over that in rectangular cubic chips is rather insensitive to surface texturing index  $n_{st}$ . The fact clearly indicates that the photon trajectory randomization by the microscopically textured surface is overwhelmed by the photon trajectory change by macroscopically deformed chip cavity. In this sense, the surface texturing process may not be necessary in geometrically deformed chips.

The slanting of all of the side walls in geometrically deformed chips may require a very sophisticated chip-dicing process. However, as shown in Fig. 11, the photon output coupling efficiency is still improved significantly by slanting only one or two side walls, compared to the conventional rectangular cubic chips.

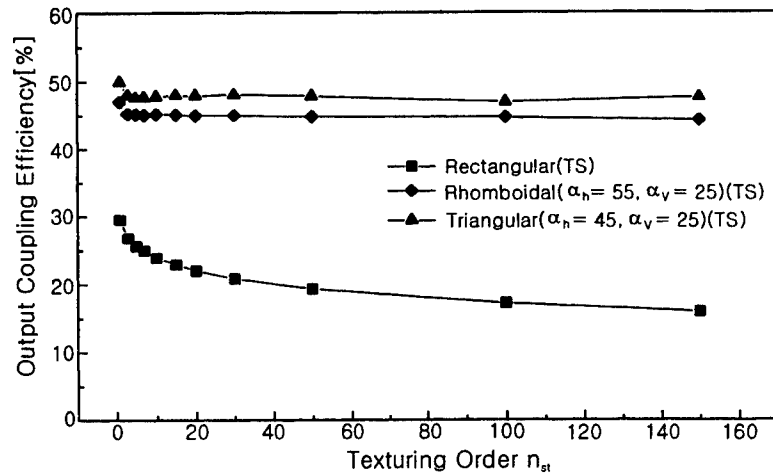


Fig. 10. The effect of surface texturing on the photon output coupling efficiency

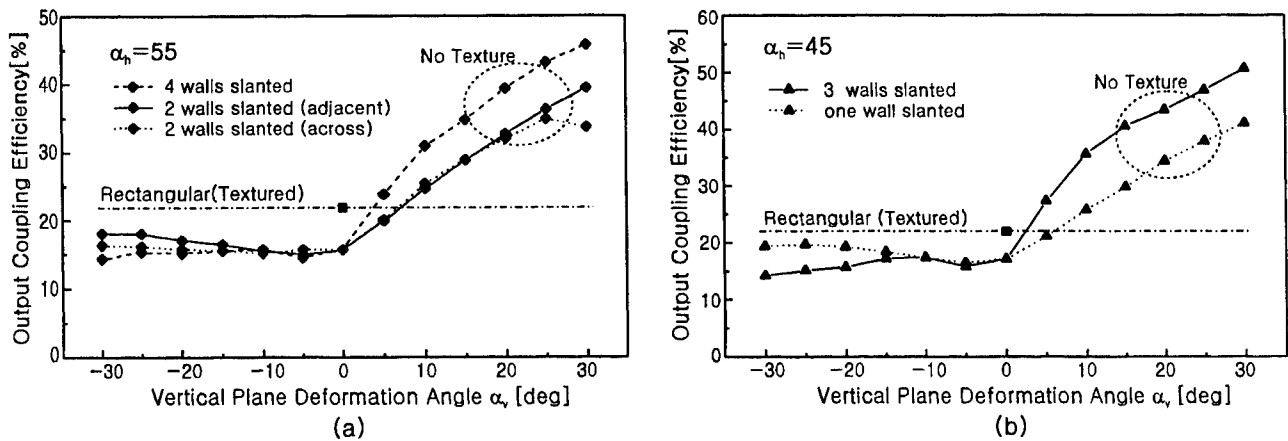


Fig. 11. Photon output coupling efficiency with only a few side walls slanted

## 6. DISCUSSINS AND CONCLUSIONS

In the case of geometrically deformed chips, photon trapping due to continued total internal reflections inside the cavity is virtually eliminated and thus, most of the photons generated in the active region are able to escape to the outside of the chip in a couple of flights. As a consequence, in the case of AlGaAs or InGaAlP systems, the photon output coupling efficiency is improved by about 100 % over that achieved in conventional rectangular cubic chips. One of the critical issues in geometrically deformed chips may be how to obtain the slanted side walls. A possible approach may be to dice chips by utilizing double slanted sawing of wafers as illustrated in Fig 12.

It is speculated that both the rhomboidal and triangular chips also have some potential in integrated chip array lamps. Some of the chip array configurations are shown in Fig. 13. When the chips are arrayed such that the side walls of neighboring chips face each other as shown in Fig. 13(a), the laterally emitted photons would be blocked or absorbed by the nearby chips. As a result, the efficiency of the integrated LED lamp would be degraded seriously below that in single chip LED lamp. However, if either rhomboidal or triangular chips are arrayed such that the neighboring side walls face each other obliquely as illustrated in Fig. 13(c) and 13(d), the optical interference between nearby chips would be virtually eliminated. The minimized optical coupling would prevent the efficiency of the integrated LED lamps from degrading seriously below that in single chip LED lamps. Integrated chip arrays with minimized optical interference may find applications in such as super-bright LED lamps and uniformly illuminated full-color pixels.

## ACKNOWLEDGEMENTS

The authors would like to acknowledge the support of University Basic Research Program sponsored by Korea Ministry of Information and Communication.

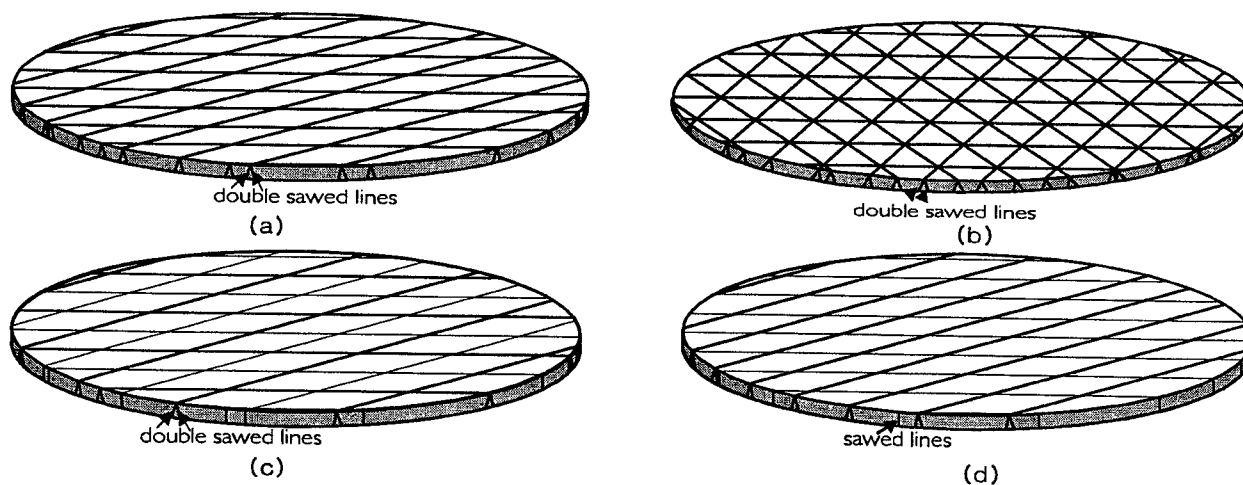


Fig. 12. A possible approach to obtain deformed chips

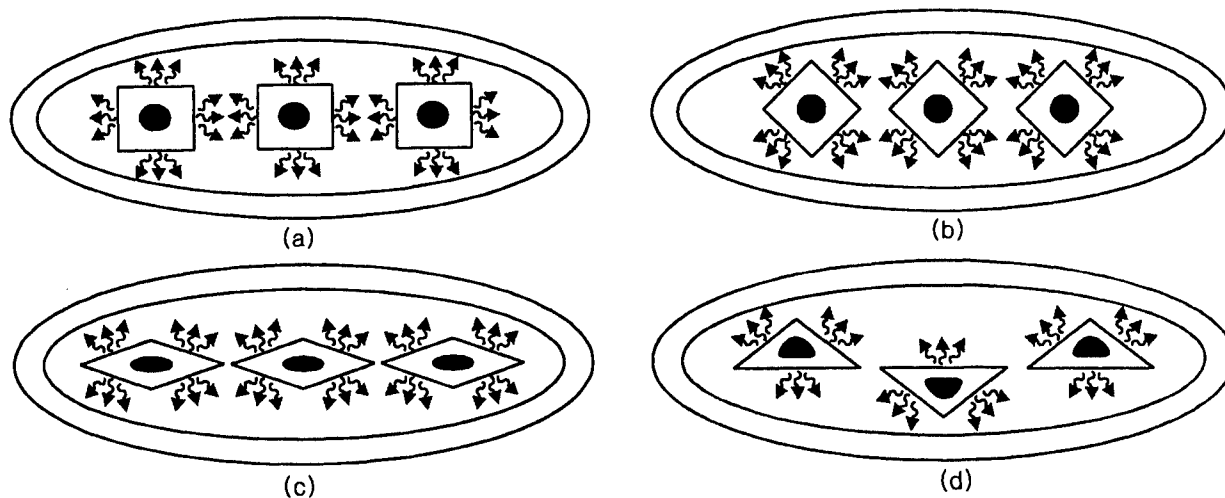


Fig. 13. Chip array configurations in integrated LED lamps

## REFERENCES

1. S. Nakamura and G. Fasol, *The Blue Laser Diode: GaN Base Light Emitters and Lasers*, Springer, Berlin, 1997.
2. S. Lee, "Design rules for high-brightness light-emitting diodes grown on GaAs substrate," *Jpn. J. Appl. Phys.*, **37**, pp. 509-516, 1998.
3. I. Schnizer, E. Yablonovitch, C. Caneau, T. Gmitter, and Scherer "30% external quantum efficiency from surface textured thin-film light-emitting diodes," *Appl. Phys. Lett.*, **63**, pp. 2174-2176, 1993.
4. S. Lee, Patents filed both in America and Japan, 1998.
5. G. Stringfellow and M. Craford, *High Brightness Light Emitting Diodes*, Academic Press, San Diego, 1997.

# Diode light sources for retinal scanning displays

Daniel C. Bertolet, Nima Bertram, John R. Lewis, and Abraham Gross

Microvision, Inc., 2203 Airport Way South, Suite 100, Seattle, WA 98134

## ABSTRACT

We present the results of an ongoing investigation into the use of directly modulated light emitting diodes and laser diodes as light sources for a retinal scanning display. Devices studied include commercially available single-mode 635 nm laser diodes, custom fabricated red edge-emitting LEDs, custom fabricated gallium nitride-based green and blue edge-emitting LEDs, and commercial LEDs. The diodes were characterized in both DC (light vs. current/voltage), and high frequency (~ 1 ns rise/fall pulse) regimes, and measured for luminance using a CCD camera in conjunction with a variable image aperture, variable NA light collection system. Results show that edge-emitting LEDs and laser diodes are each suitable for a particular range of display requirements.

**Keywords:** retinal scanning display, virtual display, laser diode, edge-emitting LED, gallium nitride, AlInGaP

## 1. INTRODUCTION

Virtual Retinal Display™ (VRD™) is a novel retinal scanning display technology being developed and commercialized at Microvision, Inc., in Seattle, Washington<sup>1,2</sup>. Retinal scanning displays generate images by raster scanning a beam of light directly to the retina, thereby eliminating the need for a traditional display screen. A retinal scanning display can be separated into four basic system components: drive electronics, light sources, scanners, and viewer optics, as depicted in Figure 1.

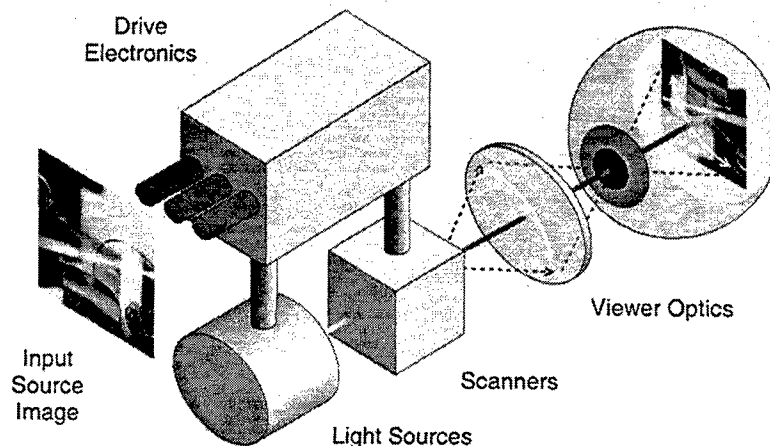


Figure 1: Virtual Retinal Display system components.

The basic display characteristics of luminance, dynamic range, uniformity, number of gray levels, and image quality are all inherently limited by the light source. Because of their compact size, low cost, and efficiency, diodes are attractive candidates for retinal scanning displays. In addition, retinal scanning displays directly illuminate the retina and therefore require a relatively small amount of optical power. Depending on the specifics of the display, light power delivered to the eye can be as low as a few hundred nW. However, because VRD optical systems are typically designed to be diffraction-limited, the light source must have relatively high luminance ( $\text{cd/m}^2$ ). In short, we desire a light source that emits from a small area over a narrow range of angles.

For a diffraction limited VRD system with specified display luminance, the system variables that determine the required luminance of the light source are resolution, exit pupil area, and overall system transmission efficiency. For example, a VRD system with luminance of  $100 \text{ cd/m}^2$  (similar to an average CRT monitor), VGA resolution ( $640 \times 480$  pixels),  $20 \times 15^\circ$  field of view, 5 mm diameter exit pupil, and optical throughput efficiency of 25% would require a light source with luminance of  $1.4 \times 10^9 \text{ cd/m}^2$ . For reference, typical commercial visible LEDs in standard lensed packages can produce a maximum of about  $1 \times 10^6 \text{ cd/m}^2$ , while a 5 mW 635 nm single-mode laser diode generates about  $2 \times 10^{12} \text{ cd/m}^2$ .

Another desirable characteristic of diode light sources is that their output can be directly modulated with drive current. Once the relationship between drive current and light output is characterized, any given schedule of display luminance, or "gray level," can be generated. The required response time for modulating the light source is determined by the display resolution (number of pixels) and the video frame rate. The minimum pixel time for a 60 Hz, non-interlaced, sinusoidally scanned, VGA resolution display is about 20 ns, which would require a minimum light source modulation rate of 25 MHz.

High efficiency LEDs and laser diodes in the red region of the spectrum are established commercial commodities. High efficiency blue and green LEDs based on gallium nitride materials have become commercially available in the past few years. Reported operation of gallium nitride laser diodes has been limited to the wavelength range of about 400 to 430 nm, which is in the violet range of visible spectrum where human eye sensitivity is very low. The world leader in the field, Nichia Chemical, Ltd. (Tokushima, Japan), plans to commercially introduce a  $\sim 400 \text{ nm}$  laser diode targeted for the optical storage market in early 1999. Unfortunately, for an RGB display, the blue wavelength needs to be in the range of 450 to 470 nm. It is projected that will be at least 1 to 3 years before blue laser diodes becomes commercially available, and even longer for green laser diodes. Thus at Microvision we have been investigating custom edge-emitting LEDs, which are capable of generating higher luminance than standard LEDs<sup>3</sup>.

## 2. EXPERIMENT

Commercial LEDs studied include 645, 595, 525, and 470 nm devices from various vendors. We have found that LED luminance has a local maximum on the chip face perpendicular to the junction plane, in the few microns of material centered around the active layer. For LEDs packaged in the typical plastic lens, we machined away the plastic encapsulant to expose the edge of the chip for luminance measurement. Laser diodes tested were 5 mW 635 nm single-mode laser diodes from Sanyo. Custom AlInGaP 650 nm edge-emitting LEDs were fabricated by an external vendor, with stripe widths from 3 to 6  $\mu\text{m}$ , using both proton implanted and dual channel ridge waveguide structures. Custom gallium-nitride based  $\sim 470$  and  $\sim 520 \text{ nm}$  quantum well edge-emitting LEDs were fabricated by an external vendor. Stripe contact widths are 3, 4, or 5  $\mu\text{m}$ , and device length is 500  $\mu\text{m}$ .

Light output and voltage versus drive current data were collected using an ILX laser diode driver and temperature controlled diode mount, and a Newport radiometer, all controlled with a Lab View (National Instruments) equipped PC. High frequency data were generated using a pulser from Avtech Ltd. (Ottawa, Canada), in conjunction with a avalanche photodiode/amplifier module from Hamamatsu with a 1 GHz bandwidth, and analyzed on a 1 GHz bandwidth digital oscilloscope. Luminance was measured using a 40X microscope objective to project an image of the emitter onto a CCD camera, which provided emitter size information. A radiometer was put in place of the CCD to measure power. If desired, the source size could be controlled by placing a variable aperture in front of the CCD. The numerical aperture of the system was varied by inserting an adjustable iris at the back focal plane of the microscope objective.

## 3. RESULTS AND DISCUSSION

### 3.1 Commercial LEDs

As described above, commercial LEDs in the standard lensed lamp package are 3 or more orders of magnitude too low in luminance for a VRD system with reasonable specifications. To further investigate the potential of commercial LEDs, we measured luminance directly from the edge of the LED chips, and also drove the LEDs to higher than rated current. Summarized in Table 1 are the luminance results for all LEDs tested. The highest luminance we have measured to date was for the Nichia green LED driven at 50 mA, which produced  $1 \times 10^8 \text{ cd/m}^2$ . In general, we found that the luminance measured at the edge of the LED is a factor of ten or so higher than the luminance of the packaged lamp. This enhancement is believed to be a result of light guiding in the junction plane, i.e., photons that are generated some finite distance in from the chip edge

can contribute to luminance. In contrast, a given area of the top surface of the LED chip only emits photons generated in the corresponding area of the thin active layer directly below.

The 10 - 90% rise and fall times of commercial visible LEDs under optimum conditions are in the range of 13 to 25 ns, as indicated in Table 1. For typical commercial LEDs, response times are inherently limited by the relatively large contact area and associated junction capacitance. For a VGA resolution VRD with a minimum pixel time of 20 ns, commercial LED response times are marginal at best. For SVGA resolution and above, they would be unacceptable. Overall, the combination of low luminance and slow response time rules out the use of commercial visible LEDs as VRD light sources.

Device	Material	Wavelength (nm)	Luminance (cd/m <sup>2</sup> )	Current (mA)	Response Time (ns)
LED	AlGaAs	645	1.0E+07	100	--
LED	AlInGaP	595	1.7E+06	40	13
LED	InGaN	525	1.0E+08	50	18 - 25
LED	InGaN	470	1.0E+07	100	15 - 25
Laser diode	AlInGaP	635	2.0E+12	50	2 - 7
EELED	AlInGaP	650	2.0E+09	140	1 - 8
EELED	InGaN	503	3.7E+08	150	0.7 - 6
EELED	InGaN	461	1.4E+08	100	--

**Table 1:** Summary of luminance and response times. EELED = edge-emitting LED.

### 3.2. Laser diodes

Single-mode laser diodes emit primarily diffraction-limited light, and thus the bulk of their output can be coupled to a VRD optical system. As mentioned above, the luminance of a single-mode 5 mW, 635 nm laser diode is  $\sim 2 \times 10^{12}$  cd/m<sup>2</sup>, which is sufficient to generate a VRD system with luminance levels approaching the limits of eye safety. We have built a monochrome VGA display with 3000 cd/m<sup>2</sup> luminance using a commercial single-mode 15 mW 635 nm laser diode. The high luminance offered by laser diodes allows the design of display systems with large exit pupils and/or partially reflective surfaces for "see-through" displays, as in the previous example.

#### 3.2.1. Light output control

Given that laser diodes can generate abundant luminance, the question is how to control the luminance. The non-linear relationship between light output and drive current, and its dependence on temperature, is well documented for laser diodes. For operation below lasing threshold, devices behave like LEDs. For typical 635 nm laser diodes, useable power below threshold is limited to a few tens of microwatts, which is enough for some low luminance VRD applications. Above lasing threshold, light output is also generally linear with drive current. If one wishes to operate the laser diode in lasing mode over the entire range of display luminance, then the dynamic range of the display (maximum luminance/minimum luminance) is determined by the maximum laser diode output, divided by the light output just above lasing threshold. For a Sanyo 5 mW, 635 nm single-mode laser diode, we have determined that the maximum dynamic range for operation above lasing threshold is about 50:1.

If both high luminance, and large dynamic range are needed, then the laser diode must be operated in both lasing and LED modes, i.e., it must be modulated across the highly nonlinear lasing threshold knee. In this case, luminance control with drive current becomes more complicated. As a test case, we defined a luminance "schedule" with a 1000:1 dynamic range, made up of 256 (8 bits) gray levels, which are spaced by equal ratiometric steps of 2.7%. This level of display fidelity is higher than most any user would ever desire, and thus is a good measure of the most stringent demands that would ever be placed on a laser diode light source. (Note that the human eye perceives proportional changes in luminance, and a 3% step change in luminance is about the minimum that can be perceived under the most ideal conditions.)

To determine how well a laser diode succeeds at delivering the above-defined luminance schedule, we built a system which measures the laser diode light output versus current characteristic across the entire range of operation at a given fixed temperature, and then calculates the drive currents necessary to produce the luminance associated with each desired gray level. We then use this drive current information to drive the laser diode to given gray levels, and then record the light output



to compare it with the expected result. Shown in Figure 2 is a plot of 20 consecutive data runs taken on a Sanyo 5 mW, 635 nm single-mode laser diode. The straight line on the log scale is the average for all 20 runs, and illustrates that basic characteristic of the desired gray level schedule is achieved. Also plotted is the standard deviation for the 20 runs, which peaks at 3.2%, at gray level 153. This maximum in error occurs in the neighborhood of the lasing threshold knee, which could be expected, since this is the region of highest nonlinearity. Nonetheless, the data shows that the laser diode can be controlled with accuracy about equal to the minimum change that can be perceived by the human eye. Note that because laser diode output is highly temperature sensitive, in a real display system either precise temperature control, or real-time recalibration could be required to achieve the above result.

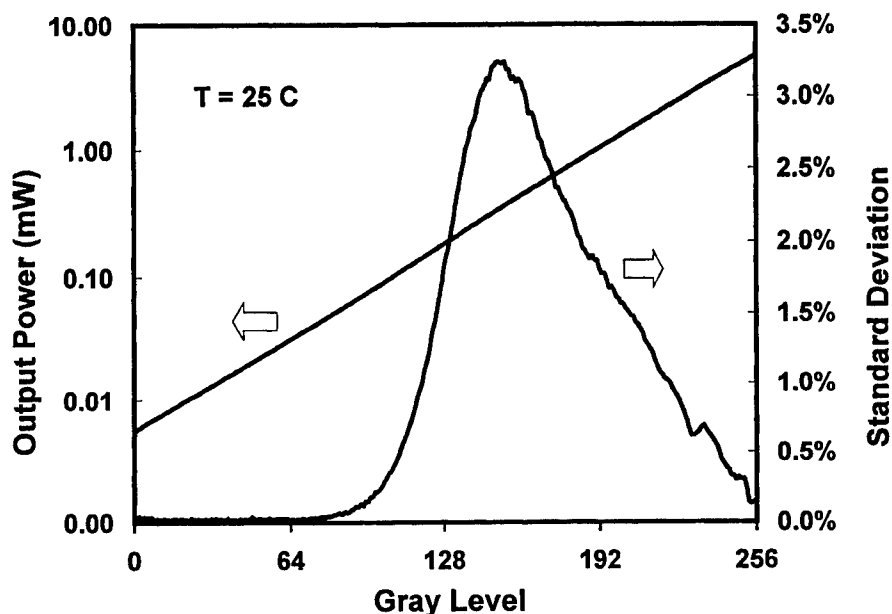


**Figure 2:** Plot of light output versus gray level for Sanyo 5 mW, 635 nm single-mode laser diode. The straight line plotted on log scale is the average of 20 consecutive runs. Standard deviation for the 20 runs reaches a maximum of 3.2% at gray level 153, which is located in the lasing threshold knee.

### 3.2.2. Response time

The stripe-contacts used in single-mode laser diodes have relatively small area, and thus response time in LED mode is typically limited by diffusion capacitance, which in turn is a function of the minority carrier lifetime. When a laser diode is modulated within lasing mode, response times can be extremely fast ( $\sim 10$  GHz or more), which is significantly faster than the requirements for a VRD system. However, when a laser diode is modulated *between* LED mode and lasing mode, an additional turn-on delay is observed, a result of the time required for the carrier density to build up to the threshold value before coherent light is emitted. The magnitude of this turn-on delay is a function of both the initial and final current injection levels. The worst case is when the diode is modulated between a very low initial current, to a current just above threshold, for which the turn-on delay is proportional to the total carrier lifetime.

In the example given in the previous section, the drive current associated with gray level "0" is typically about 10 mA for the Sanyo 5 mW, 635 nm single-mode laser diode. Shown in Figure 3 are oscilloscope plots of the rise and fall times of a Sanyo 5 mW laser diode driven by a 50 mA, 200 ns pulse, with 10 mA DC bias. The horizontal time scale is 1 ns per division. The rise and fall times of the optical output are 0.32 ns and 2.6 ns, respectively, with a turn-on delay of  $\sim 3$  ns. We took similar data over a wide range of conditions, and the results are summarized as follows:

- For modulation within lasing mode, maximum rise, fall, and turn-on delays are all in the range of 2 to 3 ns.
- For modulation both above and below lasing threshold to generate a 1000:1 dynamic range, maximum rise/fall times are in the 6 to 7 ns range, while maximum turn-on delay is 3.5 ns.

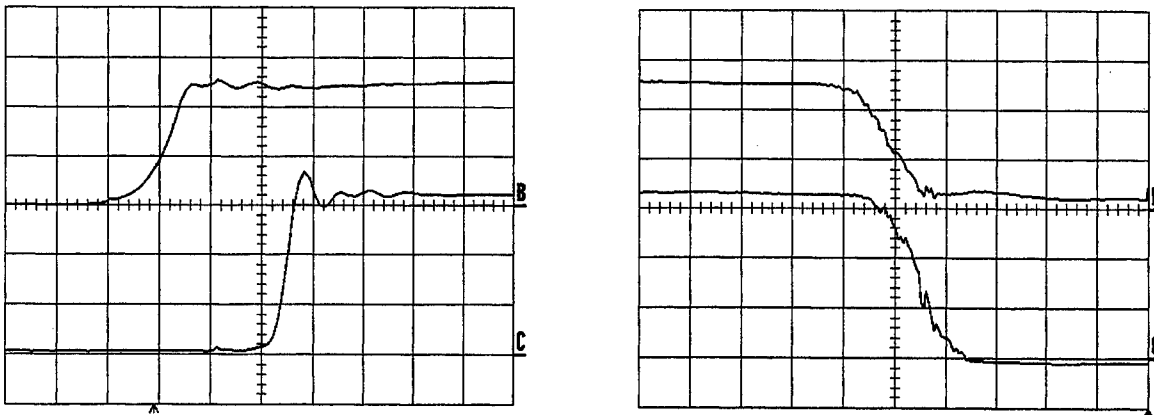


**Figure 3:** Oscilloscope plots of rise and fall times for Sanyo 5 mW single-mode 635 nm laser diode. Upper trace (B) is the drive current pulse, lower trace (C) is the optical output. Horizontal scale is 1 ns per division. Vertical scale for current trace is 20 mA per division.

### 3.3 Edge-emitting LEDs

Because laser diodes in green and blue wavelengths are not currently available, we have been investigating edge-emitting LEDs. In addition, for displays in the lower luminance ranges, it may be preferable to use LEDs instead of laser diodes, since LED output is simpler to control, and LEDs are typically cheaper and more reliable than laser diodes. Edge-emitting LEDs are similar in structure to laser diodes, and can deliver higher luminance than standard bulk, or surface-emitting LEDs<sup>5</sup>.

#### 3.3.1. Red

Total power output for the red edge-emitting LEDs ranged from 0.2 to 0.3 mW with 200 mA drive current. We were able to couple a maximum of 14  $\mu\text{W}$  into single-mode optical fiber, which translates to a luminance of  $2 \times 10^9 \text{ cd/m}^2$ . This is still 3 orders of magnitude lower than the luminance of a laser diode, but is enough to generate a VRD with luminance on par with a CRT monitor, as noted in the introduction section.

Control of LED luminance is generally simpler than the laser diode case, because LED output is nearly linear with drive current, and is relatively temperature independent. However, if a high dynamic range *and* a large number of radiometric gray levels, such as the luminance "schedule" defined in Section 3.2.1, are desired, then luminance control in the lower ranges becomes difficult. Take as an example one of our 650 nm edge-emitting LEDs operated over a drive current range of 100 mA, within which range the output is still fairly linear. To generate a 1000:1 dynamic range, the drive current for gray level "0" would be  $\sim 0.1 \text{ mA}$ . Taking the 2.7% luminance step up to gray level "1" would then require a 2.7% increase in drive current, or  $\sim 3 \mu\text{A}$ . This degree of drive current resolution would likely require specialized drive electronics, such as a D/A converter with a nonlinear transfer function.

Response time of edge-emitting LEDs is proportional to the minority carrier lifetime, which is affected by the current density. Hence, the response time is dependent on operating conditions, and in general, the smaller the drive current the slower the response. The specifics of the LED operating range for a given display is dependent on the display dynamic range and number of gray levels, which must be defined before an LED can be qualified. We have measured response times of our red edge-emitting LEDs under various conditions. In the best case measured -- 100 mA pulse with 5 mA DC bias -- the rise and fall times were 1.2 and 1.6 ns, respectively. In the worst case measured -- 1 mA pulse with 1 mA DC bias -- the rise and fall times were 8 and 6 ns, respectively.

#### 3.3.2. Blue

Shown in Figure 4 is light output and operating voltage versus drive current data for three of the blue edge emitters, one of each stripe width. The maximum total output power measured was 118  $\mu\text{W}$  from a 5  $\mu\text{m}$  stripe device driven at 180 mA. The narrower stripes put out less power, most likely because current density-dependent saturation effects set in earlier with narrower stripes. At elevated currents, the light output has become sublinear with drive current, but it has not yet rolled over.

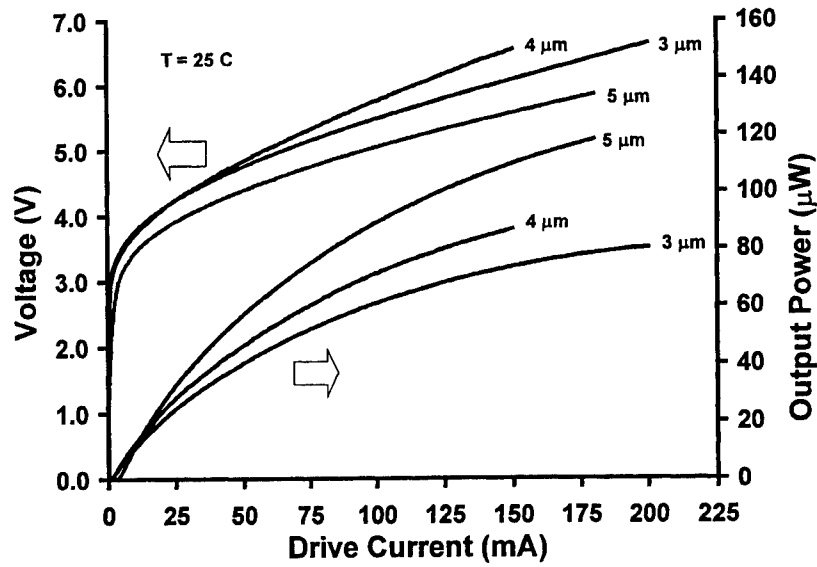


**Figure 4:** Voltage and light output as a function of drive current for blue edge-emitting LEDs with 3, 4, and 5  $\mu\text{m}$  stripe widths.

Turn-on voltages are in the range of 3.5 V, which is respectable for blue nitride LEDs. Series resistance ranges from about 10 to 17 ohms.

The emission exhibits a blue shift with increasing current density, as is typically seen in blue nitride LEDs<sup>4</sup>. The blue shift is caused by localized compositional fluctuations that produce low energy states that become saturated as current density increases. For edge-emitters this effect is more pronounced, since the current densities are up to 500 times higher than in typical commercial devices which have much larger contact area, and are driven at only 20 mA. Shown in Figure 5 are electroluminescence spectra measured at increasing drive currents (3, 25, 125 mA) for a 3  $\mu\text{m}$  stripe blue device. As can be seen, the emission peak blue shifts by a total of 9 nm, and the FWHM increases from 27 to 43 nm. For a given current, this effect is less pronounced in larger stripe widths, since current density is lower.

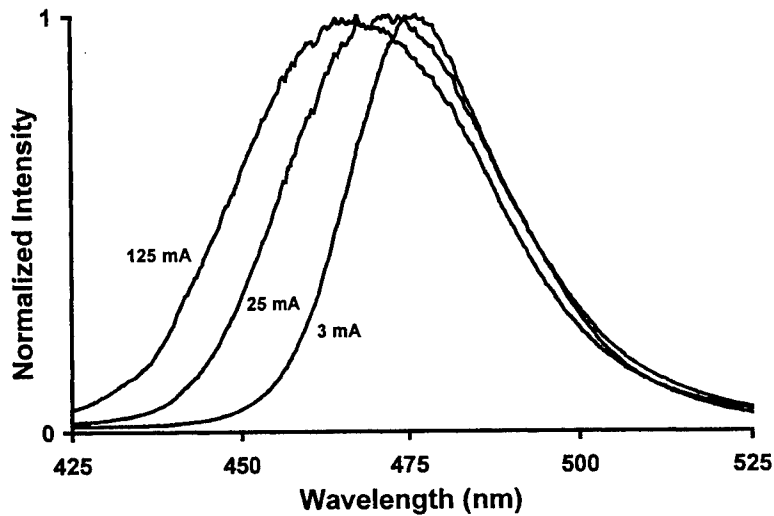


**Figure 5:** Normalized electroluminescence spectra for a 3  $\mu\text{m}$  stripe blue edge-emitting LED, driven at 3, 25, and 125 mA.

The maximum luminance measured from the blue edge-emitting LEDs was  $1.4 \times 10^8$  cd/m<sup>2</sup> for a 3  $\mu$ m stripe device driven at 100 mA, at which the emission wavelength was 461 nm. This luminance value was achieved in a measurement setup with a collection N.A. of 0.14, into which 1.9  $\mu$ W of blue power was coupled. A diffraction limited VRD optical system designed for a light source with the emitter dimensions of these LEDs would have a limiting N.A. of about 0.1, for which we could expect to couple about 1  $\mu$ W of useable optical power. Overall, the luminance of the blue edge-emitters is about an order of magnitude higher than that measured from the edge of the best commercial blue LED.

### 3.3.3. Green

Shown in Figure 6 is light output and voltage versus current data for three of the green edge emitters, one of each stripe width. The maximum total output power measured was 42  $\mu$ W. Overall, the green output power is lower than that of the blue edge-emitters, behavior that is also typical of commercial LEDs, since InGaN quantum well material quality tends to degrade at longer emission wavelengths<sup>4</sup>. Turn-on voltages are around 3.5 V, with series resistance of about 12 ohms. The voltage characteristics of the green edge-emitters are similar to those of the blue, suggesting that the p-type ohmic contacts are playing a dominant role.

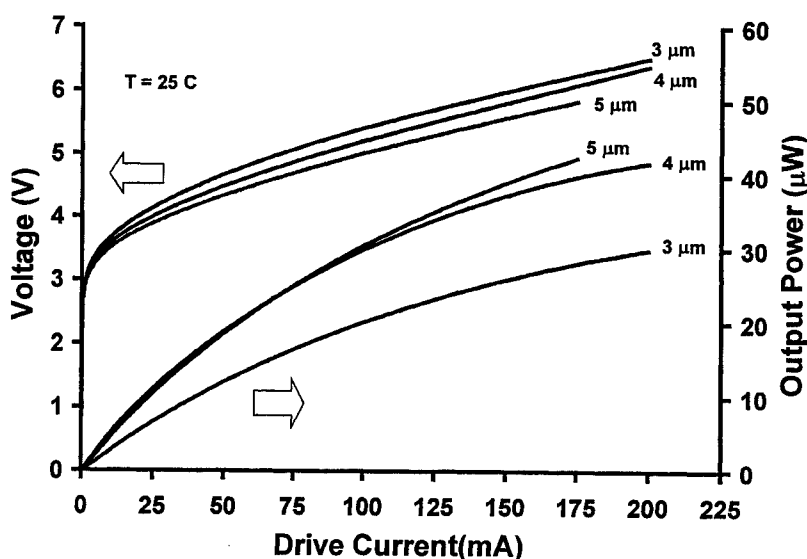


**Figure 6:** Voltage and light output as a function of drive current for green edge-emitting LEDs, with 3, 4, and 5  $\mu$ m stripe widths.

The green emission exhibits a strong blue shift with increasing current density, even more pronounced than that observed for the blue devices. The enhanced blue shift is believed to be a result of the green InGaN material containing deeper localized low energy states<sup>5</sup>. In fact, it has been reported that the emission wavelength of InGaN quantum well material is tuned not by varying the indium fraction, but by controlling growth conditions to alter the nature of the localized composition fluctuations<sup>6</sup>. Shown in Figure 7 are electroluminescence spectra measured at increasing drive current (5, 25, 125 mA) for a 3  $\mu$ m stripe device. The emission peak blue shifts by a total of 28 nm, and the FWHM increases from 36 to 46 nm.

The maximum luminance measured to date from the green devices is  $3.7 \times 10^8$  cd/m<sup>2</sup> for a 3  $\mu$ m stripe device driven at 150 mA, at which point the emission wavelength was 503 nm. In this case, the power coupled to the N.A. = 0.14 experimental setup was 1.0  $\mu$ W, and thus for a VRD optical system with N.A. = 0.1 we could expect to couple about 0.5  $\mu$ W of power. The luminance achieved with the green edge-emitter is about a factor of 4 higher than that obtained at the edge the best commercial green LED. Note that the human eye is about 2 times less sensitive to light at 503 nm compared to 520 nm, which translates to 2 times more power to generate equivalent luminance.

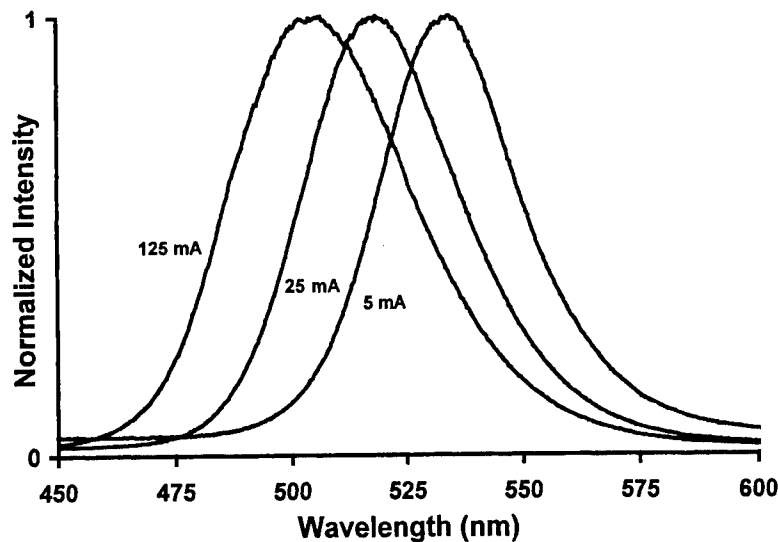


Figure 7: Electroluminescence spectra for a 3  $\mu\text{m}$  stripe green edge-emitting LED, driven at 5, 25, and 125 mA.

The results with red edge-emitting LEDs show that we can expect from about 5 to 10% of the total output power to be emitted in a single mode, which is useable light for a diffraction-limited VRD optical system. In the case of the green and blue edge-emitters, this fraction is only about 1%. We believe that for the red edge-emitters, the waveguiding layers in the structure help couple spontaneous emission into the guided, single mode<sup>7</sup>. In contrast, the green and blue edge-emitters do not contain any guiding layers other than the QW barriers, and thus we expect the guiding effect to be less prevalent. With improved materials and modified epitaxial layer designs, we believe it should be possible to attain luminance from blue and green edge-emitting LEDs that is comparable to what we have achieved with red edge-emitting LEDs. Work is ongoing in this area.

Response times were measured for a 3  $\mu\text{m}$  stripe green edge-emitter. During pulsing, the diode was held at a DC bias of 2.7 V, which produced a current of 0.1 mA, and light output of 28 nW. Thus, to produce a 1000:1 dynamic range, a maximum light output of 28  $\mu\text{W}$  would be required, which falls within the expected output power range, as shown in Figure 5. For a 100 mA, 200 ns pulse, optical output rise and fall times were 0.7 and 1.8 ns, respectively. As expected, response times lengthen as the drive current pulse intensity is decreased. The smallest pulse we tried was 0.5 mA with the same 2.7 V DC bias, which gave rise and fall times of 6 ns.

#### 4. CONCLUSIONS

We have determined that commercially available visible LEDs are not suitable for application in a VRD system with competitive specifications. In general, typical commercial LED chips emit from too large an area, and over too broad a range of angles. Commercially available single-mode red laser diodes provide enough luminance for any VRD application, and a 3000  $\text{cd}/\text{m}^2$  VGA display has been demonstrated at Microvision. We have shown that the luminance of a 5 mW, 635 nm laser diode can be controlled with a degree accuracy enabling a high fidelity display with a 1000:1 dynamic range and 256 radiometric gray levels. For the aforementioned case in which the laser diode is modulated both above and below threshold, the maximum rise/fall times are in the 6 to 7 ns range, while maximum turn-on delay is 3.5 ns. Overall, red laser diodes are good light sources for relatively high fidelity, high luminance displays.

Custom 650 nm edge-emitting LEDs generated a luminance of  $2 \times 10^9 \text{ cd}/\text{m}^2$ , with response times ranging from 1.2 to 8 ns. Custom gallium nitride based edge-emitting LEDs exhibited respectable operating characteristics, and delivered luminance of  $3.7 \times 10^8 \text{ cd}/\text{m}^2$  (green), and  $1.4 \times 10^8 \text{ cd}/\text{m}^2$  (blue). Rise/fall times of a green device ranged from 0.7 to 6 ns. Development is continuing with the nitride edge-emitters, and we believe it will be possible to achieve luminance comparable to red edge-

emitting LEDs. Overall, edge-emitting LEDs in red, green, and blue are excellent light source candidates for full color, medium-fidelity, compact, and economical VRDs.

## REFERENCES

1. Microvision, Inc. web page at <http://www.mvis.com>.
2. J. Kollin and M. Tidwell, "Optical Engineering Challenges of the Virtual Retinal Display," Proc. SPIE, vol. 2537, pp. 48 - 60 (1995).
3. M. Ettenberg, H. Kressel, and J. P. Wittke, "Very High Radiance Edge-Emitting LED," IEEE J. Quantum Electronics, vol. QE-12, pp. 360 - 364.
4. S. Nakamura, G. Fasol, *The Blue Laser Diode - GaN Based Light Emitters and Lasers* (Springer-Verlag, Berlin, 1997) 1<sup>st</sup> ed., Chapter 10.
5. S. Nakamura, Materials Research Society Fall Meeting, Symposium G, Boston, MA, 1998.
6. B Monemar, J.P. Bergman, J. Dalfors, N. Saksulv, P.O. Holtz, H. Amano, and I. Akasaki, Materials Research Society Fall Meeting, Symposium G, Boston, MA, 1998.
7. J. P. Wittke, "Spontaneous Emission Rate Alteration by Dielectric and Other Waveguiding Structures," RCA Rev., vol. 36, p. 655 (1975).

## Addendum

The following papers were announced for publication in this proceedings but have been withdrawn or are unavailable.

- [3621-04]      **MOCVD growth and characterization of AlGaIn/GaN UV emitters**  
J. Han, M. Hagerott Crawford, Sandia National Labs.; A. V. Nurmikko, Brown Univ.
  
- [3621-11]      **InGaIn/GaN LED development on GaN-on-sapphire substrates**  
K. S. Boutros, G. M. Smith, R. P. Vaudo, J. M. Redwing, Epitronics;  
E. F. Schubert, Boston Univ.
  
- [3621-16]      **Temperature-dependent performance of AlGaInP-based light-emitting diodes**  
N. F. Gardner, S. A. Maranowski, C. P. Kocot, H. C. Chui, J. W. Huang,  
M. Hueschen, P. N. Grillo, Hewlett-Packard Co.
  
- [3621-19]      **Photon emission from the GaAs quantum-well nanostructures produced by conventional lithographic and RIE technique**  
M. Manimaran, P. R. Vaya, Indian Institute of Technology/Madras (India)
  
- [3621-32]      **Layer-by-layer self-assembled multilayer films containing the organic pigment, 3, 4, 9, 10-perylenetetracarboxylic acid, and their photo- and electroluminescence properties**  
J. Shen, X. Zhang, J. Sun, S. Zou, Y. Sun, M. Gao, Jilin Univ. (China)
  
- [3621-33]      **Synthesis and characterization of CdS, CdSe, and CdSe/CdS core/shell nanoparticles by microemulsion method**  
E. Hao, B. Yang, Y. Ma, J. Shen, Jilin Univ. (China)

## Author Index

- Allerman, Andrew A., 52  
 Baets, Roel G., 221  
 Bardinal, V., 151  
 Beccard, Rainer, 170  
 Benstem, Torsten, 103  
 Bemius, Mark T., 93  
 Bertolet, Dan C., 249  
 Bertram, Nima, 249  
 Bhat, Rajaram J., 190  
 Bockstaele, Ronny, 221  
 Bogner, Georg, 143  
 Böhler, Achim, 103  
 Bojarczuk, Nestor A., 37  
 Borghs, Gustaaf, 206, 213  
 Boroditsky, Misha, 190  
 Boutros, Karim S., Addendum  
 Brown, Michael G., 28, 43  
 Carlin, Jean Francois, 151  
 Chen, Liang-Yao, 134  
 Chow, Peter P., 73  
 Chui, H. C., Addendum  
 Coccioli, Roberto, 190  
 Collins, D. A., 116  
 Coosemans, Thierry, 221  
 Dai, Ning, 134  
 Debray, Alexandra, 143  
 Deichsel, E., 198  
 Deufel, Markus, 170  
 Dhoedt, Bart, 221  
 Dill, Christian, 160  
 Dirr, Siegfried, 103  
 Döhler, Gottfried H., 206, 213  
 Dutta, Barundeb, 206, 213  
 Ebeling, Karl J., 198  
 Eberhard, Franz, 198  
 Eliashevich, Ivan, 28, 43, 116  
 Ferguson, Ian T., 64  
 Ferreira, M., 116  
 Fitzgerald, Eugene A., 179  
 Fritz, Ian J., 52  
 Gao, Manglai, Addendum  
 Gardner, Nathan F., Addendum  
 Grabherr, Martin, 198  
 Grillot, P. N., Addendum  
 Gross, Abraham A., 249  
 Guha, Supratik, 37  
 Gurary, Alexander, 43  
 Hagerott Crawford, Mary, Addendum  
 Han, Jung, Addendum  
 Hao, Encai, Addendum  
 Hardaway, Harvey, 124  
 Heber, Jörg, 124  
 Heidel, Günther, 143  
 Heremans, Paul L., 206, 213  
 Heuken, Michael, 170  
 Höhn, Klaus, 143  
 Houdré, Romuald, 151  
 Huang, Da-Ming, 134  
 Huang, J. W., Addendum  
 Hueschen, Mark, Addendum  
 Ilegems, Marc, 151, 160  
 Inbasekaran, Michael, 93  
 Jäger, Roland, 198  
 Johannes, Hans-Hermann, 103  
 Jones, Eric D., 52  
 Joos, J., 198  
 Juergensen, Holger, 170  
 Karlícek, Robert F., Jr., 28, 43, 64  
 Kern, R. Scott, 16  
 Kim, Andrew Y., 179  
 King, Roger, 198  
 Knobloch, Alexander, 206, 213  
 Kocot, Christophe P., Addendum  
 Kowalsky, Wolfgang, 103  
 Krauss, Thomas F., 190  
 Kurtz, Steven R., 52  
 Kuuslahti, Tiina, 230  
 Lee, Song Jae, 237  
 Lewis, John R., 249  
 Li, Sherman, 116  
 Li, Yuxin, 28  
 Long, Frederick H., 64  
 Ma, Yuguang, Addendum  
 Manimaran, Muthiah, Addendum  
 Maranowski, Steven A., Addendum  
 Martin, Ulrich, 198  
 Melanen, Petri, 230  
 Metzdorf, Dirk, 103  
 Michalzík, Rainer, 198  
 Miller, M., 198  
 Modine, N. A., 52  
 Möck, Peter, 124  
 Moerman, Ingrid, 221  
 Mukai, T., 2  
 Müller, Ulrich, 143  
 Nakamura, Shuji, 2  
 Nemeth, Stefan, 213  
 Nering, J. E., 116  
 Neuner, H., 103  
 Nurmikko, Arto V., Addendum  
 Oesterle, Ursula, 151, 160  
 Orsila, Seppo L., 230  
 Osinsky, Andrei, 28  
 Pessa, Markus, 230



Phillips, Chris, 124	Zawadzki, Peter A., 116
Pophristic, Milan, 64	Zhang, Rong-Jun, 134
Potemans, J., 206	Zhang, Xi, Addendum
Pullin, Mark J., 124	Zhang, Ying-Jun, 134
Qian, Dong-Liang, 134	Zheng, Yu-Xiang, 134
Redwing, J. M., Addendum	Zhou, Shi-Ming, 134
Royo, P., 151	Zou, Shan, Addendum
Saarinen, Mika J., 230	
Savolainen, Pekka, 230	
Schauler, M., 198	
Schlotter, Peter, 143	
Schmid, Wolfgang, 198	
Schöbel, Jörg, 103	
Schubert, E. Fred, Addendum	
Shen, Jiachong, Addendum	
Shen, Jun, 86	
Sipilä, Pekko, 230	
Smith, Gary M., Addendum	
Song, Seok Won, 237	
Spicher, J., 151	
Stall, Richard A., 43, 116	
Stanley, Ross P., 151, 160	
Stareev, G., 198	
Stradling, Tony, 124	
Sun, Junqi, Addendum	
Sun, Yipeng, Addendum	
Sys, Carl, 221	
Tang, Patrick J. P., 124	
Toivonen, Mika, 230	
Tozer, S. T., 52	
Tran, Chuong A., 28, 43, 64	
van Daele, Peter, 221	
Van Hove, An, 221	
Van Hove, James M., 73	
Vanwassenhove, Luc, 221	
Vatanapradit, S., 116	
Vaudo, Robert P., Addendum	
Vaya, P. R., Addendum	
Vilokkinen, Ville, 230	
Vrijen, Rutger B., 190	
Wang, Song-You, 134	
Wei, X., 52	
Wei, Yan-Feng, 134	
Windisch, Reiner, 206, 213	
Woelk, Egbert, 170	
Woo, Edmund P., 93	
Wowchak, A. M., 73	
Wright, Alan F., 52	
Wu, Weishi W., 93	
Wujkowski, Lisa, 93	
Xu, Bo, 134	
Yablonovitch, Eli, 190	
Yamada, M., 2	
Yan, Chunhui, 73	
Yang, Bai, Addendum	
Yang, Jie, 86	
Yao, H. Walter, 73	
Zavada, John M., 73	